58th KOSOMBE Autumn Conference 2021

IBEC2021

International Biomedical Engineering Conference 2021

"Digital Transformation in Healthcare"

November 10 (Wed) - 12 (Fri)

Virtual



www.kosombe.or.kr
http://conference21.kosombe.or.kr/

Hosted by The Korean Society of Medical & Biological Engineering

Organized by The Korean Society of Medical & Biological Engineering, YONSEI UNIVERSITY

Supported by IFMBE

Sponsored by

Platinum: KOREA TOURISM ORGANIZATION, NIDS 한국의료기기안전정보원, YONSEI 혁신의료기기 실증지원센터, 식품의약품안전처, 연세대학교 의과대학 의료기기산업학과

Gold: KMEDI hub, SNUH UTC 의료기기 사용적합성 테스트센터, wmit, 연세대학교 의과대학 융합의학과 디지털헬스케어전공, LORIENT, SAMJIN 삼진제약, (주)레오엘스케어, VUNO, Medi Line Active Korea, MEK, KBIOHEALTH, BIOPAC Systems Korea, MDIC, 한국수력원자력주식회사

Silver: L&C BIO, MxT Biotech, Ray, MEDIANA, OsteoSys, Hicardi MEZOO, bistos

Welcome Message

President of KOSOMBE



Dongwook Kim, Ph.D.

Dear IFMBE and KOSOMBE members,

Although the continuing pandemic of COVID-19 seems to dominate our thinking and behavior, your academic enthusiasm and growth must be a great driving force to get over this situation.

IFMBE and KOSOMBE will jointly hold the 2021 Autumn Conference as “Joint Conference of the International Biomedical Engineering Conference (IBEC2021) and the International Conference on Biomedical and Health Informatics (ICBHI2021)”

Yonsei University, which forms the organizing committee of this conference and prepares the event, started at "Gwanghyewon," the first modern hospital in Korea. It contributed greatly to the modernization of healthcare services and education and also biomedical engineering in Korea. I am pleased to prepare for this conference with the university that played a pivotal role in the establishment of our society, KOSOMBE.

'Digital Transformation in Healthcare' has been selected as the theme of this conference. Digital technology is leading the innovation in every healthcare technology sector, and we would like to identify what our roles are and how we can contribute to a prosperous future.

I hope that many members will participate in this conference and share our academic alliance and common interest as an academic community.

Sincerely,
Dongwook Kim
President of KOSOMBE

Welcome Message

Organizing Committee



Sung-Uk Kuh, M.D., Ph.D.

Dear KOSOMBE members,

Greetings! I am Sung-Uk Kuh, the Chairman of the Organizing Committee of the International Biomedical Engineering Conference 2021 (IBEC2021) as an 2021 Autumn Conference of KOSOMBE.

We are holding online conferences this year due to the ongoing COVID-19. We sincerely thank our members for their continued interest and participation.

The upcoming autumn conference aims to take a look at the fields that medical engineering needs to move forward, such as biomaterials, biomechanics, brain engineering, and medical devices. This program is designed to share the latest academic achievement with active members in each field.

The world has been suffering from an unprecedented COVID-19 pandemic since last year. Social distancing limits and hinders academic research activities.

In this challenging situation, we would like to express our sincere gratitude to all members of KOSOMBE for their efforts in academic research and fostering junior scholars. We will do our best to build a strong network among researchers by fully utilizing the online platform.

We would also like to thank the organizing committee members and sponsor representatives who helped make the autumn virtual academic conference successful.

Lastly, we appreciate the medical staff who are working hard to overcome the COVID-19 pandemic. Best wishes for the continued growth of the Korean Society of Medical & Biological Engineering.

Sincerely,

Sung-Uk Kuh

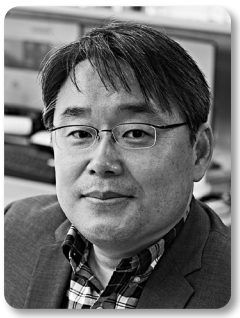
Organizing Committee Chair of IBEC 2021

Welcome Message

Academic Committee



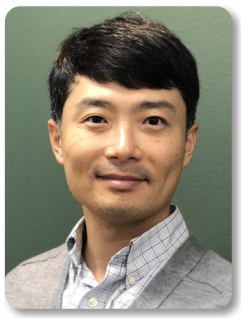
Kwang Gi Kim, Ph.D.



Won Seuk Jang, Ph.D.



Sung-Min Park, Ph.D.



Hongki Yoo, Ph.D.

On behalf of the Academic Committee of the Korean Society of Medical & Biological Engineering & International Biomeidical Engineering Committee 2021 (IBEC 2021), it is our great honor and pleasure to invite you to IBEC 2021 to be held from November 10 (Wed) to 12 (Fri), 2021 in Seoul, Korea.

The world is still going through an unprecedented period, with the prolonged COVID-19 pandemic thrusting everyone into an era of the New Normal. But thanks to the concerted efforts of everyone concerned, we have now entered a “distancing in daily life” phase whereby we may practice disease prevention while picking up on our economic and social activities and resuming our daily lives.

As such, IBEC 2021 will be held as an online congress whereby participants will be able to attend sessions on-line. Interaction is a key element in maintaining a strong bond between the members of our Biomedical Engineering community, and must continue to be fostered. Although we may not be able to see everyone face to face this time, we are preparing a rich program that participants can fully engage in and enjoy.

With the start of our presidency, IBEC proposed a new theme: ‘Digital Transformation in Healthcare’. It seeks to emphasize the importance of taking patient-centered initiatives in the digital age in order to prepare for the future and strengthen our competitiveness.

In line with the above, the Academic Committee is designing the best possible program with high-quality scientific sessions that will provide a great opportunity for all participants to keep up-to-date with the latest research findings. With ICBHI Committee, we will organize a good program.

Organization

Executive Board

	Name	Affiliation
Former President	Jinwook Choi	Seoul National University (S. Korea)
President	Dongwook Kim	Jeonbuk National University (S. Korea)
President-Elect	Dong Keun Jung	Dong-A University (S. Korea)
Vice President	Myoung Nam Kim	Kyungpook National University (S. Korea)
	Jae-Hwa Lee	Korea Medical Device Industry Cooperative Association (S. Korea)
Auditor	Min Joo Choi	Jeju National University (S. Korea)
	In Young Kim	Hanyang University (S. Korea)
Director of General Affairs	Hangsik Shin	Chonnam National University (S. Korea)
	Jongmo Seo	Seoul National University (S. Korea)
Director of Finance	Mun Ho Ryu	Jeonbuk National University (S. Korea)
	Jyung Hyun Lee	Kyungpook National University (S. Korea)
Director of Future and Vision Planning	Tae Geon Kang	Korea University (S. Korea)
	Yoonkey Nam	Korea Advanced Institute of Science and Technology (S. Korea)
Chair of Academic Program Committee	Kwang Gi Kim	Gachon University (S. Korea)
	Hongki Yoo	Korea Advanced Institute of Science and Technology (S. Korea)
	Sung-Min Park	Pohang University of Science and Technology (S. Korea)
	Won Seuk Jang	Yonsei University (S. Korea)
Editor-in-Chief (Journal of Biomedical Engineering Research)	Ki Chang Nam	Dongguk University (S. Korea)
Editor-in-Chief (Biomedical Engineering Letters)	Jae Sung Lee	Seoul National University (S. Korea)
Chair of Education Program Committee	Yonghyeon Yun	Daelim University College (S. Korea)
	Ki-Sik Tae	Konyang University (S. Korea)
	Jong-Ha Lee	Keimyung University (S. Korea)
Chair of Publication Committee	Yoonseok Yang	Jeonbuk National University (S. Korea)
	Chang-Hwan Im	Hanyang University (S. Korea)
	Sang Beom Jun	Ewha Womans University (S. Korea)
	Jin Seung Choi	Konkuk University (S. Korea)

	Name	Affiliation
Director of Information & Communications	Jaehong Key	Yonsei University (S. Korea)
	Seong Wook Choi	Kangwon National University (S. Korea)
Director of Public Relations	Wonsik Ahn	Kyung Hee University (S. Korea)
	Yun Kyung Jung	Inje University (S. Korea)
Director of Industry–Academic Cooperation	Soowon Seo	Daegu–Gyeongbuk Medical Innovation Foundation (S. Korea)
	Young Jun Song	Osong Medical Innovation Foundation (S. Korea)
	Sung Bin Park	Wonju Medical Industry Technovalley (S. Korea)
	Hyun Min Shin	Lutronic (S. Korea)
Director of International Affairs	Chulhong Kim	Pohang University of Science and Technology (S. Korea)
	Jennifer Hyunjong Shin	Korea Advanced Institute of Science and Technology (S. Korea)
Special Director for Convergence	Yung Ho Jo	National Cancer Center (S. Korea)
	Beop Min Kim	Korea University (S. Korea)
	Rena Lee	Ewha Womans University (S. Korea)
	Sung–Uk Kuh	Yonsei University (S. Korea)
	Junghwan Oh	Pukyong National University (S. Korea)
	Yoomi Kim	Ministry of Food and Drug Safety (S. Korea)

Academic Committee

	Name	Affiliation	Note
Chair of Academic Program Committee	Kwang Gi Kim	Gachon University (S. Korea)	
	Won Seuk Jang	Yonsei University (S. Korea)	
	Sung-Min Park	Pohang University of Science and Technology (S. Korea)	
	Hongki Yoo	Korea Advanced Institute of Science and Technology (S. Korea)	
Brain Engineering	Joon-Kyung Seong	Korea University (S. Korea)	Session organizer
	Chang-Hwan Im	Hanyang University (S. Korea)	
	Euiheon Chung	Gwangju Institute of Science and Technology (S. Korea)	
	Do-Won Kim	Chonnam National University (S. Korea)	
Biomedical Instrumentation	Ki Chang Nam	Dongguk University (S. Korea)	Session organizer
	Hyung-Sik Kim	Konkuk University (S. Korea)	
	Tong In Oh	Kyunghee University (S. Korea)	
	Sang Joon Lee	ilooda (S. Korea)	
Medical Imaging	Sejung Yang	Yonsei University (S. Korea)	Session organizer
	Jung-Yeol Yeom	Korea University (S. Korea)	
	Minwoo Kim	Pusan National University (S. Korea)	
	Jihoon Kang	Chonnam National University (S. Korea)	
	Hyoun-Joong Kong	Seoul National University (S. Korea)	
	Jang-Hwan Choi	Ewha Womans University (S. Korea)	
Biochip	Aram Chung	Korea University (S. Korea)	Session organizer
	Bongseop Kwak	Dongguk University (S. Korea)	
	Inhee Choi	University of Seoul (S. Korea)	
	Yun Jung Heo	Kyung Hee University (S. Korea)	
	Sehoon Jeong	Inje University (S. Korea)	
Biomedical Optics	Jae Gwan Kim	Gwangju Institute of Science and Technology (S. Korea)	Session organizer
	Chulmin Joo	Yonsei University (S. Korea)	
	Yeh-Chan Ahn	Pukyong National University (S. Korea)	
	Pilhan Kim	Korea Advanced Institute of Science and Technology (S. Korea)	
	Taesik Go	Jeonbuk National University (S. Korea)	

	Name	Affiliation	Note
Biomaterials	Suk-Won Hwang	Korea University (S. Korea)	Session organizer
	Chun Gwon Park	Sungkyunkwan University (S. Korea)	
	Hojun Kim	Korea Institute of Science and Technology (S. Korea)	
	Ki Jun Yu	Yonsei University (S. Korea)	
	Yun Kyung Jung	Inje University (S. Korea)	
	Jinmyoung Joo	Ulsan National Institute of Science and Technology (S. Korea)	
Biomechanics	Ki-Sik Tae	Konyang University (S. Korea)	Session organizer
	Dohyung Lim	Sejong University (S. Korea)	
	Tae-Soo Bae	Jungwon University (S. Korea)	
	Seungbum Koo	Korea Advanced Institute of Science and Technology (S. Korea)	
	Choongsoo Shin	Sogang University (S. Korea)	
Medical Device / Clinical Medicine	Segyeong Joo	Ulsan University (S. Korea)	Session organizer
	Yangmo Yoo	Sogang University (S. Korea)	
	Hyoungsuk Yoo	Hanyang University (S. Korea)	
	Yunseo Ku	Chungnam National University (S. Korea)	

Organizing Committee (IBEC2021)

	Name	Affiliation
Organizing Committee Chair	Sung-Uk Kuh	Department of Neurosurgery, College of Medicine, Yonsei University (S. Korea)
Organizing Committee Vice-Chair	Byungjo Jung	Department of Biomedical Engineering, College of Health Sciences, Yonsei University (S. Korea)
	Hak-Joon Sung	Department of Medical Engineering, College of Medicine, Yonsei University (S. Korea)
Committee Members	Hee Kyo Jeong	Department of Medical Device Engineering and Management, Graduate School, Yonsei University (S. Korea)
	Byeong-Ju Kwon	Department of Medical Device Engineering and Management, Graduate School, Yonsei University (S. Korea)
	Sei Young Lee	Division of Biomedical Engineering, College of Health Sciences, Yonsei University (S. Korea)
	Sungbin Park	Institute of Artificial Intelligence and Big Data in Medicine, Wonju College of Medicine, Yonsei University (S. Korea)
	Jayoung Kim	Department of Medical Engineering, College of Medicine, Yonsei University (S. Korea)
	Kyu Bom Kim	Department of Integrative Medicine, College of Medicine, Graduate School, Yonsei University (S. Korea)
	Kyuseok Kim	Department of Integrative Medicine, College of Medicine, Graduate School, Yonsei University (S. Korea)
	Hyeong-Cheon Park	Department of Nephrology, Gangnam Severance Hospital, Yonsei University (S. Korea)
	Jeong-Ho Seok	Department of Psychiatry Vice Dean, Gangnam Severance Hospital, Yonsei University (S. Korea)
	Won-Gun Koh	Department of Chemical & Biomolecular Engineering, College of Engineering, Yonsei University (S. Korea)
	Hyungsuk Lee	Division of Mechanical Engineering, College of Engineering, Yonsei University (S. Korea)

Organizing Committee (ICBHI2021)

		Name	Affiliation
Conference Committee	Conference Chair	Dongwook Kim	President, KOSOMBE Jeonbuk National University (S. Korea)
	Conference Co-Chair	Shankar Krishnan	President, IFMBE (USA)
		Sung-Uk Kuh	Yonsei University (S. Korea)
		Chulhong Kim	Pohang University of Science and Technology (S. Korea)
Organization Committee	Chair	Chulhong Kim	Pohang University of Science and Technology (S. Korea)
	Co-Chair	Dong Keun Jung	Dong-A University (S. Korea)
		Myoung Nam Kim	Kyungpook National University (S. Korea)
	Members	Jongmo Seo	Seoul National University (S. Korea)
		Tae Geon Kang	Korea University (S. Korea)
		Yoonkey Nam	Korea Advanced Institute of Science and Technology (S. Korea)
		Mun Ho Ryu	Jeonbuk National University (S. Korea)
		Jyung Hyun Lee	Kyungpook National University (S. Korea)
Program and Paper Competition Committee	Chair	Sung-Min Park	Pohang University of Science and Technology (S. Korea)
	Co-Chair	Ravi Managuli	University of Washington and Hitachi (USA)
		Paulo Carvalho	University of Coimbra (Portugal)
	Members	Kwang Gi Kim	Gachon University (S. Korea)
		Euiheon Chung	Gwangju Institute of Science and Technology (S. Korea)
		Won Seuk Jang	Yonsei University (S. Korea)
		Suk-Won Hwang	Korea University (S. Korea)
		Yeh-Chan Ahn	Pukyong National University (S. Korea)
		Changwook Jeong	Seoul National University (S. Korea)
		Hangsik Shin	Chonnam National University (S. Korea)

		Name	Affiliation
International Advisory Committee	Chair	Hongki Yoo	Korea Advanced Institute of Science and Technology (S. Korea)
	Co-Chair	Ratko Magjarevic	Vice President, IFMBE (USA)
		Ichiro Sakuma	Chair, Asian Pacific Activities Working Group, IFMBE (Japan)
		Jennifer H. Shin	Korea Advanced Institute of Technology (S. Korea)
	Members	Yung Ho Jo	National Cancer Center (S. Korea)
		Beop Min Kim	Korea University (S. Korea)
		Rena Lee	Ewha Womans University (S. Korea)
		Junghwan Oh	Pukyong National University (S. Korea)
Publicity Committee	Chair	Wonsik Ahn	Kyung Hee Universtiy (S. Korea)
	Co-Chair	Jinah Jang	Pohang University of Science and Technology (S. Korea)
		Yun Kyung Jung	Inje University (S. Korea)
	Members	Jaehong Key	Yonsei University (S. Korea)
		Seong Wook Choi	Kangwon National University (S. Korea)
		Yonghyeon Yun	Daelim University College (S. Korea)
		Ki-Sik Tae	Konyang University (S. Korea)
		Jong-Ha Lee	Keimyung University (S. Korea)
Publication Committee	Chair	Hyung Ham Kim	Pohang University of Science and Technology (S. Korea)
	Co-Chair	Chang-Hwan Im	Hanyang University (S. Korea)
		Yoon-Seok Yang	Jeonbuk National University (S. Korea)
		Sang Beom Jun	Ewha Womans University (S. Korea)
		Jin Seung Choi	Konkuk University (S. Korea)
		Jae Sung Lee	Seoul National University (S. Korea)
		Ki Chang Nam	Dongguk University (S. Korea)

Program at a Glance (IBEC2021)

10 Nov. (Wednesday)

Time	Room A	Room B	Room C
15:00~18:00	Education Committee Tutorial 1 Clinical Studies	Education Committee Tutorial 2 Non-Clinical Studies	Education Committee Tutorial 3 Usability Evaluation

11 Nov. (Thursday)

IBEC Program | Joint Session

<table>
<tr><th>Time</th><th>Room A</th><th>Room B</th><th>Room C</th><th>Room E</th></tr>
<tr><td>09:00~09:30</td><td colspan="3">Opening Ceremony (Joint Session)</td><td></td></tr>
<tr><td>09:30~10:00</td><td colspan="3" rowspan="2">Plenary Session 1 (Joint Session)</td><td></td></tr>
<tr><td>10:00~10:30</td><td></td></tr>
<tr><td>10:30~11:00</td><td rowspan="3">Biomedical Instrumentation</td><td rowspan="3">BME Award Lecture</td><td rowspan="3">Award Session 1</td><td rowspan="15">Poster Session</td></tr>
<tr><td>11:00~11:30</td></tr>
<tr><td>11:30~12:00</td></tr>
<tr><td>12:00~12:30</td><td colspan="2" rowspan="4">Lunch</td><td rowspan="4">Program Committee</td></tr>
<tr><td>12:30~13:00</td></tr>
<tr><td>13:00~13:30</td></tr>
<tr><td>13:30~14:00</td></tr>
<tr><td>14:00~14:30</td><td colspan="3">General Assembly</td></tr>
<tr><td>14:30~15:00</td><td rowspan="3">Biomaterials</td><td rowspan="3">Brain Engineering</td><td rowspan="3">Award Session 2</td></tr>
<tr><td>15:00~15:30</td></tr>
<tr><td>15:30~16:00</td></tr>
<tr><td>16:00~16:30</td><td colspan="3">Break</td></tr>
<tr><td>16:30~17:00</td><td rowspan="3"></td><td rowspan="3">Clinical Medical Devices</td><td rowspan="3">Award Session 3</td></tr>
<tr><td>17:00~17:30</td></tr>
<tr><td>17:30~18:00</td></tr>
</table>

12 Nov. (Friday)

IBEC Program | Joint Session

Time	Room A	Room B	Room C	Room D	Room E
09:00~09:30	Plenary Session 2 (Joint Session)				
09:30~10:00					
10:00~10:30	Break				
10:30~11:00	Biomedical Optics	Bio-chip	Rising Women Engineers in BME (Joint Session)	SP: Application in Digital Therapeutics (Organized by Dept. of Medical Device Engineering and Management, Yonsei Univ)	Poster Session
11:00~11:30					
11:30~12:00					
12:00~12:30	Lunch				
12:30~13:00					
13:00~13:30					
13:30~14:00	Biomechanics	Medical Imaging	SP : Application in Digital Healthcare (Organized by Dept. of Integrative Medicine, Yonsei Univ)	SP: Students Program (Organized by Medical Device Industry Graduate Schools Supported by MOHW)	
14:00~14:30					
14:30~15:00					
15:00~15:30	Closing Ceremony				
15:30~16:00					

Program in Detail

10 Nov. (Wednesday)

Education Committee Tutorial 1: Clinical Studies — **Room A (15:00~18:00)**
Session Chair: Ki-Sik Tae (Konyang University, S. Korea)

Clinical Study Process of Medical Devices at Korea Food and Drug Administratios
Yoon-Seok Kim (The Good Company Co., Ltd., S. Korea) ····· 32

Overview of Clinical Trial for Medical Devices and Clinical Trial for Software Medical Devices
Eunjeong Jeon (Promedis Co., Ltd., S. Korea) ····· 33

Quality assurance in clinical study process of medical devices
Kyuri Min (Qrio Co., Ltd., S. Korea) ····· 34

Education Committee Tutorial 2: Non-Clinical Studies — **Room B (15:00~18:00)**
Session Chair: Yonghyeon Yun (Daelim University College, S. Korea)

Common Standards and Specifications on Biological Safety of Medical Devices
Sang Sik Lee (Korea Conformity Laboratories Bio Division, S. Korea) ····· 36

Strategic Assessmentof Preclinical Evaluation for Biomedical Product in Cardiovascular Disease
Se IL Park (Yonsei University, S. Korea) ····· 37

Non-clinical Assessment for New Drug Development
Si-Whan Song (Chemon Inc. CEO, S. Korea) ····· 38

Education Committee Tutorial 3: Usability Evaluation — **Room C (15:00~18:00)**
Session Chair: Jong Ha Lee (Keimyung University, S. Korea)

Standards for Measurement of Human Factors in Usability Testing
Heecheon You (Pohang University of Science & Technology, S. Korea) ····· 40

Medical device GMP and Usability evaluation
Su Gil Hur (Korea Conformity Laboratories, S. Korea) ····· 41

HCI & Usability Evaluation of Home Healthcare Device
Bo-young Kang (Daegu Technopark, S. Korea) ····· 42

11 Nov. (Thursday)

Plenary Session 1 (Joint Session) — Room A (09:30~10:30)
Session Chair: Kwang Gi Kim (Gachon University, S. Korea)

Wearable Devices for Detection of Atrial Fibrillation and Seizure Prediction in Divers
Ki Chon (University of Connecticut, USA) ····· 44

Biomedical Instrumentation — Room A (10:30~12:00)
Session Chair: Ki Chang Nam (Dongguk University, S. Korea)

Versatile Dendritic Nanoparticles for Immunotherapy and Liquid Biopsy
Seungpyo Hong (University of Wisconsin-Madison, USA) ····· 46

Chest Electrical Impedance Tomography towards clinical use
Zhanqi Zhao (Hochschule Furtwangen University, Germany) ····· 47

Polymer-based, Miniaturized, Flexible and Long-Term Reliable Neural Interfacing Devices for Implantable and Wearable Applications
Joonsoo Jeong (Pusan National University, S. Korea) ····· 48

Remote Monitoring Systems for Individualized Health State During COVID-19 and Beyond: Opinion Piece
In cheol Jeong (Hallym University, S. Korea) ····· 49

BME Award Lecture — Room B (10:30~12:00)
Session Chair: Yangmo Yoo (Sogang University, S. Korea)

Multi-modal Imaging: Photoacoustic Imaging Plus More
Chulhong Kim (Pohang University of Science and Technology, S. Korea) ····· 51

Modulating Neutrophils for the Treatment of Severe Diseases using Biomaterials
Chun Gwon Park (Sungkyunkwan University, S. Korea) ····· 52

Award Session 1 — Room C (10:30~12:00)
Session Chair: Do-Won Kim (Chonnam National University, S. Korea), Chulmin Joo (Yonsei University, S. Korea)
Jinmyoung Joo (Ulsan National Institute of Science and Technology, S. Korea)

A-001. Non-linear Microfluidic Cell Stretching Enables Highly Effective Intracellular Delivery for Genome Editing
Chan Kwon (Korea University, S. Korea) ····· 54

A-002. Foley Catheter Assembled with Sustained Drug Releasing Polymeric layer for Reducing Catheter-related Bladder Discomfort
Cho Rim Kim (Seoul National University, S. Korea) ····· 56

A-003. Phenotyping of Breast Cancer Cells by Deep Hybrid Learning Network
Chanhong Min (Korea Advanced Institute of Science and Technology, S. Korea) ····· 58

A-004. Feasibility Test of a Stimulation Artifact-free Stimulating and Recording System for Closed-loop Therapeutic Neuromodulation
Wonok Kang (Pohang University of Science and Technology, S. Korea) ····· 60

A-005. A Portable Real-Time ECG Monitoring System Jin-Woo Jeong (Gachon University, S. Korea) ····· 62

A-006. Soft, Wireless Bioresorbable Neurochemical System for Postoperative Management of Brain-Disorders
Seung Min Yang (Korea University, S. Korea) ····· 64

Biomaterials Room A (14:30~16:00)
Session Chair: Suk-Won Hwang (Korea University, S. Korea)

Plant-inspired Tissue-adhesive, Injectable and Electroconductive Hydrogels for Biomedical Applications
Mikyung Shin (Sungkyunkwan University, S. Korea) ····· 67

Tissue engineered Constructs for in Vitro Testing Platforms
Youngmee Jung (Korea Institute of Science and Technology, S. Korea) ····· 68

Organic Mixed Conductor-based Microfiber Meshes for Efficient Bioelectronic Interfaces
Myung-Han Yoon (Gwangju Institute of Science and Technology, S. Korea) ····· 69

Brain Engineering Room B (14:30~16:00)
Session Chair: Joon-Kyung Seong (Korea University, S. Korea)

Quantitative Personality Prediction Based on Emotional EEG Responses
Dan Zhang (Tsinghua University, China) ····· 71

Targeting Neural Oscillations by Transcranial Alternating Current Stimulation
Sangtae Ahn (Kyungpook National University, S. Korea) ····· 72

Single-cell Brain Mapping using 3D Organ Profiling Techniques
Young-Gyun Park (Korea Advanced Institute of Science and Technology, S. Korea) ····· 73

Award Session 2 — **Room C (14:30~16:00)**

Session Chair: **Euiheon Chung** (Gwangju Institute of Science and Technology, S. Korea)

Tong In Oh (Kyung Hee University, S. Korea), **MinWoo Kim** (Pusan National University, S. Korea)

A-007. Novel Hybrid brain-computer interface (BCI) for Virtual Reality Applications using SSVEP-based BCI and Electrooculogram-based Eye Tracking for Increased Information Transfer Rate — Jisoo Ha (Hanyang University, S. Korea) ····· 75

A-008. Changes in Physiological Network Connectivity of body system in Narcolepsy during REM sleep — Dong Yeon Son (Seoul National University, S. Korea) ····· 77

A-009. Investigation of Electric Field Direction Sensitivity on Cortical Neuron Activation — Kyeong-Seop Park (Gwangju Institute of Science and Technology, S. Korea) ····· 79

A-010. Animal Brain-Machine Interface with Visual Feedback and Virtual Reward — Yoon Kyung Cho (Ewha Womans University, S. Korea) ····· 81

A-011. pH sensing Piezoelectric Smart Dental Implant for Peri-implantitis Monitoring — Seoyoung Lee (Sookmyung Women University, S. Korea) ····· 84

A-012. Development of a Hyperbaric Chamber Control System for Cell Experiments to Reveal the Mechanism of Hyperbaric Oxygen Therapy — Yeo-Eun Choi (Yonsei University, S. Korea) ····· 86

Clinical Medical Devices — **Room B (16:30~18:00)**

Session Chair: **Yunseo Ku** (Chungnam National University, S. Korea)

A Wirelessly-Powered Implantable Medical Devices — Byunghun Lee (Hanyang University, S. Korea) ····· 89

Biomedical Optical Spectroscopy for Clinical Diagnostics — SeungYup Lee (Kennesaw State University, Georgia Tech, USA) ····· 90

Artificial Intelligence using Electrocardiography: Strengths and Pitfalls — Joon-myoung Kwon (Sejong Hospital/Medical AI Co., Ltd., S. Korea) ····· 91

Award Session 3 — **Room C (16:30~18:00)**
Session Chair: Yun Kyung Jung (Inje University, S. Korea), Jang-Hwan Choi (Ewha Womans University, S. Korea)
Taesik Go (Jeonbuk National University, S. Korea)

A-013. Maximum Vibration Frequency Detection Method using a Piezoelectric Sensor for Skincare Device — Chang Gyu Park (Kyungpook National University, S. Korea) ····· 93

A-014. Design of a Filter Rotation System for Specular Reflection Removal of Cervicography — JaeHwang Seol (Gachon University, S. Korea) ····· 95

A-015. Generative Adversarial Network-based Image Reconstruction of Sparse-View Panoramic Radiography for Dose Reduction, and clinical evaluation — Minhyuk Choi (Seoul National University, S. Korea) ····· 97

A-016. Deep learning-based bone Marrow Edema Detection using Dual-energy CT with Multi-channel Data Fusion — ChunSu Park (Pusan National University, S. Korea) ····· 99

A-017. Simultaneous Calibration of Plane Coordinate and Depth of Interaction for Monolithic Crystal PET Detectors using Oblique Irradiation — Sangjin Bae (Seoul National University, S. Korea) ····· 102

A-018. SiPM Signal Readout for Inter-Crystal Scatter Event Identification using High Pass Filters — Hyeong Seok Shim (Seoul National University, S. Korea) ····· 104

12 Nov. (Friday)

Plenary Session 2 (Joint Session) — **Room A (09:00~10:00)**
Session Chair: Sung-Min Park (Pohang University of Science and Technology, S. Korea)

Educating Biomedical Engineers in Digital Health: Models, Challenges and Rewards — Shankar Krishnan (IFMBE, USA) ····· 107

Biomedical optics — **Room A (10:30~12:00)**
Session Chair: Jae Gwan Kim (Gwangju Institute of Science and Technology, S. Korea)

Transcranial Photobiomodulation Stimulates Brain Rhythm Powers and Hemodynamic Network — Hanli Liu (University of Texas at Arlington, USA) ····· 110

Label-free Assessment of High-risk Plaque by Multi-modal Imaging Catheter — Hongki Yoo (Korea Advanced Institute of Science and Technology, S. Korea) ····· 111

Nanostructure-based Functional Devices for Imaging and Sensing Applications
Dasol Lee (Yonsei University, S. Korea) ····· 112

Biomechanics — Room A (13:30~15:00)
Session Chair: Bomi Gweon (Sejong University, S. Korea)

Inefficient Muscular Contraction after Hemispheric Stroke
Jongsang Son (Northwestern University, USA)) ····· 114

Advancing Our Understanding of Muscle Biomechanical Properties: Implication for Neuro-and Musculoskeletal Rehabilitation
Song Joo Lee (Korea Institute of Science and Technology, S. Korea) ····· 115

Engineering Approaches of Osteoporotic Fractures: Numerical & Experimental Analyses
Taeyong Lee (Ewha Womans University, S. Korea) ····· 116

Bio-chip — Room B (10:30~12:00)
Session Chair: Aram Chung (Korea University, S. Korea)

Microfabrication Techniques Compatible with Biomaterials for Biomedical Applications
KangJu Lee (Chonnam National University, S. Korea) ····· 118

Designing High-aspect-ratio Nanostructures for Interfacing Biological System
Hyejeong Seong (Korea Institute of Science and Technology, S. Korea) ····· 119

Microfluidic Platforms with Liquid Metal-based 3D
Hyun Soo Kim (Kwangwoon University, S. Korea) ····· 120

Medical Imaging — Room B (13:30~15:00)
Session Chair: Sejung Yang (Yonsei University, S. Korea)

Understanding the Selective Mechanism of Network Vulnerability in Alzheimer's Disease Using Computational Neuroscience Approaches
Guorong Wu (University of North Carolina at Chapel Hill, USA) ····· 122

Unsupervised Learning for CT Image Enhancement
Jang-Hwan Choi (Ewha Womans University, S. Korea) ····· 123

Development of a Fully Integrated US-NM (Ultrasound-nuclear medicine) Probe
Jung-Yeol Yeom (Korea University, S. Korea) ····· 124

Rising Women Engineers in BME (Joint) — Room C (10:30~12:00)
Session Chair: Jennifer Hyunjong Shin (Korea Advanced Institute of Science and Technology, S. Korea)

Recent Progress of Optical Imaging Techniques for Diagnosis and Treatment Assessment of Breast, Ovarian and Colorectal Cancer — Quing Zhu (Washington University in St Louis, USA) ····· 126

Quantitative Histopathology using Normalized Raman Imaging (NoRI) — Seungeun Oh (Harvard Medical School, USA) ····· 127

Real-time Extended Field-of-view Ultrasound Imaging with Multi-GPU Reconstruction — Eun-Yeong Park (Stanford University, USA) ····· 128

Microphysiological Human Intestine Models to Decipher Host-microbiome Crosstalk — Woojung Shin (Harvard University, USA) ····· 129

SP: Application in Digital Therapeutics — Room D (10:30~12:00)
Session Chair: Hee Kyo Jeong (Yonsei University, S. Korea)

Guideline on Review and Approval of Digital Therapeutics — Young-Kyu Kang (Ministry of Food and Drug Safety, S. Korea) ····· 131

Development and Regulation of Digital Therapeutics, Future directions — Kwon Ho Kim (Korea Health Industry Development Institute, S. Korea) ····· 132

Digital Therapeutics in Respiratory Disease — Hee Kwon (LifeSemantics Corp., S. Korea) ····· 133

Overview of Digital Therapeutics and SaMD — Seong-ji Kang (WELT corporation/Yonsei University, S. Korea) ····· 134

SP: Application in Digital Healthcare — Room C (13:30~15:00)
Session Chair: Jihoon Kang (Chonnam National University, S. Korea)

Wearable Biosensors for Healthcare Applications — Jayoung Kim (Yonsei University, S. Korea) ····· 136

Overview of Digital Health Care & Digital Health Medical Device — Sung Hoon Kim (Yonsei University, S. Korea) ····· 137

Evaluation of Effectiveness on the Proposed Physically Interactive Controller in Bilateral Upper-extremity Exercise — Jung Hyun Park (Yonsei University, S. Korea) ····· 138

SP: Students Program (Organized by Medical Device Industry Graduate Schools Supported by MOHW)
Room D (13:30~15:00)
Session Chair: Byung-Ju Kwon (Yonsei University, S. Korea)

Major Countries Regulatory Trend of Digital Therapeutics (Korea and USA, UK, Germany)
Hanji Lee (Yonsei University, S. Korea) ····· 141

User needs analysis for multi-purpose smart neonatal incubator
Hyeonkyeong Choi (Yonsei University, S. Korea) ····· 142

Next Generation Digital Therapeutics Device: Biofeedback via VR Motion Chair
Sisu Seong (Sungkyunkwan University/Samsung Medical Center, S. Korea) ····· 143

Development of Bone Metastasis detection Algorithm on 3D CT Data made of different view images using Deep Learning-based CNN Model.
Min Seong Choi (Sungkyunkwan University, S.Korea) ····· 144

Comparison of Posterior Capsule Opacification between Hydrophobic Acrylic and Silicone Intraocular Lens after Cataract Surgery : A Systematic Review and Meta-Analysis
Yerin Kwon (Dongguk University, S. Korea) ····· 145

A Study on Improvement of the Certification System of Innovative Medical Device Software Manufacturer: Simplified Pathway based on Risk-related Certification Type
Hye Jin Kim (Dongguk University, S. Korea) ····· 146

Real-time Surgical Phase Recognition in Cholecystectomy
Sanggoo Lee (Dongguk University, S. Korea) ····· 149

Poster Session — Room E (11 Nov., 10:30~18:00 / 12 Nov., 10:30~15:00)

Biochip

P-001. All-Inkjet-Printed Alveolar Barrier Model in Microfluidic Chip for Tissue Culture ····· 151

P-002. Highly Efficient Intracellular Delivery for Cell-based Therapy using High-speed Droplet Squeezing ····· 153

P-003. Transparent ITO-IEA Cell Plate for Impedance Measurement ····· 155

P-004. Real Patient Plasma Detection Characteristics of ITO Biosensor ····· 157

P-005. Selective Neuronal Cell Adhesion on a Microelectrode Array by Electrophoretic Deposition of PLL-FITC ····· 159

P-006. Manufacture and Characteristic Evaluation of Biomimetic Structure for Drug Screening Using T-NIL Process ····· 161

P-007. Detection of Micro-particle Surface Charge Difference using DEP system ····· 163

P-008. Clogging-Free Hydroporator for Cell Engineering ····· 165

Biomaterials

P-009. Development of Biodegradable Discoidal Polymeric Particles for Effective Treatment of Lung Cancer ····· 167

P-010. Fabrication of Silk Fibroin based-Microparticle for Drug Delivery ····· 169

P-011. Skin-mimicking Phantom to Measure Transdermal Absorption of Cosmetics under Sonophoresis ····· 171

P-012. Biodegradable Discoidal Particles as Cellular Backpacks ····· 173

P-013. Near-Infrared Fluorescence Nanoparticle Targeting Ovarian Cancer for Image-guided Surgery ····· 175

P-014. Fabrication of Nanoparticles Targeting Natural Killer Cells to Prime the Cellular Activity for Anticancer Effects ····· 177

P-015. Modulating Sepsis-Associated NETosis Dysregulation Using Bioinspired DNase- I -Coated Melanin-like Nanospheres ····· 179

P-016. PEG coated MCM-48 Nanoparticles for Oral Vaccine Delivery 182

P-017. Efficient Activation of Dendritic cells with CpG-coated Functional Magnetic Nanoparticles 184

P-018. Graphene Oxide-reinforced Hydroxyapatite/Gelatin Bone Scaffolds Fabricated using Extrusion-based 3D Bioprinting 187

P-019. Cancer Cell Imaging based on Carbon Quantum Dots 189

P-020. Printing Continuous Collagen Gel at Body Fluid Temperature in Every 5 minutes 191

P-021. Comparison of Prosthetic Ankle type in Bilateral Transtibial Amputee: Micropocessor vs Conventional 193

P-022. An Analysis of Bone Conduction Hearing Aids for Speech Transmission Intelligibility Optimization by Finite Element Analysis 195

P-023. Predicting Thermal Sensation of Passenger in Subway Using A Smart Facial Mask 197

Biomedical Instrumentation

P-024. Weak Closed-loop Vibrational Stimulation Improves the Associative Memory in the Elderly 199

P-025. Evaluation of the effectiveness of Transcutaneous Vagus Nerve Stimulation on Parasympathetic Nervous System Activation with Heart Rate Variability 201

P-026. Automatic Classification of Voiding Dysfunction Patients Using Uroflow Curve 203

P-027. Exploration of Reliable Biomarkers of Non-invasive Auricular Vagus Nerve Stimulation for Healthy Adults: Pilot Study 205

P-028. Biosignal Analysis from Nose Region for Deception Detection in Thermal Imaging 207

P-029. Development of Gait Compensation Algorithm for Gait Authentication using Smartphone Sensor 209

P-030. Gender and Age Convolution Neural Network Classification using MFCC 211

P-031. Is Aryl Hydrocarbon Receptor Antagonism after Ischemia Effective in Alleviating Hepatic Ischemia-Reperfusion Injury in Rats? 213

P-032. Interpretation of Blood Pressure Errors in Clothing by Mathematical Models of Oscillometric Measurment Equipment 215

P-033. Evaluation of Antibody Aerosolization by Jet and Mesh Nebulizers 217

P-034. Comparison of Quantitative Drug Delivery Efficiency for Jet and Mesh Nebulizer 219

P-035. Development of a System to Read Sleep Patterns 221

P-036. Development of a Wireless Sensing Device with Optical Color Sensor for Monitoring Abnormal State of the Automated External Defibrillator 223

P-037. Development of Hyperbaric Oxygen Chamber Embedded System for Animal Experiment 225

P-038. Comparison of Algorithms for Screening of Cervical Intraepithelial Neoplasia using Multiple Electrodes based Electrical Impedance Spectroscopic Probe 227

P-039. Voluntary Cough Detection from Microphone Signals with Machine Learning Algorithms 229

P-040. Comparison of Stroke Volume Variations for Sleep Respiratory Events within Overnight Polysomnography using EIT monitoring 231

P-041. Simulation Study of a Channel Reduction Method for Continuous Depth-of-interaction Measurements using Single-ended Readout 233

P-042. Detection of Left Ventricular Hypertrophy from Multi-lead ECG Signal using Artificial Neural Network 235

P-043. A study on Open-anode Bio-electrochemical System for Energy Harvesting from Solid Biomass 238

Biomedical Optics

P-044. Multi-functional Optical Stimulation and Imaging System for an Ex-vivo Verification 240

P-045. Minimally Invasive Focused Ultrasound-Assisted Delivery of Nanomaterials to Retina Ganglion Cell Layer 242

P-046. Photovoltaic Retinal Prosthesis for Biphasic Stimulation using Symmetric Structure 244

P-047. Biological Fiber-based SERS Platform using Silk Fibroin Protein 246

P-048. Reflectance Investigation of EJ-510 Reflective Layer on Ceramic GAGG:Ce and GAGG:Ce Single Crystal Scintillators 248

P-049. Evaluation of Drug Transmittance Improvement in Triple-Ultrasound and Iontophoresis 250

P-050. Assessing Atherosclerotic Plaque with Precision Enhanced Multispectral Fluorescence Lifetime Imaging Microscopy 252

P-051. Sonoluminescence Counting using PMT 254

P-052. Development of High Speed and Precision Enhanced Two-photon Fluorescence Lifetime Imaging Microscopy with Optimal Repetition Rate. 256

P-053. An Experimental Animal Model of Trigeminal Axotomy and Management of Neuropathic Corneal Pain 258

Brain Engineering

P-054. Novel In-Car Environment Control System Using an SSVEP-based BCI with Visual Stimuli Presented on a Head-Up Display 260

P-055. Inter-sectional Transcranial Direct Current Stimulation for a Focal Stimulation of Deep Brain Structures: A Simulation Study 262

P-056. Semantic-hierarchical Structured Binary Quantum-behaved Particle swarm Optimization for Decoding Spoken Word Evoked Electrocorticography 264

P-057. Different Cosmetic Formulations Can Induce Distinct Neural Substrates 266

P-058. Realistic Modeling of Current Steering During Orientation Selective Deep Brain Stimulation of the Subthalamic Nucleus – The Influence of Anisotropic Conductivity 268

P-059. The Influence of Frequency Bands and Brain Region on ECoG-Based BMI Learning Performance 270

P-060. Monitoring Basal Dopamine Change using MCSWV to Identify the Roles of MAO-A and MAO-B in Dopamine Degradation 273

P-061. Quantitative Analysis on Temporal Interference-stimulation for Deep Brain Stimulation 275

P-062. Discrimination of Resting-state Functional Connectivity from Idiopathic REM Sleep Behavior Disorder Patients Based on Machine Learning with Data Augmentation 278

P-063. Effects of PPC tDCS on Vigilance Task and Alpha Power Tendency 281

P-064. Enhanced Dopamine Sensitivity using Steered Fast-Scan Cyclic Voltammetry 283

P-065. Application of Fourier transform Electrochemical Impedance Spectroscopy in Fast Cyclic Square Wave Voltammetry for the Detection of biofouling of electrodes 293

P-066. A web-based Multimodal Platform for the Evaluation and Training of Cognitive Control in Children. 296

P-067. Decoding the Performance of a Memory Task using Single-trial Intracranial EEG 297

P-068. A Computational Scheme for Optimal Control of Brain with Consideration of Activity-dependent and Homeostatic Plasticity 299

P-069. Development of an Online Endogenous Brain-Computer Interface Based on Ear-EEG 301

P-070. Optogenetic Stimulation on Rat Hippocampus for Neuromodulation 303

P-071. Coincidence Level Estimation of Bursting Spike Trains using Jittering Timestamp 306

P-072. Changes in Activated Astrocytes by the Electrical Stimulation 308

P-073. Classifying the Distracted State During Exercise using Steady State Visual Evoked Potential (SSVEP) and EEGNet 310

P-074. Effect of auditory Vagus Nerve Stimulation on Pupillometry 312

Medical Device / Clinical Medicine

P-075. Development of real Time Untact Healthcare System for an infectious Disease Patient 315

P-076. Complete Circumferential Renal Sympathetic Denervation Using a Laparoscopic Ablation System to Treat Hypertension 317

P-077. The Effectiveness of Noise Cancelling Function in Different Types of Earphones 319

P-078. Determination of the Counter-pulsation of the Pneumatic Dual-parallel Pulsatile Extracorporeal Membrane Oxygenator 321

P-079. Development of Sleep Classification Algorithm Considering Medical Significance using EEG and EOG 323

P-080. Interim Results of 2021 Horizon Scanning Service for Emerging Health Technologies in NECA H-SIGHT – Digital Therapeutics – 325

P-081. Salivary Gland Stimulation System to Promote Radioiodine Excretion 327

P-082. Total Sleep Time Estimation Using an Tri-axial Accelerometer in Daytime 329

P-083. Duty Cycle Dependence of Tumor-treating Fields on Glioblastoma Spheroid Cells 331

P-084. Development of Radio-frequency Generator for Radio-Frequency Ablation application 333

P-085. A study on the Identification of Foreign Substances in the Intubation Tube using Respiration Signals 335

P-086. A Multi – Channel Neural Stimulator with Passive Component Based on An Inductive Power Transfer 337

P-087. Evaluation of the Role Of Perfusion of the Pulsatile Pump Contributes to Pressure Fluctuations in the tube 339

P-088. Machine Learning-based Cardiac Output Estimation using Non-invasive Photoplethysmogram in Off-pump Coronary Artery Bypass Surgery 341

P-089. User Needs Analysis for Multi-purpose Smart Neonatal Incubator 343

P-090. Applying Human Factor Engineering Methods for Risk Analysis of the Breast Imaging Diagnostic System 345

P-091. Design of Expandable High-Power Ultrasound Transducer Driving System 347

P-092. A study on the Development of Parallel Robot for Laparoscopic Surgery 350

P-093. Design and Simulation of a Laparoscopic Surgical Robot by using the 3-DOF Parallel Robot 352

P-094. Design of Magnetic Traction Clip for Colonoscopic Perforation Suture 354

P-095. Development of a System Capable of Diagnosing and Treating Alzheimer's Disease: a Technique Experiment using Cadaver 356

P-096. Performance Evaluation of Magnetic Carrier Controller for Corneal Endothelial Cell Transfer 358

P-097. A Development of an Emergency Automatic Ventilator using AMBU Bag 360

P-098. Development of Mapping Catheter for Arrhythmia Interventional Procedure 362

Medical Imaging

P-099. The Noise Removal by Stationary Wavelet Transform Filter in the Phase Contrast X-ray Image using the Instantaneous Frequency 364

P-100. Low-dimensional Representations of Functional Connectivity in Migraine 366

P-101. Deep Learning-based Classification of Autism Individuals using Functional Connectivity 368

P-102. Cortical Asymmetry of Structural Connectivity in Autism Spectrum Disorder 370

P-103. PointNet++ Based Method for Automated Prediction of Tooth Crown Center of Mass, Main Axis Angle and Mesiodistal Width 372

P-104. Automatic Segmentation of Temporal Bone Structures in CT Images Using Deep Learning 374

P-105. Deep Learning Based 3D Hand Segmentation for Computer Assisted Surgery 376

P-106. A Tooth Segmentation with Self-Attention U-Net 378

P-107. Automatic Leg Veins and Arteries Segmentation based on Deep Learning in CT images 380

P-108. Ribs' Sequence Indexing using Deep learning-based method in the Chest CT images 382

P-109. MSA-Net: Multimodal Spatial Attention Network for automatic head and neck tumor segmentation in FDG-PET and CT images 384

P-110. A study of Lesion Segmentation Considering Mechanism of Ultrasound Based on Improved Transfer Learning 386

P-111. Complex Chromosome Dataset Manufacturing and Object Detection for Overlapped Chromosome Analysis. 388

P-112. Lung Cancer and Lymph Node Metastasis Segmentation on FDG PET/CT Images using Multiple Context Information 390

P-113. Segmentation Knowledge Distillation for Conjunctival Microscopic Image Analysis 392

P-114. Axial Resolution Enhancement of Optical Coherence Tomography Through STFT-based Deep Learning Approach 394

P-115. Deep Learning-based Individual Cell Detection Method to Measure Dielectrophoretic Mobility 396

P-116. Prediction of Bone Mineral Density in CT using deep learning 398

P-117. Computational Modelling of Neural Interactions Reflected in the Calcium Imaging Signals using Dynamic Causal Modelling 401

P-118. Development of Dental Biomaterials Consisting of Various Ratios of Hydroxyapatite and Tricalcium Phosphate 403

P-119. Development of a IoT Technology Based Personal Digital Pill Box 405

The Joint Conference of the
IBEC2021 and the ICBHI2021

Education Committee Tutorial 1: Clinical Studies

Session Chair: Ki-Sik Tae (Konyang University, S. Korea)

10 Nov. (Wednesday) Room A (15:00~18:00)

Clinical Study Process of Medical Devices at Korea Food and Drug Administratios
Yoon-Seok Kim (The Good Company Co., Ltd., S. Korea)

Overview of Clinical Trial for mEdical Devices and Clinical Trial for Software Medical Devices
Eunjeong Jeon (Promedis Co., Ltd., S. Korea)

Quality Assurance in Clinical Study Process of Medical Devices Kyuri Min (Qrio Co., Ltd., S. Korea)



Kim Yoon-Seok
The Good Company Co., Ltd.

임상시험에 따른 식약처 인허가 절차

Abstract

1. 의료기기 식약처 인허가 절차
   - 등급별 의료기기 인증/허가 절차에 대한 내용
   - 의료기기 인증/허가 단계에서 임상시험서가 필요한 경우
   - 의료기기 인증/허가에 제출되는 문서
2. 의료기기 임상시험계획 승인에 관한 규정
   - 자료 제출 요건
   - 면제 범위
   - 사후 관리
3. 의료기기 시험 검사 준비
   - 의료기기 시험 검사에 필요한 자료 제출 요건
   - 설계/개발 문서



Jeon, Eunjeong
Ph.D. / Public Health/ Catholic University Graduate School, Seoul, South Korea
CEO/PROMEDIS.Co.,Ltd, Seoul, South Korea
Adjunct professor, Inje University, Gimhae-si, Gyeongsangnam-do, Republic of Korea

Overview of clinical trial for medical devices and clinical trial for software medical devices

Abstract

1. Overview of medical devices
2. Authorization Procedure for Medical Devices
3. Regulations related to clinical trials for medical devices
4. Clinical trial for medical devices
5. Clinical Trial for software medical devices
6. Clinical Trial for digital therapeutic devices



Kyuri Min
QRIO (Auditor)

의료기기 임상시험 품질보증
(Medical Device Quality Assurance)

Abstract

의료기기 임상시험 및 의료기기 개발진행시 필요한 사항에 대한 강의
기술문서 시험규격 안전성 /성능
GMP (제조품질관리기준적합인정서)
ISO (13485 & 14971 & S/W Validation)
Usability (IEC 62366-1 & 60601) & Global Guideline
Risk Management (Analysis & Evaluation & Control)
Complain file list

Brief Biosketch

YONSEI University Nursing Colleage B.Sc Degree (Nursing)
Ewha Woman's University Master Special Education
YONSEI University Master Department of Integrate Medicine
BARQA (British Association of Research Quality Assurance) Auditor

The Joint Conference of the
IBEC2021 and the ICBHI2021

Education Committee Tutorial 2: Non-Clinical Studies

Session Chair: Yonghyeon Yun (Daelim University College, S. Korea)

10 Nov. (Wednesday) Room B (15:00~18:00)

Common Standards and Specifications on Biological Safety of Medical Devices
Sang Sik Lee (Korea Conformity Laboratories Bio Division, S. Korea)

Strategic Assessmentof Preclinical Evaluation for Biomedical Product in Cardiovascular Disease
Se IL Park (Yonsei University, S. Korea)

Non-clinical Assessment for New Drug Development Si-Whan Song (Chemon Inc. CEO, S. Korea)



SANG SIK LEE
MSc, DVM
Korea Conformity laboratories
Bio Division
Principal Research Engineer

Common Standards and Specifications on Biological Safety of Medical Devices

Abstract

1. Understanding of Domestic Medical Devices
2. Medical Device Act Information
3. Medical Device Certification and Authorization Process
4. ISO 10993 Biological evaluation of medical devices
5. Biological Safety tests of Medical Devices

Brief Biosketch

2010 : Graduated from Chungnam National University, Department of Veterinary Medicine
Obtaining a D.V.M. license

2010~ : Korea Conformity laboratories Toxicology Study Director



SE IL PARK, D.V.M., Ph.D.
Research associate Professor
Yonsei University College of Medicine
Cardiovascular Product Evaluation Center

Strategic assessment of preclinical evaluation for biomedical product in cardiovascular disease

Abstract

In spite of brilliant development of medical technology, cardiovascular diseases are the first leading cause of death and morbidity in most of the countries. Cardiac and vascular complications have complex multi-factorial pathologies, in which both physical and hemodynamic factors are implicated, there are limitations on reflecting the functional characteristics of the human heart. Biomedical devices for cardiovascular disease should have durability, strength and flexibility to withstand through the lifetime. Equally important are the materials' biologic properties, the most desirable of which being thromboresistance, non-calcification, anti-hemostasis and endothelialization capability. For this reason, it is one of the main advantages to use larger animals as a model of preclinical safety and efficacy testing for intravascular stents, valve replacement, and cardiac associated biomedical devices. Especially, swine models play a pivotal role for evaluating biomedical products to overcome acute and chronic myocardial infarction, as well as ischemic reperfusion injury, heart failure and cardiomyopathy. They also have offered as important pre-clinical models for investigating the system of preclinical safety and efficacy evaluation for various cardiovascular devices with new biomedical agents and relative therapy.

Brief Biosketch

2010 – 2021 Research associate Professor, Cardiovascular Product Evaluation Center, Yonsei University
2010 – 2021 Associate Researcher, Stem cell therapeutic research institute, Kyungpook National Univ.
2008 ~ 2010 Dept of Orthopedic Surgery. College of Medicine. Yeoungnam University (fellowship)
2006 – 2010 Institute of Bioscience, College of Medicine, Yeoungnam University (Researcher,)
2003 ~ 2007, Graduate school of Veterinary Medicine. Kyungpook National University (PhD)
2001 ~ 2003, Graduate school of Veterinary Medicine. Kyungpook National University (MS)
1998 ~ 2010, CEO of Veterinary Clinical Medical Center



Si-Whan Song
PhD. Seoul National University Collage of Veterinary Medicine.
Chemon Inc. CEO

Non-clinical Assessment for New Drug Development

Abstract

In the process of developing a new drug, non-clinical testing is essential. The importance of non-clinical trials is to provide scientific data necessary for clinical trials. In order to develop a new drug that is effective and safe for humans and to design an appropriate clinical trial, evaluation of the results of non-clinical trials should be conducted well. In addition, the importance of nonclinical test is emphasized because the initial dose of the phase I trial is determined using the results of the non-clinical trial. This lecture contents are an overview of non-clinical studies and brief methods of non-clinical studies, a summary of clinical initial dose setting using non-clinical results, and a strategy for conducting non-clinical trials.

Brief Biosketch

After graduating from College of Veterinary Medicine, Seoul National University. I worked for about 14 years at the Korea Research Institute of Chemical Technology (KRICT) Safety Evaluation Research Center (now KIT) since 1987. In 2000, I obtained a Ph.D. from the Department of Pharmacology, College of Veterinary Medicine, Seoul National University, and participated as a founding member of Chemon Inc. At Chemon, Korea's first private non-clinical research institute, I served as the head of the research center and the CEO, and is currently serving as the CEO. I was one of the earliest researchers to conduct a non-clinical toxicity test by introducing the GLP system in Korea. As the study director of the toxicity test, I performed general toxicity, reproductive toxicity, and carcinogenicity tests. Currently, I have played a role as a vice president and council member of the Korean Association for Laboratory Animal Science also.

The Joint Conference of the
IBEC2021 and the ICBHI2021

Education Committee Tutorial 3: Usability Evaluation

Session Chair: Jong Ha Lee (Keimyung University, S. Korea)

10 Nov. (Wednesday) Room C (15:00~18:00)

Standards for Measurement of Human Factors in Usability Testing
Heecheon You (Pohang University of Science & Technology, S. Korea)

Medical device GMP and Usability evaluation Su Gil Hur (Korea Conformity Laboratories, S. Korea)

HCI & Usability Evaluation of Home Healthcare Device Bo-young Kang (Daegu Technopark, S. Korea)



You, Heecheon
Professor
Pohang University of Science & Technology

Standards for Measurement of Human Factors in Usability Testing

Abstract

Usability is an essential aspect to be considered throughout the whole process of product design and development for better effectiveness, efficiency, and satisfaction of users with products. In this presentation, international standards that provide guidance on processes and outcomes of human-centered design and Korean standards that provide guidance on measurement of human factors would be presented. A comprehensive review of terms, concepts, processes, testing tools, measures, analysis techniques, and reporting contents of usability testing would help health professionals and medical equipment manufacturers adopt and/or develop products and service systems with better usability. Case studies would be presented to demonstrate how products are designed and tested for better usability.

Brief Biosketch

Dr. You specializes in ergonomics and product development, having over 150 journal papers and 70 patents. He has developed ergonomic designs of various products including helicopter cockpit, flight suit, and bus passenger seat using anthropometric data, human motion analysis, physiological analysis, and/or digital human model simulation. He has received over 40 awards for excellence in academic research and invention including the Alphonse Chapanis Best Student Paper Award from the Human Factors and Ergonomics Society in 1999 and 2009, Grand Prix at the 2011 Korean University Invention Fair, and Gold Prize and Special Award at the 2012 Geneva International Invention Fair.



SU GIL HUR
Principal Engineer
Korea Conformity Laboratories

Medical device GMP and Usability evaluation.

Abstract

의료기기는 사용목적과 인체에 미치는 잠재적 위해로 인해 위해도가 가장 높은 4등급에서 부터 위해도가 가장 낮은 1등급까지 총 4단계로 분류되고 있다. 이러한 의료기기를 제조/판매를 위해서는 GMP, 기술문서를 평가 받아야 한다. 의료기기는 제품 품목허가를 득하기 전에 GMP(우수 의료기기 제조관리 시스템)을 인증 받아야 한다. 현재 국내 GMP는 국제기준인 ISO 13485:2016을 준용한 "의료기기 제조 및 품질관리 기준" 요건에 충족하여야 하며, 4항(품질경영시스템), 5항(경영책임), 6항(자원관리), 7항(제품실현), 8항(측정, 분석 및 개선)으로 구성되어 있다. 국내 GMP는 총 72가지 심사기준으로 심사하여 "적합", "보완", 부적합"으로 결과를 통보하여 적용제외 항목을 제외한 모든 항목에서 "적합"을 받아야 비로소 GMP를 획득할 수 있다.

'21.01.01부터 의료기기 GMP 심사를 받기 위해서는 사용적합성 평가가 필수적이다. 사용적합성(사용성평가)에 대한 항목은 의료기기 등급에 따라 2021년부터 차등 적용하여 등급 기준으로 6개월 단계로 '21.01.01(4등급), '21.07.01(3등급), '22.01.01(2등급), '22.07.01(1등급) 수행될 예정이다. 사용성평가는 사용성 공합 프로세스를 통해 제조자가 올바른 사용과 사용오류, 즉 정상사용과 관련된 위험을 평가하고 완화시키는데 목적이 있다. 사용성평가는 정상사용 시 발생되는 사용오류를 평가하는 것으로 인위적으로 비정상 사용에서 평가하는 것이 다니다. 사용의 편리성을 위하여 의도된 사용 환경에서 유효성, 효율성 및 사용자 만족도 확립하는 사용자 인터페이스의 특성을 살피고자 IEC 62366 규격에서 사용적합성 평가를 자세히 다루고 있다.

Brief Biosketch

2006 년 KCL 에 입사하여 15 년간 의료기기 기술문서 심사, GMP 심사, 밸리데이션 평가 등 의료기기 관련업무를 수행하였습니다. 의료기기 산업발전에 기여하여 2017 년 경인지방청장 표창, 2018 년 식품의약품안전처장상을 수여하였으며, 식약처에서 지정한 '차세대 의료기기 100 프로젝트'멘토링 전문가로도 활동하였습니다.



Bo-young Kang
Principal Researcher
Daegu Technopark
Digital Transformation Agency

HCI & Usability Evaluation of Home Healthcare Device

Abstract

As life expectancy increases and medical technologies become more advanced, medical devices are being used more often at home by lay users—individuals without formal medical training. Use of healthcare devices and applications in home care settings is rapidly increasing, but the usability of these devices has not been examined systematically. This talk will introduce usability testing cases for user-centered design of home healthcare device. The purpose of usability testing is to ensure the plan for a product's functions, features and overall purpose are in line with what users want by observing how real-life people use the product. Usability testing helps identify which product benefits and functions are most desired by the user and most critical to business success. User-centered design benefits the bottom line by reducing risk, giving products a competitive edge, and more.

Brief Biosketch

Bo-young Kang is Principal Researcher at the Daegu Technopark.
As a Human-Computer Interaction(HCI) researcher, she is assisting startups, small and medium businesses. Earlier in her career, she was Senior Researcher at the Embedded Software Research Center of Kyungpook National University. She received an MSc in Computer Science with a speciality in Networks and Distributed Systems from Kyungpook National University.

The Joint Conference of the
IBEC2021 and the ICBHI2021

Plenary Session 1

Session Chair: Kwang Gi Kim (Gachon University, S. Korea)

11 Nov. (Thursday) Room A (09:30~10:30)

Wearable Devices for Detection of Atrial Fibrillation and Seizure Prediction in Divers

Ki Chon (University of Connecticut, USA)



Ki Chon
Krenicki endowed chair professor and chair of BME
University of Connecticut

Wearable Devices for Detection of Atrial Fibrillation and Seizure Prediction in Divers

Abstract

The efforts of my research group at University of Connecticut have been focused on wearable devices, biosignal processing, and development of novel algorithms for detection of atrial fibrillation (AF) and seizure prediction in Navy divers due to oxygen toxicity. My laboratory has been working on developing low-cost wearable devices and algorithms for continuous monitoring for the above-noted applications. To this end, we have been developing novel and low-cost approaches to intermittently and continuously monitor paroxysmal AF. For intermittent monitoring of paroxysmal AF, we will discuss using a smartphone's video camera to detect AF. For continuous monitoring of paroxysmal AF, we will discuss the development of a low-cost, leadless and wireless wearable device including a smartwatch. My talk will also detail our recent work on using electrodermal activity (EDA) sensors for seizure prediction due to oxygen toxicity in Navy divers.

Brief Biosketch

Ki H. Chon received the B.S. degree in electrical engineering from the University of Connecticut, Storrs; the M.S. degree in biomedical engineering from the University of Iowa, Iowa City; and the M.S. degree in electrical engineering and the Ph.D. degree in biomedical engineering from the University of Southern California, Los Angeles. He spent three years as an NIH Post-Doctoral fellow at the Harvard-MIT Division of Health Science. He is currently the John and Donna Krenicki Professor and Head of Biomedical Engineering at University of Connecticut, Storrs, CT.

He has published 184 peer-reviewed journal articles, and more than 125 book chapters, conference proceedings and abstracts to date, and has 13 U.S. patents granted. He has received more than $22M in grants from the NIH, NSF, DoD and industry. His patent concerning an algorithm for real-time detection of atrial fibrillation has been licensed to a Holter company and the Holter monitor is currently on the market. He is fellow of National Academy of Inventors, International Academy of Medical and Biological Engineering American Institute of Medical and Biological Engineering, and Asia-Pacific Artificial Intelligence Association.

The Joint Conference of the
IBEC2021 and the ICBHI2021

Biomedical Instrumentation

Session Chair: Ki Chang Nam (Dongguk University, S. Korea)

11 Nov. (Thursday) **Room A (10:30~12:00)**

Versatile Dendritic Nanoparticles for Immunotherapy and Liquid Biopsy
Seungpyo Hong (University of Wisconsin-Madison, USA)

Chest Electrical Impedance Tomography towards clinical use
Zhanqi Zhao (Hochschule Furtwangen University, Germany)

Polymer-based, Miniaturized, Flexible and Long-term Reliable Neural Interfacing Devices for Implantable and Wearable Applications
Joonsoo Jeong (Pusan National University, S. Korea)

Remote Monitoring Systems for Individualized Health State During COVID-19 and Beyond: Opinion Piece
In cheol Jeong (Hallym University, S. Korea)



Seungpyo Hong
Milton J. Henrichs Chair Professor
University of Wisconsin-Madison
Yonsei University

Versatile Dendritic Nanoparticles for Immunotherapy and Liquid Biopsy

Abstract: Dendritic polymers have drawn considerable attention to be used as a nanocarrier platform for various therapeutic agents over the past few decades. Major advantages of the macromolecules include: i) the ability to mediate strong multivalent binding; ii) efficient, controlled tumor penetration due to their sub 10 nm size and deformability; and iii) facile multifunctionalization through various conjugation chemistries. In this presentation, our recent efforts on using poly(amidoamine) (PAMAM) dendrimers for immunotherapy and biomarker development will be summarized. For immunotherapy, immune checkpoint inhibitors (ICIs), either in a form of antibody or engineered peptide, targeting PD-L1 on tumor cells were conjugated to a generation 7 (G7) PAMAM dendrimer, followed by characterization, binding kinetics measurements, in vitro cell assays, and in vivo biodistribution/efficacy study. The three independent binding measurements using surface plasmon resonance (SPR), bio-layer interferometry (BLI), and atomic force microscopy (AFM) all revealed that the dendrimer-peptide conjugates exhibited a significantly greater binding kinetics than free peptide, by up to five orders of magnitude. Such enhancement was likely achieved through the multivalent binding effect mediated by dendrimers, which was translated into improved immunotherapy efficiency and in vivo efficacy using a syngeneic mouse model. For the biomarker development, we prepared a capture surface that effectively detects circulating tumor cells (CTCs) from blood of cancer patients. The capture surface consisted of G7 PAMAM dendrimer conjugated with multiple antibodies directed toward tumor cells, along with E-selectin that induces cell rolling. The unique combination of dendrimer-mediated multivalent binding and biomimetic cell rolling resulted in substantially improved capture efficiency, as demonstrated in a series of our previous reports. Recently, we have conducted clinical pilot studies using a large cohort of patients with various cancer. Our clinical results indicate that the nano-engineered capture surfaces exhibit significantly enhanced sensitivity and specificity, which allows precise enumeration of CTCs per mL of blood. The kinetic changes of CTC numbers over the course of treatment well correlated with the clinical outcomes of individual patients. Furthermore, post-capture analysis on the captured CTCs further revealed the characteristics of the cells from individual patients, which would ultimately allow the application of most effective treatment regiments to specific patients for truly personalized medicine. All in all, the results that will be presented indicate the versatility of dendrimers to be used as a nanoscale delivery platform as well as a capture system for circulating biomarkers, demonstrating great potential to change the paradigm of currently available cancer diagnosis, prognosis, and treatments.

Brief Biosketch

Dr. Seungpyo Hong is Milton J. Henrichs Chair Professor of Pharmaceutical Sciences and Director of Wisconsin Center for NanoBioSystems (WisCNano) at University of Wisconsin-Madison (UW-Madison). He holds appointments as Adjunct Professor at the University of Illinois at Chicago (UIC) and Yonsei University, Seoul, Korea, while serving as Associate Editor for Nanomedicine: Nanotechnology, Biology and Medicine of Elsevier. Dr. Hong is also active in entrepreneurship, co-founding a biotech startup called Capio Biosciences where he serves as President. He graduated from Hanyang University in Seoul, Korea with B.S. and M.S. degrees in polymer engineering in 1999 and 2001, respectively. He then received his PhD in Macromolecular Science and Engineering at University of Michigan in 2006 and joined MIT as a postdoctoral associate in the laboratory of Prof. Robert Langer. From 2008 to 2014, he was an Assistant Professor at UIC where he was promoted to Associate Professor with tenure in 2014, and subsequently joined the UW-Madison faculty as Full Professor in 2016. To date, Prof. Hong's research has culminated in ~100 peer-reviewed articles that have ~16,000 citations and 25 issued or pending patents, while delivering over 150 invited talks worldwide and over 200 conference proceedings.



Zhanqi Zhao
Ph.D.
Furtwangen University, Germany
Fourth Military Medical University, China

Chest Electrical Impedance Tomography towards clinical use

Abstract

Chest electrical impedance tomography (EIT) is a non-invasive bedside imaging tool that captures regional lung ventilation and perfusion. Sixteen or thirty-two electrodes are typically attached to the thorax surface and imperceptible high-frequency electrical currents are injected. Resulting voltages and reconstructed regional impedance values reflect the volume changes of air and blood in the lung tissue. Chest EIT applications cover a broad field of clinical practice, including patients with acute respiratory distress syndrome, with Coronavirus disease 2019, acute exacerbation of chronic obstructive pulmonary disease (COPD) under mechanical ventilation, as well as patients with asthma, cystic fibrosis and COPD performing pulmonary function test. EIT images contain information on multiple physiological and pathophysiological processes that require further data processing depending on the intended clinical applications. The presentation introduces the motivation and technical aspects of EIT, as well as an overview of data analysis and current clinical applications.

Brief Biosketch

Dr. Zhao received his Ph.D. from Ludwig Maximilians University Munich, Germany in 2013. Since 2008, he works on lung protective ventilation and clinical applications of electrical impedance tomography. Since 2015, he is supporting over 90% of the EIT clinical studies in China. Up-to-date he has published over 80 SCI papers, among which over 50 as first or senior author. Currently he is associated with Furtwangen University Germany and Fourth Military Medical University China. He also works as consultant for several medical device companies.



Joonsoo Jeong
PH.D.
Pusan National University
Biomedical Convergence Engineering

Miniaturized and Long-Term Reliable for Neural Interfaces for Implantable and Wearable Applications

Abstract

Neural interfaces are implantable or wearables electronic devices for restoration or substitution of the impaired sensory, motor, and cognitive neural functions. Hermetic encapsulation of such devices are a critical importance for long-term stable and safe operation of the devices. Conventionally metallic packages have been most widely used for enclosure of the electronics, but they are bulky, heavy, and limited capability of miniaturization. Alternatively, polymeric materials have been recently demonstrated, but they have questionable long-term reliability. This study demonstrates liquid crystal polymer (LCP) and HfO_2 as new encapsulation and substrate materials for next-generation neural interfaces that can provide sufficient long-term reliability yet with the virtues of polymeric materials. Microfabrication, thermal deformation, monolithic integration and packaging using LCP has been developed to create a miniaturized and long-term reliable retinal prosthesis and cortical stimulator. Its functionality has been demonstrated in vivo and its long-term durability has been tested in accelerated aging test to show expected lifetime of >10 years in body condition. HfO2 is utilized as thin barrier layer for sub-milimeter sized cortical implants with distributed network. Similar technology is utilized in wearable electronics as well to create multi-functional wearable patch for healthcare monitoring applications.

Brief Biosketch

Professional Career

2018. 9 - present: Assistant professor, School of Biomedical Convergence Engineering, Pusan National University
2016. 4 – 2018. 8 : Postdoctoral Fellow, Brown University, RI, USA

Education

2015. 8 : Ph.D. in Electrical Engineering and Computer Science, Seoul National University, Korea (advisor: Sung June Kim)
2011. 2 : M.S. in Electrical Engineering and Computer Science, Seoul National University, Korea (advisor: Sung June Kim)
2009. 2 : B.S. in Electrical Engineering, Seoul National University, Korea



In cheol Jeong, PhD
Associate Professor
Hallym University, S.Korea
Icahn School of Medicine at Mount Sinai, USA

Remote monitoring systems for individualized health state during COVID-19 and beyond: opinion piece

Abstract

Since the COVID-19 pandemic, remote monitoring has rapidly emerged as a significant player in the healthcare system. In this talk, classical remote monitoring technologies and limitations will be reviewed, and the accelerating transition of medical systems to digital healthcare technologies through convergence with existing or new technologies will be discussed. Discussions will be made on how remote monitoring technology transforms current health care and what revolution it brings to healthcare workers, caregivers, patients, suppliers, and payers. An opinion will be suggested that future remote monitoring technology innovation will explore the direction of development as a technology that non-invasively tracks the progression of the disease and prevents reactive medical severe interventions. Efforts will be pointed to the research ethics mindset necessary as a global researcher to prepare for and overcome another crisis.

Brief Biosketch

In cheol Jeong is an associate professor of Artificial Intelligence Convergence School at Hallym University in South Korea and an adjunct associate professor of Population Health Science and Policy at Icahn School of Medicine at Mount Sinai in New York City, NY, USA. He was a faculty member in Hopkins inHealth Initiative at Johns Hopkins University in Baltimore, MD, USA, and a grant reviewer at National Science Foundation. One of the leading research interests in medical technology innovation focuses on developing appropriate healthcare technologies worldwide for individual/public health interventions.

The Joint Conference of the
IBEC2021 and the ICBHI2021

BME Award Lecture

Session Chair: Session Chair: Yangmo Yoo (Sogang University, S. Korea)

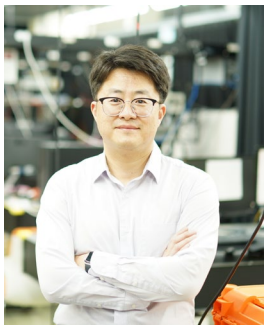
11 Nov. (Thursday) **Room B (10:30~12:00)**

Multi-modal Imaging: Photoacoustic Imaging Plus More

Chulhong Kim (Pohang University of Science and Technology, S. Korea)

Modulating Neutrophils for the Treatment of Severe Diseases using Biomaterials

Chun Gwon Park (Sungkyunkwan University, S. Korea)



Chulhong Kim
POSTECH Young Distinguished Professor and Mueunjae Chair Professor
Electrical Engineering
Convergence IT Engineering and Mechanical Engineering

Multi-modal Imaging: Photoacoustic Imaging Plus More

Abstract

Trans-energy imaging modalities have been significantly explored to overcome existing problems in conventional imaging modalities with respect to spatial/temporal resolutions, penetration depth, signal-to-noise ratio, contrast, and so on. Among them, photoacoustic imaging, an emerging hybrid modality that can provide strong endogenous and exogenous optical absorption contrasts with high ultrasonic spatial resolution, has overcome the fundamental depth limitation while keeping the spatial resolution. The image resolution, as well as the maximum imaging depth, is scalable with ultrasonic frequency within the reach of diffuse photons. In this presentation, the following topics will be discussed; (1) multiscale and multiparametric trans-energy imaging systems, (2) novel deep-learning powered image processing, (3) recent clinical study results, and (4) efforts to commercialization.

Brief Biosketch

Dr. Chulhong Kim studied for his Ph.D. degree and postdoctoral training at Washington University in St. Louis. He currently holds POSTECH Young Distinguished Professorship and Mueunjae Chair Professorship of Electrical Engineering, Convergence IT Engineering, and Mechanical Engineering at Pohang University of Science and Technology in Republic of Korea. He is also the Chief Executive Officer of Opticho Inc., a spinoff company to commercialize the preclinical and clinical photoacoustic imaging systems. He was the recipients of the Science and Technology Award of the Month for December 2021 by the Korean Minister of Science and ICT, the LINA+50 Creative Innovation Award, the 2020-2021 IEEE EMBS Distinguished Lecturer, the 2017 IEEE EMBS Early Career Achievement Award, the 2017 KAST Young Scientist Award, the 2016 Nightingale Award from IFMBE, etc. He is also elected as a member of Young Korean Academy of Science and Technology (Y-KAST). He is a Fellow of the SPIE.



Chun Gwon Park

Assistant Professor

Department of Biomedical Engineering,
Sungkyunkwan University, Suwon, Republic of Korea

Modulating neutrophils for the treatment of severe diseases using biomaterials

Abstract

Neutrophils, innate immune cells pivotal for the antibacterial and antiviral defense, fulfill their role through several cellular mechanisms, including phagocytosis. They also form neutrophil extracellular traps (NETs), a reticulated scaffold structure composed primarily of a DNA backbone and several functional proteins. NETs exert their anti-infective activity by trapping invading pathogens and killing them through virulence factor secretion. However, under serious disease conditions such as sepsis or cancer, NETs could trigger adverse reactions in the body, such as inducing tissue damage or providing shelter for dormant cancer metastasis, thereby exacerbating the disease. To effectively reduce NET-related harmful conditions and treat the diseases, we developed a long-lasting DNase-1 nanoparticle to effectively cleave NETs, thereby reducing NET-related adverse effects and helping to effectively treat various diseases.

Brief Biosketch

Prof. Chun Gwon Park is an Assistant Professor in the Department of Biomedical Engineering at Sungkyunkwan University, Korea. He received his B.S. (2009) from Hanyang University and his Ph.D. (2014) from Seoul National University. Then, Dr. Park worked as a research fellow at Harvard Medical School and Dana-Farber Cancer Institute, where he focused on biomaterials-based cancer immunotherapy until he became a faculty member at Sungkyunkwan University in 2018. His research is mainly focused on developing innovative biomaterials-based drug delivery approaches to increase the efficacy and decrease the toxicity of clinically available therapies including cancer immunotherapy. Dr. Park has published 50 peer-reviewed research papers including Science Translational Medicine, Nature Communications, Advanced Science, Biomaterials, and Science. Dr. Park was awarded domestically- or/and internationally recognized Awards including Young Scientist Award from the Korean Society for Biomaterials, Korea (2021).

The Joint Conference of the
IBEC2021 and the ICBHI2021

Award Session 1

Session Chair: Do-Won Kim (Chonnam National University, S. Korea)
Chulmin Joo (Yonsei University, S. Korea)
Jinmyoung Joo (Ulsan National Institute of Science and Technology, S. Korea)

11 Nov. (Thursday) **Room C (10:30~12:00)**

A-001. Non-linear Microfluidic Cell Stretching Enables Highly Effective Intracellular Delivery for Genome Editing — Chan Kwon (Korea University, S. Korea)

A-002. Foley Catheter Assembled with Sustained Drug Releasing Polymeric layer for Reducing Catheter-related Bladder Discomfort — Cho Rim Kim (Seoul National University, S. Korea)

A-003. Phenotyping of Breast Cancer Cells by Deep Hybrid Learning Network — Chanhong Min (Korea Advanced Institute of Science and Technology, S. Korea)

A-004. Feasibility Test of a Stimulation Artifact-free Stimulating and Recording System for Closed-loop Therapeutic Neuromodulation — Wonok Kang (Pohang University of Science and Technology, S. Korea)

A-005. A Portable Real-Time ECG Monitoring System — Jin-Woo Jeong (Gachon University, S. Korea)

A-006. Soft, Wireless Bioresorbable Neurochemical System for Postoperative Management of Brain-Disorders — Seung Min Yang (Korea University, S. Korea)

Non-linear microfluidic cell stretching enables highly effective intracellular delivery for genome editing

Chan Kwon[1,2], GeoumYoung Kang[1], and Aram Chung[1,2*]

[1]School of Biomedical Engineering, Korea University, Seoul, 02841, Republic of Korea

[2]Interdisciplinary Program in Precision Public Health, Korea University, Seoul, 02841, Republic of Korea

[*]ac467@korea.ac.kr

Abstract

A novel non-linear cell stretching microfluidic intracellular delivery platform is presented, enabling highly effective intracellular delivery of external biomolecules into various cell types. A viscoelastic fluid, methylcellulose (MC) solution, was used to achieve significant enhanced intracellular delivery. In the proposed platform, cells suspended in the MC solution were injected into a channel, where cells rapidly pass through a single constriction with a dimension slightly smaller than the cell diameter. Due to the utilization of the MC solution, a high shear force was applied to the cells, effectively generating transient cell membrane discontinuities; therefore, exogenous cargos can be transported into cells through the created membrane nanopores. With this platform, a high delivery efficiency (>97%), high throughput (>10^6 cells/min), low-cost operation (<$1), nearly clogging-free performance, and rapid delivery of various biomolecules into different immune cells were shown for cancer immunotherapy applications.

Background

Cell therapies, a potent and versatile alternative to anticancer drugs, treat disease by adjusting the expression of specific gene. For example, using chimeric antigen receptor (CAR)-engineered T cells can be shown the complete remission of refractory acute lymphoblastic leukemia (ALL) [1]. To artificially manufacture T cells which recognize cancer cells, genomic alteration is necessary.

Introduction of external biomolecules into living cells is a key step to adjust genomic property. Traditionally, viral transduction, electroporation, and lipofections are used for cellular engineering; however, these techniques are undesirable due to high cost, low cell viability, loss of cell functionality, and inconsistent delivery. Recently, microfluidic platforms have shown high possibilities as alternative solutions [2]. Among them, the cell squeezing platform gets considerable attention because of its simplicity, versatility, and high delivery efficiency. Cells are designed to pass through a series of narrow constrictions that induce cell membrane discontinuities. But the method has limitation such as serious channel clogging and low cell viability [3].

Here, a non-linear cell squeezing platform is presented using viscoelastic fluids, methylcellulose (MC) solution. Due to the high shear force given by the MC solution, significantly higher level of deformation can be achieved with the use of a single constriction with a dimension slightly smaller than the cell diameter maintaining high cell viability without channel clogging. Therefore, a high delivery efficiency, high throughput, low-cost operation, and near-zero clogging are demonstrated for various immune cell lines, providing high potential for cell-based research.

Methods

The proposed platform was fabricated by standard photolithography and PDMS soft lithography. The delivery efficiency of the cells was evaluated using flow cytometry, and cell viability was measured using a trypan blue assay.

Results and Discussion

The cells suspended in the MC solution were injected into a linear microchannel with a single narrow constriction (Figure. 1(a)) as one-step operation. As presented in Figure 1(d), close to 100% delivery efficiency for 3-5 kDa FITC-Dextran into K562 cells with a cell density of 10^6 cells/ml was demonstrated in the use of MC solution whereas nearly-zero delivery was showed for pure media. The delivery of external biomolecules into cells was affected by the flow rate, MC concentration, and channel configuration. By changing such parameters, an optimal operational condition was identified that yielded the highest delivery efficiency and cell viability (Figure. 1(e)-(h)).

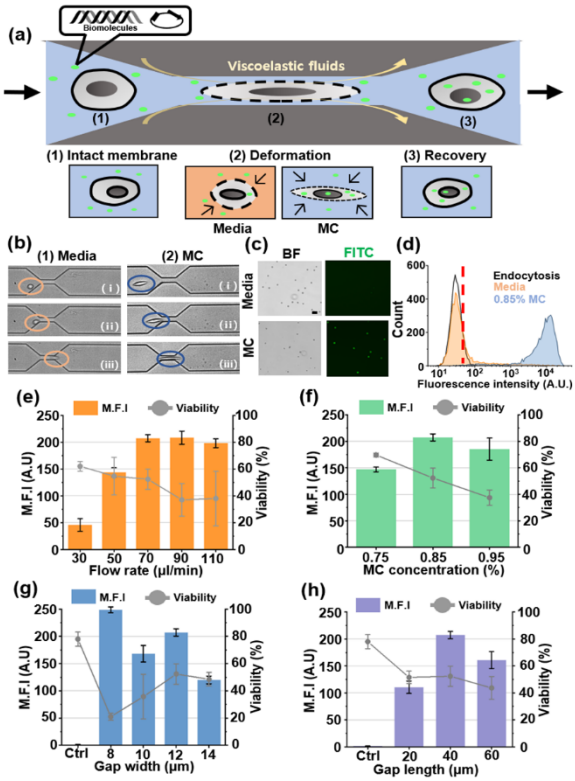


Figure.1 (a) Operating principles of intracellular delivery, (b) high-speed camera images showing cell deformation of media and MC solution, (c)-(d) fluorescence microscopy images and fluorescence intensity histograms for internalization of 3-kDa FITC-dextran into K562 cells, (e)-(h) Optimization process: MFI fold change and viability for various flow rate, MC concentration, gap width, and gap length (scale bar: 50 μm).

Under the identified optimal operation condition, a trial was executed to test various cell types and deliver different dextran sizes (3-2000 kDa) (Fig. 2(a)-(b)). As shown, the presented method was insensitive to the evaluated cell types and cargo materials. To further evaluate the possibility of the platform for functional nanomaterial delivery, EGFP mRNA was delivered into K562 cells. As shown in Fig. 2(c)-(d), approximately 97% mRNA transfection efficiency (mean fluorescence intensity fold change of close to 40) was obtained, demonstrating the potential of the platform for genome engineering.

Conclusion

We present a novel non-linear microfluidic cell stretching platform utilizing high fluidic cell shearing, which is characterized by high delivery efficiency, high throughput, nearly clogging-free, low-cost

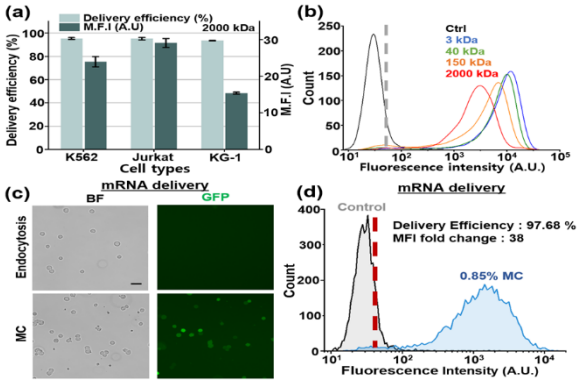


Figure.2 (a) Delivery efficiency and MFI fold change for various cell types, (b) Fluorescence intensity histograms for various FITC-dextran sizes, (c) and (d) mRNA delivery: fluorescence microscopy images and fluorescence intensity histograms for internalization of EGFP mRNA into K562 cells (scale bar: 50 μm).

operation, and simple operation. Thus, the proposed platform provides a practical, robust, and cost-effective approach that is expected to influence cell-based research and genome engineering.

Acknowledgements

This work was supported by the Samsung Research Funding and Incubation Center for Future Technology (Grant No. SRFCIT1802-03) and the National Research Foundation of Korea (NRF) funded by the Ministry of Science and ICT (No. 2021R1A2C2006224).

References

1. S. A. Grupp, M. Kalos, D. Barrett, R. Aplenc, D. L. Porter, S. R. Rheingold, D. T. Teachey, A. Chew, B. Hauck, J. F. Wright, M. C. Milone, B. L. Levine, and C. H. June, “Chimeric antigen receptor-modified T cells for acute lymphoid leukemia,” New England Journal of Medicine. 368(16), 1509-1518 (2013).
2. J. Hur, and A. J. Chung, “Microfluidic and nanofluidic intracellular delivery,” Advanced Science. 2004595 (2021).
3. A. Sharei, J. Zoldan, A. Adamo, W. Y. Sim, N. Cho, E. Jackson, S. Mao, S. Schneider, M. Han, A. Lytton-Jean, P. A. Basto, S. Jhunjhunwala, J. Lee, D. A. Heller, J. W. Kang, G. C. Hartoularos, K. Kim, D. G. Anderson, R. Langer, and K. F. Jensen, “A vector-free microfluidic platform for intracellular delivery,” PNAS. 110 (6), 2082–2087 (2013).

Foley Catheter Assembled with Sustained Drug Releasing Polymeric layer for Reducing Catheter-related Bladder Discomfort

Cho Rim Kim[a,1], Young Eun Yoon[b], Se-Na Kim[c], Min Ji Kim[a], Hong Sang Moon[b,] and Young Bin Choy[a,c,d,]

[a] *Interdisciplinary Program for Bioengineering, College of Engineering, Seoul National University, Seoul 08826 South Korea*

[b] *Department of Urology, College of Medicine, Hanyang University, Seoul 04763 South Korea*

[c] *Institute of Medical & Biological Engineering, Medical Research Center, Seoul National University, Seoul 03080 South Korea*

[d] *Department of Biomedical Engineering, Seoul National University, College of Medicine, Seoul 03080 South Korea*

chorim721@snu.ac.kr

Abstract

Foley catheters (FCs) are used in clinical settings to aid in detrusor contraction in hospitalized patients. However, an inserted FC often causes catheter-related bladder discomfort. To address this, we propose an FC abled with local, sustained release of an anesthetic drug, lidocaine. For this, a thin strand composed of poly (lactic-co-glycolic acid) and lidocaine was prepared as a drug delivery carrier, which was then assembled with the FC. Our results confirmed that the drug-releasing FC could show the pain-relief effects for up to seven days. Cystometrogram tests indicated that the drug-releasing FC could significantly alleviate a bladder discomfort compared with the FC without lidocaine. Furthermore, the expression of pain-related inflammatory markers, such as nerve growth factor, cyclooxygenase-2, and interleukin-6 in the biopsied bladder tissues was significantly lower when the drug-releasing FC was placed. Therefore, we conclude that an FC assembled with a drug-loaded polymer strand can release lidocaine to allow for the mitigation of bladder discomfort during the period of FC insertion.

Background

To drain urine and relieve urethral retention in hospitalized patients, Foley catheters (FCs) are placed in the urinary bladder through the urethra. Mostly in clinical settings, FCs are inserted for a short period of 2-4 days[1]. However, 45%–90% of these patients experience catheter-related bladder discomfort (CRBD). Usually, the CRBD associate with upregulated inflammation marker of the urethra and bladder. In addition, these patients also experience overactive bladder symptom of involuntary bladder smooth muscle contraction caused by excessive nerve transmission from the bladder detrusor muscle to the muscarinic receptor 3.

To reduce CRBD, drugs are often prescribed as oral administration and injection. However, these bolus drug need to be administered in large doses, which carries the risk of the systemic toxicity. Therefore, local anesthetic drug release could be and effective strategy to reduce CRBD. In this aspect, we suggest an FC capable of sustained release of an anesthetic drug as a single medical device entity with drug delivery functionality. In this study, we prepared a thin strand composed of poly (lactic-co-glycolic acid) (PLGA) and the anesthetic drug, lidocaine. This strand was then assembled with an FC by wounded around its surface to produce L_PLGA_FC. As the strand was present only at the surrounding surface of the FC, the detrusor contraction passage would not be blocked. After the insertion of the L_PLGA_FC via the urethra, lidocaine could be released slowly from the drug-releasing PLGA strand at the FC surface, resulting in sustained efficacy in pain relief and anti-inflammation without additional procedures for drug administration.

Methods

To prepare the lidocaine releasing FC, we prepared the strand composed of PLGA and lidocaine. For this, PLGA and lidocaine was dissolved in dichloromethane (DCM) and then electrosprayed under following conditions: needle size, 24G; tip to collector distance, 10 cm; pump speed, 20 ml/h; voltage, 20 kV. The collected sheet was cut into a 2 mm width strand and wrapped around the surface of the FC. An additional annealing process was

performed in oven at 60 ºC, for a seamless attachment between FC and the strand.

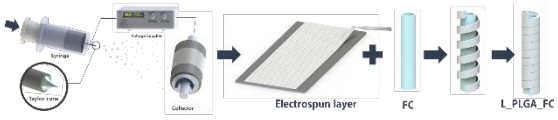


Figure 1. Manufacturing process of L_PLGA_FC.

The drug-releasing PLGA strand was analyzed with the scanning electron microscopy (SEM), Fourier transform infrared (FTIR) spectroscopy, and powder X-ray diffractometry (PXRD). The drug release profiles of the L_PLGA_FC were assessed under *in vitro* environments using phosphate-buffered saline (PBS) (pH 7.4) at 37 °C and measured by high-performance liquid chromatography. To examine *in vivo* efficacy, L_PLGA_FC was inserted in the normal or cystitis-induced bladders of rats. Cystometrogram (CMG) tests were performed to monitor bladder discomfort. Finally, bladder biopsies were performed at the end of the experiments and the tissue samples were analyzed for the expressions of nerve growth factor (NGF), cyclooxygenase-2 (COX-2), and interleukin-6 (IL-6).

Results and Discussion

As shown in the FTIR spectra, the characteristic peaks of lidocaine (e.g., 3030 cm-1: aromatic ring, 1630-1690 cm-1: carbonyl groups) were observed, indicating the prevalence of the drug on the layer. Also, the XRD patterns of lidocaine indicating the crystalline structure. However, the characteristic peaks disappeared in the drug-releasing layer, implying that the lidocaine was well distributed at the molecular level. The uniform thickness of the layer assembled around the FC was confirmed by SEM to be 51.79 ± 2.41 μm.

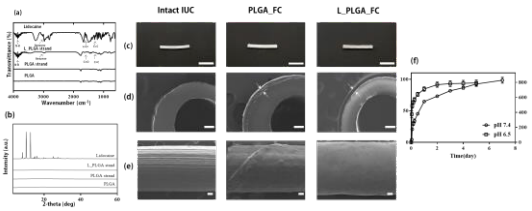


Figure 2. Characterization of the L_PLGA_FC.

L_PLGA_FC showed sustained drug release for more than 5 days at both pHs of 7.4 and 6.5. Based on the CMG analysis performed three days after FC insertion, the results indicated that the drug released from the L_PLGA_FC effects on the decreasing the average bladder pressure and increasing the average interval of detrusor contraction, meaning the L_PLGA_FC lowers the sensitivity of the bladder. Also, when tested in cystitis-induced bladders, animals treated with L_PLGA_FC showed a statistically significantly lower expression of all factors of NGF, COX-2, and IL-6 than the control groups which is known as the pain and inflammatory relevant. According to the obtained results, it can be concluded that the developed drug-delivery FC is a promising device to aid urine drainage with a minimized complication of CRBD.

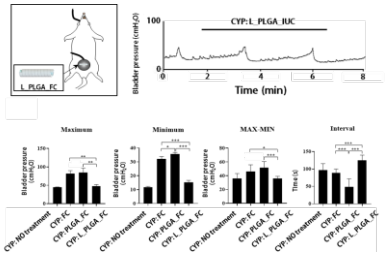


Figure 3. CMG test results.

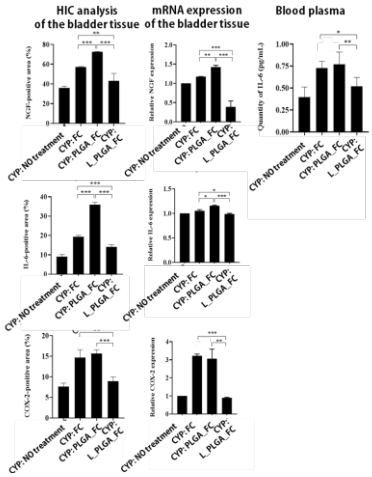


Figure 4. NGF, Cox2 and IL-6 expression.

Acknowledgements

This work was supported by Samsung Research Funding & Incubation Center of Samsung Electronics under Project Number SRFC-IT2001-01.

References

1. Aaronson, D. S., Walsh, T. J., Smith, J. F., Davies, B. J., Hsieh, M. H., & Konety, B. R. (2009).

A-003

Phenotyping of breast cancer cells by deep hybrid learning network

C. Min[1], H. Jeong[1], S. Yang[2] and J.H. Shin[1]

[1]Department of Mechanical Engineering, Korea Advanced Institute of Science and Technology, Daejeon, Korea

[2]Department of Biomedical Engineering, Yonsei University, Wonju, Korea

j_shin@kaist.ac.kr

Abstract

The complexity of high-dimensional information from dynamic responses of breast cancer cells poses a significant constraint on the phenotyping scheme based on few biomarkers. This study designed a deep hybrid learning network to classify breast cancer cell heterogeneity using single-cell morphology. Deep convolutional neural network was implemented to automatically extract more than 200 morphological features from ~40,000 cell images. Subsequently, unsupervised clustering was performed in a reduced latent state-space to investigate temporal fluctuation inherent in breast cancer. The proposed framework may serve as a cornerstone for a novel cancer diagnostic platform.

Background

Heterogeneity in breast cancer has been a critical issue in hindering accurate diagnosis at the cellular level [1]. Conventionally, biomolecular analyses like polymerase chain reaction (PCR) or immunostaining were implemented to obtain absolute expression levels of gene or proteins [2]. However, due to genomic instability inherent in cancer, heterogeneity is amplified by dynamic responses from cell proliferation, metabolism, and migration [3]. In this study, we utilized single-cell morphology, an ensemble of molecular underpinnings that can be tracked in time, to encapsulate spatiotemporal diversity. The live images of single-cell morphology were automatically segmented by a deep convolutional neural network, and a cell tracking algorithm was developed to search for a single-cell state. More than 200 morphology features were extracted and embedded in reduced latent state-space to subsequently perform unsupervised clustering to classify breast cancer cells by incorporating temporal fluctuation.

Methods

Figure.1 shows a deep hybrid learning framework for phenotyping breast cancer cells. Non-invasive breast cancer cell line MCF7 was used to model spatiotemporal heterogeneity by performing single-cell cloning. The cancer cells were seeded on a glass substrate without any chemical treatment and moved to a phase-contrast microscope (Axiovert, Carl Zeiss) for live-cell images.

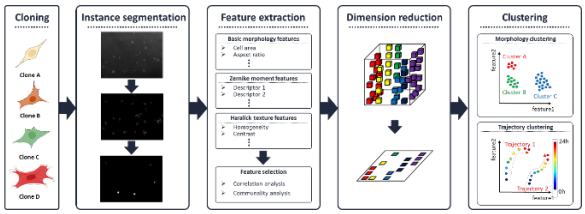


Figure 1. Deep hybrid learning framework for classifying spatiotemporal cancer heterogeneity.

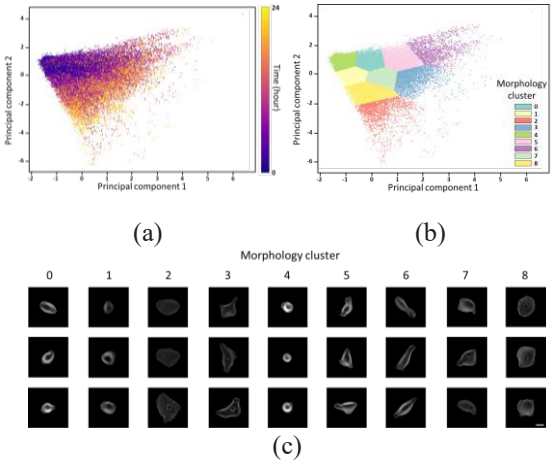
Attention Residual U-Net with binary focal loss was utilized to efficiently isolate cell boundaries from limited annotations to segment and track single-cell states. The parameters needed for learning were batch size 20, epochs 200, learning rate 0.01, and adam optimizer. Evaluation of the segmentation performance was conducted by dice coefficient and Jaccard index, which resulted in 0.6735 and 0.5097, respectively, and manual comparison of the predicted cell boundaries with real cell images. By performing morphology operation and flood fill, the inner region of the cell was labeled while segregating adjacent cells. The bounding box was set on every last frame of each cell trajectory, while its size was proportional to cell size.

From ~40,000 morphology datasets, we extracted more than 200 morphological features consisting of basic morphology, Zernike moments, and Haralick texture features. The basic morphology features such as cell area, aspect ratio, and circularity aid an intuitive

understanding of the geometric shape of a cell. Zernike moments are a range of descriptors based on the circle with its center on the centroid of the cell, which each feature displays orthogonality. Haralick texture features calculate intensity variation and discover local density inside a cell. Subsequently, communality and correlation analysis was performed for feature selection. Features with communality less than 0.4 and correlation over 0.9 were filtered out to increase the influence on the principal component and minimize the redundancy, respectively. Selected features were directly applied for principal component analysis to transform high-dimensional space into reduced two-dimensional latent space while preserving 70% of the total variance.

Results and Discussion

Figure. 2(a) shows a latent morphology state-space with the time evolution. We could observe that the initial stage of cell morphology is concentrated where principal component 1 (PC1) is low and principal component 2 (PC2) is high. The morphology states gradually matured and progressed to the direction PC1 increases. Unsupervised K-means clustering defined nine morphology clusters, as shown in Figure 2(b). The position where morphology cluster 4 resides closely aligned with the initial stage and was densely populated. In contrast, the mature stages of morphology clusters 2, 3, and 6 were highly heterogeneous. When compared with real cell morphologies depicted in Figure 2(c), the morphology cluster 4 exhibited a small, circular shape, typical of immature cells. Furthermore, cell morphologies within the cluster were highly consistent, while mature state clusters 2, 3, and 6 showed diverse shapes parallel with the reduced latent state-space.

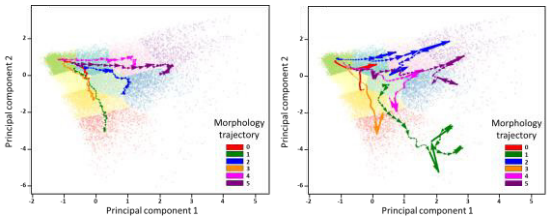


(a) (b)

(c)

Figure.2 (a) Temporal evolution of the state-space, (b) defined morphology clusters and (c) Real cell images for the clusters

Figure. 3 illustrates the dynamic pattern of cancer cell morphology due to temporal heterogeneity. Time series K-means clustering based on Euclidean distance determined six morphology trajectories with identical starting points and propagated into disparate destinations. However, by employing dynamic time warping (DTW) distance, we could visualize significant fluctuation and detailed variation in morphology for each path. Morphology trajectory 2 seemed to be very dynamic, displaying back and forth motion, whereas trajectory 0 tended to have directed motion with little variability. We captured dynamic patterns from spatiotemporal heterogeneity of breast cancer cells by unsupervised time series clustering.



(a) (b)

Figure.3 Classification of temporal heterogeneity by (a) Euclidean distance and (b) DTW distance

Acknowledgments

This research was supported by KAIST Venture Research Program for Master's and Ph.D. Students in the College of Engineering and National Research Foundation of Korea (NRF) grant funded by the Korea government (NRF-2021R1A2C3008408)

References

1. F. Pareja, C. Marchio, F. C. Geyer, B. Weigelt, J. S. Reis-Filho, "Breast cancer heterogeneity: Roles in tumorigenesis and therapeutic implications," Current Breast Cancer Reports. 9(1), 34-44 (2017).
2. K. A. Eckert, T. A. Kunkel, "DNA polymerase fidelity and the polymerase chain reaction," Genome Research. 1(1), 17-24 (1991).
3. J. R. M. Black, N. McGranahan, "Genetic and non-genetic clonal diversity in cancer evolution," Nature Reviews Cancer. 21(6), 379-392 (2021).

Feasibility test of a stimulation artifact-free stimulating and recording system for closed-loop therapeutic neuromodulation

Wonok Kang[1] and Sung-Min Park[1,2*]

[1]School of Interdisciplinary Bioscience and Bioengineering, POSTECH, Pohang, Korea

[2]Department of Convergence IT Engineering, POSTECH, Pohang, Korea

sungminpark@postech.ac.kr

Abstract

Real-time biosignal sensing in the brain or peripheral nerves is essential to implement a closed-loop therapeutic neuromodulation system and to elucidate biomarkers during therapy, however, stimulation artifact often contaminates the electrophysiological recordings and finally makes it difficult to use the recorded data. In this study, we designed a stimulation artifact-free neuromodulation system that operates in real-time and requires low computational cost. The proposed method was validated through *in silico* and *in vitro* approaches, and the results showed the potential for application to *in vivo* conditions.

Background

Electrical stimulation has received attention as a therapeutic modality for various diseases by modulating the nervous system [1]. In particular, closed-loop neuromodulation is a promising therapeutic strategy to deliver stimuli only when the patient is symptomatic, thus improving device lifetime and reducing possible side effects [2]. However, large stimulation artifacts compared to spontaneous neural activity interfere with biomarker computations, making it difficult to perform real-time patient's symptom analysis. Numerous studies have been conducted to remove artifacts from the digitized signals by back-end cancellation methods such as data reconstruction, artifact subtraction, and component decomposition. To address the challenges in recording the neural signals contaminated with stimulation artifacts, we developed a new technique that can remove artifacts even at low sampling rates by shifting the frequency component of the stimulus to outside the range of region of interest (ROI). The proposed method was validated by using computer simulations and *in vitro* experiments, demonstrating its superior performance.

Methods

A conceptual overview and validation method of the proposed closed-loop stimulation modality is shown in Figure 1. Biosignals recorded from specific region are used to detect abnormal neuronal activity in real-time. Once a signal that meets certain conditions occurs, the controller makes a modulated stimulus shape with pre-programmed parameters and delivers it to current pump.

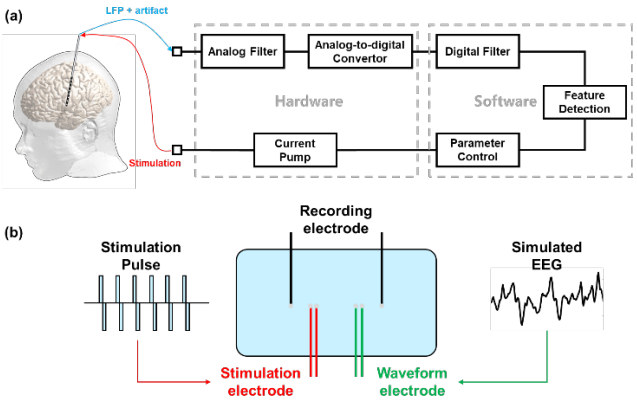


Figure 1. (a) Conceptual diagram of an artifact-free closed-loop neuromodulation system.
(b) experimental setup for performance validation.

To confirm the feasibility of our devised method, we first performed theoretical calculations. We investigated that a single frequency sinewave and a pulse stimulus several orders of magnitude larger than sinusoids could be separated. Artifact removal performance was confirmed at a range of values from high to low sampling rates to see if this technique would be plausible even at really low sampling rates. All calculations were made using custom MATLAB (MathWorks, USA) scripts.

Next, to evaluate the performance of our proposed methods in real-world conditions, *in vitro* phantom

experiments were conducted using a custom-made neuromodulation system comprised a recording module (using ADS1299, Texas Instruments, USA), a stimulation module (using DAC8580, Texas Instruments; MC34074, ON semiconductor, USA), and custom LabVIEW (National Instruments, USA) program. The phantom was made by 0.9% saline solution and the electrodes were fabricated by polyester-insulated stainless steel wires (Goodfellow, UK). To simulate the *in vivo* conditions, the actual recorded EEG data was injected to the phantom via electrodes, and stimulus artifacts much larger than that were superimposed on the phantom as shown in Figure 1, (b). Experimental results were observed and compared in both time domain and frequency domain.

Results and Discussion

Figure 2 shows simulated signals superimposed with a 130 Hz pulse stimulation and a 10 Hz sinusoidal waveform. The maximum amplitude of the pulse stimulation is thousands of times larger than that of 10 Hz signal. When the sampling rate is lowered, the huge artifacts (pulse signals) were recorded distortedly (see blue line results from 16k, 2k, and 500 SPS). However, the filtered data clearly showed a 10 Hz sinusoidal signal, almost identical to the stimulation off condition. Even at low sampling rates, sinusoidal signals were recovered regardless of the aliased artifact.

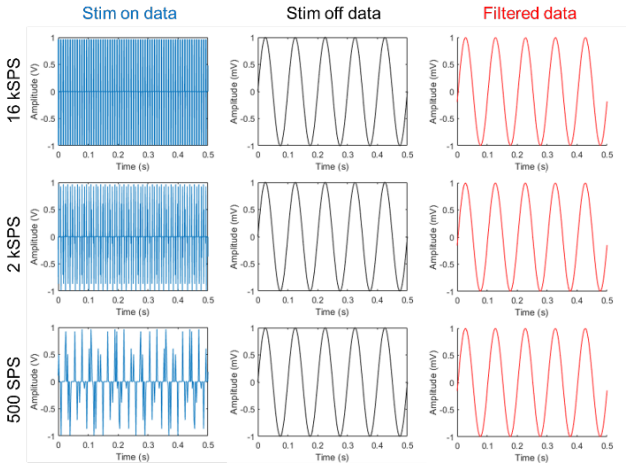


Figure 2. Time-voltage series during 10 Hz sinusoids and 130 Hz pulse stimulation sampled at 500, 2k, and 16 kSPS.

Finally, we evaluated the artifact removal method using simulated EEG signals in saline phantom. Figure 3. (a) shows the power spectral density (PSD) of the baseline, contaminated, and filtered signals. The magnified figure in the ROI (1-100 Hz) confirmed that filtered results were almost identical to the baseline, but the contaminated ones were significantly different. Figure 3. (b) also demonstrated the superior artifact-removal performance of the proposed method in time domain. With these results, we believe that this novel method has potential applications for preclinical and clinical applications.

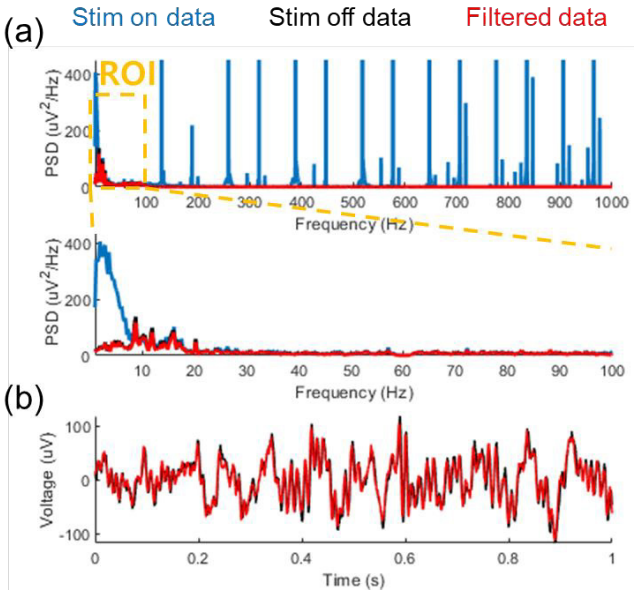


Figure 3. (a) Frequency response during stimulation in saline phantom. (b) Comparison of baseline and filtered signals in time domain.

Acknowledgements

This research was supported by the following sources: the Basic Science Research Program through the National Research Foundation of Korea (NRF) funded by the Ministry of Science and ICT (NRF-2017R1A5A1015596), the NRF funded by the Ministry of Education (2021M3H4A1A03049084), and the '2021 Joint Research Project of Institutes of Science and Technology'.

References

1. Famm, Kristoffer, et al. "A jump-start for electroceuticals," *Nature*, Vol 496, No. 7444, p.159-161, 2013.
2. Andy Zhou, Benjamin C Johnson, Rikky Muller, "Toward true closed-loop neuromodulation: artifact-free recording during stimulation," Current Opinion in Neurobiology, Vol 50, p.119-127, 2018.

A Portable Real -Time ECG Monitoring System

Jin-Woo Jeong[1], Young-Joon Kim[1]

[1]Department of Electronic Engineering, Gachon University, Seongnam, Korea

youngkim@gachon.ac.kr

Abstract

This work designs a real-time portable electrocardiogram (ECG) monitor device. The monitor can continuously monitor human ECG signals and heart rates with two electrode pads placed on the chest (lead II) and display the ECG signal on an android device via wireless communication in real-time. Both analog notch filters and digital filters were implemented to make the instrument insensitive to interference noise so that the system can be used in everyday environment. The measured ECG signal is sent to the mobile device for real time display and data logging. The monitoring device is fabricated in a small footprint (10mm × 10mm) and encapsulated in a plastic housing for portability.

Background

ECG measurements are the basis for the diagnosis of most cardiac arrhythmia and cardiovascular disease (CVD) [1]. CVD often leads to heart attacks, strokes and death [2]. Although ECG monitor has the potential benefit of screening patients which can lead to an absolute risk reduction, frequent clinical examination is inevitable [3]. The ubiquity of the internet and smartphones can support remote clinical participation, but home-based ECG measurement is still vulnerable to external noise in everyday environment, especially the powerline interference [4]. Therefore, a continuous ECG monitor device that can be used in everyday activity is necessary. Here, we present a miniaturized wireless monitor device and implementation of an ECG and heart rate logging. The proposed ECG monitor device precisely measures the physiological signal and streams the data to a commercial mobile device via standard Bluetooth. where the data is plotted in real-time. The data can be directly uploaded to a server for clinical diagnosis and a feasibility study demonstrates the potentials for a home-based care.

Methods

Figure 1 shows a block diagram of the the monitoring system. The system is divided into two sub-systems, a sensor node, and a base station, where the data is logged and displayed for real-time monitoring. In the sensor node, a single channel analog front end amplifies the ECG signal. A second order active high-pass filter and a second order active low-pass filter condition the signal. To eliminate powerline noise caused by general consumer electronics, a twin-T notch filter is implemented. The amplified ECG signal is sampled in 12-bit, 7 kSps by an analog-to-digital converter (ADC) integrated in the microprocessor (MCU). The MCU collects the data in a buffer and wirelessly transmits in every 34 ms. The sensor is interoperable with most smartphones (Bluetooth low-energy compliant Android) which can pair to the sensor node. The signal is further conditioned by a 6-tab IIR digital filter and is displayed as a real-time plot.

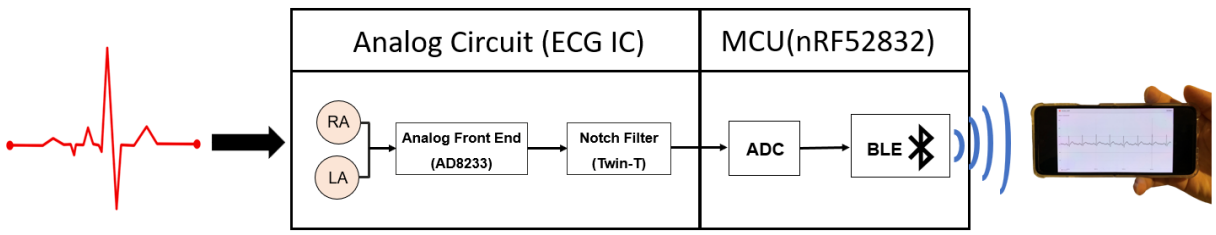


Figure 1. Schematic diagram of the measurement system architecture

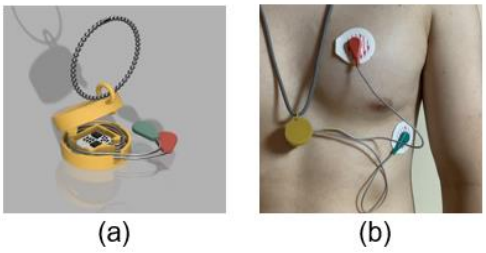


Figure.2 (a) Product design drawing through 3D printer. (b) Wearable necklace design for ECG measurement.

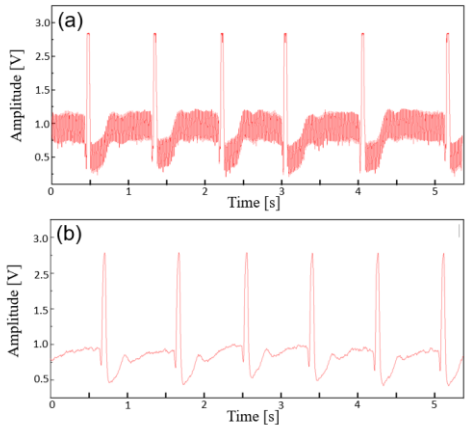


Figure 3. (a) ECG Waveform without a notch filter; (b) ECG Waveform after analog and digital filter.

The received ECG data is also saved as an individual file to be uploaded to a data server. A feasibility study is then conducted on a healthy male (age: 25) for a 50 min session continuous monitoring. A learning algorithm is applied for R-wave detection, and heart rate computation.

Results and Discussion

All of the blocks in the sensor node presented in Figure 1 are manufactured as one printed circuit board (10mm × 10mm × 0.5mm) and are encapsulated using a 3D printed photopolymer fluid material (30mm × 30mm × 40mm) as shown in Figure 2(a). A CR2032 battery is placed in the encapsulation, where the device can continuously operate for more than 48 hours. The packaging device can be used wearable in the form of a necklace (Figure 2(b)).

Figure 3 shows ECG waveforms according to the use of analog and digital filters. In order to demonstrate the influence of the powerline interference in a typical home-use, the measurement was performed at a 30-cm

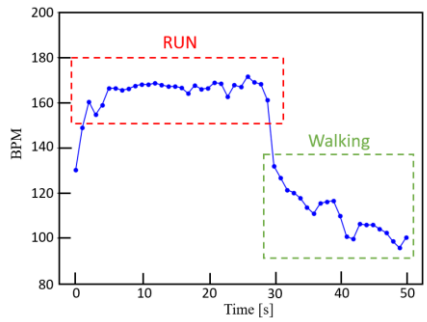


Figure 4. Continuous ECG monitoring and calculated BPM for 50 minutes.

distance from the power outlet. As it can be seen from the measurement results, significant noise reduction can be observed from the filtering. A continuous ECG monitoring is demonstrated for 50 min. An algorithm for (beats per minute) BPM calculation shows an exercise and walking session (Figure 4). The ECG signals were successfully measured and displayed through the smartphone device and it could be seen that the during a running session, the BPM was 160 to 180, and drops down to 100 after the exercise.

In this study a continuous real-time ECG monitoring device is developed and demonstrated for a remote home-base care. The measurement results and feasiblity study shows that the present work is suitable for everyday ECG monitoring.

Acknowledgements

This research was supported by the National Research Foundation of Korea (NRF-2020M3A9E4104385).

References

1. D. De Bacquer, G. De Backer, M. Kornitzer, and H. J. H. Blackburn, "Prognostic value of ECG findings for total, cardiovascular disease, and coronary heart disease death in men and women," Heart, vol. 80, no. 6, pp. 570-577, 1998.
2. J. Jin, "Screening for cardiovascular disease risk with ECG," JAMA, vol. 319, no. 22, pp. 2346-2346, 2018.
3. S. R. Steinhubl et al., "Effect of a home-based wearable continuous ECG monitoring patch on detection of undiagnosed atrial fibrillation: The mSToPS randomized clinical trial," JAMA, vol. 320, no. 2, pp. 146-155, 2018.
4. J. Piskorowski, "Digital Q-varying notch IIR filter with transient suppression," vol. 59, no. 4, pp. 866-872, 2009.

Soft, Wireless Bioresorbable Neurochemical System for Postoperative Management of Brain-Disorders

S.M. Yang[1†], J.H. Shim[1], H.-U. Cho[2], C.-H. Lee[1], D.P. Jang[2] and S.-W. Hwang[1*]

[1]KU-KIST Graduate School of Converging Science and Technology, Korea University, Seoul, Korea

[2]Department of Biomedical Engineering, Hanyang University, Seoul, Korea

smyang1991@korea.ac.kr[†], dupong76@korea.ac.kr*

Abstract

Systematic, careful management of patients with neurological disorders during unsettled peri- and post-operative period is required to ensure clinical outcomes and to manage neurosurgery-related adverse effects. Here, we present a soft, wireless, and bioresorbable neurochemical system that is designed to determine various concentrations of neurotransmitters as well as to monitor peripheral physiologies (temperature, pH, electrical activity) in a simultaneous manner. Extensive range of studies cover modifications of nanoscale materials and system-level electronics, enabling to produce exceptional performances. Such developments could pave the way for a clinically accessible neurochemical tool that not only provides reliable information for outpatients nursing, but also avoids adverse long-term effects and eliminate necessary removal procedures.

Background

Neurotransmitters are biochemical messengers that regulate essential functions of the body, which monitoring of such biochemicals plays a clinically important role in understanding and determining neurological disorders [1]. However, many research efforts have been focused on monitoring relatively physical, mechanical and electrophysiological parameters, rather than direct observation of such biochemical messengers [2]. Here, we introduce a fully implantable, bioresorbable silicon-based neurochemical analyzer incorporated with two-dimensional transition metal dichalcogenides as a completely implantable brain-integrated system that can wirelessly monitor time-dynamic behaviors of dopamine and relevant parameters in a simultaneous mode. A complete set of in vivo experiments illustrates capabilities for a potential use as a clinically accessible tool to associated neurodegenerative diseases.

Results and Discussion

Figure. 1 describes structures, mechanism, and key properties of soft, non-toxic, bioresorbable electronic brain-integrated system, designed to investigate and obtain information on neurochemicals and neurophysiologies in selective deep brain regions. The exploratory probe was systematically built with several essential components: i) electrochemical device as a primary element consisted of monocrystalline silicon nanoribbons (NRs, thickness ~300 nm) uniformly coated with a multi-dimensional heterostructure of two-dimensional transition metal dichalcogenide (2D TMD) nanosheets and iron

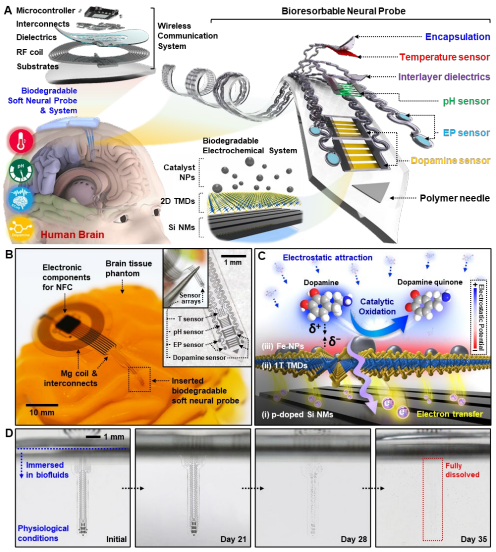


Figure 1. A) Soft, bioresorbable neurochemical systems with arrays of electronic sensors for neurotransmitters and relevant physiologies in the deep brain. B) Magnified photos of a neurochemical system inserted in the brain phantom. C) An illustration showing the key underlying mechanism of the device. D) Photographs at sequential stages of dissolution of the device during immersion in biological fluids.

nanoparticles (Fe NPs), capable of detecting

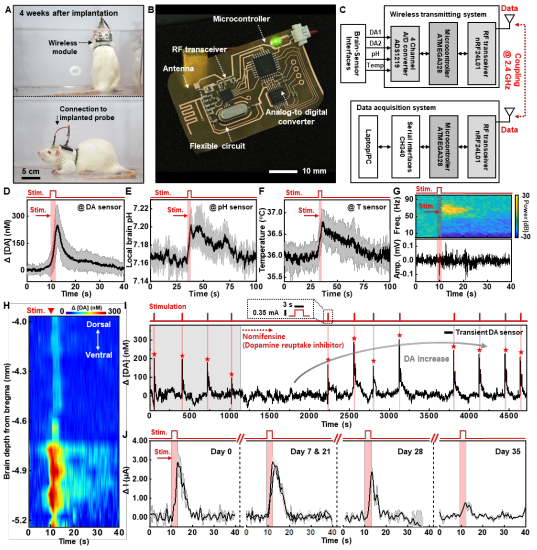


Figure 2. A) Photographs of a freely moving rat with a chronically implanted probe connected to wireless modules. B) A soft electronic module for wireless measurements and C) its operation scheme. D) Summarized instantaneous dopamine (DA) responses obtained as current changes. E, F) Observation of temporary pH and temperature fluctuations in local areas of the brain associated with the DA release. G) Local-field potential (LFP) changes related to evoked DA (top, power spectra; bottom, time series). H) Spatiotemporal DA responses. I) Real-time, continuous responses with intermittent electrical stimulations and drug (nomifensine, a DA reuptake inhibitor). J) Measured responses over a long range of timeframes, representing their stable operations for 2~4 weeks, followed by gradual degradations.

neurotransmitters with high sensitivity and selectivity over other chemical substances; ii) Peripheral electronic constituents such as pH meters, temperature sensors and electrophysiological (EP) electrodes, were assembled to analyze the correlation via simultaneously monitoring variations of diverse parameters along with the release of neurotransmitters; iii) Wireless communication system percutaneously connected to implanted brain probes via wires to transmit measured vital signals for ultimate free movements.

Photographs in Figure 2A show a freely moving rat model at 28 days post-surgery, implanted with bioresorbable electronic probes that are electrically connected to wireless modules. Soft RF wireless modules in Figure 2B can transmit measured data from implanted probes and its operation protocols are described in Figure 2C. The systems were evaluated at the dorsomedial striatum through recording physiological changes (Figure 2D, dopamine; 2E, pH; 2F, temperature; 2G, local field potential) in response to brief electrical stimulations of the medial forebrain bundle (MFB). The results from in vivo investigations demonstrate functionalities of the precise, multimodal and real-time biochemical analyzer as system-level feasibilities. Color map in Figure 2H presents recorded spatiotemporal mapping of evoked DA releases. Compared to DA activities within the grayscale region (pre-drug administration) in Figure 2I, an apparent elevation of DA signals was observed after the injection of nomifensine, indicating the strong evidence of its pharmacological DA reuptake inhibition of the dopamine transporter, DAT. Figure 2J highlights a collection of DA responses to periodic stimulations over extended periods. The results indicate stable operations over 2~4 weeks and then gradual decreases due to dissolution.

Conclusion

We investigated a wide range of measurements and analyses of neurotransmitters and relevant physiological signals via a soft, wireless bioresorbable neurochemical system. The system validates possibility for a clinically accessible tool for appropriate postoperative managements of neurosurgical procedures-induced complications, or symptoms that might be overlooked by clinicians.

Acknowledgements

This work was supported by Korea University, KU-KIST Graduate School of Converging Science and Technology Program, Technology Innovation Program (20002974) funded by the Ministry of Trade, Industry & Energy (MI, Korea), Korea Medical Device Development Fund Grant funded by the Korea Government (the Ministry of Science and ICT, the Ministry of Trade, Industry & Energy, the Ministry of Health & Welfare, and the Ministry of Food and Drug Safety) (202012D30), and the National Research Foundation of Korea (NRF) grant funded by the Korea Government (MSIP) (grant NRF-2017R1E1A1A01075027).

References

1. J. A. Frank, M. J. Antonini, P. Anikeeva, Next-generation interfaces for studying neural function. *Nat. Biotechnol.* **37**, 1013–1023 (2019).
2. H. U. Chung *et al.*, Binodal, wireless epidermal electronic systems with in-sensor analytics for neonatal intensive care. *Science* **363**, 0–13 (2019).

The Joint Conference of the IBEC2021 and the ICBHI2021

Biomaterials

Session Chair: Suk-Won Hwang (Korea University, S. Korea)

11 Nov. (Thursday) Room A (14:30~16:00)

Plant-inspired Tissue-adhesive, Injectable and Electroconductive Hydrogels for Biomedical Applications
Mikyung Shin (Sungkyunkwan University, S. Korea)

Tissue Engineered Constructs for in Vitro Testing Platforms
Youngmee Jung (Korea Institute of Science and Technology, S. Korea)

Organic Mixed Conductor-based Microfiber Meshes for Efficient Bioelectronic Interfaces
Myung-Han Yoon (Gwangju Institute of Science and Technology, S. Korea)



Mikyung Shin
PhD.
Sungkyunkwan University, Department of Biomedical Engineering

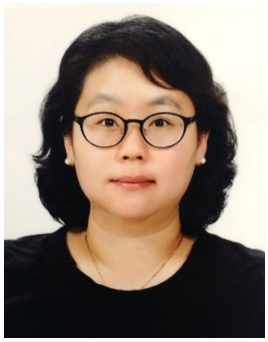
Plant-inspired tissue-adhesive, injectable and electroconductive hydrogels for biomedical applications

Abstract

Electroconductive hydrogels are promising materials for mimicking electrophysiological environments of biological system towards cardiac/neural tissue engineering, therapeutic applications, and bioelectronics. Injectable and conductive hydrogels are attractive for applications in 3D printing or for direct injection into tissues. However, current strategy of simple embedding of conductive additives (e.g., carbon materials, metal nanoparticles, and conducting polymers) has challenges to achieve stable gelation, toughness, and high conductivity. Herein, we propose two types of plant-inspired phenyl chemistry, i) rapid gallol oxidation coupled with metal reduction and ii) dynamic gallol-boronate complexation followed by exposure to biological salts for in situ fabrication of electroconductive hydrogels applicable to 3D printing and bridging of tissue defects. Our finding of phenyl chemistry would provide an insight to a variety of applications where conductive materials are needed.

Brief Biosketch

Prof. Mikyung Shin received B.S. degree in Biomedical Engineering and M.S./Ph.D. degree in Graduate School of Nanoscience and Technology, Korea Advanced Institute of Science and Technology (KAIST). She worked as a Postdoctoral Research Fellow in Department of Bioengineering, University of Pennsylvania, and currently Assistant Professor in the Department of Global Biomedical Engineering, SKKU.



Youngmee Jung
https://sites.google.com/view/kistbrel
Center for Biomaterials, Korea Institute of Science and Technology

Tissue engineered constructs for in vitro testing platforms

Abstract

Most of the tissue platforms currently being studied are lab-on-a-chip types that mimic cell environments and capillary networks, which are applied for cellular response analysis *in vitro*. However, these platforms have a limitation in clearly assessing the physiological phenomena of native tissue compared to in vivo evaluation. In this talk, I'd like to introduce simply fabricable tissue-engineered constructs mounted on the microphysiological platform with three-dimensional (3D) tissue structures like native tissues that can be applied for *ex vivo* and *in vivo* evaluation. These screening systems, in contrast to 2D in vitro models, clearly demonstrated that there is a significant difference in immune response and interaction with cells. The tissue engineering construct device has a high potential as a platform to assess various physiological and biochemical body responses.

Brief Biosketch

Dr. Youngmee Jung is currently a principal research scientist in center for biomaterials at Korea Institute of Science and Technology and is jointly appointed as an adjunct professor in school of electrical and electronic engineering at Yonsei University. She got her BSc in Chemical engineering, MSc and PhD in Biomedical engineering, at Seoul National University. She worked as a visiting scholar at Mainz University in Germany in 2007 and at Duke University in US in 2013. She is actively conducting research on 3D human tissue platform, 3D printing for regeneration, and Eco- and Human Friendly materials in various fields. She has published more than 117 peer-reviewed papers, 3 book chapters, and 40 patents issued or pending in the areas of biomaterials, polymer science, tissue engineering and regenerative medicine.



Myung-Han Yoon
Professor
School of Materials Science and Engineering
Gwangju Institute of Science and Technology

Organic Mixed Conductor-based Microfiber Meshes for Efficient Bioelectronic Interfaces

Abstract

In this research, we developed organic bioelectronic interfaces based on highly crystalline poly(3,4-ethylenedioxythiophene):polystyrene sulfonate (PEDOT:PSS) microfiber meshes to overcome the trade-off between electrical/electrochemical performance and aqueous stability. Crystalline PEDOT:PSS microfiber meshes exhibit excellent electrical/electrochemical/optical characteristics, long-term aqueous stability without film dissolution/delamination, and good viability for cardiomyocytes and neurons over several weeks while their 3D network structures with arbitrary shapes are constructed by employing the self-fusion properties of crystalline PEDOT:PSS microfibers. Furthermore, they are successfully employed for recording/stimulating the activities of cardiac tissues in a live animal with high signal fidelity and minimal vibrational artifact.

Brief Biosketch

Myung-Han Yoon received his B.S. (1999) in Chemistry and M.S. (2001) in Physical Chemistry at Seoul National University, South Korea. He finished his Ph.D. (2006) in Materials Chemistry with the guidance of Professor Tobin J. Marks at Northwestern University in US. In 2006, he moved to Harvard University as a postdoctoral fellow and focused on neuronal electronic/microfluidic interfaces. Since he joined GIST since 2010, he published more than 100 SCI journal papers (SCOPUS; h-index 35, total citation 8911) and received Excellent Research Award from Minister of Science and ICT (South Korea; 2018) and Excellent Research Award from Korean Polymer Society (2018).

The Joint Conference of the
IBEC2021 and the ICBHI2021

Brain Engineering

Session Chair: Joon-Kyung Seong (Korea University, S. Korea)

11 Nov. (Thursday) Room B (14:30~16:00)

Quantitative Personality Prediction Based on Emotional EEG Responses

Dan Zhang (Tsinghua University, China)

Targeting Neural Oscillations by Transcranial Alternating Current Stimulation

Sangtae Ahn (Kyungpook National University, S. Korea)

Single-cell Brain Mapping using 3D Organ Profiling Techniques

Young-Gyun Park (Korea Advanced Institute of Science and Technology, S. Korea)



Dan Zhang
Department of Psychology, Tsinghua University, Beijing 100084, China

Quantitative personality prediction based on emotional EEG responses

Recent advances in information technology have suggested the potential possibility to assess an individual's personality automatically. The present talk will introduce two EEG-based personality assessment studies for quantitative evaluation of people's Big Five personality. In the first study, 66 participants were invited to watch a total number of 28 video clips covering 9 typical emotion categories of amusement, joy, inspiration, tenderness, anger, disgust, fear, sadness and neutral with their 32-channel EEG signals recorded. Regression analyses were performed to predict the participants' Big Five personality trait scores using the EEG responses to these emotional video clips. A nested leave-one-out cross-validation procedure was employed with a sparse feature selection strategy to evaluate the out-of-sample personality assessment performance. The established EEG-based regression models could effectively predict the participants' self-reported personality trait scores. The prediction accuracies, measured as the correlations between the EEG-predicted personality trait scores and the self-reported scores, were 0.71, 0.72, 0.86, 0.71, and 0.82 for agreeableness, conscientiousness, neuroticism, openness and extraversion, respectively. The second study employed a similar regression analysis method but with EEG responses to positive, negative and neutral Chinese words collected from a cohort of 196 participants. The prediction accuracies were 0.50, 0.60, 0.49, 0.55, and 0.49 for agreeableness, conscientiousness, neuroticism, openness, and extraversion. A series of tests from both the internal and external validity perspective further showed that a good reliability of the obtained results. More importantly, only a brief EEG recording of 5 minutes was needed for this emotional word paradigm, demonstrating the effectiveness of the method towards practical use. Taken together, these results suggest the feasibility of quantitative personality prediction based on emotional EEG responses.



Sangtae Ahn
Assistant Professor
Kyungpook National University

Targeting Neural Oscillations by Transcranial Alternating Current Stimulation

Abstract

Neural oscillations are a fundamental mechanism that organizes the temporal relationship of activity patterns in large-scale brain networks. Transcranial alternating current stimulation (tACS) is a non-invasive brain stimulation modality that applies oscillating electrical currents to the brain via scalp electrodes. In this presentation, I talk about research studies on how tACS targets neural oscillations in animal models and human participants to entrain their spiking activity and neural oscillations. In addition, I discuss our studies on how tACS treats patients with psychiatric disorders who exhibit deficits in neural oscillations and rational designs for future neuromodulation studies.

Brief Biosketch

2020.03~present: Assistant Professor, Kyungpook National University
2016.10~2020.02: Postdoctoral Research Associate, University of North Carolina at Chapel Hill
2016.08: PhD, Gwangju Institute of Science and Technology
2012.08: MS, Gwangju Institute of Science and Technology
2010.02: BS, Chungnam National University



Young-Gyun Park
Assistant Professor
Department of Bio and Brain Engineering, Korea Advanced Institute of Science and Technology
Department of Biology, Kaist institute for Health Science and Technology, Korea Advanced Institute of Science and Technology

Single-cell brain mapping using 3D organ profiling techniques

Abstract

Brain function emerges from complex interactions among brain cells. Thus, mapping brain network in individual cell level (termed 'Single-cell brain mapping') is a prerequisite for brain engineering. In this talk, I will introduce 3D organ transformation technique (SHIELD) and labeling technique (eFLASH) that I developed, with brain mapping enabled by the techniques.

Brief Biosketch

Young-Gyun Park is an Assistant Professor of the Department of Bio and Brain Engineering at Korea Advanced Institute of Science and Technology (KAIST). He received his B.S. in Biology from KAIST in 2006 and his Ph.D. in Neuroscience from KAIST in 2011. He completed postdoctoral training at KAIST, Friedrich-Miescher Institute (Switzerland), and MIT. He aims to reveal how diverse inter-cellular interaction engender functions and dysfunctions of biological systems by inventing techniques for mapping biological networks in subcellular resolution.

The Joint Conference of the
IBEC2021 and the ICBHI2021

Award Session 2

Session Chair: Euiheon Chung (Gwangju Institute of Science and Technology, S. Korea)
Tong In Oh (Kyung Hee University, S. Korea)
MinWoo Kim (Pusan National University, S. Korea)

11 Nov. (Thursday) **Room C (14:30~16:00)**

A-007. Novel Hybrid Brain-computer Interface (BCI) for Virtual Reality Applications using SSVEP-based BCI and Electrooculogram-based Eye Tracking for Increased Information Transfer Rate
Jisoo Ha (Hanyang University, S. Korea)

A-008. Changes in Physiological Network Connectivity of body system in Narcolepsyduring REM sleep
Dong Yeon Son (Seoul National University, S. Korea)

A-009. Investigation of Electric Field Direction Sensitivity on Cortical Neuron Activation
Kyeong-Seop Park (Gwangju Institute of Science and Technology, S. Korea)

A-010. Animal Brain-Machine Interface with Visual Feedback and Virtual Reward
Yoon Kyung Cho (Ewha Womans University, S. Korea)

A-011. pH sensing Piezoelectric Smart Dental Implant for Peri-implantitis Monitoring
Seoyoung Lee (Sookmyung Women University, S. Korea)

A-012. Development of a Hyperbaric Chamber Control System for Cell Experiments to Reveal the Mechanism of Hyperbaric Oxygen Therapy
Yeo-Eun Choi (Yonsei University, S. Korea)

A-007

Novel hybrid brain-computer interface (BCI) for virtual reality applications using SSVEP-based BCI and electrooculogram-based eye tracking for increased information transfer rate

Jisoo Ha[1], Seonghun Park[2,3], Chang-Hwan Im[1,2,3*]

[1]Department of HY-KIST Bio-convergence, Hanyang University, Seoul, South Korea

[2]Department of Electronic Engineering, Hanyang University, Seoul, South Korea

[3]Department of Biomedical Engineering, Hanyang University, Seoul, South Korea

ich@hanyang.ac.kr

Abstract

Brain-computer interfaces (BCIs) based on electroencephalogram (EEG) have recently attracted increasing attention in virtual reality (VR) applications as a promising tool for controlling virtual objects or generating commands in a "hands-free" manner. Video-oculography (VOG) has been frequently used as a tool to improve BCI performance by identifying the gaze location on the screen; however, current VOG devices are generally too expensive to be embedded in practical low-cost VR head-mounted display (HMD) systems. In this study, we proposed a novel calibration-free hybrid BCI system combining steady-state visual evoked potential (SSVEP)-based BCI and electrooculogram (EOG)-based eye tracking to increase the information transfer rate (ITR) of a nine-target SSVEP-based BCI in VR environment. In our experiments with 20 participants wearing a commercial VR-HMD system, it was shown that both the accuracy and ITR of the proposed hybrid BCI were significantly increased compared to those of the traditional SSVEP-based BCI in VR environment.

Background

Brain-computer interface (BCI) is a technology that directly translates brain activities into commands to provide users with a new communication channel towards outside world. Recently, the rapid development of virtual reality (VR) technology brought about the increasing demand for new types of input devices for VR applications. For the hands-free control of VR or augmented reality (AR) devices, electroencephalo-graphy (EEG)-based BCIs have been intensively studied because of its affordability, ease of use, and portability [1]. Video-oculography (VOG) has been frequently used as a tool to improve BCI performance by identifying the gaze location on the screen; however, current VOG devices are generally too expensive to be embedded in practical low-cost VR head-mounted display (HMD) systems. In this study, we proposed a novel hybrid BCI system that simultaneously use EOG-based eye-tracking with SSVEP-based BCIs with the aim to improve the BCI performance of a nine-target SSVEP-based BCI in VR-HMD environment. Unlike the previous study by Saravanakumar and Ramasubba Reddy [2], we used the EOG and EEG signals simultaneously to select a single target among nine visual stimuli. Through experiments with 20 participants wearing a commercial VR-HMD system, it was investigated whether the BCI performance of the proposed hybrid BCI could be significantly enhanced compared to that of the conventional SSVEP-based BCI in VR environment.

Methods

Total 20 healthy volunteers were participated in the experiment. The EEG and EOG data were recorded from four electrodes attached to the scalp (Cz, O1, Oz, and O2) and two electrodes attached to the outer canthi of both eyes, respectively. Experiments were repeated on three different frequency configurations of pattern-reversal checkerboard stimuli arranged in a 3 × 3 matrix (Figure 1). When a user was staring at one of the nine visual stimuli, the column containing the target stimulus was first identified based on the user's horizontal eye movement direction (left, middle, or right) classified using horizontal EOG recorded from a pair of electrodes that can be readily incorporated with any existing VR-HMD systems. Note that the EOG can be recorded using the same amplifier for recording SSVEP, unlike the VOG system. Then, the target visual stimulus was identified among the three

visual stimuli vertically arranged in the selected column using the multivariate synchronization index (EMSI) algorithm, one of the widely-used SSVEP detection algorithms.

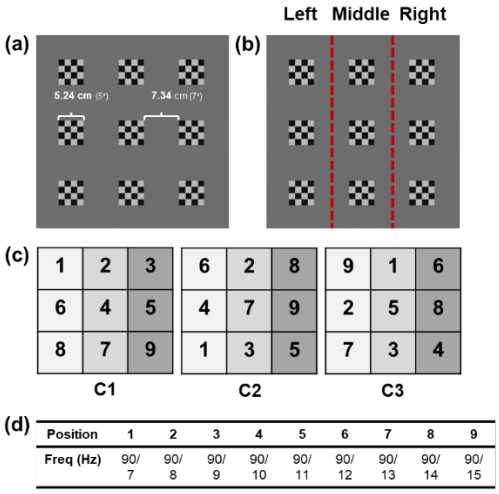


Figure 1. (a) Nine visual stimuli presented on the screen, (b) The three directions classified using EOG: Left, Middle, and Right, (c) C1, C2 and C3 represent the three different configurations of pattern-reversing frequencies. Numbers represent the positions listed in (d), (d) Pattern-reversing frequencies used for (c).

Results and Discussion

We first investigated whether the accuracy of classifying three directions (Left, Middle, and Right) using hEOG was high enough to be employed for our hybrid BCI system. The average classification accuracy was reported to be 97.74 ± 3.89%. Particularly, the classification accuracies for 11 out of 18 participants were 100%. These results suggest that the reliability of the hEOG-based eye-tracking is high enough to be employed as a reliable tool for the recognition of horizontal eye movement directions.

Statistical analyses also confirmed the superiority of the proposed hybrid BCI to the conventional SSVEP-based BCI. The SSVEP+EOG case outperformed the SSVEP-only case in the classification accuracy in (i) C1 for all window sizes except 3.5 s and 4 s, (ii) C2 for all window sizes, and (iii) C3 for all window sizes. As for the ITR, statistical significance was found in all three configurations except for the 3.5 s and 4 s window sizes in C1. The results of experiments with 18 participants suggest that the proposed system has the potential to be used as a practical hands-free control tool for VR applications, particularly for those who cannot freely move their limbs.

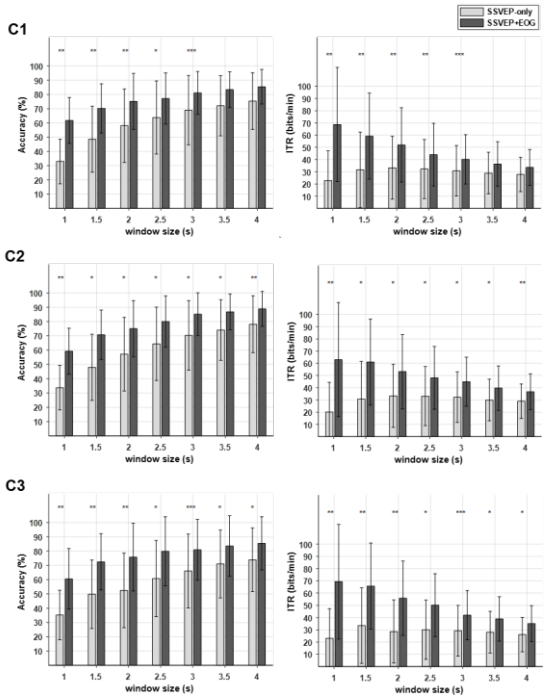


Figure 2. Comparison of the mean classification accuracies (left) and information transfer rates (ITRs, right) for SSVEP-only and SSVEP+EOG cases with respect to different window sizes for C1, C2, and C3. (*p < 0.05, **p < 0.01, ***p < 0.005, Wilcoxon signed rank test, Bonferroni-corrected).

Acknowledgements

This work was supported in part by Institute for Information & communications Technology Promotion (IITP) grant funded by the Korea government (MSIT) (2017-0-00432, Development of non-invasive integrated BCI SW platform to control home appliances and external devices by user's thought via AR/VR interface) and in part by the National Research Foundation of Korea (NRF) grant funded by the Korea government (MSIT). (No. NRF-2019R1A2C2086593).

References

1. Park, S., Cha, H.-S., and Im, C.-H. (2019). Development of an Online Home Appliance Control System Using Augmented Reality and an SSVEP-Based Brain–Computer Interface. IEEE Access 7, 163604-163614.
2. Saravanakumar, D., and Ramasubba Reddy, M. (2020). A virtual speller system using SSVEP and electrooculogram. Advanced Engineering Informatics 44, 101059-101068.

Changes in Physiological Network Connectivity of body system in Narcolepsy during REM sleep

Dong Yeon Son[1,2], Hyun Bin Kwon[1], Hyung Won Jin[1,5], Dong Seok Lee[1], Jong Hyeok Jeong[1,2], Mi Hyun Lee[3] Yu Jin Lee[3] and Kwang Suk Park[4,5]

Interdisciplinary Program of Bioengineering, College of Engineering, Seoul National University, Korea [1]
Integrated Major in Innovative Medical Science, College of Medicine, Seoul National University, Korea [2]
Department of Neuropsychiatry and Center for Sleep and Chronobiology, Seoul National University Hospital, Korea [3]
Department of Biomedical Engineering, College of Medicine, Seoul National University, Korea [4]
Institute of Medical and Biological Engineering, Medical Research Center, Seoul National University, Seoul Korea [5]
pks@bmsil.snu.ac.kr

ABSTRACT

Narcolepsy is marked by pathologic symptoms including excessive daytime drowsiness and lethargy, even with sufficient nocturnal sleep. There are two types of narcolepsy: type 1 (with cataplexy) and type 2 (without cataplexy). Unlike type 1, for which hypocretin is a biomarker, type 2 narcolepsy has no adequate biomarker to identify the causality of narcoleptic phenomenon. Therefore, we aimed to establish new biomarkers for narcolepsy using the body's systemic networks. Thirty participants (15 with type 2 narcolepsy, 15 healthy controls) were included. We used the time delay stability (TDS) method to examine temporal information and determine relationships among multiple signals. We quantified and analyzed the network connectivity of nine biosignals (brainwaves, cardiac and respiratory information, muscle and eye movements) during nocturnal sleep. In particular, we focused on the differences in network connectivity between groups according to sleep stages and investigated whether the differences could be potential biomarkers to classify both groups by using a support vector machine. Network connectivity with the TDS method may be used as a biomarker to identify differences in the systemic networks of patients with narcolepsy type 2 and healthy controls.

1. Introduction

Narcolepsy is divided into two types: type 1 (with cataplexy) and type 2 (without cataplexy). Both types present with symptoms of excessive daytime drowsiness, but type 1 involves cataplexy, which causes sudden REM sleep in the daytime. In addition, type 1 has a specific biomarker: hypocretin in the cerebrospinal fluid (CSF), which chemically controls the nervous and endocrine systems, is used to identify the cause of narcolepsy **[1]**. On the other hand, narcolepsy type 2 does not have specific biomarkers to explain the causality of the pathological phenomenon **[2,3]**. Therefore, it is essential to identify biomarkers to interpret the symptoms of patients with narcolepsy type 2. To establish new biomarkers, we focused on the interactions of the body's neurological and electronic systems and examined the differences between patients with narcolepsy and healthy controls. For this, it was necessary to quantify physiological differences in the body's network between patients with narcolepsy and controls with understandable metrics. (Narcolepsy type 2 will be referred to as "narcolepsy" from now on.) We analyzed the differences between patients with narcolepsy and healthy controls by focusing on the interactions of the physiological system during nocturnal sleep with time delay stability (TDS) method.

2. Methods and materials

15 patients with narcolepsy (8 men and 7 women; aged 24.8 ± 8.23 years) and 15 controls (7 men and 8 women; aged 27.67 ± 3.84 years) were included in the analysis and patients who were related to sleep disorder or severe mental problems were excluded. All participants conducted polysomnography (PSG) in the sleep center and their sleep stages and their pathological states were diagnosed by two clinicians. From PSG, we extracted and used 9 biosignals: brain waves (α, β, θ, δ), eye movements, chin and limb movements, heart rate and respiration rate. And sleep stages were classified as WAKE, REM (Rapid Eye Movement), LS (Light sleep which includes N1, N2 sleep), DS (Deep sleep which includes N3 sleep).

With these data, we used time delay stability method which could include temporal information by using cross-correlation based analysis. We extracted time delay indices from cross-correlation from each connection according to sleep stages, and we classified 'stable' when the time delay index remained ±1 second in the five consecutive epochs. After the process of 'stable' labeling, we got the proportion of 'stable' in each sleep stage for every connection and it represents TDS. By considering all sleep stages' TDS, we calculated proper threshold of TDS with percentile method to make connections for both of narcolepsy and control groups.

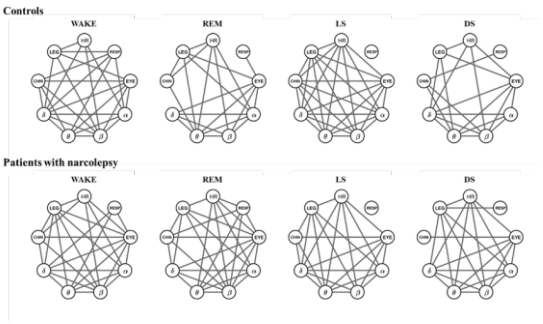


Fig. 1. Network topologies of narcolepsy and control groups

After making the topologies according to sleep stages, we compared the number of network connections between two groups and interpreted their causalities by analyzing each feature's significance. Also, we showed their possibility to be a potential biomarker to distinguish narcolepsy and control groups by classifying them with support vector machine (SVM).

3. Results

After we applied the TDS method with a threshold, we found a difference in the overall number of network connections during sleep. They showed a similar trend in WAKE, LS, DS, however, the narcolepsy group showed a significantly higher number of connections in REM sleep (p = 0.022). The narcolepsy group showed about three more connections (narcolepsy: 24.47 ± 2.87, control: 21.34 ± 2.65) compared to control group **(Fig. 2)**.

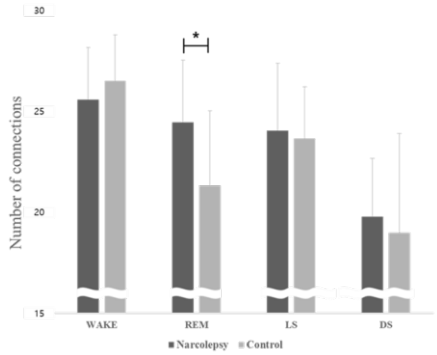


Fig. 2. Network connections between narcolepsy and control groups (* $p < 0.05$).

To identify which components in a network affect the total number of connections, we conducted a feature significance analysis. As the number of connections differed in REM sleep, we focused on REM sleep connections and visualized them using topology **(Fig. 3)**. Significant differences were observed between HR and theta (θ) brainwaves (p = 0.05), HR and eye movement (p = 0.026), and chin movement and respiration rate (p = 0.043), and their values were higher in patients with narcolepsy than in controls. Delta (δ) and alpha (α) brainwaves (p = 0.0072) and delta (δ) and theta (θ) brainwaves (p = 0.03) also showed significant differences, but they were higher in controls than in patients with narcolepsy.

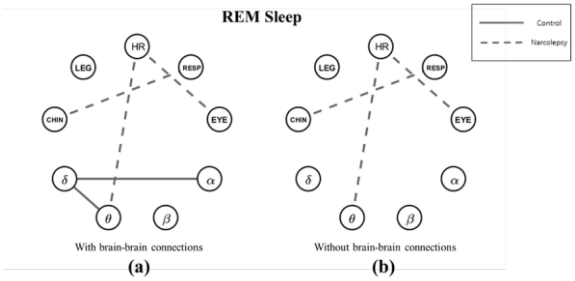


Fig. 3. Connections which showed significant difference. (a) showed all significant connections and (b) excluded brain-brain connections.

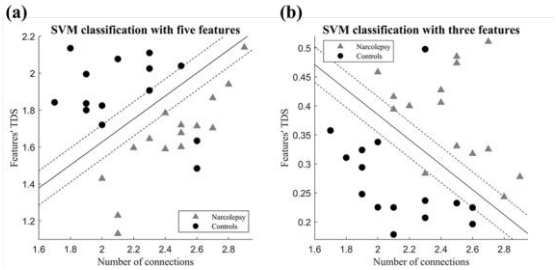


Fig. 4. Distribution of participants with number of network connections and features' TDS during REM sleep.

Some network features showed significant power affect the number of network connections: α-δ, θ-δ, θ-HR, CHIN-RESP, HR-EYE during REM sleep. We took TDS values from each network feature of REM sleep and merged them by summing them with constant weight. After calculating features' TDS, we scattered participants' data with two features: number of connections and features' TDS (**Fig. 4**). To find the best decision boundary to classify the groups, we used an SVM. As a result, when brain-brain connections were included (**Fig.4-(a)**), the sensitivity was 0.88, the specificity 1, and the accuracy 0.93. Without brain-brain connections (**Fig.4-(b)**), it was a 0.93 for sensitivity, specificity, and accuracy, respectively. These results show that the narcolepsy group has higher connectivity in brain-periphery and periphery-periphery connections, but lower in brain-brain connections in comparison to the control group during REM sleep.

4. Acknowledgements

This work was supported by the National Research Foundation of Korea (NRF) grant funded by the Korea government (MSLT) [grant number NRF-2017R1A5A1015596].

5. References

[1] Dauvilliers Y, Arnulf I, Mignot E. Narcolepsy with cataplexy. Lancet. 2007;369(9560):499-511.

[2] Eric Suni. Narcolepsy: What it is, its causes, and the steps that can help manage it. Sleep Foundation; 2021.

[3] Zhang Z, Mayer G, Dauvilliers Y, et al. Exploring the clinical features of narcolepsy type 1 versus narcolepsy type 2 from European Narcolepsy Network database with machine learning. Sci Rep. 2018;8(1):10628.

[4] Bashan A, Bartsch RP, Kantelhardt JW, Havlin S, Ivanov PCh. Network physiology reveals relations between network topology and physiological function. Nat Commun. 2012;3:702.

Investigation of Electric Field Direction Sensitivity on Cortical Neuron Activation

K. Park[1], H. Chung[1], C. Im[1], and S.C. Jun[1]

[1]School of Electrical Engineering and Computer Science, GIST, Gwangju, Korea

scjun@gist.ac.kr

Abstract

Transcranial direct current stimulation (tDCS) has garnered attention due to its usefulness in clinical applications. However, the result of tDCS is highly unpredictable because of inter-subject variability and the divergence of the neuron's orientation where it lies within the cortex. Moreover, electric field (EF) direction has been reported as a key factor for neuronal response to EF and various EF directions applied to cortical neurons render difficult prediction of neuronal response. Hence, we aimed to probe the morphological factors impacting neurons' sensitivity to electric field (EF) direction and understand cellular mechanisms of EF direction sensitivity, adopting morphologically realistic neuron models. As a result, we observed that segment orientation or segment's distance from the soma might be determining factors for EF direction sensitivity, which helps us to gain a better understanding of the neuron's cellular mechanism of EF direction sensitivity.

Background

Transcranial direct current stimulation (tDCS), delivering direct electric current non-invasively to the brain, has been spotlighted to understand brain function and to treat neurological disorders. However, limited knowledge of tDCS prevents researchers from accurately predicting the neuronal response to it, such as firing rate and membrane polarization. To conquer this obstacle, studies have attempted to investigate the effect of neuronal morphology and electric field (EF) direction sensitivity—a neuron's preferred EF direction where neurons are activated with a weaker EF—on neuron's response [1]. However, studies about the contribution of morphology on the neuronal response have been constrained on somatic polarization, without considering other neuron's compartments. Moreover, although EF direction has been reported to be a determining factor for neuronal responses, the detailed cellular mechanisms of EF direction sensitivity remain uncertain [1].

Here, our goal was to investigate the cellular mechanism of the neurons' EF direction sensitivity fully regarding each compartment, apical/basal dendrite, soma, and myelinated/unmyelinated axon. From the investigation, the findings would help us to fully understand the cellular mechanisms of neuron's EF direction sensitivity and ultimately help to predict the patient's neuronal response to tDCS more accurately on the usage of tDCS clinical treatments.

Methods

We adopted morphologically realistic cortical neuron models of Layer 1 neuroglia-form cell (L1 NGC), L2/3 pyramidal cell (L2/3 PC), and Layer 5 pyramidal cell (L5 PC), which were originally obtained from the Blue Brain Project [2] and downloadable from ModelDB [1]. In the NEURON simulator, the transmembrane potential is calculated at a unit called segment; compartments consist of several segments, and the neuron model is a series of the compartment. For neuron stimulation, when (x, y, z) is assumed as a coordinate at a center point of an arbitrary segment with the origin of soma, the calculation of extracellular potential uses the equation:

$$V_e(x, y, z) = -|E| \cdot (x\sin\theta + z\cos\theta) \quad (1)$$

Here, $V, E,$ and θ are the transmembrane potential, EF magnitude, and the polar angle, respectively (Fig. 1a). We simulated subthreshold tDCS for 50ms in total with stimulation of 5ms delay and a 45ms rectangular pulse. Also, we measured membrane polarization to quantify neuronal response to subthreshold tDCS.

Results and Discussion

We randomly chose up to 100 segments in each compartment of the basal dendrite (Basal), apical

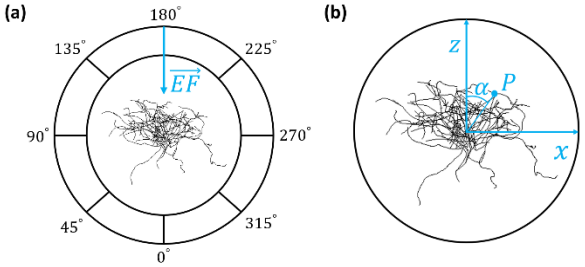


Figure 1. (a) Representation of the EF polar angle; **(b)** The angle α between the z-axis and the segment P

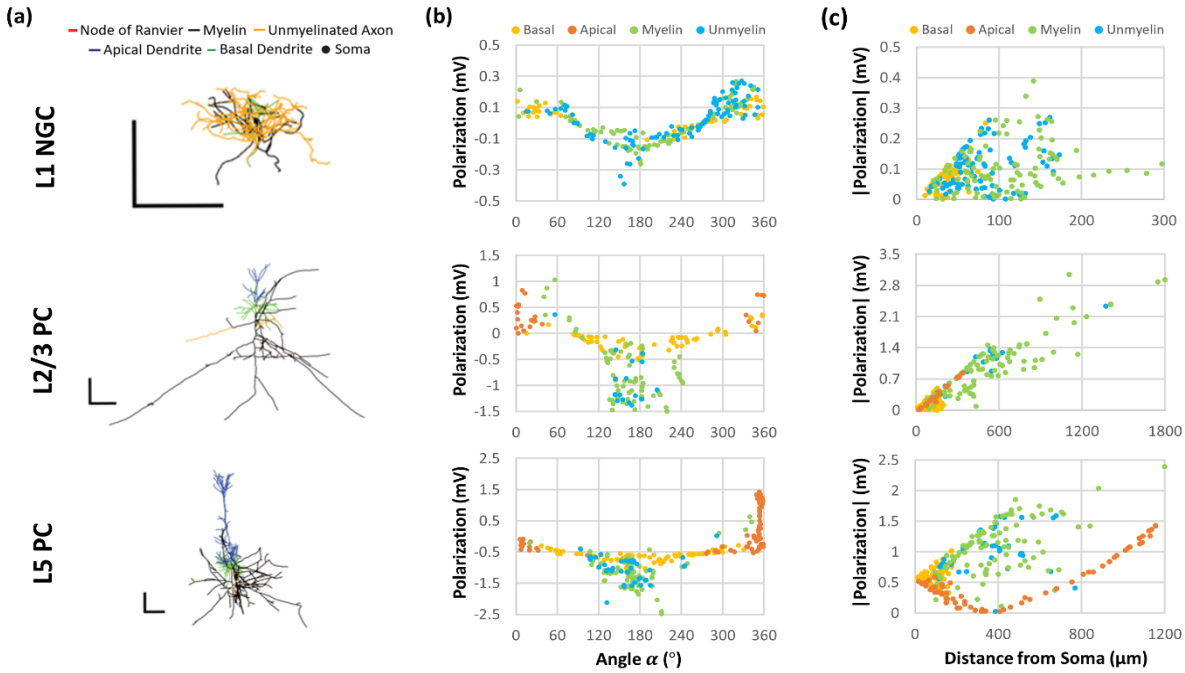


Figure 2. (a) Morphology of the neuron models with scale bars indicating 250μm; **(b)** Segment's membrane polarizations per angle α (Fig. 1b); **(c)** Absolute value of segment's polarization per segment's distance from soma

dendrite (Apical), myelinated axon (Myelin), and unmyelinated axon (Unmyelin) for each neuron model. Then we stimulated a downward 3mV/mm uniform EF (a polar angle of 180˚) and plotted the relation between α and polarization (Fig. 2b). The tendency shown in Fig. 2b is similar to a quadratic polynomial, which ideally shows symmetricity about the y-axis because the segment's distance is symmetric about the soma. We fit the segment's distance in a quadratic regression at a compartment level and measured the R-squared values. The basal compartment shows a greater R-squared value between distances: 0.74, 0.72, and 0.68 for L1 NGC, L2/3 PC, and L5 PC, respectively. As the extracellular potential is measured by eqn.1, the segment's potential values are mainly determined by the EF direction if the segment's distances from the soma are similar. The segments of the basal dendrites are similar to each other because basal dendrites locate within 250μm from the soma. Hence, in the basal dendrites, the segment's orientation was a determining factor for membrane polarization.

With the same segments selected above, we also plotted the relation between absolute polarization and the segment's distance from the soma (Fig. 2c). The segments in the apical dendrite showed the greatest correlation with the R-squared value in linear regression of 0.98 and 0.67 for L2/3 PC and L5 PC, because these segments are mostly oriented parallel to the EF orientation.

In conclusion, we showed that when segments' distances are similar, the EF direction is a key factor for membrane polarization at a segment level. Thus, the segment's population distribution of either relative orientation or relative distance from the soma is a determining force of the neuron's EF direction sensitivity. In addition, considering neuronal morphology as a distinguishing population of segments, neuronal morphological influence on neuronal EF direction sensitivity can be elucidated.

Acknowledgements

This work was supported by the Institute of Information & Communications Technology Planning & Evaluation (IITP) grant funded by the Korea government (No. 2017-0-00451) and the '2021 Joint Research Project of Institutes of Science and Technology'.

References

1. Aberra, A.S., *et al.*, *Biophysically realistic neuron models for simulation of cortical stimulation.* Journal of neural engineering, 2018. **15**(6):066023.
2. Markram, H., *et al.*, *Reconstruction and simulation of neocortical microcircuitry.* Cell, 2015. **163**(2): p. 456-492.

Animal Brain-Machine interface with visual feedback and virtual reward

Yoon Kyung Cho[1], Hyun Ji Yoo[1], Chin Su Koh[2], Tae Jun Kim[2], Jin Woo Chang[2], and Sang Beom Jun[1,3,4*]

[1]Department of Electronic and Electrical Engineering, Ewha Womans University, Seoul, Korea

[2]Department of Neurosurgery, College of Medicine, Yonsei University, Seoul, Korea

[3]Graduate Program in Smart Factory, Ewha Womans University, Korea

[4]Department of Brain and Cognitive Sciences, Ewha Womans University, Seoul, Korea

*juns@ewha.ac.kr

Abstract

Brain-machine interface (BMI) technology utilizes the neural activities recorded from the brain to control external machines or computers. In this study, visual feedback is presented to rats via real-time signal processing of the neural signal from somatosensory cortex. Combined with electrical stimulation on medial forebrain bundle as a virtual reward, the animal successfully learned how to control the location of dots in the screen using the neural activity of somatosensory cortex. After 4 days of training, the animal showed 100 % success rate for controlling the object in the screen and receiving the virtual reward.

Background

For several decades, neural interface and BMI studies have shown how the neural prostheses can effectively contribute to the rehabilitation of patients with limb amputation or paralysis. In general, in order to detect the intention for movement, previous studies have targeted the primary motor cortex which is directly related to movement. However, there exist various situations where the direct interpretation from the brain regions is impossible because of a brain damage. Therefore, needs for new approach to control machine using other brain areas are emerging. As an alternative, the primary somatosensory cortex (S1) can be a candidate. Accepting the senses is highly related to movement and it is also possible that a higher cognitive function such as attention or intention to act to control the activity of the S1 cortex in top-down manner by a higher cognitive function such as attention or intention to act. The whisker in the snout region of rodents is the most developed and plays the most important role in detecting obstacles or prey[1]. We recorded neural signals from both left and right barrel cortex (S1BF) that receive input from the whiskers. Real-time signal processing extracted a machine control signal from a local field potential (LFP) of the S1BF neural activities. The animal focus on a LCD monitor to control a movement of a dot into a target zone. Eventually, when a session is successful, the animal received virtual reward by electrical stimulation on the medial forebrain bundle (MFB), a center for pleasure and reward[2].

Methods

Figure.1 shows a scheme of operant conditioning with a neural signal recording system, electrical stimulation and display machinery. Customized multi-array electrodes are implanted into the S1BF and the MFB of Sprague Dawley rats for chronic neural recording and electrical stimulation, respectively.

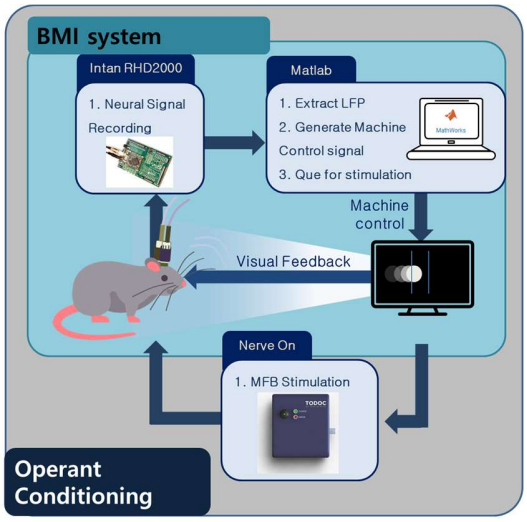


Figure 1. A scheme of BMI system with operant conditioning.

For ‘Machine Control’, the mission is to move a white dot to a target zone in a LCD monitor. During a session the monitor is set to a black background to contrast the white dot which appears at the end of left/right side of a monitor. The target zone is a center of a monitor. When the circular figure arrives at the target zone, the animal receives the virtual reward (MFB stimulation) and the dot is re-positioned to left/right starting point. During a machine control session, the rat is freely moving in an open cage (24 cm x 40 cm x 20 cm). Our assumption is based on behavioral findings that a rat’s whiskering generates differences in LFP between left and right barrel cortex during directing. Therefore we recorded the LFP from S1BF neural activities with the RHD 2000 USB interface board (Intan Technologies, LLC, LA, California, USA) at sampling rate 1 k samples/s. Especially selected range of LFP between 40 to 70 Hz was used to convert into a machine control signal. This range has been selected from previous study[3]. Comparing sum values of fast Fourier transform between 40 Hz and 70 Hz, the higher value is chosen for the direction to move at next sampling time.

For efficient learning, a simple operant conditioning was conducted before the ‘Machine Control’ session. For operant conditioning, the animals were trained for 6 days in the skinner box (Med Associates, Fairfax, Vermont, USA) for self-stimulation training (MFB stimulation). After this addiction process, the machine control session starts with getting used to the monitor setting for a day, then training starts for at least 5 days. To validate the system, we recorded every 10 sessions each day to check how many times they make a successful machine control. Each session is performed for 1 minute.

To set up this system, the main controller is implemented with Matlab software (MathWorks, Natick, Massachusetts, USA) for controlling a recording device and the stimulator, and also the real-time signal processing. For electrical stimulation, wireless stimulator Nerve-On (TODOC Co., Ltd, Seoul, Korea) was connected to a switch for enable. Stimulation parameter was set as cathodic current pulse with duration 200 us, amplitude 200 uA during 300 ms at 230 Hz.

Results and Discussion

Figure. 2 shows the success rate curve during 5 consecutive days. Success rate is higher than 70 % after first 2 days. When the circular figure arrives in the target zone by animal’s intention, the reward stimulation is delivered to MFB. As the days past, the number of success in a single session also increased (not shown in this paper) which means that the animal immediately learned how to control the circular figure shown in the monitor.

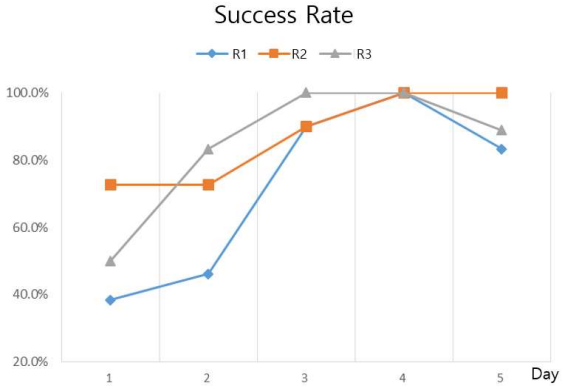


Figure.2 Success rate of machine control

Acknowledgements

This research was supported by the Korea Medical Device Development Fund grant funded by the Korea government (the Ministry of Science and ICT, the Ministry of Trade, Industry and Energy, the Ministry of Health & Welfare, the Ministry of Food and Drug Safety) (1711139110, KMDF_PR_20210527_0006) and by the National Research Foundation of Korea (NRF) grant funded by the Korea government (MSIT) (NRF-2019R1A2C1088909) and by Convergent Technology R&D Program for Human Augmentation through the National Research Foundation of Korea (NRF) funded by the Ministry of Science and ICT (NRF-2019M3C1B8090805).

References

1. DaeEun Kim, “Microphone-Based Whisker Tactile Sensors Modeling Rodent Whiskers”, Journal of Korea Robotics Society, 4(1) :33-42, 2000
2. Kong C, Shin J, Koh CS, Lee J, Yoon MS, Cho YK, Kim S, Jun SB, Jung HH, Chang JW. Optimization of Medial Forebrain Bundle Stimulation Parameters for Operant Conditioning of Rats. Stereotact Funct Neurosurg. 2019;97(1):1-9
3. Cho YK, Lee YJ, Park CJ, Lee JY, Kim TH, Koo YB, Jun SB. Brain-Machine Interface study in rodent somatosensory neural activity, The Korea

Society of Medical & Biological Engineering
2019 Nov

pH sensing Piezoelectric Smart Dental Implant for Peri-implantitis Monitoring

Seoyoung Lee[1], Gaheun Lee[1], Seyoung Yook[1], Jieun Kim[1], Seunghyun Song[1], and Eunjeong Byun[1]

[1]Department of Electronics Engineering, Sookmyung Women University Seoul, Korea

eunjbyun@sookmyung.ac.kr

Abstract

With the increased incidences of dental implantation, the long-term management of peri-implantitis is becoming increasingly important. Higher pH in gingival crevice is a critical biomarker for the bacterial manifestation; thus, the monitoring of the pH can enable early detection of peri-implantitis. In this work, we developed and verified peri-implantitis monitoring piezoelectric smart dental implant capable of harvesting energy from human oral motions and transmit RF signal at the resonant frequency of the LC transponder, which is modulated by the volumetric response of the ferrogel to the local pH change. We fabricated the proof-of-concept device and successfully measured the pH wirelessly by harvesting mechanical forces.

Background

With the continuous improvement in the health management, the incidences of dental implants have steadily increased over the years. Accordingly, the reported number of peri-implantitis (such as inflammation, sensory malfunction, or even tooth loss) is also increasing with roughly 20% of the patients suffer side effects. However, peri-implantitis is mostly symptomless and hence the early diagnosis is challenging. Thus, continuous monitoring of the occurrences of peri-implantitis through the detection of the underlying cause, bacterial manifestation, could significantly improve the oral health care.

The key biomarker of deteriorated oral health is the change of pH; in health adults, the periodontal pH in the gingival crevice is around 6.92[1]. The periodontal pH tends to increase under bacterial invasion, however, beyond 7.6 [2]. Hence, the monitoring of the local pH around the dental implant sites could lead to the early detection of the peri-implantitis. In this paper, we describe a pH sensing piezoelectric smart dental implant (Fig. 1a).

Methods

Figure 1b describes the operation principle of the pH sensing piezoelectric smart dental implant. The mechanical force from the human oral motion applied to the piezoelectric dental crown generates a pulse of electrical output. The generated power is then dissipated within the LC tank emitting the RF signal at the resonant frequency. The performance of the barium titanate ($BaTiO_3$, BTO) based piezoelectric dental crown was recently shown to be sufficient in both mechanical rigidity and electrical performance [3].

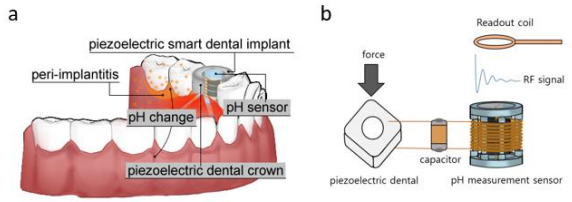


Figure 1. Schematic diagram of the pH sensing piezoelectric smart dental implant

The pH sensing is enabled through the inductance modulation by the ferrogel core. Ferrogel is a hydrogel embedded with ferromagnetic nanoparticles; this enables the volumetric response of the hydrogel to be translated to the modulation of the ferrogel core's magnetic susceptibility. Hence, under the volumetric response of the ferrogel to the local pH change, the overall inductance of the system is modulated and hence the resonant frequency ($f = \frac{1}{2\pi\sqrt{LC}}$) of the system is modulated [4].

The 3D printed mold, BTO/PVDF mixture, and the sintered BTO dental crown are shown in Fig. 2a. The scanning electron microscopy (SEM) images of the BTO grains pre-sintering and post-sintering are shown in Fig. 2b. The merging of the individual nanoparticles (~ 400 nm) into larger grains (> 5 μm) is clearly visible from the SEM images. The pH sensing element of the smart dental implant is an LC transponder with a ferrogel core. The custom 3D printed tube, wrapped with a copper wire coil, is connected to a thin copper wire immobilizing the ferrogel cores to form an inductor (Fig. 2c, e). The synthesis of ferrogel

followed the recipe in the literature reference [4]. The overall form factor of the sensor allows it to reside within the cylindrical cavity within the piezoelectric dental crown (Fig. 2a). The volumetric response of ferrogel is shown in Fig. 2d where the ferrogel exhibits isotropic volume shrinkage with a response time of 25 minutes. We note that the response time was calculated as 3τ, where τ is obtained by fitting a single exponential decay ($y(t) = y_0 + Ae^{-t/\tau}$).

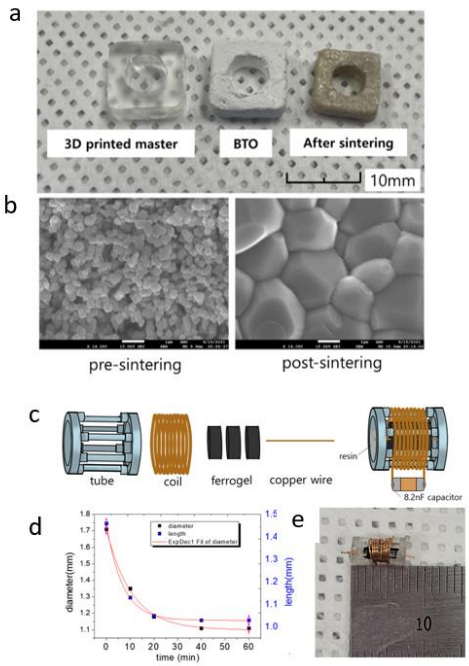


Figure 2. Fabrication process of the piezoelectric dental crown and the pH sensing ferrogel sensor

Results and Discussion

We tested the wireless pH sensing by the piezoelectric smart dental implant. The pH sensing element was immersed within a pH buffer and the force applicator provided the mechanical force to the piezoelectric dental crown and the emitted signal was measured using an external coil connected to a broadband amplifier (Fig. 3a-b). Under the applied force of 1.4 N (far below typical chewing force of 70 N [5-6]), RF signal is transmitted from the dental implant. The time trace of the amplified receiver signal is shown in Fig. 3c. We observed that the extracted resonant frequency (obtained through FFT) decrease under increasing pH (Fig. 3d). The decrease (increase) of the resonant frequency under swelling (shrinkage) of the ferrogel is assigned to the varying degree of the physical confinements imposed by the hydrogel mesh to the ferromagnetic nanoparticles.

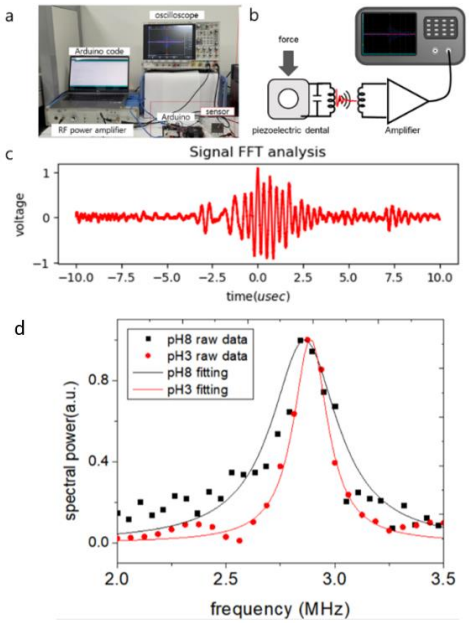


Figure 3. The wireless pH sensing by the piezoelectric smart dental implant

Acknowledgements

This work was supported by Korea Foundation for Women In Science, Engineering, and Technology (WISET) grant funded by the Ministry of Science and ICT (MSIT) under the team research program for female engineering students (grant number: WISET-2021-167).

References

1. Eggert, F. M., et al. "The pH of gingival crevices and periodontal pockets in children, teenagers and adults." Archives of oral biology 36.3 (1991): 233-238.
2. Nyako, E. A., C. J. Watson, and A. J. Preston. "Determination of the pH of peri-implant crevicular fluid in successful and failing dental implant sites: a pilot study." Archives of oral biology 50.12 (2005): 1055-1059.
3. Park, Moonchul, et al. "Human oral motion-powered smart dental implant (SDI) for in situ ambulatory photo-biomodulation therapy." Advanced Healthcare Materials 9.16 (2020): 2000658.
4. Song, S. H., et al. "A wireless chemical sensor featuring iron oxide nanoparticle-embedded hydrogels." Sensors and Actuators B: Chemical 193 (2014): 925-930.
5. F. Goldschmidtboeing et al., “Comparison of Vertical and Inclined Toothbrush Filaments: Impact on Shear Force and Penetration Depth,” Stroj. Vestn. – J. Mech. Eng., vol. 60, no. 7–8, pp. 449–461, (2014)
6. The Power of the Human Jaw,” Sci. Am., vol. 105, no. 23, pp. 493–493, Dec. 1911.

Development of a hyperbaric chamber control system for cell experiments to reveal the mechanism of hyperbaric oxygen therapy

Y.E. Choi[1], H.S. An[1], S.B. Jung[1], H.H. Yang[1], T.M. Shin[1*]

[1]Department of Biomedical Engineering, Yonsei University, Wonju, Korea

dudms923@naver.com[1], tmshin@yonsei.ac.kr[1*]

Abstract

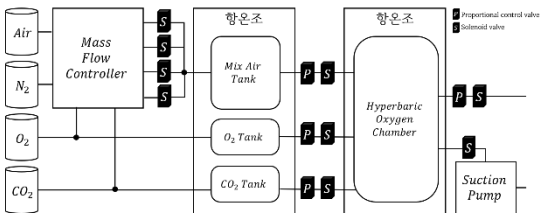
This study is a study on the development of a hyperbaric oxygen chamber control system for cell experiments that can implement custom protocols to meet cell culture conditions and create various experimental environments to clarify the mechanism of hyperbaric treatment through cell experiments. In order to meet the cell culture conditions, the developed system installed a thermostat and a water jacket in the hyperbaric oxygen chamber, and environmental data in the hyperbaric oxygen chamber are collected through six sensors. In addition, it is possible to create a quantitative mixed gas using the Mass Flow Controller so that the user can experiment in the desired atmospheric environment. Finally, for user convenience, a User Interface using Touch LCD was configured to monitor all chamber operations and the internal environment of the chamber in real time. The responsiveness of the system was confirmed through an experiment in which a step-function was applied as a pressure to evaluate the performance of the developed system. Through the developed system, it is expected to contribute a lot to the establishment of standardized standards for hyperbaric treatment by identifying the mechanism of hyperbaric oxygen therapy and incorporating it into animal experiments and clinical trials.

Background

Hyperbaric oxygen therapy is a treatment that delivers oxygen to the patient's tissue by supplying 100% concentration of oxygen to the patient at a pressure above atmospheric pressure.[1] In recent years, as the incidence of various infectious diseases, orthopedic diseases, and peripheral vascular diseases continues to increase, the importance of hyperbaric oxygen therapy is also increasing.[2] However, since the exact mechanism of hyperbaric treatment so far has not been identified, it is used based on experimental data, so the standard of the treatment protocol has not been established. Therefore, in order to reveal the mechanism of hyperbaric oxygen therapy, a preclinical experimental stage is required, and in particular, cell experiments are essential.[3] However, the existing hyperbaric oxygen chamber cannot meet the cell culture conditions and cannot provide various experimental environments. Therefore, this study developed a hyperbaric oxygen chamber control system for cell experiments so that hyperbaric oxygen therapy experiments can be conducted to reveal the mechanism of hyperbaric oxygen therapy in an in vitro environment.

Methods

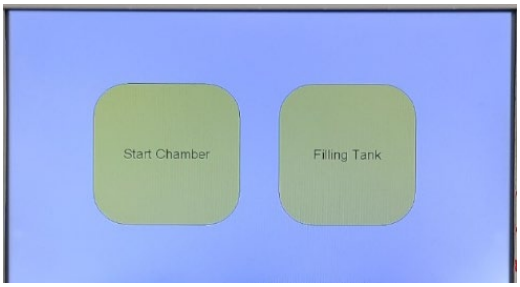
The self-produced high-pressure oxygen chamber consists of a mass flow controller that mixes gas to be used for the experiment, a tank that stores gases directly flowing into the experimental chamber, and a high-pressure oxygen chamber where high-pressure oxygen therapy experiments are conducted.



In order to maintain the temperature in the chamber at 37°C, which is a cell culture condition, the Mix Air Tank, O_2 Tank, and CO_2 Tank, which are directly introduced into the chamber, and the high-pressure oxygen chamber, which are experimented with, were placed in a thermostat. To prevent cells from drying up during the experiment, water jackets were installed inside the high-pressure oxygen chamber to maintain humidity, and two shelves were installed to arrange the cell plates.

The four gases are connected to the Mass Flow Controller so that they can be mixed at a user-defined ratio for various experimental atmospheric environments, and the mixed gas is stored in the Mix Air Tank in a thermostat. The mixed gas stored in the Mix Air Tank is used during the experimental protocol, and oxygen and carbon dioxide stored in the O_2 Tank and CO_2 Tank in the thermostat are used to maintain a 5% carbon dioxide concentration, a cell culture condition, in high concentrations of oxygen.

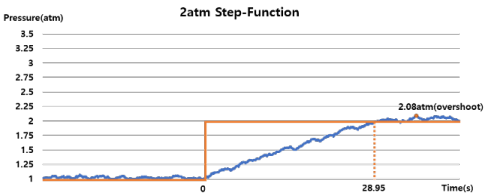
In addition, the User Interface using Touch LCD was designed for customized hyperbaric treatment protocol production for cell experiments, chamber operation, and real-time monitoring. The LCD used ADT10102BR50-14(G-Tech Display Technology, China) as a 10-inch Touch LCD, and the actual user interface is shown in Figure 2.



Finally, the responsiveness and safety of the developed automatic control system were confirmed by directing the Step-Function situation and measuring Overshoot under the target atmospheric pressure of 2 atm and 3 atm, which are mainly used during the treatment protocol.

Results and Discussion

The step-Function test results conducted by the performance test are shown in Figure 3 (a) at 2 atm and Figure 3 (b) at 3 atm at the target atmosphere. When the target air pressure was 2 atm, the target air pressure was reached 28.95 seconds after the start of pressurization, and about 8% overshoot occurred up to 2.08 atm, and when it was 3 atm, the target air pressure was reached 71.90 seconds, and about 2% overshoot occurred up to 3.04 atm.



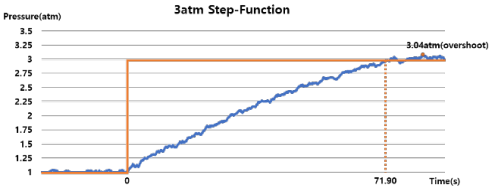


Figure.3 (a) Step-Function situation at 2atm
(b) Step-Function situation at 3atm

In the performance evaluation of the automatic control system through the production of the Step-Function situation, the pressurization speed following the complete opening was about twice as slow as when the target atmosphere was 3 atm, which is the result of the air pressure to be raised. Further experiments will be needed to determine how this rate affects cells. In addition, the actual Overshoot phenomenon is considered to be much lower because there was an error of about 5% up to 1.05 atm when the error in the Overshoot phenomenon observation was 1 atm.

In the future, it is necessary to adjust the PI coefficient according to the set pressure to minimize the overshoot phenomenon, and research should be conducted to identify the mechanism of hyperbaric oxygen therapy through cell experiments using various types of cells to prove its utility.

Acknowledgements

This study was supported by the Korea Health Industry Promotion Agency through the development of hyperbaric oxygen chambers for cell/animal research and the improvement of hyperbaric oxygen therapy devices applying clinical guidelines.(HI18C2196)

References

1. Yeonho You, Heeduck Kim, Hyun Kim, et al., “Clinical applications and contemporary trends of hyperbaric oxygen therapy in Korea”, Journal of Korean Medical Association, vol. 57, no. 7, pp. 601-606, 2014.
2. Kichang Nam, Juhwan Lee, Sungmin Kim, et al., “Performance & Safety test of Hyperbaric Chamber", The Korean Institute of Electrical Engineers, pp. 117-118, 2009.
3. "In vitro Skin Absorption Test Guidelines", Ministry of Food and Drug Safety, 2017.

The Joint Conference of the
IBEC2021 and the ICBHI2021

Clinical Medical Devices

Session Chair: Yunseo Ku (Chungnam National University, S. Korea)

11 Nov. (Thursday) Room B (16:30~18:00)

A Wirelessly-Powered Implantable Medical Devices — Byunghun Lee (Hanyang University, S. Korea)

Biomedical Optical Spectroscopy for Clinical Diagnostics
SeungYup Lee (Kennesaw State University, Georgia Tech, USA)

Artificial Intelligence using Electrocardiography: Strengths and Pitfalls
Joon-myoung Kwon (Sejong Hospital/Medical AI Co., Ltd., S. Korea)



Byunghun Lee
Assistant Professor
Hanyang University, Department of Biomedical Engineering/Electrical Engineering

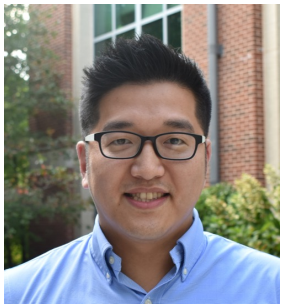
A Wirelessly-Powered Implantable Medical Devices

Abstract

Over the decades, wireless neural interfacing technology has been significantly developed to improve the patients' quality of life through surgical procedures eliminating bulky and risky interconnecting wires for chronic monitoring and treatment. Wireless neural interfaces had typically relied on the battery power, and, therefore, had a key limitation in terms of a large payload of batteries, which potentially effects on the behavior of animal subject. In addition, the limited experiment time due to the battery life was still a barrier to conducting long-term electrophysiology experiments over the span of several days, weeks, or months. In an attempt to overcome the limitations imposed by the battery charging by hardwired connection, the wirelessly-powered implantable medical devices are introduced in this presentation, which utilizes the integrated circuit (IC), inductive link, and wireless communication technologies. The presentation begins with the introduction of individual technologies for wireless implantable devices followed by and example of wirelessly-powered implants called WINeRS system.

Brief Biosketch

Byunghun Lee received the B.S. degree from Korea University, Seoul, South Korea, and the M.S. degree from Korea Advanced Institute of Technology (KAIST), Daejeon, South Korea, in 2008 and 2010, respectively. From 2010 to 2011, he worked on wireless power transfer systems for electric vehicles (OLEV project) at KAIST as a research engineer. He also received Ph.D. degree in electrical and computer engineering from Georgia Institute of Technology (Georgia Tech) in 2017. From 2017 to 2021, Byunghun Lee was an assistant professor at Incheon National University Department of Electrical Engineering. Currently, Byunghun Lee is an assistant professor at Hanyang University Department of Biomedical Engineering/Electronic Engineering and the director of Biomedical Circuit and System (BCAS) Lab.



Dr. Seung Yup Lee
Assistant Professor
Kennesaw State University
Adjunct Assistant Professor at Emory University and Georgia Institute of Technology

Biomedical Optical Spectroscopy for Clinical Diagnostics

Abstract

Cancer and cardiovascular disease are the top leading causes of death worldwide. Early detection plays a pivotal role for improved outcomes. Organ-specific microvascular monitoring holds great promise to catch early alterations in tissue morphology, physiology and metabolic status. Unfortunately, *in vivo* real-time monitoring of these microvascular metrics is often challenging due to lack of affordable and non-invasive medical devices. Non-invasive, label-free, light-based sensing technologies offer a possible cost-effective solution to this urgent clinical need. In this talk, I will discuss two specific examples of how biomedical optical spectroscopy can aid in clinical diagnostics: (1) pancreatic cancer detection and (2) stroke screening in pediatric sickle cell disease. Pancreatic cancer is lethal with a single-digit (~7%) 5-year survival rate. It is known as a silent disease where clinical symptoms are only present at the last stage, thereby impeding early detection. I will describe how visible reflectance and fluorescence spectroscopies quantitatively characterize pancreatic tissues, and then introduce a needle-compatible miniaturized optoelectronic sensor for improved diagnostics. Sickle cell disease is an inherited red blood cell disorder that has a profound effect on the brain. The risk of stroke in these patients is 250x higher than the general population. I will present how near-infrared diffuse optical spectroscopies can characterize changes in brain hemodynamics in this unique patient population.

Brief Biosketch

Dr. Seung Yup Lee is an Assistant Professor in the Department of Electrical and Computer Engineering (ECE) at Kennesaw State University. He's also an Adjunct Assistant Professor in the joint Biomedical Engineering (BME) department between Emory University and Georgia Tech (GT) wherein he finished his postdoctoral training from 2016 to 2021. He earned his Ph.D. degree in BME from the University of Michigan (UM), Ann Arbor in 2015. From 2006 to 2010, he was a research engineer in Korea Electrotechnology Research Institutes. He received his B.S. degree in ECE in 2004, and his M.S. degree in BME in 2006 from Seoul National University (SNU), South Korea. He has received several fellowships and awards including American Heart Association Postdoctoral Fellowship (2019-2020), Best Scientific Poster Award at the Southeastern Pediatric Conference (2018), Best Oral Presentation Award at the GT Postdoc Symposium (2018), Petit Scholar Mentorship (2017) at GT and UM Rackham Centennial Fellowship (2013). Dr. Lee's research program is focused on the next generation biomedical photonics technologies for clinical diagnostics and health monitoring.



Joon-myoung Kwon
M.D. M.S.
Medical AI Inc.
Sejong Hospital Group

Artificial intelligence using electrocardiography: strengths and pitfalls

Abstract

Artificial intelligence (AI) is being applied in various fields of cardiology. The primary advantage of DL is its ability to discover features of certain data that cannot be discovered from a human perspective. Since 2019, AI using ECG has been investigated to enable the diagnosis of diseases not possible through conventional ECG. Recent studies have shown that AI-enabled ECG can be used to detect heart failure, pulmonary hypertension, hyperkalaemia, and anaemia, as well as to predict the development of atrial fibrillation and cardiac arrest. Various technologies based on DL, such as the generation of precordial six-lead ECGs from limb six-lead ECGs, are being introduced to detect myocardial infarction. DL enables a model to be created using only data, i.e. without the restrictions of human ideas. Furthermore, new insights can be acquired by comparing findings obtained using DL from data only with existing medical knowledge. Although those findings and the methodology involved will inspire many researchers, further research is needed to understand the exact meaning of the former.

One limitation of DL is overfitting. Using only data without human engineering is both a disadvantage and an advantage of DL. DL is merely a method for developing an algorithm with the best accuracy limited to certain data, and the risk of overfitting exists. To guarantee real-world performance, an external validation with isolated data from a different environment is required in all DL research studies. The other disadvantage of DL is that, currently, it cannot unveil the DL decision process, i.e. the black box. In other words, although a DL model can be developed by fitting each coefficient, we cannot specifically interpret the decision process of the model.

Reference: Kwon JM, et al. Artificial intelligence using electrocardiography: strengths and pitfalls, European Heart Journal, 2021.

The Joint Conference of the
IBEC2021 and the ICBHI2021

Award Session 3

Session Chair: Yun Kyung Jung (Inje University, S. Korea)
Jang-Hwan Choi (Ewha Womans University, S. Korea)
Taesik Go (Jeonbuk National University, S. Korea)

11 Nov. (Thursday) **Room C (16:30~18:00)**

A-013. Maximum Vibration Frequency Detection Method using a plezoelectric Sensor for Skincare Device
Chang Gyu Park (Kyungpook National University, S. Korea)

A-014. Design of a Filter Rotation System for Specular Reflection Removal of Cervicography
JaeHwang Seol (Gachon University, S. Korea)

A-015. Generative Adversarial Network-based Image Reconstruction of Sparse-View Panoramic Radiography for Dose Reduction, and clinical evaluation
Minhyuk Choi (Seoul National University, S. Korea)

A-016. Deep learning-based Bone Marrow Edema Detection using Dual-energy CT with Multi-channel Data Fusion
ChunSu Park (Pusan National University, S. Korea)

A-017. Simultaneous Calibration of Plane Coordinate and Depth of Interaction for Monolithic Crystal PET Detectors using Oblique Irradiation
Sangjin Bae (Seoul National University, S. Korea)

A-018. SiPM Signal Readout for Inter-Crystal Scatter Event Identification using High Pass Filters
Hyeong Seok Shim (Seoul National University, S. Korea)

Maximum vibration frequency detection method using a piezoelectric sensor for skincare device

Chang Gyu Park[1], Seong Hwal Shin[1], Sang Kwang Bang[1], Min Gyu Park[2] ,Jeong Hyun Lee[3*]
[1]Department of Medical & Biological Engineering, Graduate School, Kyungpook National University, Daegu, 700-422, S. Korea
[2]Institute of Biomedical Engineering Research, Kyungpook National University, Daegu, 700-422, S. Korea
[3]Deptartment of Biomedical Engineering, School of Medicine, Kyungpook National University, Daegu, 700-422, S. Korea
[*]pung@knu.ac.kr

Abstract

In this paper, a frequency detection system was proposed for each operating frequency band of a device using high frequency among skincare devices. For vibration measurement, a piezo sensor DT1-028K (TE connectivity, USA) was used, and galvanic water peeler (RECLAR, Korea) was used among high-frequency skincare devices. The frequency was detected through data processing using LabVIEW (National Instruments, USA). To verify the performance of the proposed system, the performance of the proposed system was verified by comparing the maximum vibration frequency appearing at the frequency detected using the LDV (Laser Doppler Velocimeter) and the proposed system.

Introduction

Recently, as the standard of living of modern people has improved, interest in beauty is increasing[1]. In addition, the skincare device market is entering the home and personal era from the center of medical devices for hospitals. Accordingly, as the home care trend in the beauty field continues to grow rapidly, investment and development of home care skincare devices are increasing[2].

Currently, the most common skincare device is a device that uses vibration. Among them, the device using radio frequency therapy is a skincare device for improving oil, moisture, roughness, wrinkles, and pores[3]. However, the reality is that verification or clinical research on the effectiveness of skin care using cosmetic devices is lacking[4].

Therefore, in this study, a frequency detection system was proposed for each operating frequency band of a skincare device using high frequency. The proposed system uses a piezoelectric sensor DT1-028K (TE Connectivity, USA) for vibration measurement, and uses a peeler galvanic water peeler (RECLAR, Korea) among high-frequency skincare devices. In addition, the structure was designed and manufactured to be fixed between the sensor and the peeler. The signal output from the sensor passes through a bandpass filter and amplifier, and is input to the PC through the data acquisition system USB6211 (National Instruments, USA), and the frequency was detected by performing data processing using LabVIEW (National Instruments, USA). To verify the performance of the proposed system, the performance of the proposed system was verified by comparing the maximum vibration frequency appearing at the frequency detected using the LDV (Laser Doppler Velocimeter) and the proposed system.

Method

Research method

The proposed frequency detection system is configured as shown in figure 1. Vibration generated in the exfoliator was measured through a piezo sensor. At this time, a structure capable of fixing the peeling machine and the piezo sensor was designed and manufactured using a 3D printer. The signal measured by the piezoelectric sensor removes noise in a specific frequency band by the bandpass filter, and the signal amplified through the amplifier is converted to ADC(analog-digiatal converter) through the DAQ(data accusation) system and transmitted to the PC. The received data can be processed using LabVIEW and the frequency detected by the PC can be checked.

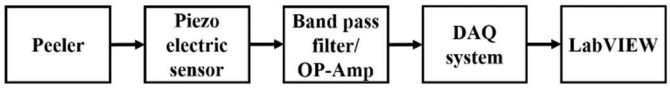


Fig. 1. Block diagram of the proposed system.

Experiments and results

The experimental environment for performance verification of the proposed system is shown in figure 2. The peeling machine operates in 100 Hz increments within 26.5 kHz to 32 kHz during operation. In the experiment, a total of three blades with different frequency characteristics were used in the experiment. The vibration generated by each blade was measured using the proposed system and LDV, and the performance of the system was verified by comparing the measured data.

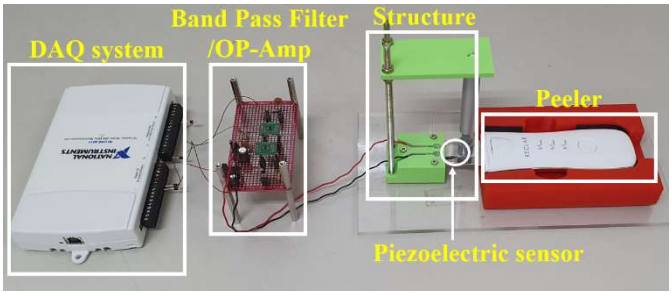


Fig. 2. Experimental environment of the proposed system.

Some of the results of measured through the proposed system and LDV are shown in figure 3. It can be seen that each result value measured using the piezo sensor and the LDV changes according to the change in the operating frequency of the peeler. Comparing the result measured using the piezo sensor and the

result measured using the LDV, it can be confirmed that the same resonance occurs at 32 kHz, which is the resonant frequency band of the blade in which the two results are used. Also, the output value according to the frequency change has a similar shape

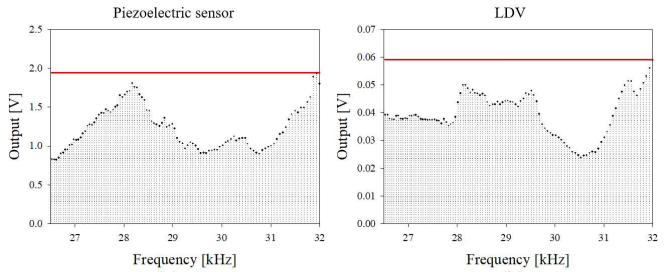


Fig. 3. Frequency detection result; (a) Piezo sensor and (b) LDV

Conclusion

In this paper, we propose a system that uses a piezo sensor to detect the operating frequency of a skincare device using high frequency waves. To verify the performance of the proposed system, a comparative experiment was conducted using the proposed system and LDV. As a result of the experiment, the proposed system and LDV were able to detect the same maximum vibration frequency. However, the measured values in different frequency bands did not match. This is due to the difference in the vibration measurement method of the two sensors. This is because the piezo sensor has a method of measuring vibration on a wide surface, and the LDV is limited to measurement at one point. Also, there was a difference in the measurement results depending on the fixing position and fixing degree of the piezo sensor. Therefore, by adjusting the elastic modulus of the damper fixing the piezo sensor to change the degree of fixation of the sensor, the difference in the result value can be reduced. It can be used for frequency detection instead of LDV, which is expensive and has a limited measurable distance, by improving the accuracy of frequency detection through supplementation and improvement of the proposed system later. In addition, it is expected that it can be used for frequency detection by device to verify the efficacy of skincare devices using vibration.

Acknowledgements

This research was supported by the National Research Foundation of Korea(NRF) grant funded by the Korea government(MSIT) (NRF-2019R1A2C2004347).

Reference

[1] Y. S. Han, J. J. Gwak, J. H. Park, J. L. Seo, Y. J. Lee, J. H. Lee, et al., “Effect of removal of the dead stratum corneum through applying ultrasound skin scrubber on facial skin,” Asian Journal of Beauty and Cosmetology, Vol. 3, No. 2, pp. 197-205, 2005.

[2] S. H. Kim, and S. G. Jung, “Design study on the Home-care Beauty Devices based on the UX; Product and service design of the vibrating cleanser,” JOURNAL OF INDUSTRIAL DESIGN, Vol. 10, No. 3, 2016.

[3] S. H. Park, and S. O. Noh, “Effect of High frequency therapy on Middle-aged wonmen's skin conditions,” Korea Academy Industrial Cooperation Society, Vol. 11, pp. 796-799, 2014.

[4] H. K. Choi, J. Y. Ryu, K. W. Lim, T. B. Choe, and M. H. Leem, “Effect of High Frequency and Ultrasound Therapy on Skin pigmentation and Wrinkle,” Asian Journal of Beauty and Cosmetology, Vol. 6, No. 3, pp. 11-20, 2008.

Design of a filter rotation system for specular reflection removal of cervicography

J.H. Seol[1,2], K.C. Yoon[2,3], K.G. Kim[1,2,3*]

[1]Department of Biomedical Engineering, College of Health Science, Gachon University, Incheon, Korea

[2]Medical Devices R&D Center, Gachon University Gil Medical Center, Incheon, Koera

[3]Department of Biomedical Engineering, College of Medicine, Gachon University, Incheon, Korea

kimkg@gachon.ac.kr

Abstract

Cervicography is one of imaging techniques for diagnosing cervical cancer. There is a specular reflection from the cervix due to the emission of light source, which can be interfered with acetowhite detection or reduce the accuracy of diagnosis. In this study, a filter rotation system is designed which can be rotated the polarizing filter. A filter could be removed the specular reflection during the diagnosis. Based on the experimental results which obtained with system, oral experiment was additionally conducted. As a result, it was succeeded in eliminating specular reflection.

1. Introduction

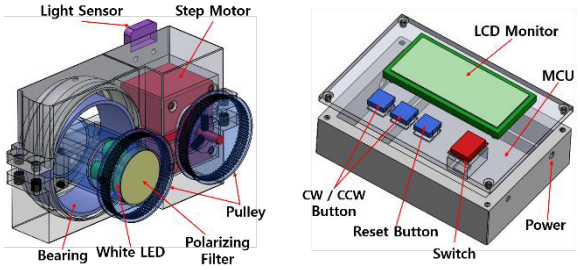
The cervicography is one of the imaging techniques for diagnosing cervical cancer. Recently, digitalized devices have advantages such as low cost, rapid reporting, and data manipulation [1]. However, there is a specular reflection from the cervix due to the emission of light source. Therefore, it will be possible to interfere with acetowhite detection or reduce the accuracy of diagnosis [2]. Modern medical images are necessary to accurate on-site diagnosis and high-resolution vision for lesion site [1].

In this study, a filter rotation system is presented that polarizing filter can rotate, and it is evaluated the system performance through the experiment. To get the realized experiment performance of proposed system, we also conducted oral experiment using cardiography digital camera.

2. Method of the system design

Figure 1 shows the entire mechanical design of the filter rotation system. From the figure 1 (b), when the power switch is pressed, the rotation angle of the step motor and luminance which collected from the light sensor is initialized. Then, it is displayed on the LCD monitor. The rotary direction can be controlled through the clockwise(CW) buttons and counter clockwise(CCW) buttons. The reset button initializes the current rotation angle in real-time.

In the Figure 1(a), a pulley which mounted on the shaft of the step motor is rotated. At the same time, the polarizing filter which mounted on the inner diameter of the pulley in the bearing also rotates together. The light sources from the white LED is irradiated through the polarizing filter. Pulley is designed with 70 teeth so that the rotation can be adjusted by 0.11° per one step. The proposed mechanism system can be designed as following to the formula of the belt power transmission system.



(a) (b)

Figure 1.(a) Rotation filter part mechanism design
(b) Control part structure design

Figure 2 shows the overall schematic design of the filter rotation system. Four and one LEDs with inner diameter of 10 and 5 are used, respectively. The LCD monitors and light sensors share the data with atmega128 in real time through I2C communication.

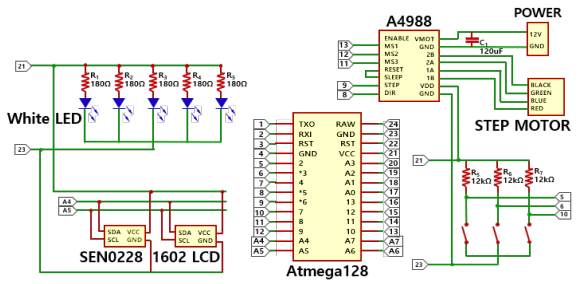
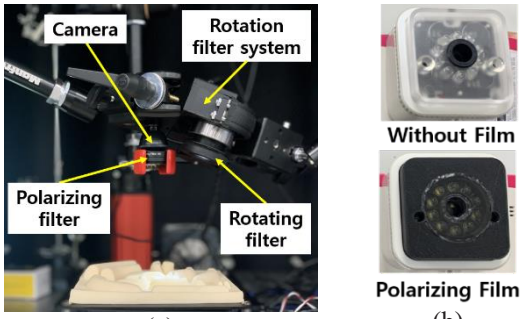


Figure 2. Schematic circuit for proposed system

Since all button switches are designed with pull-up resistors, the current which is generated from atmega128 flows to the motor driver through an external interrupt signal, when the button is pressed. In addition, a capacitor (120uF) is added to prevent sudden DC of 12V sparks.

3. Method of experiment



(a) (b)

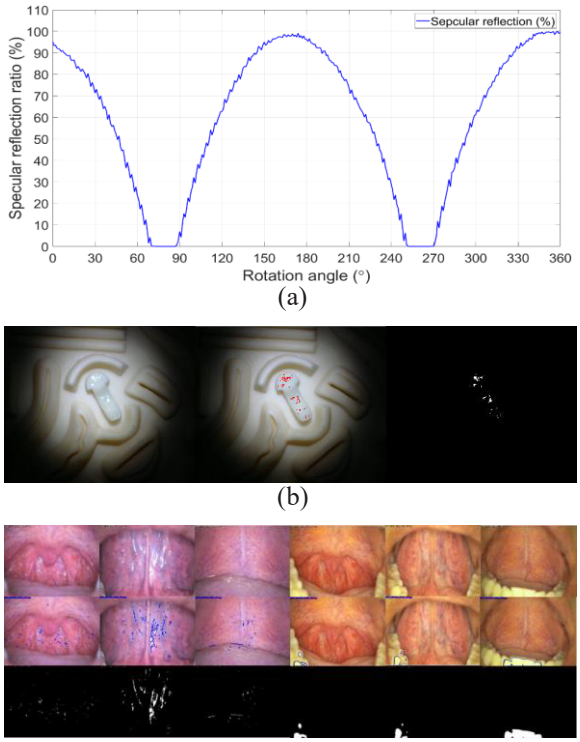
Figure 3.(a) Rotation filter system experiment
(b) Oral experiement with (Dr.cervicam C20 [1])

As shown in Figure 3(a), experiment of filter rotation system was conducted with phantom. After locating the polarizing filter at the front of the camera, the light is transmitted by polarizing filter which is mounted on the developed system. The polarizing filter rotates 1° each, rotating a total of 361 times from 0° to 360°. At the same time as the filter rotates, one photo is taken per 1° and captured a total of 361 photos. The collected data is used to analyze the results by quantifying the ratio of specular reflection through image processing.

Based on the experimental results which performed in Figure 3(a), the oral experiment is performed by attaching a polarizing film to Dr.cervicam C20 as shown in Figure 3(b). The comparison experiment was conducted between the non-film and film camera. The film was attached using UV bond because the light source of LED transmits only the polarized film.

4. Experimental results

Figure 4(b) shows the contour and binary mask image results that applied by the filter rotations system at 0°. The graph of Figure 4(a) shows the specular reflection ratio per angle with phantom experiment. As a result, it was confirmed that the signal form has a period of 180° and the specular reflection was completely removed to 0% at 80°-95° and 258°-274°. The oral experiment results with Dr.cervicam C20 is shown in Figure 4(c). it was obtained that the image color changed with the disappearance of light reflection.



(a)

(b)

(c)

Figure 4.(a) Specular reflection ratio per angle
(b) Applied contour and binary mask at 0°
(c) Oral experiment with Dr.cervicam C20

5. Conclusion

As a result, it was confirmed that there was a section where specular reflection was completely removed by using the rotation polarizing filter system. In this study, we present possibility it can be applied not only cervicography but also imaging diagnostic techniques.

Acknowledgements

This work was supported by the Technology Innovation Program (K_G012001187801, "Development of Diagnostic Medical Devices with Artificial intelligence Based Image Analysis Technology") funded By the Ministry of Trade, Industry & Energy(MOTIE, Korea)“

Reference

1. S. N. Kim, Y. H. Kim, K. H. Nam, S. K. Lee, T. S. Lee, H. S. Choi, S. J. Han, and S. C. Kim, “Development and validation of novel digitalized cervicography system,” Obstet Gynecol Sci. 59(3), 227-232 (2016).
2. V. Kudva, K. Prasad, and S. Guruvare, “Detection of specular reflection and segmentation of cervix region in uterine cervix images for cervical cancer screening” IRBM. 38(5), 281-291 (2017).

A-015

Generative Adversarial Network-based Image Reconstruction of Sparse-View Panoramic Radiography for Dose Reduction, and clinical evaluation

Minhyuk Choi[1]*, Seryong Kang[1], Jiyong Yoo[1], Su Yang[1], Sieun Choi[1], Bosoung Jeoun[2], Soyoung Chun[2], Jin Kim[2], Da-El Kim[3] and Wonjin Yi[4]

1. Department of Applied Bioengineering, Graduate School of Convergence Science and Technology, Seoul National University, Seoul, Korea

2. Interdisciplinary Program of Bioengineering, Seoul National University, Seoul, Korea

3. Medical Image Innovation Laboratory, Seoul National University, Seoul, Korea

3. Department of Oral and Maxillofacial Radiology, School of Dentistry and Dental Research Institute, Seoul National University, Seoul, Korea

cmh9101@snu.ac.kr

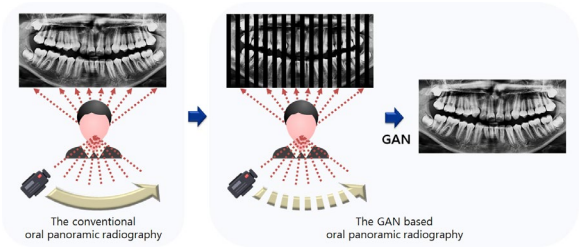
Abstract

Oral Panoramic Radiography(OPR) is a primary imaging modality system for diagnosing a patient's oral and jaw condition. The radiation dose of OPR is 3.5times and 10times higher than intra-oral and cephalometric radiography, respectively. In this study, we proposed a generative adversarial network(GAN) based image reconstruction of a sparse-view panoramic image for dose reduction. The normalized root mean square error(NRMSE), peak signal noise ratio(PSNR) and structural similarity index(SSIM) of the reconstructed images were 5.43, 0.85 and 10.83dB. Our method showed outstanding performance to the actual low dose image.

Background

Oral Panoramic Radiography(OPR) is a primary imaging modality system for diagnosing a patient's oral and jaw condition [1]. It is performed by rotating the radiation source around the patient's head, generating a 2-dimensional (2D) projection image. The radiation dose of OPR is low compared to Computed Tomography(CT), which is a 3D image. However, it is 3.5times and 10times higher than intra-oral and cephalometric radiography, respectively, 2D images used in the dental field [2]. In other words, OPR has the highest dose for the patient among dental 2D imaging systems.

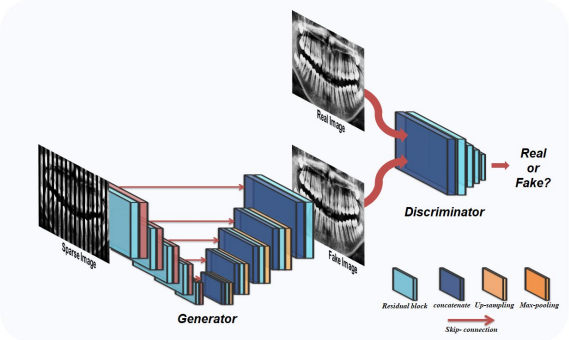
During OPR scanning, radiation may cause thyroid cancer in the patient, which may be more dangerous for pregnant women and children [3]. However, the research about dose reduction of OPR has not been much studied since the recognition that OPR has a lower dose of radiography than CT has prevailed. In this study, we proposed a generative adversarial network(GAN) based image reconstruction of a sparse-view panoramic image for dose reduction. In addition, we evaluated clinical usability by detecting dental disease in the reconstructed image.



Methods

We collected the 473 OPR images and normalized the images using histogram equalization. The resolution of images was converted to 512 by 1024 pixels for reducing the memory consumption in training. The sparse-view panoramic image was created by applying zero-padding of 8-pixel width with 8 pixels' stride. As a result, we acquired sparse-view panoramic images with half the original image dose. The images were divided into 283,94, and 96 for training, validation and test, respectively.

We used the patch-GAN for reconstructing the sparse-view image [4]. The generator in GAN was designed with five hierarchy levels using residual blocks. The skip-connection was used to prevent information loss in transferring image features from encoder to decoder. The discriminator in GAN was composed of residual blocks and distinguished the real image from the reconstructed image created by the generator with a patch of 32 by 64 pixels. We used the adversarial loss for optimizing the GAN [4].

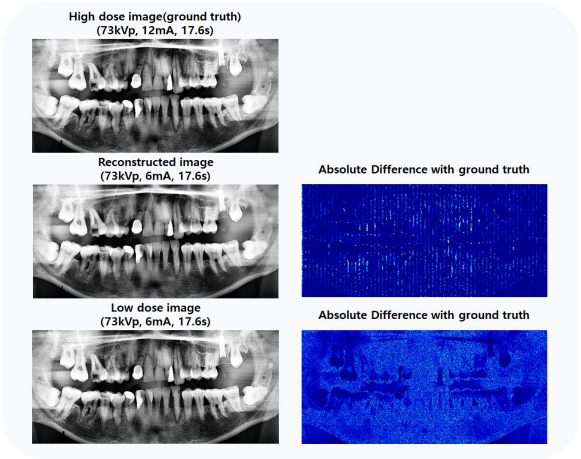


The weights of network were updated using ADAM optimizer for 300 epochs with an initial learning rate of 10^{-2}. The network was implemented in python3 using the Keras with Tensorflow backend.

For evaluation of the reconstructed image, we measured the image quality with normalized root mean square error(NRMSE), peak signal noise ratio(PSNR), and structural similarity index(SSIM), and compared the difference between low dose image and the reconstructed image. For evaluating clinical utility, dentists detected dental diseases in the reconstructed image.

Results and Discussion

The NRMSE, PSNR and SSIM of the reconstructed images were 5.43, 0.85 and 10.83dB. On the other hand, those of lose dose image were 8.35, 0.69 and 10.76dB, respectively. Our model showed outstanding performance to the low dose image. In clinical utility test, dentist detected the dental diseases with accuracy of 96%. The missing diseases were a small region that was hard to detect even in the original image. Therefore, reconstruction of sparse-view panoramic images based on GAN for dose reduction has no effect on clinical diagnosis. However, the sparse-view image was synthesized in this study, which needs further study with an actual sparse-view image.



Acknowledgements

This work was supported by the National Research Foundation of Korea (NRF) grant funded by the Korea government(MSIT) (No. 2019R1A2C2008365). This work was supported by the Korea Medical Device Development Fund grant funded by the Korea government (the Ministry of Science and ICT, the Ministry of Trade, Industry and Energy, the Ministry of Health & Welfare, the Ministry of Food and Drug Safety) (Project Number: 1711138289, KMDF_PR_20200901_0147)

References

1. B. Dannewitz, and J Muhling. "Effect of dose reduction in digital dental panoramic radiography on image quality." Dentomaxillofacial Radiology,Vol 31, p.50-55, 2002
2. Pasler, F. A., and H. Visser. "Zahnmedizinische Radiologies." Georg Thieme, Auflage, Vol 5, 1999
3. M. Wrzesien, and J.Olszewski. "absorbed doses for patients undergoing panoramic radiography, cephalometric radiography and cbct." International Journal of Occupational Medicine and Environmental Health, Vol 30, No.5, p705-713, 2017
4. P. Isola and J-Y Zhu. “Image-to-Image Translation with Conditional Adversarial Networks”, arXiv:1611.07004, 2016

Deep learning-based bone marrow edema detection using dual-energy CT with multi-channel data fusion

C.S. Park[1], D.E. LEE[1], C.K. Park[2] and M. KIM[3]

[1]Department of Information Convergence Engineering, Pusan National University, Yangsan, Korea

[2]Department of Radiology, Pusan National University Yangsan Hospital, Yangsan, Korea

[3]School of Biomedical Convergence Engineering, Pusan National University, Yangsan, Korea

cspark5484@pusan.ac.kr

Abstract

Dual-energy CT (DECT) is emerging as a great substitute for MRI for the detection of bone diseases such as Bone Marrow Edema (BME). However, it is seldomly used in clinics due to the limitation of the DECT experience. In this study, we develop deep neural networks (DNNs) to detect BME using DECT. For DNNs training, we create single-channel and multi-channel datasets where an image in every set consists of the bone region of interest. To improve generalization, we employ traditional data augmentation techniques and train DNNs. As a result, the areas under the receiver operating characteristic curve (AUC) are 90.4% and 92.8%, and the F1 Scores are 73.6% and 79.7% when the datasets are single-channel and multi-channel, respectively.

Background

MRI is the main imaging modality for detecting bone marrow edema (BME), but the clinical cost is quite high. Dual-energy CT (DECT) can be a great alternative using material decomposition techniques. Some studies reported that the disease detection rate from total DECT sections for every subject is quite high [1]. However, it is not still employed in clinics because 1) the performance is highly dependent on the DECT experience of physicians and 2) finding exact positions (sections) where BME happens is very challenging.

Currently, deep learning (DL) has been used in diverse medical imaging fields such as detection, segmentation, and classification due to its strong generalization [2]. In this study, we aim to develop a deep learning technique to assist physicians to find the BME in the region of interest (ROI). We used DECT images of 73 patients who were scanned by DECT and MRI within 1 month.

Hip bone from the top of the highest femoral head to the lowest lesser trochanter of both femurs was extracted as ROI from every DECT section to generate training/testing images. Every image was labeled by medical experts through monitoring the corresponding MR image. Augmentation techniques were applied to overcome overfitting problems caused by sample shortage and class imbalance. We developed a DL model based on convolutional neural networks (CNNs) for classifying the normal and abnormal cases from one ROI image. The diagnostic performance of DL was checked by comparing it with that of orthopedic surgeons and radiologists. In addition, we investigated the effect when we used 3 consecutive ROI images by extending 1 input channel to 3 channels under the observation that BME often spans multiple successive sections.

Methods

We used axial-water hydroxyapatite DECT images of a total of 73 patients in this study. A total of 73 cases, 50 cases were used for networks training and the rest as testing. Every case consisted of 25 to 40 DECT axial sections. For each section, one radiology professor decided ROI boxes and labelled them with the BME occurrence through monitoring the corresponding MRI section as reference (Figure 1).

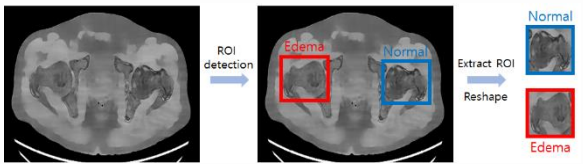


Figure 1. The process of generating training/testing images from dual-energy CT

We created single-channel and multi-channel datasets to train DNNs as shown in Figure 2. The single-channel dataset includes image data by extracting ROI from each section and resizing it to 64x64. The multi-channel dataset was made up of data consisting of three consecutive ROIs for each patient.

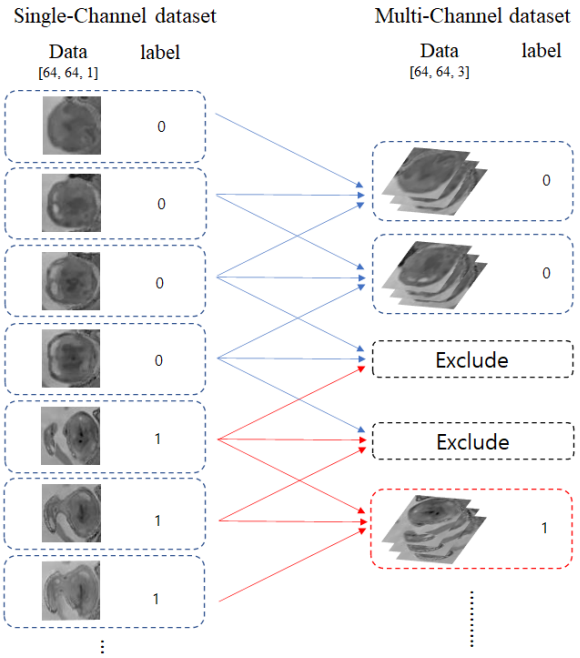


Figure 2. A framework of creating single-channel dataset and multi-channel datasets

The neural network consists of three convolutional layer, three max-pooling layer, and three fully connected layers, and a flatten layer. Each convolution layer has a rectified linear unit (ReLU) activation function and a dropout layer subsequently. The dropout rate in hidden layers, batch size and learning rate were set to 0.25, 16 and 0.001, respectively. We stopped learning early when the loss value of validation dataset was lowest. The BME probability is an output as sigmoid value. Finally, the model classified it as normal or abnormal if the value is <0.5 or ≥ 0.5, respectively.

We applied traditional data augmentation techniques such as left and right flip, up and down flip, rotation, zooming in or out on a single and multi-channel dataset to overcome the lack of total sample number and sample imbalance between normal and abnormal.

We conducted cross-validation to investigate the performance change between single-channel and multi-channel. Also, we checked the effectiveness of the augmentation. Among 50 cases in training dataset, we randomly selected 40 cases for training, and the rest for validation. For statistics, we repeated 10 times to create different subsets and measured average performance. In validation process, training results using multi-channel dataset showed better performance than single-channel dataset. In addition, we confirmed that the application of traditional image augmentation showed better performance not only in a single-channel dataset but also in a multi-channel dataset. To determine BME in the test set, we averaged outputs from 10 models trained with the different training/validation subsets as ensemble techniques.

Results and Discussion

Figure 3 shows the receiver operating characteristic (ROC) curves denoting classification results with single-channel test dataset. OS1 and OS2 are orthopedic surgeons and Rad1 and Rad2 are radiologists. OS1 and Rad2 have experience in dual-energy CT images, but others have no experience. Overall, DL outperformed the medical professionals.

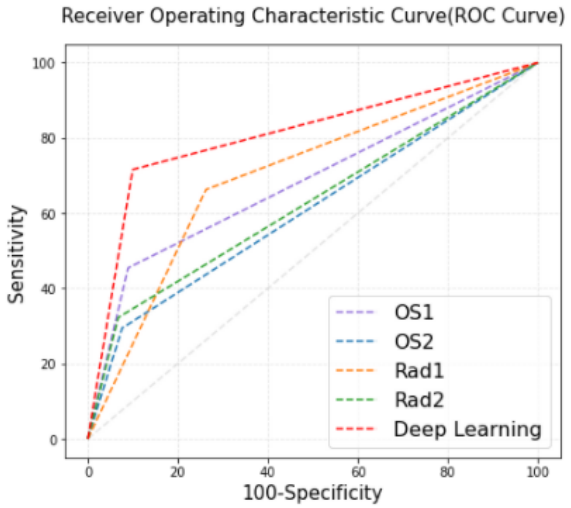


Figure 3. Receiver operating characteristic curves of classification test results

Table 1 describes the performances of the DL model using different test datasets. We showed the best performance when the dataset consisted of augmented multi-channel data.

Table 1. Performance comparison between different training datasets.

Method	Accuracy (%)	Sensitivity (%)	Specificity (%)	Precision (%)	F1 Score (%)	AUC (%)
Single Channel	81.34	56.60	92.14	75.85	64.83	87.02
Multi Channel	82.36	58.57	92.54	77.07	66.56	88.85
Single Channel + Aug	84.43	71.57	90.03	75.81	73.63	90.43
Multi Channel + Aug	**88.01**	**78.29**	**92.18**	**81.07**	**79.65**	**92.80**

We concluded that our deep learning approaches can help physicians and radiologists unfamiliar with DECT. In addition, they can contribute to finding exact single section or consecutive multiple sections where BME is extended.

Acknowledgements

This work was supported by Institute of Information & communications Technology Planning & Evaluation (IITP) grant funded by the Korea government (MSIT) (No. 2020-0-01450, Artificial Intelligence Convergence Research Center [Pusan National University])

References

1. McCollough CH, Leng S, Yu L, Fletcher JG, "Dual- and multi-energy CT: principles, technical approaches, and clinical applications", Radiology, 276:637–653, 2015.
2. Suzuki K, "Overview of deep learning in medical imaging", Radiol Phys Technol, 10:257–273, 2017.

Simultaneous Calibration of Plane Coordinate and Depth of Interaction for Monolithic Crystal PET Detectors using Oblique Irradiation

Sangjin Bae[1,2] and Jae Sung Lee[2, 3]

[1]Interdisciplinary Program of Bioengineering, Seoul National University, Seoul 03080, Republic of Korea

[2]Department of Nuclear Medicine, Seoul National University College of Medicine, Seoul 03080, Republic of Korea

[3]Brightonix Imaging Inc., Seoul, 04782, Republic of Korea

jaes@snu.ac.kr

Abstract

Positron emission tomography systems with monolithic scintillation crystals have been widely studied as an alternative to pixelated crystals due to their high spatial (*x, y* coordinate) and Depth-of-Interaction (DOI, *z* coordinate) resolution. Monolithic crystals require calibration procedures, and because DOI information is unknown for calibration sets obtained by irradiating crystals, there are difficulties in the DOI calibration. In this study, we performed optical simulations irradiating crystal perpendicularly and obliquely and trained deep learning models that estimate *x* and *z* coordinates of interaction positions. Trained models using the proposed method showed comparable results with models trained with actual interaction positions.

Background

Positron Emission Tomography (PET) detector detects gamma-ray using scintillation crystal that converts gamma-ray to low-energy photons. To estimate the position of radioactive sources with high accuracy, it is required not only estimation of *x*, *y* position of interaction, but also Depth-of-Interaction (DOI, *z*) estimation. PET detectors with monolithic scintillation crystals are investigated as an alternative for detectors with pixelated crystals and provide high spatial and DOI resolution. Machine learning-based [1] or statistics-based positioning methods were widely studied as a positioning algorithm for the monolithic crystals to utilize their high spatial resolution. This method requires a calibration set, but as long as obtaining calibration sets irradiating the crystal with gamma-rays, it is impossible to get DOI information.

Therefore, there have been several attempts to indirectly calibrate DOI, such as clustering using dispersions of light, or incident position estimation using incident angle obtained using coincidence event [2]. But, dispersion-based clustering can't fully utilize DOI resolution achievable with monolithic crystal, and in the case of incident position estimation, it required calibration sets obtained with many incident angles. Therefore, we propose a calibration process to train a deep learning model to estimate the interaction location using a dataset obtained using line sources irradiated with a small number of angles of incidence.

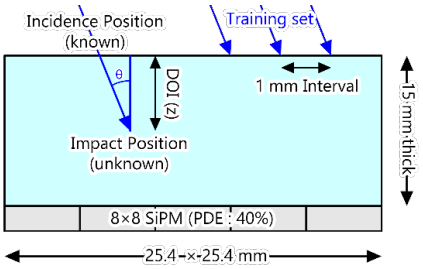


Figure 1. Simulation setup.

Methods

Assume that there is a deep learning model that estimates interaction positions (*x*, *z* coordinates) of gamma-rays, and calibration sets obtained by irradiating the line sources at known positions at three angles ($-\theta$, 0, θ). The mean square errors (MSE) between incidence positions computed using model outputs and actual incidence positions can be derived in form of the weighted sum of the square of errors of the interaction position. Therefore, we can train models to minimize position errors by minimizing the MSE of the incidence positions.

To validate the proposed concept, we performed simulations using GATE ver. 8.2 with the LUT-Davis Surface model and trained deep learning model with the PyTorch 1.9.0, a widely used Python package for deep learning. Figure 1 shows the simulation setup. 25.4 × 25.4 × 15 mm LYSO crystal (light yield: 30,000 photons MeV^{-1}, 8.4 % energy resolution at 511 keV)

was used. The lateral sides were polished, and the topside finished roughly. Teflon reflectors were attached to lateral and top surfaces. As a detector, we used an 8×8 SiPM (40 % photon detection efficiency) array, and row/column sum readout was used. We obtained calibration sets with 511 keV line sources that were parallel to the *y*-axis. Four calibration sets were obtained that spacing of incidence positions was the same (1 mm), but the incidence angle of oblique irradiation was different (15, 25, 35, 45°). The test set was obtained with a 25.4 × 25.4 mm plane source that irradiating 511 keV gamma on the crystal perpendicularly. As a model structure, 7-layer multilayer perceptron (MLP) with 192 nodes per layer was used with the ReLU activation function. We trained models using Adam optimizer, and the batch size was 256. The learning rate was 10^{-3} at the start and halved if the validation loss did not change. Max epoch was 100. We trained models using incidence information and actual interaction positions. We will call it the proposed model and the ideal model, respectively, for simplicity. Ideal models are impractical, but we trained them because it provides information about achievable resolution under the given calibration set and model structure. Proposed models are trained with different calibration sets, to evaluate the influence of the incidence angle of the calibration set on the model performance. We evaluated models using Full Width at Half Maximum (FWHM) and bias of positioning error.

Results and Discussion

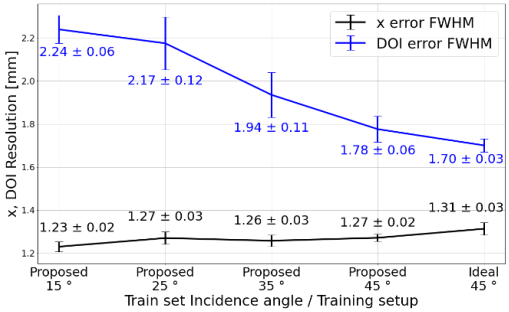


Figure 2. The resolutions of trained models

As shown in Figure 2, among the proposed models, the models trained with a 45 ° calibration set showed the best DOI resolution, with an FWHM value of 1.78 mm. The difference in spatial resolution between all models was less than 0.1 mm, which is negligible compared to the DOI resolution difference. The models trained with actual interaction positions showed the best DOI resolution among whole models, but the difference from the proposed model was less than 0.1 mm.

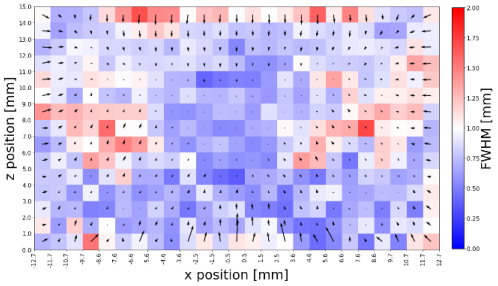


Figure 3. Bias Quiver / FWHM (Proposed, 45 °)

Figure 3 shows FWHM and quiver plot of bias of errors of the proposed model (45 °). Bias toward the center of the crystal was observed at the edge of the crystal. A large bias at the lower center of the crystal was observed in the result of the proposed model, which is not observable in the case of the ideal model. These results are thought to be because the parameters of the model were trained to reduce only the *x*-coordinate error at that location because no interaction occurred from oblique incidence at that location.

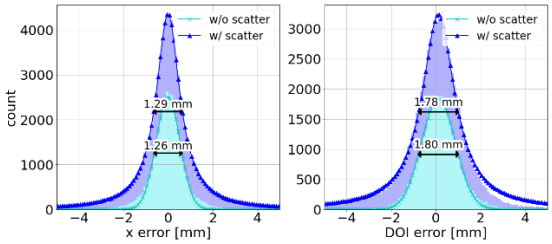


Figure 4. Spatial and DOI error histogram

Figure 4 shows the spatial and DOI error histogram of the proposed model (45 °). Long-tail in error distribution was observed for both spatial and DOI error distribution, but mainly due to events with multiple scatter. In the case of DOI, long-tail toward the negative direction was dominant, and it is thought because of the characteristics of the Compton scattering angle.

References

1. Bruyndonckx, P., Léonard, S., Tavernier, S., Lemaître, C., Devroede, O., Wu, Y., & Krieguer, M. (2004). "Neural network-based position estimators for PET detectors using monolithic LSO blocks," *IEEE Transactions on Nuclear Science*, 51(5), 2520-2525.
2. Maas, M. C., Schaart, D. R., van der Laan, D. J., Bruyndonckx, P., Lemaître, C., Beekman, F. J., & van Eijk, C. W. (2009). "Monolithic scintillator PET detectors with intrinsic depth-of-interaction correction," *Physics in Medicine & Biology*, 54(7), 1893.

SiPM Signal Readout for Inter-Crystal Scatter Event Identification using High Pass Filters

Hyeong Seok Shim[1, 2, 3], Sangjin Bae[1, 3], and Jae Sung Lee[1, 2, 3, 4]

[1]Interdisciplinary Program of Bioengineering, Seoul National University, Seoul, Korea

[2]Integrated Major in Innovative Medical Science, Seoul National University Graduate School, Korea

[3]Department of Nuclear Medicine, Seoul National University College of Medicine, Seoul, Korea

[4]Brightonix Imaging Inc., Seoul, Korea

Abstract

In this study, we propose a novel technique to estimate the amplitude of the signal from each channel of SiPM with lessened readouts, by using the time constant of the high-pass filter as the label of each channel. We summed 4 signals, all of them are filtered with different time constants, to reduce the readout and deconvoluted 4 signals from the summed signal with deep learning. We compared the R^2 value of the relation between the estimated and the true amplitude of four signals the 8 different sets of high-pass filters and found the optimal set. R^2 value of 4 signals on the best case were all above 0.99. On the worst case, the R^2 value of the signal from the second channel was below 0.8.

Background

Positron emission tomography (PET) is a functional and molecular imaging system detecting 511 keV gamma rays generated by the annihilation of a positron and an electron. 511 keV gamma rays are converted into photons inside the scintillation crystal, and SiPM detects these photons to measure the characteristics of the signals. [1] The overall performances are improved when the signals are received separately, however, since PET systems require a lot of SiPM channels, the number of readouts should be reduced. Also, to only use 511 keV gamma-ray events and reject events from Compton scattering, all events are validated with a fixed energy window. However, when 511 keV gamma rays deposit their energy partially inside the scintillation crystal, the energy of the signal is miscalculated and rejected by the energy window, thus degrade the count rate. This partial energy deposition across the crystal is called inter-crystal scatter (ICS) events. To recover such ICS events and improve the count rate, it is necessary to know each amplitude of the signal from each channel. [2]

In this study, we propose a novel technique that can estimate the amplitude of each channel with reduced readouts. We filtered the signals from four channels of SiPM with high pass filters having different time constants and summed them up. The deep learning technique was used to deconvolute four filtered signals from the summed signal. The concept was verified with not only the events which a signal comes out from one of the four channels but also the events which signals come out from two or more channels. By this technique, we expect to recover ICS events as well as positioning.

Materials and Methods

For the proof of concept, we compared the performances of 8 different sets of high-pass filters. The value of resistors and capacitors of 8 sets of high pass filters are listed in Table 1. 4 filtered signals before the summation, as well as the summed signal, were received to use as the ground truth. Figure 1 shows the circuit diagram of the experimental set-up. For deconvolution of summed signal into 4 individual filtered signals, we used a 2-layer multilayer perceptron (1023 - 128 - 4) as a model. 40,000 events were used per each setup and the ratio of the training set, validation set, and test set was 5:1:4. The learning rate began with 10^{-3} and was halved when the validation loss did not change.

		C (pF)			
		120	220	330	560
R (Ω)	Set 1	100	100	100	100
	Set 2	100	150	200	240
	Set 3	100	200	300	510
	Set 4	100	240	430	680
	Set 5	200	200	200	200
	Set 6	200	300	510	680
	Set 7	200	390	820	1600
	Set 8	200	510	1200	5000

Table 1. 8 sets of high pass filter used in the experiment

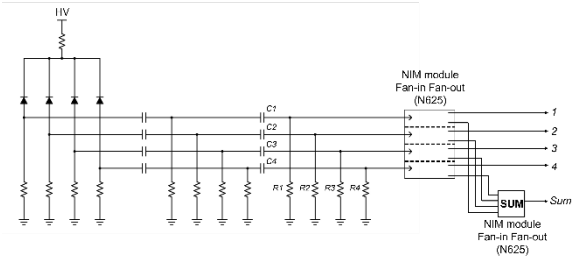


Figure 1. Circuit diagram of the experimental set-up

For the experimental setup we used 5.51 μCi ^{22}Na source for the radiation and 3.12×3.12×15 mm^3 LSO crystal array coupled with 4×4 multichannel SiPM as a radiation detector. Figure 1 shows the circuit diagram of the experimental set-up.

To compare the performance of deconvolution, we estimated the amplitude of 4 signals and compared with the true amplitude. We selected the R^2 value as the parameter to measure the precision of the performance.

Results and Discussion

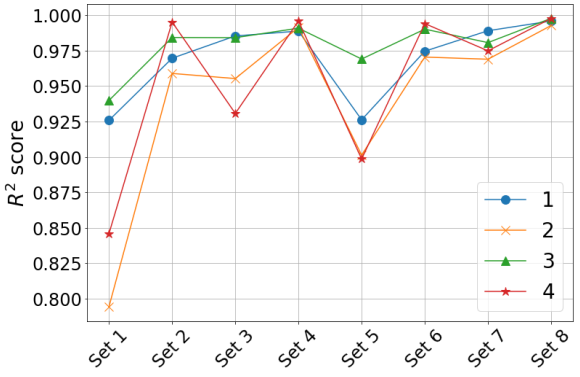


Figure 2. Each R^2 value of 4 signals on 8 sets of high pass filter

Figure 2. shows the R^2 value of 4 signals on 8 sets of high pass filters. Set 4 and Set 8 have the highest R^2 value, which means that the estimated amplitudes are most similar to the true amplitudes. Set 4 and Set 8 have maximum differences between each time constant, starting with 1.2×10^{-9} and 2.4×10^{-9} respectively. With this figure, we can know that when the difference between each time constant increases, the precision improves. Although there is a negligible difference of R^2 value between Set 4 and Set 8, since Set 8 starts with higher time constant, the minimum signal among 4 deconvoluted signals is bigger. Therefore, we plotted each relation between the estimated and the true amplitudes of 4 signals on the best case (*Set 8*) and the worst case (*Set 1*) in Figure 3.

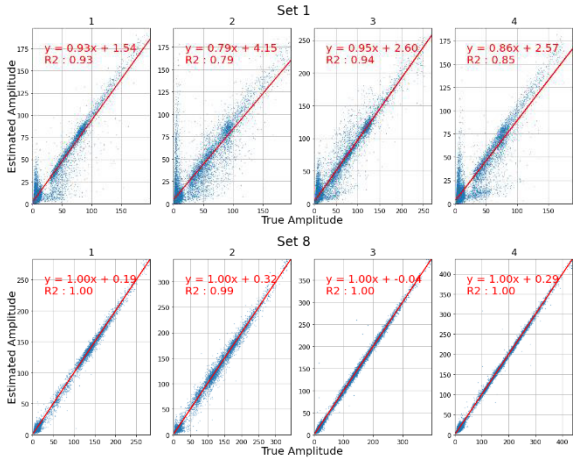


Figure 3. The relation of estimated amplitude and true amplitude of 4 signals: The best case (*Set 8*) and the worst case (*Set 1*)

All 4 R^2 values on the best case are all above 0.99 while the R^2 value of the second signal was below 0.8 on the worst case.

In conclusion, with our optimal set of high pass filters (*Set 8*), we successfully deconvoluted four signals from the summed signal by labeling each signal with different time constants of the high pass filter. With this technique, we expect to recover ICS events by precisely estimate the amplitude of the signal from each channel as well as positioning the signal.

Acknowledgements

This work was supported by grants from the National Research Foundation of Korea (NRF) funded by the Korean Ministry of Science and ICT (Grant No. 2020M2D9A1093989) and Sunway Medical Center.

References

[1] Cherry S R and Dahlbom M 2006 *PET: Physics, Instrumentation, and Scanners* (Berlin: Springer)

[2] Park, H. and J. S. Lee (2020). "SiPM signal readout for inter-crystal scatter event identification in PET detectors." Physics in Medicine & Biology 65(20): 205010.

The Joint Conference of the
IBEC2021 and the ICBHI2021

Plenary Session 2

Session Chair: Sung-Min Park (Pohang University of Science and Technology, S. Korea)

12 Nov. (Friday) Room A (09:00~10:00)

Educating Biomedical Engineers in Digital Health: Models, Challenges and Rewards

Shankar Krishnan (IFMBE, USA)

Models to Incorporate Digital Health in Biomedical Engineering Education

Shankar Krishnan

Educational program models in Biomedical Engineering (BME) especially in the undergraduate and master's levels go through continual refinement in their curricula. The major reasons at the undergraduate level are requirements from the accreditation agencies as well as the need to keep the educational program comprehensive, competitive, attractive to top quality students and faculty, financially sustainable, and successful. Technologies are advancing at rapid rates in all engineering fields and being an interdisciplinary field, BME must embrace and adopt the technologies for appropriate applications in the healthcare field. Covid-19 pandemic has triggered an array of disruptive phenomena in all our professional lives across the globe. In particular. the importance of digitalization spread across the healthcare domain has been highlighted. Based on a glimpse of the current BME programs, it is evident that inclusion of digital health is essential after careful reviews of the contents of existing curricula and necessary modifications. The key objectives of this plenary lecture are to provide a background of the overall curriculum structure in undergraduate and graduate BME programs, propose new models to incorporate digital health at various configurations, and address consequent rewards and challenges.

While many established programs with BME as a major discipline exist, some universities offer BME as a concentration or a minor field of study. There are also limitations in terms of the number of credit hours and the total duration of the program both at the baccalaureate and master's levels. The salient parameters in curriculum design include the foundational courses, the core courses and the elective courses, the number of credit hours for the lecture, lab, and capstone project components, the program educational objectives and the student learning outcomes, and additional courses in humanities and social sciences. Vital factors such as the estimated student size, available manpower and facility resources, and job and advanced studies opportunities for graduates must be prudently considered. The pervasive spread of digitalization especially in the MedTech industries and the health care delivery domain has led to the need for incorporation of digital health in the BME academic programs.

Different educational models are proposed to formulate BME curricula with varying degrees of inclusion of courses. The models could have an undergraduate minor or a concentration

or a concentration in Digital Health. The number of courses would vary with the model type. All models at the undergraduate level would also require project work or independent study in conjunction with experiential learning or internship modules. At the master's level, a sizable percentage would be in digital health related courses and the project or thesis work must be on solving current and emerging problems in digital health associated areas. It is realized that any addition of digital health components in the tightly packed curricula and over-stretched resources would have to meet the standard metrics for the success of modified or innovative programs. result in meaningful return on investment. In the current environment, it is proposed to add courses such as Health Informatics, Artificial Intelligence, Machine Learning, Interoperability, Privacy, Cybersecurity, Big Data and Predictive Analytics, Regulatory Affairs, and Data Science applied to BME and health care.

Educational models tend to have regional and national specificity and their successful outcomes will depend heavily on the commitment by the faculty, resource allocation by the Board of Trustees of public or private academic organization, and the interactions with industries, the advisory councils as well as support by the governmental agencies.

In conclusion, different models of adding digital health components in BME programs will encounter numerous challenges but will yield beneficial rewards. Purposeful intra and inter university and industry collaborations at national and international levels as well as careful planning and execution of digital health incorporation in the BME programs would pave the way to better preparation of industry-ready graduates and greater contributions by all of us to the health care field to achieve better health for all.

The Joint Conference of the IBEC2021 and the ICBHI2021

Biomedical Optics

Session Chair: Jae Gwan Kim (Gwangju Institute of Science and Technology, S. Korea)

12 Nov. (Friday) Room A (10:30~12:00)

Transcranial Photobiomodulation Stimulates Brain Rhythm Powers and Hemodynamic Network
Hanli Liu (University of Texas at Arlington, USA)

Label-free Assessment of high-risk Plaque by multi-modal Imaging Catheter
Hongki Yoo (Korea Advanced Institute of Science and Technology, S. Korea)

Nanostructure-based Functional Devices for Imaging and Sensing Applications
Dasol Lee (Yonsei University, S. Korea)



Hanli Liu, Ph.D.
Professor of Bioengineering
University of Texas at Arlington, TX, USA

Transcranial photobiomodulation enhances cerebral metabolism and electroencephalogram powers in healthy humans

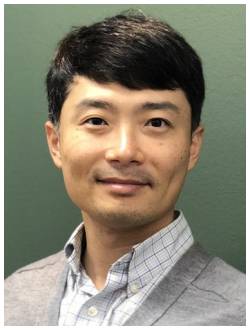
Abstract

Transcranial photobiomodulation (tPBM) is a new non-invasive means to neuro-stimulate the human brain using near infrared light. The light can be delivered regionally or globally across the human head, which has been reported by clinical studies to improve cognition or/and memory. However, few objective measures to quantify underlying mechanism of tPBM have been reported. In recent studies, our group has demonstrated that tPBM with 1064-nm laser, when being delivered regionally on the human forehead for 8 min, can significantly enhance cerebral hemodynamic concentrations, metabolic activities, and electroencephalogram (EEG) powers at both alpha and beta rhythms across the entire scalp. The hemodynamic and metabolic measurements were taken with broadband near infrared spectroscopy (bbNIRS) near the light delivery site. The measurements were performed over 25 human controls at two physical locations during a period of 3 years with consistent tPBM-induced increases in both cerebral hemodynamic and metabolic activities. Furthermore, 64-channel scalp EEG was utilized to concurrently record brain rhythms before, during, and after tPBM from 46 human subjects. The results demonstrated clearly that 1064-nm tPBM significantly increased EEG alpha and beta powers. Besides, we investigated tPBM-equivalent thermal effects on cerebral hemodynamic and metabolic activities as well as on EEG powers in the human brain. The results indicated consistently that tPBM and thermal stimulations induced significantly different responses in cerebral hemodynamics and metabolism as well as EEG alpha and beta power.

Brief Biosketch

Hanli Liu received her MS and PhD degrees in physics from Wake Forest University, followed by postdoctoral training at the University of Pennsylvania. She is a Full Professor of Bioengineering and Distinguished University Professor at the University of Texas at Arlington. She is also a Fellow of American Institute for Medical and Biological Engineering. Her expertise lies in the field of near-infrared spectroscopy of tissues, functional optical brain imaging, transcranial photobiomodulation (tPBM), and their clinical applications. Dr. Liu has published over 130+ peer-reviewed journal papers and 140+ conference proceeding papers or abstracts.

In recent years, Dr. Liu has led her team to the success of non-invasive quantification of cerebral hemodynamic and metabolic enhancement induced by tPBM with laser, facilitating tPBM as a clinical tool for cognition enhancement in healthy aging and in patients with brain disorders.



Hongki Yoo
Assocaite Professor
Department of Mechanical Engineering, KAIST

Label-free assessment of high-risk plaque by multi-modal imaging catheter

Abstract

Recent advances in optical fibers, lasers, and optical imaging technologies have introduced miniaturized fiber-based micro-endoscopy technology for use in a variety of biomedical applications. Especially, miniaturized fiber-based endoscopic imaging probes for optical coherence tomography (OCT) have been successfully translated into clinical diagnostics, including cardiology and gastroenterology. While gray-scale OCT provides only the microstructural information of biological samples, multimodal endoscopic imaging techniques using double-clad fiber can provide comprehensive information on top of the microstructure. In particular fluorescence lifetime imaging (FLIm) provides biochemical composition, inflammatory activity, and molecular information in a label-free manner. In this talk, we will present the technical advances of fiber-based micro-endoscopy technologies and its application to diagnose coronary artery disease. These newly developed endoscopic imaging technologies can provide an opportunity to investigate a variety of diseases, including cardiovascular and gastrointestinal diseases.

Brief Biosketch

Hongki Yoo is an associate professor in the Department of Mechanical Engineering, KAIST, Korea. Professor Yoo received his B.S., M.S., and Ph.D. in Mechanical Engineering from KAIST. He has worked as a postdoctoral research fellow and an instructor in Wellman Center for Photomedicine at Harvard Medical School and Massachusetts General Hospital. He led Biomedical Optics and Photomedicine Lab in the Department of Biomedical Engineering, Hanyang University, 2012-2019. After that, he joined KAIST in 2019 to lead Biomedical Optics and Optical Metrology (BOOM) Lab. His research topics include multimodal optical imaging, endoscopic imaging, optical coherence tomography, confocal microscopy, diagnostics and therapeutics of cardiovascular diasease, and machine leaning in optical imaging. For more information on Professor Yoo's research projects, please visit his website at https://boom.kaist.ac.kr



Dasol Lee
Assistant Professor
Department of Biomedical Engineering, Yonsei University,
Wonju 26493, Republic of Korea

Nanostructure-based functional devices for imaging and sensing applications

Abstract

Recently, the field of optical metamaterials that can realize unique optical properties has attracted great interest due to the rapid development of micro-/nano-fabrication technology. Optical metamaterials have exceptional advantages in realizing optical functionalities and therefore have been used in many applications. Here, recent efforts on metamaterials-based devices including super-resolution imaging platforms and basic technology applicable to high precision sensors will be discussed. First, metamaterials-based super-resolution imaging techniques of hyperlens and dielectric metasurfaces-integrated imaging systems will be introduced. Second, the basic studies and progresses on the spin Hall effect of light which refers to the spin-dependent and transverse splitting of oblique incidence will be discussed for further development and applications on ultra-sensitive biosensors. These techniques will provide an opportunity to achieve practical metamaterial devices as an important step in biomedical engineering.

Brief Biosketch

2021.09-present: Assistant Professor in Biomedical Engineering, Yonsei University
2021.03-2021.08: PIURI /BK21 Four Postdoctoral Fellow, POSTECH
2015.03-2021.02: Ph.D. in Mechanical Engineering, POSTECH
2013.03-2015.02: M.S. in Biomedical Science & Engineering, GIST
2009.03-2013.02: B.S. in Biomedical Engineering, Yonsei University

The Joint Conference of the IBEC2021 and the ICBHI2021

Biomechanics

Session Chair: Bomi Gweon (Sejong University, S. Korea)

12 Nov. (Friday) Room A (13:30~15:00)

Inefficient Muscular Contraction after Hemispheric Stroke

Jongsang Son (Northwestern University, USA))

Advancing Our Understanding of Muscle Biomechanical Properties: Implication for Neuro- and Musculoskeletal Rehabilitation

Song Joo Lee (Korea Institute of Science and Technology, S. Korea)

Engineering Approaches of Osteoporotic Fractures: Numerical & Experimental Analyses

Taeyong Lee (Ewha Womans University, S. Korea)



Jongsang Son
Research Assistant Professor
Shirley Ryan AbilityLab
Northwestern University

Inefficient muscular contraction after hemispheric stroke

Abstract

Muscle weakness is one of the severe motor impairments, which is very common in broad clinical populations including stroke. While this paresis has been explored in terms of disrupted neural signals (e.g., reduced descending excitatory neural drive, altered motor neuron behavior, and abnormal muscle synergy), there is a knowledge gap in our current understanding of the potential contribution of progressive, secondary changes in muscle intrinsic mechanical properties (e.g., muscle size, muscle architecture, and muscle material properties). In this talk, we will discuss what muscular factors are changed following stroke and how these changes are associated with muscle performance and muscular contraction efficiency.

Brief Biosketch

Jongsang Son is an Associate Research Scientist at Shirley Ryan AbilityLab and a Research Assistant Professor in the Department of Physical Medicine & Rehabilitation at Northwestern University, Chicago, United States. He obtained his Ph.D. in Biomedical Engineering from Yonsei University, Wonju, South Korea. His research priorities are to understand neuromuscular mechanisms underlying motor impairments in broad clinical populations and to investigate neuromuscular adaptations to sensorimotor stimulations. Ultimately, he hopes to translate his discoveries into practical interventions that can prevent the development of motor impairments and help people with chronic disease improve motor functions.



Song Joo Lee
Senior Research Scientist, Associate Professor
Korea Institute of Science and Technology
University of Science & Technology

Advancing our understanding of muscle biomechanical properties: Implication for neuro- and musculoskeletal rehabilitation

Abstract

The human musculoskeletal soft tissue has viscoelastic properties showing time and history-dependent behaviors. The behaviors can occur because skeletal muscle, ligament, and tendon are formed by a complex hierarchical structure, consisting of about 80% water, 3% fat, and 10% collagenous fibers, and interaction with each other. Knowing the biomechanical properties of the musculoskeletal soft tissue could be important to develop rehabilitation therapy and surgical procedures. Especially, in this talk, I am presenting my research on changes in shear elastic modulus of lumbar muscles due to changes in postures, muscle behaviors due to different speeds, and entropy of muscle activation during functional tasks. Our understanding muscle biomechanical properties can be a basis to develop diagnostic tools and effective rehabilitation strategies for patients with neurological disorders and musculoskeletal diseases.

Brief Biosketch

2020-present, Associate Editor, IEEE Trans. Neural Sys. Rehabilitation Eng.
2017-present, Associate Professor, Bio-Med, University of Science & Technology
2015-present, Senior Research Scientist, Center for Bionics, KIST
2013-2015, Postdoc. , Northwestern Univ. & Rehabilitation Institute of Chicago
2013, PhD in Biomedical Engineering, Northwestern University



Taeyong Lee
Professor
Ewha Womans University

Engineering Approaches of Osteoporotic Fractures: Numerical & Experimental Analyses

Abstract

Osteoporosis remains a prevalent problem amongst the elderly. Its prevalence is known to vary from 10-20% in patients aged 50 years and older, depending on race and assessment methods. Currently, bone mineral density (BMD) obtained from dual X-ray absorptiometry (DXA) is the golden standard in diagnosing osteopenia (-1.0 □ t □ -2.5) and osteoporosis (t > -2.5). However, following osteoporosis therapy, increases in BMD can be deceptive. While the commercially available drugs seemingly counteract bone loss due to osteoporosis and consequently reduce fracture risk, the efficacy of these drugs in treating osteoporosis is still unclear. Therefore, we aim to compare drug influences, mainly ibandronate, risedronate and raloxifene, on BMD, peak fracture load (Fcr) and buckling ratio (BR) at the femoral neck. Fcr (structural changes), derived from QCT-based finite element (FE) modelling and BR (geometric changes) will provide insight into how each drug has uniquely asserted its therapeutic effects onto the osteopenic or osteoporotic patients. Furthermore, we also hope to establish a tri-axial relationship between these three parameters which could serve as an improved tool in clinical diagnosis of osteoporosis, both in terms of specificity and sensitivity.

Brief Biosketch

Prof. Taeyong Lee is a Professor in the Department of Mechanical & Biomedical Engineering, Ewha Womans University, Korea. He received a Ph.D. degree in Biomedical Engineering from University of Wisconsin-Madison in 2001. He then worked as a post-doctoral fellow in the Orthopaedic Biomechanics Laboratory at Harvard University, followed by a research associate in the department of radiology at Johns Hopkins University. He started his academic career as an assistant professor at National University of Singapore and moved to Ewha Womans Univeristy at 2016.
He is a director of the Biomedical Mechanics and Materials Laboratory in Ewha. He has published several papers in respectable journals (including 'Nature') on the viscoelastic response of composite materials as well as biological tissues. Recently, he has been working on the design of specialized equipment for elderly including diabetic patients with regard to the foot ulcer development. By using experimental and numerical analysis of plantar shear reduction, Dr. Lee and his team successfully presented the new concept of shear mechanism in the foot using FE analysis. He is a member of ASBMR, ORS, iFAB and has served as a reviewer of several international journals.

The Joint Conference of the IBEC2021 and the ICBHI2021

Bio-chip

Session Chair: Aram Chung (Korea University, S. Korea)

12 Nov. (Friday) Room B (10:30~12:00)

Microfabrication Techniques Compatible with Biomaterials for Biomedical Applications
KangJu Lee (Chonnam National University, S. Korea)

Designing High-aspect-ratio Nanostructures for Interfacing Biological System
Hyejeong Seong (Korea Institute of Science and Technology, S. Korea)

Microfluidic Platforms with Liquid Metal-based 3D Hyun Soo Kim (Kwangwoon University, S. Korea)



KangJu Lee
Ph.D
Assistant Professor, School of Healthcare and Biomedical Engineering, Chonnam National University
Affiliate Faculty, Terasaki Institute for Biomedical Innovation

Microfabrication Techniques Compatible with Biomaterials for Biomedical Applications

Abstract

With convergence research in the limelight, "biomechanical" engineering program has been emerging in mechanical engineering fields to integrate mechanical technologies with biomedical environment. For this, it is important to understand bio-interface where micro-/nano applications will be integrated. Bio-Machine interfaces can be considered at various scales such as cell-machine, organ-machine, and human-machine, and there are various situations including overcoming and attaching the boundary surface. Microneedles developed by microfabrication can be applied to the interface and overcome biological interfaces for a variety of therapeutic purposes. Their efficient therapeutic delivery has been demonstrated not only in transdermal areas but also in non-transdermal fields such as ocular and vascular tissue over the past decades. Developing functional biomaterials accompanied by micro-/nano fabrication technologies can regulate cellular interfaces for easy transfection and selective attachment of bio factors. In this talk, several key examples of bio-machine interface-related technologies in terms of fabrication and material and possible future perspectives will be presented.

Brief Biosketch

KangJu Lee is an assistant professor the School of Healthcare and Biomedical Engineering at Chonnam National University. He earned his BS and PhD degrees in the department of mechanical engineering, Yonsei University and spent his postdoctoral career at UCLA and Terasaki Institute. His research is based on developing medical devices to delivery drugs, therapeutics and to measure biosignal with particular emphasis in microfabrication of biomaterials, 3D bioprinting, and advanced microneedles.



Hyejeong Seong
Ph.D.
Brain Science Institute, Korea Institute of Science and Technology (KIST)
Division of Bio-Medical Science and Technology, University of Science and Technology (UST)

Designing high-aspect-ratio nanostructures for interfacing biological system

Abstract

Materials with micro- and nanoscale topographies are known to be regulators of cell proliferation and differentiation. Of these topographies, high-aspect-ratio nanostructures have emerged as versatile platforms for facilitating drug/biomolecule delivery, and intracellular sensing. Here, we present a new approach for the microfabrication of high-aspect-ratio, nondegradable silicon nanoneedle arrays that can support the long-term culture of human mesenchymal stem cells (hMSCs). Through a combination of different etching processes, we were able to finely control the sharpness of the nanoneedles from 20 to 700 nm. This enabled us to investigate the influence of the nanoneedle tip diameter upon the phenotype of interfaced hMSCs. High-content, image-based profiling of 100,000 individual cells cultured on different nanoneedle arrays revealed that the nanoneedle tip diameter could be used to influence cell shape, nuclear size, and actin alignment in a controllable manner. Mechanoresponsive cell behavior, including altered expression of lamins, Yes-Associated Protein (YAP) target genes and focal adhesion genes, could also be tuned by altering the tip diameter. These results were correlated to increased nuclear membrane impingement by the sharp nanoneedles, as shown by volumetric imaging using focused-ion beam scanning electron microscopy (FIB-SEM). Our method of fabricating high-aspect-ratio nanostructures will be broadly applicable to the design of nanotopographical interfaces for biomedical devices, such as bioelectrodes and diagnostic platforms.

Brief Biosketch

Dr Hyejeong Seong gained a PhD in Chemical and Biomolecular Engineering from Korea Advanced Institute of Science and Technology (KAIST) in 2016. Following her PhD, she moved to Imperial College London to continue her career as a postdoctoral researcher, under guidance of Prof. Molly M. Stevens. After postdoctoral research, she joined Brain Science Institute at Korea Institute of Science and Technology (KIST) as a Senior Researcher in 2020.



Hyun Soo Kim
Assistant Professor
Kwangwoon University
Department of Electronic Engineering

Microfluidic platforms with liquid metal-based 3D electrodes

Abstract

Electrical detection methods commonly used in microfluidic systems can provide label-free, scalable, and cost-effective analysis. Conventionally, 2D electrode pairs are employed to analyze the target content by measuring its impedance or capacitance. Although useful, the sensitivity of 2D electrode-based detection needs to be further improved to be utilized in various microfluidic applications. 3D electrode configurations that can perform more sensitive and uniform measurement have been proposed, however, they are limited in complicated fabrication processes and requirement for expensive equipment. Here, we present novel 3D electrode fabrication methods using liquid metals, that are, a freeze casting method and a self-aligned method. The proposed 3D electrode fabrication methods enable to reduce the manufacturing cost as well as to realize the highly sensitive measurement. Two different microfluidic platforms integrated with liquid metal-based 3D electrodes, wearable pressure sensors and droplet screening systems, will be presented.

Brief Biosketch

Hyun Soo Kim received the B.S. degree in Electrical and Electronic Engineering from Yonsei University, Korea, in 2006 and received his Ph.D. in the Department of Electrical and Computer Engineering, Texas A&M University, USA in 2014. He worked as a postdoctoral research associate at Texas A&M University, USA in 2015, and joined Korea Institute of Machinery and Materials (KIMM), Korea as a senior researcher in 2017. Since 2021, he is working in the Department of Electronic Engineering at Kwangwoon University as an assistant professor. His current research interests include the development and application of organ-on-a-chip microdevices, high-throughput microbial screening platforms, wearable biosensors, and environmental toxin detection systems.

The Joint Conference of the IBEC2021 and the ICBHI2021

Medical Imaging

Session Chair: Sejung Yang (Yonsei University, S. Korea)

12 Nov. (Friday) Room B (13:30~15:00)

Understanding the Selective Mechanism of Network Vulnerability in Alzheimer's Disease Using Computational Neuroscience Approaches

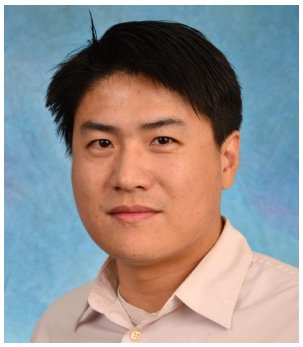
Guorong Wu (University of North Carolina at Chapel Hill, USA)

Unsupervised Learning for CT Image Enhancement

Jang-Hwan Choi (Ewha Womans University, S. Korea)

Development of a Fully Integrated US-NM (ultrasound-nuclear medicine) Probe

Jung-Yeol Yeom (Korea University, S. Korea)



Dr. Guorong Wu
Assistant Professor
University of North Carolina at Chapel Hill

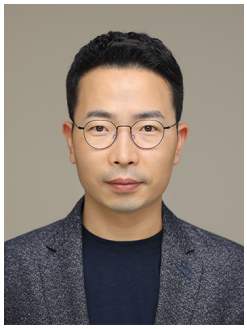
Understanding the Selective Mechanism of Network Vulnerability in Alzheimer's Disease Using Computational Neuroscience Approaches

Abstract

We are now in the era of big data. The unprecedented amount of biomedical data allows us to answer the biological questions today that we couldn't answer before. As a computer scientist, this is the most exciting time in my entire career. In the last ten years, I have been collaborating with neurology, neuroscience, genetics, and imaging experts to understand the pathophysiological mechanism of Alzheimer's disease (AD) and how AD-related genes affect aging brains. Specifically, my lab is interested in establishing a neurobiological basis to quantify the structural/functional/behavior difference across individuals and discover reliable and putative biomarkers that will allow us to come up with personalized therapy and treatment for individuals. In this talk, I would like to share my experience of integrating the domain knowledge of neuroscience into the development of computational tools for automated image analysis, image interpretation, and outcome prediction, with the focus on imaging biomarkers and the computer-assisted early diagnostic engine for AD. At the end of this talk, I will demonstrate the preliminary results of a recent research project where we aim to understand the selective mechanism of network vulnerability and resilience in AD using state-of-the-art network analysis approaches across neuroimaging and genetics data.

Brief Biosketch

Guorong Wu received the Ph.D. degree in computer science and engineering from Shanghai Jiao Tong University, Shanghai, China. He is currently an Assistant Professor at the Department of Psychiatry and Computer Science, The University of North Carolina, Chapel Hill, as an Assistant Professor. He has published more than 200 papers in international journals and conference proceedings. His research interests focus on fast and robust analysis of large population data, computer assisted diagnosis, and image guided radiation therapy. In 2016, he received the Independent Career Award from NIH for the contribution on non-invasive neurobiological basis for early diagnosis of Alzheimer's disease. He won the best paper award in MICCAI 2017. Dr. Wu is the associate editor for Neuroinformatics, Journal of Alzheimer's Disease since 2019.



Choi, Jang-Hwan
Assistant Professor
Ewha Womans University
Division of Mechanical & Biomedical Engineering

Unsupervised Learning for CT Image Enhancement

Abstract

X-ray computed tomography (CT) is an essential tool for detecting diseases and injuries. However, the risk of radiation-induced cancers is a rising concern in the medical field, and thus, low-dose computer tomography (LDCT) has become a common clinical protocol. However, as a counterpart, lowering dose leads to increased noise in the reconstructed CT images which hinders the accurate medical diagnosis. This motivated LDCT denoising to reduce noise in the LDCT images. Supervised LDCT denoising algorithms with convolutional neural networks has shown great success in their performance, and existing traditional methods rely on large amounts of labeled training data to achieve high performance. However, obtaining a sufficient amount of labeled data still remains costly, and might be even financially or physically impossible in medical domain. To overcome the limitations of existing data-dependent algorithms, we proposed unsupervised LDCT denoising by domain adaptation for the first time, and showed the possibility of using domain adaption methods for LDCT denoising. The proposed domain adaptation-based method can be applied not only to image denoising, but can be applied to other image restoration studies.

Brief Biosketch

Jang-Hwan Choi received the Ph.D. degree from Stanford University, Palo Alto, USA, in January 2015, on development of a robotic-based C-arm CT system for weight-bearing scans. In 2015, he developed a diagnosis and treatment technique for knee diseases (osteoarthritis and patellofemoral syndrome) caused by mechanical causes using weight-bearing CT and musculoskeletal modeling during his Postdoctoral Fellowship at the Stanford Medical School. Based on these findings, he has been awarded the New Investigator Recognition Award by Orthopedic Research Society, the most prestigious international society for orthopedic research. In March 2017, he was appointed as an Assistant Professor with the Division of Mechanical and Biomedical Engineering, Ewha Womans University. He also heads the Ewha Medical AI Laboratory in the division, and his laboratory conducts research on computer vision, pattern analysis, and medical informatics.



Jung-Yeol Yeom
Associate Professor
School of Biomedical Engineering, Korea University

Development of a fully integrated US-NM (ultrasound-nuclear medicine) probe

Abstract

In this talk, a fully integrated Ultrasound-Gamma (US-γ) probe and data acquisition system for intraoperative applications in introduced. This probe is designed to detect gamma radiation as well as ultrasound signal simultaneously. A readout circuit was also designed to acquire the US and Gamma signal simultaneously using a single channel. A SNR and axial resolution of 6.6 dB and 1.1 mm was achieved respectively for the US. In the case of the gamma probe, the energy resolution of full-width-half-maximum (FWHM) was 16.9% for Co-57 gamma radiation while 2.7 mm spatial resolution was acquired. Scanning experiments of a water tank with sealed radiation source and a non-radioactive plastic plate as target was also performed to assess the feasibility of the proposed dual-modality US-γ probe.

Brief Biosketch

Prof. Yeom acquired his B.Sc. from Department of Nuclear Engineering, Seoul National University in 2001, and his M.Eng./Ph.D. from the Department of Quantum Engineering and Systems Science, University of Tokyo at 2003 and 2006 respectively. He has had prior work/training experiences at Seoul National University Hospital, LG Electronics, Stanford University and Kumoh National Institute of Technology before joining Korea University. His research interests including medical imaging instrumentations including nuclear medicine and ultrasonic imaging.

The Joint Conference of the IBEC2021 and the ICBHI2021

Rising Women Engineers in BME (Joint Session)

Session Chair: Jennifer Hyunjong Shin (Korea Advanced Institute of Science and Technology, S. Korea)

12 Nov. (Friday) Room C (10:30~12:00)

Recent Progress of Optical Imaging Techniques for Diagnosis and Treatment Assessment of Breast, Ovarian and Colorectal Cancer
Quing Zhu (Washington University in St Louis, USA)

Quantitative histopathology using Normalized Raman Imaging (NoRI)
Seungeun Oh (Harvard Medical School, USA)

Real-time Extended Field-of-view Ultrasound Imaging with Multi-GPU Reconstruction
Eun-Yeong Park (Stanford University, USA)

Microphysiological Human Intestine Models to Decipher Host-microbiome Crosstalk
Woojung Shin (Harvard University, USA)



Quing Zhu
Professor
Washington University in St Louis

Recent Progress of Optical Imaging Techniques for Diagnosis and Treatment Assessment of Breast, Ovarian and Colorectal Cancer

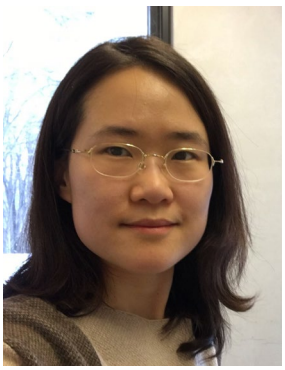
Abstract

This talk will focus on our recent progress utilizing Optical Imaging Techniques to advance diagnosis and treatment assessment of breast, ovarian and colorectal Cancer. Ultrasound imaging has co-registered with the optical imaging techniques to provide lesion morphology while optical imaging maps out lesion functional activity. The co-registered optical and ultrasound imaging techniques have implemented on hand-held probes suitable for imaging breast, ovary and rectum. This talk will also discuss roles of deep-learning in cancer diagnosis and treatment prediction as well as challenges with deep-learning in new optical imaging modalities.

Brief Biosketch

Professor Quing Zhu joined Washington University in St. Louis as a professor of the Department of Biomedical Engineering in July 2016. She also has a joint appointment in Electrical and System Engineering, and Radiology at Washington University School of Medicine in St Lois.

Professor Quing Zhu has been named a Fellow of Optical Society of American (OSA), a Fellow of SPIE- International Society for Optics and Photonics. Her research interests are focused on imaging techniques of photoacoustic, diffused light, ultrasound, optical coherence tomography for cancer detection, diagnosis and treatment assessment and prediction.



Seungeun Oh
Instructor
Harvard Medical School

Quantitative histopathology using Normalized Raman Imaging

Abstract

Stimulated Raman Scattering (SRS) microscopy visualizes the chemical composition of biological samples without any use of staining and has opened exciting opportunities in basic research as well as clinical histopathology. We created Normalized Raman Imaging (NoRI), a computational enhancement that can transform SRS images to calibrated chemical analysis. NoRI reports the chemical component at each pixel in a physical unit (mg/ml) by removing the effect of light scattering originating from samples. We demonstrated NoRI measurement of the absolute concentration of protein and lipids mass in tissues with high 3-dimensional spatial resolution. Since NoRI images show all protein and lipids, tissue microarchitecture is visualized in a similar manner as the Hematoxylin & Eosin (H&E) stained histological slides. As such, information equivalent to conventional H&E staining can be extracted from NoRI images by simply applying pink and purple pseudo-color to protein and lipids, while being free of the thin-sectioning artifacts and staining intensity variability of the conventional H&E histology. The novel and potentially critical quality of NoRI data lies in the physiological meaning of protein and lipid concentrations that are intrinsic properties specific to cell types, reflecting the health and disease states of the tissue. NoRI imaging of cells and tissues revealed quantitative biomarkers including condensation/dilution of the cytoplasm in various circumstances including mitosis entry and enrichment of lipids in the brains of Alzheimer's disease mice. Specifically, the lipid measurement is likely rich in novel information as lipid is extracted in typical paraffin-embedded histology samples. Owing to these characteristics, NoRI histology enables novel approaches in computational histology image analysis including machine learning-assisted analysis.

Brief Biosketch

Seungeun Oh, Ph.D. is an instructor at the department of Systems Biology at Harvard Medical School where she studies growth and homeostasis of cells and tissues using quantitative biophysical approaches. She utilizes label-free optical methods including quantitative phase microscopy and stimulated Raman scattering microscopy to measure protein and lipid biomass in developing or diseased tissues.



Eun-Yeong Park
Postdoctoral Scholar
Department Radiology, School of Medicine, Stanford University

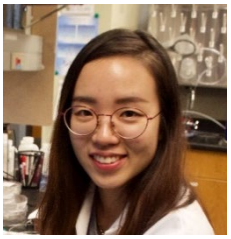
Real-time extended field-of-view ultrasound imaging with multi-GPU reconstruction

Abstract

Ultrasound (US) imaging has been routinely used for medical diagnosis and image-guided therapy thanks to the excellent safety, real-time imaging capability, and portability. New 1024 (or larger) channel imaging systems provide unprecedented opportunities to acquire data from 1D and 2D arrays with extended field-of-view (FOV) imaging. However, it is challenging to capture tissue motion or therapeutic procedures in real-time due to the enormous datasets. Here, we present a partial beamforming (BF) process with 1024-channel and multi-GPU cards for video-rate volumetric US imaging.

Brief Biosketch

Eun-Yeong Park received her B.S. and Ph.D. degrees in Electronic and Electrical Engineering from Pohang University of Science and Technology, Republic of Korea, in 2013 and 2020, respectively. Her Ph.D. work focused on the development of non-ionizing and non-invasive biomedical imaging techniques including photoacoustic/ultrasound imaging and their clinical applications. She joined the Ferrara lab at Stanford University in 2020 where she has been working on developing an ultrasound/photoacoustic dual-modal computed tomography system.



Woojung Shin, PhD
Postdoctoral Fellow
Wyss Institute for Biologically Inspired Engineering at Harvard University

Microphysiological human intestine models to decipher host-microbiome crosstalk

Abstract

Human microbiome and its crosstalk with the host play a key role in regulating human health and disease. However, it is still largely unknown how the microbiome affects the development, progression, and therapeutics of human diseases, mainly because of a lack of reliable experimental platforms. The human gut-on-a-chip is a microphysiological intestine model that closely recapitulates the intestinal microenvironment, including the three-dimensional epithelial structure, biomechanics, and physiological functions. Importantly, this innovative *in vitro* platform supports a stable and robust co-culture of the living microbiome, enabling the investigation of host-microbiome crosstalk in various gastrointestinal disease milieu. Here, we provide examples of the development and utilization of the gut-on-a-chip technology, including the mechanistic investigation of epithelial morphogenesis, the establishment of a novel platform to co-culture anaerobic bacteria, the identification of a trigger of intestinal inflammation, and the development of patient-specific intestinal disease models by integrating patient's samples. We envision that our technological innovation and findings will disseminate translational impacts in biomedical, clinical, and pharmaceutical science.

Brief Biosketch

Woojung is currently a postdoctoral researcher and an NIH/NCI F99/K00 fellow, working with Dr. Jim Collins and Dr. Don Ingber at the Wyss Institute at Harvard University. She got her expertise in human organ-on-a-chip during her PhD research at the University of Texas at Austin, working with Dr. Hyun Jung Kim. Now, she is trying to integrate synthetic biology approaches into the human organ-on-a-chip.

The Joint Conference of the IBEC2021 and the ICBHI2021

SP: Application in Digital Therapeutics

Session Chair: Hee Kyo Jeong (Yonsei University, S. Korea)

12 Nov. (Friday) Room D (10:30~12:00)

Guideline on Review and Approval of Digital Therapeutics

Young-Kyu Kang (Ministry of Food and Drug Safety, S. Korea)

Development and Regulation of Digital Therapeutics, Future directions

Kwon Ho Kim (Korea Health Industry Development Institute, S. Korea)

Digital Therapeutics in Respiratory Disease

Hee Kwon (LifeSemantics Corp., S. Korea)

Overview of Digital Therapeutics and SaMD

Seong-ji Kang (WELT corporation/Yonsei University, S. Korea)



Young-Kyu, Kang
Director
MFDS
Digital Health Devices TF

Guideline on Review and Approval of Digital Therapeutics

Abstract

Personalized medicine for patients has been trending along with the development of Information and Communications Technology (ICT), including big data and artificial intelligence.

Following this trend, the digital medical devices of today do more than detecting diseases, monitoring patients, and assisting decision making. Software as a Medical Device (SaMD) created to prevent, control and treat disabilities and diseases is taking the spotlight.

Digital Therapeutics have lower development costs and shorter development time than conventional medicine.

Furthermore, Digital Therapeutics can be used in medical fields where it is difficult to develop treatments by substituting or supplementing medicines.

The clinical field, in particular, is trending with developments like behavioral therapy, chronic disease management, and patient data collection and analysis. In order to provide proactive and predictable regulations for the novel field, it is necessary to set forth definitions, criteria for review, and the methods for approval and evaluation of digital therapeutics.

As of present, this guideline is intended to demonstrate the scope of digital therapeutics, criteria for judgement, and the methods for review and approval for the convenience of you and the enhancement of transparency in duties of review and approval.

Brief Biosketch

Dr.Young-Kyu, Kang is in charge of directing safety management of medical devices in the Ministry of Food and Drug Safety (MFDS), South Korea.

He holds an appointment as Director of Digital Health Devices TF in MFDS. Under his leadership, professional review and approval of SaMDs including Artificial Intelligence, mobile app, DTx, and U-Healthcare has been conducted and guidelines on review and approval of relevant products have been developed to support rapid commercialization of them. With this, he also serves as the chair of the AIMD working group of International Medical Device Regulators Forum (IMDRF) and has been participated in the international affairs with the aim of harmonizing the regulation in Korea globally.

Kim KwonHo
Researcher
KHIDI(Korea Health Industry Development Institute)
Department of Medical Devices & Beuaty-Cosmetics Industry

Development and Regulation of Digital Therapeutics, Future directions

Abstract

As the continuously COVID-19, mental health disorders such as depression and insomnia are on the rise caused by health concerns, job loss, isolation and uncertainty, etc. Digital therapeutics (DTx) has emerged as a therapeutic approach for the management, or treatment of these disorders through a cognitive behavior therapy (CBT). DTx have already been approved in such as the FDA, CE, PMDA etc. and are being used in clinical practice. On the other hands, there is still no product approved by the MFDS. The current status of domestic development and future support directions will be discussed compared with oversee cases.



Hee Kwon
BS, Nursing Science
LifeSemantics Corp.

Digital Therapeutics in Respiratory Disease

Abstract

Definition of Digital Therapeutics
Requirements for Digital Therapeutics
Development : Digital Therapeutics versus Investigational New Drug
Digital Therapeutics under development in Korea
How digital therapeutics are used in respiratory diseases
Why digital therapeutics are needed for respiratory diseases

Brief Biosketch

2013. 01 ~ Present LifeSemantics Corp. - Head of department DH/DTx
2009. 06 ~ 2012. 10 ICON(ex PRA Health Sciences) - Clinical Team Manager
2005. 10 ~ 2009. 01 ADM Korea – Sr. Clinical Research Associates

Publication

1. An mHealth Management Platform for Patients with Chronic Obstructive Pulmonary Disease (efil breath): Randomized Controlled Trial. (Kwon H, Lee S, Jung EJ, Kim S, Lee JK, Kim DK, Kim TH, Lee SH, Lee MK, Song S, Shin K.)
2. An mHealth Management Platform for Pulmonary Rehabilitation for Non-small Cell Lung Cancer. (Sojung Park, MD, PhD ; Ji Youn Kim, BSc ; Jae Cheol Lee, MD, PhD ; Hyeong Ryul Kim, MD, PhD ; Seungjae Song, PhD ; Hee Kwon, BSc ; Wonjun Ji, MD ; Chang Min Choi, MD, PhD)
3. Development and Validation of a Multidisciplinary Mobile Care System for Patients With Advanced Gastrointestinal Cancer: Interventional Observation Study (Soh JY, Cha WC, Chang DK, Hwang JH, Kim K, Rha M, Kwon H.)
4. Remote Management of Poststroke Patients With a Smartphone-Based Management System Integrated in Clinical Care: Prospective, Nonrandomized, Interventional Study (Do Yeon Kim ; Hee Kwon ; Ki-Woong Nam ; Yongseok Lee ; Hyung-Min Kwon ; Young Seob Chung)



Dr. Seong-ji Kang
WELT corporation
Yonsei university School of Public health

Overview of Digital Therapeutics and SaMD

Abstract:
Digital therapeutics (DTx) deliver medical interventions directly to patients using evidence-based, clinically evaluated software to treat, manage, and prevent a broad spectrum of diseases and disorders. DTx products are held to the same standards of evidence and regulatory oversight as traditional medical treatments. Those are regulated in the category of SaMD.

Because of their easy accessibility, record of improving outcomes, ability to integrate into care management workflows, delivery of real-world insights, and increased reimbursement by payors, DTx products are becoming critically important tools for clinicians and patients.

And the information collected from digital biomarkers are integrated within care management workflows to provide valuable insights that support health management and value-based care.

Brief Biosketch

Dr. Kang graduated as medical doctor of Yonsei university. He started his career as public health doctor in the Ministry of health & welfare, and he operated the first trial of digital health project in Korean goverment. After that he joined as the first medical doctor in Samsung electronics to take in charge of healthcare strategy. He nominated on FORBES cover as 2030 Power Leader in 2018.

The Joint Conference of the IBEC2021 and the ICBHI2021

SP: Application in Digital Healthcare

Session Chair: Jihoon Kang (Chonnam National University, S. Korea)

12 Nov. (Friday) Room C (13:30~15:00)

Wearable Biosensors for Healthcare Applications

Jayoung Kim (Yonsei University, S. Korea)

Overview of Digital Health Care & Digital Health Medical Device

Sung Hoon Kim (Yonsei University, S. Korea)

Evaluation of Effectiveness on the Proposed Physically Interactive Controller in Bilateral Upper-extremity Exercise

Jung Hyun Park (Yonsei University, S. Korea)

Jayoung Kim
Assistant professor
Department of Medical Engineering, College of Medicine,
Yonsei University, Seoul, Republic of Korea



Wearable Biosensors for Healthcare Applications

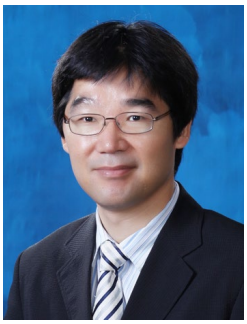
Abstract

Wearable biosensors represent a promising opportunity to continuously and non-invasively track human physiology through dynamic measurements of chemical markers in bio-fluids such as sweat, tears, saliva, and interstitial fluid. Such biosensing platforms can thus offer real-time biochemical information toward a more comprehensive view of a wearer's health, performance, or stress at the molecular level. The growing recent interest in wearable and mobile technologies has led to increased research efforts toward the development of non-invasive biomarker monitoring platforms. Continuous biomonitoring addresses the limitations of finger-stick blood testing and provides the opportunity for optimal therapeutic interventions. My research is focused on developing wearable electrochemical biosensors towards non-invasive health monitoring opportunities and evaluating the potential impact of such wearable point-of-care devices on our daily life. The innovative biosensing technology was demonstrated by successful electrical signal transduction of biomolecular reactions. It was further developed into various wearable form-factors using printing technology, offering wearer's conformity, flexibility, and stretchability. The wearable biosensors could measure a broad spectrum of biomarkers such as metabolites, electrolytes, hormones, and various small molecules in non-invasive biofluids, demonstrating clinical values through human studies.

These advances, opportunities, and future perspectives will be discussed through interdisciplinary approaches, such as materials engineering, printed electronics, and medical engineering.

Brief Biosketch

Jayoung Kim is an assistant professor in the Medical Engineering Department at Yonsei University, College of Medicine. Prior to that, she was a post-doctoral scholar in the Department of Chemical Engineering at Stanford University, working with Prof. Zhenan Bao. She earned her Ph.D. in the Material Science and Engineering Program at the University of California San Diego (UCSD) under Dr. Joseph Wang's supervision in 2018. Her Ph.D. thesis is focused on the development of wearable electrochemical biosensors for healthcare applications. She received her B.S. (2010) and M.S. (2012) in Chemistry from Yonsei University with a focus on developing nanomaterial-based electrochemical biosensors under Prof. Won-Yong Lee's supervision. Her research interests include a wide range of biosensors and bioelectronics for healthcare applications, bio-energy harvesting systems, printed electronics, bio-catalysis, and electrochemistry.



Kim Sung Hoon
M.D., Ph.D.
Yonsei University Wonju College of Medicine,
Dept of Rehabilitation Medicine
Yonsei University, Wonju Severance Christian Hospital Medical device Clinical Trial center

Overview of digital health care & digital health care medical dievice

Abstract

We live in a world where big medical data are being compiled. Many people make use of biometric information gathered by a variety of health care devices linked to smartphones, such as Fitbit devices. In addition, the development of medical information management schemes and the introduction of health information systems have greatly increased the possibility of using medical records stored in medical institutions. With the development of sensor technology and analytical capabilities, we have gained new knowledge through big data, stemming from the collection of data that was not important in the current medical area. Digital health care is moving toward creating value while creating utility as well based on data collected beyond the level of those collected by sensors. Only organizations that have quickly entered the market and accumulated data and have already developed advanced algorithms based on the data can be competitive. However, digital health care companies that survive in the market will lead the change and will reorganize the health care sector. In addition, a big data-based health care platform can help increase the number of e-patients through patient participation.

Brief Biosketch

- **Professor, Yonsei University, Wonju Severance Hospital, Dept of Rehbilitation Medicine**
- **Director,** Yonsei University, Wonju Severance Christian Hospital Medical device Clinical Trial center
- **Director,** Yonsei University, Wonju Severance Christian Hospital Medical device Safety Monitoring center

Evaluation of effectiveness on the proposed physically interactive controller in bilateral upper-extremity exercise

Jung Hyun Park, Tae Young Um, Kyuseok Kim, Kyu Bom Kim***

Department of Integrative Medicine, Yonsei University College of Medicine, Seoul, Korea

Introduction: Upper extremity disorders mainly occur the post-stroke cases and existing exercise and rehabilitation equipment is well-known to treat an affected neural network, intensively. However, when patient has severe activity restriction, this approach could be reduced the effect of treatment and had an inherent risk of injury. To overcome these problems, a bilateral exercise outperformed because the healthy neural network compensates the affected neural network, and it induces the brain plasticity. In this study, we implemented the evaluation of effectiveness on the proposed physically interactive controller (PIC) in bilateral upper-extremity exercise. Here, the PIC was able to the various motions including the extension, flexion, pronation, and supination of bilateral upper-extremity. A comprehensive evaluation of the exercise was performed by measuring electromyography (EMG) for actual muscle movement and electroencephalography (EEG) for patient's participation.

Materials and methods: The proposed PIC consists of a spherical balance ball, (ADXL335, Analog Device corp.) which measures 3-axis (*e.g.*, pitch, roll, and yaw) acceleration at real-time, a cradle to comfortable place the forearm of both upper extremities, and the button attached on the handle to receive the additional information. The maximum inclination for the proposed PIC in each direction is front of 22^0, rear of 28^0, and left and right of 16^0, respectively, and a difference of about 2^0 occurs depending on the length of the user's forearm. This experiment was conducted on the adults (8 males and 2 females, average age of 25 ± 1.7). EMG signal was measured by attaching sensors to the deltoid, biceps brachii, triceps brachii, and elbow according to the reference manual. EEG signal was also measured in 32 locations of the scalp according to the international 10-20 electrode placement method. To evaluate the effectiveness, root mean square (RMS), event-related desynchronization/event-related synchronization (ERD/ERS), and concentration index (CI) factors were measured. In particular, ERD/ERS was obtained by calculating the relative amplitude between measured and reference time series signal as the movement intention, and CI consists of some beta waves for the theta wave in the frequency domain. In addition, a conventional controller (CC) was used as a control group to compare with the

performance of the proposed PIC in condition which provides different type of movements (*e.g.*, finger extension and flexion).

Results and discussion: The activation of the triceps brachii during the extension of the upper extremity and that of the biceps brachii and deltoid during the flexion were significantly shown in the basic motion experiment of proposed PIC (p<0.05). Moreover, the proposed PIC indicated that the significantly larger ERD (p<0.05) and CI (p<0.05), compared to those of CC. However, because of the several outliers causes low reproducibility, ERS showed the opposite result (p<0.1). Moreover, a significant difference (p<0.05) is also shown in the task of pressing button of proposed PIC and CC, which is the same type of movement, indicating that the movement intention may appear differently even if the actual movement is the same.

Conclusion: The proposed PIC demonstrates that it was possible to more activation of brain as well as the actual muscle movement rather than CC. Furthermore, it may be employed to exercise the rehabilitation based on the result of the high concentration. Nevertheless, in the study, ERS did not show reliable results, and it will be solved by performing repeated experiments or identifying factors that affect them. In addition, more meaningful analysis can be expected by conducting cohort studies on the patients incorporating with normal and upper extremity disorders. These problems can be overcome through continuous R&D.

The Joint Conference of the IBEC2021 and the ICBHI2021

SP: Students Program (Organized by Medical Device Industry Graduate Schools Supported by MOHW)

Session Chair: Byung-Ju Kwon (Yonsei University, S. Korea)

12 Nov. (Friday) Room D (13:30~15:00)

Major Countries Regulatory Trend of Digital Therapeutics (Korea and USA, UK, Germany)
Hanji Lee (Yonsei University, S. Korea)

User needs analysis for multi-purpose smart neonatal incubator
Hyeonkyeong Choi (Yonsei University, S. Korea)

Next Generation Digital Therapeutics Device: Biofeedback via VR Motion Chair
Sisu Seong (Sungkyunkwan University/Samsung Medical Center, S. Korea)

Development of Bone Metastasis detection Algorithm on 3D CT Data made of different view images using Deep Learning-based CNN Model.
Min Seong Choi (Sungkyunkwan University, S. Korea)

Comparison of Posterior Capsule Opacification between Hydrophobic Acrylic and Silicone Intraocular Lens after Cataract Surgery : A Systematic Review and Meta-Analysis
Yerin Kwon (Dongguk University, S. Korea)

A Study on Improvement of the Certification System of Innovative Medical Device Software Manufacturer: Simplified Pathway based on Risk-related Certification Type
Hye Jin Kim (Dongguk University, S. Korea)

Real-time Surgical Phase Recognition in Cholecystectomy
Sanggoo Lee (Dongguk University, S. Korea)



Hanji Lee
Master's course
Department of Medical Device Engineering & Management,
Yonsei University, Seoul, Korea

Major Countries Regulatory Trend of Digital Therapeutics (Korea and USA, UK, Germany)

Abstract

Digital therapeutics are health or social care interventions delivered either wholly or significantly through a smart device to induce a behavioral change in the patient. Digital Therapeutics are cost-effective and can improve patient engagement and bring about substantial changes in patient health. Factors such as the increasing incidence of preventable chronic diseases, rising focus on preventive healthcare, need to control healthcare costs, and rising investments in digital therapeutics are driving the market growth.

In the Major Countries (Korea and USA, UK, Germany) Digital therapeutics are clinically approved evidence-based software and managed as a medical device. Since Digital Therapeutics have limitation in applying previous regulatory methods, a new regulatory approach is required. It is essential to understand major countries regulations well and to develop medical device regulatory tailored to each regulatory authority.

Brief Biosketch

[Education]

2020.03 – Present: Yonsei University, Medical Device Engineering and Management, M.S.
2015.03 – 2019.08: Gachon University, Biomedical Engineering, B.S.

[Experience]

2019.06 – Present: Yonsei University, Medical Device Design & Usability Lab, Researcher
2020.03 – 2020.11: Synex Consulting Ltd., Market Research, Researcher
2015.11 – 2018.09: Gachon University, Multi Modality Medical Imaging Lab, Researcher



Hyeonkyeong Choi
Master's course
Department of Medical Device
Engineering & Management, Yonsei University,
Seoul, Korea

User needs analysis for multi-purpose smart neonatal incubator

Abstract

An estimated 15 million infants were born preterm worldwide and this number is rising. (WHO,2018). The neonatal incubator is an important medical device of life support, as the survival rate of low birthweight and preterm infants. In this study, we combine multiple functions such as warmer, patient monitoring with ECG, NIBP, SpO2, RESP, TEMP, phototherapy to neonatal incubator. We expect that this newly designed incubator, multi-purpose smart incubator, can improve workflows in NICU. In order to reduce risk and improve patient safety, it is important to incorporate user human factors into the medical device design process. In the human factors engineering process, it is recommended to make user population participate in user interface design and evaluate the device. To define industrial design needs, participatory design was applied gathering user preferences on design elements of neonatal incubators. Our research identified user needs and preferences for multi-purpose neonatal incubator. Human factors engineers translated those into functional and design needs as design inputs for the design process.

Brief Biosketch

Master's Degree in Medical Device Engineering & Management, Graduate school of Yonsei University(03/2021-present)
Researcher, Medical Device Development and Usability Laboratory in Yonsei University



Sisu Seong
Sungkyunkwan University, The master's course
Sungkyunkwan University
Department of Medical Device Management and Research
Samsung Medical Center,
Research Institute for Future medicine

Next Generation Digital Therapeutics Device: Biofeedback via VR Motion Chair

Abstract:

After our society had recently made our life adjustments to the Fourth Industrial Revolution, in 2020, the Covid-19 pandemic was suddenly imposed upon us. Thus, we have been living with conditions in a world that we have never experienced before. The medical devices industry has started to research the next generation devices that remain relevant to current medical devices. One research thus breaks the mold in which the historically accepted notion on medical devices had been so that software is to be regarded as a medical device as well: SaMD. Therefore, we are ready to develop a new type of medical devices: the digital therapeutics device.

This study examines primarily the definition of the digital therapeutics device correlated with the present market conditions. Based on the current situation, it has been found that the market will demand for a multi-dimensional model to supplement solutions to resolve the existing problems. This study aims to develop a system whose effects are to reduce depressions and anxiety through biofeedback via VR motion chair that is interactive with other devices. It is not only a software program but also a set of instructions that show how to operate the medical device, namely AI, and assist the doctors how to treat their patients. It is the next generation digital therapeutics device.

Acknowledgements:

This research was supported by a grant from the Korea Health Technology R&D Project through the Korea Health Industry Development Institute (KHIDI) and funded by the Ministry of Health & Welfare, Republic of Korea (grant number: HR21C0885).

Brief Biosketch

SAIHST: Samsung Advanced Institute for Health Sciences & Technology

The Master's Course in Department of Medical Device Management and Research



Choi Min seong
Master's degree
Sungkyunkwan University, Dept of Medical Device Management and Research
: Research Institute for Future Medicine, Samsung Medical Center

Development of Bone Metastasis detection Algorithm on 3D CT Data made of different view images using Deep Learning-based CNN Model.

Abstract

Bone metastasis is a type of cancer that occurs when primary cancer cells invade the bone tissue as they travel through blood vessels or lymphatic vessels and thus penetrating the blood vessel wall. This sometimes causes extreme pain and paralysis due to bone fracture. Bone metastasis lesion is relatively simple but easy to miss in CT image reading due to decreased concentration of radiologists. The dataset includes 502 patient cases, age range from 27 to 96 years old. The primary goal of this study is to develop an AI algorithm for predicting and diagnosing bone metastasis cancer lesions using abdominal CT images. While the existing model only used the axial view 2D images of Abdominal CT for training, we planned to use 3D data of coronal view images. So, axial and coronal view images will be used to construct 3D dataset. The previous model structure is composed of 15 convolution layers and 5 pooling layers based on basic cnn network. In this study, to train the newly constructed 3D image dataset, we are going to use V-Net and Volumetric CBAM as 3D CNN models. Then, the ensemble technique will be applied to the models which are trained from each two different 3D images of different views. Through this, we expect better performance than existing 2D model.

As a result of this study, improved cancer detection system can shorten CT image reading time and also improve the prognosis of patients with bone metastasis through rapid treatment. Furthermore, economic effects can be expected by reducing unnecessary inspection costs.

Brief Biosketch

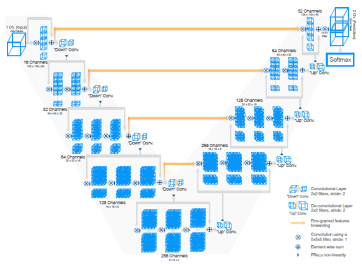
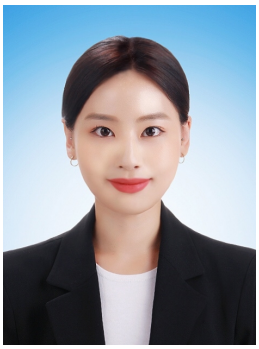


Fig. 2. Schematic representation of our network architecture. Our custom implementation of Caffe [5] processes 3D data by performing volumetric convolutions. Best viewed in electronic format.



Yerin Kwon
M.S. Student
Department of Medical Devices Industry, Dongguk University,
Seoul, Korea

Comparison of Posterior Capsule Opacification between Hydrophobic Acrylic and Silicone Intraocular Lens after Cataract Surgery : A Systematic Review and Meta-Analysis

Abstract:
Hydrophobic acrylic intraocular lens (IOL) is one of the most frequently used materials in cataract surgery currently. Posterior capsule opacification (PCO) is a well-known long-term complication of cataract surgery, impairing vision and adversely affects the prognosis of IOL delamination. Therefore, a systematic review and meta-analysis were conducted to provide an updated evaluation of the long-term complications and visual function after implantation with hydrophobic acrylic and silicone intraocular lenses. In this study, we found that hydrophobic acrylic IOLs exhibited a higher PCO value and Nd:YAG capsulotomy rate compared with silicone IOLs over long-term use exceeding 6 years. Therefore, this study may serve as a standard of reference for using hydrophobic acrylic IOLs due to increased life expectancy.

Brief Biosketch

- Education: A bachelor's degree of department of Medical Biotechnology, Dongguk University and currently in a master's degree course of Medical Device Industry, Dongguk University.
- Experience: Participated as a research assistant of MFDS service project, "A study on the improvement of combination product groups."
- Training: Registration for Euro Convergence 2021 leading by RAPS.

A Study on Improvement of the Certification System of Innovative Medical Device Software Manufacturer
: Simplified Pathway based on Risk-related Certification Type

H.J. Kim[1], Y.N. Hwang[2] and J.Y. Kwon

Department of Medical Devices Industry, Dongguk University, Seoul, Korea

Department of Medical Biotechnology, Dongguk University-Bio Medi Campus, Gyeonggi-do, Korea

gpalwls1123@naver.com

Abstract

Software as a Medical Device(SaMD) Manufacturers of Korea with excellent R&D and quality management systems are certified through 'the certification system of innovative medical device software manufacturer' and receive the benefit of being exempt to some document to be submitted upon application for the approval. However, the current certification system of manufacturer certifies manufacturer for each item of medical device. Therefore, the purpose of this study is to develop a simplified pathway for certified manufacturer that applies for certification of manufacturer with new item. First, based on the FDA Pre-cert program, the risk-related certification types were classified and the simplified pathway was proposed. And then, detailed assessment criteria for each pathway were derived through the software safety class-specific requirements of IEC 62304. Through the results of this study, more efficient and systematic certification system will be possible.

Background

Innovative medical devices are medical devices that are have significantly improved or are expected to improve safety and effectiveness compared to existing medical devices or treatments through the application of advanced technologies such as information and communication technology, biotechnology, and robot technology. Among medical devices designated as innovative medical devices, medical device software developed and manufactured alone is called innovative medical device software. The U.S. FDA is operating 'the Pre-Cert program' which allows pre-certified medical device software developer can determine the streamlined premarket review pathway for their product [1]. Similarly, In Korea, 'the certification system of innovative medical device software manufacturer' has been in effect since May 2020, and through this, certified manufacturers with excellence in R&D related personnel·organization·activity, manufacturing and quality management systems are exempted to some document to be submitted upon application for the approval process. However, this certification system has limitation that if a manufacturer is receive designation as an innovative medical device for another item, it must obtain certification of manufacturer again for the item. also, manufacturers are evaluated and certified through the same assessment criteria regardless of the risk of the software, which can lead to inefficient assessment procedure. Therefore, in this study, we intend to develop simplified pathway of certification through the classification of risk-related certification types and propose the detailed assessment criteria for each pathway.

Methods

1. Classification of risk-related certification type and simplification pathway of certification by types

1) FDA's Pre-Cert program: SaMD risk category and streamlined premarket review process

FDA Pre-Cert program classifies SaMD risk category by adding sub-category to the SaMD risk category (I~IV) proposed by IMDRF [2]. The premarket review pathway (No review or Streamlined review) determined for SaMD from pre-certified companies, depending on the risk category of the SaMD and the level of precertification of the organization.

2) MFDS's Certification system for innovative medical device software manufacturer: Medical device software classification and certification process

MFDS's certification of manufacturer does not establish their own risk-related classification system for innovative medical device software. Instead, medical device is given the classes by item of medical devices announced by MFDS [1,2,3,4]. also, medical device software manufacturers should classify the

software safety class of IEC 62304 through risk analysis.

The current certification system of manufacturer is carried out in the order of certification of manufacturer after designation of innovative medical devices, so, companies must obtain certification of each item designated as an innovative medical device. This process can lead to overlapping assessments when an existing certified manufacturer applies for certification of manufacturer for a new item.

2. Derivation of assessment criteria of simplified pathway

1) Requirements for each safety class of IEC 62304

IEC 62304 is a standard for medical device software life cycle processes, providing a system of life cycle processes related to activities and tasks necessary for safe design and maintenance of medical device software and requirements for each process [3]. This standard requires that software safety class be divided through risk analysis, and the requirements for each safety class are also different.

2) Assessment criteria for certification of innovative medical device software manufacturer

The certification of innovative medical device software manufacturer evaluates the excellence in personnel, organization, activity related R&D and the manufacturing and quality management system [4]. Among them, assessment criteria of the excellence in manufacturing and quality management system are highly related to the life cycle processes and activities required by the IEC 62304 standard.

Results and Discussion

1. Risk-related certification type of innovative medical device software manufacturer

Table 1 Matrix using the classes by the item of medical device and the software safety class

① \ ②	1	2	3	4
A	I(1)	I(3)	II(5)	II(8)
B	II(2)	II(6)	II(9)	III(11)
C	III(4)	II(7)	III(10)	III(12)

Table 1 is a matrix using the classes by item of medical devices announced by MFDS (①) and the software safety class of IEC 62304 (②). Each class represents a higher risk in the order of A, B, C and 1, 2, 3, 4. Through this, 12 sub-types related to risk of medical device software were divided, and sub-types were classified into three types of certification of innovative medical device software manufacturer. (Type I, II, III).

2. Simplified pathway based on certification type and assessment criteria for each pathway

Table 2 simplified pathway based on certification type

Classification of type of certification		evaluation criteria for certification	
type	**Sub-type**	**Initial certification**	**New item certification**
III	(10)~(12)	ⓐ	ⓒ
II	(4)~(9)		
I	(1)~(3)		ⓑ

Table 2 shows a simplified pathway for certified manufacturers that apply for certification with a new item according to the three types of certification.

Through the matching between software safety class-specific requirements of IEC 62304 and the existing assessment criteria of certification of innovative medical device software manufacturer, detailed assessment criteria for each pathway were derived.

In Table 2, When a manufacturer obtain certification for the first time, the same assessment criteria ⓐ are applied regardless of the software risk. Because this case is the initial certification, all existing assessment criteria for certification are applied. When a certified manufacturer applies for certification of manufacturer with a new low-risk medical device software (Type I), assessment criteria ⓑ are applied. According to IEC 62304, class A does not required some processes (software structure design, software integration and integration testing, software system testing, software risk management). Therefore, assessment criteria ⓑ exempt detailed assessment criteria of the excellence in manufacturing and quality management system related to the aforementioned process. In the case of high-risk medical device software (Type II, III) items in the same situation, assessment criteria ⓒ are applied. Assessment criteria ⓒ include all existing criteria of the excellence in manufacturing and quality management system, but exempt criteria of the excellence in R&D related personnel·organization·activity that is no significant change for each item. (if there is a significant change, relevant must be submitted.)

Through the results of this study, manufacturers can reduce the burden of submitting duplicate document

and regulators are also expected to be able to operate more efficient and systematic certification system through risk-related certification types.

Future research can be conducted on a comprehensive innovative medical device software manufacturer certification system that considers the level of excellence and maturity of manufacturers in terms of quality management as well as risk-related types of innovative medical device products.

Acknowledgements

This research was supported by the training program for advanced medical device industry professional manpower of Korea Health Industry Development Institute (KHIDI) funded by the Ministry of Health and Welfare, Republic of Korea.

References

1. FDA (2019), "Developing a Software Precertification Program: A Working Model v1.0″

2. IMDRF (2014), IMDRF/SaMD WG/N12FINAL:2014; Software as a Medical Device(SaMD): Possible Framework for Risk Categorization and Corresponding Consideration

3. IEC 62304/FDiS (2006), Medical device software — Software life cycle processes

4. MFDS (2021), "Information on the procedures and standards for certification of innovative medical device software manufacturing companies (Civil Complaint Guide)"



Sanggoo Lee
M.S. Student
Department of Medical Devices Industry, Dongguk University,
Seoul, Korea

Real-time Surgical Phase Recognition in Cholecystectomy

Abstract:
In the computer assisted interventions(CAI), surgical workflow recognition is very important subject. It could be applied to improve communication with an operator and nurse in modern operating room, educational materials and automatic surgery machine in the future. In this paper, we propose a training method for phase recognition of cholecystectomy in real-time during surgery without other information and schemes. Also, we introduce our end-to-end two-stream CNN-LSTM model. The result of this study is performed by using the open-source data Cholec80. We report the accuracy of 85.6% for phase recognition in cholecystectomy in real-time.

Brief Biosketch
I graduated from Dongguk University and received a bachelor's degree. I majored in Bio-Medical Engineering. And now, I'm majoring in Medical Device Industry in Dongguk University for master degree.
I'm studying deep learning using medical images, and learning regulation or policy for this medical device. Specifically, I am interested in surgical workflow recognition such as surgical phase recognition, surgical tool localization, surgical tool segmentation and surgical event detection.

The Joint Conference of the
IBEC2021 and the ICBHI2021

Poster Session

P-001

All-Inkjet-Printed Alveolar Barrier Model in Microfluidic Chip for Tissue Culture

Dayoon Kang[1], Wookyeom Kim[2], Yunji Lee[3], and Sungjune Jung[1,2,3,*]

[1] School of Interdisciplinary Bioscience and Bioengineering, POSTECH, Pohang, Republic of Korea

[2] Department of Mechanical Engineering, POSTECH, Pohang, Republic of Korea

[3] Department of Materials Science and Engineering, POSTECH, Pohang, Republic of Korea

sjjung@postech.ac.kr

Abstract

With the outbreak of new respiratory viruses and high mortality rates of lung diseases, physiologically relevant models of human lung tissue are urgently needed to study disease pathogenesis, drug efficacy, and toxicology. In this research, we present a three-layered human alveolar barrier model by printing four alveolar cell lines with an unprecedented thickness of approximately 10 μm. High-resolution inkjet printing enabled fabrication of the alveolar barrier model with the optimal three-layered structure by the drop-on-demand deposition of alveolar cells. Furthermore, the microfluidic chip was used for culturing the inkjet bioprinted alveolar barrier model for biomimetic blood flow at the epithelial-blood barrier interface. We investigated proliferation, multilayered structure, and functionalities such as tight junction and surfactant secretion of the printed alveolar barrier cultured in a microfluidic chip. The bioprinted alveolar barrier models and microfluidic chip could be a 3D-manufacturable alternative to traditional cell culture and animal models for pathological and pharmaceutical applications.

Background

Histologically, viral respiratory disease, which can damage lung tissues, has spread globally, countless people in the world have suffered. There is an urgent need for morphologically and functionally relevant, yet reliably manufacturable and customizable models of human lung tissue to study disease pathogenesis, drug efficacy, and toxicology[1]. Researchers have made great efforts to fabricate biomimetic *in vitro* 3D alveolar barrier tissue models in various ways. However, the difficulty of *in vitro* alveolar barrier tissue modeling still lies in the challenge to recapitulate the very thin and complex architecture with three-layered structure as well as spatial arrangements and populations of multiple cell types composing the tissue. Meanwhile, bioprinting technology is one of the emerging technologies that can be used to fabricate a 3D tissue model of a complex structure. Bioprinting enables an automated deposition of cells and biomaterials in a 3D manner for the highly controlled and customized production of tissue models[2]. Additionally, a microfluidic chip enables biomimic the dynamic microenvironment and key functions of organ units[3].

Methods

Fig.1 shows the inkjet printing process for the fabrication of an ultrathin, three-layered alveolar barrier model. The fabrication of a very thin, three-layered alveolar barrier model was accomplished via the precise inkjet printing of these cells and collagen in a Transwell with a 10 μm porous membrane, endothelial cell ink, collagen ink, and fibroblast-containing collagen ink were printed in a layer-by-layer manner. The all-inkjet-printed alveolar model was air-exposed cultured for 14 days until its structure and functions were further evaluated and analyzed.

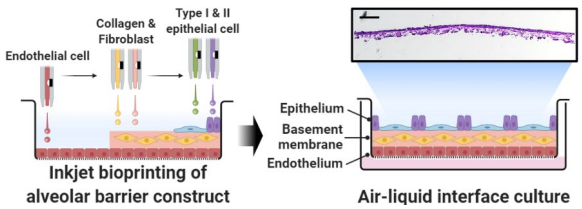


Figure. 2(a) shows the chip mold design and the product manufactured using laser assisted 3D printer, and Figure. 2(b) is the chip manufactured with PDMS.

To optimize tissue culture process in the microfluidic chip, the flow rate of the cell culture medium inside the microtubule was controlled, and we selected 50 µl/hr as the flow rate suitable for supplying nutrients to the tissue without leakage.

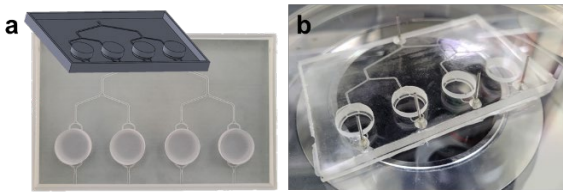


Figure.2 (a) Design and fabrication of microfluidic chip mold and (b) fabricated microfluidic chip

Results and Discussion

Figure. 3(a) shows single-flash jetting images of the bio-inks. All the bio-inks were ejected with an 80-µm-sized piezoelectric nozzle at a jet speed of ≈3 m/s. A precisely adjusted bipolar actuation waveforms and pneumatic pressures enabled the patterning of cell-laden drops with high resolution and stability. Figure. 3(b) shows cell viability obtained by analyzing cells stained with calcein AM (green, live cells) and ethidium homodimer-1 (red, dead cells). The results show high cell viability of >90% in the printed groups, which were close to the values of pipetted control groups. This high survival rate was consistently found for all the human cell types used in this work.

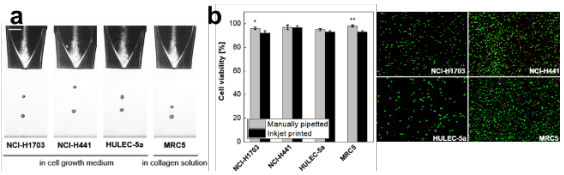


Figure.3 (a) Single-flash images of inkjet-printing of cells (b) viability of cells immediately after printing

Figure. 4(a) shows its clear three-layered structure with homogeneous distributions of epi- and endothelial cells on both sides of a collagen basement membrane. The unprecented thickness of the inkjet-printed alveolar model was measured to be 12 ± 1.1 µm by using a high-resolution stylus profiler (Data was not shown). Immunostaining was performed to confirm that the function of the cultured tissue inside the microfluidic chip was maintained. Figure 4(b) shows the tight junction formation and pulmonary surfactant secretion, which are representative functions of the alveoli. The image of the epithelium surface confirmed that the tight junction protein, ZO-1, was highly expressed over the entire area. The image of the apical surface showed a thin film containing the pulmonary surfactant, SP-A, that lines the gas-exchanging surface of the epithelium.

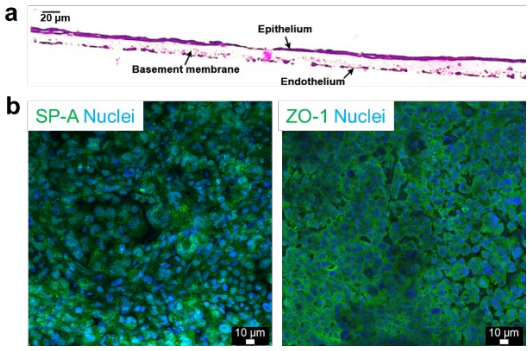


Figure.4 (a) A cross-sectional image of alveolar barrier model was stained with H&E (b) Immuno-staining of specific proteins (green) and nuclei (blue)

In this study, we aimed to recapitulate the morphological, functional, and microenvironmental features of human alveolar barrier tissue by high-resolution inkjet bioprinting and microfluidic chip. The results show that the 3D structured model maintained the key properties of alveoli, in the process of being cultured in the chip. All-inkjet-printed alveolar barrier model and microfluidic chip for tissue culture would have the potential to become a new enabling platform for studying respiratory physiology.

Acknowledgements

D.K., and W.K., contributed equally to this work. This work was supported by the National Research Foundation of Korea (NRF) grants funded by the Korean government (NRF-2018R1A2A3075391 and NRF-2020R1C1C1015018) and and Global R&D Activities through the Korea Center for Women In Science, Engineering and Technology(WISET) funded by Ministry of Science and ICT.

References

1. Langhans, Sigrid A. "Three-dimensional in vitro cell culture models in drug discovery and drug repositioning." Frontiers in pharmacology 9 (2018): 6.
2. Moroni, Lorenzo, et al. "Biofabrication strategies for 3D in vitro models and regenerative medicine." Nature Reviews Materials 3.5 (2018): 21-37.
3. Wu, Qirui, et al. "Organ-on-a-chip: Recent breakthroughs and future prospects." Biomedical engineering online 19.1 (2020): 1-19.

P-002

Highly efficient intracellular delivery for cell-based therapy using high-speed droplet squeezing

You-Jeong Kim[1], Ha-Sung Lee[1], and Aram Chung[1]

[1]Department of Biomedical Engineering, Korea University, Korea

ac467@korea.ac.kr

Abstract

We present a versatile droplet-based intracellular delivery platform leveraging droplet microfluidics with mechanical cell permeabilization. The delivery of external biomolecules was achieved by passing droplets containing a cell with target cargos through a single constriction at a high speed. The platform enables highly efficient gene transfection of immune cells using mRNA, and plasmid DNA with high scalability and can thus find potential application in cancer immunotherapy.

Background

Intracellular delivery of biomolecules, including DNAs, RNAs, proteins, and nanoparticles, into living cells is one of the important steps in engineering innate cell functions. As shown as Fig. 1, conventional strategies for intracellular delivery include lipofection, viral transduction, electroporation, and microinjection; however, they are limited due to their genotoxicity, inconsistency, low scalability, high cost, and/or time and labor consuming process [1]. To address these limitations, several microfluidic approaches have been introduced [2]. In particular, the cell squeezing platform, which is introduced by Armone Sharei, is already effective enough to approval for clinical applications (NCT04084951). However, the approach is limited because of failure of delivering plasmid DNA and large nanoparticles, wastefulness of delivery cargo, and channel clogging. To overcome these limitations, a high-speed droplet squeezing platform is introduced that can be considered as a next-generation intracellular delivery platform

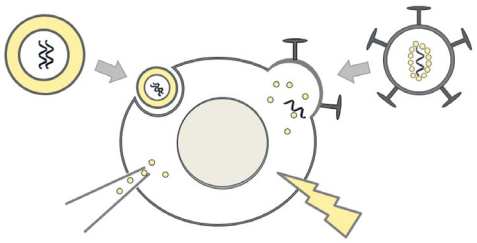


Figure 1. Conventional intracellular delivery strategies: (clockwise from top left) lipofection, viral transduction, electroporation, and microinjection.

Methods

A high-speed droplet squeezing platform mold was prepared by etching a silicon wafer using a deep reactive ion etching process, and polydimethylsiloxane (PDMS) microfluidic channels were created using standard soft lithography. Leukemia cell lines were cultured according to standard protocols. The cells mixed with the target molecules and recyclable oil were pumped into a microchannel by the syringe pump. Opti-MEM (Thermo Fisher) was used to transfect the mRNA or plasmid DNA. Additionally, 3 and 2000 kDa FITC-dextran (Sigma-Aldrich, USA), 996 nt EGFP-mRNA (TriLink BioTechnologies, USA), or 7.9 kbp pGreenPuro plasmid DNA (System Biosciences, USA) was used. After delivery, droplets were collected and coalescence by 1H,1H,2H,2H-Perfluoro-1-octanol (PFO) solution. The delivery efficiency of the cells was analyzed using flow cytometry, and cell viability was measured using a standard trypan blue assay.

Results and Discussion

The high-speed droplet squeezing platform comprises three functional units: a droplet generation part, droplet acceleration part and cell membrane disruption part. Cells and biomolecules are first co-encapsulated into droplets (Fig. 2A(1)) that allows stable droplet generation; additional sheath fluids are introduced to accelerate the droplets for efficient and clogging free cell mechanoporation (Fig. 2A(2)) when drops pass through a single constriction at a high speed (Fig . 2A(3)). During droplet squeezing, the cell membrane

is permeabilized and the cargos in the droplet are designed to transport into cells through the created discontinuities in the membrane (Fig. 2A(4)).

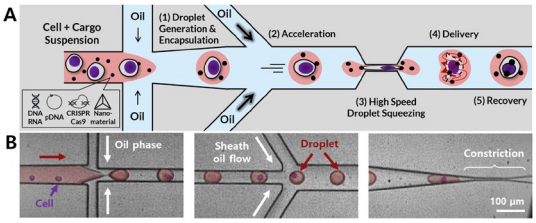


Figure 2. (A) High-speed microscopy images showing the intracellular delivery by high-speed droplet squeezing. (B) Design and operating principles of our platform.

To characterize the high-speed droplet squeezing platform performance, 2000 kDa FITC-dextran was delivered using different channel geometry and flow conditions (Fig. 3A). As shown in Fig. 3C-D, nearly 100% delivery efficiency was achieved with a minimum of 80% cell viability.

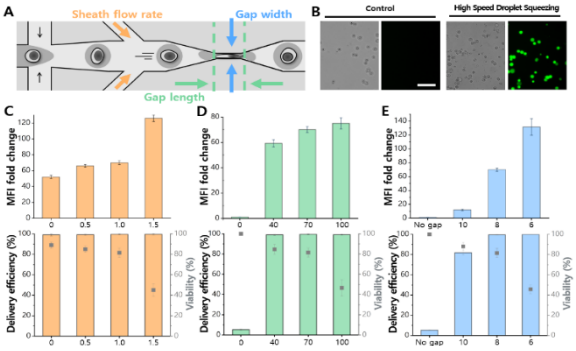


Figure 3 : (A) Parameters of the high-speed droplet squeezing device (B) Bright field and fluorescence image of 3kDa FITC-dextran delivery into K562cells. Scale bar represents 100 μm. (C-E) 2000kDa FITC-dextran delivery into K562 cells at different operational conditions. Mean fluorescence intensity (MFI), Delivery efficiency, and viability for different (C) sheath flow rate, (D) gap length and (E) width.

Using the identified optimal channel geometry and flow conditions that also consider cell viability, approximately 98% of EGFR mRNA (Fig. 4A) and more than 62% of plasmid DNA (Fig. 4B) was delivered into K562 cells. Compared to Vect platform, which is similar to cell squeezing, 67.7% of delivery efficiency was reported, even if they use concentration of 100-200 μg/mL [3]. In addition, cell squeezing method has critical disadvantages in that it cannot deliver plasmid DNA [4]. However, using our high-speed droplet squeezing platform with the size of 7.9kbp pDNA, as shown in Fig 4B, it showed an efficiency of over 60%.

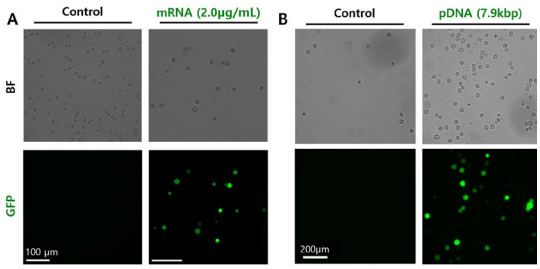


Figure 4 : Bright field and fluorescence image of (A) 2.0μg/mL of EGFP-mRNA, and (B) 7.9kbp size of plasmid DNA delivery.

.Acknowledgements

This work was supported by the National Research Foundation of Korea (NRF), funded by the Ministry of Science and ICT (No. 2021R1A2C2006224).

References

1. Stewart, M., Sharei, A., Ding, X. *et al. In vitro* and *ex vivo* strategies for intracellular delivery. *Nature* **538,** 183–192 (2016)
2. Jeongsoo Hur and Aram. J. Chung, Microfluidic and nanofluidic intracellular delivery, *Advanced Science*, 2021, pp. 2004595
3. Anna Liu, Muhymin Islam, Nicholas Stone, Vikram Varadarajan, Jenny Jeong, Samuel Bowie, Peng Qiu, Edmund K. Waller, Alexander Alexeev, Todd Sulchek, Microfluidic generation of transient cell volume exchange for convectively driven intracellular delivery of large macromolecules, Materials Today, 2018, Volume 21, Issue 7, Pages 703-712
4. Armon Sharei, Janet Zoldan, Andrea Adamo, W ooYoung Sim, Nahyun Cho, Emily Jackson, Shir ley Mao, Sabine Schneider, Min-Joon Han, Abigail Lytton-Jean, Pamela A. Basto, Siddharth Jhunjhunwala, Jungmin Lee, Daniel A. Heller, Jeon Woong Kang, George C. Hartoularos, Kwang-Soo Kim, Daniel G. Anderson, Robert Langer, Klavs F. Jensen, Vector-free microfluidic delivery platform, Proceedings of the National Academy of Sciences Feb, 2013, 110 (6) 2082-2087; DOI: 10.1073/pnas.1218705110

P-003

Transparent ITO-IEA cell plate for impedance measurement

Sang-Keun Sung[1] and Hyung Jin Kim[1,]

[1] Digital Health Care Research Center, Gumi Electronics and information Technology Research Institute (GERI), South Korea

hjkim745@geri.re.kr

Abstract

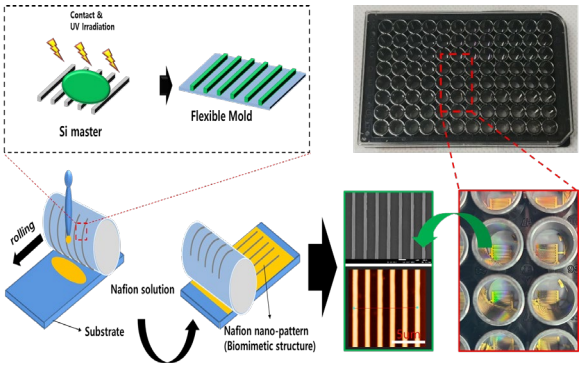
Transparent Indium Tin Oxide-Interdigitated Electrode Array (ITO-IEA) cell plate is a technology that can not only monitor the physiological and morphological changes of cells through a microscope, but also quantify the state and response of cells in real time through electrical impedance. In order to monitor the image and analyze the electrical impedance, an electrode was fabricated using transparent ITO, and an environment similar to that of the body was created by combining a nano structure, thereby realizing an accurate ecological response of the cell. We observed DIC and fluorescence of H9c2 cells using a transparent ITO-IEA cell plate, and analyzed impedance optimization for each frequency through IEA. The transparent ITO-IEA cell plate is expected to be applicable to stem cell-based drug screening and various bio fields.

Background

Currently, there is active progress worldwide to develop vaccines and therapeutics against COVID-19. In screening technology for new drug development in such an atmosphere, absorbance measurement method, in which a substance produced by an enzyme absorbs light of a specific wavelength and develops a different color before and after the enzyme reaction, is often used. but the most important problem in screening technology by optical analysis is that How to detect and quantify or image light emitted from a sample, and fluorescence is measured quantitatively by attaching a fluorescent compound to cells in culture. In the process of attaching fluorescence, the cells have to undergo dehydration or immobilization, so it has a disadvantage in that live cells cannot be measured in real time. Cell monitoring using Interdigitated Electrode Array (IEA)-based electrical impedance or resistance spectroscopy is a non-destructive technology that quantifies the state and response of cells in real time by measuring the morphological changes and the degree of cell adsorption as electrical impedance. However, since electrodes using Au are usually used, there is a disadvantage that images cannot be obtained at the same time. Therefore, we intend to secure a technology that can increase the accuracy of cell morphological changes and cell differentiation by simultaneously analyzing electrical signals and visualization based on transparent ITO-IEA and nanostructures.

Methods

Figure.1 shows a product in which a nanostructure is fabricated by a flexible printing method, and a film in which IEA and nanostructures are fused is attached to a commonly used cell plate. To fabricate a transparent cell plate, first, an IEA pattern was formed using photolithography, and then ITO was deposited using a sputter. Since PET was used as a substrate, it was deposited at room temperature, and RF power of 300W was applied to improve conductivity. After that, ITO-IEA was manufactured by removing unnecessary ITO through lift-off.



To obtain a nanostructure, hydrophilicity was given through O2 plasma treatment on the ITO-IEA film to improve adhesion, and a nanostructure was formed by the Roll-to-plate technique, which is one of the flexible printing processes. The roll-to-plate technique was carried out with hand-made equipment, and in the

case of nanopatterns using Nafion material, it was possible to produce a structure with the most uniform large area at 125 degrees. Finally, the cell plate and the film were combined to prevent the solution from leaking from the cell plate.

Results and Discussion

Figure. 2 is data measured by AFM of a large-area nanostructure using Nafion material. In order to apply a general cell plate, it was necessary to implement a large-area nanostructure, and when a 600nm-high structure was applied using the roll-to-plate technique, it was confirmed that a 400nm-high nanostructure was formed in the cell plate area. As the nanostructure was formed, the solvent contained in the solution was evaporated to form a structure having a height of 400 nm.

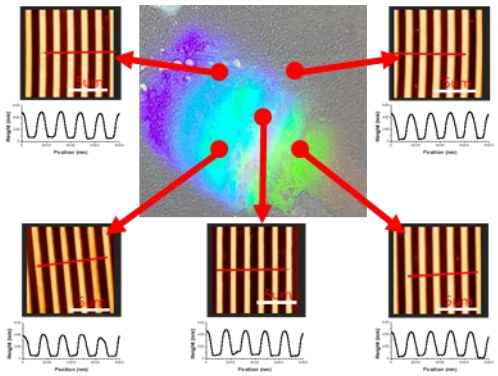


Figure.2 (a) Uniformity of large-area nanostructures using flexible substrates

Figure.3(a) shows that 100nm, 200nm, and 300nm thick ITO-IEA was fabricated, and H9c2 cells, which are myocardial myocytes, were cultured to observe the cell status and morphological changes. As a result of incubation, the ecological characteristics of cells even up to 300 nm ITO-IEA could be observed through images, and (b) impedance could also be measured at the same time. However, it was confirmed that the 100nm-thick ITO-IEA was significantly affected by the surrounding environment due to lower conductivity than the metal material, reducing the measurement reliability. In addition, the impedance for each frequency of 10Hz to 100kHz was able to verify the result that the impedance decreases as the frequency increases, which is a typical characteristic of IEA, without the resonance phenomenon that may occur due to the electrode design. Through this study, absorbance measurement and electrical resistance spectroscopy were simultaneously applied in real time for more objective quantification, and it is expected that raw live cells can be directly analyzed through impedance analysis instead of fluorescence analysis.

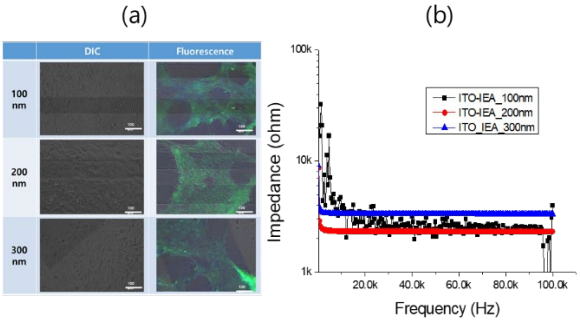


Figure.3 (a) DIC and Fluorescence of H9c2 cells
(b) ITO-IEA Impedance by thickness

Acknowledgements

This work was partly supported by Institute of Information & communications Technology Planning & Evaluation (IITP) grant funded by the Korea government(MSIT) (No.2021-0-01302, Development of a Roll-to-plate-based large-area drug screening system, 50%) and Korea Institute for Advancement of Technology(KIAT) through the International Cooperative R&D program. grant funded by the Korea government(MOTIE) (No.P0004638, Development of a drug screening system to suppress breast cancer metastasis, 50%)

References

1. J. S. Choi, D. H. Kim, "Nanopatterned Nafion Microelectrode Arrays for In Vitro Cardiac Electrophysiology" Adv. Funct. Mater., Vol 30,1910660, 2020
2. S. H. Ahn, and L. J. Guo. "Large-Area Roll-to-Roll and Roll-to-Plate Nanoimprint Lithography: A Step toward High Throughput Application of Continuous Nanoimprint." ACS Nano, Vol 3. No. 8, p.2304-2310, 2009

P-004

Real patient plasma detection characteristics of ITO Biosensor

D. H. Kim and H.J. Kim

[1]Digital Health Care Research Center, Gumi Electronics and information Technology Research Institute, Gumi, Korea

hjkim745@geri.re.kr

Abstract

Liver cancer biosensor have been developed using indium tin oxide (ITO) thin film transistor. In this study, we developed an ITO transistor for detecting quantitative label-free detection of alpha-fetoprotein (AFP) in liver cancer patient plasma. The surface characterization of the ITO biosensor was performed by atomic force microscopy (AFM) in order to individual steps of antibody immobilization. The quantitative detection of AFP was performed by measuring shift in the I-V transfer characteristics of ITO transistor. The electrical detection of liver cancer using ITO biosensor could be a viable model to optimize low-cost, flexible electronics used in biosensor applications.

Background

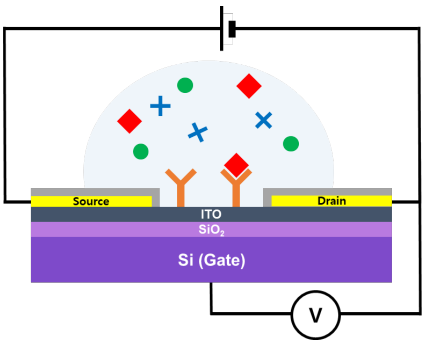
Liver cancer is one of the major malignant tumors with a poor prognosis and high recurrence rate, seriously threatening human health. Alpha-fetoprotein (AFP) is a plasma protein that is produced by the liver and the yolk sac during fetal development [1]. In adults, an elevation in this protein can be exclusive to specific malignancies such as hepatocellular carcinoma (HCC), yolk sac tumors, and metastatic disease to the liver. In the clinical setting, an elevated AFP level and a liver mass translate to a diagnosis of hepatocellular carcinoma [2]. Therefore, detecting AFP in an early, rapid, sensitive and reliable way is significant important for early diagnosis and future treatment of HCC. Although various analytical methods for the detection of AFP have been reported, it is difficult to find results using actual patient's plasma. In this study, we developed ITO biosensor and performed quantitative detection of AFP in human patient plasma.

Methods

Figure.1 shows a schematic diagram of detection method of ITO biosensor. The ITO biosensor was fabricated using an radio frequency (RF) sputtering system, and the target used was an In_2O_3/SnO_2 (90/10 wt%) component target. The source and drain electrodes of the ITO biosensor were made of titanium (Ti) and gold (Au), and were manufactured by thermal evaporation under vacuum conditions (5.0×10^{-6} torr).

As surface functionalization process for antibody immobilization, the ITO biosensor was first immersed in a mixture of 2% APTES in toluene for 30 min to achieve covalent modification of the channel surface, followed by rinsing with toluene. The silanized sensor was immersed in 2.5% glutaraldehyde solution for 30 min. The sensor was washed three times in Di water, followed by incubation in anti-AFP (50 μg/mL) was dropped to immobilize on the channel surface and it was placed in a constant temperature and humidity chamber for 2 hours. Then the anti-AFP-immobilized ITO biosensor was washed three times with 0.01 × PBS. BSA solution (1 wt%) was added for 60 min to block non-specific adsorption and washed 3 times with 0.01 x PBS. The surface modified ITO-TFT was evaluated using atomic force microscopy (AFM; AFM5300E, Hitachi, Japan).

For detection of AFP using ITO biosensor, the transfer characteristics of the ITO biosensor was measured using a digital source meter (Keithley 2400). The ITO biosensor was performed at a gate bias (V_G) of -7 to 7 V of and a drain-source voltage (V_{DS}) of 0.5 V. For AFP detection, the drain-source current (I_{DS}) characteristics of the ITO channel region before and after antigen-antibody reaction in 0.01 × PBS (pH 7.4) solution were evaluated and compared. Each AFP concentration was prepared by dissolving in 1 × PBS. After the antibody specifically binds to the antigen, the sensitivity of the ITO biosensor was evaluated by evaluating the change in the threshold voltage.



Results and Discussion

Figure. 2 shows an evaluation of reproducibility of ITO-TFT at various AFP concentrations. Each of five samples was measured to evaluate the reproducibility of ITO biosensor at each concentration of AFP. At the AFP concentrations of 1, 20, 50, 100, and 200 ng/mL, ΔV_{th} values were 0.48±0.11 V, 0.78±0.11 V, 1.21±0.07 V, 1.43±0.08 V and 1.87±0.22 V. The V_{th} value of the ITO biosensor bound to AFP showed a positive shift compared with before the binding.

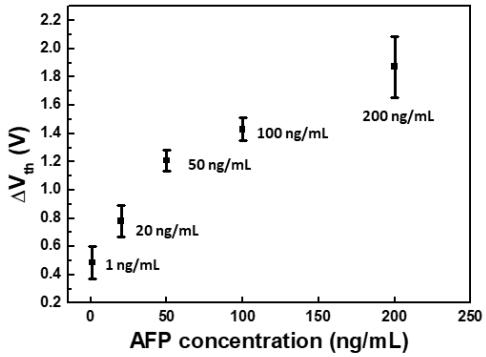
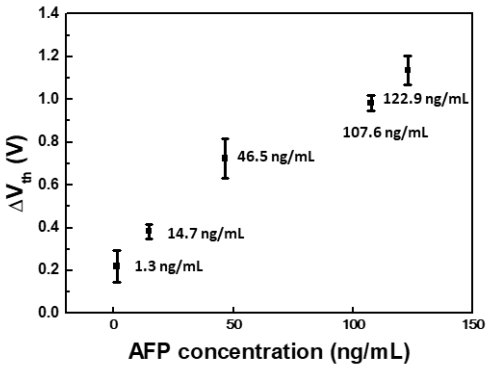


Figure.3 shows an evaluation of reproducibility of ITO-TFT at various AFP concentrations in human patient plasma. Five sensors per each sample were used to evaluate the sensitivity of the ITO biosensor, where AFP concentrations in patient plasma were 1.3, 14.7, 46.5, 107.6, and 122.9 ng/mL. The AFP binding and measurement process was progressed as same as those used for the detection of AFP in PBS. The AFP binding and measurement process was the same as that used for AFP detection in PBS, but an additional washing process was performed to remove non-specific protein binding in the patient's plasma. The Vth values of the ITO biosensor were 0.23±0.07 V, 0.39±0.03 V, 0.72±0.09 V, 0.98±0.03 V and 1.13±0.06 V. As in the previous PBS experiment, the ITO biosensor confirmed that the V_{ht} value increased as the AFP concentration in the patient's plasma increased.



Acknowledgements

This work was supported by Institute of Information & communications Technology Planning & Evaluation (IITP) grant funded by the Korea government(MSIT) (No.2021-0-01302, Roll-to-plate-based large-scaled drug screening system development)and Nano·Material Technology Development Program through the National Research Foundation of Korea(NRF) funded by Ministry of Science and ICT (No.NRF2021M3H4A407927511)

References

1. C. Bergstrand, "Alphafetoprotein in paediatrics," Acta Pædiatrica, vol. 75, pp. 1-9, 1986.
2. T. S. Lim, D. Y. Kim, K.-H. Han, H.-S. Kim, S. H. Shin, K. S. Jung, *et al.*, "Combined use of AFP, PIVKA-II, and AFP-L3 as tumor markers enhances diagnostic accuracy for hepatocellular carcinoma in cirrhotic patients," *Scandinavian journal of gastroenterology,* vol. 51, pp. 344-353, 2016.

P-005

Selective neuronal cell adhesion on a microelectrode array by electrophoretic deposition of PLL-FITC

Dongjo Yoon[1], Daejeong Kim[1] and Yoonkey Nam[1]

[1] Department of Bio and Brain Engineering, KAIST, Daejeon, REPUBLIC OF KOREA

ynam@kaist.ac.kr

Abstract

The relationship between structural connectivity and functional activity of neuronal network is the central questions in the neurophysiology. In vitro neuronal network models cultured on microelectrode array (MEA) have been used as one of the strategies. Engineering techniques to control the structural connectivity have been developed using soft lithography. These strategies had to require an additional fabrication process of producing stencil used in soft-lithography. In this research, we applied electrophoresis deposition (EDP) technique to pattern the neuron-adhesive molecule without stencil. The electrodes applied voltage could attach neurons. The higher intensity of applied voltage induced the larger neuron adhesive area around electrode. This technique will be used as an easily neuronal patterning technique on MEA without an additional microfabrication process.

Background

The relationship between structural connectivity and functional activity of neuronal network is considered as one of the central questions in the neurophysiology. As a strategy to study this relationship, in vitro neuronal network models cultured on microelectrode array (MEA) have been used. Engineering techniques to control the structural connectivity of neuronal network have been developed using soft lithography. In particular, the strategy which guides the growth of neuron by using the patterned neuronal adhesive molecules is one of the approaches [1]. This strategy has to require an additional fabrication process of producing stencil used in soft-lithography for each pattern. In this research, the positive charged neuron-adhesive molecule which is poly-L-lysine could be selectively coated in the electrode region by using electrophoresis deposition (EDP) technique without stencil. Also, it could be used as a cell patterning technique that can control the neuron attached area around the electrode according to the applied voltage intensity.

Methods

A. Electrophoresis deposition (EPD)

Microelectrodes of MEA (59 channels: 40 μm diameter, 200 μm inter electrode spacing, 1 reference electrode) were electropolymerized with PEDOT:PSS (poly(3,4-ethylenedioxythiophene) polystyrene sulfonate) before EPD (Figure.1a). To confirm the coating of the neuron-adhesive molecule on the MEA, poly-L-lysine conjugated with FITC was used. PLL-FITC (poly-L-lysine-FITC, 0.3 mg/mL in 70% ethanol solvent) solution was loaded on MEA. EPD was done by potentiostatic mode using two-electrode system (working electrode: microelectrodes, reference/counter electrode: platinum wire) (Figure.1b). Charged voltage range was -1 V to -3 V and charged period was 10 minutes.

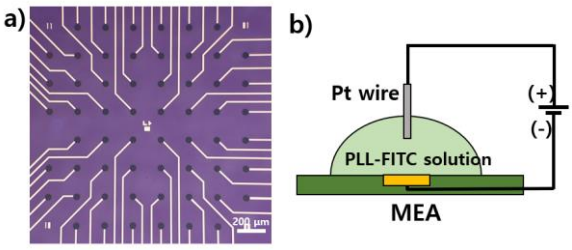


Figure 1. a) MEA image. b) Electrophoresis deposition set-up schematic illustration.

B. Cell culture

Primary neuronal culture was performed by using the dissociated hippocampal neurons of E18 Sprague-Dawley rat. Neurons were cultured on MEA which EPD was performed. The plated cell density was around 800 cells/mm^2.

Results and Discussion

A. Fluorescence and cell image after EPD

Under the several voltage condition, the coating pattern of PLL-FITC and the attachment area of neurons were investigated (Figure.2). It was confirmed that the larger the intensity of voltage applied, the larger the spread area around the electrode (Figure.2a-d). Also, it was confirmed that the neuron adhesive area increased as the intensity of the voltage increased (Figure.2A-D). In the case of the -2 V condition, neurons form clusters only near the electrode (Figure.2E). For the -3 V condition, it can be seen that neurons are widely attached from the electrode to a far range (Figure.2F). The area which neurons can be attached could be adjusted according to the intensity of the applied voltage.

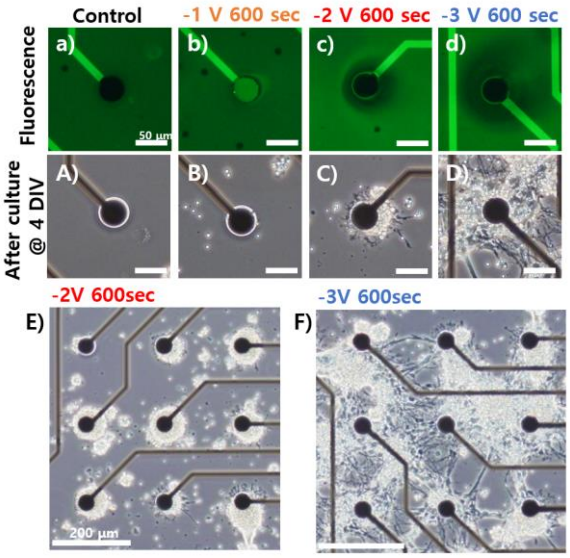


Figure.2 Fluorescence image after EPD. a~d) different the applied voltage condition, A~F) phase contrast image after cell culture.

B. Cell attached electrode ratio and the spread area of PLL-FITC

The ratio of neurons attached electrode was related with the applied voltage condition (Figure.3a). At -1 V, only 48.7% of the electrodes were attached with neurons. About -2 V and -3 V conditions, 92.9% and 90.7% of electrodes were attached with neurons. As the EPD voltage intensity increased, electrodes had more neuron adhesive condition.

Several electrodes were selected and EPD was performed under conditions of -2 V and -3 V. At -3 V condition, it had the wider spread area of PLL-FITC exceeded the adjacent periphery of the electrodes (Blue box at Figure.3b). Neurons could be attached to these spread areas (Figure.3c). At -2 V condition, it was confirmed through the cell image (Figure.3c) that the conditions were not formed to sufficiently attach the neurons on spread area. Neurons were attached only near the electrodes to form cluster (Figure.3c). According to the intensity of the applied voltage, the neuron attached area could be made variety.

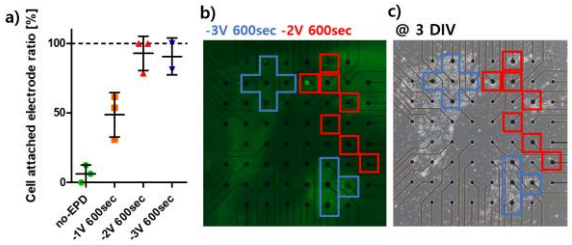


Figure.3 a) cell attached electrode ratio for diverse the applied voltage conditions. mean±sd. N=3 chips. # of electrodes of each condition on a chip =16, 13, 14, 16 electrodes. b) fluorescence image after EPD, c) phase contrast image after cell culture.

Conclusion

By applying EPD technique to MEA, it had been shown that neurons can be selectively attached on electrodes. The neurons adhesive area and probability to the electrode can be adjusted by the variety intensity of voltage. It is preliminary study for neuron patterning technique on MEA that can easily pattern without an additional microfabrication process.

Acknowledgements

This work was supported by the National Research Foundation of Korea grant funded by the Korean government (MSIP) (NRF-2018R1A2A1A05022604, NRF-2021R1A2B5B03001764).

References

1. R. Fricke, P.D. Zentis, L.T. Rajappa, B. Hofmann, M. Banzet, A. Offenhäusser, S.H. Meffert., "Axon guidance of rat cortical neurons by microcontact printed gradients," *Biomaterials*, vol. 32, no. 8, pp. 2070–2076, 2011.

P-006

Manufacture and Characteristic Evaluation of Biomimetic Structure for Drug Screening Using T-NIL Process

Suhan Lee[1] and HyungJin Kim[1,*]

1Digital Health Care Research Center, Gumi Electronics and Information Technology Research Institute, Gumi 39253, South Korea

hjkim745@geri.re.kr

Abstract

Nafion is a synthetic polymer with ion conductivity and has the characteristics of free movement of cation. In this study, we used this characteristic to evaluate the electrical properties of cells and to produce biomimetic structures. The production of nanopatterns using conventional Nafion was limited in the application of bio-sensor by using sheet type, which is in the form of a membrane. Therefore, a biomimetic structures was produced using the T-NIL process to easily perform thin film and pattering on the various substrate and electrode. Four types of mold were compared for the production and improvement of nanopatterns, and the shape was improved according to post-processing. This enabled the production of a large-area structure applicable to 96-channel cell culture plate. Using the drug screening cell culture plate, directional migration according to cell growth and impedance change according to drug treatment could be confirmed

Background

NIL (Nanoimprint lithography) technology is a widely used in the manufacture of various nanopatterns and devices. In particular, thermal nanoimprint lithography (T-NIL) using heat is a method of making a patterns by heating a polymer, and has the advantage of being able to produce a pattern of several nm up to 8 inches or more. Screening technology for new drug development has the disadvantage of not being able to measure living cells in real time because materials produced by enzymes absorb light of a specific wavelength and show up before and after the reaction. Thus, research is being conducted to measure the real-time change of cells using electrodes with new research methods, and we intend to secure a technology that measures not only the real-time change of cells using electrodes but also the morphological change of cells and electrical signals simultaneously by manufacturing patterns similar to in-vivo.

Methods

Figure 1 is a schematic diagram for manufacturing a cell biomimetic structure using T-NIL technology, and a 96-well nanoIEA plate in which a cell biomimetic structure is applied on the IEA electrode using the schematic diagram.

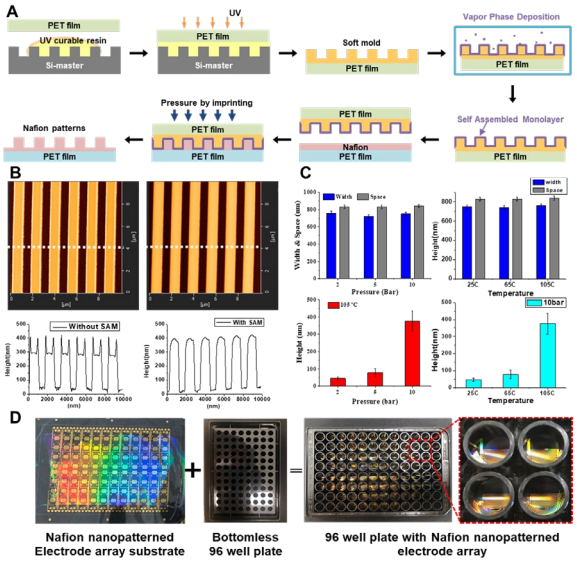


Fig. 1(a, d) 96well nanoIEA plate was manufactured by applying photolithography technology on PET film as a substrate, and a large-area cell biomimetic structure was manufactured using T-NIL technology after spin coating the ion conductivity polymer. Figure 1(b) As an optimization method for manufacturing a cell biomimeticl structure, the pattern result is obtained by self-assembled monolayers (SAMs) treatment to increase mold heterogeneity. Figure 1(c) The temperature (25℃, 65℃, 105℃) was changed to three conditions to confirm the optimal heat and pressure conditions, which are the most important factors in the T-NIL process, and the pattern was produced by changing the patterning result according to pressure at 105℃.

Results and Discussion

Figure 2 is the result of fluorescence staining to confirm the alignment of cells according to the nanopatterns of a biomimetic structure, and the alignment of breast cancer cells cultured in nafion nanostructures made under optimization conditions (10 bar, 105°C) for pattern production. In a nafion layer without a pattern, it was confirmed that cells grew randomly from 0°C to 90°C, and in the nanopatterned nafion layer, it was confirmed that cells grew in the same direction as the pattern..

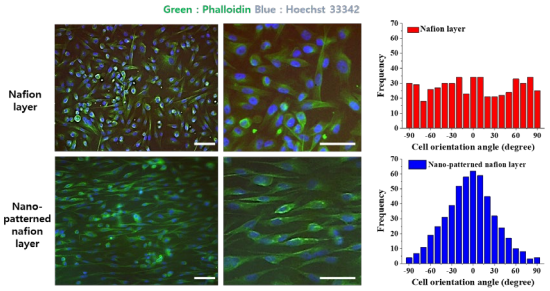


Figure 3(a) is the impedance result of 72 hours of cultivation of breast cancer cells by applying a plate without a cell biomimetic structure, and Figure 3(b) is the impedance result of 72 hours of cultivation of breast cancer cells by applying a plate with a cell biomimetic structure. When there was a cell biomimetic structure, it was confirmed that the impedance increased rapidly by affecting the initial culture rate and area. Through this study, real-time changes in living cells could be identified and analyzed directly, and cell alignment and rapid impedance change rates similar to those of the human body could be identified depending on the presence or absence of a cell biomimetic structure

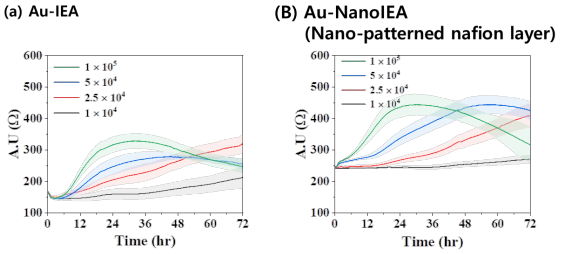


Figure 3(a) Results of measuring breast cancer cell impedance in a nafion thin film, and (b) Results of measuring impedance in a cell biomimetic structure.

Acknowledgements

This work was partly supported by Institute of Information & communications Technology Planning & Evaluation (IITP) grant funded by the Korea government(MSIT) (No.2021-0-01302, Development of a Roll-to-plate-based large-area drug screening system, 50%) and Korea Institute for Advancement of Technology(KIAT) through the International Cooperative R&D program. grant funded by the Korea government(MOTIE) (No.P0004638, Development of a drug screening system to suppress breast cancer metastasis, 50%)

References

1. JS Choi, Adv. Funct. Mater. 2020, 1910660
2. Alec S. T. Smith, Nano Lett. 2020, 20, 1561−1570

P-007

Detection of Micro-particle Surface Charge Difference using DEP system

K.I. Yeo[1], G.J. Min[1], and S.W. Lee[1]

[1]Department of Biomedical Engineering, Yonsei University, Wonju, Korea

yusuklee@yonsei.ac.kr

Abstract

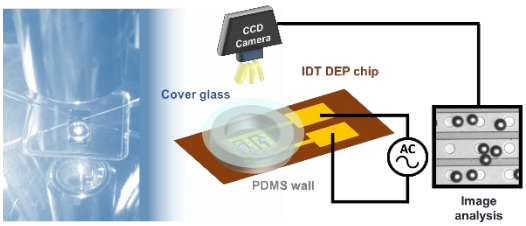
Dielectrophoresis (DEP) based measuring system can be specialized in measuring electrical properties of a given sample using multi-probe introduced in microfluidic devices. Here, we developed DEP sensor using negative DEP force exerted on the polystyrene microparticles. Different chemical functional group on the homogenous particles creates different surface charges on the microparticles. Surface conductivity changes of the microparticles in different surface conductivity conditions are measured by particle movement. As a result, our method which selectively detect different surface charge particles can be practically applied as a simple and efficient device for various detection purpose.

Background

Biosensors have been developed for the detection of diverse analytes including antibodies, DNA, cells and small molecules [1]. Among these, electrical transduction is commonly used in a wide array of biosensors. This carries multiple advantages such as high sensitivity, low cost for manufacturing, miniaturized device size, simplicity, and is a label-free method. However, electrochemical sensors have some difficulties such as implementing multiple probes. Dielectrophoresis has been used with many bio-particles (cells, bacteria, viruses, DNA) for trapping, alignment, separation, and detection [2]. Especially, dielectrophoresis-based sensors are able to conduct an easy and simple detection procedure with robust aqueous sensing and have advantages from the combined transduction methods of both optical and electrical measurement systems using numerous probe particles [3]. We developed the DEP based multi-probe detection system using micro-sized polystyrene particles. We implemented micro-particles as surface charge detection probes. To detect the surface charge difference of multiple particles, we used DEP chip which can create vertical movements of micro-particles, which occurred by the n-DEP force. These movements were detected by particle images and we calculated particle height by the radius calculation of the defocused image of the particles.

Methods

Figure.1 shows a schematic image of the DEP based micro-particle surface charge detection system. On the fabricated DEP chip, donut shaped PDMS reservoir was attached. After the particle contained liquid is injected, cover glass was placed on the top of the PDMS wall. For the alignment of the particles, 0.6V of input AC voltage was applied on the DEP chip. Images of the particles were observed through the microscope combined with CCD camera. For the particle height detection, input frequency was manipulated from 100 kHz to 500 kHz with the 1kHz interval. Each Captured image was analyzed with MATLAB for the particle radius calculation.



Results and Discussion

Figure. 2(A) shows the particle radius when the particles are landed on the surface and the microscope lense height is changed from the focused point. When the defocusing height is increased, the radius of the particle images are increased. Figure. 2(B) shows when the frequency input is changed the observed images show the different particle radius due to the different vertical nDEP force. Based on the above

results, Figure. 2(C) shows the particle height depending on the input frequency changes. This shows that the increased input frequency makes higher nDEP force inducing increased particle height.

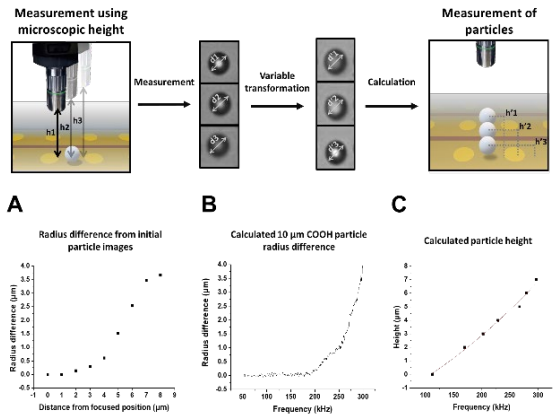


Figure.2. (A) Particle radius difference between focused and defocused particle image based on the defocusing distance. (B) Data of radius difference between focused particle on the landed position and measured image while frequency from 300 kHz to 50 kHz. (C) Height of COOH immobilized 10 μm particle while input frequency from 300 kHz to 50 kHz.

Figure 3(A) shows that the Re[CM(f)] depending on the surface charge of the micro-particle. when frequency increased, the absolute value of the Re[CM(f)] is increased which makes the higher nDEP force. The higher surface charge on the particle, the more increased change in Re[CM(f)] is shown as the frequency increased. Therefore, the nDEP force exerted on the microparticle is different depending on their surface charge. Figure 3(B) shows the calculated vertical height while input frequency changes. COOH and plain particle shows different vertical height due to their difference in surface charge. Therefore, our system can detect the surface charge of particles in microfluidic system by observing the vertical height of the micro-particle image.

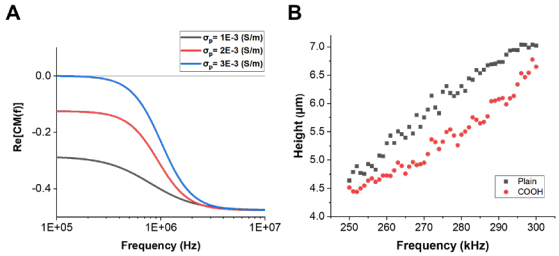


Figure 3. (A) The calculated real part of CM factor against input frequency spectrum for the microparticle with different surface conductivity ($\sigma_p = 1\times10^{-3}$, 2×10^{-3}, 3×10^{-3}). (B) Calculated vertical height of the plain and COOH particle depending on the frequency range domain.

References

1. Chalklen, T., Jing, Q. & Kar-Narayan, S. Biosensors based on mechanical and electrical detection techniques. Sensors (Switzerland) 20, 26–37 (2020).
2. Chen, Q. & Yuan, Y. J. A review of polystyrene bead manipulation by dielectrophoresis. RSC Adv. 9, 4963–4981 (2019).
3. Rahman, N. A., Ibrahim, F. & Yafouz, B. Dielectrophoresis for biomedical sciences applications: A review. Sensors (Switzerland) 17, 1–27 (2017).

P-008

Clogging-Free Hydroporator for Cell Engineering

Gi-Beom Kim[1,2,3] and Aram J. Chung[1,2,3,*]

[1]Department of Biomedical Engineering, Korea University, Seoul, Korea

[2]Interdisciplinary Program In Precision Public Health, Korea University, Seoul, Korea

[3]MxT Biotech, Seoul, Korea

[*]ac467@korea.ac.kr

Abstract

There have been many approaches for internalization of external biomolecule for cell engineering. However, these approaches showed limitations in throughput, internalization efficiency and/or cell viability. As the substitutes for them, some approaches applied with the microfluidic system have been popularized due to high scalability, but they had critical trouble; channel clogging due to debris, cells and their secretion. In this study, we designed a microfluidic system for internalizing external biomolecules into the cells without clogging by maximizing the inertial vortices in the channel. We optimized the channel design in its geometries and dimension for eliminating potential clogging sources perfectly with maintaining high delivery efficiency and cell viability. This novel clogging-free microfluidic platform enables fully automated hydroporation system, which is crucial in the industrial production of engineered cells.

Background

Immunotherapy has become more important owing to its therapeutic effect and no severe side effects occurred when using chemotherapy or radiotherapy. For immunotherapy, intrinsic function of immune cells should be engineered and reprogrammed by internalizing biomolecules into the cells. There are many roads for internalizing external biomolecules into cells for engineering intrinsic cell functions. Traditionally, microinjection, electroporation, viral transduction and lipofection were extensively used; however, they are limited in efficiency, cell viability, loss of functionality and/or throughput. To overcome these drawbacks, microfluidics has allowed a wide variety of new solutions, demonstrating high potential for effective intracellular delivery.[1] However, most microfluidic approaches critically suffer from the channel clogging issue.

Recently, we presented a microfluidic intracellular delivery platform termed “Hydroporator” (HP) and demonstrated its superior performance on engineering human primary stem and immune cells using a T-shaped microchannel with a cavity.[2] To completely eliminate any potential clogging, in this work, we reconstructed the cavity design and the channel dimension to maximize the inertial vortices developed near the cavity.

Methods

The silicon mold for microfluidic device was fabricated using conventional photolithography and DRIE method. And microfluidic device was fabricated by standard soft lithography process using PDMS and bonded with slide glass using O_2 plasma treatment and heat treatment.

Delivery processes of FITC-dextran were done using K562 cells, MDA-MB-231 cells and NK-92 cells. They were cultured according to the protocols provided by ATCC.

For preparation of hydroporation process, the cells were resuspended in growth media with 0.3mg/ml of FITC-dextran. The cell suspension with delivery materials was injected into the microfluidic device using the syringe pumps. After the process, the cells were incubated for 18h or 24h. And the fluorescent intensity of cells was measured using flow cytometry for quantifying the efficiency for internalization of FITC-dextran. We assumed 5% of ‘Control’ group was expressing fluorescence due to internalization of FITC-dextran by endocytosis.

To measure cell viability, trypan blue and PI staining was used. Trypan blue was used after the delivery process and washing step. PI staining was done after 18h incubation.

Results and Discussion

We reconstructed the design of the previous HP, which has the cavity on a T-shaped junction to eliminate potential clogging. (Figure.1) Its geometry and dimension was optimized for maximizing the inertial vortex in the microfluidic channel to enhance internalization performance and reduce the opportunities for clogging. The operating principles of 'Clogging-Free Hydroporator' (*cf*-HP) are shown as Figure.1.

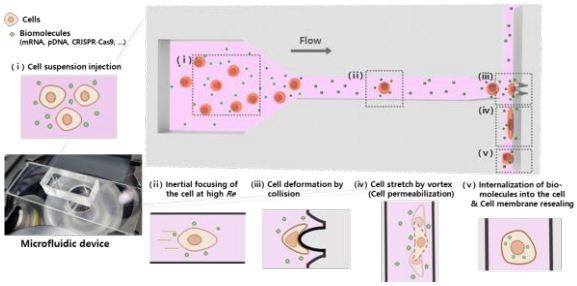


Figure 1. Microfluidic device design and its operating principles.

We demonstrated the performance for intracellular delivery when using the newly reconstructed *cf*-HP. (Figure.2) Both 3kDa and 2000kDa FITC dextran was internalized well into the cells with high efficiency of over than 95%. When using *cf*-HP, clogging occurrence frequency reduced significantly, and it showed no significant difference in the internalization performance when compared with HP.

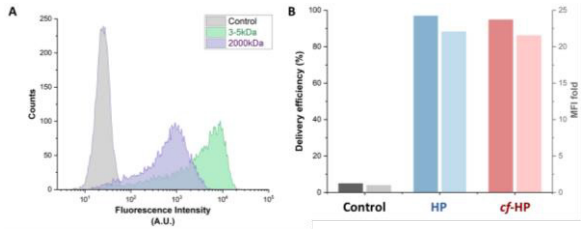


Figure.2 (A) Fluorescence intensity histograms of the 3kDa- and 2000kDa FITC-dextran delivery tests using *cf*-HP with K562 cells and (B) comparison in internalization performance between the previous HP and *cf*-HP in 2000kDa FITC-dextran delivery.

Repetitive 2000kDa FITC-dextran delivery tests using K562 cells were done for demonstrating reduction when using *cf*-HP. (Figure.3) In all the tests, no severe clogging occurred. Debris, which can induce channel clogging, were flushed away due to the flow with high *Re* and inertial vortex in the T-shaped junction. This clogging-free process enables consistent and highly efficient internalization for every cell during the entire process time. It is crucial for maximizing the yield of treated cells. Even when clogging occurred, it showed no significant reduction in internalization performance because no severe channel clogging is not formed that would interfere cell deformation.

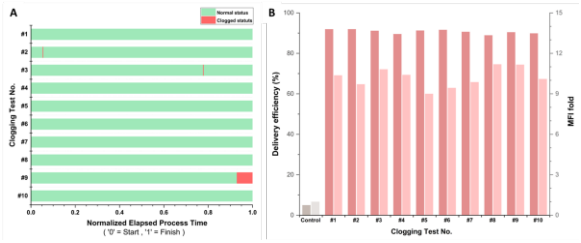


Figure.3 (A) Repetitive tests for measuring clogging occurrence frequency and (B) internalization performance of each test using 2000kDa FITC-dextran with K562 cells.

Acknowledgements

This research was supported by the National Research Foundation of Korea (NRF), funded by the Ministry of Science and ICT (No. 2021R1A2C2006224) and the Samsung Research Funding and Incubation Center for Future Technology (grant no. SRFC-IT1802-03).

References

1. Jeongsoo Hur, and Aram J. Chung, "Microfluidic and Nanofluidic Intracellular Delivery", *Adv. Sci.*, 8, 15, 2198-3844 (2021).
2. Jeongsoo Hur, Inae Park, Kyung Min Lim, Junsang Doh, Ssang-Goo Cho, and Aram J. Chung, "Microfluidic Cell Stretching for Highly Effective Gene Delivery into Hard-to-Transfect Primary Cells", ACS Nano, 14, 11, 15094–15106 (2020).

P-009

Development of Biodegradable Discoidal Polymeric Particles for Effective Treatment of Lung Cancer

Sanghyo Park[1], Gahee Kim[1], Hyeyoun Cho[1], Seonmin Choi[1], Susmita Aryal[1] and Jaehong Key[1]

[1]Department of Biomedical Engineering, Yonsei University, Wonju, Korea

jkey@yonsei.ac.kr

Abstract

Lung cancer is the disease with the highest incidence and mortality worldwide. The physicochemical properties of drug carriers are important for the effective delivery of drugs into the body. In this study, 3μm discoidal polymeric particles (DPPs) were developed using a top-down fabrication method that can precisely control physicochemical properties. Currently, most nanoparticles (e.g., prodrugs, passive targets, active targets) are delivered only 0.7% to the lung, whereas the developed 3μm DPPs are delivered about 70%. The therapeutic effect was evaluated by loading these particles with an anticancer agent in terms of survival rate, body weight, and histology staining. These findings demonstrated a promising result as a novel lung cancer delivery system that minimizes existing chemotherapy's side effects and increases therapeutic effects.

Background

Worldwide, the incidence and mortality of cancer are reported as rank one [1]. In particular, the incidence and mortality of lung cancer are the highest. Lung cancer is difficult to diagnose early due to vague symptoms, and current therapeutic methods such as chemotherapy, surgery, and immunotherapy are still limited. Chemotherapy is the most usual method of treating lung cancer. However, chemotherapy also affects normal cells, causing many side effects [2]. The surgical method may be impossible depending on the degree of cancer progression, and it is also a very invasive method. Immunotherapy has a limitation in that it is only effective for specific patients. Accordingly, many studies have been conducted on targeting drug carriers that specifically deliver drugs to only cancer cells [3-5]. In the case of the top-down fabrication method, the size and shape of particles can be uniformly adjusted, and the discoidal particles have a large surface area that can easily contact and stay at the thin and tortuous blood vessels surrounding tumors [6-7]. In this study, doxorubicin-loaded discoidal polymeric particles (DOX-DPPs) were prepared by a top-down fabrication [8-10], and these particles were systemically injected into a lung cancer mouse model. The results were evaluated in terms of survival rate, body weight, and histology staining.

Methods

Discoidal polymeric particles were produced by the nanoimprint lithography method [8-10]. A silicon template with a diameter of 3 μm and a height of 1.49 μm was fabricated by electron beam lithography. A polydimethylsiloxane (PDMS) template was made using a PDMS solution on the silicon template. A polyvinyl alcohol (PVA) template engraved with the same pattern as the Silicon template was produced using a PVA solution for the PDMS template. Poly(lactic-co-glycolic acid) (PLGA), a biodegradable polymer, was dissolved in dichloromethane (DCM) and chloroform ($CHCl_3$), and doxorubicin, an anticancer drug, was dissolved in dimethyl sulfoxide (DMSO) and added. After loading the polymer solution on the PVA template, it was dried for 5 minutes to vaporize DCM and $CHCl_3$ co-solvent. PVA template was dissolved in Deionized (DI) water (RT, 600ml) to produce particles. The debris generated while producing particles were removed using a Nylon filter (pore size: 100 μm) and a Membrane filter (pore size: 1.2 μm), and then particles were obtained through centrifugation.

Results and Discussion

As a result of confirming the morphology characteristics of DPPs through a microscope, it was confirmed that particles with uniform size and shape were produced (Figure 1(A)). All treatments were injected at 2-day intervals 4 times until 9 days via intravenous injection at the same doses. Free DOX (2mg/kg), DOX-DPPs (1mg/kg, DOX at 0.2mg/kg), DPP(1mg/kg) were injected. As shown in Figure 1B, Lung cancer progressed in PBS-treated and DPP-

treated mice rapidly. On the other hand, free DOX-treated and DOX-DPP treated mice showed a reduction of metastatic tumor nodules and green fluorescence protein (GFP) signal in the lung (Figure 1B). As a result of survival, it was confirmed that 60% of the DOX-DPP group was alive on the 9 days (Figure 1C). In addition, all treatments showed stable body weight (Figure 1D). Hematoxylin and eosin (H&E) staining indicate that the size of metastatic nodules in free DOX and DOX-DPP groups was smaller than PBS and DPP groups. Furthermore, the concentration of doxorubicin in free DOX group was 10-fold less than DOX-DPP group, the size and number of metastatic cancer nodules have no statistically difference (Figure 1E).

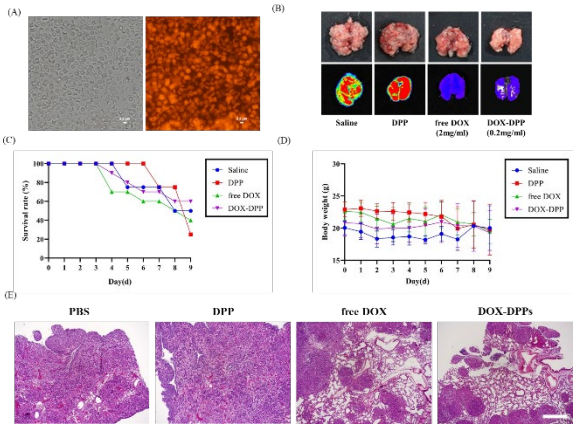


Figure 1. In vivo anti-tumor efficacy of DOX-DPPs. (A) Morphology of the DOX-DPPs observed by microscope. (B) Photographs of lungs obtained from the metastatic lung cancer on C57BL/6 mice. (C) Ex-vivo images of cancer cells in lung after various treatments. (D) Time-independent body weight curves of mice after various treatments. (E) Histological sections of lung tissues were observed by microscope under 200 X magnification.

Acknowledgments

This work was supported by grants from the National Research Foundation of Korea (NRF), No. 2018R1-D1A1B07042339 and No. 2019K2A9A2A08000123.

References

1. SUNG, Hyuna, et al. Global cancer statistics 2020: GLOBOCAN estimates of incidence and mortality worldwide for 36 cancers in 185 countries. *CA: a cancer journal for clinicians*, 2021, 71.3: 209-249.
2. PEARCE, Alison, et al. Incidence and severity of self-reported chemotherapy side effects in routine care: A prospective cohort study. *PloS one*, 2017, 12.10: e0184360.
3. MANISH, Gupta; VIMUKTA, Sharma. Targeted drug delivery system: a review. *Res J Chem Sci*, 2011, 1.2: 135-8.
4. MASOOD, Farha. Polymeric nanoparticles for targeted drug delivery system for cancer therapy. *Materials Science and Engineering: C*, 2016, 60: 569-578.
5. ZHANG, Gen; ZENG, Xin; LI, Ping. Nanomaterials in cancer-therapy drug delivery system. *Journal of biomedical nanotechnology*, 2013, 9.5: 741-750.
6. DECUZZI, P., et al. Size and shape effects in the biodistribution of intravascularly injected particles. *Journal of Controlled Release*, 2010, 141.3: 320-327.
7. BLANCO, Elvin; SHEN, Haifa; FERRARI, Mauro. Principles of nanoparticle design for overcoming biological barriers to drug delivery. *Nature biotechnology*, 2015, 33.9: 941-951.
8. KEY, Jaehong, et al. Soft discoidal polymeric nanoconstructs resist macrophage uptake and enhance vascular targeting in tumors. *ACS nano*, 2015, 9.12: 11628-11641.
9. PARK, Jun Young, et al. Biodegradable micro-sized discoidal polymeric particles for lung-targeted delivery system. *Biomaterials*, 2019, 218: 119331.
10. KEY, Jaehong, et al. Engineering discoidal polymeric nanoconstructs with enhanced magneto-optical properties for tumor imaging. *Biomaterials*, 2013, 34.21: 5402-5410.

P-010

Fabrication of Silk Fibroin based-Microparticle for Drug Delivery

Hyeyoun Cho[1], Susmita Aryal[1], Hwijin Jang, Ho Tien Son[1], Seungho Choi[1], and Jaehong Key[1]

[1]Department of Biomedical Engineering, Yonsei University, Wonju, Korea

jkey@yonsei.ac.kr

Abstract

The protein polymer obtained from Bombyx mori silk, silk fibroin, is a biopolymer and can be used as a drug delivery carrier. It has advantages such as non-toxicity, biocompatibility, biodegradability, renewability, and a slow rate of degradation in vivo. In nature, silk fibroin is soluble in water. Therefore, it is necessary to convert the water-soluble structures into a water-insoluble β-sheet structure. For conversion to the β-sheet structures, 1,1,1,3,3,3-hexafluoro-2-propanol (HFIP) was used. The silk fibroin-HFIP solution was loaded on a PVA film fabricated by nanoimprint technology. The average diameter and zeta potential of the particle produced in this way were measured to 3.17± 0.33μm and -20.3 ± 1.6mV, respectively. The silk fibroin particles will be loaded with therapeutic drugs as a drug delivery carrier.

Background

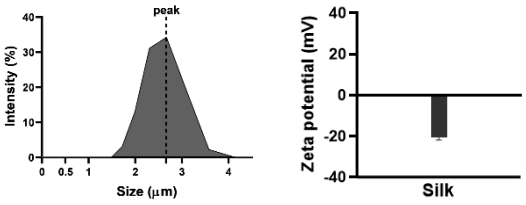
Biopolymers have received more and more attention over the past decades as a drug delivery system. Silk fibroin, obtained from Bombyx mori silk, is a protein polymer that has been widely studied in various fields such as biomedicine, cosmetics, and structural materials. It has properties of non-toxicity, biocompatibility, biodegradability, renewability, and a slow rate of degradation in vivo [1]. Also, particles made of silk fibroin can be efficiently loaded with drugs through methods such as physical encapsulation, chemical coupling, and surface absorption. In nature, silk fibroin contains random coils, α-helical structures, and amorphous structures. However, in order to create stable three-dimensional silk fibroin-based particles, conversion to β-sheet structures is required. Silk fibroin is composed of a heavy chain (H-chain) and a light chain (L-chain). There are 12 hydrophobic blocks and 11 hydrophilic blocks in the H-chain, which is a contributor of β-sheet structures. Hydrophobic β-sheet blocks are formed by intermolecular hydrogen bonding, van der Waals force, and hydrophobic interaction [2]. Random coils and α-helical structures have water-soluble properties. Under external stimulation such as the addition of organic solvents and ultrasound, change in temperature, and pH value, random coils and α-helical structures can be transformed into β-sheet structures. The β-sheet structures are water-insoluble.

Methods

Bombyx mori silk cocoons have a water-insoluble outermost layer called sericin. Silk cocoons were cut into pieces and boiled in an aqueous solution of 0.02M Na_2CO_3 to remove sericin. After washing with DI water three times, it was squeezed out excess water and dried in an oven at 60℃ overnight. The extracted silk fibroin was dissolved in a 9.3M LiBr solution in

an oven for 4 hours. Silk fibroin-LiBr solution was dialyzed in deionized (DI) water in dialysis membrane tubing for 48h [3]. The supernatant was removed by centrifugation, and then the pellet was lyophilized. The lyophilized silk fibroin was dissolved in 1,1,1,3,3,3-hexafluoro-2-propanol (HFIP) at room temperature with continuous stirring [4]. The solution had water-insoluble properties and was loaded on the PVA template. PVA template was produced through sequential steps. A 3μm discoidal wafer was fabricated using e-beam lithography technology. PDMS solution was transferred onto this wafer. The PDMS template showed the wafer pattern. Then, water-soluble PVA solution was transferred to the PDMS template and dried in an oven. Silk fibroin-HFIP solution was loaded on the PVA template. The loaded PVA template was dissolved in DI water for 2h with continuous stirring. After removing the undissolved PVA template and large debris with a 100μm Nylon filter, particles were obtained on a 1.2μm Membrane filter. The obtained particles were lyophilized [5].

Results and Discussion



(a) (b)

Figure.1 Characteristics of silk fibroin based-microparticles (a) hydrodynamic diameters and (b) zeta potential.

The physicochemical properties of silk microparticles were characterized, as shown in Figure 1. The particle size distribution and zeta potential were confirmed through Dynamic Light Scattering (DLS) analysis. DLS determined particle properties by measuring the intensity of light scattered from a suspension or solution. Measurements were performed using Zetasizer Nano. The average diameter and zeta potential of silk fibroin particles were measured in an aqueous solution resulting in 3.17± 0.33μm and -20.3 ± 1.6mV. In this experiment, micro-sized particles were produced using a biopolymer called silk fibroin. The microparticles using silk fibroin will be further studied to be used as a drug delivery carrier by loading therapeutic drugs.

Acknowledgments

This research was partially funded by grant numbers 2018R1D1A1B07042339, 2019K2A9A2A08000123, and Leaders in Industry-university Cooperation+ Project supported by the Ministry of Education and National Research Foundation of Korea.

References

1. Ya Ma, Brandon S.B.Canup, Xiaoling Tong, Fangyin Dai, Bo Xiao, "Multi-Responsive Silk Fibroin-Based Nanoparticles for Drug Delivery", Chem. (2020).
2. Narges Johari, Lorenzo Moroni, Ali Samadikuchaksaraei, "Tuning the conformation and mechanical properties of silk fibroin hydrogels", European Polymer Journal. volume 134 (2020).
3. Danielle N Rockwood, Rucsanda C Preda, Tuna yucel, Xiaoqin Wang, Michael L Lovett & David L Kaplan, ″Materials fabrication from Bombyx mori silk fibroin″, Nature Protocols, 1612-1631 (2011).
4. Kelvin O,Moseti, Taiyo Yoshioka, Tsunenori Kameda, Yasumto Nakazawa, "Structure Water-Solubility Relationship in α-Helix-Rich Films Cast From Aqueous and 1,1,1,3,3,3-Hexafluoro-2-Propanol Solutions of S. c. ricini Silk Fibroin", Melecules, 24(21):3945 (2019).
5. Jaehong Key, Santosh Aryal, Francesco Gentile, Jeyarama s. Ananta, Meng Zhong, Melissa D.Landis, Paolo Decuzzi, "Engineering discoidal polymeric nanoconstructs with enhanced magneto-optical properties for tumor imaging", Biomaterials. volume 34, 5402-5410 (2013).

P-011

Skin-mimicking phantom to measure transdermal absorption of cosmetics under sonophoresis

Gahee Kim[1], Hwijin Jang[1], Hyeyoun Cho[1], Seonmin Choi[1], Sanghyo Park[1], and Jaehong Key[1]

[1]Department of Biomedical Engineering, Yonsei University, Wonju, Korea

jkey@yonsei.ac.kr

Abstract

The cosmetic industry has rapidly grown. Recently, functional cosmetics, including various ingredients, are in demand. Recently, much attention has been paid to the development of cosmetics that increase absorption into the skin. A sonophoresis is one of the methods to increase the transdermal absorption of cosmetics. Therefore, this study suggests the skin-mimicking phantom to measure the transdermal absorption of cosmetics under sonophoresis quantitatively. The skin-mimicking phantom was prepared by a simple and cheap method using PDMS and Strat-M™ membrane. This method demonstrates the quantitative and repeated results of transdermal absorption of cosmetics under sonophoresis.

Background

The cosmetics industry has grown rapidly as one of the markets with growth potential. In 2017, the global cosmetics market was valued at USD 464.8 billion, showing a high growth rate of 5.2% compared to the previous year, and is projected to grow at a compound annual growth rate (CAGR) of 5% until 2022 [1]. For this reason, there is a need to develop functional cosmetics, including various ingredients desired by consumers. However, due to the skin barrier of the stratum corneum, the outermost layer of the skin with low permeability, no matter how effective cosmetics are, they may not be able to exert their effect sufficiently when applied to the skin [2]. Therefore, various physical and formulation approaches are being studied to effectively overcome the obstacle of the skin and promote transdermal absorption.

Physical approaches include 1) iontophoresis, a method to increase skin permeation of ionic drugs by changing the electrical environment of the skin by giving the skin potential difference, 2) a drug penetration method using high voltage, and 3) sonophoresis, which allows drugs to penetrate the skin through the bio-membrane using ultrasonic waves. Formulation approaches include various nanoparticle designs such as nano-emulsions, liposomes, elastic liposomes, and polymeric micelles [3]. In this study, a skin-mimicking phantom was manufactured to quantitatively evaluate the degree of penetration of ingredients in a mask pack used for skincare with the sonophoresis effect. It is expensive and dangerous to evaluate the absorption of cosmetics directly in humans. Also, the ethical issue of animal experiments is strengthened worldwide. Therefore, the Franz diffusion cell is generally used [4,5]. The method of evaluating skin absorption using a Franz diffusion cell is to analyze and evaluate the degree and amount of permeation with time by HPLC. However, when measuring the degree of absorption using the Franz diffusion cells in the sonophoresis method, it is not possible to use an ultrasonic device other than the standard diameter of the Franz diffusion cell of 5 to 25 mm because of the glass characteristics that frequency may vary depending on the internal solvents. Besides, there is a limitation in that expensive pieces of equipment are essential to evaluate skin penetration characteristics.

Therefore, this study suggests a skin-simulating phantom manufactured using PDMS with good moldability, customized according to various sizes of ultrasonic devices. The result demonstrates a quantitatively calculable method of transdermal absorption of various cosmetics at a low cost.

Methods

PDMS: elastomer (10: 1, w/w) was mixed, put in a mold, and hardened to produce a skin-mimicking phantom. Inside the phantom. DI + Ethanol 1:1 mixed solution was filled with an aqueous solution according to the in vitro with the guidelines for absorption of in

vitro skin absorption guidelines presented by the Ministry of Korean Food and Drug Safety [6]. A magnetic stirrer was used to circulate the aqueous solution inside the phantom, and the aqueous solution was injected and discharged using syringes located on both sides of the phantom. In order to promote percutaneous absorption using sonophoresis, SONOCARE, an ultrasound device for dermatology developed by Newpong Co., was used. SONOCARE devices offer single frequencies (1, 3, and 10 MHz). Strat-M™ Membrane, Transdermal Diffusion Test Mode, and Strat-M Membrane were used as skin substitutes on the skin-simulating phantom.

Strat-M Membrane was placed on the fabricated PDMS skin-simulating phantom. The lower surface of the membrane is in contact with the DI + Ethanol 1:1 mixed aqueous solution so that the absorbed cosmetics can be mixed with the aqueous solution. After applying 200 μl of Mk mask pack cosmetics produced by Mangil Co. on the membrane, fix it using an ultrasonic device. Ultrasound was applied according to the user conditions of various ultrasonic frequencies, and 800 μl of the aqueous solution was injected and discharged according to the ultrasonic treatment time (1, 3, 5, 7, 9 minutes). At this time, the absorbance of the discharged aqueous solution for each time was measured in the 290 nm absorbance wavelength. From the measured absorbance, the transdermal absorption of cosmetics was obtained by reverse estimation according to the standard curve in the range of 0 to 1 mg/ml of cosmetics.

Results and Discussion

The skin-mimicking phantom manufactured using PDMS is 5.4 cm in diameter and 1.3 cm in height according to the size of the ultrasound device SONOCARE. The absorption of Mk mask pack cosmetics was measured using the manufactured skin-simulating phantom. At a single frequency, it was confirmed that absorption increased with time in the order of 1 MHz, 3 MHz, and 10 MHz.

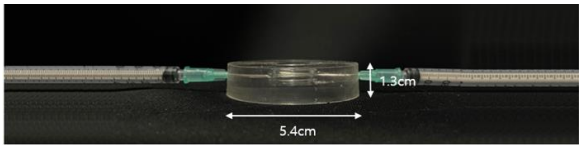


Figure 1. Skin-mimicking phantom fabricated using PDMS

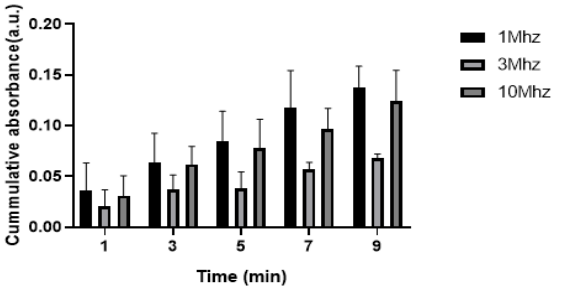


Figure 2. Absorption measurement of MK mask pack cosmetics using the skin-mimicking phantom

Based on the results of this study, it was confirmed that the skin-mimicking phantom produced in this study measure the absorption of cosmetics with the ultrasonic device. These results also suggest the possibility that the skin-mimicking phantom proposed in this study will enable quantitative analysis of various cosmetics.

Acknowledgments

This work was supported by Leaders in INdustry-university Cooperation+ Project supported by the Ministry of Education and National Research Foundation of Korea.

References

1. ”KOSME 산업 분석 레포트-화장품”, 융합금융처, 2019
2. NAIK, Aarti; KALIA, Yogeshvar N.; GUY, Richard H. Transdermal drug delivery: overcoming the skin’s barrier function. *Pharmaceutical science & technology today*, 2000, 3.9: 318-326.
3. LEE, Sung-Joo; LEE, Soon-Hong; PARK, Seung-il. A study on skin permeability enhancement of active substances in cosmetics using nanobubble technique. *Journal of the Korean Applied Science and Technology*, 2020, 37.4: 1041-1051
4. FRANZ, Thomas J. Percutaneous absorption. On the relevance of in vitro data. *Journal of Investigative Dermatology*, 1975, 64.3: 190-195
5. FRANZ, Thomas J. The finite dose technique as a valid in vitro model for the study of percutaneous absorption in man. *Current problems in dermatology*, 1978, 7: 58-68.
6. 식품의약품안전처, 생체 외 피부흡수 가이드라인 Guideline for in vitro Skin Absorption method, 2009.

P-012

Biodegradable Discoidal Particles as Cellular Backpacks

Susmita Aryal[1], Sanghyo Park[1], Gahee Kim[1], Hyeyoun Cho[1], Seonmin Choi[1], and Jaehong Key[1]

[1]Department of Biomedical Engineering, Yonsei University, Wonju, Korea

jkey@yonsei.ac.kr

Abstract

Cells are promising as carriers that can enhance nanomedicine delivery. Cells that can carry a theranostic cargo, either immobilized on the cell surface or internalized, can enable precise delivery and allow the transport of nanomedicines across complex physiological barriers. The effective use of cells as a carrier for nanomedicine transport and delivery requires careful selection of the chemical strategies that are used to load the cell-based carriers with their cargo[1]. This study demonstrates the SCC7 cancer cells conjugated with 5µm discoidal Poly(lactic-co-glycolic acid)-Polyethylenimine-maleimide-PEG$_{5000}$-succinimidyl valerate (PLGA-PEI-PEG) as a cellular backpack immobilizing on the cell surface.

Background

Various malignant cancer cells overcome biological barriers in the body and have the ability to migrate via blood vessels or lymphatic vessels. This study explores the feasibility of SCC7 cancer cells to facilitate the transport of 5µm PLGA-PEI-PEG DPPs. The PEG chains that make up the particle corona were functionalized with maleimide groups to allow covalent conjugation of the particles to thiol groups on the cell surface. Confocal microscopy was used to examine the localization and distribution of DPPs on the cell surface.

Materials

Polyvinyl alcohol (PVA), acid-terminated poly-lactide-co-glycolide (PLGA, lactide:glycolide = 50:50, M_w = 24000-38000 g/mol), dichloromethane (DCM), chloroform ($CHCl_3$), dimethyl sulfoxide (DMSO), N-Hydroxysuccinimide (NHS), dicyclohexyl carbodiimide (DCC), polyethylenimine, Maleimide-PEG$_{5000}$-succinimidyl valerate, and Sylgard 184 elastomer were utilized for synthesis. All reagents and solvents were used without further purification.

First, PLGA was dissolved in DMSO and reacted with DCC and NHS. Then branched PEI was added in PLGA solution. The unreacted materials were removed by dialysis and lyophilized. PLGA-PEI DPPs were synthesized by top-down fabrication method using nanoimprint lithography technique as reported earlier[2]. After fabrication of PLGA-PEI DPPs, 1 mg of particles was mixed with 5 mg of maleimide-PEG$_{5000}$-succinimidyl valerate and dissolved in DI water. The reaction mixture was left on an orbital shaker at 300 RPM at room temperature for 60 min. Excess PEG was removed by centrifuge, and particles were resuspended in DI water (Figure 1).

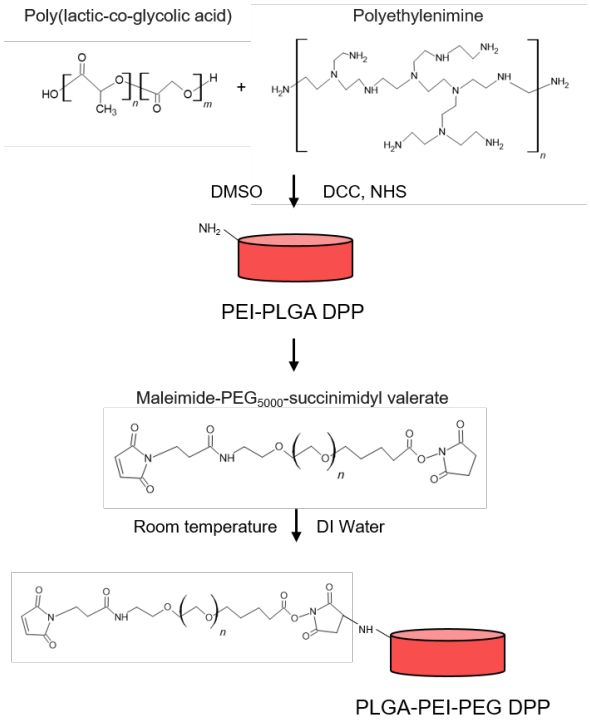


Figure 1. Schematic diagram of PLGA-PEI-PEG DPP synthesis process as a cellular backpack

Results

The coating of PEG_{5000}-succinimidyl valerate was confirmed with zeta potential changes measured by Zetasizer. The Zeta potential of PLGA-PEI DPPs was 14.5mV which was decreased to -16.2 mV after PEG_{5000}-succinimidyl valerate coating (Figure 2A). The attachment and localization of DPPs on the cell surface were confirmed directly after 6 hours by confocal microscopy (Figure 2B).

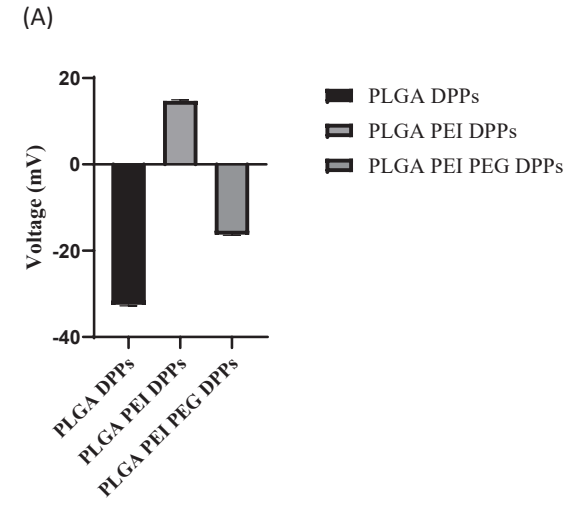


Figure 2. (A) Zeta potential of PLGA, PLGA- PEI, and PLGA-PEI-PEG DPPs, (B) confocal microscopy of DPPs attached on the SCC7 cell surface.

Conclusion

The attachment of PLGA-PEI-PEG DPPs stays only on the cell surface without internalization. It is believed that the cell surface has a negative charge and PLGA too. Therefore, charge-charge interaction cannot happen. PLGA-PEI DPPs were able to be attached to the cell surface because PLGA-PEI has a positive charge. Despite PLGA-PEI-PEG DPPs having a negative charge, it shows a stable attachment on the cell surface, which explains the result PEG chains that make up the DPPs corona were functionalized with maleimide groups to allow covalent conjugation of the particles to thiol groups on the cell surface. These results suggest the possibility that PLGA-PEI-PEG DPPs can be utilized as a cellular backpack. These studies will be studied in more depth through in vivo experiments in the future.

Acknowledgments

This work was supported by grants from the National Research Foundation of Korea (NRF), No. 2018R1-D1A1B07042339 and No. 2019K2A9A2A08000123.

References

1. Ayer, Maxime, et al. "T Cell-Mediated Transport of Polymer Nanoparticles across the Blood–Brain Barrier." *Advanced healthcare materials* 10.2 (2021): 2001375.
2. Key, Jaehong, et al. "Soft discoidal polymeric nanoconstructs resist macrophage uptake and enhance vascular targeting in tumors." *ACS nano* 9.12 (2015): 11628-11641.

P-013

Near-Infrared fluorescence nanoparticle targeting ovarian cancer for image-guided surgery

Seonmin Choi[1], Sanghyo Park[1], Gahee Kim[1], Hyeyoun Cho[1], Hwijin Jang[1], and Jaehong Key[1]

[1]Department of Biomedical Engineering, Yonsei University Gangwon-do, Korea

jkey@yonsei.ac.kr

Abstract

Indocyanine Green (ICG) is widely used as an imaging agent in near-infrared (NIR) fluorescence image-guided surgery. However, ICG has limitations, including poor stability, short half-life, and non-specific targeting. In this study, NIR fluorescence emitting nanoparticles that target cancer cells were synthesized with ICG and hyaluronic acid (HA) to improve the margination of ovarian cancer. This study showed that the efficiency of HA-ICG-PLGA nanoparticles is superior to that of free ICG with bio-stability and target specificity. The particles were about 200 nm in diameter, known as a proper size for enhanced permeability and retention effect to cancer. Moreover, the particles demonstrated higher fluorescence intensity in CD44 overexpressed ovarian cancer cells (SK-OV-3 cells) than CD44 function blocked cells via CD44 receptor-mediated endocytosis. This study proposes the potential of HA-ICG-PLGA nanoparticles for use in NIR fluorescence image-guided surgery for CD44 overexpressed ovarian cancer.

1. Introduction

Cancer is one of the leading diseases of mortality and incidence worldwide. In women, gynecological cancer is included in the world's top 10 cancers. It is the fifth-highest mortality cancer due to its difficulty in early detection and local cancer [1, 2]. Cancer treatment includes chemotherapy and radiation therapy, but surgery is known to be the most effective way. Visualization in surgery to remove these tumors determines the outcome of the surgery. Real-time imaging techniques play an important role, as treatment of local areas such as ovaries requires possible minimum invasive surgery to be performed [3, 4].

Fluorescence imaging has the advantage of being applied to the role of real-time imaging during surgery. Unlike CT and X-ray, fluorescent materials have the advantage of being inexpensive and convenient to carry. In addition, near-Infrared, a wavelength band mainly used in fluorescence imaging, is a region that can escape the interference of auto-fluorescence of body cells such as mitochondria. For this reason, near-infrared fluorescence-based imaging is widely used [4].

Indocyanine green (ICG), used in image-guided surgery, is an FDA-approved therapeutic NIR fluorescent substance with its biocompatibility and biodegradability characteristics [5]. However, limitations such as non-specific targeting and short half-life due to rapid clearance make ICG have a problem of not specifically targeting cancer cells, resulting in side effects such as cancer recurrence [6].

In this study, a nano-drug delivery system using PLGA was used to overcome these limitations. PLGA is a polymer approved by the FDA as a biodegradable and biocompatible substance. Compared to ICG, PLGA nano-carriers can overcome the limitations of ICG by improving its stability in the body [7]. Furthermore, it is known that CD44 receptors are over-expressed in cancer cells and new blood vessels. Hyaluronic Acid (HA), which reacts to these CD44 receptors through receptor-ligand binding, was used to increase target specificity [8]. PLGA-based nanoparticles combined with ICG and HA are expected to contribute to the efficiency and accuracy of image-guided surgeries by overcoming the limitations of existing ICGs.

2. Method and Materials

The particles used in the experiment were PLGA-based nanoparticles (NP) loaded with ICG and coated with HA. The particles were made through the oil in water (O/W) emulsion method and amide coupling. Combining PLGA-amine polymer, which is synthesized with PLGA and polyethyleneimine (PEI) via DCC-NHS coupling, and ICG, ICG encapsulated NPs can be obtained. By

coating hyaluronic acid on the particles via charge-charge interaction, HA-ICG-PLGA NPs were prepared.

The size and zeta-potential of the particles were confirmed via dynamic light scattering (DLS). SK-OV-3 cells (CD44 over-expressed ovarian cancer cells) were cultured with DMEM. Culture medium with different concentrations of nanoparticles (1.0, 0.5, 0.25, 0.125, 0.06 mg/mL) was added to the cells, followed by incubation for 24 h under light-protected conditions. With the CCK-8 assay solution, cytotoxicity was evaluated by measuring optical density. A culture medium with nanoparticles (0.5 mg/mL) was added to the cells, followed by incubation for 24 h under light-protected conditions. With the DAPI solution, cellular uptake was evaluated in the same way as cytotoxicity. For the blocking experiment, a medium containing HA(5mg/ml) was incubated with cells for 2h before treating nanoparticles (HA+). Cellular uptake in the blocking experiment group was evaluated in the same way as above. Cells without pretreatment before treating nanoparticles were called HA- and cells pretreated with HA were called HA+.

3. Result and Discussion

A previous study confirmed that the size and zeta-potential of the synthesized nanoparticles were 200.0 ± 48.83 nm (PDI <0.2) and 32.9 ± 5.67 mV. Wilhelm S, et al. reported that although it varies depending on the tumor cells, it is suitable for enhanced permeability and retention effect (EPR effect) for nano-sized particles range from 100 nm to 400 nm [9].

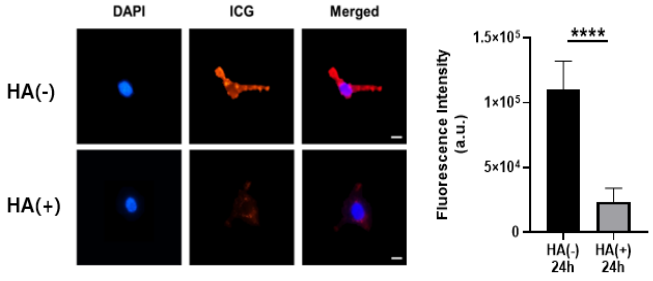


Figure 1. ICG fluorescence intensity in cytoplasm of CD44 over-expressing ovarian cell group (HA-) and HA pretreated ovarian cell

SK-OV-3 cells were selected to confirm the responses of the nanoparticles against ovarian cancer. Experiments with these cells assessed the cytotoxicity, cellular uptake, and blocking test. In the cytotoxicity experiment of the nanoparticles, the viability of the cells after treatment was significantly decreased at a concentration of more than 0.5 mg/ml. With the concentration of 0.5 mg/ml, the cellular uptake experiment and blocking experiment were confirmed. The fluorescence images shown in Figure 1 demonstrate that the cells treated with nanoparticles exhibited red fluorescence of ICG in the cytoplasm. This means that the nanoparticles were internalized in the ovarian cancer cells. Moreover, the fluorescence intensity in the cell group without pretreating HA was 4.7 fold higher than that in the cell group which pretreated HA. With these results, it can be predicted that hyaluronic acid effectively introduces particles into cancer cells with CD44 receptor-mediated endocytosis and that active targeting can play a role. These particles plan to further evaluate in image-guided surgeries.

4. Acknowledgements

This work was supported by grants from the National Research Foundation of Korea (NRF), No. 2018R1D1A1B07042339 and No. 2019K2A9A2A08000123.

5. Reference

1. Siegel, R.L., et al., *Cancer Statistics, 2021.* CA Cancer J Clin, 2021. **71**(1): p. 7-33.
2. Miller, K.D., et al., *Cancer statistics for adolescents and young adults, 2020.* CA Cancer J Clin, 2020. **70**(6): p. 443-459.
3. Esposito, C., et al., *Image-Guided Pediatric Surgery Using Indocyanine Green (ICG) Fluorescence in Laparoscopic and Robotic Surgery.* Front Pediatr, 2020. **8**: p. 314.
4. Peiyuan Wang, Y.F., Lingfei Lu, Lu Liu, Lingling Fan, Mengyao Zhao, Yang Xie, Congjian Xu, Fan Zhang, *NIR-II nanoprobes in-vivo assembly to improve image-guided surgery for metastatic ovarian cancer.* Nature Communications, 2018. **9**: p. 2898.
5. Holloway, R.W., et al., *Detection of sentinel lymph nodes in patients with endometrial cancer undergoing robotic-assisted staging: a comparison of colorimetric and fluorescence imaging.* Gynecol Oncol, 2012. **126**(1): p. 25-9.
6. Zan, M., et al., *Near-infrared light-triggered drug release nanogels for combined photothermal-chemotherapy of cancer.* Biomater Sci, 2015. **3**(7): p. 1147-56.
7. Manchanda, R., et al., *Preparation and characterization of a polymeric (PLGA) nanoparticulate drug delivery system with simultaneous incorporation of chemotherapeutic and thermo-optical agents.* Colloids Surf B Biointerfaces, 2010. **75**(1): p. 260-7.
8. Bartolazzi, A., et al., *Interaction between Cd44 and Hyaluronate Is Directly Implicated in the Regulation of Tumor-Development.* Journal of Experimental Medicine, 1994. **180**(1): p. 53-66.
9. Wilhelm S,et al. Analysis of nanoparticle delivery to tumours. Nat Rev Mater 2016;1:16014.

P-014

Fabrication of Nanoparticles Targeting Natural Killer Cells to Prime the Cellular Activity for Anticancer Effects

Na Kyeong Lee[1], and Chun Gwon Park[1*]

[1] Department of Intelligent Precision Healthcare Convergence, Sungkyunkwan University, Suwon, Korea, SKKU Institute for Convergence, Sungkyunkwan University (SKKU), Suwon, Gyeonggi 16419 Republic of Korea.

chunpark@skku.edu

Abstract

Natural killer cells (NK cells) are critical to the innate immune system. They give rapid responses to cancer cells and virus-infection through various receptors on the cell surface. Recently, the importance of NK cells is increasing because they can directly attack cancer cells and regulate adaptive immune cells. In this study, we fabricate nanoparticles (NPs) targeting NK cells as a platform of the target delivery system. Our goals are to reduce undesired systemic side effects and enhance therapeutic effectiveness through concentrating immune-activation compounds into NK cells.

To establish proof of concept, F(ab')2 fragment of NK cells targeting antibody is conjugated on the surface of PLGA-PEG-Mal NPs through the reaction between free sulfhydryl groups in the hinge region of antibody and maleimide on the NPs surface. To confirm the binding ability of the NPs to target cells *in vitro* and *in vivo*, antibody conjugated NPs loaded with DiD were used and fluorescent signal was analyzed by flow cytometry. As a result, up to 80% of the NK cell population is targeted by antibody-conjugated nanoparticles, whereas unconjugated NPs are not. This result demonstrates that antibody conjugated NPs can bind to NK cells with minimized non-specific binding and show their potential as a target delivery platform.

Background

Antibodies(Abs) have been widely used as active pharmaceutical ingredients, targeting ligands, and biosensing molecules in pharmaceutical and biomedical fields [1]. Abs are often chemically conjugated or physically adhered to the surfaces of biomaterial-based nanoparticles (NPs) to ensure specific targeting or/and enhanced bioactivity due to their high specificity, remarkable diversity, and high availability [2]. As an attractive target immune cell for anticancer treatment, natural killer cells (NK cells) are part of the innate immune system. They give rapid responses to cancer cells and virus-infection through various receptors on the cell surface. Recently, the importance of NK cells is increasing because they can directly attack cancer cells and regulate adaptive immune cells. In this study, we fabricate nanoparticles (NPs) targeting NK cells as a platform of the target delivery system. Our goals are to reduce undesired systemic side effects and enhance therapeutic effectiveness through concentrating immune-activation compounds into NK cells.

Methods

Poly(lactic-co-glycolic acid) (PLGA) NPs were prepared by using conventional emulsification methods. The size, morphology, and zeta potential of the NPs were analyzed by using a Malvern Zetasizer Nano ZS system (Malvern Instruments, MA, USA), dynamic light scattering (DLS), and a JEM-7500F (Akishima, Japan) scanning electron microscope (SEM).

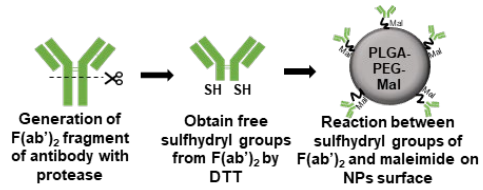


Figure 1 shows the fabrication process of antibodies conjugation to NPs (f(ab')2 NPs) for target delivery. F(ab')2 fragment of NK cells targeting antibody was conjugated on the surface of PLGA-PEG-Mal NPs through the reaction between free sulfhydryl groups in the hinge region of Abs and maleimide (Mal) on the NPs surface. The protease cleaved Abs to fc and f(ab')2 and only the f(ab')2 portion was used to prevent unspecific binding by the Fc region and to

control the direction of the Abs on the surface of NPs. The generation of f(ab')2 fragments were confirmed by non-reducing SDS-PAGE gel stained with Commassie Brilliant Blue. And DTT was used to obtain a free thiol group from the hinge region of the abs for interaction with Mal on surface of NPs.

To validate the immune cell targeting ability of NPs *in vitro*, mouse splenocytes were co-incubated with fluorescently labeled NPs. The fluorescent signal of NPs from targeted immune cells was collected by flow cytometry. To evaluate the immune cell targeting ability of NPs *in vivo*, fluorescently labeled NPs were injected to mouse via tail vein. After 1,3 or 6 h from injection, mouse spleen, lymph node (LN) and blood were collected for verification of NPs binding to targeted immune cells.

Results and Discussion

Figure. 2 indicated the successful cleavage of Abs by protease. The band of whole Abs was shown in 150 kDa. On the other side, the band on 115 kDa and 25 kDa indicated f(ab')2 and fc portion respectively.

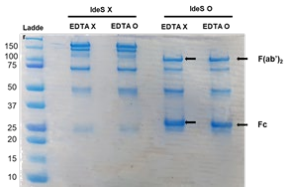


Figure.2 Non-reducing SDS-PAGE gel stained with Commassie Brilliant Blue for confirmation of f(ab')2 fragments after protease cleavage.

Figure.3 demonstrates the size, morphology and zeta potential of PLGA-PEG-Mal NPs and F(ab')2 NPs. The average sizes of the non-conjugated-PLGA-PEG-Mal NPs and f(ab')2 NPs were measured with DLS to be 193 and 201 nm, respectively (Fig. 3A and B). The zeta potentials of PLGA-PEG-Mal NPs and f(ab')2 NPs were -22.3 mV and -6.78 mV, respectively (Fig. 3C). The less negative zeta potential of the antibody-conjugated NPs can therefore be explained by the presence of antibodies on the NPs' surface.

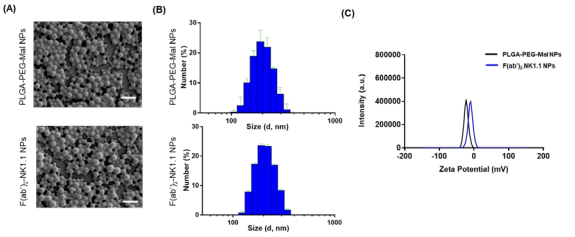


Figure. 3 Characterization of PLGA NPs and Abs conjugated PLGA NPs. (A) SEM image of NPs (scale bar=0.5 μm). (B) Size distribution of NPs. (C) Zeta potential of NPs.

In vitro and in vivo binding ability of NPs to targeted immune cells, NK cells, were shown in Figure 4. As NK cells targeting ligand, anti-mouse NK1.1 Abs were conjugated to NPs. Fluorescently labeled NK1.1+NPs with DiD were then co-incubated with mouse splenocytes or injected to via mouse tail vein. DiD signal from NK cells confirmed by flow cytometry indicate the specific binding of NPs to NK cells. *In vitro*, NK1.1+NPs targeted to up to 75.66% of NK cells in 30 minutes, and it was confirmed that they target up to 80% or more as the incubation time increases (Fig. 4A and B). And the i.v. injected NPs successfully targeted NK cells in spleen, LN and blood of mouse (Fig. 4C). The fluorescence signal of NPs generally peaks at 1 hour, and then decreases over 3 and 6 hours, indicating the clearance of the NPs.

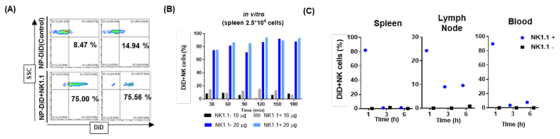


Figure. 4 Binding ability of NPs *in vitro* and *in vivo*.

Acknowledgements

This work was supported by the National Research Foundation of Korea (NRF) grant funded by the Korean government (MSIT) (NRF-2019R1A4A1028700 and NRF-2019R1C1C1006300). This work was supported by the Fourth Stage of Brain Korea 21 Project of the Department of Intelligent Precision Healthcare and IBS-R015-D1.

References

1. KS Kim, J Kim, DH Kim, HS Hwang, and K Na, Biomater. Sci. 6, 1217 (2018).
2. Schmid, D., Park, C.G., Hartl, C.A. et al., *Nat Commun* 8, 1747 (2017)
3. Liu, S., Galat, V., Galat4, Y. et al. J Hematol Oncol 14, 7 (2021)

Modulating Sepsis-Associated NETosis Dysregulation Using Bioinspired DNase-Ⅰ-Coated Melanin-like Nanospheres

Y.Y. Lee[1,2] , C.G. Park[2] , Y.B. Choy[1]

[1] Department of Biomedical Engineering, Seoul National University College of Medicine, Seoul, Korea

[2] Department of Biomedical Engineering, Sungkyunkwan University, Suwon, Korea

chunpark@skku.edu

Abstract

We report that DNase-I-coated melanin-like nanospheres (DNase-I pMNSs) mitigate sepsis-associated NETosis dysregulation, thereby preventing further progression of the disease. Recombinant DNase-I and poly(ethylene glycol) (PEG) were used as coatings to promote the lengthy circulation and dissolution of NET structure. Our data indicate that the application of bioinspired DNase-I pMNSs reduce neutrophil counts and NETosis-related factors in the plasma of SARS-CoV-2 sepsis patients, alleviates systemic inflammation, and attenuates mortality in a septic mouse model. Given this, our findings suggest that the NET degradation with DNase-I pMNSs may also reduce the lung injury and have potential application in the treatment of COVID-19 related diseases.

Background

The current outbreak of severe acute respiratory syndrome coronavirus 2 (SARS-CoV-2) began in December 2019. Globally, the number of confirmed cases and mortality rates of coronavirus disease 2019 (COVID-19) have risen dramatically. Currently, there are no FDA-approved antiviral drugs and there is an urgency to develop treatment strategies that can effectively suppress SARS-CoV-2-mediated cytokine storms, acute respiratory distress syndrome (ARDS), and sepsis. SARS-CoV-2 infections are associated with both impaired adaptive immune responses and uncontrolled inflammatory innate immune responses, which lead to local and systemic tissue damage.

Neutrophil extracellular traps (NETs) are reticular structures consisting of a DNA backbone and a number of functional proteins that are formed through a process known as NETosis. SARS-CoV-2 infections may impair adaptive immune responses as well as induce uncontrolled inflammatory innate immune responses, which cause local and systemic tissue damage. These phenomena are typically associated with elevated levels of NETosis markers, such as cell-free DNA (cfDNA), myeloperoxidase (MPO), and neutrophil elastase (NE). These factors correlate with increased disease severity and poor clinical outcome. It is particularly challenging to treat patients that exhibit high levels of NETosis. Consistent with this, an approach that inhibits NETosis has significantly increased the survival in pulmonary sepsis.

Methods

Figure.1 Long-acting DNase-1 was prepared as previously described [15, 16]. Primary nanoparticles were prepared with the FDA-approved polymer, PLGA, via a conventional single emulsification method (**Figure 1**). To prepare bare nanoparticles (PLGA NP), 400 mg PLGA was dissolved in 5 mL DCM and then poured into a 20 mL solution of 1% PVA. The resulting polymer solution was sonicated for 10 min at 40% amplitude with 1 sec on and 1 sec off using a Q700 sonicator (Qsonica, LLC, Newtown, CT, USA). The prepared emulsions were poured into 5 mL DI water and residual DCM was allowed to evaporate overnight at room temperature with magnetic stirring. The PLGA NPs (400 mg) were resuspended in 20 mL 10 mM, pH 8.5 Tris buffer and coated with a bio-adhesive made of polydopamine (PD, 100 mg dopamine in 1 mL water) with vigorous stirring at 4℃ for 3 h. The bio-adhesive nanoparticles (PLGA-PD NPs) were collected by centrifugation at 17,000 rpm for 20 min, resuspended in 5 mL Tris buffer (10 mM, pH 8.5) containing 50 mg DNase-1 and 50 mg poly(ethylene glycol), and stirred at 4 ℃ for 3 h. The resulting DNase-1-coated NPs were then collected and washed with DI water to prepare PLGA-

PD-PEG-DNase-1 NPs (referred to as long-acting DNase-1).

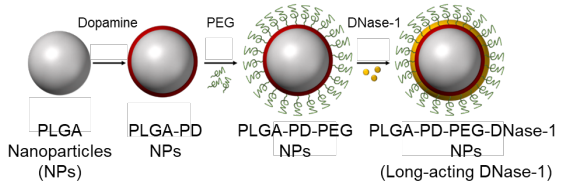


Figure 1. Preparation of long-acting nanoparticulate DNase-1.

To validate

Results and Discussion

Figure. 2(a) shows the effects of DNase-1 on DNA degradation, we treated the plasma of COVID-19 patients with sepsis with the free DNase-1 and long-acting DNase-1. The results showed that both forms of DNase-1 significantly reduced cfDNA levels (Fig. 4A) and that exposure of DNase-1 to the plasma of COVID-19 patients with sepsis increased the activity of DNase-1 (Fig. 4B). We also observed markedly reduced NET levels, MPO activity, and NE levels in neutrophils of COVID-19 patients with sepsis upon treatment of the DNase-1 formulations (Fig. 4C–E).

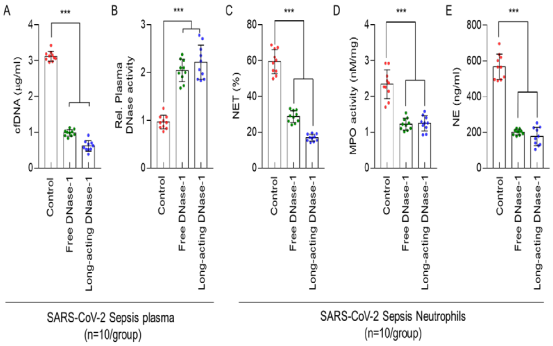


Figure.2. NETosis index and cytokine production in free DNase-1- or long-acting DNase-1-treated SARS-CoV-2 Sepsis patients' plasma and PBMCs.

Figure.3 demonstrates exogenous administration of the DNase-1 formulations in a cecal ligation and perforation (CLP)-treated septic mouse model. The CLP model is an in vivo model in which NETosis, CRS, and multiple organ failure (MOF) syndrome can be induced. Because similar phenotypes are also observed in severe cases of SARS-CoV-2-infected patients, the CLP model can be used to represent the SARS-CoV-2-induced sepsis symptoms of patients with COVID-19. With the current limitations and no alternatives being available, the CLP model was considered to be an applicable in vivo model for the current setting. To confirm the anti-septic effects of DNase-1, CLP-treated mice were intravenously injected with phosphate-buffered saline (PBS; control group), free DNase-1 (100 units), or long-acting DNase-1 (100 units) at 12 h and 24 h post CLP-treatment. All of the CLP-treated mice died within 78 h of the CLP procedure when no DNase-1 treatment was given, demonstrating the high mortality seen for the CLP-treated sepsis model. Even with the administrations of free DNase-1, the septic mice died quickly with none of the CLP-mice (0 %) surviving at 96 h after CLP induction. This lack of an in vivo effect of free DNase-1 may have been due to the short half-life of DNase-1 [29]. Intriguingly, the long-acting DNase-1 conferred a 50% survival rate for the CLP-treated septic mice at 96 h. Ultimately, these mice fully recovered.

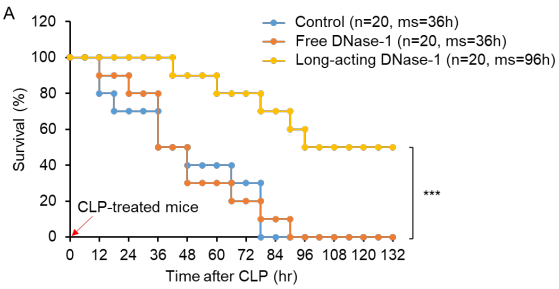


Figure.3. Anti-septic effects of long-acting DNase-1 in mouse septic model.

Acknowledgements

This research was supported by the National Research Foundation of Korea (NRF) grant funded by the Korea government (MSIT) (2019R1C1C1006300, 2019R1A4A1028700, 2018R1C1B6001120, and 2018M3A7B4071204) and the Ministry of Education (2018R1D1A1B07050422, and 2017R1A6A3A04005573).

References

1. J. Park, R.W. Wysocki, Z. Amoozgar, L. Maiorino, M.R. Fein, J. Jorns, A.F. Schott, Y. Kinugasa-Katayama, Y. Lee, N.H. Won, "Cancer cells induce metastasis-supporting neutrophil extracellular DNA traps ", Sci Transl Med, 8(361), (2016).
2. P. Mehta, D.F. McAuley, M. Brown, E. Sanchez, R.S. Tattersall, J.J. Manson, "COVID-19:

consider cytokine storm syndromes and immunosuppression", Lancet. 395(10229)., 1033-1034 (2020).

P-016

PEG coated MCM-48 nanoparticles for oral vaccine delivery

Chang Hee Min[1,+], Se Na Kim[1,+], Young Bin Choy[1,2,3,*]

[1]Institute of Medical & Biological Engineering, Medical Research Center, Seoul National University, Seoul, Korea

[2]Interdisciplinary Program in Bioengineering, College of Engineering, Seoul National University, Seoul, Korea

[3]Department of Biomedical engineering, Seoul National University College of Medicine, Seoul, Korea

*ybchoy@snu.ac.kr

+ These authors contributed equally to this work

Abstract

Oral vaccination has been considered as a convenient strategy compared with other conventional means. However, this method poses some problems, such as low antigen stability, and low targeting efficiency. To resolve those problems, we modified the MCM-48 nanoparticles as oral vaccine delivery carriers. For upregulated antigen loading, the pores of MCM-48 were expanded with long chain amine. (i.e. MCM-48-LP). For enhanced delivery to the M cells, polyethylene glycol (PEG) was grafted on the surface of the particles. Then ovalbumin (OVA) was impregnated as a model antigen (i.e. OVA@PEG-MCM-48-LP). The *in vitro* antigen release study exhibited that the OVA@PEG-MCM-48-LP contained more than half of OVA at simulated gastric environment, and could sustained OVA release at simulated intestinal environment. The confocal image revealed that FITC labelled PEG-MCM-48-LP could be well localized in M cells. However, FITC labelled MCM-48-LP could not be observed around the M cell. From these data, we propose the PEG-MCM-48-LP as a potential carrier for oral vaccine delivery.

Background

Treatment and prevention of infectious diseases is emerging as an important social problem in many countries. The most widely used method for preventing infectious diseases is vaccine administration. Currently, vaccines are administered mainly through injection administration (intramuscular injection, subcutaneous injection) in clinical practice. However, due to the invasive administration method, requirement of skilled medical personnel, low patient-friendliness, and the cost of establishing a cold chain system to maintain the safety of vaccine injection formulations are considered as disadvantages. Although oral vaccines have been developed to solve these problems, there are still problems to be overcome, such as antigen degradation in the gastrointestinal environment, low antigen loading efficiency, and low delivery efficiency to target site. In order to solve the limitations of oral vaccines, our research team increased the antigen loading efficiency by expanding the pores of the particles, and coated polyethylene glycol (PEG) on the surface to increase the antigen delivery efficiency of MCM-48 mesoporous silica. MCM-48 is a 3D pore-structured mesoporous silica particle with a large specific surface area and large pore volume, and has the advantages of high biocompatibility and surface modification in various ways. In this study, MCM-48 applied with pore expansion technology was used as a vaccine carrier to effectively load a larger amount of model antigen. In addition, by coating the surface of MCM-48 with PEG, mucosal permeability was imparted to the particles, increasing the efficiency of particle delivery to Peyer's patch, the target immune site of the oral vaccine.

Methods

MCM-48 was synthesized by the modified Stöber synthesis method [1], and then the pores of the particles were expanded through post-thermal treatment [2]. 1.01 g of cetrimonium bromide and 4.10 g of F127 were dissolved in a mixture of 167.64 g of tertiary distilled water, 72.78 g of ethanol, and 41.76 g of ammonium hydroxide solution (29 wt%), and then 3.6 g of tetraethyl orthosilicate was added. After stirring at 1000 rpm for 1 minute, the mixture was synthesized at 25℃ for 24 hours. A white solid precipitate was obtained by centrifugation, washed thoroughly with water and ethanol, and dried. To expand the pores of the particles, 0.6 g of MCM-48 and 0.75 g of dimethylhexadecylamine were added to 22.5 g of water and reacted at 130° C. for 72 hours. After the reaction was completed, white solid precipitate was washed with water and ethanol, and

then centrifuged to obtain MCM-48 with expanded pores (i.e. MCM-48-LP).

In order to coat the PEG on the surface of the particle, an amine group was attached to particles surface. And then, PEG is coated on the surface of the particle through NHS/EDC reaction (i.e. PEG-MCM-48-LP). PEG-MCM-48-LP were loaded with albumin from egg white (OVA) as a model antigen (i.e. OVA@PEG-MCM-48-LP). In vitro OVA release experiments were carried out in a shaking incubator at 37 °C using pH 1.2, 6.8, and 7.4 phosphate buffer saline (PBS) solutions. The amount of released OVA was measured using a bicinchoninic acid assay. Peyer's patch targeting efficacy was assessed under in vivo environments using the fluorescein-labelled nanoparticles herein (i.e. FITC-MCM-48-LP, and FITC-PEG-MCM-48-LP).

Results and Discussion

The X-ray diffraction analysis results with the MCM-48 displayed a well resolved characteristic pattern as previously reported. Through the scanning electron microscope image, it was confirmed that MCM-48, MCM-48-LP, PEG-MCM-48-LP, all were spherical particles with a size of about 200 nm. The expanded pores of MCM-48-LP particles were confirmed by comparative analysis through transmission electron microscope images of MCM-48 and MCM-48-LP. (See Figure 1)

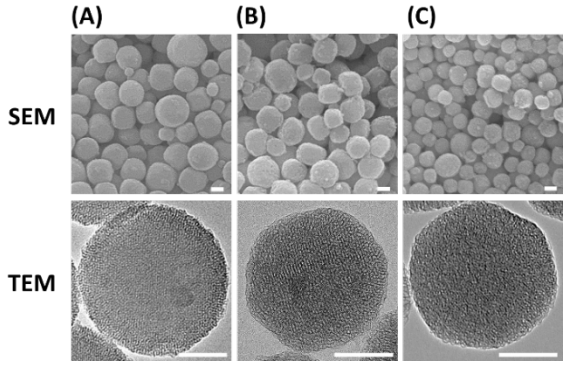


Figure 1. SEM, TEM image of (A) MCM-48, (B) MCM-48-LP, (C) PEG-MCM-48-LP (Scale bar = 100 nm)

As a result of calculation using the BET and BJH equations, pore volume of particles was increased from 0.9 to 1.82 cm^3/g, and the average pore diameter increased from 2.1 to 4.9 nm, respectively. The PEG-MCM-48 exhibited a characteristic Fourier-transform infrared spectroscopy peak at 2929 cm^{-1} that was attributable to the C-H asymmetric vibration from $-CH_2$, indicating the presence of PEG. However, MCM-48-LP particles didn't present specific FTIR peak.

The *in vitro* OVA release test exhibited that the OVA@PEG-MCM-48 contain more than 65% of the antigen even after the first 2 hours, and sustained release of the antigen loaded in the particles from 2 hours to 48 hours. The confocal microscopy image of mice Peyer's patch revealed that FITC labelled PEG-MCM-48 could be well localized in Peyer's patch. However, FITC labelled MCM-48 could not be observed around the Peyer's patch. Judging from this, in the case of MCM-48-LP, even when administered orally, it is trapped in the mucosal layer of the intestinal tract and cannot reach the Peyer's patch, the target immune organ of the oral vaccine, but in the case of PEG-MCM-48-LP, it passes through the mucosal layer, It was determined that the Peyer' patch could be reached.

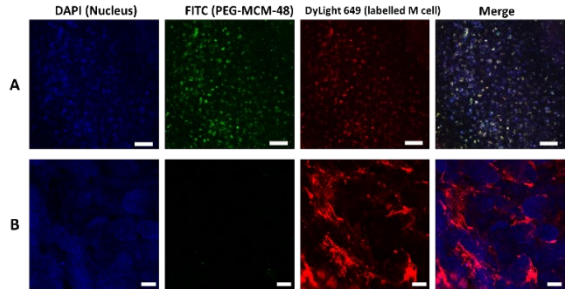


Figure 2. Confocal fluorescence image of mice Peyer's patch, demonstrating the uptake of (A) FITC-PEG-MCM-48-LP and (B) FITC-MCM-48-LP

Acknowledgements

This work was supported by Samsung Research Funding & Incubation Center of Samsung Electronics under Project Number SRFC-IT2001-01

References

1. Tae-Wan Kim, Po-Wen Chung, and Victor S.-Y. Lin, "Facile Synthesis of Monodisperse Spherical MCM-48 Mesoporous Silica Nanoparticles with controlled Particle Size", Chemistry of Materials, Vol. 22, No. 17, 2010
2. Michal Kruk, Mietek Jaroniex, Abdelhamid Sayari, "New insights into pore-size expansion of mesoporous silicates using long-chain amines", Microporous and Mesoporous Materials, Vol. 35, 2000

P-017

Efficient Activation of Dendritic cells with CpG-coated Functional Magnetic Nanoparticles

Jaesung Lim[a,b], Se-Na Kim[c], Jun-Hyeok Han[d], Hee Seung Seo[a,b], and Chun Gwon Park[a,b,e,f]*

[a]Department of Biomedical Engineering, Sungkyunkwan University (SKKU), Suwon, Korea

[b]Department of Intelligent Precision Healthcare Convergence, SKKU, Suwon, Korea

[c]Department of Biomedical Engineering, Seoul National University College of Medicine, Seoul, Korea

[d]Department of Biomedical-Chemical Engineering, The Catholic University of Korea, Bucheon, Korea

[e]Biomedical Institute for Convergence at SKKU (BICS), Suwon, Korea

[f]Center for Neuroscience Imaging Research, Institute for Basic Science (IBS), Suwon, Korea

chunpark@skku.edu

Abstract

Modulation of the postoperative immune-suppressive environment is crucial for tumor treatment. Herein, we demonstrate immune-modulating magnetic nanoparticles. These nanoparticles were synthesized by a heat-up method and coated with a CpG oligonucleotide capable of activating the immature dendritic cells. CpG-coated magnetic nanoparticles were treated to bone marrow-derived dendritic cells (BMDCs), upregulating activation markers such as CD80, CD86, CD40, and MHC2 molecules, suggesting the nanoparticles-mediated maturation of BMDCs.

Background

There are various agonists capable of changing the tumor microenvironment by activating immune cells. One of them, the CpG oligonucleotide (ODN) was well-known as a toll-like receptor (TLR) 9 activator. It promotes maturation of dendritic cell playing a pivotal role in immune system as antigen-presentation cells that could elicit both innate and adaptive immunity. Here, we have conjugate CpG oligonucleotide to the magnetic nanoparticles via electrostatic interaction, which could be delivered to naive DCs, leading to more efficient activation than when CpG is freely delivered to 4T1 tumor baring model. These CpG on MNPs capable of DC maturation and delivered tumor-associated antigen (TAA) to naïve T cell and resident DCs in lymph node. Activated immunity could elicit the localized inflammatory response, which could prevent tumor recurrence and metastasis, and increase survival rate.

Methods

The Zn/Fe magnetic nanoparticles (MNPs) were synthesized following a slightly modified heat-up procedure [1]. The PEI coated-magnetic nanoparticles were prepared following modified three-step process [2]. The morphology of magnetic nanoparticles was analyzed by high resolution transmission electron microscopy (HRTEM; JEM-2100F, JEOL, USA) and scanning electron microscopy (FESEM; JSM-7600F, JOEL, USA). The size distribution and surface charge of prepared nanoparticles were measured by dynamic light scattering (DLS; ZetaSizer Nano ZS, Malvern, UK). In order to estimate the content of organic materials and Zn/Fe magnetic core, thermogravimetric analysis of the samples were carried out in nitrogen atmosphere. The degree of binding between the cationic MNPs and CpG was estimated by a gel retardation assay. CpG-coated PEI/d/CA-MNPs was compared with an equal amount of the PEI/d/CA-MNPs (0.5 mg), and different weight ratio of CpG [CpG*(PEI/d/CA-MNPs), w/w]. Prepared samples were co-incubated at room temperature. Every supernatant was mixed with a gel loading dye and

loaded to an 1% agarose gel. A ChemiDoc™ XRS+ Imaging System (Bio-Rad, USA) that contains an ultraviolet transilluminator was used to visualize and document the gel. Prepared nanoparticles were structurally analyzed by Fourier-transform infrared (FT-IR) spectroscopy with potassium bromide disc on a Vertex 70 (Bruker, USA). Cytotoxicity of CpG coated nanoparticles was measured by D-Plus™ CCK cell viability assay kit The absorbance of the solution was detected at 450 nm by using a microplate reader (SynergyHTK multimode, Winooski, VT, USA). The BMDCs were prepared following modified process [3, 4]. In day 6, proliferating immature DCs were harvested as non-adherent and loosely adherent clusters of cells. 200 µl of reactant media was added each groups for 24 hours at 37 ℃. To analyze the maturation markers of BMDCs, cells were labeled by fluorescence conjugated antibodies for zombie violet, CD11c, CD80, CD86, CD40, and MHC II (Biolegend, USA). The prepared samples were assessed by flow cytometry (Beckman coulter, USA)

Results and Discussion

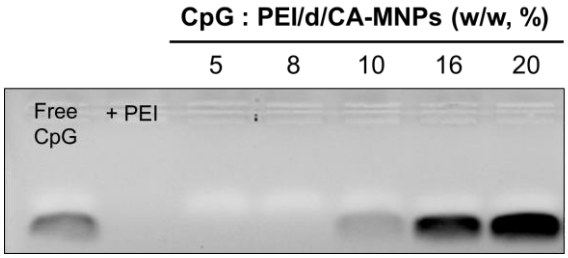


Figure 1. Gel retardation assay using CpG-B (5′-TCCATGACGTTCCTGACGTT-3′)

The cationic MNPs were fabricated by surface modification with modified three-step process [2]. Gel retardation assay was used to determine the binding capacity of PEI/d/CA-MNPs and CpG-B to identify the proper ratio PEI/d/CA-MNPs with CpG-B (Fig 1). In these experiments, various concentrations of PEI/d/CA-MNPs were complexed with a CpG-B and then subjected to 1% agarose gel electroporation. The bands of CpG*(PEI/d/CA-MNPs) were confirmed at % weight ratio of 10, 16, 20. This results indicate that the unbounded CpG was still remaining in supernatant after co-incubation at 10, 16 and 20 % CpG groups.

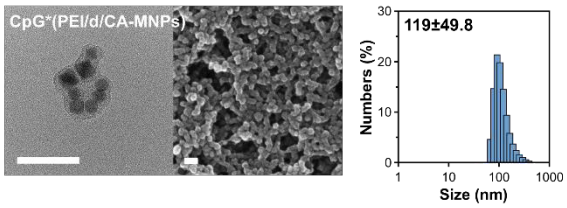


Figure 2. The morphology of CpG-coated MNPs and its size distribution

The 8% CpG-coated (PEI/d/CA/MNPs) measured its morphology and size by HRTEM, FESEM and DLS compared to other groups, and its value was 119±49.8 nm (Fig 2). We next measured the zeta-potential to estimate the change of surface charge on each nanoparticle (Fig 3).

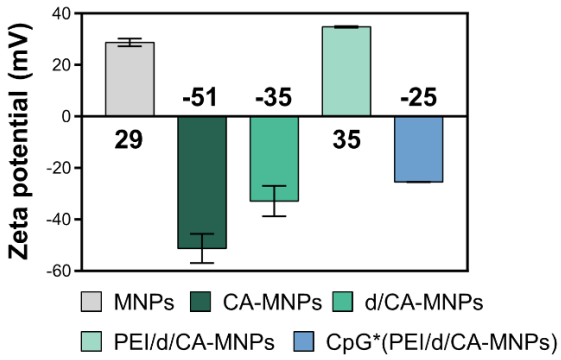


Figure 3. Zeta potential analysis

First, the MNPs, coated with OA, was shown 29 mV. The CA-MNPs d/CA-MNPs were negatively charged at −51 and −35 mV, respectively, whereas PEI/d/CA-MNPs were switched at +35 mV. CpG*(PEI/d/CA-MNPs) were switched to negative charge, at -25 mV. Taken together, these results indicate that cationic MNPs and CpG had been successfully immobilized on the surface of MNPs with a core-shell structure. In addition, to confirm the chemical change in surface of nanoparticles, we performed Fourier-transform infrared spectroscopy (FT-IR) analysis. Specific characteristic peaks of oligonucleotide were detected in CpG*(PEI/d/CA-MNPs), the PO^{-1} and PO^{-2} scissoring were detected in 1051 and 1100 cm-1, respectively (Fig 4).

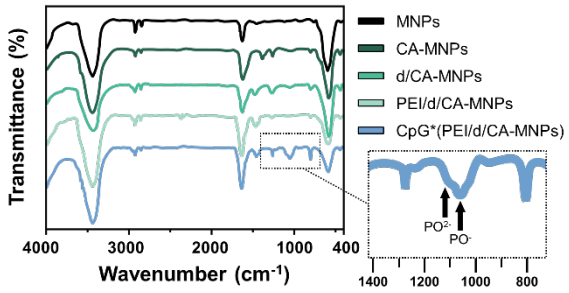


Figure 4. FT-IR analysis of CpG*(PEI/d/CA-MNPs)

To determine whether the MNPs were toxic or not, we first evaluated their cytotoxicity by CCK assay with L-929 cells (Fig 5). When L-929 cells were treated with various concentrations of CpG*(PEI/d/CA-MNPs), the cell survival rate was greater than 90%, up to a concentration of 20 μg/mL, but the cell survival rate was lower than 80% at a concentration of 80 μg/mL.

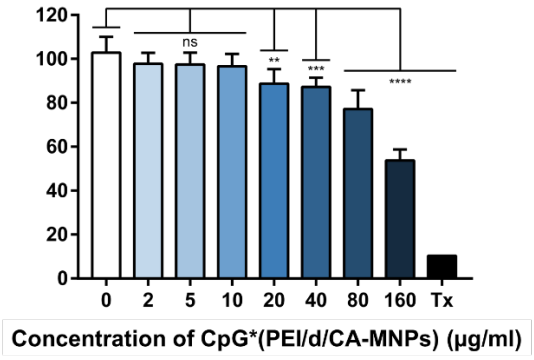


Figure 5. Cytotoxicity of CpG*(PEI/d/CA-MNPs) *in vitro* (n=5)

From this result, we decided the BMDCs treated concentration as 10 ug/ml of CpG*(PEI/d/CA-MNPs), and compared degree of expression of activation marker by flow cytometry (Fig 6).

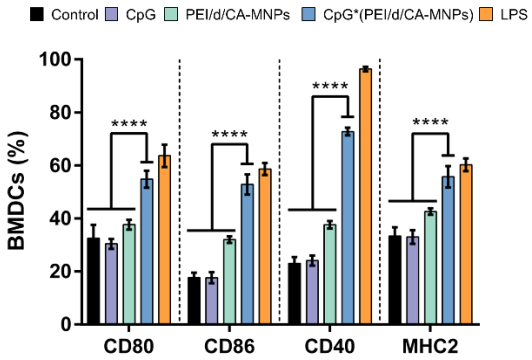


Figure 6. Live/CD11c^{+} BMDCs maturation test by CpG*(PEI/d/CA-MNPs) (n=8, 10 ug/ml)

Every single markers was over-expressed in CpG-coated MNPs compared to other groups except LPS. This result indicates the same dose of CpG more activate BMDCs effectively when they conjugated with cationic MNPs.

Acknowledgments

This work was supported by the National Research Foundation of Korea (NRF) grant funded by the Korea government (2019R1C1C1006300, 2019R1A4A1028700). This work was also supported by the BK21 FOUR Project.

Reference

1. Jang, J.T., et al., Critical Enhancements of MRI Contrast and Hyperthermic Effects by Dopant-Controlled Magnetic Nanoparticles. Angewandte Chemie-International Edition, 2009. 48(7): p. 1234-1238.
2. Kim, K.S., et al., Multifunctional nanoparticles for genetic engineering and bioimaging of natural killer (NK) cell therapeutics. Biomaterials, 2019. 221: p. 119418.
3. Inaba, K., et al., Generation of Large Numbers of Dendritic Cells from Mouse Bone-Marrow Cultures Supplemented with Granulocyte Macrophage Colony-Stimulating Factor. Journal of Experimental Medicine, 1992. 176(6): p. 1693-1702.
4. Gorska, S., et al., Distinct Immunomodulation of Bone Marrow-Derived Dendritic Cell Responses to Lactobacillus plantarum WCFS1 by Two Different Polysaccharides Isolated from Lactobacillus rhamnosus LOCK 0900. Applied and Environmental Microbiology, 2014. 80(20): p. 6506-6516

P-018

Graphene oxide-reinforced hydroxyapatite/gelatin bone scaffolds fabricated using extrusion-based 3D bioprinting

H.Y. Lee[2], J.M. Yoo[2], and S.Y. Nam[1,2]

[1]Department of Biomedical Engineering, Pukyong National University, Busan, Republic of Korea

[2]Industry 4.0 Convergence Bionics Engineering, Pukyong National University, Busan, Republic of Korea

synam@pknu.ac.kr

Abstract

3D printing technology has been widely applied to precisely fabricate 3D tissue engineered scaffolds with designed shape and porosity. In this study, we fabricated graphene oxide (GO) reinforced HA/gelatin composite scaffold using micro-extrusion-based 3D bioprinter under optimized printing parameters. The results demonstrate the great potential of using GO in the fabrication of composite bone scaffolds with improved mechanical properties for applications in bone tissue engineering.

Background

Recently, 3D printing technology has been widely applied to precisely fabricate 3D tissue engineered scaffolds with designed shape and porosity. Especially, bioceramic-based composites with favorable osteogenic ability have been proposed for fabrication of bone scaffolds and have also gained an interest in tissue engineering and regenerative medicine [1]. Among various combinations of bioceramic-based composites, hydroxyapatite (HA)/gelatin composites have been frequently suggested, thanks to their synergistic advantages of gelatin and HA, which mimic organic and inorganic constituents of bone as well as enhance mechanical properties and osteogenic activities. However, HA/gelatin composites still have limitations for preclinical and clinical applications such as low fracture toughness, poor tensile strength, and weak wear resistance.

Graphene oxide (GO) is the highly oxidized form of graphene, a single atom-thick layer of sp2-bonded carbon atoms in a honeycomb lattice, and is rapidly rising as a potential material for reinforcement of ceramic-based composites due to its outstanding intrinsic mechanical properties. Also, functional groups of GO such as hydroxyl, carboxyl, and epoxy groups can provide a chance to easily interact with other biomolecules and biomaterials via both covalent and noncovalent strategies.

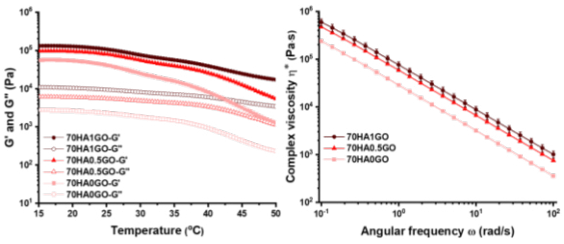
Therefore, in this study, fabrication of 3D printed bone scaffolds using HA/gelatin composites reinforced with GO was demonstrated to improve their mechanical properties with maintaining appropriate printability. The physiochemical and rheological properties of GO-reinforced composites were quantitatively and qualitatively analyzed and compared with controls. Also, compressive and flexural strength of the 3D printed scaffolds were measured after optimization of printing parameters.

Methods

The HA powder (< 200 nm particle size, nGimat), type-A gelatin (Sigma Aldrich) and GO, which was prepared by the oxidation of natural graphite powder according to the Hummer's method, were used to fabricate HA/gelatin/GO composite scaffolds using an extrusion-based 3D bioprinter with a 21G nozzle (diameter = 0.51 mm) [2]. After the fabrication, the scaffolds were transferred into a solution of glutaraldehyde (GA) (0.25 %w/v) for 24 h at 25 °C for crosslinking. Mechanical properties were assessed using the universal testing machine (LR5K Plus, LLOYD instruments). Chemical analysis was carried out with X-ray diffraction (XRD) (X'Pert-MPD, Philips), Fourier-transform infrared (FT-IR) spectroscopy (Spectrum X, PerkinElmer) and thermo gravimetric analysis (TGA) (Pyris 1, Perkin Elmer). The rheological measurements were performed with a rheometer (TA Instruments, HR-2) using a 20 mm parallel plate.

Results and Discussion

Figure. 1 shows the rheological assessment of HA/gelatin/GO composites. As shown in the figure, the results indicated a distinct rise of the storage modulus (G'), loss modulus (G"), and complex viscosity with the increase of the GO concentrations from 0% to 1%. Furthermore, all composite groups show shear-thinning behaviors, which is prerequisite for the proper extrusion.



(a) (b)

Figure. 1. (a) Oscillatory temperature ramp test. (b) Complex viscosity as a function of angular frequency.

According to each rheological property of HA/gelatin/GO composite group, the range for appropriate printing was considered and optimized to maximize the printability of HA/gelatin/GO composites (Figure. 2).

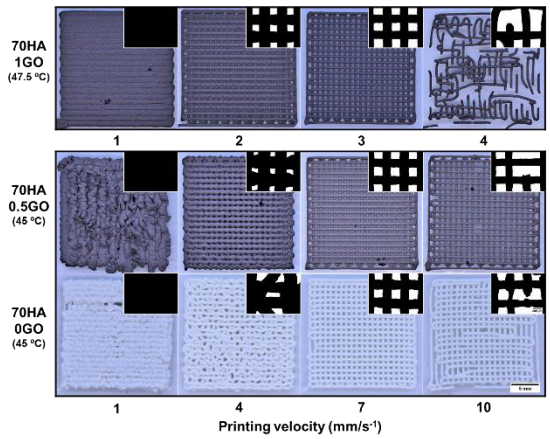
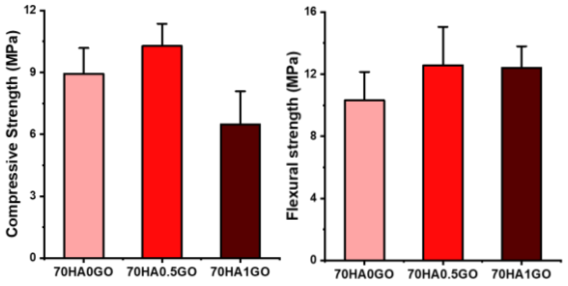


Figure. 2. Printability assessment of HA/gelatin/GO composites under different printing parameters.



(a) (b)

Figure. 3. (a) Compressive strength and (b) Flexural strength of the 3D printed HA/gelatin/GO composite scaffolds.

Figure. 3 demonstrates the reinforcement effect of GO on the 3D printed HA/gelatin/GO composite scaffolds. Specifically, the addition of 0.5% GO shows the highest compressive strength (10.28 ± 1.08 MPa) and flexural strength (12.58 ± 2.47 MPa) compared to that of 0% GO (compressive strength: 8.94 ±1.24 MPa, flexural strength: 10.31 ± 1.84 MPa)

Acknowledgements

This research was supported by Basic Science Research Program through the National Research Foundation of Korea (NRF) funded by the Ministry of Education (NRF- 2021R1I1A3040459).

References

1. Lee, H., Yoo, J.M. and Nam, S.Y., 2021. Additive Fabrication and Characterization of Biomimetic Composite Bone Scaffolds with High Hydroxyapatite Content. Gels, 7(3), p.100.

2. Yang, K., Feng, L., Hong, H., Cai, W. and Liu, Z., 2013. Preparation and functionalization of graphene nanocomposites for biomedical applications. Nature protocols, 8(12), pp.2392-2403.

P-019

탄소 양자점 기반의 암세포 이미징

성제훈[1], 김준서[1], 정윤경[1*]

인제대학교 의용공학부 & 나노융합공학부[1]

Cancer Cell Imaging based on Carbon Quantum Dots

Je Hun Sung[1], Jun Seo Kim[1], Yun Kyung Jung[1*]

School of Biomedical Engineering & Department of Nanoscience and Engineering, Inje University, Republic of Korea

*ykjung9@inje.ac.kr

Abstract

Carbon quantum dots (CQDs) are highly photoluminescent nanomaterials used as biosensors due to their low toxicity, good biocompatibility, and stable optical properties. In this study, we developed anti-EGFR antibody-functionalized CQDs which can specifically bind to epidermal growth factor receptor (EGFR) overexpressed on the surface of human cervical cancer cells (HeLa). We successfully demonstrated the specific cancer cell imaging by anti-EGFR antibody-functionalized CQDs by confocal fluorescence microscopy. Since CQDs exhibits low toxicity, anti-EGFR antibody-modified CQDs developed in this work can be utilized as a biocompatible nanoprobe to detect cancer cells.

1. 연구 배경

암은 세포주기 조절이 되지 않아 세포 분열이 끊임없이 진행되는 질병으로 모든 조직에서 발병 가능성이 존재한다. 암이 진행될 경우 암세포의 전이가 발생하여 사망률이 증가하며, 암이 초기에 검출될 경우 생존율이 현격히 증가한다.

Carbon quantum dots (CQDs)은 수 nm의 크기를 가진 형광을 방출하는 나노 물질로, 생체 독성이 거의 없고, 우수한 생체 적합성을 가지며 목적에 따른 표면 개질화가 가능하여 바이오메디컬 분야에서 유용하게 사용될 수 있는 물질이다 [1]. 또한 특정 파장의 빛을 조사하면 가시광선 영역에서 근적외선 영역에 이르는 빛을 방출하여 바이오센싱 분야에서 활발한 연구가 이루어지고 있다.

암세포는 다른 정상 세포에 비해 빠르고, 불규칙한 증식을 하기 때문에, 정상 세포보다 대사과정이 더 빠르게 진행된다. 암세포는 활발한 대사과정을 수행하기 위해 세포의 성장, 분열, 생존 및 사멸을 조절하는 세포막 수용체 그룹인 표피 성장 인자 수용체 (EGFR)를 과발현 한다. 본 연구에서는 암 세포 탐지 및 형광 이미징을 위해 EGFR에 특이적으로 결합하는 anti-EGFR 항체를 CQDs 표면에 수식하여 암 세포를 특이적으로 검출할 수 있도록 하였다. 암 세포 탐지를 위한 모델 세포로서 자궁경부암 세포주인 HeLa 세포를 사용하였으며, anti-EGFR 항체가 수식된 CQDs와 HeLa 세포의 배양 시 CQDs 표면의 anti-EGFR 항체와 HeLa 세포에 과발현 된 EGFR의 특이적 결합을 통한 암 세포의 형광 이미징을 평가하였다.

2. 연구 방법

실험에 사용된 CQDs 는 citric acid (CA), ethylenediamine (EDA)로 구성되었다. CQDs 는 CA, EDA 의 다양한 몰 비 (CA : EDA = 1 : 5, 1 : 6 및 1 : 7)에 따라 제조하였다 (그림 1a) [2]. 표적 리간드인 표피 성장 인자 수용체(EGFR)는 1-ethyl-3-(3-dimethylaminopropyl) (EDC) 및 N-hydroxysuccinimide (NHS) 반응을 통해 최종적인 Anti-EGFR 항체 수식된 CQDs 가 합성되었다 (**그림 1a**).

Anti-EGFR 항체-CQDs 표면의 Anti-EGFR 항체와 HeLa 세포의 EGFR의 특이적인 결합에 의한 HeLa 세포의 형광 추적 이미지는 Anti-EGFR 항체-CQDs (200 μg/mL) 용액으로 처리된 HeLa 세포 (2×10^4 cells/well)의 공 초점 현미경을 통한 세포 형광 이미지로 관찰하였다 (**그림 1b**).

200 μg/mL의 농도의 Anti-EGFR 항체-CQDs로 처리된 HeLa 세포 (7×10^3 cells/well)에 대한 세포 독성은 cell counting kit-8 (CCK-8)를 이용하여 평가되었다.

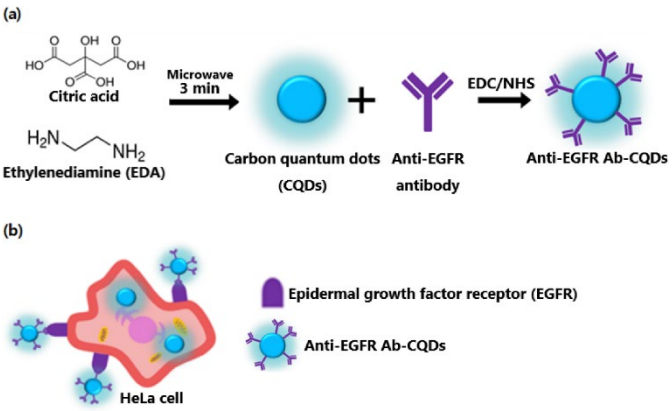


그림 1. (a) Anti-EGFR 항체로 기능화된 CQDs 합성 과정 및 (b) Anti-EGFR 항체-CQDs 기반 HeLa 세포 탐지 및 형광 이미징의 개략도

3. 연구 결과

제조된 CQDs는 분광광도계의 흡광도 측정을 통해 광학적 특성을 분석하였다 (**그림 2**). 그 결과, 250 nm에서 숄더 피크, 350 nm에서의 흡수 피크 강도를 관찰할 수 있었다 (**그림 2a**). 또한, CQDs에 350 nm 여기(excitation) 시 약 460 nm에서 최대 형광 방출(emission) 피크를 보였다 (**그림 2b**). CQDs에 조사하는 여기 파장을 300 – 370 nm 범위로 10 nm씩 변화시켰을 시, 형광 방출 피크가 변하지 않아 CQDs가 여기 파장에 대한 독립적인 방출 거동을 보이는 것을 확인하였다.

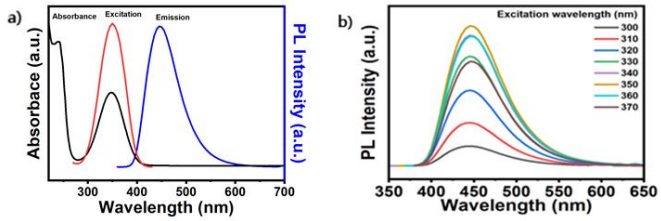


그림 2. (a) CQDs의 흡수(적색 선), 여기(녹색 선), 방출(청색 선) 스펙트럼 및 (b) CQDs의 여기 파장 독립적 형광 방출 스펙트럼

HeLa 세포의 형광 추적은 공 초점 현미경을 통한 Anti-EGFR 항체-CQDs와의 반응을 통해 관찰하였다. 250 μg/mL 농도의 Anti-EGFR 항체-CQDs를 처리한 HeLa 세포에서 푸른색의 강한 형광 신호를 관찰할 수 있었으며, 이는 CQDs 표면의 Anti-EGFR 항체와 HeLa 세포의 표피 성장 인자 수용체(EGFR)가 결합하여 CQDs가 HeLa 세포 내부로 내재화되었음을 알 수 있었다 (**그림 3a**). 반면, 아무것도 수식되지 않은 CQDs를 처리한 HeLa 세포에서는 매우 약한 형광 신호만 관찰되었으며 이는 Anti-EGFR 항체로 수식되지 않은 CQDs는 세포에 거의 결합되지 않았음을 보여주는 것이다 (**그림 3b**). 따라서, Anti-EGFR 항체-CQDs를 사용하여 암 세포의 형광 탐지가 가능함을 확인하였다.

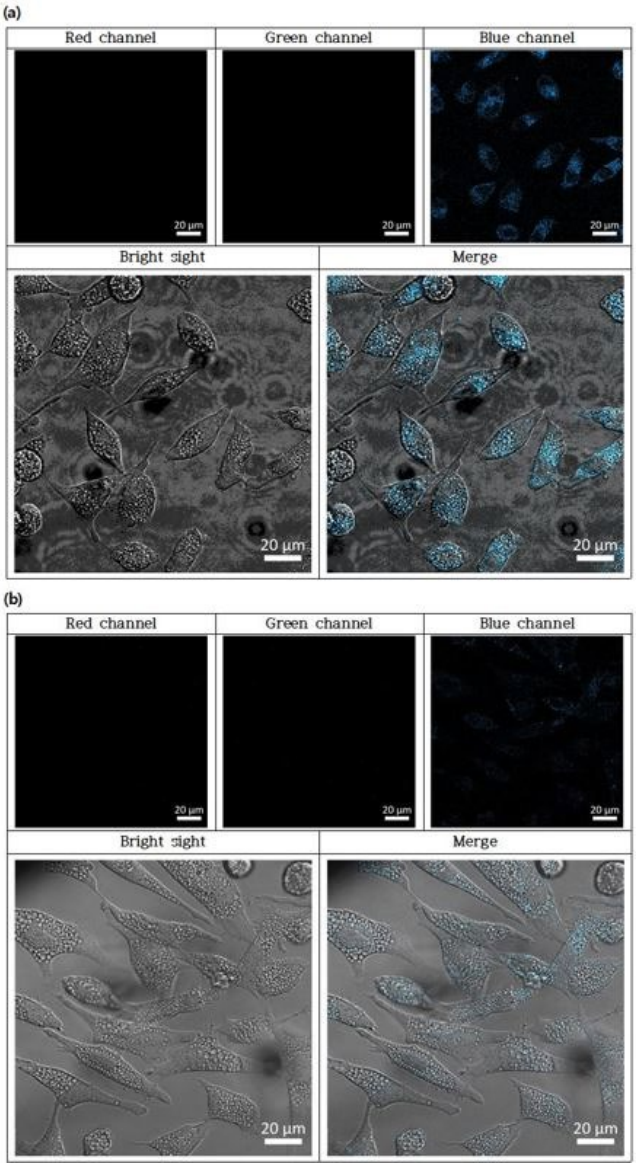


그림 3. (a) 250 μg/ml 농도의 Anti-EGFR 항체-CQDs 및 (b) 항체를 수식하지 않은 CQDs를 처리한 HeLa 세포의 이미지

제작된 Anti-EGFR 항체-CQDs의 HeLa 세포에 대한 세포 독성은 CCK-8 분석을 통해 평가되었다 (**그림 4**). Anti-EGFR 항체-CQDs를 상이한 농도 (0 – 500 μg/mL)로 HeLa 세포에 처리하고 24시간 뒤의 세포생존율을 확인하였다. 모든 농도에서 HeLa 세포는 90% 이상의 높은 생존율을 보였다. 이를 통해, Anti-EGFR 항체-CQDs는 낮은 세포 독성으로 암 세포의 탐지 및 형광 이미징을 위한 바이오센서로 활용될 수 있음을 입증하였다.

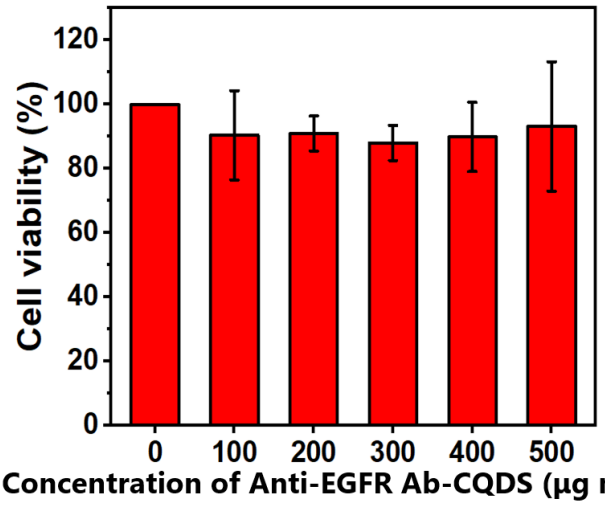


그림 4. 상이한 농도의 Anti-EGFR 항체-CQDs로 처리된 HeLa 세포(7 X 10^3 cells/well)의 세포생존율 그래프

4. 참고 문헌

[1] Yang, Zhi, et al. "Nitrogen-doped, carbon-rich, highly photoluminescent carbon dots from ammonium citrate." *Nanoscale* 6.3 (2014): 1890-1895.

[2] Wang, Duo, et al. "A highly selective and sensitive fluorescence detection method of glyphosate based on an immune reaction strategy of carbon dot labeled antibody and antigen magnetic beads." *Journal of agricultural and food chemistry* 64.30 (2016): 6042-6050.

P-020

Printing continuous collagen gel at body fluid temperature in every 5 minutes

H. J. Lim* and D.H. Hong*

Department of Electrical, Electronic, and Computer Engineering, University of Ulsan, Ulsan, Republic of Korea

* These two authors equally contributed.

bbdbbdbbd97@gmail.com

damhi1106@naver.com

Abstract

Hydrogels mixed with collagen and alginate are frequently used in bio-ink of three-dimensional bio-printer. This study investigated the optimized gelating condition of collagen only without alginate. To verify newly created hydrogel support, we made printing patterns and checked that printing patterns. Finally, the most ideal form is the composite hydrogel that has undergone pre-heating for 15 minutes at room temperature (26℃) and 15 minutes in the refrigerator (4℃), and then post-heating for 10 minutes in an oven (40℃).

Background

Damaged organs are difficult to return to their original state. In this case, many patients receive organ transplants, but the procedure for organ transplants is complicated. In addition, organ transplantation has disadvantages such as having to wait for organ donation without promise, genetic conditions between the recipient and the donor, and various side effects including secondary infection.

"3D Bio Printing" has a plan to solve various problems with organ transplantation. It takes less time than waiting for organ donation because we culture and print cells that make up the body. In addition, there is no need to determine the biocompatibility of organ donors and it can be customized for patients due to the nature of printing.

"Bio Ink" is the core of 3D Bio Printing. The bio ink studied up to date is a complex hydrogel support in which alginate is combined with collagen. Alginate has the advantage of reducing the time for collagen to gel, but there is a risk of cytotoxicity. In view of this, instead of using alginate, we use a property of collagen that is sensitive to temperature. We make a hydrogel support that is gelled with only pure collagen and have made that the temperature and time is to be changed.

Methods

2.1 Test of appropriate Gel.

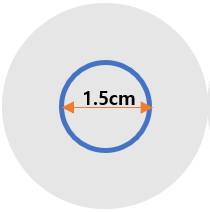


Figure 1

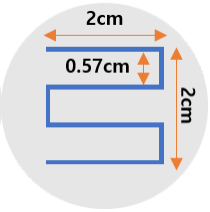


Figure 2

Figure1. Curve pattern sheet that we made

Figure2. Straight line pattern sheet that we made

We constructed a circular curved pattern with a thickness of 0.8 mm and a diameter of 20 mm and 15 mm. (figure 1) In addition, a straight line with a thickness of 0.8 mm was composed of a straight pattern with a width of 20 mm, a length of 20 mm, and a width of 5.7 mm.(figure 2)

After the observation of post heating is completed, using a micropipette, add 2 ml of D.I water along the wall surface of the 35mm cell culture dish. If the form of the composite hydrogel drawn along the pattern was maintained in 2ml of D.I. water, we judged that to be an appropriate gel.

2.2 Materials

We added 100 ㎕ of 10X PBS and 100 ㎕ of Collagen (type I) to 1ml microfuge tubes and mixed them using a vortexmixer, and then we added 0.5M NaOH 16 ㎕ and mixed again using a vortexmixer. We prepared a

collagen protocol by adding 784 $\mu\ell$ of Wilton's edible coloring red water (by Wilton) and then mixing.

2.3 Printing method of composite hydrogel

Put collagen protocol in 1 ml of syringe prepared by putting it in the freezer, connect the nozzle and 0.8 mm of glass pipet and install it on the syringe pump. Set at a speed of 0.1 rate. Place the pattern sheets under the 35mm cell culture dish and print the collagen protocol along the pattern.

2.4 Experiments of composite hydrogel

	Pre-heating[min]	Post-heating[min]
I	none	In oven 10
II	In oven 10	
III	In room temperature 10	
IV	In refrigerator 10	
V	In room temperature 10 + In refrigerator 10	

Table1. The experiments order

In Experiments I, we observed the pattern results that one in Pre-heating for 0 minutes, post-heat in the oven for 10 minutes. After then In Experiments II, Experiments III, Experiments IV, and Experiments V, post-heating proceeds equally in an oven for 10 minutes, and each experiment is performed again after making a change in pre-heating time. The pre-heating process that made the change is as follows. Experiments II was pre-heated in an oven for 10 minutes, Experiment III at room temperature for 10 minutes, Experiment IV at refrigerator for 10 minutes, and Experiment V at room temperature for 10 minutes and in the refrigerator.

Results and Discussion

3.1 Results

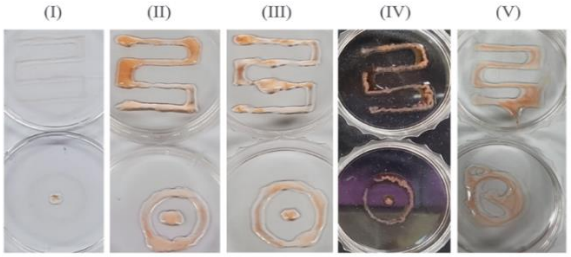


Figure3. Pictures of Experiments I, Experiments II, Experiments III, Experiments IV and Experiments V

In Experiments I, the results of gel with a faint form were observed. In Experiment II, the gelation inside the nozzle was fast, so a partially lumped collagen gel was observed. In Experiment III, a collagen gel made of short pieces was confirmed. In Experiment IV, a winding collagen gel was observed. In Experiment V, the form of continuous collagen gel was observed.

3.2 Conclusion and Discussion

After 10 minutes at room temperature (26°C) then 10 minutes at refrigerator (4°C) (pre-heating process), a composite hydrogel after 15 minutes at oven (40°C) (post-heating process) was most continuously output.

If the composite hydrogel produced in this study can be produced in 3D, the role of collagen as an artificial organ can be expected. However, since there is a discontinuous strand of the composite hydrogel, and the hydrogel strand is not a neat straight line, the task for this part must be preceded. In addition, manual 3D printing, which draws along the pattern while holding the nozzle by hand, causes problems such as inconsistency with the planned pattern due to the operator's hand shaking. Therefore, research on automatic printing using a machine should be conducted for a certain output.

Acknowledgements

This work was supported by the Ministry of Science and ICT, Republic of Korea (NRF-2020R1F1A1075779) and by the Practical technology development medical microrobot Program (R&D Center for Practical Medical Microrobot Platform, HI19C0642) funded by the Ministry of Health and Welfare (MOHW, Republic of Korea) and the Korea Health Industry Development Institute (KHIDI, Republic of Korea).

References

1. Skardal A, Devarasetty M, Kang HW, Mead I, Bishop C, Shupe T, et al. “A hydrogel bioink toolkit for mimicking native tissue biochemical and mechanical properties in bioprinted tissue constructs”, Acta biomaterialia, 25 24-34, 2015

P-021

Comparison of Prosthetic Ankle type in Bilateral Transtibial Amputee: Micropocessor vs Conventional

Jong Hu Jeon[1], Hee Seung Yang[1], Eui Jin Ahn[1], Woo Sob Sim[2], Dong Young Ahn[2], Jin Yang Kim[2], Seul Bin Na Lee[2], Min Jo[2], Min Hee Cho[2] and Pyoung hwa Choi[2]

[1]Department of Rehabilitation Medicine, Veterans Health Service Medical Center, Seoul, Korea

[2]Center of Prosthetics and Orthotics, Veterans Health Service Medical Center, Seoul, Korea

yang7310@naver.com

Abstract

Prosthetic ankles aim to mimic physiological ankle mobility to enhance ambulation in various environments. A microprocessor-controlled prosthetic ankle (MPA) shows advantages compared to a conventional prosthetic ankle (CPA), and its commercialization has started. Bilateral amputees compared to unilateral amputees have disadvantages in ambulation, as they lack the support of a healthy leg. We present the case of a bilateral transtibial amputee, wherein we compared the first MPA made in South Korea to a CPA by gait analysis.

Introduction

Though the development of medical technology and prolonged lifespan, the frequency of loss of the lower extremities is gradually increasing due to complications of diabetes, peripheral vascular disease, and other chronic diseases [1-2]. From 2005 to 2050, prevalence of amputation is expected to be more than double [3]. The prosthetic ankle replaces the ankle joint function of the amputee. It is divided into structure and function (SACH, single axis, energy storage, etc.) [4]. In addition, there is a MPA that detects the user's motion to provide joint angle control and fixation. However, microprocessor-controlled prosthetic foot is not widely used due to its dependence on a small number of products, low walking assistance ability, high weight and price. Therefore, new MPA has been developed in South Korea. It detects gait cycle by using the sensors (IMU and pressure) and then actively assists the gait through the motor when push-off motion. In this study, we compared cases of applying conventional prosthetic ankle (CPA) to patients with bilateral transtibial amputees with microprocessor-controlled prosthetic ankle (MPA) developed in Republic of Korea, and examined the advantages through gait analysis and subjective satisfaction of patients.

Methods

A 70-year-old man presented with bilateral transtibial amputations secondary to trauma from a Vietnam War landmines. The individual was otherwise in a good physical condition, and his functional K-level was 3. Radiological examination revealed that his right leg had been amputated 9.9 cm below the tibial plateau and his left leg was amputated 7.5 cm below the tibial plateau. Both stump shapes were cylindrical. He had a 10° flexion contracture of the left limb due to an old distal femur fracture deformity. The socket had a total-surface-bearing design that used a silicon liner with a pin and shuttle locking suspension, and a CPA (Vari-Flex®, Ossur, Iceland) was provided. Both sides have been wearing the same prosthetic feet. The subject wore a MPA (RoFT®, HUGO dynamics, South Korea) for 4 weeks. We performed gait analysis on wearing CPA and MPA after 4 weeks. The patients were instructed to walk at a self-selected pace along a 10-m walkway. Spatiotemporal, kinematic, and kinetic data of the lower limbs (Table 1 & Figure 1) were obtained through gait analysis (Motion analysis Corp.®, Santa Rosa, USA).

Table 1. Gait parameters of CPA and MPA

	CPA		MPA	
	Right	Left	Right	Left
Temporal-spatial data				
Forward velocity (m/s)	63.8±2.91		57.3±4.37	
Step legth (cm)	45.72±3.17	43.91±3.30	41.71±3.61	44.96±2.56
Cadence (step/min)	85.07±1.92	85.83±1.80	78.79±3.18	79.11±3.55
Step width (cm)	28.31±1.03		28.08±0.99	
Stance time (%)	70.58±1.51	68.13±2.45	69.95±1.80	62.09±1.79
Swing time (%)	29.42±1.51	31.87±2.45	30.05±1.80	37.91±1.76
Initial double support time (%)	21.43±1.45	16.81±0.91	16.83±1.51	15.26±1.59
Single support ime (%gait cycle)	31.87±2.45	29.42±1.51	37.91±1.76	30.05±1.80
Kinematic data				
Stance-phase ankle plantar/dorsiflexionROM (°)	19.19±0.93	17.15±0.72	23.30±1.11	19.86±1.51
Stance-phase knee flexion (°)	10.82±2.50	-	15.62±4.06	-
Kinetic data				
First peak vertical GRF (BW)	0.95±0.03	1.09±0.02	-	1.02±0.05
Second peak vertical GRF (BW)	0.95±0.03	0.95±0.02	-	0.95±0.01
Peak acceleration GRF (BW)	0.12±0.01	0.19±0.02	0.14±0.04	0.21±0.02
Peak deceleration GRF (BW)	-0.19±0.01	-0.12±0.02	-0.30±0.05	-0.12±0.03
Peak ankle plantarflexion moment (Nm/Kg)	1.09±0.12	0.90±0.08	0.91±0.09	0.58±0.17
Peak positive ankle power (W/kg)	0.67±0.12	0.21±0.05	0.45±0.10	0.25±0.21
Peak negative ankle power (W/kg)	-1.07±0.05	-1.08±0.12	-0.71±0.17	-0.64±0.16
Second peak positive hip power (W/Kg)	0.30±0.11	0.73±0.27	0.37±0.13	0.90±0.30

** Values are presented as mean ± Standard deviation

Results and Discussion

The spatiotemporal parameters of both sides showed increased swing time and decreased stance time. Likewise, single support time increased, whereas double support time decreased. Among the kinematic parameters, both ankle plantar/dorsiflexion range of motion (ROM) and right knee flexion increased (Figure 1. a&b) in the stance phase. Moreover, the negative ankle power increased in the early stance phase bilaterally (Figure 1. c). Increasing stability was observed as single time and swing time increased. Although ankle force did not increase, knee and ankle ROM in the stance phase increased. Further questionnaire based investigations on satisfaction, mobility, and pain revealed excellent results (Figure 2).

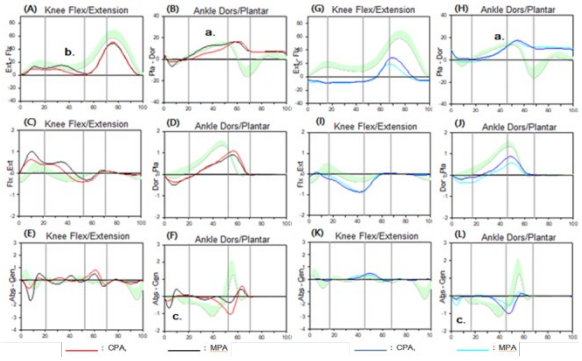
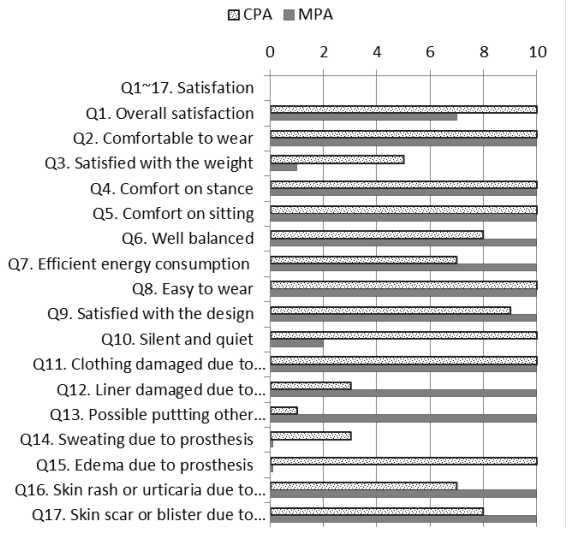
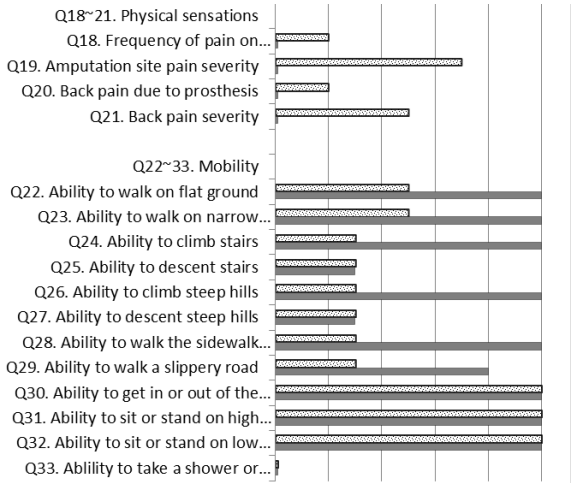


Figure 1. Knee and ankle angle of range-of-motion, Knee flexion/extension and ankle dorsiflexion/plantarflexion moment (N·m/Kg), Knee and ankle power (W/kg) during the gait cycle





** Q1~17 & Q22~33 Greater mean indicates more satisfaction
*** Q18~21 Lesser mean indicates more satisfaction

Figure 2. Questionnaires for MPA and CPA

Conclusion

MPA proved helpful for knee and ankle mobility in the bilateral transtibial amputee gait, and patient satisfaction showed good results. Thorough understanding of each prosthesis allows the prescription of a proper device considering the patient's characteristics. We present the first case of applying an MPA developed in South Korea to patients with a rare case of bilateral transtibial amputation.

References

1. You chul, Kim, Jong rak Choi, and Oh hun Kwon., "A Study of Amputee Rehabilitation in Korea." New Medical Journal, Vol. 33, No. 4, 1990
2. Dillingham, Timothy R., Liliana E. Pezzin, and Ellen J. MacKenzie., "Limb amputation and limb deficiency: epidemiology and recent trends in the United States." Southern medical journal, Vol. 95, No. 8, 2002
3. Ziegler-Graham, K., MacKenzie, E. J., Ephraim, P. L., Travison, T. G., and Brookmeyer, R. "Estimating the prevalence of limb loss in the United States: 2005 to 2050." Archives of physical medicine and rehabilitation, Vol. 89, No. 3. 2008
4. Fey, Nicholas P., Glenn K. Klute, and Richard R. Neptune. "The influence of energy storage and return foot stiffness on walking mechanics and muscle activity in below-knee amputees." Clinical Biomechanics, Vol. 26, No. 10, 2011

An Analysis of Bone Conduction Hearing Aids for Speech Transmission Intelligibility Optimization by Finite Element Analysis

D.Y. Kim*, H.L. Kang*, Y.H. Choi*, H.I. Koh*, S.D. Na**, and M.N. Kim***

*Department of Medical & Biological Engineering, Graduate School, Kyungpook National University

** Department of Biomedical Engineering, Kyungpook National University Hospital

*** Department of Biomedical Engineering, School of Medicine, Kyungpook National University

kimmn@knu.ac.kr

Abstract

Recently, a study on the rehabilitation of hearing loss on the actuator of a bone conduction hearing aid is in progress. The bone conduction actuator is preferred a simple structure, an ear canal insertion type actuator using a piezoelectric body and to vibrate a non-surgical way. In this paper, a finite element analysis (FEA) method for the output characteristics according to the structural change of the ear canal insertion-type bone conduction piezoelectric actuator is proposed. The correlation with resonance was demonstrated by applying a virtual spring constant value. The proposed method analyzed the frequency characteristics due to the adjustment of the spring constant of the elastic body based on FEA. As a result of the experiment, it was confirmed that the resonance frequency can be adjusted to a specific band.

Background

Recently, according to various types and symptoms of hearing loss, the discomfort of patients with hearing loss is increasing. Various rehabilitation methods are recommended according to the type and symptoms of such hearing loss. Hearing aids are recommended during rehabilitation, and bone conduction hearing aids are typically used. Bone conduction hearing aids compensate for a specific frequency loss by using the actuator of the hearing aid. Hearing aids are divided into electromagnetic type and piezoelectric type actuator according to the driving method. In addition, the positional approach is divided into attachment to the mastoid and insertion into the ear canal. Recently, bone conduction actuator has a simple structure, and ear canal insertion type actuator using piezoelectric body in a non-surgical way has been studied [1]. The ear canal insertion type piezoelectric actuator can change the output characteristics of the actuator due to structural changes. Therefore, compensation for the frequency loss is required using the output characteristics of ear canal insertion type piezoelectric actuator. In this paper, the FEA method for the characteristics according to the structural change of the ear canal insertion-type bone conduction piezoelectric actuator is proposed. The proposed method attempts to compensate for the lost frequency by inserting an elastic body into the actuator to form the resonance band of a specific frequency.

Methods

A bridge-structured piezoelectric actuator that can stimulate the temporal bone when the actuator is inserted into the limited space of the ear canal was used [2]. The role of the bridge structure is to convert the vibration direction of the piezoelectric body from a vertical direction to a horizontal direction.

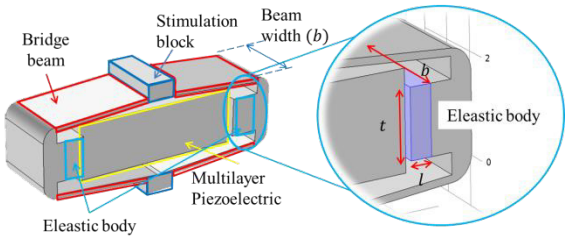


Fig. 1. Proposed actuator with elastic body

Fig. 1 shows the piezoelectric actuator of the proposed bridge structure. Here, the resonance frequency of the piezoelectric actuator is considered in order to stimulate the outer wall of the ear canal.

The resonance is one that can derive sufficient efficiency even with a relatively small input. The resonance frequency can improve the vibration transmission efficiency when the natural frequency and an excitation frequency meet. In order to control the resonance frequency, an experiment was conducted by inserting the elastic body between the piezoelectric body and the structure. Insertion of the elastic body into the actuator is one of the factors determining the mechanical resonance frequency of the actuator by the spring constant value of the elastic body. Eq. 1 and 2 are equation for spring constant and resonance frequency.

$$k = \frac{A}{l}E \tag{1}$$

$$\omega_n = \sqrt{\frac{k}{m}} \tag{2}$$

Here, k is the spring constant, A is the cross-sectional area, l is the thickness, E is the elastic modulus, ω_n is the resonance frequency, and m is the mass. The cross-sectional area A is expressed as the product of the width b and the height t in Fig. 1. Eq. 1 is an equation to obtain the spring constant of the elastic body. Here, the spring constant is proportional to the cross-sectional area and Young's modulus, and inversely proportional to the thickness. Eq. 2 is a natural frequency equation. Here, the natural frequency is proportional to the spring constant and inversely proportional to the mass. In this way, the resonance frequency of the actuator is determined based on the calculation of the mass and the applied spring constant of the actuator. Therefore, it is possible to compensate for the loss of a specific frequency by adjusting the elastic body for patients in need of bone conduction hearing aid.

Results and Discussion

The spring constant values used in the FEA were applied to 0, 100, 1000, and 10000 N/m. Fig. 2 shows the output characteristics of the actuator to which different spring constants of the elastic body are inserted. Here, the resonance frequencies of 0 to 10000 N/m are 1.45, 1.467, 1.483, and 1.628 kHz. As shown in Fig. 2, it can be confirmed that the insertion of the elastic body and the change in the spring constant value of the elastic body are proportional to the resonance frequency. In this paper, the FEA method for the characteristics according to the structural change of the piezoelectric actuator inserted into the ear canal is proposed.

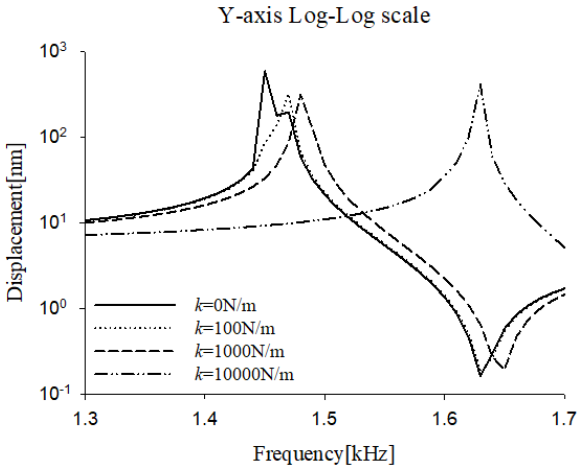


Fig. 2. Result of FEA, 1.3 to 1.7 kHz zoom

The elastic body was inserted as a structural change, and the characteristics were analyzed by adjusting the spring constant value, which is a variable of the elastic body. As a result, it was confirmed that the spring constant affects the output as shown in Eq. 1 and 2. Therefore, it was confirmed that it is possible to compensate for the frequency loss band. In addition, the resonant frequency of the actuator is determined by electrical equivalent circuit modeling. Electrical equivalent circuit modeling consists of R, L, and C, and there are two states: series resonance and parallel resonance. The negative resonance after 1.6 kHz is the anti-resonant frequency, and is generated by parallel connection of the RLC circuit. It is expected that it can be used in fields other than the hearing aid actuator based on this experiment in the future.

Acknowledgements

This study was supported by the National Research Foundation of Korea (NRF) grant funded by the Korea government (MSIP) (No. 2017M3A9E2065284, 2019R1C1C1009013).

References

[1] D.Y. Kim, S.D. Na, K.W. Sung, and M.N. Kim, “Ear Canal Insertion-Type Piezoelectric Bone Conduction Actuator Of Bridge Structure,” *Journal of Mechanics in Medicine and Biology*, Vol. 20, No. 10, pp. 1-11, 2020.

[2] S. Stenfelt, “Model Predictions for Bone Conduction Perception in the Human,” *Hearing Research*, Vol. 340, pp. 135-143, 2016.

Predicting Thermal Sensation of Passenger in Subway Using A Smart Facial Mask

Seong Eun Yoon[1], Md Hasib Fakir[2], Proma Dutta[3], Jung Kyung Kim[4]

[1]Mechanical Engineering, Graduate School, Kookmin University, Seoul 02707, Republic of Korea

[2, 3]Department of Integrative Biomedical Science and Engineering, Graduate School, Kookmin University, Seoul 02707, Republic of Korea

[4]School of Mechanical Engineering, Kookmin University, Seoul 02707, Republic of Korea

jkkim@kookmin.ac.kr

Abstract

A thermal-sensation model for prediction of individuals by assembling sensors into a face mask is developed in this study. Personal micro-climate is controlled through the current developed model. Thermal sensation factors such as skin temperature, exhaled breath temperature and heart rate are monitored by incorporating wearable sensors in to the face mask. A random forest classification model was also build for each participant to calculate the accuracy of our modeling. This paper represents a noninvasive procedure of measuring the physiological data to predict personal thermal sensation model that can be an aid to the comfort level of indoor surroundings. This setup also be used for observing and recording other health data like respiration rate etc.

Background

Almost Ninety percent of the people stays in indoor environment for having a comfortable zone. This behavior is even more reinforced these days due to COVID-19 outbreak. The existing HVAC system is always trying to achieve individual thermal satisfaction in a space as each person is subjective to ambient condition and at local level it is not possible to centralize the system for temperature control [1]. Development of personalized thermal-sensation model can be a help in this aspect [2]. core body temperature has direct correlation with Thermal comfort. The Core temperature can be measured by nonintrusive means using NIR imaging technique. Piacentini et al. [3] found that for asthmatic patients, exhaled breath temperature (EBT) can be a biomarker. These studies denote that skin temperature and heart rate are useful terms for thermal sensation. Specially use of EBT in Thermal comfort modelling has the highest popularity in current literature.

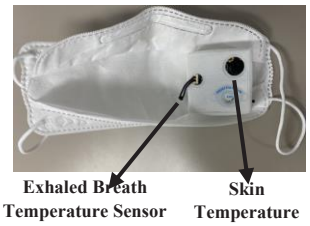
Due to the COVID-19 situation, especially in Korea, most of the people (asymptomatic and symptomatic) are wearing masks despite their controversial preventative efficacy. Researchers are working to add some improvement in the functionality of mask through the incorporation of electronic and biochemical sensors to monitor individual health condition as mask has become the new normal in the present world.

Methods

The whole experiment was conducted with 20 healthy participants among them everyone was male including 9 foreigners and 11 Korean personal. The data were collected from three sessions of experiment for each participant with around 80 minutes per session in the Subway station where the route was from the Gierum to the Sadang Station on Line no.4 of Seoul Subway, South Korea.

The smart Face mask Device was controlled by Arduino Nano BLE where infrared temperature sensor MLX90614 measured the skin temperature of the subject on the cheek, and the exhaled breath temperature(EBT) inside the mask was measured using thermistor NXFT15XH103FA2B130(a negative temperature coefficient sensor with a resistance of 10K ohm at 25°C) in Fig 1. Participants also gave their Thermal Sensation preference by voting every 5 minutes on a 7-point scale according to ASHREA through a smartphone application called “Smart Face Mask” which was also developed by us. It was developed through MIT App Inventor provided by Google and managed by MIT to monitor different physiological parameters in real time. In addition, the subject's thermal sensation votes were collected every 5 minutes and the data was set up to be stored as CSV files along with other physiological data, which connects to Android Bluetooth and Arduino nano 33 BLE's Bluetooth module. Android 5+ devices can run this app.

(a)



(b)

3	Hot
2	Warm
1	Slightly Warm
0	Neutral
-1	Slightly cool
-2	Cool
-3	Cold

Fig 1. Smart face mask with embedded physiological sensors: (a) inside view of the mask showing the physiological sensors and (b) thermal-sensation scale to receive the vote.

The recorded per second data were organized into per minute average values and analyzed. Spearman's rank correlation coefficients were calculated for each data set to determine their correlation with thermal sensation. The normality of the data was analyzed through Shapiro–Wilk tests. Significant differences among the mean values of the TSV were identified by Kruskal–Wallis tests.

Results and Discussion

The importance and accuracy of each measurement for personal thermal sensation prediction were determined using the random forest classifier machine learning model used for thermal sensing prediction. Several decision trees were generated for random selection of different input features to predict for every tree. Final class prediction was taken from the voting majority. This bagging method improved the model's reliability for new data by reducing variance.

A useful innovation can be achieved by adjusting the current face mask device for the monitoring of respiratory rate. This study shows a Predictive Model for Personal Thermal Sensation considering EBT, skin temperature, heart rate etc. physiological parameters which were collected through a Smart face mask. The novel contribution to this field was using EBT as predictive factor for thermal comfort.

This study mainly focused on the individual health parameters for prediction which were almost neglected by the other current population model based studies. The overall accuracy average was 77% in Fig 2 for predicting Thermal Sensation with our Smart Face Mask.

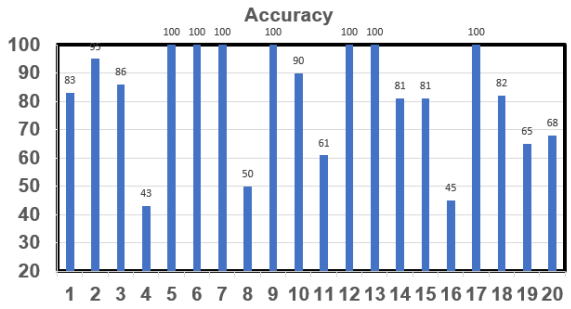


Fig 2. Accuracy of the individual prediction model with various combinations of predictive features.

It was also noticed that, there were variations in physiological and psychological reactions of individual subjects even being in the same ambient state. The reason behind these variances might be the mental stress and activity level or the circadian rhythm of the participants. Based on various factors e.g. BMI, gender, age heart rate can be analyzed in future.

Acknowledgements

This research was supported

References

[1] A. Aryal and B. Becerik-Gerber, "Energy consequences of comfort-driven temperature setpoints in office buildings," *Energy Build.*, vol. 177, no. March 2019, pp. 33–46, 2018, doi: 10.1016/j.enbuild.2018.08.013.

[2] M. K. Shourav, J. Choi, and J. K. Kim, "Visualization of superficial vein dynamics in dorsal hand by near-infrared imaging in response to elevated local temperature," *J. Biomed. Opt.*, vol. 26, no. 02, p. 026003, 2021, doi: 10.1117/1.jbo.26.2.026003.

[3] G. L. Piacentini *et al.*, "Exhaled air temperature in asthma: methods and relationship with markers of disease," *Clin. Exp. Allergy*, vol. 37, no. 3, pp. 415–419, 2007, doi: 10.1111/j.1365-2222.2007.02663.x.

P-024

Weak closed-loop vibrational stimulation improves the associative memory in the elderly

H.W. Jin[1,2], D.Y. Son[1,3], J.H. Jeong[1,3] and K.S.Park[2,4]

[1]Interdisciplinary Program in Bioengineering, College of Engineering, Seoul National University, Seoul, 03080, South Korea

[2]Institute Medical and Biological Engineering, College of Medicine, Seoul National University, Seoul, 03080, South Korea

[3]Integrated Major in Innovative Medical Science, College of Medicine, Seoul National University, Seoul, 03080, South Korea

[4]Department of Biomedical Engineering, College of Medicine, Seoul National University, Seoul, 03080, South Korea

jinhyungwon@snu.ac.kr

Abstract

Despite of the importance of sleep, the effect of sleep is not clearly revealed yet. Various researches endeavour to figure out the method how to improve the sleep quality. In this research, unrecognizable closed-loop vibrational stimulation under the bed mattress during 90 min nap sleep was applied to the elderly to prove the effect of the vibrational stimulation on memory consolidation. To measure the effect of the vibrational stimulation, semantically related word-pair task was employed in both SHAM ans STIM condition. The result of the word-pair task shows the vibrational stimulation during sleep slightly improves memory consolidation.

Background

Sleep has an important meaning as it occupies one-third of our whole lives, yet the purpose and the effect of sleep is not clearly revealed scientifically. Some researches show sleep helps to consolidate and reform important memories [1]. Various researches endeavour to measure and estimate the quality of sleep. Many researchers are eager to find out how to improve the quality of sleep. In previous research, the depth of slow-wave sleep and declarative memory consolidation are improved when weak closed-loop vibrational stimulation is applied during sleep [2]. However one of the restriction of the experiment is the fact that the 12 participants of the experiment are all young age adults under the age of 30s. Most of the young age adults have good memory so that it was hard to testify how much the closed-loop vibration during sleep can effect on the memory consolidation. Thus the same method of the experiment was applied to the elderly during nap sleep. The purpose of this research is to measure the effect of the closed-loop vibration during sleep on memory consolidation.

Methods

Twenty elderly volunteers (mean age 56.5 ± 5.1 SD) participated in the experiments. Participants were recruited by posts on hospital bulletin boards. This cohort research was approved by Institutional Review Board (IRB) of Seoul National University Hospital. The study only included health elderly participants with no sleep-related disorders, and the age ranging from 45 to 65.

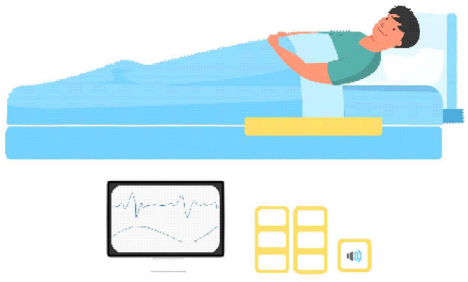


Figure 1. Schematic experiment structure.

Each participant was tested under two experimental conditions : vibration stimulation condition (STIM) and non-stimulation condition (SHAM). Vibration stimulation in unrecognizable power from under the topper of the bed mattress was applied in STIM condition during 90-min nap sleep. To define the size of the unrecognizable power of the vibration for the participants, each participant was applied to the vibration power test in the same condition of the experiment right before the nap sleep. To measure the effect of the memory consolidation, 54 semantically related Korean word-pair task was employed. Learning task right before the sleep and the test task right after nap sleep were employed in both SHAM and STIM condition to compare the effect on the memory consolidation. Also ECG and respiration were measured during the nap sleep for bio-signal analysis.

Results and Discussion

As the suggested rule of the word-pair task, the only participants who succeeded to employ the task over 60 points of 100 in the learning task. Also some outlier cases were deducted from the test result. Figure. 2 shows the result of the word-pair task in each SHAM and STIM condition.

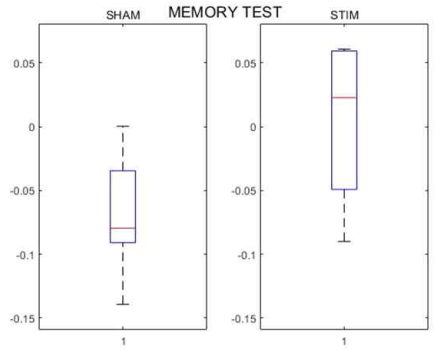


Figure.2 Memory test result in SHAM and STIM.

In SHAM condition, it showed 7%p decrease of the test score in average comparing the before and the after nap sleep. In STIM condition, it showed 2%p increase of the test score in average comparing the before and the after nap sleep. The result of the word-pair task shows the vibrational stimulation during sleep slightly improves memory consolidation.

Acknowledgements

This work was supported by the National Research Foundation of Korea (NRF) grant funded by the Korea government (MSLT) [NRF-2017R1A5A1015596]

References

1. Brendon O. Watson, and Gyorgy Buzsaki, "Sleep, Memory & Brain Rhythms", Daedalus, Vol. 144, Issue 1, 2015.
2. Sang Ho Choi, Hyun Bin Kwon, Hyung Won Jin, Heenam Yoon, Mi Hyun Lee, Yu Jin Lee, and Kwang Suk Park, "Weak closed-loop vibrational stimulation improves the depth of slow-wave sleep and declarative memory consolidation", Sleep, Vol. 44, Issue 6, 2021.

Evaluation of the effectiveness of Transcutaneous Vagus Nerve Stimulation on Parasympathetic Nervous System Activation with Heart Rate Variability

S.J Lee[1*], D.H Kang[1] , J.H Kim[1], Y.S Choi[1] and I.Y. Kim[1]

[1]Department of Biomedical Engineering, Hanyang University, Seoul, Korea

[*]seungjaelee@hanyang.ac.kr

Abstract

The tVNS, a type of electroceuticals, innervates the vagus nerve that regulates the PSNS. Recent studies on tVNS have been reported that tVNS is effective in relieving symptoms of diseases. However, each study has been reported the results using different stimulation parameters. In this study, we analyzed the HRV to evaluate the activation of PSNS, when pulse width was changed. Twenty subjects participated in the experiment. pNN20 showed statistical significance between baseline period and stimulation period when the pulse width is 1000 μs (Paired t-test; $p = 0.032$). And through one-way ANOVA between three sessions, statistical significance was showed in pNN20 ($p = 0.031$) and pNN30 ($p = 0.047$) between differences of baseline period and stimulation period. We confirmed that PSNS can be innervated with our tVNS system and that activation of PSNS is better when the pulse width is long.

Background

Electroceuticals is a compound word of electronic and pharmaceutical, and is a new method that stimulates organs, tissues, and nerve with electrical signals to produce therapeutic effects. Vagus nerve stimulation, a type of electroceuticals, stimulates the vagus nerve that regulates the parasympathetic nerve system (PSNS) [1]. Recently, several studies have been reported to be effective in alleviating symptoms of certain diseases through transcutaneous vagus nerve stimulation (tVNS), which non-invasive stimulation of auricular branch of vagus nerve (ABVN), but stimulation parameters are still different depending on the study. In this study, heart rate variability (HRV) was analyzed to evaluate the activation of PSNS when pulse width, one of the stimulation parameters, was changed.

Methods

The tVNS system was consisted of two clip electrodes and stimulator TPD-NH1 (NuEyne, Korea). Electrocardiography (ECG) signals were recorded using MP150 (BIOPAC Systems Inc., USA) to extract HRV parameters. During the experiment, the subject stared at the monitor while sitting in the right position in the chair. The monitor played a peaceful video to prevent sleepiness and to focus the subject. Figure 1 shows the experimental environment described above.

The stimulation parameters were 10 Hz frequency, 500 μs or 1000 μs pulse width, and $2 \times I_M$ mA amplitude, when I_M is minimum amplitude to detect stimulation. The waveform was biphasic symmetric square pulse.

The stimulating site of tVNS was cymba concha and stimulating site of sham stimulation is earlobe. All stimulations were applied to the left ear, since stimulating left ABVN innervates atrioventricular node, otherwise stimulating right ABVN innervates sinoatrial node [2].

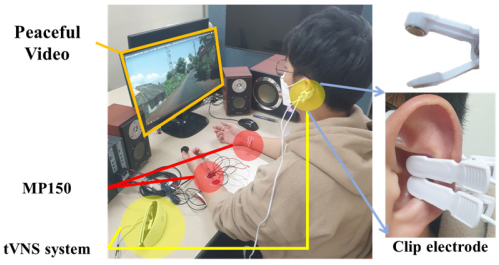


Figure 1. Experimental environment

One stimulation session consisted of three periods (baseline period, stimulation period, and recovery period), and each period is 6 minutes. The experimental protocol was divided into three sessions according to the stipulating site and pulse width. The experimental protocol and conditions of each session are described in Figure 2. The order of session was randomized to minimize the bias of order. There was a break period of 2 minutes between each session.

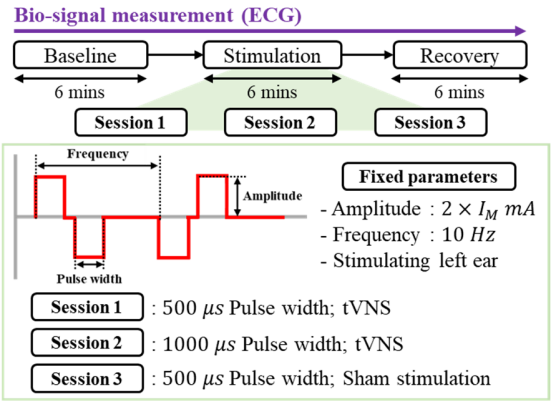


Figure 2. Experimental protocol

Results and Discussion

Subjects were recruited from healthy adult male and female in their 20s and 30s ($N = 20$; 10 Female; $Mean\ age \pm Standard\ deviation = 25.7 \pm 3.93$).

All data satisfied normality through normality test, and all statistical analysis used a parametric test (Paired t-test, One-way ANOVA).

In session 2, pNN20 showed statistical significance between baseline period and stimulation period (Paired t-test; $p = 0.032$). In session 1 and session 3, there was no HRV parameter that showed statistical significance.

Between three sessions, pNN20 showed statistical significance between differences of baseline period and stimulation period (One-way ANOVA; $p = 0.032$). Also, pNN30 showed statistical significance (One-way ANOVA; $p = 0.045$). As a post hoc analysis, Bonferroni test was performed. Between session 1 and session 2, statistical significance was showed in pNN20 ($p = 0.031$) and pNN30 ($p = 0.047$) between differences of baseline period and stimulation period.

Since the pNN20 and pNN30 are HRV parameters that indicate activation of the PSNS, our results indicates that our tVNS system and stimulation parameters can activate PSNS. Moreover, the result from the Bonferroni test for differences of baseline period and stimulation period indicates that the degree of activation of the PSNS is better at 1000 μs pulse width than the 500 μs pulse width suggested by Badran et al. (2018) [3].

Our study has various limitations, some of which are for stimulation electrodes. we used two clip electrodes for tVNS stimulation. A spring for fixing the electrode position is contained in the clip electrode. Since the spring inside, the clip electrodes would have pressed the ear from both back and forth. As a result, most subjects complained of pain caused by the clip electrodes itself. Pain is known to activate SNS. And it was possible that activation of PSNS was suppressed due to activation of SNS by pain. That is, it was possible that the effect of tVNS on the PSNS due to the pain caused by the clip electrode was not properly reflected in the HRV parameters. Another limitation of the clip electrode is that the size of the electrode was large in comparison with the stimulation site. For this reason, there is a possibility that the stimulation was not applied to the exact stimulation site. Additionally, we had a break period of 2 minutes between sessions, which may not have been enough to be called a wash-out period. In other words, the tVNS stimulation of the previous session would have affected the subsequent session. We tried to minimize this effect by randomizing the order of sessions, but there would have been an effect.

In this study, we confirmed that PSNS can be activated with our tVNS system and that activation of PSNS is better when the pulse width is long. We will conduct tVNS experiments using new electrodes to compensate for the limitations described above, and at the same time, we will build new protocols including sufficient wash-out period between sessions.

Acknowledgements

This work was supported by the National Research Foundation of Korea (NRF) grant funded by the Korea government (MSIT) (No. NRF2020R1F1A1074431).

References

1. Capilupi, Michael J., Samantha M. Kerath, and Lance B. Becker. "Vagus nerve stimulation and the cardiovascular system." Cold Spring Harbor perspectives in medicine 10.2 (2020): a034173.
2. Kaniusas, Eugenijus, et al. "Current directions in the auricular vagus nerve stimulation I–a physiological perspective." Frontiers in neuroscience 13 (2019): 854.
3. Badran, Bashar W., et al. "Short trains of transcutaneous auricular vagus nerve stimulation (taVNS) have parameter-specific effects on heart rate." Brain Stimulation 11.4 (2018): 699-708.

P-026

Automatic Classification of Voiding Dysfunction Patients Using Uroflow Curve

Jonghyeok Jeong[1,2*], Seongkeun Park[3], Jeehoon Kim[1], Dongyeon Son[1,2], Hyunbin Kwon [1], Dongseok Lee[1]
Hyungwon Jin[1,5], Sangjun Yoo[4], Hwancheol Son[4], Jinwook Choi[3,5] and Kwang Suk Park[3,5]

Interdisciplinary Program of Bioengineering, College of Engineering, Seoul National University[1]
Integrated Major in Innovative Medical Science, College of Medicine, Seoul National University[2]
Department of Biomedical Engineering, College of Medicine, Seoul National University[3]
Department of Urology, College of Medicine, Seoul Metropolitan Government - Seoul National University Boramae Medical Center[4]
Institute of Medical and Biological Engineering, Medical Research Center, Seoul National University[5]
wjdwhdtks@bmsil.snu.ac.kr

Abstract

Uroflowmetry is one of the most frequently first used tests for patients with urination discomfort. Because uroflowmetry is noninvasive, inexpensive and simple, uroflowmetry is widely used in urology. From uroflowmetry, urologists can get uroflow curves. The uroflow curves provide extremely valuable diagnostic data for voiding dysfunction. In this paper, we propose a deep learning based approach to the automatic classification for distinguishing normal people from patients who have urination discomfort by considering 805 cases of medical data, which are confirmed by three highly experienced urologists. The classification performance shows 95.6 % for accuracy and 91.3 % for Cohen's Kappa.

1. Introduction

Uroflowmetry is simple and non-invasive test to identify patients' voiding dysfunction. This test measures rate of urine flow (Q) during urination. From these uroflowmetry result, urologists obtain following parameters: void volume, maximum flow rate, voiding time, average flow rate, time to reach maximum flow rate. These parameters show patients' voiding condition. Nazeeh Alothmany et al. interpreted these parameters for accurate diagnosis [1]. The ability of interpretation of uroflow curves from uroflowmetry result is critical.

Chang et al. showed automatic classification for interpreting normal and abnormal uroflowmetry curves using grading-based approach [2]. We hypothesized that using uroflowmetry results, deep learning can be good method to distinguish normal people from patients who have voiding dysfunction. The purpose of this research is to prove that using uroflow curve ,the deep learning system can predict whether people have voiding dysfunction or not.

2. Method

In this study, uroflowmetry measurements of 805 subjects were included. The number of subjects who don't have any voiding dysfunction were 378 and the number of subjects who have voiding dysfunctions such as bladder outlet obstruction (BOO) and under active bladder (UAB) were 427.

In Uroflowmetry, all subjects drank enough water before the experiment. When subjects want to urinate, they were asked to privately urinate into a special funnel that collects the urine into a container connected to a measuring instrument. The measuring instrument measures each subject's rate of urine flow (Q). Fig. 1 shows the example of uroflowmetry result. All uroflow curves were measured up to 60 ml/sec for rate of urine flow and 200 sec for time.

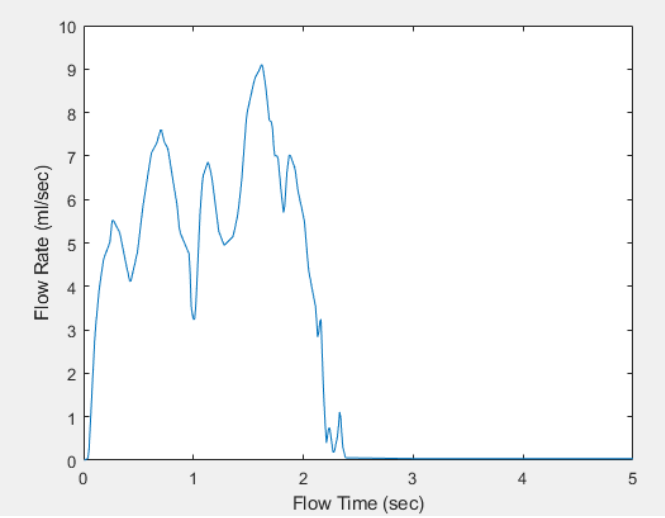


Fig. 1. Example of uroflowmetry result

Each subjects' uroflow signal was sampled to 10 Hz with cubic spline interpolation. Sampled uroflow signals were converted into 2-D images which size is 350 by 350. All uroflow images were normalized.

We used convolution neural network (CNN) as deep learning model. CNN is a good deep learning network for image classifier. Our CNN model was used as binary classifier to distinguish normal people from patients. The normalized images were used in our CNN model. The process for automatic classifier of normal people and patients is illustrated in Fig. 2. We used 644 subjects' normalized uroflow images as training data and 161 subjects' normalized uroflow images were used as test data.

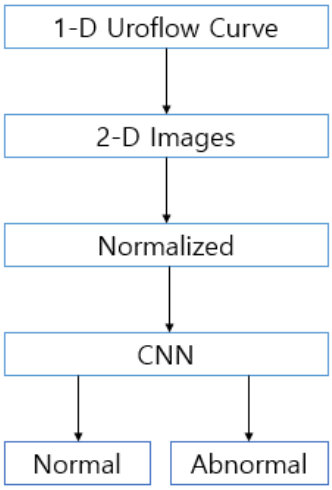


Fig. 2. Automatic Classification Process

3. Results

In Fig. 3, we show the confusion matrix for predicting normal people and patients who have voiding dysfunction. The accuracy of prediction result is 95.6 %. The sensitivity is 94.2 % and the specificity is 97.3 %. We calculated Cohen's kappa, a statistic for assessing inter-reader agreement. The Cohen's kappa is 91.3 %

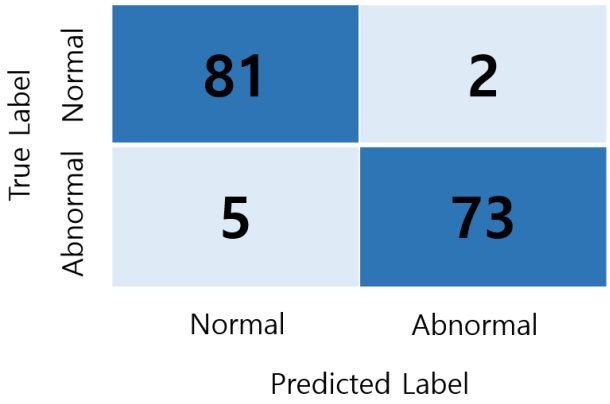


Fig. 3. Confusion Matrix of Result

4. Discussion

The aim of this study is to distinguish normal people from patients who have voiding dysfunction automatically. Based on uroflow curve, our deep learning model shows good performances of predicting normal or not. Our research shows possibility that using deep learning model is good method at interpreting uroflow curve for predicting whether people have voiding dysfunction or not.

5. Reference

[1] Alothmany, N., Mosli, H., Shokoueinejad, M., Alkashgari, R., Chiang, M., & Webster, J. G. (2018). Critical review of uroflowmetry methods. *Journal of Medical and Biological Engineering*, *38*(5), 685-696.
[2] CHANG, Y., SHEI-DEI YANG, S. T. E. P. H. E. N., CHUANG, Y., SHEN, J. H., LIN, C. C., & LI, C. E. Automatic Classification of Uroflow Patterns via the Grading-based Approach.

Exploration of reliable biomarkers of non-invasive auricular vagus nerve stimulation for healthy adults: pilot study

D.H. Kang[1*], S.J. Lee[1], J.H. Kim[1], Y.S. Choi[1] and I.Y. Kim[1]

[1]Department of Biomedical Engineering, Hanyang University, Seoul, Korea

[*]donghun2296@hanyang.ac.kr

Abstract

Transcutaneous vagus nerve stimulation (tVNS) has shown clinical effects in various diseases. The stimulus of tVNS induces the activation of the branch of the vagus nerve (VN), which relayed to the brainstem, especially the nucleus of the solitary tract (NTS) and the locus coeruleus (LC). This provides the unique entrance the way to the central nervous system (CNS). Despite the clinical effects, there has been no clearly established mechanism and biomarker of tVNS. In this study, we applied tVNS to 4 healthy men to demonstrate the potential of EEG spectral powers as a biomarker of tVNS and compare the effects of the four stimulus durations on the EEG spectral powers.

Background

tVNS has shown similar clinical effects with invasive vagus nerve stimulation (iVNS). Despite its clinical effects, there is a lack of studies that established reliable biomarkers of tVNS. Most of the afferent fibers of VN end in NTS. Through NTS and other further regions of the brainstem like LC, the CNS can be modulated using vagus nerve stimulation (VNS). That is, the brain activity is inevitably involved in the clinical mechanism of tVNS, and it is reasonable that the modulated brain activity can be analyzed with electroencephalogram (EEG) [1-2].

We hypothesize that tVNS could induce the brain modulation forward relieving hyperarousal and it could be measured by EEG spectrum analysis. In aspect of hyperarousal theory, higher frequency band EEG power will decrease, and lower frequency band EEG power will increase after tVNS. Also, we design a protocol in which the effect of stimulation duration on the EEG can be evaluated.

Methods

4 healthy young male adults (26.5±0.58) participated. They were requested not to drink any alcohol and caffeine 24 hours before the experiment. The tVNS was delivered using the stimulator TPD-NH1 (NuEyne, Korea) combined with the electrodes (tVNS technologies, Germany). The threshold intensity was first measured. While the intensity began at 0.1mA and was increased by 0.2mA, participants were asked to find the intensity as a moderately strong, but not painful sensation. The two threshold values, from the two consecutive threshold measurements, were averaged and the averaged value was selected as intensity for the following experiment. The stimulus location was cymba conchae of the left ear. The stimulation with 20 Hz inter-pulse frequency and 200 μs pulse width was delivered as a biphasic waveform.

EEG was recorded during a block (baseline, stimulation, and recovery) continuously using LX3232-RF (Raxtha, Korea). In 10-20 measuring system, F4-M1, C4-M1, O2-M1, F3-M2, C3-M2, O1-M2, Fz-Cz and Cz-Oz (active channel– reference channel) were measured. Power spectrum of two frequency bands (alpha: 8-13Hz, delta: 0.1-4Hz) were analyzed for each channel. Mean power values of frontal (F3, F4, Fz), central (C3, C4, Cz), and occipital (O3, O4) channels were calculated across all subjects. The mean value of recovery session was compared with the baseline session. Electrode connection was confirmed by jaw clenching and eye blinking. Both baseline and recovery sessions continued for 5 minutes, and four kinds of stimulation sessions (1min, 5min, 10min, and 15min) were assigned to each block in randomized order. Thus, a block consisted of baseline, stimulation, and recovery, and each participant received four blocks, which had different and randomly assigned stimulation periods (Figure 1). Participants were required to close their eyes during the experiments.

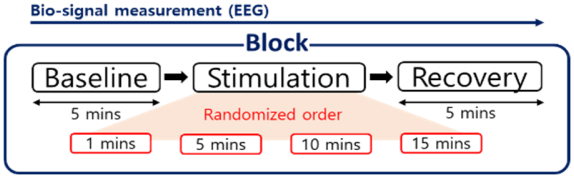


Figure 1. Experimental protocol

			Power [μV^2]											
Stimulation Period			1min			5 min			10 min			15 min		
Session			Pre	Post	Trend	Pre	Post	Trend	Pre	Post	Trend	Pre	Post	Trend
Frequency band	Alpha	Frontal	13.5	14.7	↑	13.4	14.6	↑	13.0	23.7	↑	14.5	13.5	↓
		Central	14.4	15.2	↑	14.0	14.1	↑	14.4	25.4	↑	15.2	13.5	↓
		Occipital	21.2	18.2	↓	19.8	15.3	↓	22.3	33.3	↑	23.3	19.9	↓
	Delta	Frontal	42.4	110.9	↑	39.8	79.5	↑	42.2	77.9	↑	73.3	125.3	↑
		Central	41.3	100.4	↑	58.4	85.5	↑	43.9	86.9	↑	78.6	130.9	↑
		Occipital	38.7	79.7	↑	45.1	58.1	↑	47.6	123.1	↑	95.0	151.5	↑

Table 1. Mean power values of alpha and delta frequency band for all channels, frontal channels (F3, F4, Fz), central channels (C3, C4, Cz), and occipital channels (O3, O4)

Results and Discussion

In all stimulation blocks, the mean delta powers of whole channel groups increased in recovery compared to baseline (Table 1). In 1-min block, the mean alpha powers for occipital channels decreased, and the powers for the other channel groups increased. In 5-min block, the mean alpha powers for both frontal and central channels increased, but it decreased for occipital channels. For the case of 10-min block, the mean alpha powers for whole channel groups increased. In 15-min block, the mean alpha power for the whole channel groups decreased. We could identify the attenuation of alpha power and the augmentation of delta power in power spectrum density plot (Figure 2).

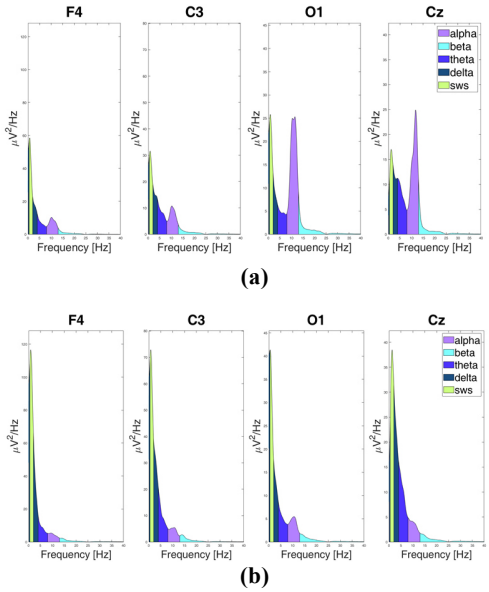


Figure 2. Power spectrum density of one subject for 4 channels (F4, C3, O1, Cz) (a) Baseline (b) Recovery

In the previous studies, after short (3.4s) tVNS, alpha oscillations were attenuated [1]. Another study observed that tVNS induced an increase in EEG delta frequency activity [2]. In this study, although, the mean delta power of whole channel groups increased after tVNS, only 15-min tVNS reduced the alpha oscillation for the whole channel groups (Figure 2). We thought of some limitations of this study. First, the number of subjects was not enough to observe a meaningful result. Second, the stimulus periods under 15 minutes were insufficient to induce a hyperarousal-relieving effect. Third, we should have needed to check the participants' state, for example, drowsy, many thoughts, or tension, to confirm that no differences of subjects' state between the baseline and recovery session existed, but the only impact of tVNS.

In conclusion, we demonstrated the attenuation of alpha oscillation and the increase of delta frequency power after 15-minutes tVNS. Thus, we found the EEG power spectrum as a biomarker of tVNS. Considering the limitations, we will modify the experimental protocol and plan a second pilot study to check the reproducibility of the results in a more controlled environment. Also, the next experiment will involve heart rate variability (HRV) analysis to check the parasympathetic effect of tVNS simultaneously as well.

Acknowledgements

This work was supported by the Technology Innovation Program (Alchemist Project, 20012461) funded By the Ministry of Trade, Industry & Energy (MOTIE, Korea)

References

1. Sharon, Omer, Firas Fahoum, and Yuval Nir. "Transcutaneous vagus nerve stimulation in humans induces pupil dilation and attenuates alpha oscillations." Journal of Neuroscience 41.2 (2021): 320-330.
2. Ricci, Lorenzo, et al. "Transcutaneous Vagus Nerve Stimulation Modulates EEG Microstates and Delta Activity in Healthy Subjects." *Brain Sciences* 10.10 (2020): 668.

P-028

Biosignal analysis from nose region for deception detection in thermal imaging

M.S. Kim[1], J.Y Kim[1], B.R Nam[2], J.K Choi[2], K.M Choi[1], S.J Choi[2] and I.Y. Kim[1,2]

[1]Department of Biomedical Engineering, Hanyang University, Seoul, Korea

[2]Department of Electronic Engineering, Hanyang University, Seoul, Korea

myeongsu1213@hanyang.ac.kr

Abstract

Deception detection system determines deception by the physiological response of the autonomic nervous system. Among them, thermal imaging for deception detection can measure in face temperature changes as physiological changes caused by fight or flight response. Previous research has discussed that the nose region is the main facial region investigated in relation to vasoconstriction and vasodilatation among regions of interest (ROI). However, there is still a lack of research to analyze biosignal features of the nose region using deception. In this paper, the temperature signal at the nose tip and the respiration signal at the nostril will be simultaneously extracted and analyzed. In addition, we propose a meaningful feature that determines whether there is deception through the temporal feature. As a result, the max, std, max-min features in the respiration signal are meaningful.

Background

When a person deception, their action and beliefs are inconsistent, resulting in cognitive dissonance. A person's physiological changes due to such cognitive dissonance cannot be hidden, so it can be measured by deception detection. Contact deception detection measures changes in blood pressure, respiration rate, and electrodermal activity [1]. However, there is a disadvantage in that movement is limited due to wearing the equipment. To compensate for this disadvantage, study have been underway on non-contact deception detection [2]. Thermal imaging can measure changes in face temperature as a result of a fight or flight response, such as changes in respiratory rate, sweat production, constriction and dilation of blood vessels, and facial micro-muscle movement. However, there are lack of research to analyze the nose region in deception [3][4]. Therefore, in this study, respiration and temperature are simultaneously analyzed through the nostrils and the nose tip in the nose region. In addition, meaningful deception indicators are identified through statistical testing from temporal characteristics that can know the overall characteristics of deception data.

Methods

Figure 1 is an experimental protocol that was advised by a criminal investigator. The deception detection protocol selects one of three cards and answers "아니오" to all seven questions. At this time, the selected cards were labeled as 'deception', the unselected cards as 'truth', and the rest as 'unrelated questions'. The research team proceeds with a deception induction experiment on 120 subjects. A FLIR T620 camera was used, and thermal images were acquired at a distance of 90cm from the subject. The equipment has 640 × 480 pixels resolution, 0.04°C thermal sensitivity, 30 frames per second, and 28-38°C temperature measurement range.



Figure 1. Experiment protocol.

Figure 2 shows the data preprocessing process. The length of the video to be analyzed was a video clip from the start of the answer to 10s after the answer. To automatically extract a region of interest (ROI) from the acquired thermal image, the Tracking API provided by OpenCV was used. The Tracking API automatically tracks the object by selected the ROI region to be tracked. Acquire time-series signals from all thermal images by averaging each frame element in the nose tip and nostril regions with the selected ROI region. So, in the end, the respiratory signal of the

nostrils and the temperature signal of the nose tip are extracted.

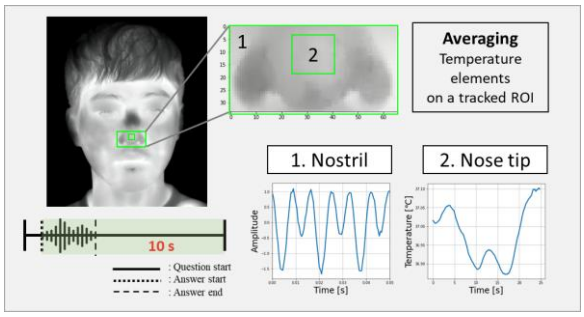


Figure 2. Data preprocessing.

The movement of the face creates noise in the signal. Signal processing was performed to remove noise. The noise was removed through a moving average filter with a window size of 30 for both the extracted respiration and temperature signals. Respiration was set to 0 by spline interpolation in order not to affect the temperature increase with time. And then, the high-frequency signal was removed by performing a fast fourier transform. In previous research [5], temporal features that can know the typical range, slope, and change of the signal were effectively utilized. In addition, peak to peak, max-min features were extracted to decide the interval between respirations. Figure 3 shows the extracted signal and temporal features.

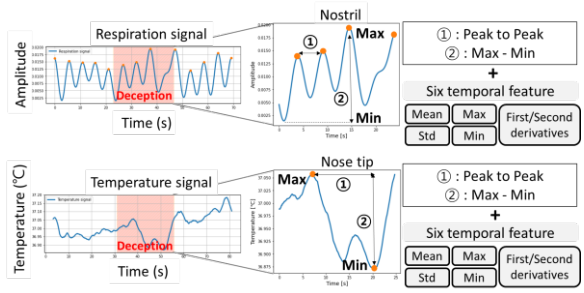


Figure 3. Extracted signal and temporal features

Results and Discussion

Table 1 shows the ranking of meaningful features using paired samples t-test, a statistical testing method. As a result, it was found to be a meaningful deception indicator (p-value <0.05) at max, std, and max-min in the respiratory signal. The temperature signal showed a different temperature type for each subject, and some subjects showed a latency response. In addition, the temporal feature in previous research [6] has a disadvantage in that temporal information is lost. In the future, we plan to analyze it with 1d class activation mapping, a deep learning algorithm that can find out which part of the deception is activated over time. Therefore, we develop an algorithm that can simultaneously analyze and visualize changed temperature and respiration over time for each ROI region to deliver information to the criminal investigator.

	Signal	Feature	Method	p-value (<0.05)
1	**Respiration**	**Max**	Paired samples t –test	**0.002**
2	**Respiration**	**Std**	Paired samples t –test	**0.003**
3	**Respiration**	**Max-Min**	Paired samples t –test	**0.013**
4	Respiration	Mean	Paired samples t –test	0.06

Table.1 Statistical testing results.

Acknowledgements

This research was supported by the Bio & Medical Technology Development Program of the NRF funded by the Korean government, MSIP(NRF-2017M3A9E1064781).

References

1. I. Pavlidis, J. Levine, “Thermal Image Analysis for Polygraph Testing” (2002).
2. JMC Vendemia, Detection of deception (2003).
3. Pavlidis, Ioannis, James Levine, and Paulette Baukol. "Thermal image analysis for anxiety detection." Proceedings 2001 International Conference on Image Processing (Cat. No. 01CH37205). Vol. 2. IEEE, (2001).
4. Cho, Youngjun, Simon J. Julier, and Nadia Bianchi-Berthouze. "Instant stress: Detection of perceived mental stress through smartphone photoplethysmography and thermal imaging." JMIR mental health 6.4 (2019).
5. Hossain, M.Z.; Gedeon, T. Classifying posed and real smiles from observers’ peripheral physiology. In Proceedings of the 11th International Conference on Pervasive Computing Technologies for Healthcare, Barcelona, Spain, 23–26 (2017).
6. Derakhshan, Amin, et al. "Identifying the Optimal Features in Multimodal Deception Detection." Multimodal Technologies and Interaction 4.2 (2020).

P-029

Development of gait compensation algorithm for gait authentication using smartphone sensor

S.B. Lee[1*], J.S. Lee[1] and I.Y. Kim[1]

[1]Department of Biomedical Engineering, Hanyang University, Seoul, Korea

*soobin2113@hanyang.ac.kr

Abstract

Gait authentication using a smartphone sensor provides unconscious/continuous personal authentication without interfering with the user's daily life. In this study, 3-axis accelerometer and Euler angle were acquired from the thigh, which is most related to a smartphone(when the user puts the smartphone in the pants pocket). We suggest the compensation algorithm regardless of how the smartphone is located in the pocket. Also, We verify the permanence of the algorithm by measured the multiple days dataset (three times with an interval of 2 days). Our study utilizes a gait cycle dataset of 10 participants at their comfortable walking speed. The experimental results indicated the user authentication rates of 99.2% (training model) and 70.5% (test model).

Background

With the advancement of computing and networking technologies in smartphones, it has become possible to handle various tasks such as financial and business at the same time. Since it deals with personal information, the importance of information security is also emerging.

The most commonly addressed mobile security methods are authentication mechanisms such as the PIN, patterns, passwords, face, fingerprint and iris. However, there is a disadvantage that inference is possible because it is based on the user's knowledge (PIN, patterns, password). In addition, there is the inconvenience of usability that interaction is required every time the lock is released. To overcome this problem, we need to develop an authentication algorithm that cannot be inferred and can be used continuously.

Gait has different characteristics for each individual according to the difference in height and the difference in acceleration according to walking speed.[1] And, since the measurement system is built into the existing commercial equipment, it can be applied immediately. In addition, it has the advantage of being able to perform unconscious and continuous personal authentication without interfering with daily life. It is necessary to develop an algorithm capable of gait authentication regardless of the sensor's state or time.

Methods

1. Data collection

We have recorded biometric gait data from 10 participants (3 females, 7 males) using a bno055 IMU (9-axis accelerometer, gyroscope, magnetometer) sensor. It was measured on the right thigh, which is most related to the smartphone as shown figure 1. At the same time, measure 3-axis accelerometer, Euler angle with a sampling rate of 100Hz. Participants were asked to walk 700m (50m*14) at their comfortable speed. Data is acquired over 3 days to confirm the permanency of the algorithm.

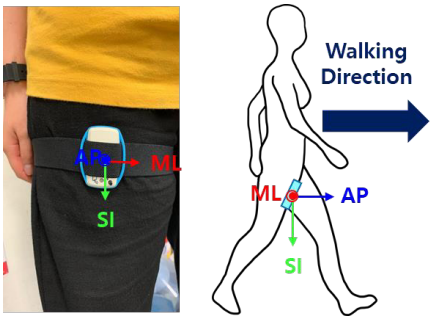


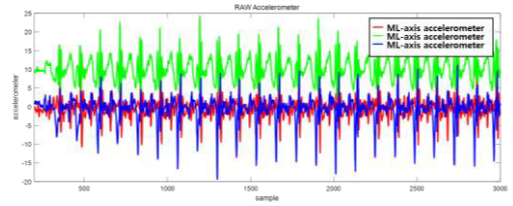
Figure 1. Sensor placement and orientation (ML: Medial Lateral, SI :Superior Inferior, AP: Anterior Posterior)[2]

Human body acceleration during walking appears by combining movement, gravity, and noise. To analyze only human movement, the accelerometer component for gravity and noise have to remove.

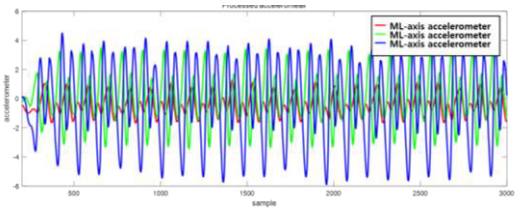
2. Noise removal & Gravity extraction

Considering the characteristics of typical gait data has frequency range [3], cut off frequency = 2.5, 5th Butterworth low pass filter is used. The noise accelerometer component is removed using the low pass filter.

Quaternions can be used to measure reference earth gravity. Therefore, it is possible to extract how much the sensor rotates relative to the reference gravity. After compensation by a rotation matrix, remove the gravity accelerometer component as shown figure 2.(b).



(a)



(b)

Figure 2. (a) Raw accelerometer data

(b) Accelerometer data without gravity component

3. Gait cycle segmentation & sample normalization

Then, the gait length is estimated to analyze the gait based on the gait cycle. Estimate the gait length using the pitch component that can see the most prominent periodic change. When FFT (Fast Fourier Transform) is performed with the pitch signal, the frequency for the peak component is the periodic component. Divide this by the sampling rate (100Hz) to obtain the gait length. Also, for easy analysis of the gait cycle rate, it is normalized into 100 samples as shown figure 3.

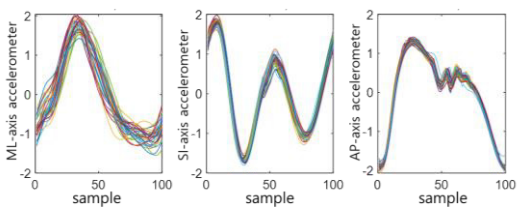


Figure 3. Segmented and normalized cycle

4. Feature extraction

The feature is extracted to user authentication using the individual's differentiation within the gait cycle. Individual gait pattern analysis was conducted by referring to the 1d feature used in [4].

Results and Discussion

Identification is performed using the extracted 1d feature to verify the validity of the algorithm. Generate a training model with gait cycle data for 10 participants as 1 day, and a test model with the remaining 2 days. Classification is performed using a linear SVM. The accuracy of the training model for 1 day is 99.2%, and the accuracy of the test model for 2 days is 70.5%.

Currently, identification was performed using a classifier app in Matlab. In the future, the final goal of the authentication algorithm will be developed and applied. In addition, it is necessary to build more databases and develop more efficient feature detection algorithm.

Acknowledgements

This research was supported by Basic Science Research Program through the National Research Foundation of Korea (NRF) funded by the Ministry of Education (2021R1I1A1A01055813)

References

1. D.A. Winter Biomechanics and Motor Control of Human Movement (3rd edition), John Wiley and Sons (1990)
2. Tchelet, Keren, Alit Stark-Inbar, and Ziv Yekutieli. "Pilot study of the EncephaLog smartphone application for gait analysis." *Sensors* 19.23 (2019): 5179.
3. Dehzangi, Omid, et al. "Motion-Based Gait Identification Using Spectro-temporal Transform and Convolutional Neural Networks." *Advances in Body Area Networks I*. Springer, Cham, 2019. 407-421.
4. Sunarya, Unang, et al. "Feature analysis of smart shoe sensors for classification of gait patterns." *Sensors* 20.21 (2020): 6253.

P-030

Gender and Age convolution neural network classification using MFCC

K.M Choi[1], B.R Nam[2], J.Y Kim[1], M.S. Kim[1], J.K Choi[2], S.J Choi[2] and I.Y. Kim[1,2]

[1]Department of Biomedical Engineering, Hanyang University, Seoul, Korea

[2]Department of Electronic Engineering, Hanyang University, Seoul, Korea

ckm303@hanyang.ac.kr

Abstract

In recent years, Voice-related crimes such as phone scams are increasing. In previous studies, gender and age were classified using scripts, but this classification cannot be used in actual criminal investigations. To overcome the shortcomings, free speech dataset was used, and Convolution Neural Network (CNN) was used for age and gender classification. CNN was trained by extracted features of speech data. In order to improve the performance, the highest accuracy was obtained in Gammatone Frequency Cepstral Coefficients (GFCC) when various improved Mel Frequency Cepstral Coefficients (MFCC) were tested. With this method, we obtained of 92% accuracy in gender and 50% in age classification.

Background

The major crimes in the last decade, Voice-related crimes such as phone scams are increasing. Profiling the Suspect's voices can be helpful for investigators as it can be used as evidence to reduce suspects or induce confessions. The reason that an individual can be profiled using a voice signal which has information about the vocal cords and the vocal track filter. Figure. 1 shows that the voice signal in the frequency domain is expressed as the product of the vocal track filter and the vocal source. The difference in the vocal tract filter appears different depending on the person [1]. In previous papers, MFCC and Mel-spectrogram were mainly used to extract features in speech signals [2][4]. In various previous papers, MFCC has low accuracy in noisy environments. MFCCs are difficult to use due to noise in environments that require profiling such as Phone scams. Therefore, we propose a gender and age classification system suitable for profiling by extracting robust features through performance comparison of various advanced MFCCs.

Methods

2.1 Dataset

The dataset used in this paper is Korean free conversation voice of AI-hub. The data consists of files recorded in the studio and files using voice chat. Voice data was collected at the same rate by gender and consists of data of over 2000 speakers and a total of over 4000 hours of utterance. Each data is labeled with gender, age, regional dialect, and education level. Speech consists of free speech with a length between 2 and 15 seconds. The sampling rates of all voices are fixed at 16000 Hz

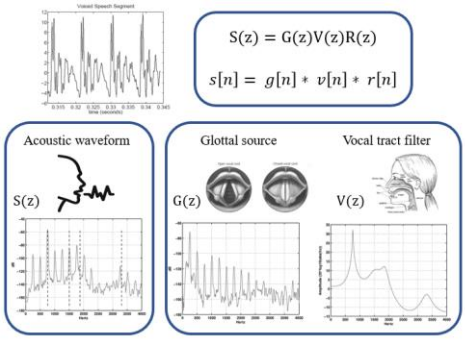


Figure1. Voice signal expressed by vocal tract filter and vocal source

2.2 Feature extraction

The features were extracted using utterances of 5 seconds consisting of 100 males and 100 females of various regions and age groups. As the features used, Mel-Frequency Cepstral Coefficient (MFCC) was mainly used and extracted through the process shown in the Figure2 below. For performance comparison, delta MFCC, delta-delta MFCC, Power Normalized Cepstral Coefficients (PNCC) [5], Basilar-membrane Frequency-band Cepstral Coefficient (BFCC) [6], Gammatone Frequency Cepstral Coefficients (GFCC), Lateral Floating-Capacitor-Coupled (LFCC), Linear Predictive Coding (LPC) [3], Normalized Gammachirp Cepstral Coefficients (NGCC), Perceptual Linear Prediction (PLP) [3], Rasta-PLP [3],

and Linear Predictive Cepstral Coding (LPCC) [6] were used.

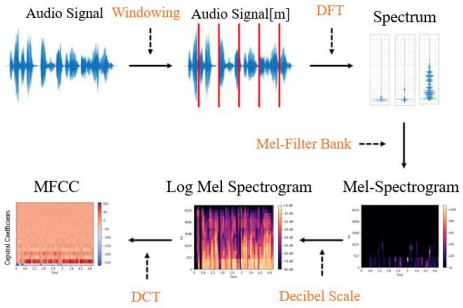


Figure2. MFCC feature extraction

3. Result and Discussion

Genders were classified by 3-layers convolutional neural network using the extracted feature points. As a result, when MFCCs were extracted by feature points, the accuracy of gender classification was about 82% as shown in the Figure.3. As shown in Figure. 4, when delta MFCC, delta-delta MFCC, PNCC, BFCC, GFCC, IFCC, LPC, NGCC, PLP, Rasta-PLP, and LPCC were used for gender classification, GFCC obtained relatively good accuracy (92%). When classifying gender-mixed data from 10s to 50s, it showed an average of 35% accuracy, and when male age was predicted through the classified files, 40% accuracy was confirmed, and when only female age was predicted, the accuracy was up to 50%. In the age classification, various features were used for comparison, but no significant difference was found. Overfitting occurs in both age and gender classification. It is necessary to add batch normalization and dropout layer. In order to improve accuracy, it is necessary to adjust the parameters of the age and gender classification system.

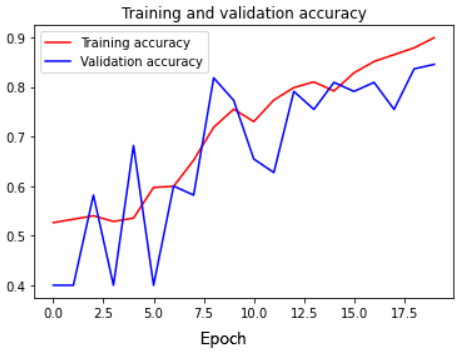


Figure3. Results of gender classification using CNN

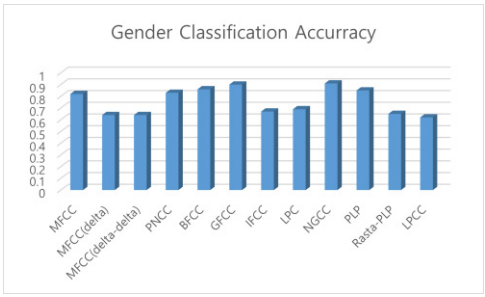


Figure4. Results of gender classification using advanced MFCC

Acknowledgements

This research was supported by the Bio & Medical Technology Development Program of the NRF funded by the Korean government, MSIP(NRF-2017M3A9E1064781).

References

1. Hamlet, Sean Michael," Comparing Acoustic Glottal Feature Extraction Methods with Simultaneously Recorded High-speed Video Features for Clinically Obtained Data." (2012).
2. Tiwari, Vibha," MFCC and its applications in speaker recognition," International journal on emerging technologies 1.1, 19-22 (2010).
3. Gupta, Kartiki, and Divya Gupta," An analysis on LPC, RASTA and MFCC techniques in Automatic Speech recognition system. " 2016 6th international conference-cloud system and big data engineering (confluence). IEEE, (2016).
4. Shen, Jonathan, et al. "Natural tts synthesis by conditioning wavenet on mel spectrogram predictions." 2018 IEEE International Conference on Acoustics, Speech and Signal Processing (ICASSP). IEEE, (2018).
5. Kim, Chanwoo, and Richard M. Stern. "Power-normalized cepstral coefficients (PNCC) for robust speech recognition." IEEE/ACM Transactions on audio, speech, and language processing 24.7, 1315-1329 (2016)
6. Gulzar, Taabish, Anand Singh, and Sandeep Sharma. "Comparative analysis of LPCC, MFCC and BFCC for the recognition of Hindi words using artificial neural networks." International Journal of Computer Applications 101.12, 22-27 (2014)

P-031

Is Aryl Hydrocarbon Receptor Antagonism after Ischemia Effective in Alleviating Hepatic Ischemia-Reperfusion Injury in Rats?

Jae-Im Kwon[1,2], Hwon Heo[2], Joongkee Min[2], Sang Tae Kim[2], Chul-Woong Woo[2*†],Dong Cheol Woo[2*†]

mri.dcwoo@gmail.com

Abstract

Aryl hydrocarbon receptors (AhRs) have been reported to be important mediators of ischemic injury in the brain. Furthermore, the pharmacological inhibition of AhR activation after ischemia has been shown to attenuate cerebral ischemia-reperfusion (IR) injury. Here, we investigated whether AhR antagonist administration after ischemia was also effective in ameliorating hepatic IR injury. A 70% partial hepatic IR (45-minute ischemia and 24-hour reperfusion) injury was induced in rats. We administered 6,2',4'-trimethoxyflavone (TMF, 5 mg/kg) intraperitoneally 10 minutes after ischemia. Hepatic IR injury was observed using serum, magnetic resonance imaging-based liver function indices. This study demonstrated that inhibition of AhR activation after ischemia was effective in ameliorating IR-induced liver injury in rats.

Background

Hepatic ischemia-reperfusion (IR) injury commonly occurs during liver transplantation or resection and is considered a leading cause of liver damage and dysfunction. The mechanisms of hepatic IR injury have been extensively investigated, but nevertheless remain largely unclear. The aryl hydrocarbon receptor (AhR) is a ligand-activated basic helix-loop-helix/Per-ARNT-Sim transcription factor known to mediate toxic and carcinogenic effects of xenobiotics. Recent studies have suggested that cerebral ischemia induces AhR activation and exacerbates neuronal damage. This is because L-kynurenine (L-Kyn), an endogenous ligand of AhR, is accumulated in the brain during ischemia and triggers the activation of AhR. L-Kyn is produced in a significant amount in the liver through the degradation of L-tryptophan by tryptophan-2,3-dioxygenase (TDO),[1] it is more likely to accumulate in the liver than in the brain due to ischemia. This means that ischemia-induced AhR activation and tissue damage after reperfusion could be greater in the liver than in the brain.

Methods

Sprague-Dawley rats (male; 8 weeks old; Orient Bio, Pyeongtaek, Republic of Korea) were used in the experiments. Based on previous studies, a 70% partial hepatic IR injury model was established in rats.[2] Briefly, the abdominal cavity was exposed by a midline incision, and the portal triad (hepatic artery, portal vein, and bile duct), which supplied the left lateral and median lobes, was clamped (Fig. 1). The clamp was removed 45 minutes after ischemia developed.

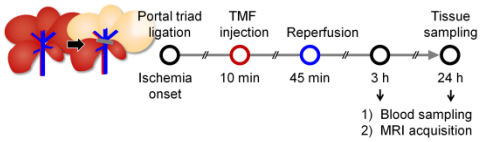


Figure 1. Schematic diagram of the experimental procedure.

As the AhR antagonist, 5 mg/kg of 6,2',4'-trimethoxyflavone (TMF) (Sigma-Aldrich, St. Louis, MO, USA) dissolved in dimethyl sulfoxide (DMSO) Sigma-Aldrich) was used. All treatments were administered via intraperitoneal injection. The rats were randomly divided into the following: (1) a sham group with no IR modeling or vehicle injection (n = 8); (2) a control group with IR modelling and vehicle injection (n = 8); and (3) a TMF group with IR modeling and administration of the drug at 10 minutes after ischemia (n = 8). MRI was performed on a 9.4 T MRI system (Agilent Technologies, Santa Clara, CA, USA) with a 63-mm transmit/receive volume coil. MRI data were obtained at 3 and 24 hours after reperfusion. MRI images were obtained before and 20 minutes after administration of Gd-EOB-DTPA (25M/kg, Primovist, Bayer Korea, South Korea). All MRI data were analyzed using the ImageJ software (National Institutes of Health, Bethesda, MA, USA) by an observer blind to grouping information. The mean the signal intensities (SIs) values and T1 relaxation time were measured on T1-weogjted gradient echo images (T1-WIs) and T1 maps obtained before and 20 minutes after Gd-EOB-DTPA administration. Region of interests (ROIs) were manually placed at identical locations on the hepatic parenchyma and paravertebral muscle. Two ROIs were randomly placed in the liver and paravertebral muscles in the T1-WIs and T1 maps

before and after Gd-EOB-DTPA administration. MRI-based liver function indices were calculated from the SI measurements or T1 relaxation time before (SI-pre, T1-pre) and 20 minutes after (SI-post, T1-post) Gd-EOB-DTPA administration as follows: (1) relative enhancement (RE) of the liver = (SI-post – SI-pre)/SI-pre; (2) LMR = SI-post of the liver/SI-post of the muscle; (3) T1-post = T1-post values of the liver; and (4) ΔT1 = T1-pre – T1-post.[3] Blood samples were obtained from the rats' jugular veins 3 and 24 hours after reperfusion. The samples were centrifuged at 2,000 r/minutes for 14 minutes to obtain serum for analysis. The activities of serum of alanine aminotransferase (ALT) and aspartate aminotransferase (AST) were determined with a biochemical analyzer (7180, Hitachi, Tokyo, Japan).

Results and Discussion

Figure. 2 shows MRI-based liver function indices. The SIs of the liver in T1-WIs obtained at 3 and 24 hours after reperfusion were higher in all three groups at 20 minutes after the administration than those before the administration of Gd-EOB-DTPA, Fig. 2 (A). Conversely, the T1 values of the liver in T1 maps were lower in all three groups 20 minutes after the administration than those before the administration of Gd-EOB-DTPA. The relative enhancement (RE) values at 24 hours after reperfusion were significantly higher in the control group than in the sham group ($P < 0.01$), Fig. 2 (B). The RE values at 3 and 24 hours after reperfusion were significantly lower in the TMF group than in the control group ($P < 0.05$ and $P < 0.001$, respectively). The ΔT1 values at three hours after reperfusion were significantly higher in the TMF group than in the sham group. The ΔT1 values at 24 hours after reperfusion were significantly higher in the control group than in the sham group ($P < 0.001$). The ΔT1 values at 24 hours after reperfusion were significantly lower in the TMF group than in the control group ($P < 0.01$).

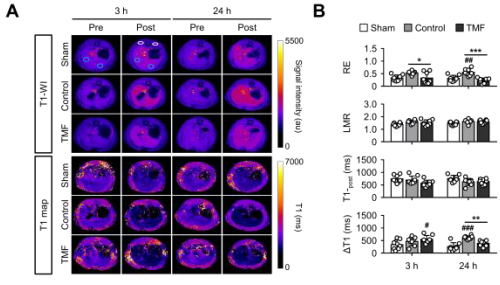


Figure 2. Effect of 6,2',4'-trimethoxyflavone (TMF) treatment on magnetic resonance imaging-based liver function indices.

Figure. 3 shows changes in serum ALT and AST levels. Compared with the sham group, the control and TMF groups had significantly higher serum ALT and AST levels at 3 and 24 hours after reperfusion ($P < 0.05$, Fig. 2A, B). The serum ALT levels were significantly lower in the TMF group than in the control group at 3 ($P < 0.001$) and 24 ($P < 0.01$) hours after reperfusion. The serum AST levels were significantly lower in the TMF group than in the control group at 3 hours after reperfusion ($P < 0.001$).

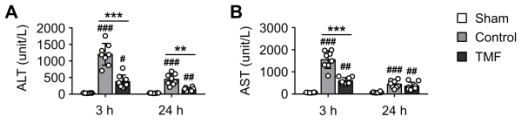


Figure 3. Reduction of serum levels of alanine aminotransferase (ALT) and aspartate aminotransferase (AST) by TMF treatment.

Acknowledgements

We thank the Magnetic Resonance Core Facility at the ConveRgence mEDIcine research cenTer (CREDIT), Asan Medical Center, for the MRI data acquisition and analysis. We would like to thank Editage (www.editage.co.kr) for English language editing. This study was supported by a grant (2019IL0602) from the Asan Institute for Life Sciences, Asan Medical Center, Seoul, Republic of Korea and the Basic Science Research Program through the National Research Foundation of Korea (NRF-2018R1C1B6003879).

References

1. Green, A. R., Woods, H. F. & Joseph, M. H. Tryptophan metabolism in the isolated perfused liver of the rat: effects of tryptophan concentration, hydrocortisone and allopurinol on tryptophan pyrrolase activity and kynurenine formation. Br J Pharmacol 57, 103-114, doi:10.1111/j.1476-5381.1976.tb07660.x (1976).
2. Karatzas, T., Neri, A. A., Baibaki, M. E. & Dontas, I. A. Rodent models of hepatic ischemia-reperfusion injury: time and percentage-related pathophysiological mechanisms. J Surg Res 191, 399-412, doi:10.1016/j.jss.2014.06.024 (2014).
3. Haimerl, M. et al. Gd-EOB-DTPA-enhanced MRI for evaluation of liver function: Comparison between signal-intensity-based indices and T1 relaxometry. Sci Rep 7, 43347, doi:10.1038/srep43347 (2017).

P-032

Interpretation of blood pressure errors in clothing by mathematical models of oscillometric measurment equipment

Jeonghoon Kim[1], Jongshill Lee[1] , Inyoung Kim[1] and Hoonki Park[2]

Department of Biomedical Engineering Hanyang University[1,]

Department of Family Medicine Hanyang University[2]

kjhoon6075@hanyang.ac.kr

Abstract

Automatic blood pressure measurement with oscillometric is most common blood pressure measurement method that can be done at home. Several error factors can be applied to automatic blood pressure measurement by unskilled individuals. Using a cuff while clothing on the arm is one of the common error factors. This study provides an interpretation of how blood pressure measurements in clothing cause blood pressure errors. Oscilometric and auscultatory measurements were performed for three error conditions from a total of 26 subjects. Through measurements, ABP(auscultation blood pressure), OBP(oscilometric blood pressure) and OMWE(Oscillometric Waveform Envelope) were acquired. OMWE was fitted on the exponential function model to explaining the Volume and Pressure relationship of arterial. The Fitted OMWE was used to obtain exponential function coefficients parameter **"a"** and **"b"**. Parameter "a" has a positive correlation with the ability to expand blood vessels, and parameter "b" has a positive correlation with the ability to contract blood vessels. Both parameters had getting lower in error conditions compared to bare arm conditions. However, only parameter "a" had decreasing significantly. OMWE based on the parameter "a" and "b" was simulated to determine the effect of this change. And OBP was measured using SOMWE(Simulated OMWE). significant blood pressure over estimation were confirmed under error conditions. Statistical results can be interpreted as the conclusion that "OMWE in error condition" reflects suppressed arterial expansion ability compared to bare condition. This can lead to over estimation and means that clothing blood pressure measurement should be avoided regardless of the significant degree.

Background

Automatic blood pressure measurement methods using oscilometric methods have become more active at home. However, since measurements at home are measured by non-experts, they are exposed to various error factors. A paper summarizing the error factors in blood pressure measurement [1] explains that wearing a cuff on clothes is one of the error factors, and at the same time, it is not significant. A review paper synthesizing previous studies on clothing error [2] showed that this clothing error causes excessive blood pressure measurement, but is not significant.

However, all clothing thickness measurement methods used in previous studies are not clearly specified, so they involve limitations that cannot be regarded as quantified results.

Because of these limitations, in order to clearly analyze the error impact, it can be said that a qualitative study approach that clearly analyzes the measurement path, in which error factors appear as errors, is more appropriate than a simple quantitative study approach to compare measurement results.

This study estimates the arterial characteristics of the measurer from OMWE data obtained during the oscillometric method, and identifies the difference in OMWE in bare and clothing measurements conditions, finally uses SOMWE to confirm the occurrence of BP errors.

Methods

Figure 1a shows the experimental protocol. In each segment, stethoscope and oscillometric methods were performed simultaneously. In clothing conditions, correct blood pressure was calculated as the average value of preceding and following blood pressure.

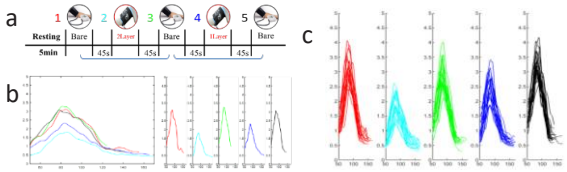


Figure 1

The error conditions were composed of two types depending on the thickness, with a thickness of 3.5 mm for thick clothing and 1.5 mm for thin clothing. All conditions used are three conditions, including bare arm condition.

Figure 1b shows each OMWE measured under three error conditions. Figure 1c shows that all extracted OWMEs are plotted at the same location according to the measurement protocol.

To confirm the effect of the extracted parameters a and b on the OMWE form, the extracted parameters a and b were entered into the OMWE model presented in previous study [3] to obtain the simulated OMWE (SOMWE) and measure BP therefrom.

Previous studies [3] argued that the high pressure range slope and low pressure range slope (Parameters a and b) of the semlLog scaled oscillogram can be used as coefficients of the fitting index function.

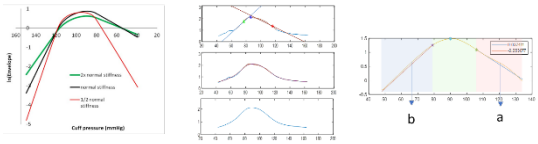


Figure 2

The extracted OMWE was subjected to Gaussian fitting to be converted into an exponential function form and then semilog scaling. Figure 2 describes the process of extracting the described parameters.

Results and Discussion

Data were obtained from 26 subjects (Male=17). The oscillometric method was divided into two methods according to the algorithm.Two methods are the LAA and MAA methods.

Table 1 shows the results of measurement blood pressure (acultation, LAA, MAA). Table 2 shows the results according to the error conditions of the extracted parameters a and b. Table 3 shows the OBP measurement results extracted from SOMWE.

Table 1

Measurement	Conditions	Mean Error		P-value	
		SBP	DBP	SBP	DBP
Auscurtartory	Thick-Bare	**+3.88mmHg**	**+4.04mmHg**	**P < .005 ***	**P < .005 ***
	Thin-Bare	+2.48mmHg	+1.80mmHg	P = .079	P = .062
Oscillometric (LAA)	Thick	**+10.96mmHg**	**+4.04mmHg**	**P < .001 ****	**P < .010 ***
	Thin	+2.48mmHg	- 3.42mmHg	P = .142	P = .937
Oscillometric (MAA)	Thick	**+9.92mmHg**	**+3.60mmHg**	**P < .001 ****	**P < .010 ***
	Thin	+1.52mmHg	- 1.16mmHg	P = .410	P = .095

Parameter a significantly decreased. The decrease in parameter b was not significant. This means that clothing can cause distortion on the OMWE by creating a response that seems to hinder arterial expansion.

Measurement errors identified in SOMWE blood pressure indicate that distorted OMWE can lead to overestimation of measured blood pressure.

Table 2

Conditions	Mean Error		P-Value	
	a	b	a	b
Bare–Thick	**+ 0.0105**	+ 0.0043	**P < .001 ****	P = .111
Bare–Thin	**+ 0.0082**	+ 0.0009	**P < .005 ***	P = .695

From these results, we were able to obtain a interpretation of pathway in which clothing causes distorted OBP. However, the results of this study cannot explain the effect of clothing error in stethoscope blood pressure measurement.

In follow-up studies, an explanation of the measurement error of the stethoscope method should be considered together.

Table 3

Conditions	Mean & Confidence Interval					
	LAA SBP			LAA DBP		
Bare_1	**136.66**	[136.47 ~ 136.84]	.009	**110.82**	[110.70 ~ 110.96]	.004
Thick	**137.29**	[137.04 ~ 137.53]	.015	**111.28**	[111.12 ~ 111.46]	.007
Bare–2	**136.53**	[136.32 ~ 136.75]	.012	**110.76**	[110.62 ~ 110.91]	.006
Thin	**136.93**	[136.65 ~ 137.22]	.021	**110.04**	[110.84 ~ 111.25]	.011

Conditions	Mean Error		P-value	
	LAA SBP	LAA DBP	LAA SBP	LAA DBP
Thick-Bare	**+0.6293**	+0.4610	**P < .001 ****	**P < .001****
Thin-Bare	**+0.3990**	+0.2766	**P < .050 ***	**P < .050***

Acknowledgements

This work was supported by the National Research Foundation of Korea(NRF) grant funded by the Korea government(MSIT) (No. 2021R1F1A1060660).

References

1. Kallioinen, Noa, et al. "Sources of inaccuracy in the measurement of adult patients' resting blood pressure in clinical settings: a systematic review." Journal of hypertension 35.3 (2017): 421.
2. Seguret, David, et al. "Blood pressure measurements on a bare arm, over a sleeve or below a rolled-up sleeve: a systematic review and meta-analysis." *Journal of hypertension* 38.9 (2020): 1650-1658.
3. Babbs, Charles F. "Oscillometric measurement of systolic and diastolic blood pressures validated in a physiologic mathematical model." *Biomedical engineering online* 11.1 (2012): 1-22.

P-033

Evaluation of antibody aerosolization by jet and mesh nebulizers

K.H. Chang[1], S.W. Hong[1], H.M Park[2], C.J. Woo[1], B.J. Park[3] and K.C. Nam[1]

[1]Department of Medical Engineering, Dongguk University College of Medicine, Gyeonggi-do, Korea

[2]Graduate Program of Biomedical Engineering, Yonsei University, Seoul, Korea

[3]Department of Electrical & Biological Physics, Kwangwoon University, Seoul, Korea

kichang.nam@gmail.com

Abstract

Aerosol therapy using nebulizers is a key way of delivering drugs to the lungs of people with respiratory disease. In recent years, clinical studies have been conducted to deliver therapeutic antibodies by nebulizers for the treatment of asthma and COVID-19, but still no standard treatment for nebulization of antibodies. Moreover, there are few literature studies on the nebulization performance using antibodies in various types of nebulizers. The purpose of this study was to evaluate the in vitro aerosolization performance such as aerosol size, output rate, nebulization time, residual volume and reservoir temperature during nebulization of immunoglobulin G (IgG) by jet and vibrating mesh nebulizers. The jet nebulizer maintained a constant output rate regardless of the concentration of the antibody solution, whereas the mesh nebulizer decreased as the antibody concentration increased.

Background

Nebulizer has the advantage of minimizing toxicity and side effects that occur during intravenous or oral drug delivery as it can deliver a high concentration of drug to the lungs through with a small amount of drug [1]. Most drugs approved for nebulizers are small molecules like corticosteroids, beta-sympathomimetics, muscarinic antagonists, and antibiotics, with the exception Pulmozyme®, which is the only one protein therapeutics for cystic fibrosis. To treat asthma and COVID-19, many clinical trials have recently been conducted to deliver therapeutic antibodies directly to the lungs with a nebulizer [2]. However, antibody drug as protein can be affected by various physical factors such as temperature change and cavitation that occur during operation of the nebulizer, and also have high viscosity, which can lead to poor pulmonary delivery efficiency [3]. According to the principle of operation, the nebulizer is divided into three types: jet, ultrasonic and mesh (static and vibrating) nebulizers. Pulmonary drug delivery efficiencies also vary due to differences in aerosolization properties between nebulizers. Also, there are little literature studies on nebulization performance using therapeutic antibodies in different types nebulizers. This study evaluated *in vitro* aerosolization characteristic (aerosol size, residual volume, nebulization time and output rate) and reservoir temperature changes at various IgG concentrations in jet and vibrating mesh nebulizers.

Methods

Two nebulizers were assessed; a jet nebulizer (PARIr: PARI LC Sprint nebulizer with red nozzle, PARI GmbH) and a vibrating mesh nebulizer (SM3 nebulizer KTMED Co.). IgG prepared at 1, 10, 20, 40 mg/mL with water and stored refrigerated until use. Aerosolization properties were evaluated using 2 mL of each IgG solution. Aerosol sizes (Dv50) of IgG solutions were measured directly using laser diffraction (Spraytec). Nebulizer weights were measured before and after nebulization or at 1min intervals and nebulization times were also recorded. Residual volumes were determined gravimetrically. The temperature changes of the IgG solution in the reservoir during nebulization were measured at 1min intervals using a K-type thermocouple probe with a digital multimeter (FLUKE-87-5).

Results and Discussion

Table 1. Aerosol size (Dv(50) emitted by PARIr and SM3 nebulizers at each IgG concentration.

IgG conc. (mg/mL)	The Fifty Percent Volume Diameter (Dv(50) (μm))	
	PARIr	SM3
0 (saline)	2.998 ± 0.071	7.073 ± 0.116
1	3.206 ± 0.042	6.755 ± 0.121
10	3.096 ± 0.072	6.742 ± 0.187
20	3.186 ± 0.011	6.533 ± 0.049
40	2.903 ± 0.059	6.016 ± 0.013

In Table 1, the aerosol sizes of PARIr was constant at 3μm regardless of the IgG concentration, while SM3 decreased from 7μm to 6μm, and the aerosol size of SM3 is about 2 times larger than that of PARIr. Table 2 showed the residual volume, nebulization time, and output rate of PARIr nebulizer similar to saline.

Table 2. Aerosolization characteristics for PARIr nebulizer at each IgG concentration.

IgG conc. (mg/mLl)	Aerosolization characteristics		
	Residual Vol. (mL)	Nebulization time (min)	Output Rate (mL/min)
0 (saline)	0.564 ± 0.010	9.178 ± 0.019	0.153 ± 0.002
1	0.560 ± 0.016	8.778 ± 0.048	0.164 ± 0.001
10	0.611± 0.056	8.694 ± 0.127	0.160 ± 0.008
20	0.625± 0.024	8.667 ± 0.167	0.159 ± 0.004
40	0.632± 0.005	8.722 ± 0.096	0.157 ± 0.001

Unlike saline, SM3 nebulizer generates many air bubbles during nebulization in the IgG solution. Therefore, after the IgG solution is rapidly emitted, the remaining air bubbles are nebulized, resulting in an incomplete nebulization pattern that quickly decreases the output rate and increases the residual volume. In addition, it was confirmed that the SM3 nebulizer increased the nebulization time as the output rate decreased as the IgG concentration increased.

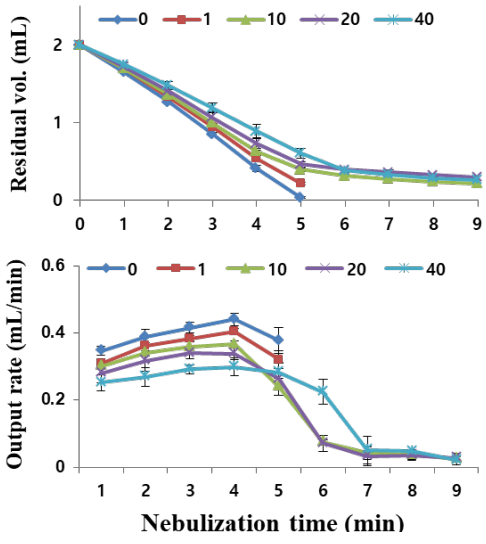


Figure 1. Aerosolization characteristics for SM3 nebulizer at each IgG concentration.

PARIr was increased to about 17°C within 1 min of nebulization in all IgG concentration and maintained until nebulization is finished, while SM3 increased up to about 30°C.

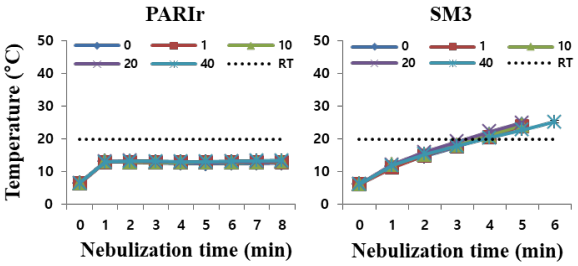


Figure 2. Temperature change of IgG solution during nebulization by PARIr and SM3 nebulizer

These results demonstrated that the jet nebulizer showed constant aerosolization characteristic regardless of the IgG concentration, whereas the mesh type nebulizer was affected. The temperature elevated by the SM3 nebulizer is not expected to affect the activity or function of IgG, as it is lower than the denaturation temperature of IgG, 65°C. Better understanding the aerosolization characteristic for therapeutic antibody in various type of nebulizer is critical to support the selection and development of suitable nebulizers for antibody nebulization. Further studies are needed on the stability and pulmonary delivery efficiency of the emitted antibodies by nebulizer.

Acknowledgements

This work was supported by the National Research Foundation (NRF) Grant funded by the Korea government (MSIT) (NRF-2020R1A2C1101048).

References

1. H. H. Gangured, M. A. Chordiya, N. S. Baste, and C. D. Upasani, “Approaches and devices used in pulmonary drug delivery system: A review,” Asian J Pharm. Res. Health Care. 4, 11–27 (2012).
2. ClinicalTrial.gov. Clinical trials found for nebulizer and antibody. Available at: https://clinicaltrials.gov/ct2/results?term=nebulizer+antibody& Search=Search.
3. A. A. Matthews, P. L. Rachel Ee, and R. Ge, “Developing inhaled protein therapeutics for lung diseases,” 1, 11 (2020).

Comparison of quantitative drug delivery efficiency for jet and mesh nebulizer

H.M. Park[1], K.H. Chang[2], S.W. Hong[2], C.J. Woo[2], B.J. Park[3] and K.C. Nam[2,*]

[1]Graduate Program of Biomedical Engineering, Yonsei University, Seoul, Korea

[2]Department of Medical Engineering, Dongguk University College of Medicine, Gyeonggi-do, Korea

[3]Department of Electrical & Biological Physics, Kwangwoon University, Seoul, Korea

kichang.nam@gmail.com

Abstract

Nebulizer is a medical device used to treat respiratory diseases that delivers aerosolized drugs to lung. Drug delivery amount depends on the breathing pattern and type of nebulizer. It has been reported that the drug delivery amount of mesh nebulizers is higher or similar than that of jet nebulizers. However, due to the structural characteristics of the nebulizer, it is difficult to quantitatively compare the drug delivery efficiency due to the difference in the residual volume. In this study, a developed respiratory simulator was applied to test drug delivery efficiency quantitatively using three breathing patterns under the constant output in the nebulizers.

Background

A nebulizer is a medical device used for respiratory treatment. Depending on the type of nebulizer, the drug delivery amount is different due to the difference because the output rate, particle size, and residual volume [1]. There is a report that the drug delivery amount of mesh nebulizer is higher than that of jet nebulizer. But, it is difficult to compare the quantitative drug delivery efficiency of the nebulizer due to difference of nebulization characteristics. Also, the drug delivery amount is different depending on the breathing pattern caused by the disease [2]. In this study, the quantitative drug delivery efficiencies of nebulizers were compared under the constant output using a developed respiratory simulator.

Methods

The respiratory simulator consist of a linear actuator (Scipia, Korea), a stepper motor (Nema 57 56 Stepper motor, JingJiang Tech. Co., China), motor driver (TB6600, DFRobot, China), a flow sensor (SMF3000, Sensirion, Switzerland), an air cylinder (MDB1B50-600, SMC Co., Japan), and an airway model [3] using UV-curable resign (VisiJet M3, 3D Systems, USA) [4]. A disposable filter (Proguard-EX, GMS Korea, Korea) for aerosol collection is located between the airway model and flow sensor. The breathing patterns generated by the respiratory simulator are shown in Table 1. The nebulizers used are shown in Table 2.

Table 1. Breathing patterns generated by the respiratory simulator

Breathing pattern	Tidal volume (mL)	I:E ratio	Respiration rate (bpm)
Normal adult [2]	500	1:2	15
Asthma [2]	290	1:2.5	22
COPD [5]	500	1:3	15

Table 2. Used nebulizers in the study

Type	Model	Abbreviation
Jet	PARI BOY SX-red nozzle (PARI GmbH, Germany)	JN-PARIr
	PARI BOY SX-blue nozzle (PARI GmbH, Germany)	JN-PARIb
Static mesh	NE-U22 (Omron Healthcare, Japan)	SMN-U22
	NE-U150 (Omron Healthcare, Japan)	SMN-U150
Vibrating mesh	NE-SM1 NEPLUS (KTMED Co., Korea)	VMN-SM1
	NE-SM3 (KTMED Co., Korea)	VMN-SM3

The test drug is 2 mL of 0.1% salbutamol solution as defined in ISO 27427:2013 [6]. For comparison of drug delivery efficiency, a nebulized test was performed for each nebulizer using a respiratory simulator until the output reached 1.3mL because JN-PARIb nebulizer had the highest residual volume (~ 0.7 mL) [4]. In order to compare the delivery efficiencies of nebulizers for each breathing pattern, delivered doses were compared versus those obtained for the normal adult breathing pattern. The drug

collected in the filter was eluted with distilled water and quantified using UV spectroscopy.

Results and Discussion

The drug delivery amount of the nebulizer is shown in Table 3. Generally the mesh nebulizer was reported to have a higher drug delivery amount than the jet nebulizer [1], but some mesh nebulizers was not. VMN-SM1 had the highest delivery efficiency in all breathing patterns because delivered dose was the highest. The drug delivery amount may be different due to the output rate and particle size [1].

Table 3. Delivered dose (mg) and Delivery efficiency (%) [4]

Nebulizer	Normal adult		Asthma		COPD	
	DD (mg)	DE (%)	DD (mg)	DE (%)	DD (mg)	DE (%)
JN-PARIr	0.197 ± 0.020	15.14 ± 1.57	0.138 ± 0.021	10.51 ± 1.59	0.130 ± 0.012	9.97 ± 0.92
JN-PARIb	0.147 ± 0.004	11.31 ± 0.28	0.092 ± 0.011	7.13 ± 0.73	0.088 ± 0.010	6.80 ± 0.74
SMN-U22	0.171 ± 0.009	13.12 ± 0.71	0.111 ± 0.004	8.49 ± 0.35	0.108 ± 0.011	8.56 ± 0.32
SMN-U150	0.211 ± 0.008	16.16 ± 0.59	0.155 ± 0.002	11.92 ± 0.15	0.115 ± 0.008	8.82 ± 0.63
VMN-SM1	0.248 ± 0.013	19.04 ± 0.98	0.218 ± 0.007	16.74 ± 0.56	0.177 ± 0.028	13.59 ± 2.19
VMN-SM3	0.156 ± 0.008	12.01 ± 0.65	0.112 ± 0.011	8.63 ± 0.88	0.093 ± 0.008	7.18 ± 0.59

Figure 1 show the drug delivery efficiency compared to the normal adult pattern. The drug delivery efficiency of nebulizers was followed by asthma (62.6 ~ 87.9%) and COPD (54.6 ~ 71.4%) compare to normal adult. As shown in Table 1, the tidal volume of asthma was lower than that of COPD, but respiration rate and inspiration phase were higher, so that the delivery efficiency of asthma was higher or similar to that of COPD. In breathing pattern, the higher the tidal volume, respiration rate and inspiration phase, the higher the drug delivery amount [2].

Since the outputs of all nebulizers are set identically, quantitative drug delivery efficiency is comparable. The limitations of this method are not considered for emitted dose and concentration variation during nebulization.

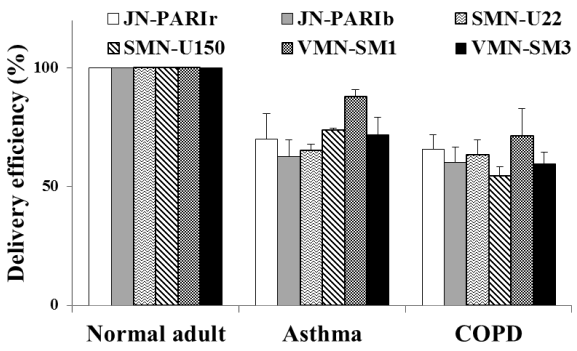


Figure 1. Comparison of drug delivery efficiency for nebulizers between each breathing patterns [4]

Acknowledgements

This work was supported by the National Research Foundation (NRF) Grant funded by the Korea government (MSIT) (NRF-2020R1A2C1101048).

This presentation is part of the published articles (Park et al. BioMed Eng OnLine Vol. 20, No. 59, 2021).

References

1. Ari A, "Jet, ultrasonic, and mesh nebulizers: an evaluation of nebulizers for better clinical outcomes", Eurasian J Pulmonol, Vol. 16, 2014.
2. Bennett G, Joyce M, Sweeney L, MacLoughlin R, "In vitro study of the effect of breathing pattern on aerosol delivery during high-flow nasal therapy" Pulm Ther. Vol. 5, No.1, 2019.
3. Cheng KH, Cheng YS, Yeh HC, Swift DL, "Measurements of airway dimensions and calculation of mass transfer characteristics of the human oral passage", J Biomech Eng., Vol. 119, , No.4, 1997.
4. Park HM, Chang KH, Moon SH, Park BJ, Yoo SK, Nam KC, "In vitro delivery efficiencies of nebulizers for different breathing patterns", BioMed Eng OnLine Vol. 20, No. 59, 2021.
5. Abdelrahim ME, Plant P, Chrystyn H, "In-vitro characterisation of the nebulised dose during non-invasive ventilation", J Pharm Pharmacol., Vol. 62, No.8, 2010.
6. ISO 27427:2013: Anaesthetic and respiratory equipment-nebulizing systems and components. In: International Organization for Standardization 2013.

P-035

Development of a system to read sleep patterns

H.H. Yang[1], S.B. Jung[1], H.C. Kim[1], S.H. Nam[1], T.M. Shin[1*]

[1]Department of Biomedical Engineering, Yonsei University, Wonju, Korea

hahee2538@naver.com[1], tmshin@yonsei.ac.kr[1*]

Abstract

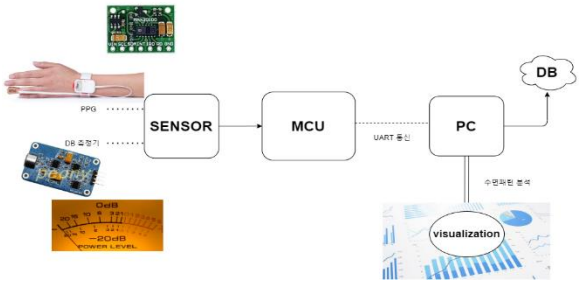
Continuous snoring and sleep apnea hinder deep sleep and cause chronic fatigue in daily life. If respiratory disorders occur frequently during sleep, the sympathetic nervous system is overactivated in our body to prevent the continuation of respiratory disorders. Overactivation of the sympathetic nervous system poses a risk to cardiovascular relations. However, the polysomnography test, which diagnoses sleep apnea currently being performed, is subject to many restrictions. Therefore, in this study, a real-time monitoring system for snoring intensity through sound detection sensors and oxygen saturation levels and heart rate through SpO_2 sensors was developed so that sleep patterns could be recognized at home. Using the developed system, it is expected that the initial response of sleep apnea patients will be easy by determining the severity of snoring and sleep apnea, and recognizing sleep patterns that they did not know.

Background

Developing a system to determine the severity of snoring and sleep apnea, snoring is a very common symptom, and obstructive sleep apnea is found in 70% of adults with snoring. However, most of the patients do not feel the symptoms themselves and are not well aware of them even in serious situations. In addition, patients with severe obstructive sleep apnea will have a mortality rate of about three times higher from cardiovascular disease or cerebrovascular disease within 10 years than normal people. Currently, polysomnography is typically performed to diagnose sleep apnea. In general, polysomnography is conducted by skilled experts in specialized centers, and costs and investments such as facilities, manpower, and equipment are required, resulting in temporal, spatial, and economic burdens for patients. Therefore, in this study, a home sleep pattern monitoring diagnosis system was developed to compensate for these limitations.

Methods

The hardware block diagram of the system developed in this study is shown in Figure 1. An audible signal detection microphone amplifier KB4500W (K-bell, Korea) was used to detect snoring signals, and a SpO_2 sensor MAX30102 (ANALOG DEVICES, USA) was used to measure apnea during sleep. The MCU used Atmega 4809 (Microchip, USA), which was visualized using the LabView program after calibrating the values obtained through the aforementioned sensors through ADC.



< Figure.1 System block diagram >

1. Snoring signal measurement.

1.1 Snoring signal detected with dB value.

The sound signal detected through the audible signal microphone amplifier KB4500W is output as a value that has passed through the MCU's ADC, which requires a process of converting it into dB, a unit of sound. Therefore, an experiment was conducted to examine the ADC value at that time by providing a source of sound source that pays a constant dB value to KB4500W. The experiment was conducted in a quiet room without external noise. The volume of the sound source was adjusted and classified into a total of 10 types at 5 dB intervals from 40 dB to 85 dB, and each dB corresponding to the sound source was provided to KB4500W. A total of three experiments were conducted for 90 seconds according to each dB value. The ADC value output according to the volume of the source corresponding to each applied dB was output and stored, and the ADC value corresponding to each dB was averaged to be derived. Through this, dB = 49.219 x ln (ADC value) - 68.733 which is the calculation formula of the dB estimate was derived.

1.2 Snoring count

When the sound signal entered the audible signal microphone amplifier KB4500W was converted to dB and output using UART communication, it was classified as weak snoring when the dB value was 60 to 69 dB, usually snoring when it was 70 to 79 dB, and slightly severe snoring when it was 80 to 89dB. Monitoring was conducted by LabView, and when a signal corresponding to each range occurred, a phrase indicating the seriousness of snoring appeared.

2. SpO_2 and heart rate measurement.

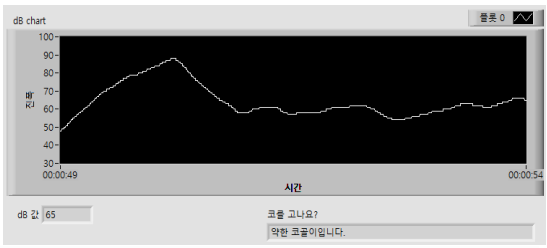
For real-time data monitoring, the I2C communication speed was set to 100 kHz and the UART communication speed was set to 115200bps. Two LEDs (IR, RED) of the MAX30102 sensor are switched to each other at regular intervals according to the sampling rate set. Data is stored in the form of FIFO DATA with an 18-bit ADC resolution, and after receiving 6-byte packet-type data through I2C communication, data is divided into 3 bytes to process RED and IR LED values, respectively. Data is received at a sampling rate of 250ms period. SpO_2, for heart rate calculation, the AC value obtained by removing the average value (DC) based on 100 data was derived. After the threshold calculation, data with peak values were stored through the peak detection algorithm, and when peak exists more than once, it was considered normal and pulse rate bpm per minute was calculated. In order to obtain the degree of oxygen saturation, the ratio of AC values for each DC value of IR and RED LEDs is calculated, and then SpO_2 values are derived using Equations 2.1 and 2.2 through calibration.

$$SpO_2 = aR^2 + bR + c \quad \text{< Equation 2.1 >}$$

$$R = \frac{AC_{red}/DC_{red}}{AC_{ired}/DC_{ired}} \quad \text{< Equation 2.2 >}$$

Results and Discussion

Figure 4 is a front panel showing the result according to the snoring signal when the snoring signal is detected.



< Figure.4 Reading the snoring intensity using the dB>

Figure.6 shows the SpO_2 and bpm values calculated through the algorithm. It was confirmed that the user's breathing condition was monitored in real time.



< Figure.6 Observation of SpO_2 and BPM. >

It is believed that the system developed in this paper can check the user's sleep pattern and prevent emergency situations in advance. In the future, development will be carried out in a wrist-wearing band type that is easier to carry, taking advantage of the wearable characteristics of the device, and wireless communication will be added to develop an alarm to the guardian in case of an emergency.

References

1. Fleetham J, Ayas N, Bradley D, Fitzpatrick M, Oliver TK, Morrison D, et al. Canadian Thoracic Society 2011 guideline update: diagnosis and treatment of sleep disordered breathing. Can Respir J 2011;18(1):25-47.
2. Kimoff RJ. To treat or not to treat: can a portable monitor reliably guide decision-making in sleep apnea? Am J Respir Crit Care Med 2011;184(8):871-2.

Development of a wireless sensing device with optical color sensor for monitoring abnormal state of the automated external defibrillator

Su-hyun Oh[1], Yoon-Seok Oh[2], Jeong-Won Park[2], Qun Wei[2], Hyo-Chan Jeon [3]

[1]Department of Advanced Materials Engineering, Keimyung University, Daegu, Korea

[2]Department of Biomedical Engineering, Keimyung University, Daegu, Korea

[3]CU Medical Co., Ltd., Seoul, Korea

weiqun@kmu.ac.kr

Abstract

Automated external defibrillator (AED) is a portable electronic device that automatically diagnoses the life-threatening cardiac arrhythmias of ventricular fibrillation and pulseless ventricular tachycardia, and is able to treat them through defibrillation, the application of electricity which stops the arrhythmia, allowing the heart to re-establish an effective rhythm. The AED installed in medical institutions or public institutions must always be available. However, due to difficulties in management and lack of human resources, problems of not recognizing medical devices in abnormal conditions often arise and become social issues. In this study, the goal is to develop a wireless sensing device that can identify abnormal conditions of the AED and notifying managers using IoT technology to increase the usability of AED at all times.

Background

It is estimated that about 100,000 AEDs have been distributed in South Korea. With the enactment of legislation on the supply of AEDs, the supply of AEDs is on the rise. Until now, developing a attached device to manage status of the AEDs has been presented by each AED manufacturer, however, due to the size of the device is difference of each brand, so an integrated management system that can manage all AEDs are required [1,2].

In order to ensure the constant usability of the AED that can be used immediately in an emergency. In this study, a service that monitor and notify the abnormal status of the AED in a short time with technology that senses abnormal status of medical devices and IoT network technology is presented. The developed device is using optical color sensor and with WIFI and LTE-M wireless communication technology, the device can monitor the abnormal status by sensing the color of the LED of the AED, and send the message to the management office to maintain the device in real time.

Methods

Figure.1 shows manufactured PCB of proposed wireless sensing device with optical color sensor. The device was manufactured based on analysis of user or administrator needs. AED anomaly classification and detection sensor development. The device was designed based on ARM processor (STM32L4,ST, USA). It has built a new architecture to reach best-in-class ultra-low-power figures thanks to its high flexibility. It offers dynamic voltage scaling to balance power consumption with processing demand, low-power peripherals available in Stop mode, safety and security features, smart and numerous peripherals, advanced and low-power analog peripherals such as op amps, comparators, and etc. Also, the color sensor (TCS3200, AMS, USA) is a programmable color light to frequency converter combines configurable silicon photodiodes and a current to frequency converter on a single monolithic CMOS integrated circuit. The output is a square wave (50% duty cycle) with frequency directly proportional to light intensity (irradiance). In addition, a multi-mode LPMA module offers best-in-class power performance for global LTE-M, NB-IoT, and GNSS networks is designed in this device. The wireless module (HL7800, Sierra, USA) for Cat-M1/NB1 worldwide networks is fully compliant with the 3GPP Release 13. It provides a low-cost, best-in-class power technology for low-bandwidth IoT applications with extended reach beyond traditional cellular. This module is ideal for simple static sensor applications, or real-time fixed or mobile applications such as

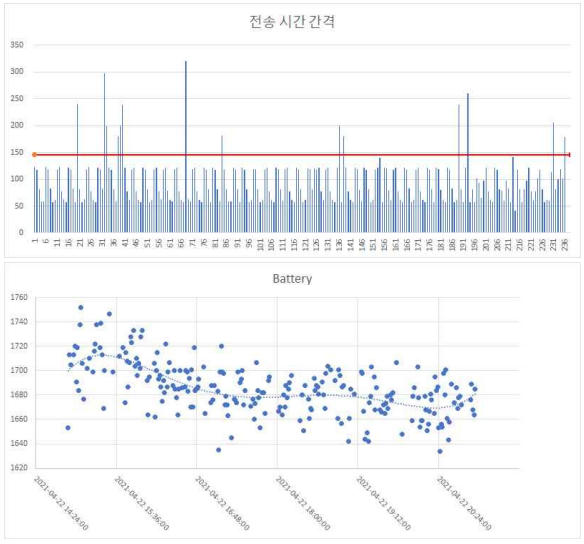
asset tracking, industrial equipment monitoring, consumer wearable devices, smart city deployments, healthcare applications and agricultural monitoring devices.



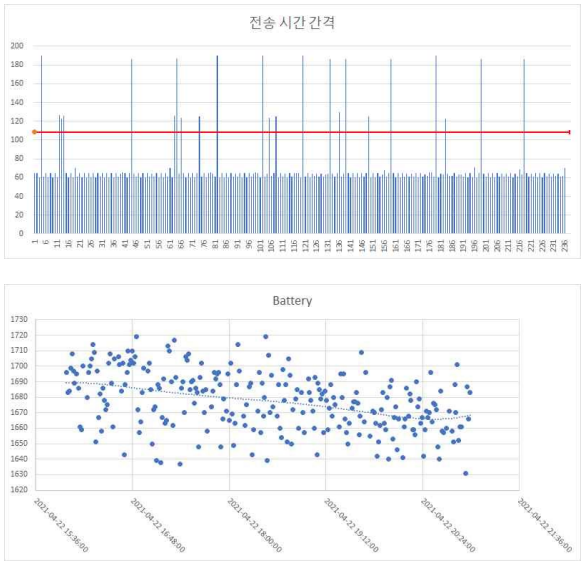
Figure 1. Manufactured PCB of proposed wireless sensing device with optical color sensor.

Results and Discussion

Figure. 2 shows the experimental results of developed wireless sensing device with optical color sensor to monitor the AED. The test for product development that can be managed in the optimal AED state by checking the AED status has been successfully carried out, and a review will be conducted for response in the market, commercialization, and mass production. It is highly likely to be used as a product that can manage the state of the previously sold AED. Students were able to directly practice the principle of prototype production by participating in the project.



(a)



(b)

Figure.2 (a) The AED in normal status and (b) the AED in abnormal status that measured by the proposed device.

Acknowledgements

This research was supported by the Daekyung Innovative University Project (HuStar), promoted by Daegu City. Also, this research was supported by the Bisa research Grant Program of Keimyung University in 2018.

References

1. Woollard, Malcolm et al. “Skill acquisition and retention in automated external defibrillator (AED) use and CPR by lay responders: a prospective study.” Resuscitation vol. 60,1 (2004): 17-28. doi:10.1016/j.resuscitation.2003.09.006
2. Woollard, Malcolm et al. “Optimal refresher training intervals for AED and CPR skills: a randomised controlled trial.” Resuscitation vol. 71,2 (2006): 237-47. doi:10.1016/j.resuscitation.2006.04.005

Development of Hyperbaric Oxygen Chamber Embedded System for Animal Experiment

S.H. Nam[1], H.C. Kim[1], H.S. An[1], Y.E. Choi[1] and T.M. Shin[1*]

[1]Department of Biomedical Engineering, Yonsei University, wonju, Korea

tjdrhd9387@naver.com

Abstract

Hyperbaric oxygen therapy is a treatment that allows patients to inhale 100 percent oxygen in 2.4 to 2.8 atmospheric pressure, as much as 5 atmospheric pressures. 100% oxygen inhalation in hyperbaric environments is a treatment method in which more oxygen is dissolved in the blood and transported to tissues and organs. So, it often used to treat decompression sickness, carbon monoxide poisoning, high-altitude medical problem, and diabetes mellitus. But there has been no case globally yet that the mechanism for hyperbaric oxygen therapy has been revealed. It is necessary to experiment on animals before treatment is performed on humans to identify the mechanism of hyperbaric oxygen therapy. Therefore, in this study, the hyperbaric oxygen chamber for animal experiment with various gas ratios and pressure control was developed using Mess Flow Controller (MFC).

Background

Hyperbaric oxygen therapy is a treatment that allows patients to inhale 100% oxygen in an environment of 2.4 to 2.8 atmospheres and as high as 5 atmospheres, unlike atmospheric pressure. When 100% oxygen is absorbed in a hyperbaric environment, more oxygen than conventional oxygen melts into the blood and transports it to tissues and organs, and in this case, the oxygen concentration in plasma, not hemoglobin, can treat certain areas. The treatment effect is shown through continuous experiments, but it is not standardized or systematized, so various experiments and studies are needed due to the lack of mechanism and method of hyperbaric oxygen treatment.

Therefore, in this study, to develop hyperbaric oxygen therapy and find a new mechanism, a hyperbaric oxygen chamber embedded system for animal experiments was developed. Existing oxygen, general atmosphere, and nitrogen and carbon dioxide are quantitatively mixed and used through MFC, and all systems in the chamber are designed to be controlled and monitored by operators through LCD attached to the front.

Methods

The hyperbaric oxygen chamber embedded system for animal experiments developed in this study can control the gas ratio, pressure, and experimental time desired by the operator through the User Interface. The overall system flow chart is shown in Figure 1.

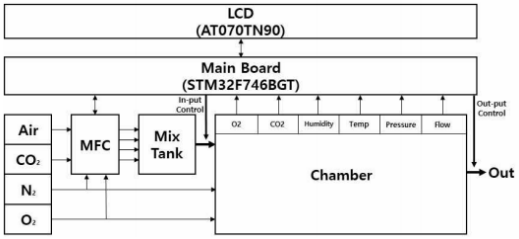


figure 1. Hardware block diagram of the developed system.

For system control, a regulator that converts 5V to 3.3V from an external power source was attached to supply power to the MCU. MCU is Cortex M7 based STM32F746BG (STMicroeletronics Ins, USA) was used, and the actual appearance of the developed module is as shown in Figure 2.



figure 2. Developed actual board (TOP)

P-M-1 (Omega Inc, Korea) and HX92BC (Omega Inc, Korea) were used to measure temperature and humidity, respectively, while oxygen and carbon dioxide sensors used AO2 (City Technology Ins, USA)

and GC-0018 (CO2Metoer Ins, USA), respectively. MFC used KRO_4000S (Teledyne Hastings Instruments, USA), HFC-303 (Teledyne Hastings Instruments, USA) as MFC Valve, and actual photos are shown in Figure 3.



Figure 3. MFC's actual appearance.

A proportional control valve (EPV-312B) was used as the proportional control valve, and XOR110 (Texas Instruments Ins, USA) was used as the integrated circuit. The PID control method was used to control the solenoid valve according to the pressure, and the opening and closing of the valve was adjusted through fertilizer between the value through the pressure sensor and the value input by the operator. The PID algorithm used is the same as Figure 4.

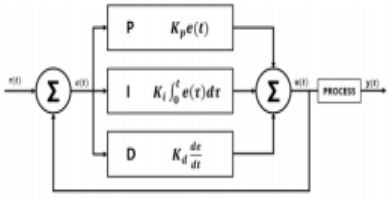


Figure 4. PID notification figure.

Results and Discussion

In this study, the performance evaluation of the developed hyperbaric oxygen chamber's automatic control and programming algorithm was performed, and animal experiments included general mouse wound experiments, diabetic mouse wound experiments, and carbon monoxide poisoning mouse recovery experiments.

First, since there was no hyperbaric oxygen chamber for animal experiments as a performance evaluation, it was compared with the standard of the Ministry of Food and Drug Safety. It operated within the reference value in all parts, and the size of the chamber was relatively small, so there was little change in temperature during pressurization or decompression. When the target was 3ATA, up to 3.04ATA showed 1.3% overshoot. The experimental results are shown in Figure 5.

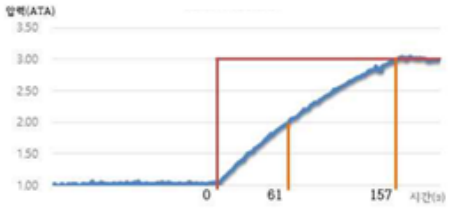


Figure 5. 3ATA pressure function test.

The result of the wound experiment was Figure 6, and the treatment effect was proportional to the treatment time.

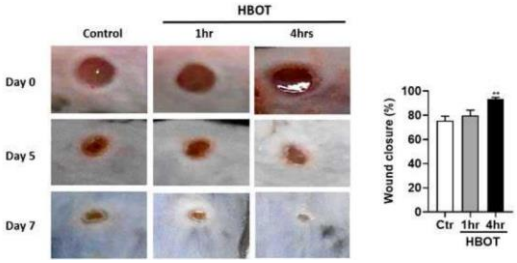


Figure 6. The results of the wound mouse experiment.

In the case of diabetic mice, the higher the pressure at the same time, the better the results, and in the case of acute carbon monoxide-addicted mice, the best results were found at 2.7 ATA.

Hyperbaric oxygen therapy is certainly an effective treatment. Automatic control design was performed according to the existing medical hyperbaric oxygen room standards, and the therapeutic effect was proved through animal experiments. There were no errors during machine operation during animal experiments, and all experiments were safely completed. Therefore, the hyperbaric oxygen chamber for animal experiments developed in this study is expected to greatly help find treatment standards for hyperbaric oxygen therapy in the future.

References

1. LEACH, R. M.; REES, P. J.; WILMSHURST, P. Hyperbaric oxygen therapy. Bmj,1998,317.7166: 1140-1143.
2. TIBBLES, Patrick M.; EDELSBERG, John S. Hyperbaric-oxygen therapy. New England Journal of Medicine,1996,334.25: 1642-1648.

Comparison of Algorithms for Screening of Cervical Intraepithelial Neoplasia using Multiple Electrodes based Electrical Impedance Spectroscopic Probe

Jinwon Mok[1,2], Tingting Zhang[2,3], Jun Beom Heo[1,2,4], Dong Choon Park[4] and Tong In Oh[1,2,3]

[1] Department of Medical Engineering, Graduate School, Kyung Hee University, Seoul, Korea

[2] Impedance Imaging Research Center, Kyung Hee University, Seoul, Korea

[3] Department of Biomedical Engineering, College of Medicine, Kyung Hee University, Seoul, Korea

[4] Department of Obstetrics and Gynecology, Saint Vincent's Hospital, The Catholic University of Korea, Korea

tioh@khu.ac.kr

Abstract

As cervical cancer screening is generally performed on adult women, the diagnosis of cervical intraepithelial neoplasia (CIN), a pre-stage of cervical cancer, has been increasing. This study acquired impedance spectra in the frequency range of 0.625 to 100 kHz for 136 samples using an electrical impedance spectroscopic probe composed of multiple active electrodes. We extracted various features from measurements and evaluated the performance of the classification algorithms to distinguish between normal and CIN

Background

Cervical cancer is the fourth most common cancer among women worldwide. Fortunately, it is highly preventable with the early diagnosis and timely treatments of cervical intraepithelial neoplasia (CIN), since cervical cancer is also one of the most successfully treatable forms of cancer [1]. A simple Papanicolaou smear test has relatively low sensitivity, and anxiety persists due to delays until the result is received [2]. In addition, various diagnostic methods require high cost, and treatment through conization is highly likely to induce side effects and complications and may leave fatal sequelae. Therefore, it is necessary to diagnose CIN in clinical practice, which is an early stage of cervical cancer, with high sensitivity, low cost, and non-invasive, and to screen in real-time. The EIS probe system using multiple active electrodes was recently developed and evaluated its performance [3]. This system will be developed for a CIN screening tool as measuring the electrical impedance spectrum in the frequency range of 0.625 to 100 kHz non-invasively. In order to develop an algorithm for screening CIN from measured data, it is necessary to use information that is robust against noise and represents the characteristics of CIN and normal samples clearly. In this study, we basically used the measured frequency difference spectrum. Additional parameters of the extracellular space R, intracellular space S, and the capacitance C values were extracted by using the Cole-Cole model. We intend to develop an algorithm for screening CIN by adding clinical factors such as the patient's age and menopause. We compared the performance of screening systems using each classification algorithm such as Logistic Regression, Decision Tree, and Random Forest using 136 cervical samples. Finally, the sensitivity, specificity, accuracy, precision, and F1-Score according to the use of each algorithm were evaluated. The combination of all known information will provide deep insight into the characteristics of cervical tissue and inspire future advanced techniques for classifying normal and CIN cases via EIS data.

Methods

136 women with informed consent were enrolled in this study approved by the IRB of St. Vincent's Hospital of The Catholic University of Korea (VC17TNSI0126).

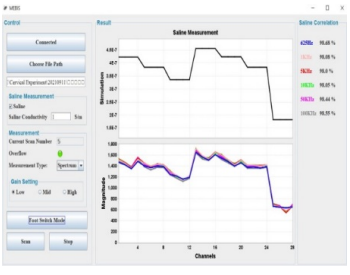
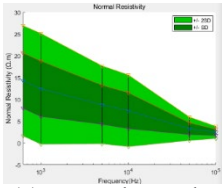
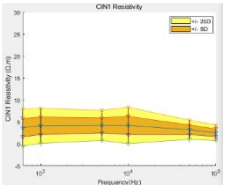


Figure 1. Quality verification and calibration for multiple electrodes based electrical impedance spectroscopic probe

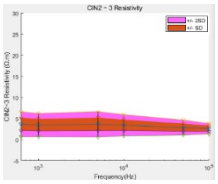
Before measurement, we verified the performance of the multiple electrodes based electrical impedance spectroscopic probe and calibrated it using 1 S/m saline. As shown in Figure 1, the measured data has a high correlation with the simulation data.



(a) Normal samples



(b) CIN 1 samples



(c) CIN 2/3 samples

Figure 2. Reconstructed resistivity spectrum [Ω·m] for each category of cervical tissues (CIN stages)

The pathology reports for each sample were classified into three stages: Normal, CIN1, and CIN23. From the multiple data measured between several pairs of electrodes, we reconstructed resistivity at each operating frequency [3]. Figure 2 shows the average and two times standard deviation regions of resistivity spectra for samples grouped by each CIN stage. We extracted extracellular space resistance of R, intracellular space conductance of S, and the capacitance of C values when fitting the measured spectrum to the Cole-Cole model. Additionally, age and menopause data were collected. The classification algorithm was applied using the widely used Logistic Regression, Decision Tree, Random Forest techniques, and the measured values. All information, including impedance spectrum, Cole-Cole parameters, age, and menopause, were used for training each classification algorithm. And we applied separated data for verifying the developed classification models. Finally, the performance was compared and evaluated by extraction with a confusion matrix.

Results and Discussion

We proposed the multi-channel EIS system and probe with multiple active electrodes to screen cervical cancer using impedance spectroscopic measurement. The impedance measurement value for each CIN step was identified, and the frequency spectrum displayed differently for each pathology was calculated and confirmed. In addition, we were able to distinguish between Normal and CIN with our data using the classification algorithm, and meaningful results were obtained through the confusion matrix in Table.1.

	Logistic Regression	Decision Tree	Random Forest
Accuracy (%)	82.2	89.1	94.6
Sensitivity (%)	61.3	93.3	97.7
Specificity (%)	92.3	88.8	92.4
Precision (%)	79.4	82.3	89.8
F1-Score	0.69	0.87	0.93

Table 1. Performance evaluation of the classification algorithm using the sensitivity, specificity, accuracy, precision, and F1-Score.

From the results of various algorithms, we confirmed the contribution of each feature, accuracy, sensitivity, specificity and precision of each classification algorithm were evaluated. The F1 score with a value between 0 and 1 is a harmonic means of recall and precision, and the random forest algorithm showed the best performance among the three algorithms. In the future, we plan to measure more electrical and mechanical properties of tissue to improve the performance of screening devices. Multi-electrode screening probe-based bioimpedance spectroscopy is a promising cervical screening tool that is cost-effective, non-invasive, and real-time and advantageous, especially in developing countries. In the future, we expect to see and diagnose the suitability of the EIS system for clinical use as a screening tool.

Acknowledgements

This research was supported by Basic Science Research Program through the National Research Foundation of Korea (NRF) funded by the Ministry of Education (NRF-2020R1I1A1A01066649), and the National Research Foundation of Korea (NRF) grant funded by the Korea government (NRF-2020R1A2C1008975 and NRF 2019R1A2C1086807).

References

1. P. A. Cohen, A. Jhingran, A. Oaknin, and L. Denny, “Cervical cancer”, The Lancet, 393(10167), 169-182 (2019)
2. M. H. Mayrand, E. Duarte-Franco, I. Rodrigues, S. D. Walter, J. Hanley, A. Ferenczy, and E. L. Franco, “Human papillomavirus DNA versus Papanicolaou screening tests for cervical cancer”, N. Engl. J. Med, 357(16), 1579-1588 (2007)
3. D. C. Park, "Electrical bioimpedance spectroscopy based multi-electrode screening probe for the identification of cervical intraepithelial neoplasia (CIN).", Gynecologic Oncology 159, 356 (2020)

Voluntary cough detection from microphone signals with machine learning algorithms

Sang-Ho Han [1], Nam-Gyun Kim [2] and Mun-Ho Ryu [3,4]

[1]Department of Healthcare Engineering, Jeonbuk National University, Korea

[2] Research Center, Color Seven Co. Ltd., Korea

[3]Division of Biomedical Engineering, Jeonbuk National University, Korea

[4]Research Center of Healthcare & Welfare Instrument for the Aged, Jeonbuk National University, Korea

mhryu@jbnu.ac.kr

Abstract

Cough frequency and severity of cough provide useful information for the diagnosis of upper respiratory diseases. In this study, a cough detection method from microphone signals microphone is proposed. Voluntary cough signals and non-cough signals such as rest state, throat clearing, and speaking were collected from health subjects. Various tabular algorithms (a convolution neural network with 40 Mel-frequency cepstral coefficients (MFCCs) and a recurrent neural network with 40 MFCCs) and time-series algorithms (a random interval decision tree, random interval spectral forest, and random convolution kernel transform)) were applied and compared.

Background

Cough frequency and severity of cough provide useful information for the diagnosis of upper respiratory diseases [1]. The gold standard method for counting coughs is to count cough sounds from audio recordings manually [2], but this method is subjective, labor-intensive and time-consuming. Regarding the sensor types, most of the studies used audio signals [3] or accelerations signals [4]. Also, most of these studies used algorithms specialized for tabular data even though cough signals are time-series. Recently, time-series machine learning algorithms have been introduced in various fields [5]. In this study, a cough detection method from microphone signals. Voluntary cough signals and non-cough signals such as rest state, throat clearing, and speaking were collected from health subjects. Various tabular algorithms (a convolution neural network with 40 Mel-frequency cepstral coefficients (MFCCs) and a recurrent neural network with 40 MFCCs) and time-series algorithms (a random interval decision tree, random interval spectral forest, and random convolution kernel transform)) were applied and compared.

Methods

Data acquisition system

A sensor board with a microphone sensor (SPH0645LM4H, 18-bit, I2S, 3.50 x 2.65 x 0.98 mm^3, Knowles, IL) was used to capture acoustic signals (Figure 1). The captured microphone signals were read by a processor board (Adafruit Feather M0 Adalogger, ARM Cortex M0 processor, 48 MHz, 51 x 23 x 8 mm^3, Adafruit Industries LLC, NY) and transmitted to a PC at 4000 Hz.

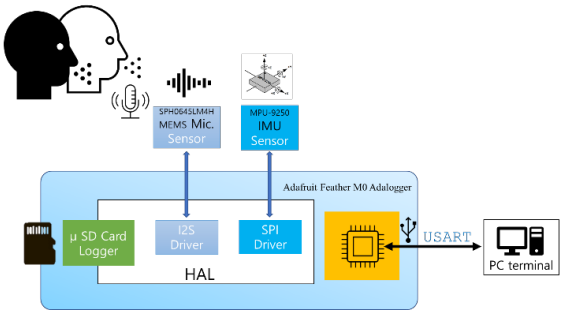
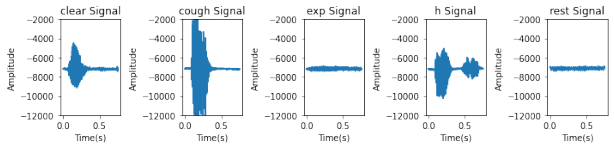


Figure.1 System block diagram

Microphone signals were collected from ten healthy subject. The microphone board was attached to the subject's thorax. Regarding the signal classes, voluntary cough (“cough”) and non-cough signals such as clearing the throat (“clear”), expiration (“exp”), pronunciation of alphabet H (“h”), and resting (“rest”) were considered.

Data preparation

Each sample was collected for 2 s with 4,000 Hz (Figure 2). Each collected sample with 8,000 points were segmented into 3,000 points automatically and trimmed manually if necessary.



Time-series methods

Random interval forest method: this method split the time-series data into random intervals, extract features (mean, standard deviation, and slope), and a decision tree is trained.

RISE method: the random interval spectral forest (RISE) is similar to the random interval forest methods but uses a single time series interval per tree and uses spectral features instead of summary statistics.

ROCKET method: the random convolution kernel transform (ROCKET) randomly generates a great variety of convolution kernels and extracts two features for each convolution. ROCKET uses various many kernels to capture patterns at different frequencies and scales.

ANN methods

CNN (convolution neural network): a convolution layers with 40 kernels and another layer with 20 kernels were stacked and max-pooled with a pooling size of 2. After that, a drop-out layer with a ratio of 0.4 was applied to prevent over-fitting during training. 40 Mel-frequency cepstral coefficients (MFCCs) with window length 1,024 and hop length 256 were used as features.

LSTM (long short-term memory): two LSTM layers with 100 units were stacked and a drop-out layer with a ratio of 0.4 was applied to prevent over-fitting during training. 40 Mel-frequency cepstral coefficients (MFCCs) with window length 1,024 and hop length 256 were used as features.

Results and Discussion

The applied algorithm showed different performances (Table 1). The ROCKET showed the best classification accuracy (98.00%), and the CNN showed the second best accuracy (97.40%). The LSTM and the Random interval forest showed similar performances. The RISE showed the lowest accuracy (83.56%).

Table 1. The algorithm performances

algorism	accuracy (%)
Random interval forest	92.53
RISE	83.86
ROCKET	98.00
CNN	97.40
LSTM	94.40

References

1. Morice A. Fontana GA, Sovijarvi AR, Pistolesi M, Chung KF, Widdicombe J, O'Connell F, Geppetti P, Gronke L, De Jongste J, Belvisi M, Dicpinigaitis P, Fischer A, McGarvey L, Fokkens WJ, Kastelik J. The diagnosis and management of chronic cough. Eur Respir J 2004; 24: 481-492.
2. Hall JI, Lozano M, Estrada-Petrocelli L, Birring, S., & Turner, R. The present and future of cough counting tools. J Thorac. Dis. 2020; 12: 5207.
3. Birring S, Fleming T, Matos S, S., Raj, A. A., Evans, D. H., & Pavord, I. D. The Leicester Cough Monitor: preliminary validation of an automated cough detection system in chronic cough. Eur Respir J 2008; 31: 1013-1018.
4. Mohammadi H, Samadani A-A, Steele C, Chau, T. Automatic discrimination between cough and non-cough accelerometry signal artefacts. Biomed Signal Processing and Control. 2019; 52: 394-402.
5. Löning M, Bagnall A, Ganesh S, Kazakov, V., Lines, J., & Király, F. J. sktime: A unified interface for machine learning with time series. arXiv preprint arXiv:190907872 2019.

Comparison of Stroke Volume Variations for Sleep Respiratory Events within Overnight Polysomnography using EIT monitoring

Tae Wook Chang [1,2] and Tong In Oh [1, 2, 3]

[1] Department of Medical Engineering, Graduate School, Kyung Hee University, Seoul, Korea

[2] Impedance Imaging Research Center, Kyung Hee University, Seoul, Korea

[3] Department of Biomedical Engineering, College of Medicine, Kyung Hee University, Seoul, Korea

tioh@khu.ac.kr

Abstract

Patients with obstructive sleep apnea (OSA) demonstrate both acute and chronic hemodynamic changes due to their disease. We continuously monitored the stroke volume (SV) from EIT images when the overnight polysomnography of eight OSA patients. Percentile changes of SV were processed and analyzed during and after each of six different sleep breathing disorder events with reference to the mean SV in the pre-event. Apnea and arousal hypopnea cases produced the large SV increment after finishing the event. We required additional research to observe and index the hemodynamic changes for various sleep breathing disorders using the non-invasive monitoring method.

Background

OSA (Obstructive Sleep Apnea) is a phenomenon in which airflow is reduced or temporarily suspended due to occlusion around the upper airway during sleep [1]. The repetitive respiratory events that characterize OSA are followed by abrupt increases in heart rate and pulmonary and systemic artery pressure and sudden decreases in right and left ventricular stroke volume [2]. Because of these dramatic hemodynamic oscillations during sleep, many clinicians and investigators have postulated a connection between sleep-disordered breathing and cardiovascular morbidity and even mortality [3]. Although knowledge of the hemodynamic consequences of sleep apnea has grown in recent years, much remains to be studied using non-invasive hemodynamic monitoring methods.

Overnight polysomnography (PSG) is used as the standard method to diagnose and evaluate the severity of OSA [4]. It could detect a variety of sleep respiration disorders such as apnea and hypopnea during sleep. However, it could not include measurements for hemodynamics because there is no proper non-invasive monitor. Recently, the Electrical Impedance Tomography (EIT) device successfully presented the capability of measuring beat-to-beat stroke volume (SV) during varying volume states [5]. In this study, we continuously monitored SV changes during the overnight polysomnography (PSG) using an AirTom-R device (BiLab, Korea), as shown in Figure 1, which produces 100 frames per second. The change in SV at each category of sleep breathing disorder events was evaluated with reference to the SV just before the event, and we additionally observed the change in SV after finishing the event.

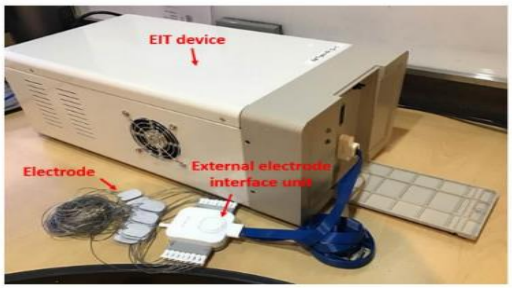


Figure 1. AirTom-R system for monitoring of SV.

Methods

Simultaneous measurements of PSG and EIT were performed on eight male subjects aged from 19 to 75 years old with IRB approval (no. 2021-09-022) from Kyung Hee University Medical Center. As summarized in Table 1, all participants in the experiment were OSA patients with an apnea hypopnea index (AHI) of 5 or higher. We determined the period and type of event for the following six types of sleep breathing disorder from PSG results - the flow limitation (FL), respiratory effort related arousal (RERA), arousal hypopnea (H*a*), arousal &

desaturation hypopnea (H*ad*), desaturation hypopnea (H*d*) and apnea (A).

We separately calculated the percentile difference between the mean of SV from 20 consecutive heartbeats before and after each specific sleep breathing disorder event. If there are less than 20 beat-to-beat SVs for each pre-event and post-event section, that section was excluded from the analysis. Within the event section, the average SV was computed using all detected beat-to-beat SVs. Additionally, we calculated the percentile SV change during events with reference to the mean SV obtained at the pre-event period. Statistical difference between the percentile changes of the mean SV for each section was analyzed using the paired t-test to present the variation of hemodynamics due to respiratory sleep disorders.

Table 1. Sleep respiratory events from PSG analysis.

No	Age	BMI	FL	RERA	Hypopnea				Apnea				Total	AHI
					Ha	Hd	Had	All	OA	MA	CA	All		
1	38	37.4	4	3	13	24	17	54	549	3	2	554	615	89.9
2	65	23.0	67	12	60	32	75	167	31	17	0	48	294	35.5
3	68	27.5	7	32	27	7	157	191	59	0	0	59	289	58.9
4	67	24.0	2	7	19	5	13	37	91	14	0	105	151	32.9
5	35	26.0	66	67	87	11	31	129	3	0	0	3	265	22.5
6	48	29.7	23	11	45	53	145	243	75	0	0	75	352	53.0
7	19	27.9	31	33	23	14	18	55	0	0	0	0	119	6.4
8	24	27.4	7	2	23	89	215	327	151	1	0	152	488	80.2

Results and Discussion

Figure 2 graphically presents the relative percentile change in mean SV for the six types of sleep breathing events mentioned earlier. We observed noticeable SV increments after apnea and arousal hypopnea (Ha) events. These were expected to be the effect of arousal. However, interestingly, in the case of Had, the SV did not increase relatively much. Figure 2 graphically presents the relative percentile change in mean SV for the six types of sleep breathing disorder events mentioned earlier. From the results, the SV was significantly decreased during the apnea event. In addition, we observed noticeable SV increments after apnea and arousal hypopnea (Ha) events. These were expected to be the effect of arousal. However, interestingly, in the case of Had, the SV did not increase relatively much. In the three different types of hypopnea, the increases in SV were different after finishing the event. However, in the cases of FL and RERA, there were no differences in SV due to events. We need to examine the stroke volume and blood pressure changes due to the obstructive and central apneas including other sleep breathing disorder events.

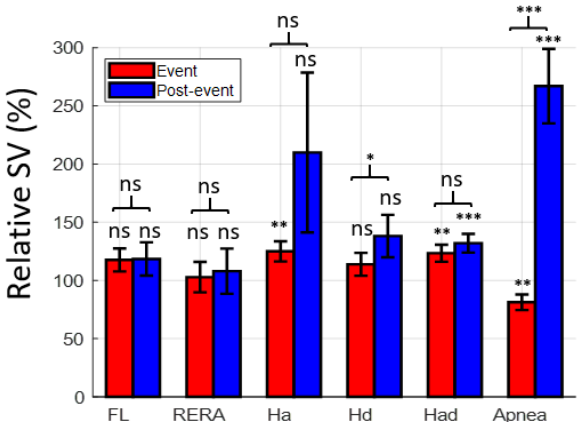


Figure 2. Relative percentile changes of stroke volume during and after sleep respiratory events with reference to the mean SV in the pre-event. (ns: no difference, *: $p < 0.05$, **: $p < 0.01$, ***: $p < 0.001$)

Acknowledgements

This work was supported by a grant from the Industrial Strategic Technology Development Program (20006024) funded by the Ministry of Trade, Industry & Energy (MOTIE) in Korea and the National Research Foundation of Korea (NRF) grant funded by the Korea government (NRF-2020R1A2C1008975).

References

[1] W. W. Flemons. "Obstructive sleep apnea", New England Journal of Medicine 347(7), 498-504 (2002).

[2] J. W. Weiss, S. Remsburg, E. Garpestad, J. Ringler, D. Sparrow, and J. A. Parker. "Hemodynamic consequences of obstructive sleep apnea", Sleep 19(5), 388-397 (1996).

[3] J. W. Weiss, S. H. Launois, A. Anand, and E. Garpestad. "Cardiovascular morbidity in obstructive sleep apnea", Progress in cardiovascular diseases 41(5), 367-376 (1999).

[4] C. H. O'CONNOR, K. S. Thornley, and P. J. Hanly. "Gender differences in the polysomnographic features of obstructive sleep apnea", American journal of respiratory and critical care medicine 161(5), 1465-1472 (2000).

[5] R. E. Ko, G. Y. Jang, C. R. Chung, J. Y. Lee, T. I. Oh, G. Y. Suh, Y. M. Kim, and E. J. Woo. "Noninvasive beat-to-beat stroke volume measurements to determine preload responsiveness during mini-fluid challenge in a swine model: A preliminary study." Shock 56(5), 850-856 (2021).

Simulation study of a channel reduction method for continuous depth-of-interaction measurements using single-ended readout

Minseok Yi[1,2,3*], Jae Sung Lee[1,2,3,4]

[1]Interdisciplinary Program in Bioengineering, Seoul National University College of Engineering, Seoul 03080, Korea

[2]Integrated Major in Innovative Medical Science, Seoul National University College of Medicine, Seoul 03080, Korea

[3]Department of Nuclear Medicine, Seoul National University College of Medicine, Seoul 03080, South Korea

[4]Brightonix Imaging Inc., Seoul 04782, South Korea

[*]minseok0408@snu.ac.kr

Abstract

A feasibility study for readout channel reduction in single-ended continuous DOI (cDOI) encoding method using triangular teeth-shaped reflector strips and a silicon photomultiplier (SiPM) array was conducted based on GATE Monte Carlo optical simulation. In this study, we successfully demonstrated that the variation estimation circuit in conjunction with symmetric charge division network can be applied to the cDOI PET detector development without noticeable degradation in DOI encoding performance and with significantly reduced readout channel number.

Background

Depth of interaction (DOI) estimation availability in Positron Emission Tomography (PET) detector has become an indispensable factor for the enhancement of spatial and timing resolutions by correcting parallax error. Recent research interest has been given to DOI encoding with single-ended readout using crystal scintillators coupled to silicon photomultiplier (SiPM) pixels in favor of cost reduction and electronics simplicity [1,2].

Our group proposed and conducted a proof-of-concept prototype PET system investigation using cost-effective single-ended continuous DOI (cDOI) estimation method based on a single-layer pixelated crystal optically coupled to digital SiPM and triangular teeth-shaped reflector strips (Figure 1) [3,4]. However, when using analog SiPM arrays, it is necessary to introduce additional channel reduction strategy in front-end circuit level to scale it up to system level.

Therefore, in this study, we conducted simulation investigation of the possibility of electronic readout channel reduction using symmetric charge division (SCD) circuit network integrated with variation estimation circuit. The variation estimation circuit was simply configured with 1-dimensional charge division circuit (1D-CDC) and an operational amplifier voltage adder [5]. The method worked outstandingly in terms of channel reduction with negligible difference in DOI estimation performance comparing to the conventional simple SCD method.

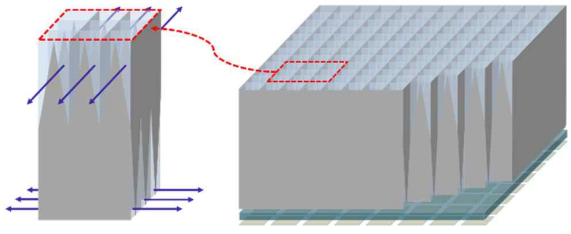


Figure 1. cDOI detector configuration

Methods

1) Detector design and simulation

The GATE Monte Carlo simulation toolkit was used to simulate the light spreading method using crossed triangular teeth-shaped reflector strips. With such design of reflector strips used, the optical photons generated by a scintillation event can only disperse through the partially uncovered surfaces of the crystals. Hence, the interaction position in the z-direction can be estimated using different light dispersion patterns along the x-, and y- direction of the photon detector array.

The simulated detector consisted of a 12×12 array of unpolished LSO crystals (2 mm×2 mm×20 mm, 2.1 mm pitch) optically coupled to an 8×8 SiPM array that features a 3.2 mm sensor pitch. An epoxy lightguide of 0.1 mm thickness was inserted between the crystal array and the SiPM for more effective light dispersion. A light yield of LSO crystal and the quantum efficiency of the SiPM were assumed to 30000 photons per MeV and 50 %, respectively. During the optical simulation, the optical photons were assumed to be reflected with a reflectivity of 98 % on the surfaces of the reflectors defined using the UNIFIED model.

2) Readout circuit design and analytical modeling

The simultaneous computation of the first and the second moments of the projected light distribution was realized by a modified symmetric charge division (SCD) circuit network (Figure 2(a)). The modified SCD network was constructed by feeding the symmetrically divided output current from each SiPM anodes into a 1-dimensional charge division circuit (1D-CDC), whose each nodes are also consequently fed into a summing amplifier.

While the modification in SCD network being made, the circuit components have to meet few constraints. First, the anode charge divider resistor R_L should be sufficiently larger than the CDC resistor R_D so that the summed current does not flow backward to the SCD network. Second, it is preferable to utilize current sense amplifiers (CSA) at the both ends of the 1D CDC resistor chain while a voltage sense amplifier (VSA)

should be used as at the summing stage. Along with that, the summing resistor R_S should also be larger enough than R_D to keep the summation circuit from extracting too much current. With the constraints met, the modified SCD circuit network can be analytically modeled as Eq 1~10 using Kirchoff theorems and superposition. All notations are as denoted in (Figure 2(b)) and $U_{i,k}$ refers to the voltage caused by the current J_i at position k. The index i was shifted from 1, 2, …8 to -7/2, -5/2, …7/2 for the sake of symmetry of the equations.

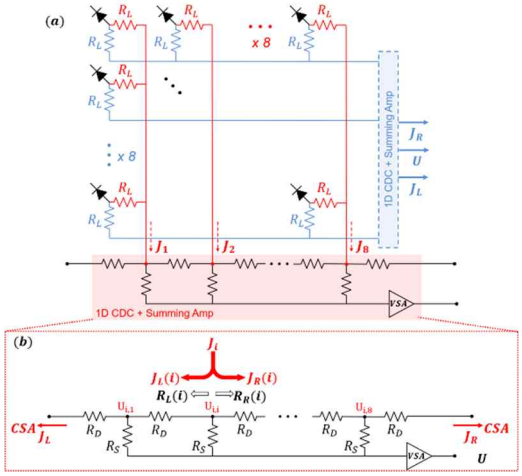


Figure 2. (a) Circuit Diagram (b) Circuit Notations

$$R_{L,R}(i) = \left(\frac{n+1}{2} \pm i\right) R_d \quad \text{(Eq.1)}$$

$$J_{L,R}(i) = J_i\left(\frac{R_{R,L}(i)}{(n+1)R_d}\right) = J_i\left(\frac{1}{2} \mp \frac{i}{n+1}\right) \quad \text{(Eq.2)}$$

$$J_{L,R} = \sum_i J_{L,R}(i) = \sum_i J_i\left(\frac{1}{2} \mp \frac{i}{n+1}\right) \quad \text{(Eq.3)}$$

$$\frac{J_R - J_L}{J_R + J_L} = \frac{\sum_i J_i \frac{2i}{n+1}}{\sum_i J_i} = \frac{2}{n+1}\frac{\sum_i i J_i}{\sum_i J_i} \quad \text{(Eq.4)}$$

$$\langle i \rangle = \frac{n+1}{2} \cdot \left(\frac{J_R - J_L}{J_R + J_L}\right) \quad \textbf{(Eq.5)}$$

$$U_{i,i} = J_i \frac{R_d}{n+1}\left(\left(\frac{n+1}{2}\right)^2 - i^2\right) \quad \text{(Eq.6)}$$

$$U_i = \sum_k U_{i,k} = U_{i,i}\left(\frac{n+1}{2}\right) \quad \text{(Eq.7)}$$

$$U = \sum_i U_i = \sum_i J_i \frac{R_d}{n+1}\left(\left(\frac{n+1}{2}\right)^2 - i^2\right)\left(\frac{n+1}{2}\right) \quad \text{(Eq.8)}$$

$$\langle i^2 \rangle = \left(\frac{n+1}{2}\right)^2 - \frac{2U}{R_d(J_R + J_L)} \quad \textbf{(Eq.9)}$$

$$\sigma^2 = \langle i^2 \rangle - \langle i \rangle^2 = \left(\frac{n+1}{2}\right)^2 \left\{1 - \left(\frac{J_R - J_L}{J_R + J_L}\right)^2 - \frac{8U}{R_d(n+1)^2(J_R + J_L)}\right\} \quad \textbf{(Eq.10)}$$

Results and Discussion

Figure 3(a) and (b) show representative variation difference histogram and 2-dimensional variance scatter plot calculated with the optical simulation and the analytically modeled modified SCD circuit network, respectively. The DOI resolution was calculated by averaging full width half maximum of the variance difference histogram for each irradiation depth and was estimated to be 1.37 mm and 1.84 mm at the center and the edge of the detector, respectively. An exceptionally linear relationship between calculated variation difference and DOI is shown in Figure 3(c). Figure 3(c) also comparatively shows DOI estimation linearity performance using conventional SCD network and the modified SCD network in which 8 + 8 = 16 and 3 + 3 = 6 output channels are needed, respectively. Two methods yield almost same result showing that an effective channel reduction has been achieved without performance degradation.

The cDOI method takes advantage of the difference in light dispersion among crystals and because the most outer surface

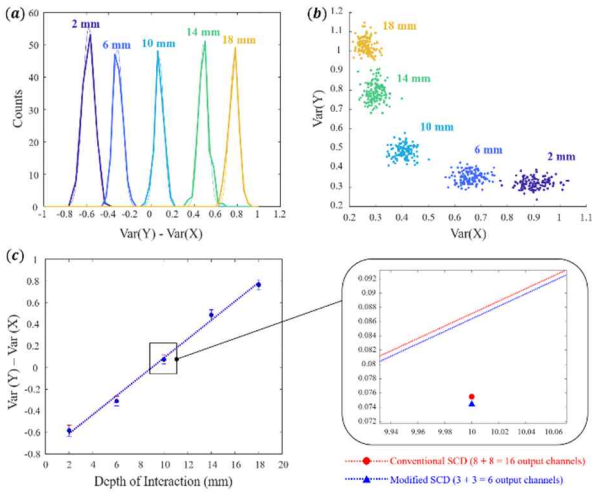


Figure 3. (a) Calculated Variance Difference Histogram (b) 2D Variance map (c) Calculated Variance Difference (Conv-SCD & Mod-SCD) vs. DOI

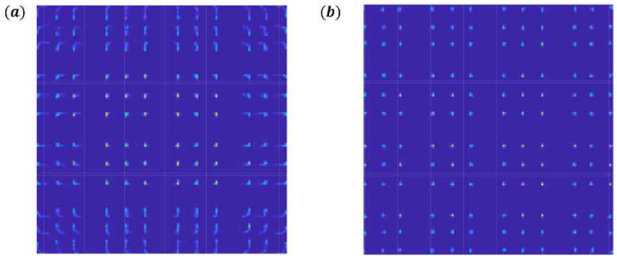


Figure 4. (a) Flood map before DOI compensation
(b) Flood map after DOI compensation

of the crystal array is completely enclosed with reflective materials, more light reflection at the detector periphery brings positional shift of the crystal peak position depending on the DOI position (Figure 4(a)). Therefore, the DOI information achieved from the light dispersion variance was used to quantize the 3D flood map into 5 layers with DOI of 0mm ~ 4 mm, 4 mm ~ 8mm, 8 mm ~ 12 mm, 12 mm ~ 16 mm, and 16 mm ~ 20 mm, respectively. Consequently, the 5 layers were aligned with the middle layer based on the average centroid position of each layer at each crystal. All crystals in 12×12 array were clearly separated (Figure 4(b)).

Acknowledgements

This work was supported by grants from the National Research Foundation of Korea (NRF) funded by the Korean Ministry of Science and ICT (Grant No. 2020M2D9A1093989) and Sunway Medical Center.

References

[1] Pizzichemi M et al. 2016 A new method for depth of interaction determination in PET detectors, Phys. Med. Biol. 61 4679

[2] A. LaBella et al. 2019 Prism Mirror Light Guide for Enhanced Gamma Ray Localization in PET IEEE Nuclear Science Symposium and Medical Imaging Conference (NSS/MIC), pp. 1-4

[3] Ito M et al. 2013 Continuous depth-of-interaction measurement in a single-layer pixelated crystal array using a single-ended readout Phys. Med. Biol. 58 1269–82

[4] M. S. Lee et al. 2017 Prototype pre-clinical PET scanner with depth-of-interaction measurements using single-layer crystal array and single-ended readout, Phys. Med. Biol., vol. 62, no. 10, pp. 3983-3996

[5] Lerche C W et al 2005 Depth of gamma-ray interaction within continuous crystals from the width of its scintillation light-distribution IEEE Trans. Nucl. Sci. 52 560-72

P-042

Detection of left ventricular hypertrophy from multi-lead ECG signal using artificial neural network

Jiseung Ryu[1], Yerin Lee[1], Sena Lee[1], Youngjun Park[2], Solam Lee[3,4*], Sejung Yang[1*]

Department of Biomedical Engineering, Yonsei University, Wonju, Republic of Korea[1]

Department of Internal Medicine, Yonsei University Wonju College of Medicine[2]

Department of Dermatology and Institute of Hair and Cosmetic Medicine, Yonsei University Wonju College of Medicine, Wonju, Republic of Korea[3]

Department of Preventive Medicine, Yonsei University Wonju College of Medicine[4]

fbwkdrns77@yonsei.ac.kr, yerin001@hotmail.com, bluesky9707@naver.com,

pyj@yonsei.ac.kr, solam@yonsei.ac.kr, syang@yonsei.ac.kr

Abstract

Initial diagnosis of Left Ventricular Hypertrophy (LVH), a risk factor for cardiovascular disease, is important. LVH diagnostic methods using electrocardiogram have been studied, but classification performance has been low. Conventional diagnostic methods and machine learning algorithms do not perform well in LVH diagnosis. However, deep learning-based algorithms compensate for these shortcomings and show the possibility of good performance. In our study, we develop an algorithm that can diagnose LVH using deep learning-based algorithms and Electrocardiogram (ECG).

Background

Recently, as people's tastes have become westernized, the increase in nutritional imbalance due to changes in diet and excessive stress are considered major factors in the occurrence of various diseases. In particular, overloaded blood vessels and high blood pressure led to changes in the myocardium and an increase in the inner wall of the left ventricle.[1] As a result, the prevalence of Left Ventricular Hypertrophy (LVH) was increased. LVH is a risk factor for cardiovascular diseases such as heart failure and arrhythmia, and is one of the causes of increased mortality rate. Since it is the earliest stage of heart change caused by hypertension, the importance of LVH diagnosis is emphasized.[2]

Currently, Chest PA (X-ray), Computed Tomography (CT), Magnetic Resonance Imaging (MRI), and Echocardiography are being performed to diagnose LVH in clinical trials. Echocardiography is the most accurate method among LVH diagnostic methods [3], However, there are limitations in universal use due to high cost and long waiting time. Another diagnostic method, CT, also has a high-test cost problem and a risk of radiation exposure. In order to solve the above problem, an LVH diagnosis method using Electrocardiography (ECG) has been studied. ECG is a simple, non-invasive, and economical test method that is most commonly used in primary care. Previous studies have proposed several diagnostic criteria, such as Sokolow Lyon, Cornell, and Framingham criteria, to identify LVH. Since the diagnostic criteria were based only on changes in the QRS voltage of ECG, the rate of agreement between actual LVH and diagnostic findings was low. Demographic features such as gender, age, and BMI are also known to affect QRS voltage.[4] Therefore, a diagnostic model using Machin Learning (ML) was also studied, but the classification results were low.[5] These days, convolutional neural networks and deep learning (DL) algorithms using accumulated big data are in the spotlight.[6] It learns and analyzes the given information by itself to automatically extract the features necessary for image classification. DL algorithms complemented the shortcomings of ML techniques that relied on existing algorithms and achieved state-of-the-art performance in extensive classification identification tasks in the medical field. In this study, we developed neural networks to diagnose LVH using ECG. Here, we compared the classification results according to gender and developed neural networks considering gender and age.

Methods

This study included ECG acquired in Yonsei University Wonju Severance Christian Hospital, Wonju, Korea from October 2010 to February 2020. The recorded electrocardiogram was 8-Lead(I,II,V1,V2,V3,V4,V5,V6), and 4-Lead(III,aVF,aVR,aVL) was added through vector calculation. The sampling rate was recorded at 500 Hz for 10 seconds. The signal used in the experiment consisted of 5000 samples, and signal processing such as normalization or noise reduction was not performed.

The value obtained by dividing the LV mass index measured during the patient's echocardiography by the body surface area (BSA) was used on the label. If one patient

underwent echocardiography several times, an initial label was used. Based on the echocardiography measurement date, the ECG recorded within 31 days before and after was found and matched with the label. Data were classified into four classes through measurement values and classification criteria. Each data was classified as LVH when the echocardiography value was higher than 117 g/m^2 for male and higher than 101 $g/m^2$for female. All LVH data were labeled as 1 and normal data were labeled as 0. In order to guarantee uniformity of model during learning procedure, the four classes were under-sampled based on the smallest class, 'Moderately ordinary'. As a result, a uniform dataset

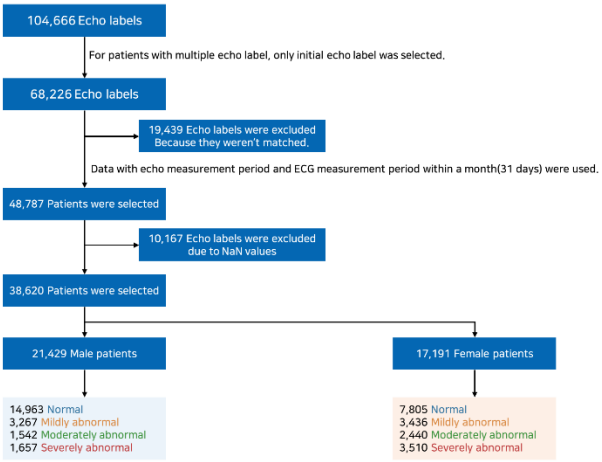


Figure 1. A study flowchart

of 6,168 male data and 9,760 female data was obtained. For all experiments conducted, the training set, validation set, and test set were divided at a ratio of 4:3:3. Division of dataset was performed on a patient basis to prevent overlapping personnel between datasets.

	Male				Female			
	Normal range	Mildly abnormal	Moderately abnormal	Severely abnormal	Normal range	Mildly abnormal	Moderately abnormal	Severely abnormal
LVH Criteria								
LV mass index by BSA 2D	<102	103-116	117-130	>130	<88	89-100	101-112	>112
Data composition								
No. of unique patients	14,963	3,267	1,542	1,657	7,805	3,436	2,440	3,510
Mean (SD)	85.27 (14.41)	108.73 (3.97)	122.66 (4.07)	155.08 (45.68)	73.37 (13.02)	94.07 (3.43)	106.08 (3.40)	134.35 (30.77)

Table 1. Data characteristics

In this study, a total of three experiment was conducted. The first experiment was conducted with male patient data, the second experiment was conducted with female patient data, and the last experiment was conducted with all data. In the last experiment, gender and age of the patient were added to the dataset. The performance of three types of CNN models was compared in each experiment. LeNet, one of the basic models used in the image classification field, was used as the first CNN model. The encoder part of image segmentation model U-Net was used as the second CNN model. The last CNN model, ResNet, maintains the original information using short cut connection even though the depth of the model gets deeper. The layers of all three models were adjusted to learn electrocardiogram in our dataset. The first model is composed of 16 layers, the second model is composed of 40 layers, and the last model is composed of 188 layers. The number of output nodes in all models was designed to be two. Cross entropy loss was used as the loss function of the model. Adam optimizer was used with 0.001 of learning rate for 50 epochs. The maximum size that each model could allocate to over NVIDIA GeForce RTX 2080Ti was used as a batch size. Pytorch was used as the framework for model learning.

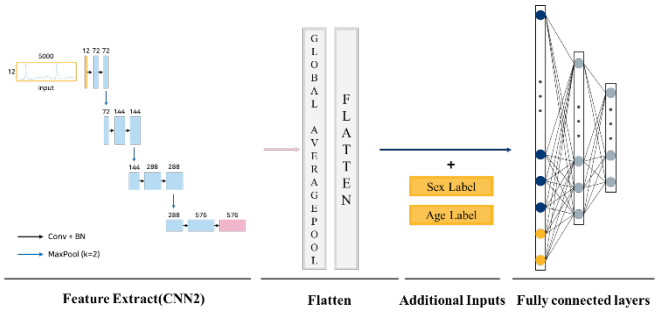


Figure 2. Overview of experiment 3 using CNN2

The area under the receiver operating characteristics curve (AUROC) was used as the main result of the classification model. AUROC, accuracy, sensitivity, specificity, positive prediction value (PPV) and negative prediction value (NPV) were measured using optimal cutoff calculated by Youden index.

Results and Discussion

Figure 3 and Table 2 show the results of CNN models learned with ECG datasets. CNN models that learned only male data showed AUROC of 0.736-0.748. On the other hand, CNN models that learned only female data showed relatively high AUROC of 0.829-0.853. Since the amount of male data were smaller than female data in moderately abnormal class, the classification result was relatively lower in male data. CNN models that learned the entire gender showed AUROC of 0.886-0.913, which is best result of all three experiment. This seems to indicate adding gender and age information had a positive effect on classification. Overall, sensitivity and PPV showed higher values than specificity and NPV. The second model showed highest results among three models in all experiments.

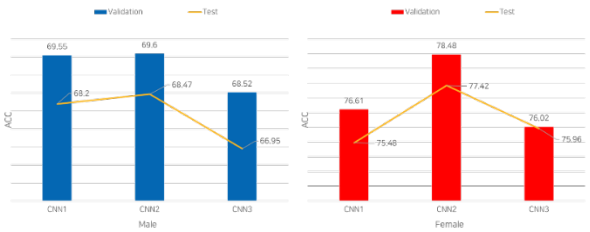


Figure 3. Comparing the performance of experiment1 and experiment2

Several studies reported LVH diagnostic criteria and analysis models but not shown high classification results. Some studies suggested diagnostic models that utilize ECG features and demographic information together. Through this study, we confirmed that the CNN model has a possibility to diagnose LVH using only ECG, gender, and age information.

	Model Performance						
	Val ACC	Test ACC	AUROC	Sensitivity	Specificity	PPV	NPV
Male							
CNN1	65.55%	68.20%	0.7364	61.88%	74.51%	70.83%	66.16%
CNN2	69.6%	68.47%	0.7480	65.87%	71.06%	69.48%	67.56%
CNN3	68.52%	66.95%	0.7393	54.10%	79.80%	72.82%	63.49%
Female							
CNN1	76.61%	75.48%	0.8293	77.04%	74.05%	72.96%	78.02%
CNN2	78.48%	77.42%	0.8539	82.93%	72.43%	73.21%	82.36%
CNN3	76.02%	75.96%	0.8418	80.99%	71.38%	72.00%	80.51%
All genders + Demographic features							
CNN1	83.7%	81.63%	0.8944	85.74%	75.83%	83.36%	79.02%
CNN2	85.27%	84.67%	0.9137	89.53%	77.80%	85.06%	84.03%
CNN3	82.3%	81.86%	0.8867	89.85%	70.59%	81.18%	83.13%

Table 2. Performance metrics

However, it was difficult to confirm the performance of male data due to insufficiency of the male data. The male heart is larger than the female heart, resulting in a significant change in QRS amplitude. Since there is a possibility of increase in classification performance of male data, verification using additional dataset is required. In addition, only a single data source was used in this study and thus external validation was not performed. Many neural network models do not reach same performance on external datasets obtained from different environments. Verification using additional dataset should be conducted for better generalization.

Acknowledgements

This research was supported by the 'BK21 FOUR (Fostering Outstanding Universities for Research)' in 2021 (II21SS7606007).

References

1. SungHee Yang, JinSoo Lee, Changsoo Kim, “The Accuracy of Echocardiography and ECG in the Left Ventricular Hypertrophy”, The Korea Contents Association, Vol.16, Issue 2, Pages.666-672, 2016.
2. MinJung Cho, “Left Ventricular Hypertrophy and Prelude to Hypertensive Cardiovascular Diseases from the Pediatric Cardiologist’s Point of View”, the Korean society of pediatric nephrology, Vol.15, no.1, Pages14-21,2011
3. Devereux RB, Alonso DR, Lutas EM, Gottlieb GJ, Campo E, Sachs I et al., “Echocardiographic assessment of left ventricular hypertrophy: comparison to necropsy findings.”, Am J Cardiology, Vol.57, issue 6, Pages 450-458, 1986.
4. Rider OJ, Ntusi N, Bull SC, Nethononda R, Ferreira V, Holloway CJ et al., “Improvements in ECG accuracy for diagnosis of left ventricular hypertrophy in obesity.”, BMJ Heart, Vol.120, issue 19, Pages 1566-72, 2016
5. Fernando De la GS, Maria Elena RI, Elias Abraham RD, et al., “Improvement of electrocardiographic diagnostic accuracy of left ventricular hypertrophy using a Machine Learning approach”, PLoS One, 2020 May 13;15(5): e0232657.
6. JoonMyoung Kwon, KiHyun Jeon, HyueMee Kim, MinJeong Kim, et al., “Comparing the performance of artificial intelligence and conventional diagnosis criteria for detecting left ventricular hypertrophy using electrocardiography”, EP Europace, Vol.22, issue 3, Pages 412-419, 2020

A study on open-anode bio-electrochemical system for energy harvesting from solid biomass

Jonghoon Lim [1] and Yoonseok Yang [1,2]

[1]Department of Healthcare Engineering, Jeonbuk National University

[2]Division of Biomedical Engineering, Jeonbuk National University

[1]**hun6949@gmail.com,** [1,2]**ysyang@jbnu.ac.kr**

Abstract

Microbial Fuel Cell (MFC) can produce electrical energy by decomposing organic waste. Most MFCs take liquid organic waste and therefore, need extra pretreatment for extraction of liquid from mixed waste. However, there are abundant solid biomass which could provide large electricity if harvested properly. This study proposed an open-anode MFC which can be installed in a biomass-rich environment so that it can generate electricity by freely contacting organic matter in surroundings, and supporting eco-system favorable to the survival and activation of exo-electrogenic microorganisms. A prototype of Tubular-type open-anode air-cathode MFC (T-MFC) was developed and tested by using vermicompost medium. The experimental results proved not only its feasibility and easy-installation but also the advantage of its open-anode structure for energy harvesting from solid biomass by allowing the biologic environments favorable to microorganisms.

Background

Microbial Fuel Cell (MFC) utilizes microorganisms to decompose organic matter, and to produce electricity. Though there are plenty of solid organic waste around us such as biomass and food waste, studies using solid organic matter as its substrate have not been conducted as extensively as those using liquid organic matter as substrates. In this study, we proposed a Tubular-type open-anode air-cathode MFC (T-MFC) which can generate electricity by decomposing solid organic biomass when installed into biomass-rich environments.

Methods

It is important to maintain an environment favorable for the survival and activation of exo-electrogenic microbial species to improve the performance of MFC, especially for processing solid biomass. Since the microorganisms live interacting with their surrounding eco-system, the typical MFC structures which separate them from their own environment into enclosed anodic chamber with small inlet and outlet port only allowing liquid organic substrate have limited functionalities. Therefore, we designed and implemented a T-MFC which enables a direct contact between its anodic surface and surrounding environment full of microbial communities and variety of solid organic biomass. The microbial fuel cell used in this study has two cylindrical layers constructed by a 3D-printed frame as shown in Figure.1. In Figure.1(a), a cylindrical anodic surface is formed by attaching a carbon paper whose area is 263.76cm^2 and fits the outermost frame. Figure.1(b) shows PEM (Proton Exchange Membrane) and cathode (carbon paper with 20% Pt) which are attached together on the inner cylindrical frame to keep the cathodic space separate from outside for increased output electric power. The PEM and the cathode have the same area of 163.28cm^2. The innermost space is extended in axial direction to airway, which implements an air-cathode.

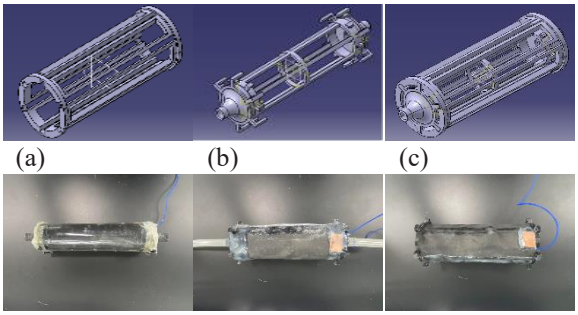


Figure 1. Development of T-MFC. (a) Anode frame, (b) PEM and cathode frame, (c) Assembled model, (d) Anode attachment,(e) PEM and cathode attachement with airway connected, (f) Assembled model

The surrounding environments of T-MFC contain microbial communities, organic biomass, and even bigger symbiotic organisms, such as earthworms[1]. Figure 2. shows the arrangement of the T-MFC for

experiment. Two identical T-MFC's were built and placed in the 2.5kg of vermicompost and 500ml of worm juice was inoculated in the medium to help the growth of a biofilm on the anodic surface prior to the experement. To explore the collaborating effect with the surrounding eco-system, earthworms were added to the T-MFC1 medium as shown in Figure.2, which simulated a natural living environments of the *geobacter* species[2].



Figure 2. Exploration of T-MFC performance in different surroundings

The output voltages were measured with different load conditions to analyze its characteristics and output performance. At earlier stages, open-circuit voltages (OCV) were measured until output stabilized. Then closed-circuit voltages (CCV) were measured with different dc resistance values (100 Ω, 200 Ω, 500 Ω, 1K Ω, 2K Ω, 5K Ω, and 10 K Ω). The data acquisition device (NI9215, National Instruments, USA) and the data acquisition software (LabVIEW-2009, National Instruments, USA) were used for recording of the measured data. Figure 3 shows the experimental setup.

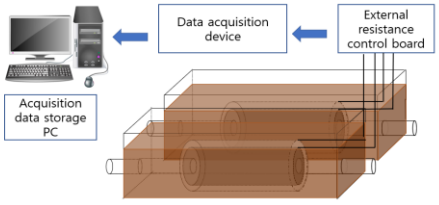


Figure 3. Experimental setup

Results and Discussion

Figure 4 shows the measured voltages of the T-MFC1 and T-MFC2 with various load conditions. Their I-V characteristics are also shown in Figure 5. The output voltages and powers shown in Figure 4 verify that the both T-MFC are capable of generating electricity by using solid biomass in the surrounding environment. Moreover, the higher voltage and power values of T-MFC1 prove the beneficial effect of collaborating with its surrounding allowed by the open-anode structure. The proposed T-MFC seems to support the symbiotic interactions between the exo-electrogenic microorganisms and their surroundings since it does not separate themfrom their eco-system.

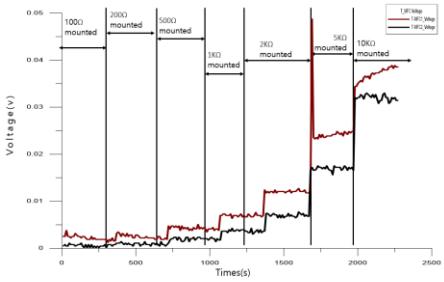


Figure 4. Output voltage of both T-MFCs under different load conditions

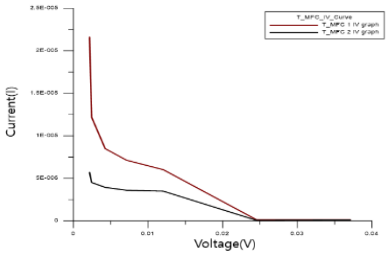


Figure 5. The I-V characteristics of both T-MFCs

The developed T-MFC verifed its feasibility of energy harvesting from solid biomass. The experimental results also showed that T-MFC is suitable for maintaining the favorable biologic eco-system of microorganisms and their interactions, which is important for significant improvement in bioelectrochemical technology.

Acknowledgements

This research was supported by Basic Science Research Program through the National Research Foundation of Korea (NRF), funded by the Ministry of Science and Technology Information and Communication. (NRF-2019R1F1A1061503).

References

[1] D. Thakuria, O. Schmidt, D. Finan, D. Egan, and F. M. Doohan, "Gut wall bacteria of earthworms: a natural selection process," The ISME journal, vol. 4, no. 3, pp. 357-366, November 2009

[2] S.Y Yoon, J.J. Yeo and Y.S. Yang, "Energy harvesting from food waste by inoculation of vermicomposted organic matter into Microbial Fuel Cell(MFC)," in Proc. of 2015 IEEE SENSORS, pp. 1-4, Busan, South Korea, November 2015

Multi-functional optical stimulation and imaging system for an ex-vivo verification

Seonghoon Jo[1] and Kyungsik Eom[1]

[1]Department of Electronics Engineering, Pusan National University, Busan, 46241 South Korea

jayjo2005@gmail.com

Abstract

Retinal prosthesis based on optical neural stimulation has been spotlighted due to its high spatial and temporal resolution. In this study, we designed a system to optically stimulate and image a sample at the same time. The proposed system used a digital micromirror device (DMD) based optical stimulation system to generate patterned stimulation light and shared optical path to optically stimulate and image simultaneously. This multi-functional optical stimulation and imaging system can serve as a neuromodulation and imaging tool for *ex-vivo* verification.

Background

In the medical and engineering fields, many attempts to restore vision are underway. Retinal prosthesis based on electrical stimulation is widely used to induce vision recovery by electrically stimulating the nerve, but it has a fundamental problem in that the electronic device needs to be implanted in the body, and the resolution is low since the electric charge spreads in the nervous tissue in three dimensions [1]. Retinal prosthesis based on optical neural stimulation has been spotlighted in stimulating targets due to its high spatial and temporal resolution. [2] Before the development of an optical artificial vision device for vision recovery, it is necessary to verify and optimize the optical neural interface technology *in vitro*. We developed a system for patterned light illumination and imaging the stimulated sample. A digital micromirror device (DMD) based illumination system and Köhler illumination system have been used for the optical stimulation and even illumination of the sample, respectively. The optical paths have been shared by using dichroic mirrors. We got the images of the 1954 USAF resolution test chart, fluorescence bead, and single-pixel stimulation light, and quantitatively evaluated them with MATLAB (Mathworks Inc.) and ImageJ (National Institute of Health, USA) to characterize our system.

Methods

Figure.1 shows a schematic of the multi-functional optical stimulation and imaging system (MOSIS). The trans-illumination light from the Köhler illumination system which is composed of LED1 (λ = 780nm, M780L3, Thorlabs Inc., Newton, New Jersey, USA), two convex lenses (L1(f=35 mm, AC254-35-A, Thorlabs), L2(f=50mm, AC254-50-A, Thorlabs)), and two slits (S1, S2) illuminates a sample stage uniformly across the field of view and pass an objective lens (N.A = 0.5, 20X, UMPLFLN 20XW, Olympus). For fluorescence imaging, illumination light from LED2 (λ = 565 nm, 6.1W, SOLIS-565C, Thorlabs Inc., Newton, New Jersey, USA) pass through collimating lens L3 (f= 60 mm, LB1723-A, Thorlabs) and reflected at BS2(dichroic beam splitter & filter set, MDF-MCHA, Thorlabs). Then, light travels to the sample substrate through optical components in the system. The size of the patterned stimulation light by DMD (DLP3010-EVM-LC, Texas Instruments) was controlled by minifying lens ML (f = 200 mm, AC254-200-AB, Thorlabs), and the light pass through a tube lens TL1 (f = 200 mm, TTL200-B, Thorlabs). Then, the patterned light reflected by dichroic mirror BS1 (FF484-FDi01-25x36, Semrock) travels to the sample substrate. Light coming from the sample substrate passes a tube lens TL2 (f = 200 mm, TTL200-A, Thorlabs) and is focused on the CMOS camera (Blackfly S BFS-U3-19S4M, FLIR) with the resolution of 1616 x 1240 pixels (pixel size: 4.5μm). The sample stage is translated manually in x, y, and z directions.

DLP EVM GUI program was used to control pixels in the DMD of the DLP module. We updated the input images in HD (1280 x 720 pixels) resolution which matches the resolution of DMD (1280 x 720 pixels, pixel size: 5.4 μm x5.4 μm) into a DLP module for patterned stimulation. The stimulation light has been observed by placing a mirror on the sample stage and taking the reflected light with a CMOS camera.

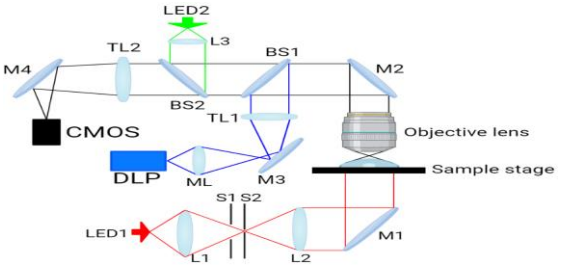


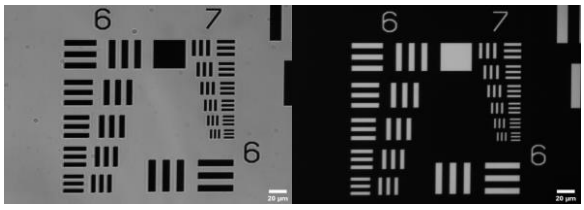
Figure 1. A schematic of the multi-functional optical stimulation and imaging system.

We used a fluorescent bead (Fluorescent Polystyrene, 0.7-0.9 μm, Sphero^{TM}) diluted in a 1:10 mixture of beads and water and drop it on a filter paper to observe the particle. We applied 565 nm LED light to excite the beads. Emission light was delivered to the CMOS camera through the filter set BS2(dichroic mirror: 578 nm, emission filter: 641 ± 37.5 nm, excitation filter: 578 ± 10.5 nm).

To characterize the system, we used ImageJ to measure the field of view and MATLAB to measure the full-width half maximum of the point spread functions of the fluorescent bead and a single-pixel stimulation light.

Results and Discussion

Figure. 2 (a) and (b) shows the bright field and dark field image of the 1951 USAF resolution test chart. The field of view of the system was 321 μm x 247 μm, and it was calculated with ImageJ considering the bar width of the USAF target. Figure. 2 (a) and (b) also show that our system can resolve element 6, group 7 of the target, whose line width is 2.17 μm**.** Regarding that the size of a retinal ganglion cell (RGC) is about 10 μm, this system can be seen that has sufficient resolution to image a single RGC.

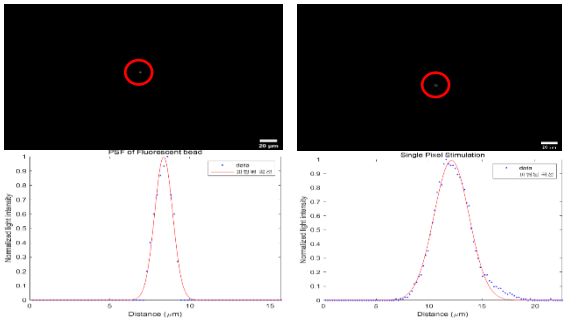


(a) (b)

Figure.2 (a) Bright-field (b) Dark-field imaging of 1951 USAF resolution test chart, scale bar: 20 μm

Figure.3 (a) exhibits an image and point spread function (PSF) of a single fluorescent bead. The PSF of the bead was obtained using the Gaussian fitting function in MATLAB. The resolution of the fluorescent image was about 1.6 μm, calculated with full-width half maximum (FWHM) of the PSF. Although the resultant resolution could not meet the expected resolution, 0.6893 μm, it appears that activation of a single RGC upon light stimulation can be sufficiently observable.

Figure.3 (b) illustrates an image and PSF of a single-pixel stimulation light. The size of a single-pixel stimulation light was about 3.85 μm. This result shows that we may be able to conduct a single RGC level stimulation with our system.



(a) (b)

Figure.3 (a) Image (top) and PSF (bottom) of a single fluorescent bead, (b) image (top) and PSF (bottom) of a single-pixel stimulation pattern

With these results, it seems that our system can be served as a neuromodulator and imaging tool for *ex-vivo* verification of further works.

Acknowledgments

This work was supported by the National Research Foundation of Korea (NRF) grant funded by the Korea government (MSIT) (2020R1C1C1010505) and by BK21PLUS, Creative Human Resource Education and Research Programs for ICT Convergence in the 4th Industrial Revolution

References

1. K. Eom, J. Kim, J. Choi, T. Kang, J. Chang, K. Byun, S. Jun, and S. Kim, “Enhanced Infrared Neural Stimulation using Localized Surface Plasmon Resonance of Gold Nanorods”, *Small* **10**, 3853-3857 (2014).
2. H. Jung, H. Kang, and Y. Nam, "Digital micromirror based near-infrared illumination system for plasmonic photothermal neuromodulation, "*Biomed. Opt.* Express 8, 2866-2878 (2017)

P-045

Minimally Invasive Focused Ultrasound-Assisted Delivery of Nanomaterials to Retina Ganglion Cell Layer

Younghoon Park[1*],Junewon Park[2],Jaewoo Shin[2],Chanho Kong[2], Wonseok Chang[2], Jinwoo Chang[2], Kyungsik Eom[1]
[1]Department of Electronics engineering, Pusan National University, Pusan, Republic of Korea
[2]Department of Neurosurgery, Yonsei University college of Medicine, Seoul, Republic of Korea

*yhunp93@gmail.com

Abstract

Focused ultrasound-assisted nanomaterial delivery to the retinal ganglion cell layer is demonstrated by intravenous injection of two nanomaterials, Dextran and gold nanoparticles (“AuNP”). Focused ultrasound (“FUS”) can evoke cavitation with microbubbles injected with nanomaterials, creating transient pores on the blood-retinal barrier (“BRB”), allowing nanomaterials to cross the barriers. After sonication with FUS, confocal and two-photon emission images of Dextran and AuNP are taken. Retinal images show Dextran and AuNP placed in the retinal layers and are the result of passing through the BRB via FUS.

Background

Degenerative retinal diseases such as macular degeneration (AMD), retinitis pigmentosa (RP), and Stargard's disease damage photoreceptors and cause blindness. For vision recovery, various methods of electrical, optical, magnetic, and acoustic neuronal stimulation have been proposed to stimulate retinal ganglion cells that are still alive while photoreceptors are damaged.

The eye as a bio-optical tissue has a clear optical path and can efficiently use light energy, so optical neural stimulation is suitable for the eye as the target. In addition, light stimulation with a combination of nanomaterials has shown more advantages in terms of neuron responsiveness, stimulation efficiency, spatial resolution, and reduced levels of radiation exposure, so these methods have been proposed for a new visual prosthesis. [1] However, prior to the promising use of photostimulation with nanomaterial combinations, the non-invasive delivery of nanomaterials to the retinal ganglion cell layer needs to be well studied.

Intravenous injection(“IV”) is the least invasive method of other nanomaterial injections. However, because of the blood-retinal barrier (“BRB”), this method is not a substitute for the delivery of nanomaterials in the retinal ganglion cell (“RGC”) layer. BRB is the wall formed by the complex solid junction between the endothelium of retinal blood vessels and the retinal pigment epithelium. When nanomaterials are injected intravenously, they cannot cross this barrier and are just trapped in blood vessels.

Here, FUS is used to increase the permeability of nanomaterials. When the ultrasonic pressure reaches the target, the microbubbles injected together with the nanomaterials collapse violently, causing biological effects and physical reactions. Microbubbles mechanically disrupt the integrity of blood vessel walls and cell membranes, increasing their permeability to nanomaterials [2], and ultimately the nanomaterials pass through the BRB and are placed in the RGC layer.

Methods

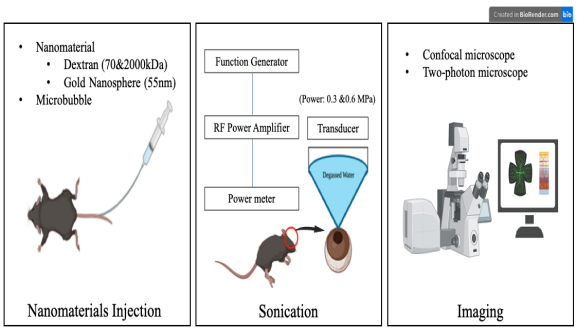


Figure 1. Experimental Process

Figure 1 shows the experimental process of focused ultrasound-assisted delivery of nanomaterials to the RGC layer, which involves three steps: nanomaterial injection, sonication, and imaging. Nanomaterial injections begin with dextran due to the benefits of biocompatibility, resizing, and available optical imaging. 70 kDa (≈10 nm) (2 mg / 50 µL) was injected intravenously into peritoneal anesthetized mice (C57BL / 6) via a tail veil together with microbubbles (1.2 µl/30 mg). After injection, a focused ultrasound transducer was attached to the cornea of one eye of the mouse eyeball and the retina was subjected to FUS treatment (0.3 MPa) for 120 seconds. The retina was separated from the sonicated eye and prepared for imaging. A confocal microscope (Carl Zeiss, LSM 980)

was used to image the dextran with a focus on the retinal ganglion cell layer. This layer can be identified by RGC cell staining with Dapi and anti-RBPMS. Then, 2000 kDa (≈55 nm) dextran and 55 nm gold nanospheres (0.2 mg / 30 g) are injected in sequence for sonication and imaging. For gold nanospheres ("AuNS"), a two-photon microscope (Carl Zeiss, LSM780) is used for the contrast between autofluorescence and the AuNS signal. The RGC layer is identified in a brightfield image containing spherical cells approximately 10 μm in diameter.

Results and Discussion

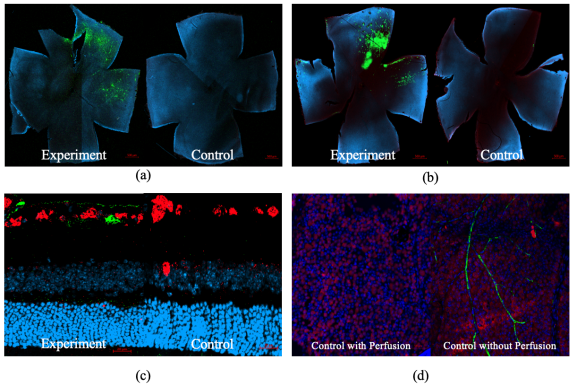


Fig. 2 (a) Confocal image of flat retinal of 70 kDa dextran, (b) Confocal image of flat retinal of 2000 kDa dextran, (c) Confocal image of retinal paraffin section of 70 kDa dextran, (D) Control group with and without perfusion

Figure 2 shows a confocal microscope image of Dextran. The blue, red, and green signals represent Dapi (ex/em: 345/455 nm), anti-RBPMS (ex/em: 633/648 nm), and 70 kDa Dextran (ex/em: 555/568 nm), respectively. Treatment of FUS distinguishes between experiments and controls. Only experimental samples show dextran ("green") on the retina, but no dextran appears in the control retinas of flat-mounted and paraffin-section retinas (Figures 2 (a) and 2 (c)). Figure 2 (d) shows a control sample with and without perfusion. The control without perfusion showed the vascular shape of dextran, but the perfusion control could not find dextran anywhere. Figure 2. (b) shows a 2000 kDa dextran (ex/em: 488/519 nm) confocal microscopic image of the retina. The result is the same as 70 kDa. This means that larger-sized nanomaterials can pass through the BRB via FUS.

Figure 3 shows the case of 55nm AuNS. In the bright-field image, spherical cells with a diameter of about 10 μm were observed, from which the RGC layer was identified. Two-photon Luminescence("TPL") images are taken with a wide range of emission wavelength (ex/em: 750 nm / 415 - 686 nm), and the presence of AuNS in the retina is confirmed by the difference in light intensity.

This study shows that 70 kDa and 2000 kDa dextran and 55 nm AuNS are injected into the retina and observed. The result of nanomaterials to the retina is that focused ultrasound can help nanomaterials coming out of BRR. This minimally invasive method of delivering nanomaterials to the RGC layer is expected to be used in nanomaterial-based optical neural stimulation for visual acuity restoration.

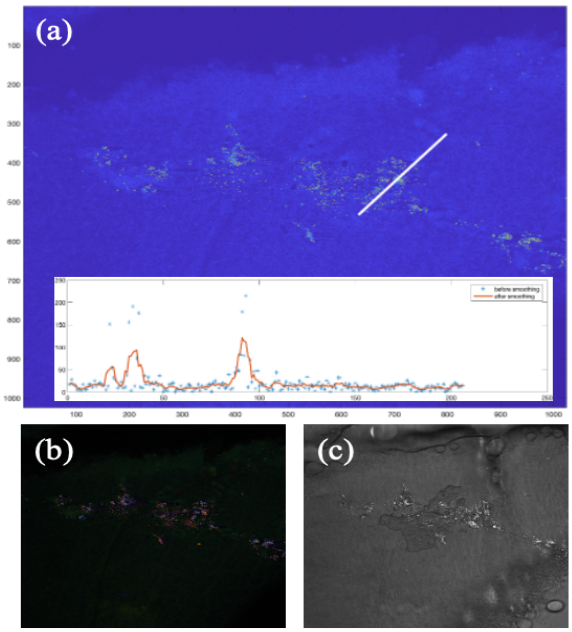


Figure.3 (a) Intensity profile in TPL Image, (b) TPL Image, (c) TPL and Merged TPL and Bright field image for 55nm AuNP

Acknowledgements

This work was supported by National Research Foundation of Korea (NRF) grant funded by the Korea government (MSIT) (2020R1C1C1010505) and by BK21PLUS, Creative Human Resource Education and Research Programs for ICT Convergence in the 4th Industrial Revolution

References

1. Eom, K.; Kim, J.; Choi, J.M.; Kang, T.; Chang, J.W.; Byun, K.M.; Jun, S.B.; Kim, S.J. Enhanced Infrared Neural Stimulation using Localized Surface Plasmon Resonance of Gold Nanorods. *Small* **2014**, *10*, 3853-3857.
2. Wan, C.; Li, F.; Li, H. Gene therapy for ocular diseases meditated by ultrasound and microbubbles (Review). *Molecular Medicine Reports* **2015**, *12*, 4803-4814.

Photovoltaic retinal prosthesis with biphasic stimulation & flexibility

Jaewook Lee[1] Kyungsik Eom[1], Heesoo Jeong[2], Sangbeom Jun [2]

[1]Department of Electrical Engineering, Pusan National University, Busan, Korea

[2] Department of Electronic and Electrical Engineering, Ewha Womans University, Seoul, Korea

wodnr5093@pusan.ac.kr

Abstract

Photovoltaic retinal prostheses in the form of arrays using photodiodes are manufactured and inserted into the eyes of patients with retinal disease to restore vision. However, these prosthetics with photodiodes in series have a limitation that stimulate with monophasic characteristics which charges can be accumulated. This study demonstrates biphasic stimulation to retina by photovoltaics, which can perform the charge balanced stimulation. The photodiodes are arranged in both directions, and biphasic stimulation can be created by switching each light exposure region.

1. Background

Several visual recovery devices have been developed that are attached above or below the retina to acquire visual information lost due to diseases such as retinitis pigmentosa ("RP") and age-related macular degeneration [1]. In addition, the system using a double photovoltaic diode does not use wired or wireless power supply, so it has the advantages of relatively convenient operation, light weight, non-enlargement, and less sequelae [2]. However, in the case of a device manufactured in a hexagonal shape by arranging diodes in series, the output is formed in a monophasic type, and there is a limitation that the operation speed is not fast enough, and the tissue can be damaged. To improve this, we separated the solar-cell in both directions and placed it in a biphasic form. In addition, to sequentially apply the light source to the separated space, a DLP Projector equipped with Digital Mirror Device ("DMD") chip were used to control it.

2. Methods

2.1 System Overview

In Figure 1, the DLP Projector (DLP2010evm-lc, Texas Instruments, Texas, USA) is controlled using the provided software (DLP EVM GUI). The photovoltaic device is a Solar-cell Array by soldering one pair of solar cells (KXOB25-04X3F-TB, ANYSOLAR Ltd, Gyeonggi-do, Republic of Korea) to the PCB bidirectionally in a target of one pixel. MEA System (Multi Channel Systems MCS GmbH, Reutlingen, Germany) is included a Microelectrode Array (MEA, 60pMEA200/30iR-ITO-pr), Amplifier (MEA 1060-Inv-BC), Power supply (PS40W), Temperature controller (TC02), Data acquisition Device (USB-ME64-System) and Software (MC Rack). Nerve stimulation targets were prepared through Retina dissection from rat eyeballs.

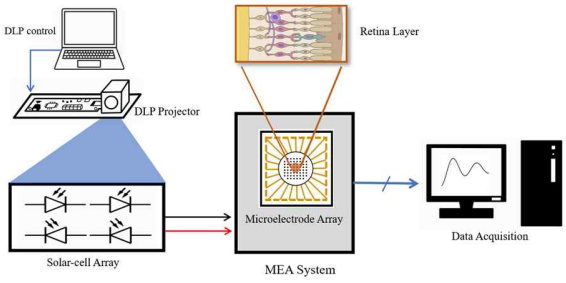


Figure 1. Current injection and recording setup for retinal nerve stimulation

2.2 Stimulus signal generation

The DLP Projector's lens was located at $14\,us$ from the Solar-cell array. Figure 2. depicts the shape of the current from the solar-cell array according to the area of the irradiated light. If the current flowing through Load Z is negative when irradiated to the top

of the solar-cell array (Figure 2. (a)) for the first time Phase duration ("P_{D1}") from DLP Projector, when the same interval P_{D2} is irradiated to the lower side (Figure 2. (b)), the positive current flows through Load Z. The time pattern for a total of period time (" P ") seconds divided into P_{D1}, IPH_I (Inter-phase interval), P_{D2}, and IP_I (inter-pulse interval) and the area of the irradiated light are controlled using a Software.

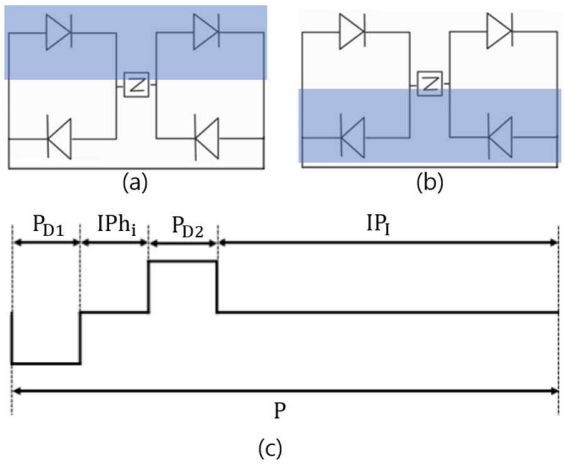


Figure 2. (a) Top area of the solar-cell array and (b) Bottom area of the solar-cell array, (c) Shape of the current from the solar-cell array

2.3 Stimulation and recording via the MEA system

The prepared retina layer is placed on the MEA. Solar-cell Array consists of two ports per cell, and channels can be selected by cathode and anode. It is connected to 2 of the 60 Golden Pins in the MEA. The recording had a sampling frequency of 25kHz from the MEA and was passed through a 2nd order Butterworth type of High Pass Filter (1Hz) and Low Pass Filter (5kHz). Nerve stimulation was observed through a trigger based on the signal of the Solar-cell Array.

3. Results and Discussion

In the state of normal activity, the light source used in the DLP projector is Blue LED, and P_{D1}, P_{D2} and IPH_I are set at $500us$, and P is set at an interval of 5s. The current was observed when the intensity of 100, 300mA was applied to the nerve. At this time, the voltages measured at the Golden pin of the MEA were 1.85V, 2.21V, and the irradiance was measured as $38.5W/m^2$, $72.538.5W/m^2$. Figure 3. is raw data obtained from MEA, and the observed potential level is larger at 300mA than 101mA. In this case, the stimulation artifact was observed as saturated at $-3.4mV$.

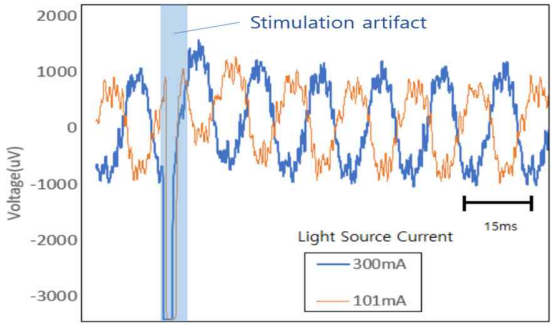


Figure 3. Raw data following stimulation artifact recorded by MEA

This system is a preliminary experiment in which the retinal layer was stimulated using a system constructed in vitro. Results will be derived through additional data processing, and the results will be quantitatively analyzed, and a mathematical model will be established through EIS measurement. Lastly, we plan to construct a system by fabricating a flexible organic photovoltaic device that can perform the role of an existing solar-cell array into a device that can be inserted into the eyeball.

4. Acknowledgements

This work was supported by National Research Foundation of Korea (NRF) grant funded by the Korea government (MSIT) (2020R1C1C1010505) and by BK21PLUS, Creative Human Resource Education and Research Programs for ICT Convergence in the 4th Industrial Revolution

5. References

[1] Sachs, H. G., Gabel, V.-P., "Retinal ©replacement—the development of microelectronic retinal prostheses—experience with subretinal implants and new aspects, Graefe's Arch Clin Exp Ophthalmol, 2004,242:717–723.

[2] Mathieson, K., et al." Photovoltaic retinal prosthesis with high pixel density", Nature Photonics, Vol. 6, 2015,391-396.

P-047

Biological fiber-based SERS platform using silk fibroin protein

Taeyoung Kang[1], Yongjun Cho[2], Seung Ho Choi[3] and Kyung Min Byun[1,2,*]

[1]Department of Electronics and Information Convergence Engineering, Kyung Hee University, Korea

[2]Department of Biomedical Engineering, Kyung Hee University, Korea

[3]Department of Biomedical Engineering, Yonsei University, Korea

*kmbyun@khu.ac.kr

Abstract

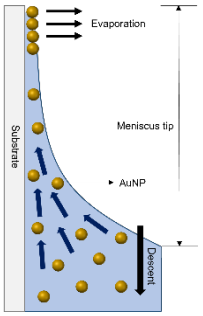
Naturally occurring silk material has gained much attention in biomedical applications due to its unique optical characteristics. As silk fibroin, a fibrous protein with a semi-crystalline structure has advantages of biocompatibility and no inflammatory response in vivo, it has been employed as a substrate or an encapsulation material in the fields of neural prosthetics, tissue engineering and drug delivery. In this study, we applied a biological silk material to surface-enhanced Raman scattering (SERS) scheme and realized a high sensitivity detection based on silk optical fiber and gold nanoparticles. Deposition of gold nanoparticles were successfully achieved via convective self-assembly method. From SERS experiments using 4-ABT analytes, we found that gold nanoparticles attached on a silk optical fiber presented a high sensitivity as well as a fairly good linearity and a wide dynamic range. Our silk-based fiber optic SERS platform has a potential for sensitive and reliable healthcare monitoring in vivo.

Background

To realize a non-invasive detection in vivo, biological and biocompatible materials have been investigated actively in recent years. Among various optical detection schemes, SERS (Surface-enhanced Raman Scattering) detection platforms have been studied by incorporating biological substrates and metallic nanostructures, thereby signals of target analytes are significantly amplified as a result of field-analyte interactions. Electromagnetic enhancement by LSPR (Localized Surface Plasmon Resonance) in the vicinity of metallic nanostructures can improve the SERS sensitivity [1]. In this study, biological silk fibroin obtained from silk cocoons is employed as a biocompatible SERS substrate [2]. Gold nanoparticles are deposited on the outer surface of the core of silk optical fibers using CSA (Convective Self-Assembly) method. Using 4-ABT analytes, SERS performance of silk fiber is compared with the case of multi-mode fiber.

Methods

Fabrication process of silk-based SERS platform is as follows. A silk fibroin solution is obtained from the original silk through Kaplan's method [3]. The prepared silk fibroin solution is changed into a silk powder via low temperature vacuum drying. The silk powder is then dissolved for 48 hours using HFIP (hexafluoroisopropanol) and the solution is extracted into a syringe to produce silk optical fibers. The multimode fiber is also prepared by removing a cladding layer through a wet etch process.



When the silk fiber is placed vertically on the surface of gold nanoparticle solution, a meniscus is formed on the fiber surface by capillary phenomenon. When evaporating the gold nanoparticle solution for 3 hours, uniform deposition of gold nanoparticles on the fiber surface is achieved.

In SERS experiment, 4-ABT is used as a Raman probe material to investigate the properties of silk optical fibers and multimode fibers using convective self-assembly method. The optical fibers are dipped in

a 100 nM 4-ABT solution for 15 minutes, then cleaned with ethanol and distilled water, and the Raman signals are measured and analyzed.

Results and Discussion

Figure 2 shows the FE-SEM images to confirm the morphological characteristics of the silk optical fiber surface. Through a CSA method, gold nanoparticles are bound to the silk surface with a uniform distribution. Since a silk fibroin is hydrophilic, gold nanoparticles are well attached without additional surface treatment.

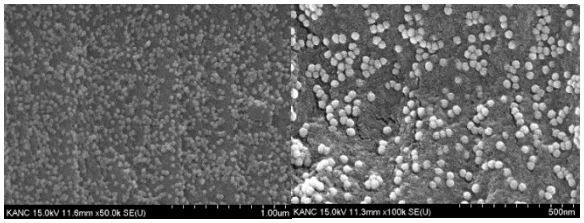


Figure 2. FE-SEM images of silk fiber based on CSA technique

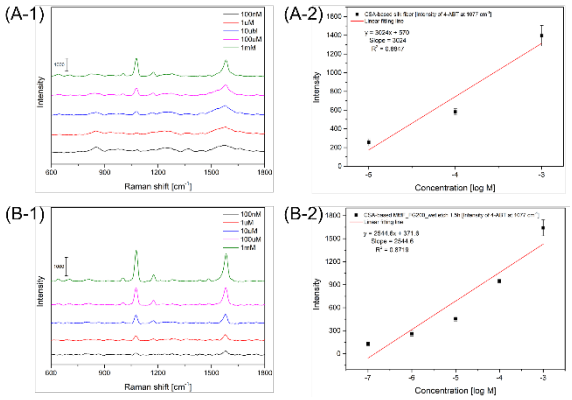


Figure 3. Experimental results of sensitivity and linearity performance for (A) silk optical fiber and (B) multimode fiber

In Figure 3, SERS spectra of 4-ABT for silk and multimode fibers are measured at the concentrations varied in the range of 100 nM to 1 mM. For a silk fiber, LOD (Limit of Detection) of 4-ABT is determined to be 10 uM. For multimode fibers, LOD is determined to be 100 nM. Figure 3 also shows linear regression analysis of SERS intensities of 4-ABT at 1077 cm^{-1} at various concentrations. Slope and coefficient of determination (R^2) are highly associated with sensor sensitivity and linearity. For the slope and the coefficient of determination, the performance of silk optical fibers is highly comparable to the results of multimode fibers. A silk optical fiber presents a high sensitivity as well as a fairly good linearity and a wide dynamic range

In this study, silk optical fibers are successfully implemented as a SERS substrate and gold nanoparticles are deposited uniformly using CSA method. We demonstrate that a high sensitivity and a high linearity of silk optical fibers is comparable to the results of commercially available multimode fibers. Our silk-based fiber optic SERS platform has a potential for sensitive and reliable healthcare monitoring in vivo.

Acknowledgements

This study was supported by the National Research Foundation of Korea (2019R1A2C2091068).

References

1. Haes, Amanda J., and Richard P. Van Duyne. "A nanoscale optical biosensor: sensitivity and selectivity of an approach based on the localized surface plasmon resonance spectroscopy of triangular silver nanoparticles." Journal of the American Chemical Society, Vol 124, No.35, p10596-10604, 2002.
2. Koh, Leng-Duei, et al. "Structures, mechanical properties and applications of silk fibroin materials." Progress in Polymer Science, Vol 46, p86-110, 2015.
3. Rockwood, Danielle N., et al. "Materials fabrication from Bombyx mori silk fibroin." Nature protocols, Vol 6, No.10, p1612-1631, 2011.

Reflectance Investigation of EJ-510 reflective layer on ceramic GAGG:Ce and GAGG:Ce single crystal scintillators

Abdallah Elmughrabi[1,2], Alima Melis[3], Sangsu Kim[4], Shinhaeng Cho[5], Chansun Park[6], Jung-Yeol Yeom[2,3]
[1]Department of Bio-Microsystem and Technology, Korea University, Seoul 02841, Republic of Korea
[2]Interdisciplinary Program in Precision Public Health, Korea University, Seoul 02841, Republic of Korea
[3]School of Biomedical engineering, Korea University, Seoul 02841, Republic of Korea
[4]Department of Radiation Oncology, Chonnam National University Medical School, Gwangju 61469, Republic of Korea
[5]Department of Display and Semiconductor Physics, Korea University, Sejong 30019, Republic of Korea
[6]BK21 FOUR R&E Center for Precision Public Health, Korea University, Seoul 02841, Republic of Korea
jungyeol@korea.ac.kr

Abstract

Reflectors for inorganic scintillators have been used to preserve the scintillation light inside and enhance collection efficiencies. In this study, we studied a reflective layer using paint type EJ-510 reflector material for its feasibility of substituting conventional film type reflectors. EJ-510 reflective layer, painted on GAGG:Ce scintillators, showed competitive reflectance compared to ESR (enhanced specular reflector), and Teflon tape. Light output was evaluated by excitation of ^{137}Cs source when ceramic and single-crystal scintillators were coupled to a photomultiplier tube (PMT). The tested EJ-510 reflector showed possibilities to be a cost-effective reflector for scintillators in radiation detection.

Background

Inorganic scintillator is a material which luminescence emits near ultraviolet or visible photons when it absorbs high energy ionizing radiation as gamma rays. The scintillation lights are detected on the photodetector. Those scintillators have been used in many applications such as high energy physics, security, and nuclear medicine. Cerium-doped gadolinium aluminum gallium garnet (GAGG:Ce) has promising properties such as high light yield, high density, and fast decay time [1].

Characterization of scintillators using suitable reflectors, for maximizing the light collection to the photodetector is needed to reduce the backscattered photons as shown in Fig. 1 [2]. There are different kinds of reflectors, one is Lambertian reflectors such as Teflon PTFE tape, and the other is specular reflectors such as ESR (enhanced specular reflector) film.

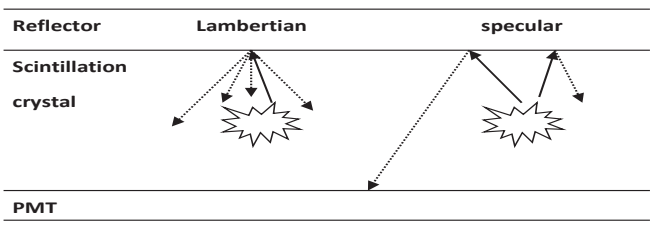


Figure 1. Schematic diagram of a reflection process inside the inorganic scintillator wrapped with different reflectors solid lines indicate the emitting scintillation photons and dashed lines show reflected photons.

In this study, we studied the performance of a white paint (EJ-510, Eljen Technology) as a reflector. The EJ-510 paint is a bright white paint of titanium dioxide pigment. For comparison, several reflective materials were prepared: (1) ESR film (3M), (2) Teflon tape, and (3) EJ-510.

We investigated the reflectance and spectral performances of ceramic GAGG:Ce and single-crystal GAGG:Ce scintillators. The effectiveness of EJ-510 reflective layers on the scintillators is discussed. Its performance, when compared to conventional ones, has not been reported with GAGG:Ce scintillators.

Methods

All reflectors were put on the mechanically polished ceramic GAGG:Ce and GAGG:Ce single crystal with dimensions of $5 \times 5 \times 2$ mm^3. The ESR reflector was manufactured as a reflection cap covering 5-side of the scintillator. To avoid the dependency of the Teflon tape's thickness, all scintillators are wrapped with 4 layers of it. Painting with EJ-510 was conducted 3 times on the surface as uniform as possible.

In Fig. 2, each sample was optically coupled to a photomultiplier tube (PMT) using silicone optical grease (BC-630, Saint-Gobain) to evaluate their spectral performances. Samples were kept in a dark box, irradiated

with a ^{137}Cs γ-ray source, and supplied with a voltage of -900 V. The output signal from the PMT was sent to a digitizer (DT5730, CAEN) for the data acquisition.

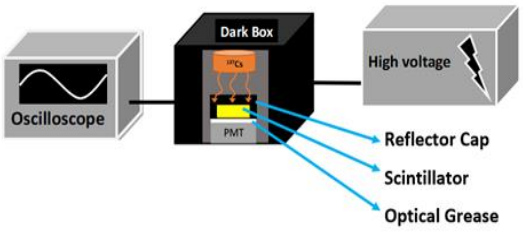


Figure 2. Gamma-rays measurement excited by ^{137}Cs source.

The reflectance measurement was performed using a UV–Vis–NIR spectrophotometer (Agilent Technologies, Cary 5000) with internal diffuse reflectance accessory (DRA). The baseline reflectance was calculated by the baseline correction using a reference material (PTFE) [3].

Results and Discussion

The light output (signal output) result acquired using different reflectors is shown in Fig. 3. Among them, GAGG:Ce single crystal using ESR showed the best light output. The light output with EJ-510 reflector was relatively lower than that of other reflectors due to light absorption and loss in the reflector but the reflectance may be enhanced in further study by controlling the amount of EJ-510.

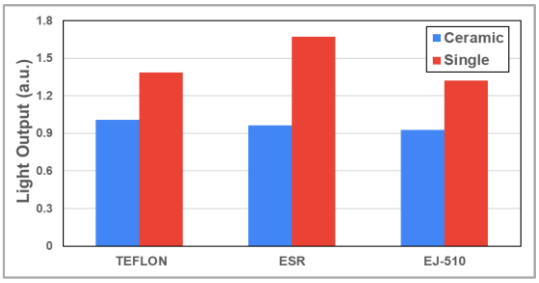


Figure 3. The light output of ceramic GAGG:Ce and GAGG:Ce single crystal with different reflector configurations.

The reflectance measurements were carried out by normalizing data to that of PTFE (reference). Ceramic GAGG:Ce with EJ-510 showed a reflectance of 84% and GAGG:Ce single crystal with EJ-510 demonstrated the reflectance of 86% compared to reference near wavelength of 540 nm. EJ-510 is a water-soluble paint that does not require any etching or cutting tools, and potentially could be used along with ESR and Teflon PTFE, making it a promising candidate for future scintillator applications, especially for large scale fabrication or complex shapes.

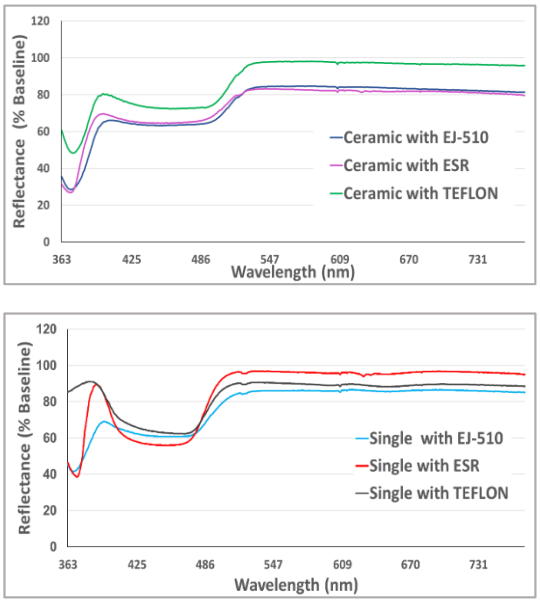


Figure 4. Normalized Reflectance of ceramic GAGG:Ce and GAGG:Ce single crystal with different reflectors.

Acknowledgment

This research was supported in part by National Research Foundation of Korea (NRF-2020R1I1A1A01070761, NRF-2020R1A2C2007376, NRF-2020R1C1C1007296), and Korea Institute of Energy Technology Evaluation and Planning (KETEP) grant funded by the Korea government (MOTIE) (20214000000070, Promoting of expert for energy industry advancement in the field of radiation technology)

References

[1] C. Park *et al.*, "Performance comparison between ceramic Ce:GAGG and single crystal Ce:GAGG with digital-SiPM," *J. Instrum.*, 2017, doi: 10.1088/1748-0221/12/01/P01002.

[2] M. Janecek and W. W. Moses, "Measuring light reflectance of BGO crystal surfaces," *IEEE Trans. Nucl. Sci.*, 2008, doi: 10.1109/TNS.2008.2003253.

[3] Agilent Technologies, *Diffuse Reflectance Accessories (DRAs)*. 2021.

P-049

Evaluation of Drug Transmittance Improvement in Triple-Ultrasound and Iontophoresis

Sangmin Shim, Yongheon Kim, Subin Park, Hyunseon Yu and Byungjo Jung*
Department of Biomedical Engineering, Yonsei University, Wonju, Gangwon-do, 26493, South Korea
* bjung@yonsei.ac.kr (e-mail address for corresponding author)

Abstract

Triple ultrasound is an equipment currently used in many dermatologists. It is used for skin regeneration, wound healing, and anti-aging through an increase in HSPs(Heat Shock Proteins) and a decrease in MMPs(Matrix Metalloproteinases) by stimulating the skin using principles such as LDM. Triple ultrasound has the advantage of being able to stimulate it from the nearest epidermis to the subcutaneous fat because the transmittance depth is different for each frequency. When used in combination with ionophoresis, which is effective in drug delivery, the experiment was conducted by comparing it with 1 MHz used for ultrasound drug delivery. As a result of the experiment, the combination of triple ultrasound and ionophoresis showed higher drug permeation than 1MHz ultrasound.

Background

As interest in skin beauty increases, related technologies are being developed. Through clinical trials using dual ultrasound like LDM, many studies have been conducted on skin tightening, skin rejuvenation, anti-aging and improvement of wrinkle. In an experiment using 1,3 MHz ultrasound, erythema related to rosacea and acne were reduced [1]. As high frequency ultrasound was used, MMPs (Matrix Metalloproteinases) decreased and HSPs(Heat Shock Proteins) increased, resulting in a decrease in chronic wound over time after treatment through wound healing [2][3]. With the development of technology, research on triple ultrasound beyond double ultrasound is underway, and clinical trials using it are also underway.

It has been found that ultrasound influences drug delivery as well as a wound healing on tissue. The biggest hindrance to drug delivery is the stratum corner. Ultrasound can reduce its effects and improve drug delivery through physical methods.

There are many reasons for increasing drug delivery through ultrasound, including thermal effect and cavitation effect. The thermal effect increases ultrasonic energy by lengthening the irradiation time, increasing the surface temperature of the medium, increasing drug delivery. The cavitation effect repeats expansion and contraction of bubbles caused by ultrasonic waves and increases drug delivery due to the impact when bubbles collapse. Several related studies have also been conducted, and among them, the most important effect is known as the cavitation effect [4].

There are various techniques as well as ultrasound used for drug delivery. Among them, iontophoresis increases the drug by using electrostatic repulsion by flowing the same polarity current as the drug. In addition, drug delivery is increased using electroosmotic. Currently, iontophoresis is used in many areas from vitamin C to anesthetics [5].

In this experiment, the superiority of drug delivery was measured by comparing the results of simultaneous irradiation with triple ultrasound and iontophoresis and the case of single irradiation at 1 MHz. Since it was expected that ultrasound of three frequencies would show a lower effect than 1 MHz in drug delivery, it was combined with iontophoresis to increase drug delivery.

Material and Methods

The drug used in the experiment is glycerol, which is a representative material of an optical clearing agent. When applied to the skin, moisture in the skin comes out and glycerol enters. Because glycerol has a refractive index that is similar to that of the human body, glycerol reduces scattering of light and increases transmission. Therefore, it is possible to quantitatively measure the high transmission of light in a deep region of the tissue through OCT [6].

For optical analysis of drug delivery, OCT (OQ Labscope 2.0, Lumedica, USA) and glycerol (70%) were used. For the sample, pig skin was used. For accurate measurement, 30 single t-pictures were acquired and averaged to acquire one picture (Figure 1). This process was repeated 3 times to obtain a total of 3 average images. The irradiation site was set by placing a 4cmx4cm frame on the sample, and 0.5ml of glycerol was evenly applied. The ultrasonic device was provided by ElimTek, and the ultrasonic device was operated in two modes. In test1, 1MHz outputting 1W/cm2 was applied for 5 minutes, and in test2, 1,3,10MHZ+iontophoresis outputting 1W/cm2 was performed for 5 minutes. And then, the drug was wiped off and images were taken by OCT. Since the stratum corneum surface of each pig's skin is different, the before and after analysis was performed based on a certain area below a certain depth from the surface (Figure 2). Since the pig skin tissue was non-uniform for each sample group, control, test1, and test2 were sequentially performed to maintain as uniform conditions as possible.

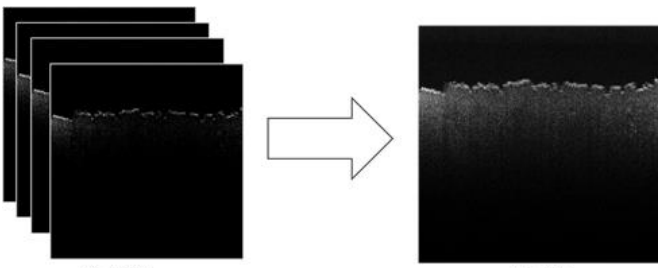


Figure 1. Average 30 images into one image.

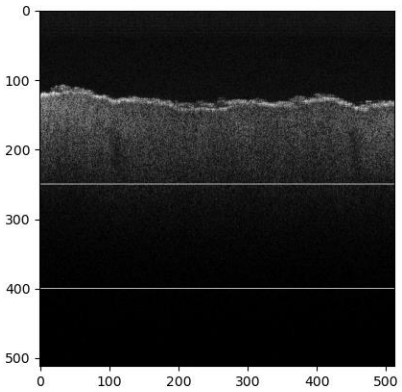


Figure 2. Porcine skin OCT image designating a region of interesting.

Results and Discussion

As shown in Figure 3, test1 showed an increase in light transmission of 57% compared to control, and test2 showed an increase of 114% compared to control. This shows that 1,3,10 MHz and ionophoresis show better drug delivery effects than using only 1 MHz. 1,3,10 MHz has been found to be effective in improving skin and inflammation through clinical trials, and studies on drug delivery have not been conducted. In future experiments, it is thought that additional experiments are needed to measure drug delivery using 1,3,10 MHz. In this study, it was an experiment to verify the effectiveness of 1,3,10 MHz when used in combination with ionophoresis, which has an excellent effect on drug delivery,

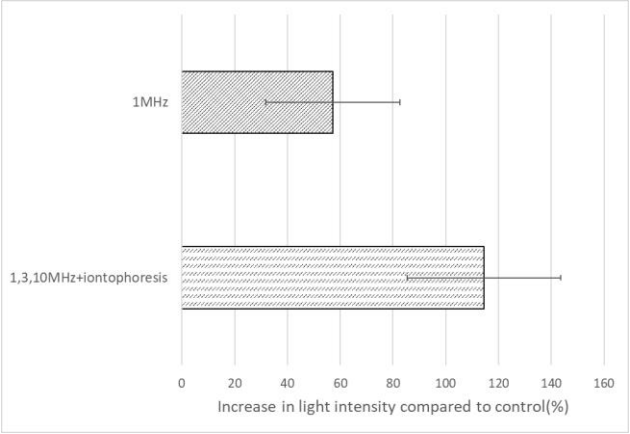


Figure 3. Measurement the light intensity of ROI of 1MHz and 1,3,10MHZ+iontophoresis based on control.

on the premise that it is not effective in drug delivery and is effective in improving skin texture and wrinkles. Through this experiment, using 1,3,10 MHz and iontophoresis at the same time can be expected to show good effects on skin care as the benefits of skin wrinkle improvement and sound healing and drug delivery increase.

Acknowledgements

This work was supported by the Technology development Pr ogram(S2845027) funded by the Ministry of SMEs and Startu ps(MSS, Korea)

References

[1] Kim, Y. J., Moon, I. J., Lee, H. W., Won, C. H., Chang, S. E., Lee, M. W., ... & Lee, W. J. (2021). The Efficacy and Safety of Dual-Frequency Ultrasound for Improving Skin Hydration and Erythema in Patients with Rosacea and Acne. Journal of Clinical Medicine, 10(4), 834.

[2] Kruglikov, I., & Kruglikova, E. (2011). Dual treatment strategy by venous ulcers: Pilot study to dual-frequency ultrasound application. Journal of Cosmetics, Dermatological Sciences and Applications, 1(4), 157.

[3] Lee, W. S., Park, E. S., Kang, S. G., Tak, M. S., & Kim, C. H. (2018). Successful treatment of recalcitrant remaining postoperative wounds by dual-frequency ultrasound. Medical Lasers; Engineering, Basic Research, and Clinical Application, 7(2), 74-78.

[4] Lavon, I., & Kost, J. (2004). Ultrasound and transdermal drug delivery. Drug discovery today, 9(15), 670-676.

[5] Huh, C. H., Seo, K. I., Park, J. Y., Lim, J. G., Eun, H. C., & Park, K. C. (2003). A randomized, double-blind, placebo-controlled trial of vitamin C iontophoresis in melasma. Dermatology, 206(4), 316-320.

[6] Son, T., & Jung, B. (2015). Cross-evaluation of optimal glycerol concentration to enhance optical tissue clearing efficacy. Skin Research and Technology, 21(3), 327-332.

P-050

Assessing atherosclerotic plaque with precision enhanced multispectral fluorescence lifetime imaging microscopy

J. Han[1], S. Kim[2,3], H. J. Kim[3], H. S. Nam[1], J. W. Song[3], J. W. Kim[3] and H. Yoo[1]

[1]Department of Mechanical Engineering, Korea Advanced Institute of Science and Technology, Daejeon, Korea

[2]Department of Cardiology, Korea University Ansan Hospital, Gyeonggi-do, Korea

[3]Cardiovascular Center, Korea University Guro Hospital, Seoul, Korea

h.yoo@kaist.ac.kr

Abstract

Fluorescence lifetime, the decaying rate of fluorescent signal, has intrinsic optical properties in biological tissue samples. Atherosclerotic plaque, characterized according by the composition of biochemical components, such as low-density-lipoprotein (LDL), macrophage, collagen, and smooth muscle cells, emit autofluorescence signal under ultra-violet (UV) excitation. Here, we developed high-resolution fluorescence lifetime imaging microscopy to assess vulnerability of atherosclerotic plaque and characterize biochemical components. Pixel-wise matching with 4 different histology enabled robust validation that FLIM-derived parameters is highly correlated with biomedical components. Statistical analyses of FLIM-derived parameters validate the custom-built FLIM system for diagnosis of vulnerability of atherosclerotic plaque.

Background

Atherosclerosis is characterized by the plaque formation on the arterial wall, which accumulates lipids and cell debris, leading to inflammation. There are some key biochemical compositions in the mechanism of atherogenesis. While lipid-rich macrophage, known as foam cell provoke inflammation in coronary artery, generating vulnerable plaque. And, smooth muscle layer developed in artery stabilizes artery and suppress lipid core to rupture. With stabilizing, collagen-rich region developed, and collagen layer stabilize the plaque. Thus, it is essential to characterize tissue components of the arteries to study and manage atherosclerosis. Fluorescence lifetime imaging microscopy (FLIM) is an optical imaging technique for measuring fluorescence lifetime, defined as a fluorescence decay rate of a fluorescent sample. FLIM can obtain biochemical information with autofluorescence emitted by collagen, elastin, and lipids for characterizing atherosclerosis [1]. In this study, we developed a multispectral FLIM to visualize high-resolution and precision enhanced FLIM images of arterial sections. We were able to characterize and validate the tissue components using the FLIM images through one-to-one matching with the histological images.

Methods

We developed a FLIM microscopy system using a 355 nm excitation light and three emission bands whose central wavelengths are 390 nm, 452 nm, 542 nm to characterize atherosclerotic tissue components, including collagen, elastin, macrophages, and lipids [2]. Imaging fluorescent reference slide, and resolution target, this developed system was validated to have high-resolution and high-precision. With multiple scanning and stitching technique of cross-sectional atherosclerotic plaque, we successfully obtained full cross-sectional image of artery. We performed *ex vivo* FLIM imaging of coronary artery sections of atherosclerotic swine. We processed matching sections to obtain histological stainings, including H&E, PSR, PM2K, a-SMA and ORO to validate the components of atherosclerotic plaque.

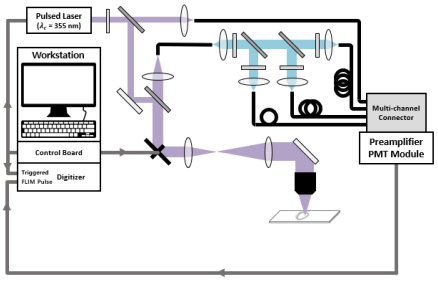


Figure 1 Schematic of developed FLIM system

Results and Discussion

Figure. 2 shows a high-resolution FLIM images obtained from developed systems. Lifetime images were shown by intensity weighted. Since different spectral bands were designed to target different fluorophores, we calculated the intensity ratio by channel 2 intensity divided by channel 1 intensity and also utilized as FLIM parameters to assess atherosclerotic plaque. 4 types of histological staining of provide multi-components such as lipids, macrophage, collagen, and smooth muscle cells which are main components of atherosclerotic plaque.

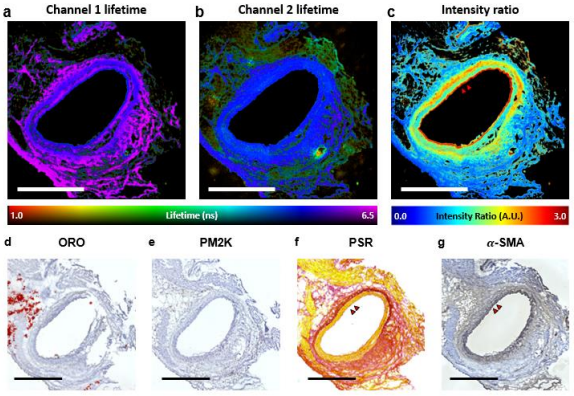


Figure.2 FLIM images obtained from developed FLIM and co-registered histology.

Matching with histology can glimpse the viability of differentiating plaque based on FLIM parameters (channel 1 lifetime, channel 2 lifetime, intensity ratio). We manually segmented and classified 5 different (lipid core, foam cell, fibrosis, media and adventitia). legions based on 4 types of histology. Within randomly selected 100 pixels of one-way analysis of variance (ANOVA) turns out to be there are significant difference between lipid core and other plaque type with $p<0.0001$ at channel 2 lifetime and intensity ratio (Figure 3). Also, among other types of plaque they have different FLIM parameters with statistically significant ($p<0.05$).

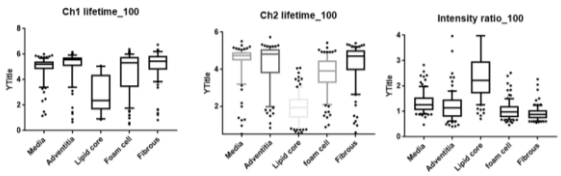


Figure.3 Box plots of FLIM parameters for 5 different types of plaque.

Also, Figure 4 shows the correlation analysis between FLIM parameters and four types of binary quantified histology. Four types of main atherosclerotic components are highly correlated with intensities and lifetimes of channel 2 with statistical significance. $p < 0.005$)

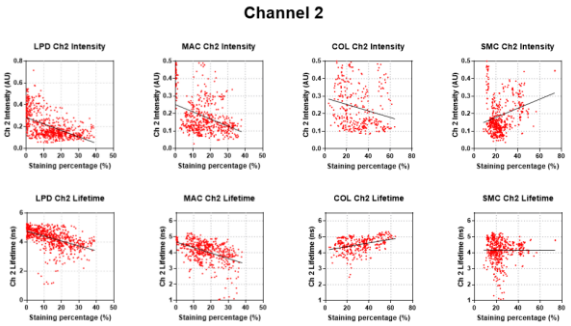


Figure.4 Correlation between FLIM parameters and biochemical components at channel 2.

In conclusion, we developed multispectral FLIM to assess atherosclerotic plaque in biochemical respects with label-free manner. And, with histological validation and statistical analysis, we found the feasibility to characterize biochemical components of atherosclerotic plaque and classify different plaque types. This analysis can be utilized as a diagnostic tool for detecting and determine the vulnerability of atherosclerotic plaque in label-free manner.

Acknowledgements

This study was supported by Samsung Research Funding center of Samsung Electronics under Project Number G01210323

References

1. Park J, Pande P, Shrestha S, Clubb F, Applegate BE and Jo JA. Biochemical characterization of atherosclerotic plaques by endogenous multispectral fluorescence lifetime imaging microscopy. *Atherosclerosis*. 2012;220:394-401.
2. Nam HS, Kang WJ, Lee MW, Song JW, Kim JW, Oh WY and Yoo H. Multispectral analog-mean-delay fluorescence lifetime imaging combined with optical coherence tomography. *Biomed Opt Express*. 2018;9:1930-1947.

Sonoluminescence counting using PMT

Hyun Jae Song[1], Tai-kyung Song[1] and Min Joo Choi[2,3]

[1]Department of Engineering, Sogang University, Seoul, Korea

[2]Department of medicine, Jeju National University, Jeju, Korea

hjsong@sogang.ac.kr

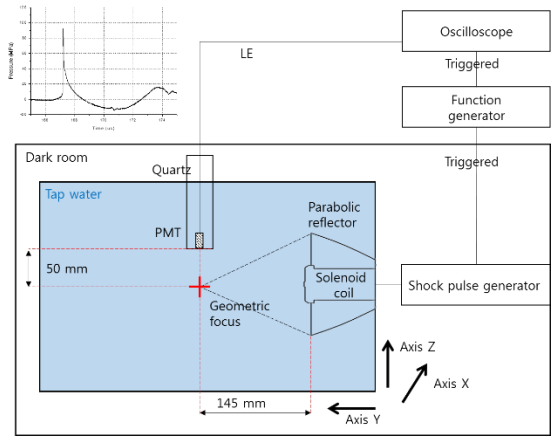
Abstract

Sonoluminescence generated by shock waves is difficult to measure and characterize because its size and location are not constant. In this paper, the cavitation phenomenon caused by the shock wave was characterized by counting the number, not the size, of the SL signal accumulated several times. When the experiment was repeated 200 times, more SL numbers were observed in the 2nd than in the 1st, and from 120 times on, the ratio of the 1st and 2nd collapse signals to the total accumulated signals converged to 0.27 to 0.72.

Background

When the cavitation bubble caused by the shock wave, the sonoluminescence (SL) phenomenon in which light is generated appears. In addition, since the location or size of the SL signal is occurred inconsistently, it is difficult to characterize its characteristics. In this paper, we try to characterize the SL phenomenon qualitatively by counting the number of SL signals repeatedly measured with PMT.

Methods



1) Shock pulse production

The shock wave generator is used by separating the generator part of an electromagnetic (EM type) extracorporeal shock wave lithotripsy (Rifle, HnT Medical, Rep. Korea) used in clinical practice. 1 uF Capacitor is charged and discharged with high voltage, and vibration pulse is generated by vibrating the converter copper plate. The generated vibration pulse is reflected by the parabolic reflector and focused at the focal point to generate a shock wave pulse of high pressure. It has a maximum pressure of 91.7 MPa and a minimum pressure of -12.5 MPa when measured using a broadband optical hydrophone (FOPH 200, RP acoustics, Germany).

2) PMT

Light emission as a result of strong cavitation near the focal point is measured using a Photo Multiplier Tube (H10721-110, Hamamatsu, Hamamatsu City, Japan) in a dark room. The data output is a current output type, and the measurable rise time is 0.57 ns. Measurements were made at a position 50 mm vertically away from the focal position.

3) Measurements

A trigger signal is generated using a function generator in a water tank located in a dark room, and a shock wave generator and an oscilloscope (HDO6104A, Teledyne LeCroy, USA) are synchronized. The signal measured by the PMT is collected by setting the sampling rate of the oscilloscope to 10 GS/s (0.1 ns). The shock wave generator capable of adjusting the output level from 1 to 10 is set to level 6, which is an intermediate level among levels 2 to 10, except for level 1, where no pulses were generated intermittently in this experiment. The data collection is performed 100 times and the shock wave generation interval is set to be at least 30 seconds, so that there was no change in the state of the medium due to the preceding shock wave. Tap water is used and the water temperature is maintained at 25 degrees, the same as room temperature.

Results and Discussion

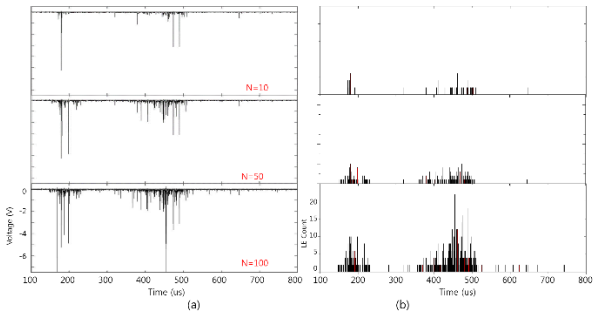
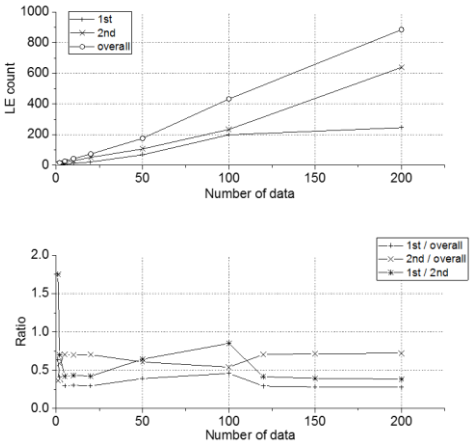


Figure 2 shows the SL signal and counting results according to the accumulated number of times. SL signals repeatedly occurred at similar times in all data. When the generated SL signals are counted, it is very similar to the result of accumulating the SL signals. The total number of generated LE signals increased linearly with the number of data accumulations.



As shown in Figure 3, even when the 1st and 2nd signals were divided, the same was the same, and the number of 2nd signals was about twice as large as that of 1st.

When the SL signals, which do not show a clear trend in the size or time of occurrence, were counted in units of 1 us, they showed a linear increase according to the number of accumulations in both the 1st and 2nd times. It was confirmed that the ratio converges to 0.27 and 0.72, respectively. A study according to the change in the strength of the shock wave generator or the PRF is needed in the future.

Acknowledgements

This research was supported by Basic Science Research Program through the National Research Foundation of Korea (NRF) funded by the Ministry of Education, Science and Technology (NRF-2017R1A2B3007907) and Korea Medical Device Development Fund grant funded by the Korea government (the Ministry of Science and ICT, the Ministry of Trade, Industry and Energy, the Ministry of Health & Welfare, the Ministry of Food and Drug Safety) (KMDF-PR-20200901-0010-2021-04)

References

1. Coleman, A. J., et al. "Acoustic emission and sonoluminescence due to cavitation at the beam focus of an electrohydraulic shock wave lithotripter." Ultrasound in medicine & biology 18.3 (1992): 267-281.
2. Kang, Gwansuk, et al. "Characterization of the shock pulse-induced cavitation bubble activities recorded by an optical fiber hydrophone." The Journal of the Acoustical Society of America 135.3 (2014): 1139-1148
3. Choi, Min Joo, Gwansuk Kang, and Jung Sik Huh. "Geometrical characterization of the cavitation bubble clouds produced by a clinical shock wave device." Biomedical engineering letters 7.2 (2017): 143-151.
4. Matula, Thomas J., et al. "In vitro sonoluminescence and sonochemistry studies with an electrohydraulic shock-wave lithotripter." Ultrasound in medicine & biology 28.9 (2002): 1199-1207.

P-052

Development of high speed and precision enhanced Two-photon Fluorescence Lifetime Imaging Microscopy with optimal repetition rate

Jeonggeun Song[1], Juehyung Kang[1], Hyeong Soo Nam[1], Ungyo Kang[1], Hyun-Jung Kim[2], Jin Won Kim[2] and Hongki Yoo[1]

[1]Department of Mechanical Engineering, KAIST, Daejeon, Republic of Korea

[2]Cardiovascular Center, Korea University Guro Hospital, Seoul, South Korea

H.yoo@kaist.ac.kr

Abstract

Two-photon fluorescence lifetime imaging microscopy (TP-FLIM) is one of the most famous tools in the life science and biomedical. In general, TP-FLIM uses 80MHz repetition rate femtosecond pulsed laser and time-correlated single photon counting (TCSPC). However, because average power is limited by phototoxicity, there is a limitation in obtaining high-quality images. In this study, we developed TP-FLIM utilizing analog-mean-delay method (AMD) with optimal repetition rate. In order to find the optimal repetition rate, the relationship between repetition rate and TP-FLIM performance such as SNR, lifetime precision, and photobleaching was analyzed and validated by tissue imaging.

Background

Fluorescence lifetime imaging microscopy (FLIM) has been used for research field of biomedical and life science. Since fluorescence lifetime imaging provides information of fluorophore types, and local biochemical environment, it is used in various applications such as metabolism, FRET, and structural analysis. In particularly, two-photon fluorescence lifetime imaging microscopy (TP-FLIM) utilizing near infrared femtosecond pulsed laser has advantages such as large penetration depth, optical sectioning ability, and low phototoxicity [1]. However, the time-correlated single photon counting (TCSPC) typically used in TP-FLIM system require long acquisition time because it requires a large number of pulses. Using analog mean delay method (AMD) instead of TCSPC can easily reduce acquisition time with a smaller pulse [2]. However, for the typically used commercial laser source, a high repetition rate of 80Mhz is usually used, which is inappropriate for optimizing TP-FLIM system with AMD method.

We developed high speed and precision enhanced two-photon fluorescence lifetime microscopy by adjusting repetition rate. Computer simulations demonstrate that repetition rates lower than 80MHz enable fast and highly sensitive FLIM imaging. The effects of the pulse repetition rate of the TP-FLIM on SNR, lifetime precision, photobleaching and imaging speed was analyzed and validated.

Methods

Figure.1 shows a set-up for the TP-FLIM system. The Ti:S femtosecond pulsed laser (λ = 800 nm) with a 76MHz repetition rate was used. The pulse picker was used to control the excitation beam repetition rate of 1 to 19 MHz to find the optimal repetition rate. Excitation beam passes dichroic mirror (FF705-Di01-25x36, Semrock). Some of the reflected parts from dichroic mirror used as IRF signal. The microscope field of view (400um x 400um) was formed by Galvano-resonance with 4KHz resonant frequency. The emitted fluorescence passed through the emission filter (FF01-550/200-36, Semrock) and was

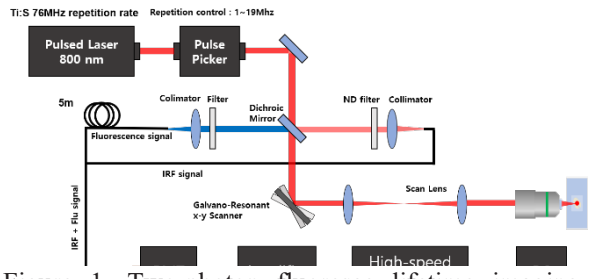
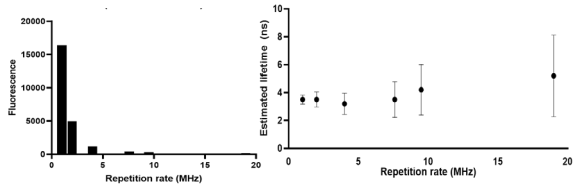


Figure 1. Two-photon fluoresce lifetime imaging system

Collimated to 440um multimode fiber and is measured with single photomultiplier along with IRF signal. The delay line (5m) was made by multimode fiber for avoiding overlapping IRF and fluorescence signals. Fluorescence was measured at intervals of about 22 ~25ns than IRF signal. It is amplified through an amplifier (C6438-01, Hamamatsu) of 50MHz bandwidth the finally measured through a workstation 400MHz sampling rate digitizer (PX14400D, Signatec). The obtained digitized signal was processed by imaging software to obtain the fluorescence intensity and fluorescence lifetime images. Fluorescent microscope slide (FSK5, Thorlabs) and mouse kidney tissue was used for analysis and validate.

Results and Discussion

Figure. 2(a) shows the change in fluorescence according to the repetition rate when fluorescence microscope slide fluorescence lifetime imaging with 5mW average power. The fluorescence at 1MHz repetition rate was 176 times higher than the fluorescence at 19MHz. Figure. 2(b) shows the change in fluorescence lifetime measured by AMD method. AMD method precision can be enhanced by sufficient fluorescence.



(b) (b)

Figure 2. (a) Microscope slide fluorescence and (b) Microscope slide fluorescence lifetime

Figure.3(a) shows fluorescence intensity and fluorescence lifetime weighted mouse kidney tissue images. Figure. 3(b) shows the SNR utilizing region of interest (ROI) at the tissue and background. The SNR of 1MHz repetition rate imaging is 23.6 times higher than 19MHz repetition rate imaging.

Figure.4(a) shows the photobleaching of biological specimen according to the repetition rate. When imaging was performed for 10 minutes, the amount of fluorescence decreased by twice as much as 9.5MHz at 1MHz. Figure. 4(b) the number of frames used in the averaging method to obtain images of the same SNR and the degree of photobleaching risk accordingly. This comparative analysis can provide a method of finding an appropriate repetition rate suitable for an experimental environment.

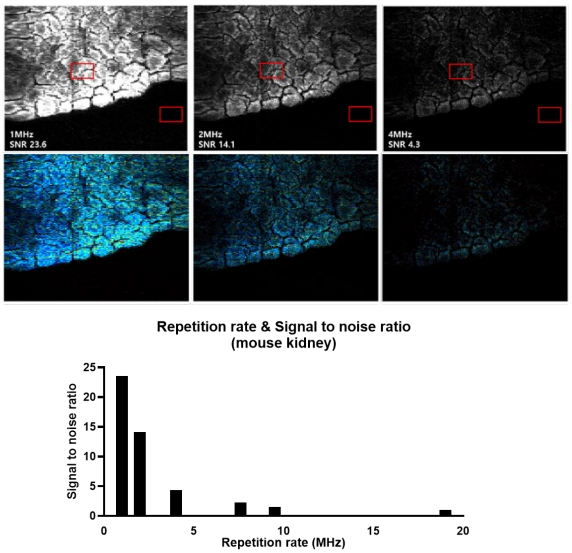
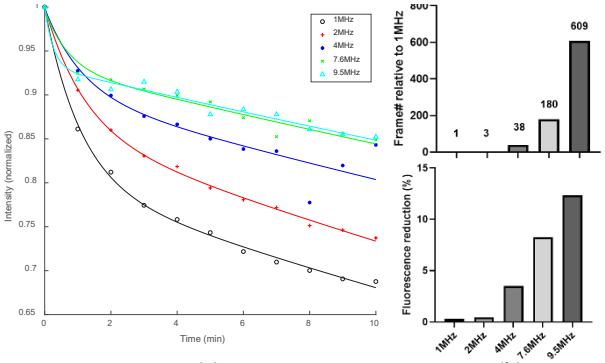


Figure 3 (a) Mouse kidney fluorescence lifetime images. (b) Fluorescence signal to noise ratio



(a) (b)

Figure 4 (a) Photobleaching of mouse coronary artery and (b) Acquisition time for high quality images.

Acknowledgements

I sincerely thank Jue Hyung Kang, Hyeong Soo Nam, JeongMoo Han, Ungyo Kang, and Professor Hongki Yoo for their great help and advice on this research.

References

1. W.R.Zipfel, R.M. Williams, and W.W.Webb, “Nonlinear magic:multiphoton microscopy in the biosciences,” Nature biotechnology, vol. 21, no. 11, pp. 1369-1377, 2003
2. S. Moon, Y. Won, and D. Y. Kim, “Analog mean-delay method for high-speed fluorescence lifetime measurement,” Optics express, vol. 17, no. 4, pp. 2834-3849, 2009

P-053

An experimental animal model of trigeminal axotomy and management of neuropathic corneal pain

Mohd. Afzal Khan[1], Kyung Chul Yoon[2], Euiheon Chung, *[1, 3]
[1]Department of Biomedical Science and Engineering, Institute of Integrated Technology (GIST) Gwangju 61005, Republic of Korea
[2]Department of Ophthalmology, Chonnam National University Medical School and Hospital Gwangju 61005, South Korea
[3]AI Graduate School, GIST, 123 Cheomdangwagi-Ro, Buk-gu, Gwangju 61005, Republic of Korea
**Corresponding author: ogong50@gist.ac.kr*

Abstract

Neuropathic pain in the cornea is caused by a primary nervous system lesion or dysfunction. However, neuropathic corneal pain (NCP) is a poorly described condition at the moment. Patients with NCP are notoriously difficult to treat, and there are few evidence-based clinical guidelines for their care. In current study, we will acquire a novel experimental model of trigeminal axotomy after transection and holding ciliary nerve. For pain assessment in rodents, the corneal hypersensitivity to mechanical (manual von Frey filaments) and chemical (eye wiping test) stimulation were measured to check response with (surgical animals) and without (sham animals) transection of ciliary nerve. These results will provide a preliminary data related with the development of translational pain research and the development of innovative methods to evaluate pain in laboratory rodents. Moreover, this serves a baseline data for future therapeutic approach that may accelerate the regeneration process of corneal nerves after trigeminal axotomy.

I. Background

The cornea defends and preserve the eye from alienated and exotic substance. Ophthalmic surgical procedures such as corneal transplant, radial keratotomy, photorefractive keratectomy and laser-assisted in-situ keratomileusis (LASIK), trigger and provoke corneal nerve severance and impairment. Rodents prototype manifest to be significant and pivotal in the research and analysis of human ocular physiological mechanism and the growth and spreading of ailment and indisposition. It was already studied that corneal sensory innervation is supplied by ciliary nerves which is derived from ophthalmic division of the trigeminal nerve. Patients with NCP are notoriously difficult to treat, and there are few evidence-based clinical guidelines for their care.

III. Materials and Methods

1. Animal surgery

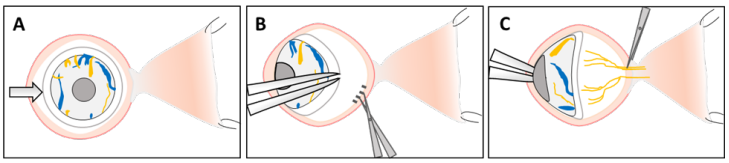


Figure 1. Representative schematic displaying steps for the evocation of trigeminal axotomy. A. Lateral canthotomy. B. Soft and connective tissue preparation C. Ciliary nerve transected (full and partial).

2. Behavior tests for pain assessment

I. Corneal mechanical sensitivity

Mechanical corneal sensitivity was monitored using von Frey filaments. Various forces of calibrated von Frey filaments (0.02–0.16 g) were applied to the center of the cornea of immobilized mice. The mechanical threshold corresponded to the eye-blink response at a given time.

II. Eye wiping test

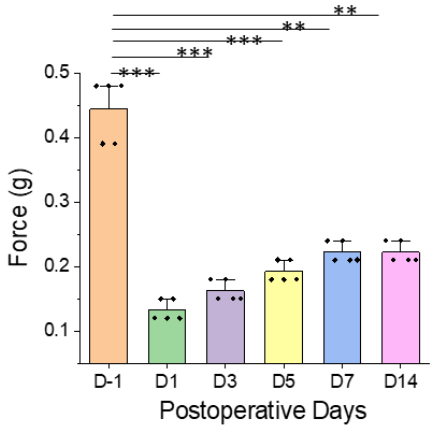
For the adaptation period, animals were placed in an individual chamber for 10 minutes, each day for 3 days. A 10 µl drop of hypertonic solution (NaCl 2M) were applied to the surgical and non-surgical eye and the animal were placed in an individual cage. The number of eye wipes will be counted during 30 s

II. Result and Discussion

1. Corneal mechanical sensitivity

The corneal mechanical sensitivity threshold (g) of ipsilateral eye (before and after surgery) for surgical (full transection and partial clasp) and sham animals were measured using von Frey filaments. Results are expressed as the mean ± SD from D-1 to D14 post-surgery (n=5).



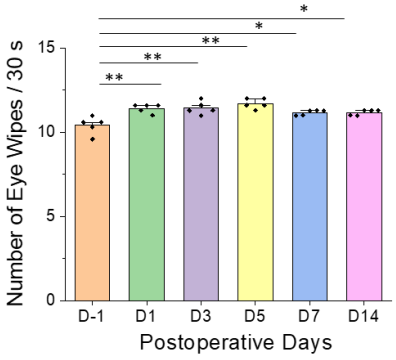


Partial injury model

2. Eye wiping test

The number of eye wipes was measured after an application of 2M NaCl (30 seconds) for ipsilateral eye (before and after surgery) for surgical (full transection and partial clasp) and sham animals. Results are expressed as the mean ± SD from D-1 to D14 post-surgery (n=5).





Partial injury model

3. Histopathology of mouse cornea.

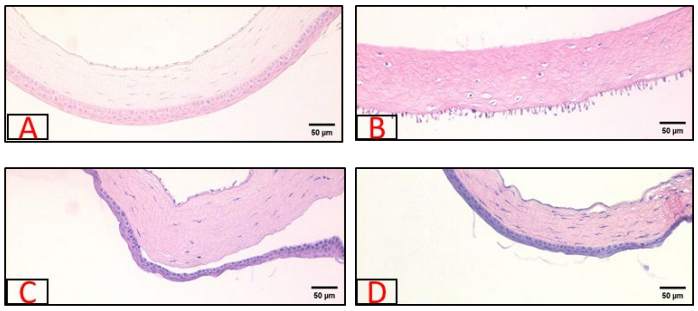


Figure 6. Representative images of H&E stained cornea sections from 11 to 12 week-old mouse. A: Naive. B: Full transection. C: Partial injury. D: Sham. Images were captured using a 20x objective lens, scale bars represent 50 µm.

Conclusion:

1. In our study, we developed a new experimental model in rodents to study NCP through surgical axotomy of the ciliary nerve of the trigeminal nerve.

2. Moreover, this serves for a future therapeutic approach that may accelerate the regeneration process of corneal nerves after trigeminal axotomy

References

1. H. Takefumi Yamaguchi, et al. Bilateral Nerve Alterations in a Unilateral Experimental Neurotrophic Keratopathy Model: A Lateral Conjunctival Approach for Trigeminal Axotomy. PLOS ONE. 2013. https://doi.org/10.1371/journal.pone.0070908.

2. Fanny Joubert, et al. Effects of corneal injury on ciliary nerve fibre activity and corneal nociception in mice: A behavioural and electrophysiological study. Eur J Pain. 2019. https://doi.org/10.1002/ejp.1332.

P-054

Novel In-Car Environment Control System Using an SSVEP-based BCI with Visual Stimuli Presented on a Head-Up Display

S. Park, M.-S. Kim, and C.-H. Im*

Department of Electronic Engineering, Hanyang University, Seoul, Korea

ich@hanyang.ac.kr

Abstract

Negligence of looking forward of drivers is one of the major reasons of car accidents. In the present study, we proposed a new in-car environmental control system using brain-computer interface (BCI). In a simulated driving situation, the participants could control the car environment by staring at a visual stimulus presented on a head-up display, without pressing a button or changing their gaze out of the front screen. In the comparison between manual and BCI control conditions, participants showed both higher reaction rate and shorter reaction time in the BCI control condition, compared to the manual control condition. The proposed in-car environment control system might contribute to a safer driving.

Background

While controlling the in-car environment such as temperature and ventilation is necessary for comfortable driving experience, it often makes the drivers to neglect to look forward and distracts driver's attention, causing severe car accidents. Brain-computer interface (BCI) is a technology that enables the direct communication between a user and external devices, and BCI might be a plausible solution to this situation. In the present study, we proposed a steady-state visual evoked potential (SSVEP)-based BCI system to control in-car environment, to help lowering the occurrence of car accidents. The performance of the proposed system was evaluated using a lab-made driving simulator system.

Methods

A total of 22 healthy adults (13 males and nine females, aged 24.9±3.4 years) participated in the experiment. All participants had normal or corrected-to-normal vision, and none of them had a history of psychiatric or neurological disease.

To implement a simulated driving environment, we designed a custom driving map in AirSim open-source platform [1] using Unity 3D (Unity Software Inc., CA, USA), and the simulated driving environment was presented on a 49-inch TV (LG electronics Inc., Seoul, Republic of Korea), as shown in Figure 1(a). The vehicle was controlled using a gaming wheel and pedals (PXN-V900, ShenZhen PXN Electronics Technology Co., Ltd., Shenzhen, China). To elicit SSVEP responses, we adopted a visual stimulus that changes its size and color concurrently. The visual stimulus was presented via a digital light processing (DLP) projector (EP728, New Taipei City, Taiwan), on a light reflection film (440*300 mm) attached on a tempered glass panel with a size of 700*240*80 mm (width*depth*height), as shown in Figure 1(b).

The experiment consisted of two different driving tests: 1) obstacle avoidance and 2) car-following. In the obstacle avoidance test, there were four obstacles that unexpectedly appeared on a driving course, and the participants were instructed to stop the vehicle as soon as possible to avoid the collision. In the car-following, the participants were instructed to follow a preceding vehicle that ran at a sinusoidal speed profile, trying to travel along the centerline of the lane. Also, the participants were instructed to drive at a speed slower than 60 km/h in city, and 100 km/h in highway.

In addition, each driving test consisted of two control conditions: 1) manual and 2) SSVEP-BCI. In manual control condition, the participants were required to execute car environment control command by manually pressing a button (Figure 1(c)), while the participants were required to control the car environment by staring at a visual stimulus presented on the head-up display. The obstacle avoidance driving test was conducted before the car-following test, and for each driving test, both control conditions were conducted in a random order. Consequently, each

participant conducted total four runs {(2 driving tests) * (2 control conditions) = 4}.

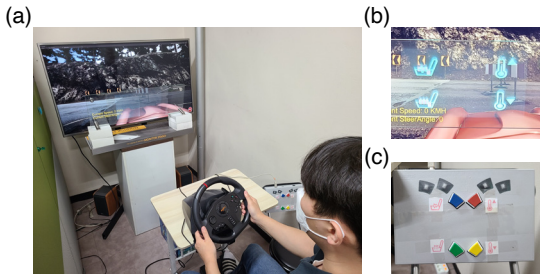


Figure 1. The real pictures of experimental environment and two control modalities. (a) The driving simulator; (b) The visual stimulus presented on head-up display; (c) The buttons for manual control

The EEG data were recorded at a 2,048 Hz sampling rate from 9 electrodes (Cz, POz, PO3, PO4, PO7, PO8, Oz, O1, and O2), using Biosemi ActiveTwo system (Biosemi, Amsterdam, The Netherlands). The recorded EEG data were down-sampled to 512 Hz, and then re-referenced to Cz. The re-referenced data were band-pass filtered with 2 and 54 Hz cutoff frequencies, using a zero-phase Butterworth infinite impulse response filter. A recently developed algorithm called extension of multivariate synchronization index (EMSI) [2] was adopted for the classification of the SSVEP responses, and all the EEG data analysis was conducted with a custom real-time software developed using MATLAB (MathWorks, Inc., MA, USA).

Results and Discussion

The car environment control accuracy in manual and SSVEP-BCI control conditions were 98.3% and 82.4%, respectively. In the obstacle avoidance driving test, the participants showed a significantly shorter reaction time in SSVEP-BCI than manual control condition (Figure 2(a)). Also, the ratio of the obstacles that the participants did not react among all obstacles was significantly higher in manual than SSVEP-BCI control condition (Figure 2(b)). In addition, the distance between the centerline and the vehicle was significantly shorter in SSVEP-BCI than in manual control condition (Figure 3(a)). While a significant difference was not observed in the comparison of speed difference between the preceding vehicle and the participant's vehicle, however, in city driving situation where the participants were instructed to drive at a speed lower than 60 km/h, the speed difference between the two vehicles was significantly shorter in SSVEP-BCI than manual control condition (Figure 3(b)). It might imply that the proposed car environmental control system based on SSVEP-BCI could contribute to a safe driving, and consequently lower the occurrence of car accidents.

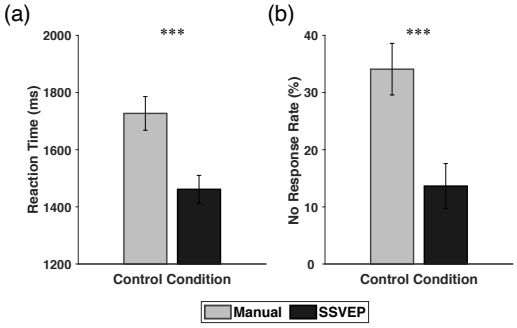


Figure 2. Driving performance comparison between control conditions for obstacle avoidance driving test. (a) Response time; (b) No response rate.

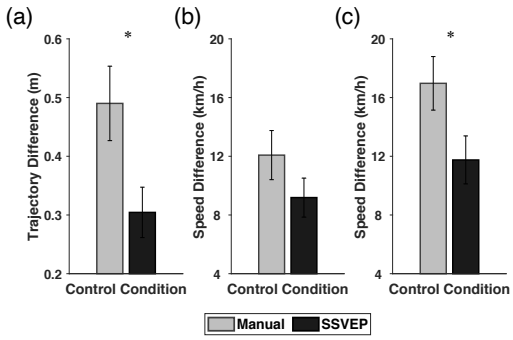


Figure 3. Driving performance comparison between control conditions for car-following driving test. (a) Trajectory difference; (b) Speed difference (total); (c) Speed difference (city).

Acknowledgements

This work was supported by Institute for Information & communications Technology Promotion (IITP) grant funded by the Korea government (MSIT) (2017-0-00432, Development of non-invasive integrated BCI SW platform to control home appliances and external devices by user's thought via AR/VR interface).

References

1. https://microsoft.github.io/AirSim
2. Y. Zhang, D. Guo, D. Yao, and P. Xu, "The extension of multivariate synchronization index method for SSVEP-based BCI", Neurocomput. 269, 226-231 (2017).

P-055

Inter-sectional Transcranial Direct Current Stimulation for a Focal Stimulation of Deep Brain Structures: A Simulation Study

Da Som Choi[1†], Sangjun Lee[1†], Jimin Park[1] and Chang-Hwan Im[1, 2, 3*]

1 Department of Electronic Engineering, Hanyang University, Seoul, Republic of Korea

2 Department of Biomedical Engineering, Hanyang University, Seoul, Republic of Korea

3 Department of HY-KIST Bioconvergence, Hanyang University, Seoul, Republic of Korea

dawesomii@gmail.com

Abstract

Transcranial direct current stimulation (tDCS) has been widely used for the modulation of neurons in neocortical regions. However, it is difficult to send electric fields to deep brain structures while avoiding the stimulation of overlying cortex. Recently, inter-sectional short pulse (ISP) stimulation was proposed as a new technique to selectively induce neural activities at neurons of subcortical structures. To overcome the limit of tDCS, in this study, we suggested a novel stimulation approach, inter-sectional tDCS (IS-tDCS), combining tDCS with ISP stimulation. IS-tDCS applies sequentially different current patterns at each time point; every current pattern sends a sufficient electric field for the modulation to a specific target deeply sited in the brain continuously while the electric field in the non-target regions at each time point is distributed differently. Through the computational simulations, our results demonstrated that IS-tDCS can deliver a continuous electric field to the target over time whereas a discontinuous stimulation in unwanted regions, compared to the conventional tDCS. The proposed stimulation can be used to improve the overall efficacy of noninvasive deep brain stimulation.

Background

Transcranial direct current stimulation (tDCS) has been highlighted as a promising technique that can modulate cortex excitability. However, the conventional transcranial direct current stimulation (tDCS) has a low performance on the stimulation of deep brain regions while avoiding the stimulation of cortical regions [1]. Intersectional short pulse (ISP) stimulation was proposed recently as a new technique to achieve a focal stimulation of deep brain structures [2]. Different pairs of electrodes generate currents sequentially in a short time, and the individual electric field generated from each electrode pair is focally delivered to the target. To address the shortcoming of tDCS, we suggest a novel stimulation approach, inter-sectional short – transcranial direct current stimulation (IS-tDCS), combining the concept of ISP stimulation with multi-channel tDCS. IS-tDCS can achieve a focal stimulation of the target sited in deep brain regions by injecting different current patterns obtained from 61 channels over time, which can continuously stimulate the target to induce tDCS-like aftereffects whereas non-target regions were only stimulated for the duration not sufficient for inducing aftereffects of tDCS. Thus, we hypothesize that IS-tDCS has an advantage on a more focal stimulation of the deep brain structure compared to the conventional tDCS.

Methods

Finite element (FE) head model was constructed with a magnetic resonance image (MRI), and the surface point at the head of the right hippocampus was set as a region of interest (ROI). The electric field in the entire domain were calculated by solving a quasi-static Laplace equation. By using the Globalized Bounded Nelder Mead optimization, we determined *n*'th current pattern at *n*'th time point. For the first current pattern, the objective function that can maximize the electric field along a desired direction at the target region while minimizing the electric field intensity in non-ROI regions was set, as follows:

$$w_1 \cdot \int_{\Omega_{\text{non-ROI}}} |\mathbf{E}^n| d\Omega \; - \; w_2 \cdot \int_{\Omega_{\text{ROI}}} \left(\mathbf{E}^n(\mathbf{r}) \cdot \mathbf{d}(\mathbf{r})\right) d\mathbf{r} \; (n = 1), \; (1)$$

Here, $|\mathbf{E}^n|$ and $\Omega_{\text{non-ROI}}$ represent the electric field intensity in n'th time point and the non-ROI regions, respectively. $\mathbf{E}^n(\mathbf{r})$ and $\mathbf{d}(\mathbf{r})$ denote the electric field intensity vector at n'th time point and a dimensionless

unit vector field representing the desired direction for the electric field at location $\boldsymbol{r}$ in ROI (Ω_{ROI}), respectively. We set the desired direction to x-direction in this study. The values of w_1 and w_2 are the weight factors, which were empirically determined to maximally minimize the objective function for each time point. From the second current pattern, we modified the objective function to determine the n'th current pattern that can be able to avoid the regions strongly stimulated in all prior time points from first to n-1'th. We set the objective function that can minimize the electric field at the highly stimulated deep brain regions where the electric field is larger than 70% of the maximum electric field in the prior time point until n-1'th time point, as follows:

$$w_1 \cdot \int_{\Omega_{\text{non-ROI, high}}} |\mathbf{E}^n| d\Omega \; - \; w_2 \cdot \int_{\Omega_{\mathrm{ROI}}} \left(\mathbf{E}^n(\mathbf{r}) \cdot \mathbf{d}(\mathbf{r})\right) d\mathbf{r}$$

$$(n \geq 2) \, , \, (2)$$

where $\Omega_{\text{non-ROI, high}}$ denotes the non-ROI regions highly stimulated in the previous time points. The optimization of the current patterns was repeated until five current patterns were obtained. To validate the feasibility of IS-tDCS that can reduce continuous stimulation of unwanted regions as we hypothesized, we evaluated the overlapped area in neocortical regions and overlapped volume in deep brain regions where the electric field is larger than 0.2 V/m for all time points, and we compared those to the conventional multi-channel tDCS (which is the same condition as the case at the first time point).

Results and Discussion

Figure. 1 depicts the regions where the electric field intensity remains above 0.2 V/m in the time duration from the first to n'th time point. As the number of the used time points increased, both non-ROI neocortical and deep brain regions continuously stimulated in all the time points were reduced.

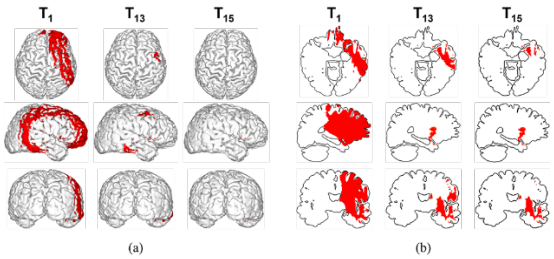


Figure.1 (a) Neocortical regions and (b) deep brain regions where the electric field intensity is higher than 0.2 V/m for the time duration from the first to n'th time points.

Figure. 2(a) shows that the target point in the head of the right hippocampus maintained 0.2 V/m, and Figure. 2(b) shows that the other deep brain structures were not continuously stimulated by IS-tDCS. Thus, the constant direct currents are dominantly delivered to the head of the right hippocampus which is the target in the current study.

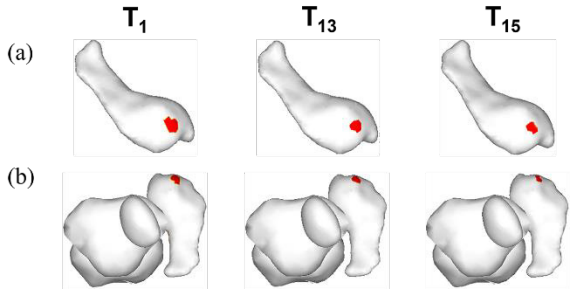


Figure. 2 Overlapped regions in (a) the right hippocampus and (b) other deep brain regions where the electric field intensity is higher than 0.2 V/m for the time duration from the first to n'th time points.

From these results, non-targeted regions would be discontinuously stimulated when applying the current patterns consecutively for five time points whereas the targeted region would be continuously stimulated over time. It is demonstrated that the regions where the electric field larger than 0.2 V/m kept being delivered over time were markedly reduced when employing different current patterns sequentially compared to when employing only one current pattern of the first time point. It suggests that IS-tDCS can allow for a more focal stimulation of the target than the conventional multi-channel tDCS.

Acknowledgements

This research was supported by the Brain Research Program through the National Research Foundation of Korea (NRF) funded by the Ministry of Science, ICT & Future Planning (No. NRF-2019M3C7A1031278).

References

1. Huang Y, Parra LCJBs. Can transcranial electric stimulation with multiple electrodes reach deep targets? 2019;12(1):30-40.

2. Vöröslakos M, Takeuchi Y, Brinyiczki K, Zombori T, Oliva A, Fernández-Ruiz A, et al. Direct effects of transcranial electric stimulation on brain circuits in rats and humans. Nature communications. 2018;9(1):1-17.

P-056

Semantic-hierarchical structured binary quantum-behaved particle swarm optimization for decoding spoken word evoked electrocorticography

Dongseok Kim[1] and Jihwan Woo[1, 2]

[1]Department of Electrical, Electronic and Computer Engineering, University of Ulsan, Republic of Korea

[2]Department of Biomedical Engineering, University of Ulsan, Republic of Korea

jhwoo@ulsan.ac.kr

Abstract

The meaning of spoken words is processed semantically by the human brain. Inspired by the brain's information processing mechanisms, we developed a semantic-hierarchical structured binary quantum-behaved particle swarm optimization (SH-BQPSO) feature selection algorithm. This proposed algorithm decodes the semantic grouping of words and then decodes the sub-word. Our study demonstrate that this approach effectively reduces the number of features while improving accuracy.

Background

In the brain-computer interface(BCI) system, brain signals are used to assess the overall state of the brain, brain activity, and user intention. Decoding methods are being studied to obtain more information about spoken word stimuli that evoke cortical responses. Features in the brain signals that are unrelated to the task of processing cause overfitting and reduce decoding accuracy. Therefore, a feature selection algorithm that reduces the dimensionality of datasets by eliminating many irrelevant and redundant features is necessary to improve decoding performance. Binary quantum-behaved particle swarm optimization (BQPSO) is an evolutionary search algorithm based on swarm intelligence theory, originally proposed by Sun et al. in 2007 [1]. Separately, Na et al. (2019) suggested a semantic hierarchical decoding model inspired by information processing mechanisms in the brain [2]. Here, we propose a semantic-hierarchical structured BQPSO (SH-BQPSO) that applies this semantic-hierarchical approach to the BQPSO algorithm.

Methods

Six native Korean-speaking participants were enrolled in this study. Subdural electrodes were implanted at the locations of their epileptic seizure foci and used to carry out clinically indicated ECoG signal monitoring. Eight monosyllabic Korean words, which were semantically categorized into two groups, were presented to each participant by the speaker. The first four words are the semantic group of the face, and the other four are numbers. Each word was randomly presented 80-110 times with a duration of 275-498 milliseconds (ms). Electrode grids were placed on either the left or right brain hemispheres of the study participants. The cortical maps in Figure 1 show only the language area of electrode locations for all participants. These locations were mapped relative to the Montreal Neurological Institute (MNI) average brain map coordinates using the Matlab Surfstat toolbox (The Mathworks Incorporated, USA). Decoding was carried out on ECoG signals from 13 electrodes located either in Broca's area, Wernicke's area, or primary auditory cortex.

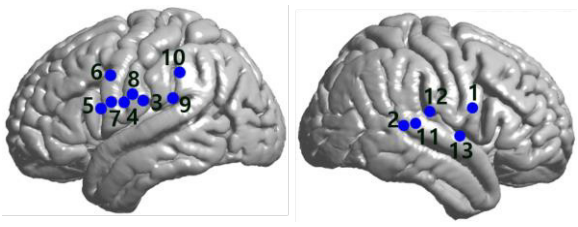


Figure 1. The language area was mapped onto 13 subdural electrodes in study participants. Left: left hemisphere for P3(electrode 3-5), P4(6), and P5(7-10). Right: right hemisphere for P1(1), P2(2), and P6(11-13).

Event-related spectral perturbation (ERSP) was used to extract task-related features of ECoG signals. The feature used to decode ECoG signals was calculated by averaging the ERSP in each frequency band (delta, theta, alpha, beta, low-gamma, high-gamma I, high-gamma II) with a 50% overlapped 100ms time window. Each ERSP was calculated from a set of 20-27 epochs. In total, four ERSP sets were obtained.

For feature selection using the BQPSO algorithm, particles are set as a binary string with a length equal to the number of features. In the binary string, 1 represents the selected feature, and 0 represents the excluded feature. Because feature selection has two goals, improving accuracy and reducing the number of features, the evaluation function for updating each particle was calculated as the weighted sum of decoding accuracy and the *norm*(F_{num}). The *norm*(F_{num}) is the normalizing function that re-arranges the number of selected features so that they are equal to the accuracy range. F_{num} denotes the number of selected features. The weight combination [w1, w2] for the evaluation value calculation contains 10 pairs of combinations, from [0.1, 0.9], [0.2, 0.8], etc., up to [1, 0]. Decoding accuracy was calculated over a 4-fold cross-validation process using a support vector machine (SVM) classifier.

We have developed an SH-BQPSO method that combines the BQPSO algorithm with the semantic-hierarchical model, thereby improving decoding accuracy. In the SH-BQPSO algorithm, the feature subset for word group classification is optimized first, before the feature subset of sub-words is optimized. In the second sub-word feature optimization step, decoding accuracy used for feature subset evaluation is calculated by counting the correct answers in both word groups and sub-word.

Results and Discussion

Figure 2 shows the comparison of the performances of the standard BQPSO and the SH-BQPSO algorithms. Because accuracy and the number of selected features were calculated for feature subset evaluation in this study, these two variables, obtained from the global best case, were used to compare the two algorithms.

Figure 2 (a) shows the average *norm*(F_{num}) and accuracy of 13 electrodes according to the weighted combination of the evaluation function. The rightmost case is [w1, w2] = [1, 0]. In the BQPSO method, the accuracy is the maximum 48.7%, and the minimum is 27.4% depending on the weight combination, and *norm*(F_{num}) is 31.3%, 16.7%. In SH-BQPSO, maximum and minimum accuracies were 64.4% and 56.8%, respectively, and *norm*(F_{num}) was 26.5% and 18.2%. These results indicate that reducing the number of selected features in the SH-BQPSO method has a smaller effect on accuracy relative to the BQPSO method.

Figure 2 (b) shows the *norm*(F_{num}) and accuracy for the 13 electrodes. The SH-BQPSO method showed a decrease in the number of selected features by -22.5% to 1.32% (mean -9.82%), when compared to the BQPSO method. These differences were statistically significant ($p<0.001$). Accuracy showed a gain of 18.8% to 57.9% (mean 35.4%) ($p<0.001$) with the SH-BQPSO method, relative to the BQPSO method. These results indicate that the SH-BQPSO algorithm is superior to the BQPSO algorithm for the feature optimization of spoken word-evoked cortical responses measured using ECoG signals.

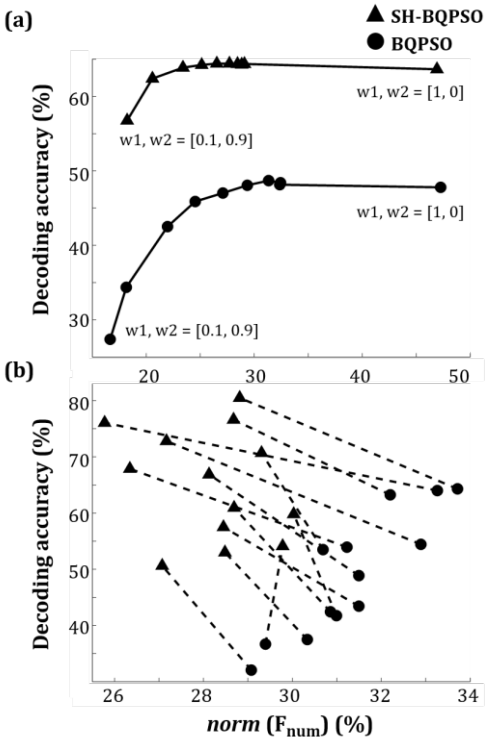


Figure 2. Comparison of the accuracy and selected features between the BQPSO and SH-BQPSO algorithms over 13 electrodes in study participants.

Acknowledgements

This research was supported by grants from the National Research Foundation of Korea (NRF-2020R1A2C2003319)

References

1. J. Sun, W. Xu, W. Fang, and Z. Chai, "Quantum-behaved particle swarm optimization with binary encoding", ICANNGA., Springer, Berlin, Heidelberg, 376-385 (2007).
2. Y. Na, I. Choi, D. P. Jang, J. K. Kang, and J. Woo, "Semantic-hierarchical model improves classification of spoken-word evoked electrocorticography", J. Neurosci. Methods., 311, 253-258 (2019).

Different Cosmetic Formulations Can Induce Distinct Neural Substrates

Hye-Ran Cheon[1,2], Gusang Kwon[3], and Han-Jeong Hwang[1,2*]

[1]Department of Electronics and Information Engineering, Korea University, Sejong, Korea

[2]Interdisciplinary Graduate Program for Artificial Intelligence Smart Convergence Technology, Korea University, Sejong, Korea

[3]Amorepacific R&D Center, Yongin, Korea

*hwanghj@korea.ac.kr

Abstract

In this study, we investigated the difference of neural substrates between different cosmetic formulations using electroencephalography (EEG) and classified the emotions evoked by different cosmetic formulations using EEG features. EEG data were measured while five subjects applied two positive and one negative cosmetic formulations. Event-related desynchronization (ERD) was relatively increased in negative formulation as compared to positive formulation, and the highest classification accuracy was 71.84%, demonstrating the possibility of decoding different emotions evoked by different cosmetic formulations. The result could be used to develop a neuromarketing system to propose customized cosmetic products.

Background

Cosmetic products have a variety of formulations. Applying cosmetics to the skin evokes emotions related to the texture of formulations, regardless of the effect of the product. Some formulations cause positive feelings, such as softness and moistness, while others cause negative feelings of stickiness or greasiness. Traditionally, questionnaires and survey were used to measure the emotions evoked when applying cosmetics. However, this method cannot capture a real-time response for cosmetic formulation-related emotions and can be flawed by the respondent's incorrect remembrance. For this reason, researchers proposed a new method using neurophysiological data to measure cosmetic formulation-related emotions [1, 2]. By using neurophysiological measures, it is possible to acquire more objective and quantifiable emotion-related data while using cosmetics. The purpose of this study was to compare the emotions evoked by the application of different cosmetic formulations using electroencephalography (EEG), and to automatically classify the emotions using EEG features based on machine learning technique.

Methods

Five subjects aged between 31 and 56 (4 females, 1 male) participated in the study. All subjects were healthy, and none of them had skin allergies, neurological or psychiatric disorders. Before the experiment, three locations of the subjects' left forearm were marked to deliver three different formulations, including two positive formulations (P1, P2) and one negative formulation (N). Each of the formulations was repeatedly applied three times in a random order. After applying each formulation using a pipette, a 10 sec baseline was given and then the subjects were instructed to apply the formulation for 20 sec using the right hand.

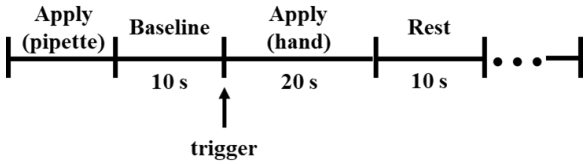


Figure 1. Experimental paradigm.

The EEG data were acquired using CGX Quick-20r (Cognionics Inc., San Diego, CA, USA) with twenty dry electrodes attached on the scalp according to international 10-20 system. A1 electrode was placed on the left earlobe as ground and reference electrode. The P3 electrode was excluded from further analysis due to severe physiological artifacts. The raw EEG data were band-pass filtered between 0.5 – 55 Hz and down-sampled at 200 Hz. The filtered EEG data were epoched for an interval of -1 – 20 sec based on the onset of the hand apply period. Independent component analysis (ICA) was applied to the epoched

data to remove physiological artifacts, such as electrooculography (EOG) and electromyography (EMG).

We performed event-related spectral perturbation analysis to investigate event-related (de)synchronization (ERD/ERS) and estimated mean ERD/ERS values over the time and channel for six different frequency bands (delta: 0.5 – 4 Hz, theta: 4 – 8 Hz, alpha: 8 – 12 Hz, beta: 12 – 30 Hz, gamma: 30 – 55 Hz, all: 0.5 – 55 Hz) to confirm the distinct ERD/ERS between the different formulations.

Classification of each formulation was performed for each frequency band using mean ERD/ERS values as features; one feature was extracted per channel. Data augmentation was performed using a 1 sec of window size with 50% overlap to increase the number of samples. Each augmented data was normalized to the range of 0 to 1 to reduce the variation between subjects. To prevent the overfitting issue, a subject-wise 5x5-fold cross-validation method was used to estimate classification accuracy. Support vector machine (SVM) model was used as a classifier with Fisher score for feature selection.

Results and Discussion

Figure 2 shows the difference of mean ERD/ERS values between positive and negative formulations for six frequency bands when applying each formulation. The negative formulation showed relatively stronger ERD compared to the positive formulation in general, but significant difference between formulations was not observed.

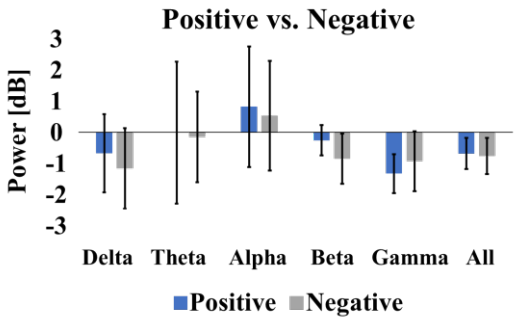


Figure 2. Grand-average ERD/ERS values of all subjects during applying the different formulations.

Figure 3 shows the average classification results with respect to the number of features. Overall, the beta band showed the highest classification accuracy, and in particular, the highest accuracy of 71.84% was observed when using six features selected by Fisher score in beta frequency band.

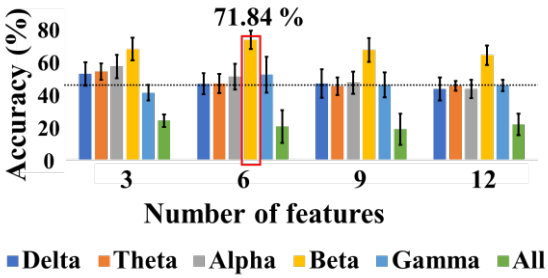


Figure 3. Average classification accuracies for six frequency bands with respect to the number of features.

In this study, we investigated the differences in EEG when different types of formulations were applied to the skin. As a result, the negative formulation showed relatively stronger ERD patterns as compared to the positive formulation and the highest classification accuracy of 71.84 % was shown, demonstrating the feasibility of decoding emotions induced by different formulations using EEG. In the future work, we attempt to acquire sufficient data in order to increase classification performance with more advanced classification algorithms such as deep learning.

Acknowledgements

This research was supported by a grant of the Korea Health Technology R&D Project through the Korea Health Industry Development Institute (KHIDI), funded by the Ministry of Health & Welfare, Republic of Korea (grant number : HP20C0083) and Institute for Information & Communications Technology Promotion (IITP) grant funded by the Korea government (MSIT) (No. 2017-0-00451).

References

1. D. Gabriel, E. Merat, A. Jeudy, S. Cambos, T. Chabin, J. Giustiniani and E. Haffen, “Emotional effects induced by the application of a cosmetic product: A real-time electrophysiological evaluation”, Appl. Sci., 11(11), 4766 (2021).
2. H. Singh, M. Bauer, W. Chowanski, Y. Sui, D. Atkinson, S. Baurley, M. Fry, J. Evans, and N. Bianchi-Berthouze, “The brain’s response to pleasant touch: an EEG investigation of tactile caressing”, Fron. Hum. Neurosci., 8, 893 (2014).

Realistic modeling of current steering during orientation selective deep brain stimulation of the subthalamic nucleus – The influence of anisotropic conductivity

C. Cheong[1], C. Im[2] and S. C. Jun[2]

[1]School of Life Science, Gwangju Institute of Science and Technology, Gwangju, Republic of Korea

[2]School of Electrical Engineering and Computer Science, Gwangju Institute of Science and Technology, Gwangju, Republic of Korea

scjun@gist.ac.kr

Abstract

Orientation selective deep brain stimulation (OS-DBS) is a new strategy of deep brain stimulation which enables to steer current and stimulate axons along a preferred direction. In this study, a realistic computational model was used to measure the direction of current in subthalamic nucleus. Two cases (isotropic or anisotropic white matter) were compared. We observed from simulation study that OS-DBS may steer current direction to the desired direction, however the direction of current is substantially influenced by anisotropic conductivity of white matter.

Background

Deep brain stimulation of the subthalamic nucleus (STN) is an established treatment for Parkinson's disease [1]. It is important to stimulate axons along hyperdirect pathway, while avoiding stimulating internal capsule fibers of passage to minimize side effects such as paraesthesia and involuntary muscle contraction. Based on the fact that the hyperdirect collaterals and the internal capsule fibers of passage are almost perpendicular to each other, a new approach to target the hyperdirect pathway selectively has been proposed. Orientation selective deep brain stimulation (OS-DBS) is the new method of DBS that uses three leads to steer electric current to a desired direction so that axons in that direction can be preferentially stimulated [2]. However, to the best of our knowledge, OS-DBS of STN has not yet been tested for humans. In this study, anatomically realistic computational model based on human MRI data set was developed to estimate the direction of current in STN in OS-DBS.

Methods

A publicly accessible and unidentified MRI data set consisting of T1-weighted MRI and diffusion tensor image (DTI) was obtained from the Human Connectome Project. STN was manually segmented using Multi-contrast PD25 atlas [3]. SimNIBS function 'headreco' was used to generate surface meshes of scalp, skull, cerebrospinal fluid (CSF) layer, gray matter, white matter, ventricles, and eyes [4]. Surface meshes of three Medtronic 3389 DBS leads were generated and positioned in that the center of the lowest contacts of three leads is at the centroid of STN voxels. Surface meshes of encapsulation layers consisting of cells grown around the DBS leads after surgery were also created. Encapsulation layers were modeled as isotropic homogeneous tissues with 0.25 mm thickness around DBS leads inside CSF layer. All of the surface meshes were merged into a single surface mesh and a volumetric mesh consisting of 6.3 million tetrahedra was generated using 'iso2mesh' toolbox [5]. Figure 1 shows the cross section of the final volumetric mesh crossing the first lead.

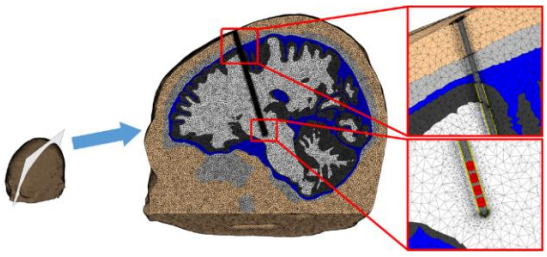


Figure.1 Cross section of the volumetric mesh – scalp (apricot), skull (light gray), CSF (blue), gray matter (dark gray), white matter (white), encapsulation layer (yellow), lead shafts (medium gray), and lead contacts (red).

The volumetric mesh was imported into COMSOL Multiphysics v5.2. Figure 2(a) shows the geometry of three DBS leads and STN voxels. The lowest contacts were the constant current source or sink. Figure 2(b) shows the definition of the angle θ. If the direction of axons to be stimulated (stimulation angle) is θ, current amplitudes of three contacts were set as

$I_1 = -\cos(\theta)$ [mA]

$I_2 = -\cos(\theta - 120°)$ [mA]

$I_3 = -\cos(\theta + 120°)$ [mA] ,

where positive current means a current source and negative current means a current sink [2]. All other contacts were set as perfect conductors and lead shafts were set as insulators.

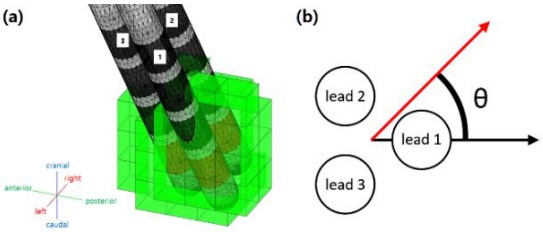


Figure. 2 (a) Three DBS leads and STN voxels. (b) Stimulation angle θ (direction of the red arrow).

Two cases were considered: the case where the conductivity of white matter is isotropic and the case where it is anisotropic. In the first case, conductivity of white matter was set to 0.126 S/m. In the second case, conductivity matrix of each voxel was set as

$$\sigma = S \begin{bmatrix} 10^{2/3} & 0 & 0 \\ 0 & 10^{-1/3} & 0 \\ 0 & 0 & 10^{-1/3} \end{bmatrix} S^T \times 0.126 \text{ [S/m]}$$

where S is an orthonormal eigenvector. Conductivity matrices of the voxels were linearly interpolated to assign conductivity to all tetrahedra of white matter. In each case, the average current densities toward varying directions of θ's was calculated inside STN voxels, excluding encapsulation layers and leads.

Results and Discussion

Figure 3 shows the average current densities toward varying θ's for 6 stimulation angles: 0˚, 30˚, 60˚, 90˚, 120˚, and 150˚. In the case of isotropic white matter, most current densities headed toward the stimulation angle, while small amount of current densities was directed perpendicularly with respect to the stimulation angle. In the case of anisotropic white matter, although distortions toward the direction between about θ=30˚ and θ =60˚ was shown, similar tendency to the previous case was observed. This result suggests that OS-DBS generates current primarily to desired direction and therefore enables orientation-selective stimulation at STN. Also, it should be noted that orientation selectivity of current may be influenced by anisotropy of white matter tissue.

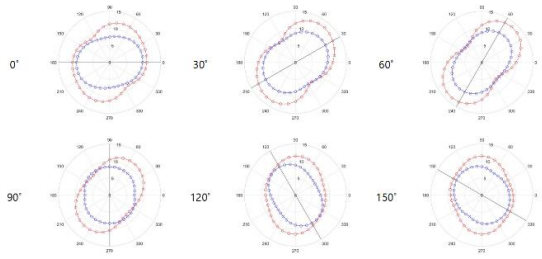


Figure. 3 Average current densities [A/m^2] toward varying θ's; anisotropic (red) and isotropic (blue) cases.

Acknowledgements

This work was supported by the Institute of Information & Communications Technology Planning & Evaluation (IITP) grant funded by the Korea government (No. 2017-0-00451) and the '2021 Joint Research Project of Institutes of Science and Technology.

References

1. A. L. Benabid, S. Chabardes, J. Mitrofanis, and P. Pollak, "Deep brain stimulation of the subthalamic nucleus for the treatment of Parkinson's disease", The Lancet Neurology, 8(1), 67-81, 2009.
2. L. J. Lehto, A. Canna, L. Wu, A. Sierra, E. Zhurakovskaya, J. Ma, C. Pearce, M. Shaio, P. Filip, M. D. Johnson, W. C. Low, O. Gröhn, H. Tanila, S. Mangia, and S. Michaeli, "Orientation selective deep brain stimulation of the subthalamic nucleus in rats", Neuroimage, 213, 116750, 2020.
3. Y. Xiao, V. Fonov, M. M. Chakravarty, S. Beriault, F. A. Subaie, A. Sadikot, G. B. Pike, G. Bertrand, and D. L. Collins, "A dataset of multi-contrast population-averaged brain MRI atlases of a Parkinson′ s disease cohort", Data in brief, 12, 370-379, 2017.
4. J. D. Nielsen, K. H. Madsen, O. Puonti, H. R. Siebner, C. Bauer, C. G. Madsen, G. B. Saturnino, and A. Thielscher, "Automatic skull segmentation from MR images for realistic volume conductor models of the head: Assessment of the state-of-the-art", Neuroimage, 174, 587-598, 2018.
5. Q. Fang and D. A. Boas, "Tetrahedral mesh generation from volumetric binary and grayscale images", In 2009 IEEE international symposium on biomedical imaging: from nano to macro (pp. 1142-1145). Ieee, 2009.

The Influence of Frequency Bands and Brain Region on ECoG-Based BMI Learning Performance

Seokbeen Lim[2,†], Wongyu Jung[1,†], Youngjong Kwak[2], Jeongeun Sim[2], Jinsick Park[2] and Dong Pyo Jang[2,*]

[1]Department of Electronics and Computer Engineering, Hanyang University, Seoul, Korea
[2]Department of Biomedical Engineering, Hanyang University, Seoul, Korea
[†]Contributed equally to this work
[*]dongpjang@hanyang.ac.kr

Abstract

Numerous brain-machine interface (BMI) studies have shown that various frequency bands (alpha, beta, and gamma bands) can be utilized in BMI experiments and modulated as neural information for machine control after several BMI learning trial sessions. In addition to frequency range as a neural feature, various areas of the brain, such as the motor cortex or parietal cortex, have been selected as BMI target brain regions. However, although the selection of target frequency and brain region appears to be crucial in obtaining optimal BMI performance, the direct comparison of BMI learning performance as it relates to various brain regions and frequency bands has not been examined in detail. In this study, ECoG-based BMI learning performances were compared using alpha, beta, and gamma bands, respectively, in a single rodent model. Brain area dependence of learning performance was also evaluated in the frontal cortex, the motor cortex, and the parietal cortex. The findings indicated that BMI learning performance was best in the case of the gamma frequency band and worst in the alpha band (one-way ANOVA, $F = 4.41$, $p < 0.05$). In brain area dependence experiments, better BMI learning performance appears to be shown in the primary motor cortex (one-way ANOVA, $F = 4.36$, $p < 0.05$). In the frontal cortex, two out of four animals failed to learn the feeding tube control even after a maximum of 10 sessions. In conclusion, the findings reported in this study suggest that the selection of target frequency and brain region should be carefully considered when planning BMI protocols and for performing optimized BMI.

Background

The brain-machine interface (BMI) was designed to restore sensorimotor functions in people in need of rehabilitation, as well as to control external devices using patterns of electrical signals generated by cortical neurons in the brains of people using neuroprosthetics [1, 2].

Electrocorticography (ECoG) has an advantage in that it is possible to record a signal of better quality than that of scalp EEG because electrodes are placed on the surface rather than being inserted into the brain [3, 4]. Thus, many researchers have continued to report findings from BMI studies with ECoG signals on the motor cortex. They showed that features of gamma-band on the motor cortex have potential for use in BMI studies [3, 5-7].

Analogous to motor learning, if the process of BMI learning is similar to a motor learning task [8], the animal should be able to modulate not only the gamma band of brain oscillation but also the oscillation of the alpha and beta bands for BMI learning and external device control [9-11]. Although these studies show the applicability of various frequency bands to BMI [9, 10], there are few studies demonstrating how learning efficacy, such as learning speed and capability, may differ depending on frequency band, raising the question of whether a particular frequency may be optimal. In addition to frequency band, various areas of the brain have been selected previously as targets for inserting an electrode. Traditionally, the motor cortex has been the main target, but recently, other areas, including the parietal cortex, have been targeted as the brain cortex for use in BMI applications [12]. However, although the selection of target frequency and brain region appears to be crucial to obtaining optimal BMI performance, the direct comparison of BMI learning performance as it relates to brain region and frequency band has not been examined in detail.

Thus, for this report, two comparison studies were performed to validate ECoG-based BMI learning performance with respect to spectrum power band (alpha, beta, and gamma bands) and brain region (the frontal cortex, the motor cortex, and the parietal cortex).

Methods

A. Brain-Machine Interface (BMI) Learning session: Feeding tube control by ECoG Signal

We conducted an ECoG-based BMI learning session by making the animal neural control of the water feeding tube. For ECoG signal acquisition, two screw-type recording electrodes were implanted on the skull. Before the BMI learning session, the animals were deprived of water for about 12 h to encourage them to perceive water as a reward. A single BMI learning trial consisted of a ready state (5 s) and a learning state (15 s), as shown in Figure 1A (BMI learning session box). After finishing the ready state, a 4.5 kHz beep sound alerted the animal to recognize the beginning of the learning state. In this state, the feeding tube was controlled based on their ECoG signals. The feeding

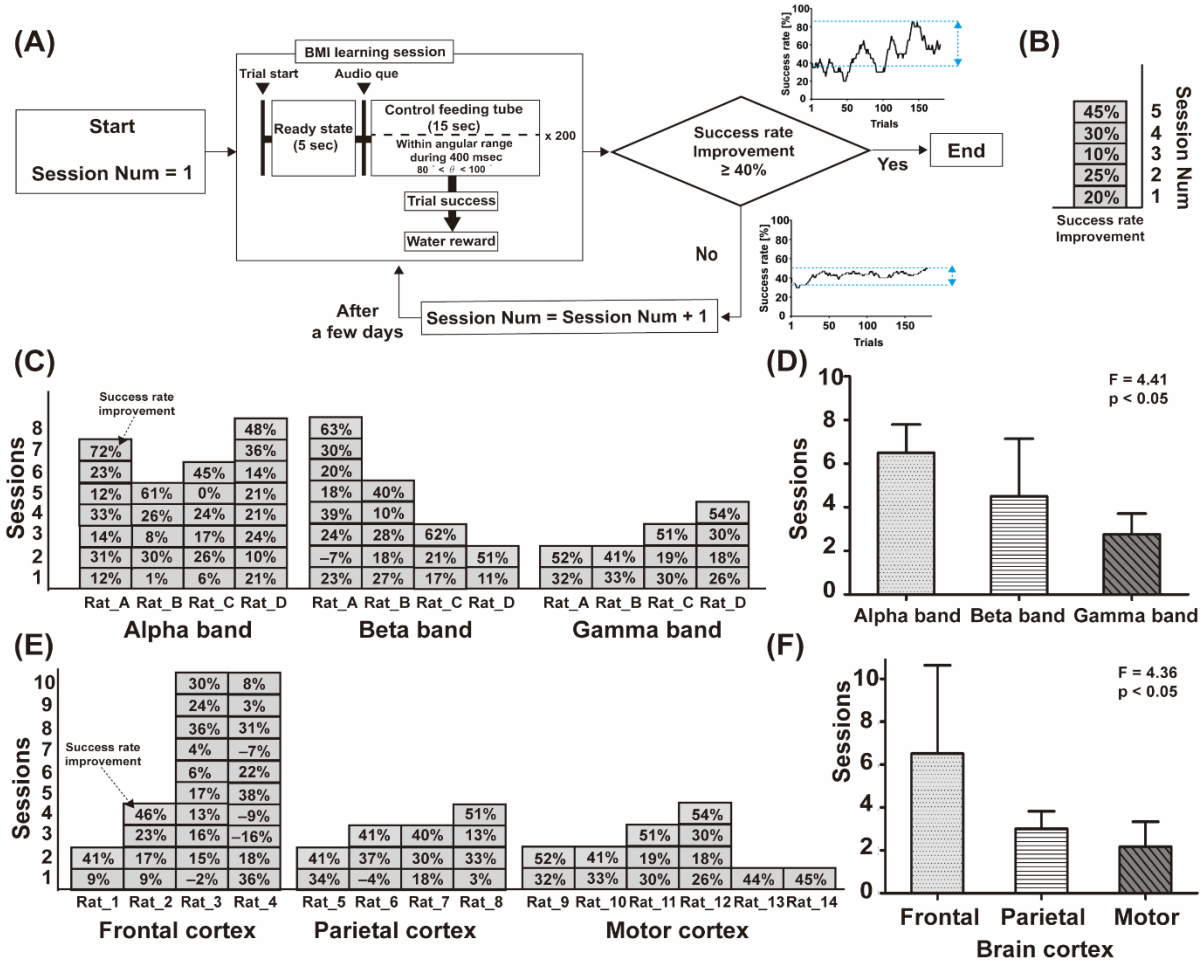


Figure 1. BMI learning protocol and learning results. (A) The repeated multiple BMI learning session protocol. The BMI learning session was repeated until the success rate improvement condition was satisfied. (B) The number of conducted sessions and success rate improvement of each session. (C) Total sessions and success rate improvements for frequency-dependent BMI learning of each animal. (D) Average sessions for successful frequency-dependent BMI learning. (E) Total sessions for brain-area-dependent BMI learning of each animal (frontal and parietal cortex group, n = 4; motor cortex group, n = 6), (F) Graphs of average sessions for successful brain-area-dependent BMI learning.

tube angular position was updated with the averaged spectrum power that was calculated from ECoG data within a specific frequency band (i.e., a 30–55 Hz gamma band) at intervals of 200 ms. The subjects were required to keep a feeding tube at specific angular ranges (between 80° and 100°) for 400 ms. If they succeeded in maintaining a feeding tube at those ranges, they could take in water as a reward, and it was counted as a success trial. If not, within 15 s after the beep sound, the trial was recorded as a fail trial.

To evaluate BMI learning performance, we obtained a learning curve with the success rate calculated as the ratio of the number success trials among 20 consecutive trials. In addition, success rate improvement was defined to estimate BMI learning performance as the difference between the first success rate and maximum success rate within the session.

B. The BMI Learning Performance Comparison Protocol: Frequency and Brain Region

Two comparison studies were designed and conducted to validate ECoG-based BMI learning performance with respect to spectrum power band and brain region. In the first study, the effect of frequency band on BMI learning performance was evaluated with alpha (8–13 Hz), beta (13–30 Hz), and gamma (30–55 Hz) bands in the rat with the electrode placed on the primary motor cortex. BMI learning performance for one of the frequencies was validated with repeated multiple BMI learning session protocols because it could be influenced by various factors such as daily conditions. First, the animal performed a BMI learning session by modulating the specific frequency power of the ECoG for feeding tube control as described in the previous section. If the success rate improvement in the BMI learning session was not

greater than 40% (empirically defined criterion), the same BMI learning session was performed again a few days later (Figure 1A). The BMI learning sessions were repeated until success rate improvement was above the criterion. The maximum number of sessions was 10. Finally, we recorded the number of sessions conducted for fulfilling the 40% success rate improvement criterion. After finishing this protocol with a specific frequency, the entire protocol was conducted again at the other two frequencies with the same animal. Four rats were used in this frequency comparison study.

In the second study, the influence of brain region on BMI learning performance was evaluated at the frontal cortex, the motor cortex, and the parietal cortex. Recording electrodes were implanted in one of three brain regions in the animal. BMI learning performance was validated using the repeated multiple BMI learning session protocol. All protocols were conducted with a gamma frequency band. A total of 14 rats took part in this study (four rats per frontal and parietal cortex, six rats to the motor cortex).

C. Subject and electrode location

Fourteen healthy, adult Sprague Dawley rats (300-350 g, male, Koatech, Pyeongtaek, Korea) were used in the ECoG-based BMI learning experiments. In the frequency-dependent BMI learning study, two recording electrodes were implanted the bilateral primary motor cortex (AP: +2 mm, ML: ±3 mm). In the case of the brain area-dependent BMI learning experiment, the recording electrodes were implanted in the bilateral frontal association cortex (AP: +5.64 mm, ML: ±1.9 mm), the bilateral medial parietal association cortex (AP: –4.08 mm, ML: ±2.1 mm), and the bilateral primary motor cortex (AP: +2 mm, ML: ±3 mm). All experiments procedures were approved by the Hanyang University Institutional Animal Care and Use Committee (IACUC No. 2019-0151A).

Results

A. BMI Learning Performance Comparison Study for Frequency Bands

As shown in Figure 1C, in the case of "Rat_A", the animal met the criterion after seven sessions in the case of the alpha frequency band, and after eight sessions in the case of the beta band. In contrast, only two sessions were conducted for the gamma frequency band. As shown in Figure 1D, the subjects finally succeeded in BMI learning after 2.8 ± 1.0 sessions in the gamma band, 4.5 ± 2.6 sessions in the beta band, and 6.5 ± 1.3 sessions in the alpha band. The animals showed significantly faster learning performance when the gamma band was used (One-way ANOVA, $F = 4.41$, $p < 0.05$).

B. BMI Learning Performance Comparison Study on Brain Region

The animals succeeded in BMI learning after 2.2 ± 1.2 sessions in the case of the motor cortex, 3.0 ± 0.8 sessions in the case of the parietal cortex, and 6.5 ± 4.1 sessions in the case of the frontal cortex (Figure 1E, 1F). Animals showed significantly better BMI learning performance when the motor cortex was used (one-way ANOVA, $F = 4.36$, $p < 0.05$). As shown in Figure 1E, in the case of the frontal cortex area, two animals (Rat_3 and Rat_4) failed to show learning performance above the success rate improvement criterion even after the maximum of 10 sessions.

Conclusion

In this study, we implemented a rodent ECoG BMI system and compared BMI learning performance using multiple frequency bands and brain regions. The findings indicated that BMI learning performance was best in the case of the gamma frequency band and worst in the alpha. In brain area-dependence experiments, better BMI learning performance was shown in the primary motor cortex. The findings presented in this study suggest the selection of target frequency and brain region need to be carefully considered in planning future BMI studies.

Acknowledgements

This research was supported by the National Research Foundation of Korea (NRF) funded by the Ministry of Science and ICT (NRF-2019M3C7A1031278) and was supported by the Technology Innovation Program (Alchemist Project, 20012461) funded By the Ministry of Trade, Industry & Energy (MOTIE, Korea). This paper was published in *Sensors*, 2021.

References

[1] J. J. Shih, D. J. Krusienski, and J. R. Wolpaw, "Brain-computer interfaces in medicine," *Mayo Clin Proc,* vol. 87, no. 3, pp. 268-79, Mar 2012, doi: 10.1016/j.mayocp.2011.12.008.

[2] M. M. Shanechi, "Brain-Machine Interface Control Algorithms," *IEEE Trans Neural Syst Rehabil Eng,* vol. 25, no. 10, pp. 1725-1734, Oct 2017, doi: 10.1109/TNSRE.2016.2639501.

[3] E. C. Leuthardt, G. Schalk, J. R. Wolpaw, J. G. Ojemann, and D. W. Moran, "A brain–computer interface using electrocorticographic signals in humans," *J Neural Eng,* vol. 1, no. 2, pp. 63-71, 2004/06/01 2004, doi: 10.1088/1741-2560/1/2/001.

[4] H. Choi *et al.*, "Improved prediction of bimanual movements by a two-staged (effector-then-trajectory) decoder with epidural ECoG in nonhuman primates," (in English), *J Neural Eng,* vol. 15, no. 1, Feb 2018, doi: ARTN 016011

[5] T. Costecalde *et al.*, "A Long-Term BCI Study With ECoG Recordings in Freely Moving Rats," *Neuromodulation,* vol. 21, no. 2, pp. 149-159, Feb 2018, doi: 10.1111/ner.12628.

[6] J. D. Wander *et al.*, "Distributed cortical adaptation during learning of a brain-computer interface task," *Proc Natl Acad Sci U S A,* vol. 110, no. 26, pp. 10818-23, Jun 25 2013, doi: 10.1073/pnas.1221127110.

[7] Y. Guo, R. A. Foulds, S. V. Adamovich, and M. Sahin, "Encoding of forelimb forces by corticospinal tract activity in the rat," (in English), *Front Neurosci-Switz,* Original Research vol. 8, no. 62, 2014-May-01 2014, doi: 10.3389/fnins.2014.00062.

[8] N. Censor, D. Sagi, and L. G. Cohen, "Common mechanisms of human perceptual and motor learning," *Nat Rev Neurosci,* vol. 13, no. 9, pp. 658-64, Sep 2012, doi: 10.1038/nrn3315.

[9] J. R. Wolpaw and D. J. McFarland, "Control of a two-dimensional movement signal by a noninvasive brain-computer interface in humans," (in eng), *P Natl Acad Sci USA,* vol. 101, no. 51, pp. 17849-17854, 2004, doi: 10.1073/pnas.0403504101.

[10] B. Engelhard, N. Ozeri, Z. Israel, H. Bergman, and E. Vaadia, "Inducing gamma oscillations and precise spike synchrony by operant conditioning via brain-machine interface," *Neuron,* vol. 77, no. 2, pp. 361-75, Jan 23 2013, doi: 10.1016/j.neuron.2012.11.015.

[11] A. Dubey and S. Ray, "Comparison of tuning properties of gamma and high-gamma power in local field potential (LFP) versus electrocorticogram (ECoG) in visual cortex," *Sci Rep,* vol. 10, no. 1, p. 5422, Mar 25 2020, doi: 10.1038/s41598-020-61961-9.

[12] R. A. Andersen, S. Kellis, C. Klaes, and T. Aflalo, "Toward More Versatile and Intuitive Cortical Brain-Machine Interfaces," (in English), *Curr Biol,* vol. 24, no. 18, pp. R885-R897, Sep 22 2014. [Online].

Monitoring basal dopamine change using MCSWV to identify the roles of MAO-A and MAO-B in dopamine degradation

Hyun-U Cho[1], Jeongeun Sim[1], and Dong-Pyo Jang[1*]

Dept. of Biomedical Eng., Hanyang University, Seoul, Korea[1]

*dongpjang@gmail.co.kr

Abstract

Monoamine oxidase (MAO) has been attributed to the degradation of monoamine neurotransmitters including dopamine(DA) in the brain. Among two types of MAO, MAO-B has been widely accepted as a key enzyme responsible for DA degradation, and this belief led to a notion that the symptomatic relief of MAO-B inhibitors for patients with Parkinson's disease is most likely due to an increase in extracellular DA concentration. However, direct evidence of this notion has been lacking. Here we demonstrate that MAO-A, but not MAO-B, mainly contributes to striatal DA degradation by utilizing in-vivo basal electrochemical monitoring of extracellular DA with recently developed multiple-cyclic square wave voltammetry(MCSWV). We conclude that MAO-A and MAO-B have different roles in the degradation of DA: MAO-A regulates extracellular dopamine level whereas MAO-B has less effect on striatal DA level.

Background

Monoamine oxidase (MAO) is an enzyme that catalyzes the oxidative deamination of biogenic amines [1]. MAO inhibitors are prescribed to patients with depression and Parkinson's disease (PD) to increase DA secretion within the brain [2]. MAO exists in two isoenzymes, MAO-A and MAO-B, with different substrate specificities and roles in the metabolism of neuroactive monoamines, such as dopamine (DA), norepinephrine, and serotonin in the brain. DA has traditionally been thought to be degraded by both MAO-A and MAO-B due to a positive therapeutic effect of both inhibitors for Parkinson's disease (PD) patients. However, many studies show ambiguous results upon the major role of MAO-A and MAO-B in DA degradation [3]. In this study, we investigated the contributions of MAO-A and MAO-B in striatal DA degradation by in vivo multiple-cyclic square wave voltammetry (M-CSWV) techniques accompanied with inhibitory drug study. Given these findings, we differentiate the roles of MAO-A and MAO-B in DA degradation.

Methods

R Rodents were anesthetized with intraperitoneal urethane (1.6 g/kg, i.p.) and stabilized on a stereotaxic frame. Two holes with a diameter of 0.5-1.0 mm were drilled in the skull for the implantation of a carbon fiber microelectrodes (CFM, AS4, d = 7μm l = 80 ~ 100 μm) and Ag/AgCl reference electrode. Electrode coordinates were defined by rat brain atlas based on the skull position using bregma as a reference point with coordinates anteroposterior (AP), mediolateral (ML), and dorsoventral (DV). The CFM was placed in the right hemisphere in the striatum (AP +1.2 mm; ML +2.0 mm; DV -4.5 to -5.5 mm).

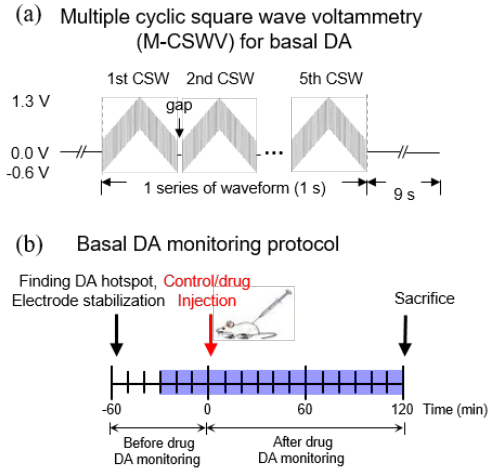


Figure 1 (a) Schematic design of multi cyclic square wave voltammetry (M-CSWV) (b) Experimental schedule for tonic DA monitoring.

Once an optimal CFM recording site was identified, rats were constantly measured with M-CSWV recording system for monitoring tonic DA concentration. Five cyclic square waveforms, which consisted of a large-amplitude square wave modulation on top of a symmetric staircase voltammogram was applied in sequence at a frequency of 0.1 Hz. Data collection and analysis of MCSWV

was performed using a commercial electronic interface (NIUSB-6363, National Instruments) with a base-station PC, a home-made current-to-voltage amplifier without an analog filter to preserve sharp current responses to the square pulse and software written in-house using LabVIEW 2016 (National Instruments, Austin, TX). Data processing is done by MATLAB (MathWork Inc., Natick, MA) which included temporal averaging, filtering, and simulating background currents. Basal DA response was extracted from the 2-dimensional voltammogram, indicated by oxidation peaks seen in red in the region-of-interest marked with a circle at the range of 0.2 V to 0.45 V. For the pharmacological test, selegiline (10 mg kg−1; i.p.) and clorgiline (10 mg kg−1; i.p.) was selected for selective MAO-A and MAO-B inhibition. All inhibitors were dissolved in DI water and injected 500 uL with a single dose, respectively.

Results and Discussion

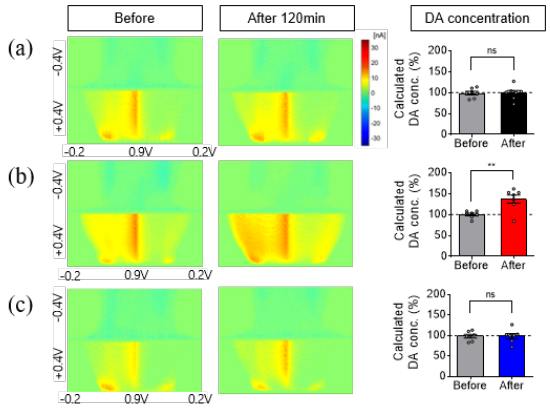


Figure 2. The representative changes in tonic DA level monitored by M-CSWV in response to treatment with saline control, MAO-A inhibitor (clorgiline, 10 mg kg^{-1}), and MAO-B inhibitor (selegiline, 10 mg kg^{-1}) (N = 7, 6, and 7). Representative pseudo-color plots demonstrate the tonic DA level in response to M-CSWV before (left) and after 120 minutes (middle) from drug administration. The changes in tonic DA concentration changes were quantified (right).

Figure. 2 shows the result of MCSWV, whether MAO-A or MAO-B is engaged in the maintenance of the basal DA level. At first, we confirmed that vehicle injection did not significantly alter the basal DA concentration after 2 hours of observation (98.97 ± 6.28%). However, MAO-A inhibition by clorgiline (10 mg kg−1) caused a significant increase in the basal DA level after 120 min (147.29 ± 6.39%), whereas MAO-B inhibition by selegiline (10 mg kg−1) did not (91.83 ± 7.16%). These findings indicate that MAO-A inhibition elevates basal DA level in the striatum while MAO-B does not change DA level in the striatum.

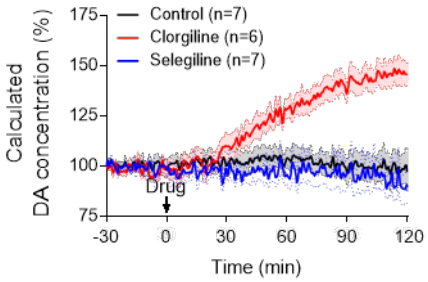


Figure 3. Quantification of the time-dependent changes in tonic DA concentrations

In conclusion, in vivo electrochemical monitoring of DA currents using M-CSWV revealed that the acute pharmacological inhibition of MAO-B by selegiline did not affect basal DA levels, which was inconsistent with the traditional belief in the treatment for improving the DA deficient state such as PD. Additionally, our findings demonstrate MAO-A, but not MAO-B, is mainly responsible for tonic DA levels in the striatum by mediating DA degradation. Our results would be important to differentiate the obscure roles of MAO-A and MAO-B in DA metabolism and support the idea that MAO-B is not involved in DA degradation but is associated with other neurotransmitters.

Acknowledgements

This research was supported by the National Research Foundation of Korea (NRF) grant funded by the Korea government (MSIT). (No. 2021R1A2B5B02002437).

References

1. Shih, J. C., Chen, K. & Ridd, M. J. "Role of MAO A and B in neurotransmitter metabolism and behavior" Pol J Pharmacol., 51, 25-29 (1999)
2. Finberg, J. P. & Rabey, J. M. "Inhibitors of MAO-A and MAO-B in Psychiatry and Neurology" Front Pharmacol., 7, 340, (2016)
3. Fornai, F. *et al.* "Striatal dopamine metabolism in monoamine oxidase B-deficient mice: a brain dialysis study." J Neurochem., 73, 2434-2440, (1999)

Quantitative analysis on Temporal Interface-stimulation for Deep Brain Stimulation

Jeongju Moon[1], Bonjae Koo[1], and Kyungsik Eom[1]
[1]Department of Electronic Engineering, Pusan National University, Pusan, Korea
kseom@pusan.ac.kr

Abstract

Recently, Temporal Interference (TI) stimulation has emerged as a Deep Brain Stimulation ("DBS") technique. However, studies on neural response to carrier or delta frequency and current amplitude are insufficient. This study presents seven responses and conduction block as a result of applying temporal interface("TI") stimulation(1kHz to 100kHz, 1mA to 200mA) to neurons. The tendency of the responses varied depending on the carrier frequency and delta frequency. As the carrier or delta frequency increases, the threshold value of each response also tends to increase.

Background

Neurostimulation can improve the quality of life of people suffering from severe paralysis and severe loss of various sensory organs, and is also used to relieve pain in patients with severe chronic pain. In particular, DBS has been shown to be effective against movement disorders such as Parkinson's disease and dystonia, as well as disorders such as depression and obsessive-compulsive disorder. One of the DBS methods is transcranial magnetic stimulation ("TMS"), which is widely used in clinics because it is non-invasive. However, TMS systems have a limited trade-off between depth penetration and the focal point of the induced electric field.

Temporal interference (TI) stimulation is a potential non-invasive method that promises stimulation in the deep brain region. The concept of TI stimulation is to deliver multiple electric fields at relatively high but slightly different frequencies. A neural membrane with the inherent low-pass filtering of electrical signals makes it impossible for nerve electrical activity to follow high frequency. [1] Therefore, during TI stimulation, neurons in the brain do not respond directly to these high-frequency electric fields. However, due to the small frequency difference, the two application fields can eventually form temporally interfering fields with envelope modulation at different frequencies to track neural responses. Here, we present a study of the response to TI stimuli using Python and NEURON, depending on carrier frequency, delta frequency, and current amplitude.

Methods

We use the code of [1]. Figure. 1 shows the experimental set-up. There are two pairs of electrodes on the x-y plane, and the electrodes of the first electrode pair are located at (5,5), (-5,5)and the electrodes of the second are located at (5,-5), (-5, -5). The neuron is located on the x-axis, the middle point of the two electrode pairs.

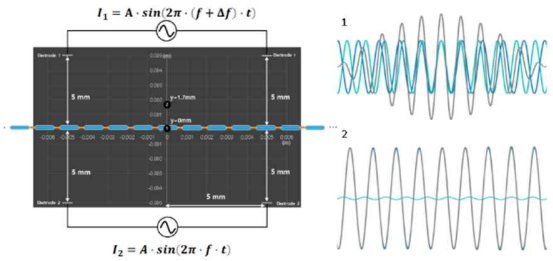


Figure. 1 Simulation set-up

For TI-stimulation, a sine waveform signal with the frequency, f_1, was applied to the first electrode pair and a sine waveform signal with the frequency, $f_2 = f_1 + \triangle f$, was applied to the second electrode pair.

The electrode is assumed to be an ideal current source, and the potential field generated from the current source is calculated by Equation :

$$V(x,y,z) = \frac{I_0}{4\pi\sqrt{\sigma_{xx}\sigma_{yy}\sigma_{zz}}} \frac{1}{\sqrt{\frac{(x-x_s)^2}{\sigma_{xx}} + \frac{(y-y_s)^2}{\sigma_{yy}} + \frac{(z-z_s)^2}{\sigma_{zz}}}} \quad \text{(Equation 1) [1]}$$

Overall potential field is calculated using Equation :

$$V_{total}(x,y,z,t) = V_1(x,y,z)\sin(2\pi f_1 t) + V_2(x,y,z)\sin(2\pi f_2 t) \quad \text{(Equation 2) [1]}$$

To describe the electrical properties of neurons, an isotropic infinite space with a diagonal conductivity

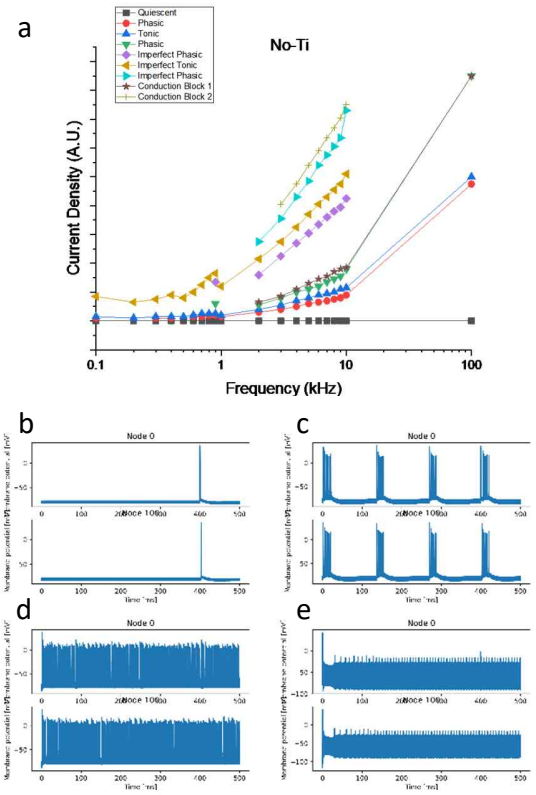
tensor was assumed and set to σ_{xx}= 0.6, σ_{yy} = 0.083, σ_{zz} = 0.083.

We use myelinated marmalian axon model and nueron morphology is composed of 100 node of ranvier, including myelin sheath. The 50th node of Rangvier was placed at (0, 0).

TI-stimulation was applied for 500ms and test pulse was applied at 0th node to check whether the action potential by test pulse reached to the 100th node.

In the case of non-TI stimulation, the simulation was carried out by increasing the carrier frequency from 5 Hz to 100 kHz, and the current amplitude from 1 mA to 200 mA in each carrier frequency. In the case of TI stimulation, the simulation was carried out by increasing the carrier frequency from 100 Hz to 100 kHz and the amplitude of the current from 1mA to 200 mA in each carrier frequency. In the case of TI stimulation, simulation was conducted repeatedly changing the test pulse injection time.

Results and Discussion



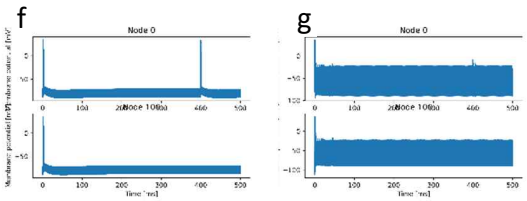
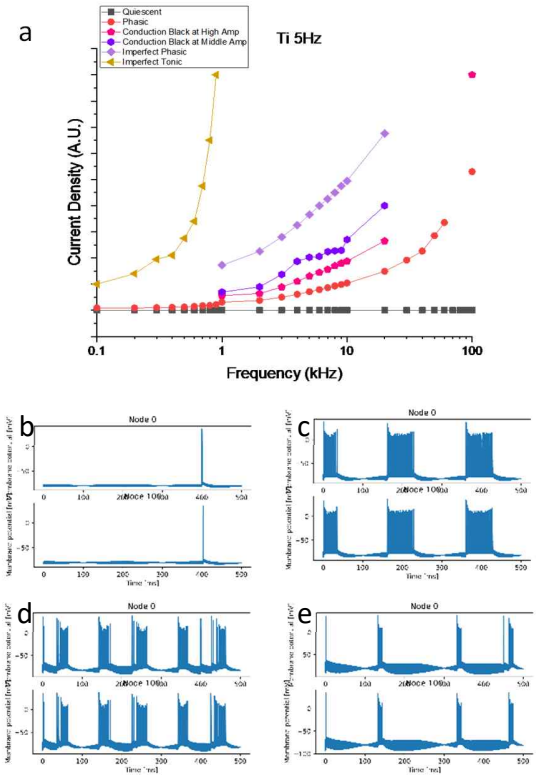


Figure. 2 TI-stimulation simulation results when delta frequency is 0Hz

(a) Threshold value of response of TI-stimulation according to carrier and delta frequency

(b-g) Response of TI-stimulation when carrier frequency is 10kHz

Figure. 2 shows the simulation results when delta frequency is 0Hz. Figure. 2(a) shows the threshold value in which each response appears according to the carrier frequency, and Figure. 2(b)-(g) show the typical responses in neuron when the carrier frequency is 10 kHz. There are six kinds of responses; quiescent, phasic, tonic, imperfect phasic, imperfect tonic, conduction block, as neurons' reactions to non-TI stimulation.



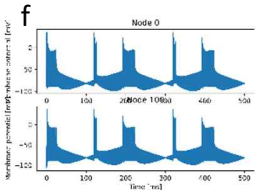


Figure. 3 TI-stimulation simulation results when delta frequency is 5Hz
(a) Threshold value of response of TI-stimulation according to carrier and delta frequency
(b-g) Response of TI-stimulation when carrier frequency is 10kHz

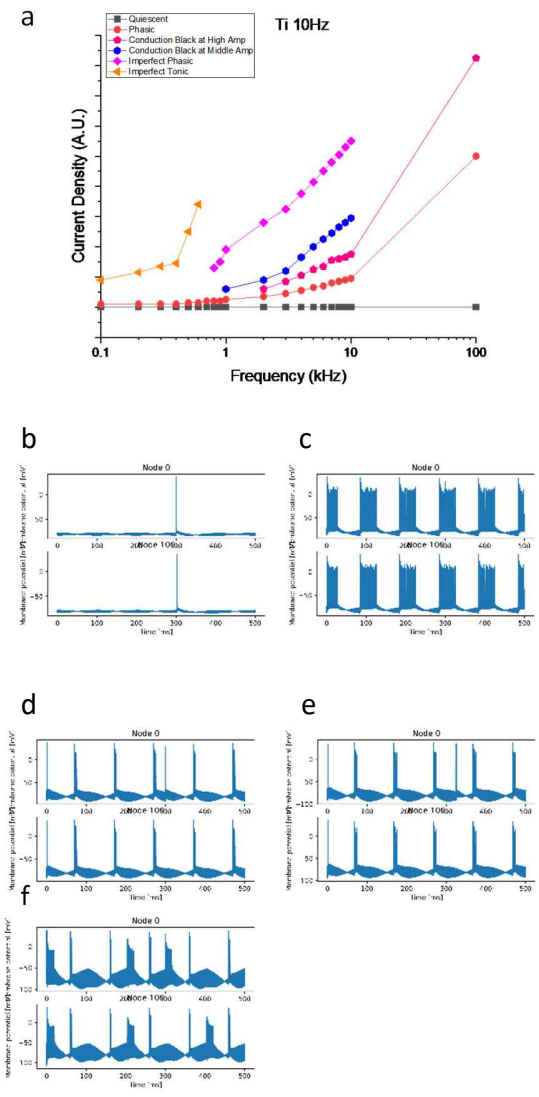


Figure. 4 TI-stimulation simulation results when delta frequency is 10Hz
(a) Threshold value of response of TI-stimulation according to carrier and delta frequency
(b-g) Response of TI-stimulation when carrier frequency is 10kHz

Figure. 3 and 4 shows the simulation results when delta frequency is 5Hz and 10Hz respectively. Figure. 3(a) and 4(a) shows the threshold value in which each response appears according to the carrier frequency, and Figure. 3 and 4(b)-(f) show the typical responses in neuron when the carrier frequency is 10 kHz. There are six kinds of responses; quiescent, phasic, conduction block at high amplitude of membrane potential, conduction block at middle amplitude of membrane potential, imperfect phasic, imperfect tonic, as neurons' reactions to non-TI stimulation.

In the future study, by simulation of neuron's response according to carrier and delta frequency not confirmed in this study, carrier frequency, delta frequency, and current intensity can be optimized according to the purpose of TI-stimulation. However, since this study used the mammalian neuron model and was conducted under various approximations and assumptions, the actual biological experiment results may be slightly different, but it is thought that it can help determine carrier frequency, delta frequency, and current intensity when conducting actual biological experiments of TI-stimulation.

Acknowledgements

This work was supported by National Research Foundation of Korea (NRF) grant funded by the Korea government (MSIT) (2020R1C1C1010505) and by BK21PLUS, Creative Human Resource Education and Research Programs for ICT Convergence in the 4th Industrial Revolution

References

1. Ehsan Mirzakhalili, Beatrice Barra, Macro Capogrosso, and Scott F. Lempka, “Biophysics of Temporal Interference Stimulation”, Cell Systems 11, 557-572, 2020.

Discrimination of resting-state functional connectivity from idiopathic REM sleep behavior disorder patients based on machine learning with data augmentation

H. Kim[1], J. I. Byun[2], J. I. Huh[1], M. J. Kim[1], P. Seo[1], J. S. Sunwoo[3], K. Y. Jung[4], and H. K. Kim[1]

[1]Department of Biomedical Engineering, Yonsei University, Wonju, Korea
[2]Department of Neurology, Kyung Hee University Hospital at Gangdong, Kyung Hee University College of Medicine, Seoul, South Korea
[3]Department of Neurosurgery, Seoul National University Hospital, Seoul, South Korea
[4]Department of Neurology, Seoul National University Hospital, Seoul National University College of Medicine, Seoul, South Korea

khkim0604@yonsei.ac.kr

Abstract

idiopathic REM sleep behavior disorder (iRBD) is a prodromal period of neurodegenerative disorders. Neuroimaging biomarkers for iRBD have not been developed yet. In this study, we tried to develop a convolutional neural network (CNN) classifier which discriminates iRBD patient from normal controls based on resting-state functional connectivity . Due to the problem of data insufficiency, we applied data augmentation methods and evaluated their effectiveness for improving the performance of classification . The data augmentation using interpolation and extrapolation was found to be effective, while the generic image augmentation method was not suitable for the connectivity matrices.

Background

iRBD is a prodromal stage of α-synucleinopathies such as dementia with lewy bodies, Parkinson's disease [1]. iRBD has been known to be associated with cognitive impairments such as visuospatial function, memory, and attention. Underlying neural mechanisms of cognitive dysfunction in iRBD patients remain unclear. In this study, we tried to discriminate the brain functional connectivity of iRBD patients from that of normal control using convolutional neural network based on resting-state fMRI. However, training of neural network has limitation in terms of small dataset size. It has been reported that data augmentation improved a classification performance in many non-medical problems such as image classification task [2]. In this work, we applied three data augmentation method and investigated the performance improvement of augmentation.

Methods

Twenty healthy subjects (68.05 ± 3.39 years) and 50 drug-naïve iRBD patients (65.84 ± 6.75 years) participated in this study. Before the experiment, subjects assessed cognitive function with two sets of cognitive tests: Montreal cognitive assessment (MoCA) and the Korean version of the Consortium to Establish a Registry for Alzheimer's Disease (CERAD-K). Subjects underwent structural MRI and resting-state functional MRI. Subjects were instructed to keep their eyes closed with relaxed state. T1-weighted sMRI was acquired by 3T Siemens Biograph mMR 3T scanner (Siemens Healthcare Sector, Germany) with a single sequence; echo time (TE) was 1.89 ms, repetition time (TR) of 1670 ms, dimension of 256×256, and an isotropic voxel size of 1 mm. BOLD fMRI was acquired for 8 minutes using a TE of 30 ms, TR of 3000 ms, dimension of 128×128, and an voxel size of 1.9×1.9×3.0 mm. As a magnetic field needs to be saturated, after 10 scans of resting-state fMRI images were processed using a CONN-fMRI FC toolbox with Statistical Parametric Mapping (SPM) and MATLAB software. Images were preprocessed using a default preprocessing pipeline for volume-based analysis. The residual BOLD time series was band-pass filtered (0.009-0.08Hz) and linearly detrended. After preprocessing, functional connectivity networks were inferred using the Pearson correlation between BOLD time series in a duration of 10 seconds in each epoch from pairs of brain regions from Harvard-Oxford Atlas. A total dataset of 1,120 samples (320 samples for normal control, 800 samples for iRBD patients) was used for classification. To avoid class imbalance, the 320 data samples from iRBD patients were randomly selected. To inflate the

original training data, four data augmentation methods were applied and evaluated (Figure. 1). N times as much original training data was augmented (N=2, 3, 5, 10 for interpolation, N=5 for other augmentation techniques).

A. Generic augmentation methods

In computer vision studies, image augmentation has been widely used and shown to be effective for a wide range of image classification tasks. We applied simple image data augmentation technique using albumentation library [3]. We used multiple schemes (Random Gamma, Blur, Motion Blur, Optical Distortion) to apply transformation to training data. Each scheme has a chance to be applied to input data with a probability of 0.2.

B. Interpolation

A new artificial data sample was generated by an interpolation of two training images which were randomly selected from mini-batch as follows:

$$(1)\quad \mathrm{I}' = (I_1 - I_2)\lambda + I_2$$

I' is the new sample. I_1 and I_2 are randomly selected input samples, λ is a parameter which controls a degree of interpolation. λ was randomly set in the range of {0, 1} at each split of training data.

C. Extrapolation

A new artificial data sample was generated by an extrapolation of two training images which were randomly selected from mini-batch as follows:

$$(2)\quad \mathrm{I}' = (I_2 - I_1)\lambda + I_2$$

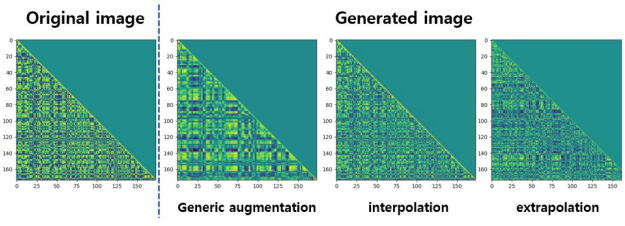


Figure.1. Example images of functional connectivity matrix (left: original image, right: new image generated by data augmentation methods)

We used convolutional neural network (CNN) for classifying iRBD patients from normal control. The CNN classifier included three convolutional layers, followed by ReLU and max pooling layer and three fully connected layers and one dropout layer. A stratified 10-fold cross validation was applied to evaluate a performance of the CNN classifier.

Results and Discussion

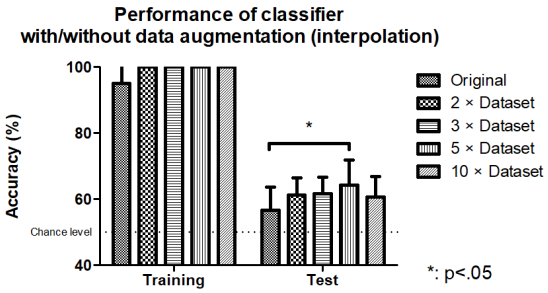


Figure.2. Classification performance with/without data augmentation method (interpolation)

Figure. 2. shows the training and test performances of the CNN classifier with both original and augmented training data using interpolation augmentation method. Original dataset means that no augmentation method is applied. 'N × Dataset' denotes N times larger than original training dataset. The training accuracy using augmented dataset was 100.0±0.0 %, whereas the training accuracy using original dataset was 95.14±14.59 %. Applying data augmentation enables stable learning of CNN classifier. The test performance using '5×Dataset' was significantly larger than the test performance from original dataset (original: 56.72±6.88 %, 5×Dataset: 64.22±7.54 %; t: -2.2, p<.05, independent sample t-test). The CNN classifier using '10×Dataset' as input showed relatively poor test performance. It can be interpreted that too much augmented data cause overfitting during training phase. The five times of the original dataset, therefore, was generated via augmentation (generic augmentation, extrapolation).

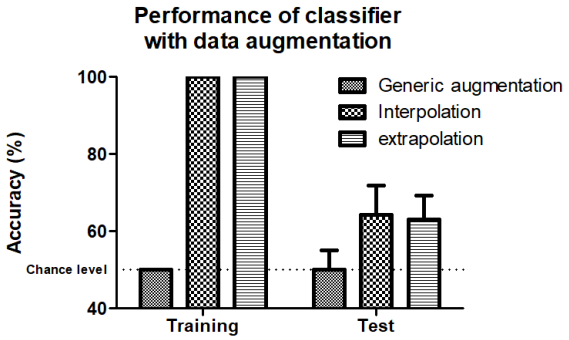


Figure.3. Classification performance with data augmentation method

Figure. 3. shows the training and test performances of the CNN classifier using each data augmentation method. The CNN classifier using interpolation and extrapolation augmentation trained successfully and showed test accuracy of 64.22±7.54 % for interpolation, and 63.12±6.06 % for extrapolation, which showed improvement of performance compared with original dataset (no augmentation). However, the CNN classifier using generic image augmentation method failed to learn and predict the data correctly. The generic data augmentation was developed for natural images in the manner of transforming intensity, shape, and color of images. It may not be appropriate for brain functional connectivity. On the other hand, interpolation and extrapolation could generate realistic images of brain connectivity matrix, so that the classifier using these augmentations showed improvement of performance.

Acknowledgements

This research was Supported by the Brain Research Program through the NRF of Korea. Grant number: 2017M3C7A1029485

References

[1] E. Matar and S. J. G. Lewis, “Rem sleep behaviour disorder: Not just a bad dream,” *Med. J. Aust.*, vol. 207, no. 6, pp. 262–268, 2017.

[2] C. Shorten and T. M. Khoshgoftaar, “A survey on Image Data Augmentation for Deep Learning,” *J. Big Data*, vol. 6, no. 1, 2019.

[3] A. Buslaev, V. I. Iglovikov, E. Khvedchenya, A. Parinov, M. Druzhinin, and A. A. Kalinin, “Albumentations: Fast and flexible image augmentations,” *Inf.*, vol. 11, no. 2, pp. 1–20, 2020.

Effects of PPC tDCS on vigilance task and alpha power tendency

S.H. Kang[1], J.Y. choi[1] and S.C. Jun[1]

[1]School of Electrical Engineering and Computer Science, Gwangju Institute of Science and Technology, Gwangju, Korea

scjun@gist.ac.kr

Abstract

Transcranial Direct Current Stimulation (tDCS) applied to Posterior parietal cortex (PPC) has garnered attention due to its ability to improve the performance of phasic alertness task and executive vigilance task. PPC tDCS has been reported to reduce resting alpha power after the cognitive task. Here, we aimed to confirm the effects of PPC tDCS on the performance improvement in cognitive tasks by modifying and re-organizing experimental paradigms. As a result, we found a notable increase in phasic alertness, while executive accuracy did not. In addition, the alpha power during the resting state was maintained by the PPC tDCS intervention. These results may provide noteworthy clues to understanding the efficacy of tDCS.

Background

There have been attempts to investigate the effect of PPC tDCS on human behavior. Current study suggests that PPC tDCS modulate the alertness of subject [1]. While "Phasic alertness" means the vigilance obtained by an additional cue which is presented before the input request, PPC tDCS could enhance subject's vigilance as the level of phasic alertness [1]. The authors in [1] suggested this result as modulating effect of PPC tDCS on alerting network. Also, PPC tDCS may mitigate the increment of alpha power as well as the decrement of executive vigilance during the task [1]. "Executive vigilance" means the agility of response for congruent and incongruent cues. An executive vigilance decreases as repeating the task and the resting alpha power increases, however, PPC tDCS mitigates these effects [1,2]. In this study, we tried to reproduce previous results and to verify the effect of PPC tDCS on vigilance with a modified version of the vigilance task.

Methods

In the experiment, we used ANTI-Vea task to see both phasic alertness and executive vigilance. We recruited 13 participants and they visited the laboratory twice for experiencing tDCS and SHAM stimulation (each visiting day was separated into two weeks). These participants were healthy adults. During the task session, participants were subjected to handle ANTI-Vea task (Figure 1). Each participant responded to the six types of visual cues, as shown in figure 1-(b). The number of the total trial is 64 and each type of cue was displayed in random order. Half of the trials includes tone cue which is introduced to measure phasic alertness. Participants should press "space bar" for the arrows arranged unevenly (25% of total trials) and it is used for measuring executive vigilance.

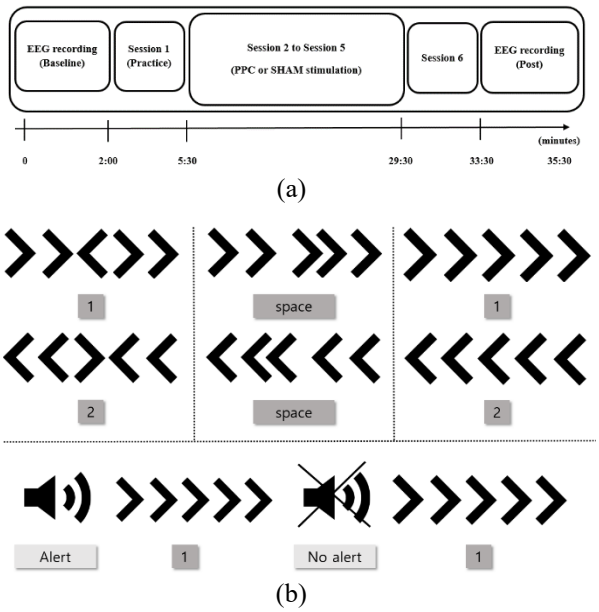


Figure 1. Timeline(a) and ANTI-Vea Task(b)

After the experiment, we did a statistical analysis to point out the meaningful results. To do this, we applied student paired t-test and correlation analysis to ANTI-Vea task results. Also, we measured alpha power by using EEGLAB Toolbox in MATLAB environment. We calculated relative alpha power (8-13 Hz) during the task (from session 1 to session 6) based on the resulting alpha power state in the baseline (see Figure 1-(a)). We measured 3 EEG channels (Fz, Cz, and Pz) and applied a bandpass filter (1 – 50 Hz) for

preprocessing. Then we removed EEG epochs showing artifacts using amplitude threshold and visual inspection.

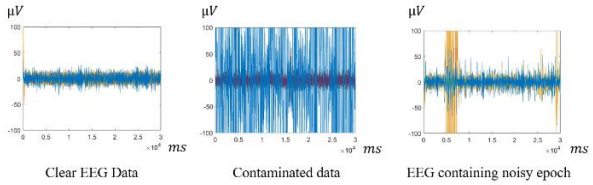


Figure 2. Examples of the EEG epochs

Results and Discussion

Previous research indicated that the accuracy of the executive vigilance task gradually decreases during the experiment [1]. However, our experiment didn't show an overall decrement during the task. In addition, there was a report that the vigilance task accuracy of PPC tDCS groups should be higher than the SHAM tDCS groups [1]. But there is no notable accuracy difference in our results. In the meantime, we found a significant contrast in the accuracy difference for the phasic alertness task (upper panel of Figure 3, session 6).

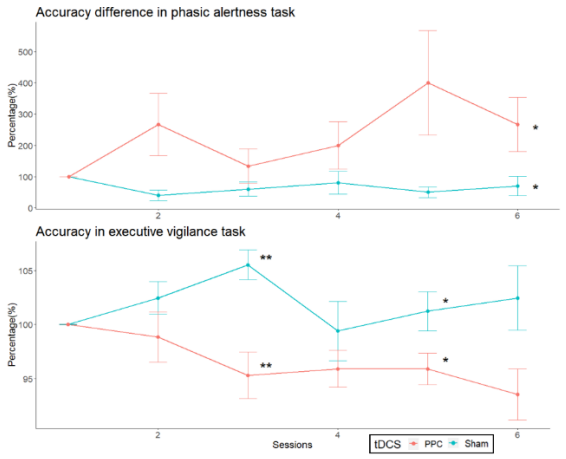


Figure 3. Relative analysis of accuracy difference of phasic alertness and accuracy of executive vigilance. (*: p value < 0.05, **: p value < 0.01)

In alpha power tendency, we observed that PPC tDCS diminished alpha power difference between baseline and end of the task (Figure 4). This indicates that the PPC tDCS may regulate the tendency of alpha power decrement. However, there is a previous report that alpha power increased after the vigilance task and PPC tDCS mitigated this alpha power increment [1], which was not relevant to our result.

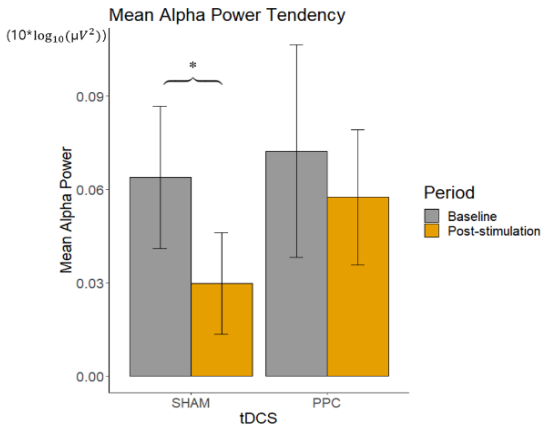


Figure 4. Mean alpha power tendency (*: p value < 0.05)

There may have several points for the controversial results. One of the main causes may be the difficulty of the task. In the previous research [1], the accuracy of the executive vigilance task was about at most 85 percent per session, while our experiment was an average of 93.79 percent accuracy. This suggests that a ceiling effect may occur due to the ease of task.

In conclusion, PPC tDCS group has a notable increment in accuracy difference of phasic alertness task. Further, alpha power decrement was mitigated by PPC tDCS. Although we observed different results from previous studies, we believe that it would be an important report for understanding the effect of tDCS.

Acknowledgements

This research was supported by the Institute of Information & Communications Technology Planning & Evaluation (IITP) grant funded by the Korea government (No. 2017-0-00451).

References

1. F. G. Luna, R. Román-Caballero, P. Barttfeld, J. Lupiáñez, and E. Martín-Arévalo. "A high-definition tDCS and EEG study on attention and vigilance: Brain stimulation mitigates the executive but not the arousal vigilance decrement," Neuropsychologia, 142:107447, 2020.
2. L. K. McIntire, R. A. McKinley, J. M. Nelson, and C. Goodyear. "Transcranial direct current stinulation versus caffeine as a fatigue countermeasure," Brain Stimulation, 10:1070-1078, 2017.

P-064

Enhanced dopamine sensitivity using Steered Fast-Scan Cyclic Voltammetry

Y. Kang[1,*], A.Goyal[2,3,*], S. Hwang[1], C. Park[1], H. U. Cho[1], J. Park[1], K. E. Bennet[2,4], K. H. Lee[2,5], Y. Oh[2,5,**], D.P.Jang[1,**]

[1]Department of Biomedical Engineering, Hanyang University, Seoul, Republic of Korea

[2]Department of Neurosurgery, Mayo Clinic, Rochester MN 55905, USA

[3]Mayo Clinic Medical Scientist Training Program, Mayo Clinic, Rochester MN 55905, USA

[4]Division of Engineering, Mayo Clinic, Rochester, MN 55905, USA

[5]Department of Biomedical Engineering, Mayo Clinic, Rochester, MN 55905, USA

* These authors contributed equally.

** Corresponding authors. YO and DPJ supervised all aspects of this work equally.

dongpjang@hanyang.ac.kr

Abstract

Fast-scan cyclic voltammetry (FSCV) is a technique for measuring phasic release of neurotransmitters with millisecond temporal resolution. The current data is captured by carbon fiber microelectrodes, and non-Faradaic current is subtracted from background current to extract the Faradaic redox current through a background subtraction algorithm. FSCV is able to measure neurotransmitter concentrations in vivo down to the nanomolar scale, making it a very robust and useful technique for probing neurotransmitter release dynamics and communication across neural networks. In this study, we describe a technique that can further lower the limit of detection of FSCV. By taking advantage of a "waveform steering" technique and by amplifying only the oxidation peak of dopamine to reduce noise fluctuations, we demonstrate the ability to measure dopamine concentrations down to 0.17 nM. Waveform steering is a technique to dynamically alter the input waveform to ensure the background current remains stable over time. Specifically, the region of the input waveform in the vicinity of the dopamine oxidation potential (~ 0.6 V) is kept flat. Thus, amplification of the input waveform will amplify only the Faradaic current, lowering the existing limit of detection for dopamine from 5.48 nM to 0.17 nM, a 32-fold reduction and for serotonin, it lowers the limit of detection from 57.3 nM to 1.46 nM, a 39-fold reduction compared to conventional FSCV. Finally, the applicability of steered FSCV to in vivo dopamine detection was also demonstrated in study. In conclusion, steered FSCV might be used as a useful neurochemical monitoring tool for enhancing detection sensitivity.

Background

Dopamine (DA) is an essential neurotransmitter in the brain, responsible for modulating a wide array of functions, including motivation, pleasure, and movement[1, 2]. Dysfunction in dopaminergic dynamics is known to play a critical underlying role in several neuropathological disorders such as Parkinson's Disease, addiction, obsessive-compulsive disorder, and Tourette's syndrome[3, 4]. Therefore, furthering our understanding of the mechanisms of DA release and transmission in the central nervous system is of great importance to inform future development of therapies for these disorders. To measure DA in the brain in real-time, microdialysis and electrochemical methods are typically employed[5, 6]. The former has been primarily utilized for sampling DA with high selectivity and sensitivity. While it boasts sub-nanomolar sensitivity and high selectivity using high-performance liquid chromatography, it suffers from low spatiotemporal resolution. Measurements can be taken once every minute[7], at best, and the high diameter of the microdialysis cannula leads to a low spatial resolution as well as tissue damage. This tissue damage has been shown to confound in vivo measurements[8]. All of these drawbacks taken

together limit future application for microdialysis for probing in vivo neurotransmitter dynamics.

In contrast, electrochemical methods combined with carbon fiber microelectrodes boast high spatiotemporal resolution. For example, fast-scan cyclic voltammetry (FSCV) utilizes a triangular input voltammetric waveform that sweeps from -0.4 V to 1.3 V at 400 V/s, with a scan repetition time of 10 Hz[9, 10]. Carbon fiber microelectrodes have diameters of less than 10μm, minimizing tissue damage and inflammation[11], both of which can confound in vivo measurements. For these reasons, FSCV has been utilized for decades as the preferred method to measure synaptic release of DA and other neurotransmitters in vivo, both in animals and in humans. In addition, recent technical advancements in FSCV have been made to meet biological needs to measure low concentrations of neurotransmitters with high specificity by waveform optimization, material development, and signal processing[9, 12]. Although the sensitivity of FSCV has been improved since its inception, there is still demand for improvement to enable further investigation into biological phenomena. The current limit of detection of FSCV algorithms, assuming an optimized research set up with limited noise, has been reported to be around 15nM at carbon fiber microelectrodes[10, 13]. Unfortunately, this is still insufficient for certain applications, such as measuring spontaneous (non-induced) neurotransmitter release[14-16].

Previous attempts to increase FSCV sensitivity have employed a variety of methods, including increasing the scan rate[17] and utilizing square wave voltammetry with relatively large amplitude and sampling rate (1 mega sample/sec)[18]. The limit of detection has been lowered to 0.17 nM using multiple cyclic-square wave voltammetry, but this technique was designed to only measure tonic resting levels of neurotransmitters, and not phasic release[19]. In addition, square wave voltammetry employs waveforms with relatively low temporal resolution (1 scan every few seconds), so the technique lacks the temporal resolution necessary to record spontaneous activity, which occurs several times per second[14]. Another noteworthy attempt to increase sensitivity to DA was by changing the shape of the input waveform, and amplifying it, to change the shape of the resultant voltammogram[20]. This was able to reduce the limit of detection to DA down to 127 pM; however, the technique employed made use of a specially prepared potentiostat for use in in vitro solutions, and it has not been tested in the in vivo environment. Further, the algorithm for generating a particular voltammogram was not discussed and the waveform optimization procedure takes up to 10 minutes.

In this study, we employ a waveform steering technique to control the input waveform to modify the resultant voltammogram to achieve a flat background current at voltages near the oxidation potential of DA (~ 0.6 V). A pre-amplifier specifically designed to amplify only the oxidation current from the redox currents obtained from the steered input waveform is also discussed. This technique lowers the limit of detection of DA to 0.17 nM (170 pM), and is employable both in vitro and in vivo, making it a very useful modification to FSCV for applications requiring a very low limit of detection.

Methods

FSCV input waveform

Steered FSCV requires the use of conventional FSCV, which uses a waveform that increases from -0.4 V to 1.3 V at a rate of 400 V/sec and then returns to -0.4 V (Figure 1). The input waveform is about 8.5 ms long and is applied every 100 ms.

Data I/O system and analysis

After application of the input waveform, the resulting electrochemical redox data was collected by the carbon-fiber microelectrode and passed through a pre-amplifier to an NI-DAQ board (NI USB-6251, 16-bit, National Instrument). The output range of the digital to analog converter (DAC) for controlling the waveform output and the offset controller is ±10V, and the input range of the analog to digital converter (ADC) for receiving the voltammogram is ±10V, and each has a resolution of 16 bits. The NI-DAQ board passed the resultant digital data to the computer for analysis.

Custom acquisition software was written using LabVIEW 2016, and has functions to adjust the FSCV input waveform parameters, implement the waveform steering technique through NI USB-6251 control, and synchronize the flow-injection apparatus. Using two analog input channels, the output values from the current-to-voltage converter (IVC) and the extra amplifier module were simultaneously acquired in the form of 2 byte signed integer. The raw data is continuously saved to the hard drive. For postprocessing, the saved data was analyzed with

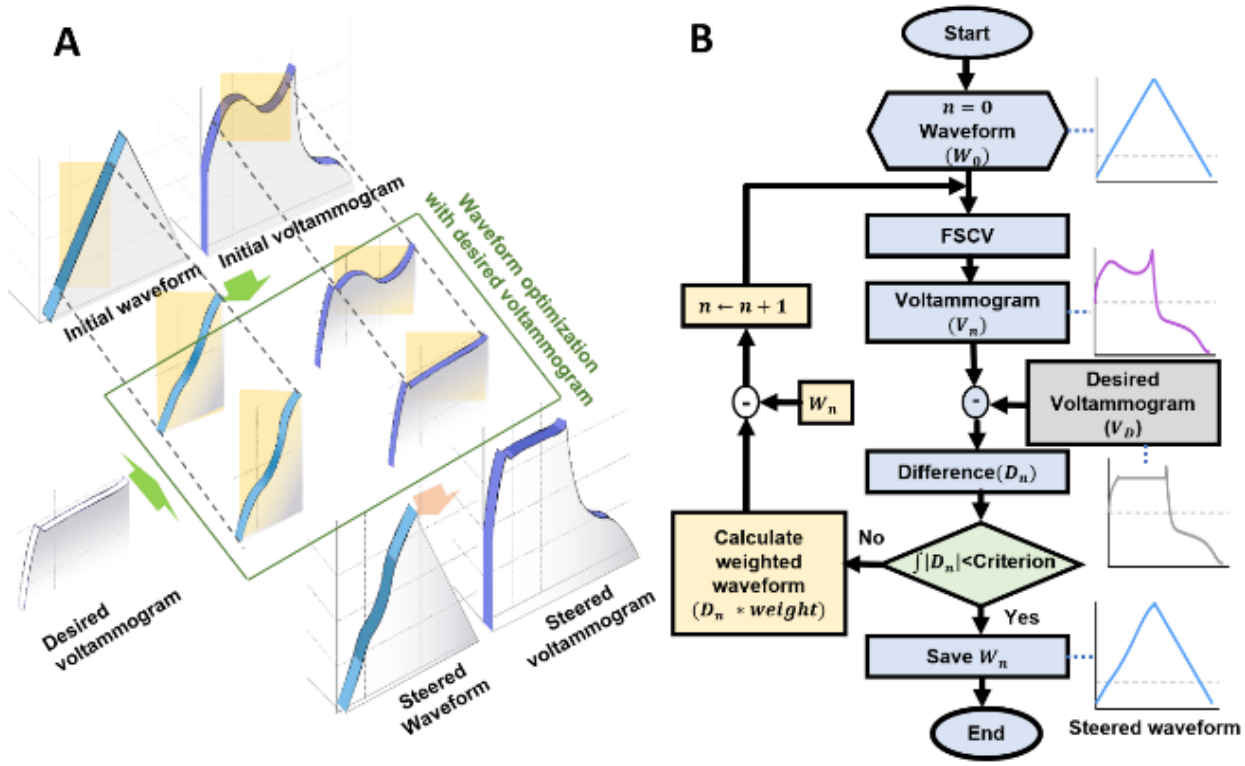


Figure 1 - *Description of the waveform steering technique.* (A) The initial voltammogram is the output of the initial input waveform. When waveform optimization is performed using the desired voltammogram, a steered input waveform is generated to generate a steered voltammogram of the same shape as the desired voltammogram. (B) A feedback algorithm for deriving the steered input waveform. By comparing the desired voltammogram with the output voltammogram from the input waveform, the input waveform is iteratively updated to generate a steered waveform to output the desired voltammogram.

custom software written in LabVIEW 2016, and has signal processing and data display functions such as background subtraction and filtering. All figures were prepared using GraphPad Prism 6 (GraphPad Software, San Diego, CA, USA).

Flow cell apparatus

A flow injection system was used for in-vitro experiments. The flow-injection system was composed of a syringe pump (Harvard Apparatus, Hollisoton, MA), a six-port switching valve (Rheodyne, Rohnert Park, CA), and an electrochemical flow cell, all connected using Teflon tubing. The syringe pump was set at a flow rate of 2 ml/min, the CFM was placed in the center of the flow cell, and the injection of buffer solution and analyte was controlled by controlling the 6-port switching valve. The six-port switching valve was connected to the DO port of the NI-DAQ system and synchronized with the waveform output.

Solutions

Dopamine, 5-HT, and Trizma base were purchased from Sigma-Aldrich (St. Louis, MO). Tris buffer was made as discussed previously18. Briefly, sodium chloride, Trizma base, water, and hydrochloric acid are mixed to achieve a buffered solution with pH = 7.4. 1 mM dopamine and 5-HT stock solutions were made by dissolving each neurotransmitter in Tris buffer, and each stock was used to create dilutions.

Fabrication of carbon-fiber microelectrodes

CFMs were fabricated using an established standardized CFM design previously reported15. Briefly, a single carbon fiber (AS4, diameter = 7 µm; Hexel, Dublin, CA) was inserted into a silica tube (20 µM ID, 90 µM OD, 10 µM coat with polyimide; Polymicro Technologies, Phoenix, AZ). The connection between the carbon fiber and the silica tubing was sealed with epoxy resin. The other end of the silica tubing was then attached to a nitinol (Nitinol

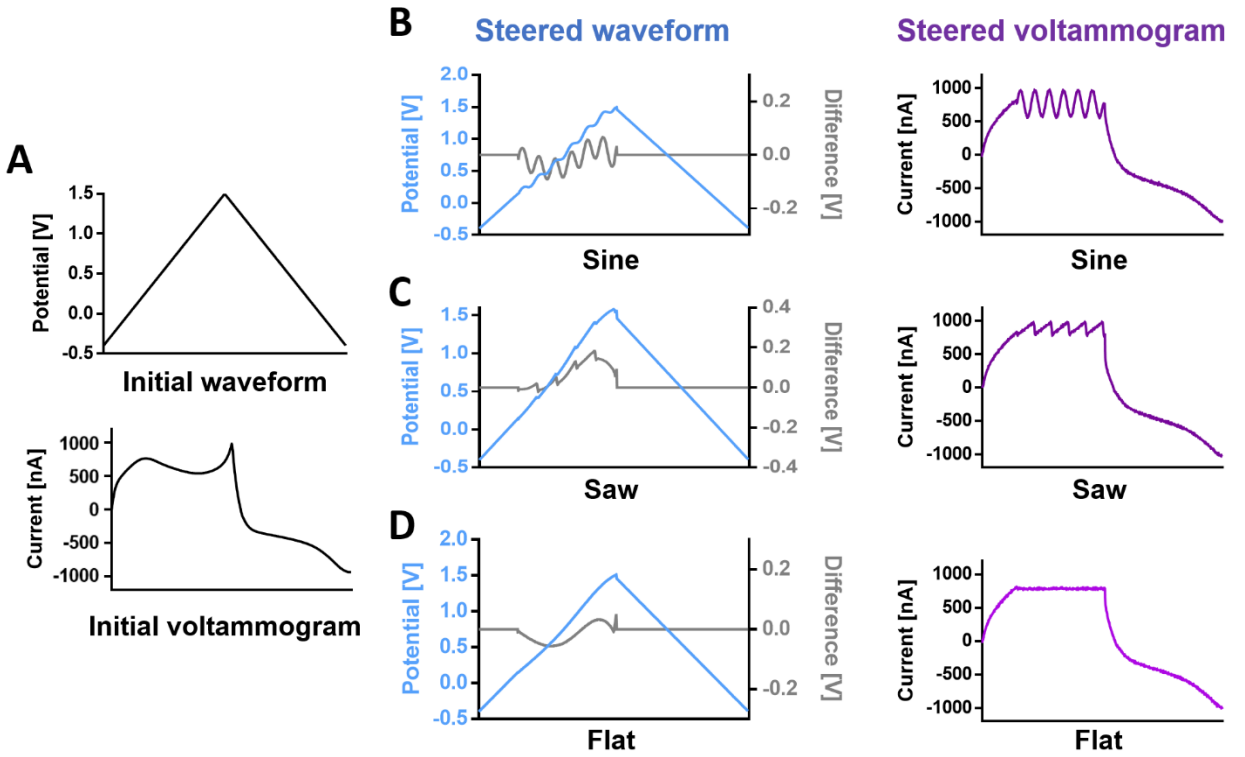


Figure 2 – Output voltammograms from various input waveforms. (A) Triangle waveform used to perform conventional FSCV. (B,C) Difference (gray) between the steered waveform (blue) used to acquire a steered voltammogram (purple) including sine wave or saw tooth wave and the initial waveform used in conventional FSCV. (D) Difference (gray) between the steered waveform (blue) to derive a voltammogram with a flat oxidation region.

#1, an alloy of nickel and titanium; Fort Wayne Metals, IN) extension wire with a silver-based conductive paste. The silia and nitinol wire were insulated with polyimide tubing (0.0089″ID, 0.0134″OD, 0.00225″ WT; Vention Medical, Salem, NH) up to the carbon fiber. The exposed carbon fiber was then trimmed under a dissecting microscope to a length of 50 µm. Teflon-coated silver (Ag) wire (A-M systems, Inc., Sequim, WA) was prepared as an Ag/AgCl counter-reference electrode by chlorinating the exposed tip in saline with a 9 V dry cell battery. CFMs were pretested in a flow cell prior to coating deposition with a PEDOT:Nafion deposition solution, which minimized the effect of in vivo biofouling.

In vivo experiments

Male Sprague-Dawley rats were used for in vivo experiments. Rats were anesthetized with urethane (Sigma Aldrich, 2.24 g/kg, i.p.) and head-fixed to a stereotactic frame (David Kopf Instruments, Tujunga, CA). One burr hole was made above the dorsal striatum (AP +1.2, ML 2.0, DV -4.5), one was made above the medial forebrain bundle (MFB; AP -4.6, ML 1.4, DV -8.4), and one made in the contralateral cortex for reference electrode placement. A carbon fiber microelectrode was lowered to about 1 mm above the dorsal striatum, and a stimulating electrode (twisted bipolar stimulating electrode—Plastics One, MS 303/2, Roanoke, VA, with the tips separated by 1 mm) was lowered to the MFB. Optimal positioning of the carbon fiber microelectrode was determined by measuring evoked DA signal in response to MFB stimulation (2 ms pulse width, 60 Hz, 300 uA, 1 sec stimulation) and lowering the depth by 0.1 mm after each stimulation. Once the optimal depth was determined, data collection began. Dopamine was evoked in the dorsal striatum through electrical stimulation of the MFB every 10 minutes. Waveform steering was performed before each stimulation.

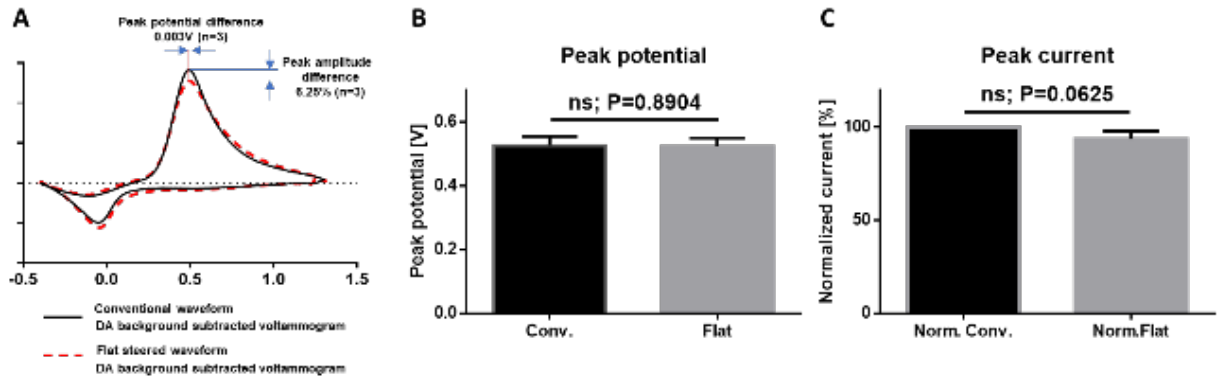


Figure 3 – Change in DA response to different input waveforms (original triangle waveform and flat steered waveform). (A) Background-subtracted voltammograms obtained by using conventional FSCV (black) and a flat steered waveform (red). (B) The location of the oxidation peak of DA shows a difference of about 3 mV. (C) The amplitude of the currents shows no significant difference.

Results and Discussion

Waveform steering technique

The waveform steering technique is designed to induce a desired shape of a voltammogram by modifying the input waveform during conventional FSCV (Figure 1). Figure 1A shows that the voltammogram changes as the waveform and properties required for the waveform steering technique change. When the initial waveform is input, the initial voltammogram is output, and the waveform is changed through comparison with the desired voltammogram. Finally, when the optimized steered waveform is input, a steered voltammogram in the same form as the desired voltammogram can be obtained. Figure 1B shows the algorithm for generating a steered waveform. The initial input waveform (W_0) can be of any form, but here the standard FSCV waveform is depicted. The voltammogram obtained with this waveform is then subtracted from the desired voltammogram V_D to obtain a difference DN, where N is the iteration number. The area of this difference over the desired section (the vicinity of the DA oxidation potential) is then compared to a pre-established criterion. If the difference exceeds the minimum criterion, it is multiplied by a weighting factor that is determined in advance. Weighting factors can range from 0.001 to 0.005. A smaller weighting factor will lead to a highly optimized input waveform, at the cost of an increased number of iterations, leading to longer optimization time. This weighting serves to adjust the waveform to be applied on the next iteration. The time to generate the optimized steered waveform differs depending on the voltammogram type and weight setting, but since FSCV applies the waveform every 100ms, the waveform is usually optimized within 10 seconds.

Using the waveform steering technique, various types of voltammograms can be derived. Figure 2A shows the voltammogram that can be obtained using the conventional triangular waveform, and the middle column shows the steered waveform (blue solid line) to obtain voltammograms of sine wave (Figure 2B), saw tooth wave (Figure 2C), and flat form (Figure 2D). The right column shows the voltammogram that results from the input waveform in the middle column. From this, it is seen that any desired voltammogram shape can be generated by using the waveform steering technique. One interesting point is that the difference between the initial waveform and the flat steered waveform was quite small (range < 0.05 V; Fig 2D, gray, solid line).

In conventional FSCV, the magnitude of the non-Faradaic current is significantly larger than that of the Faradaic current. Thus, a large amplification must be used to measure the concentration of a small amount of neurotransmitter. In this case, since the magnitude of the non-Faradaic current also increases, it may be impossible to measure beyond the measurement range of the analog to digital converter (ADC). Therefore, by flattening the non-Faradaic current (Fig. 2D), the change in the size of the current due to amplification can be effectively ignored. It is important to derive a flat steered voltammogram by applying a waveform steering technique because the DC type current can be selectively removed by using a pre-amplifier.

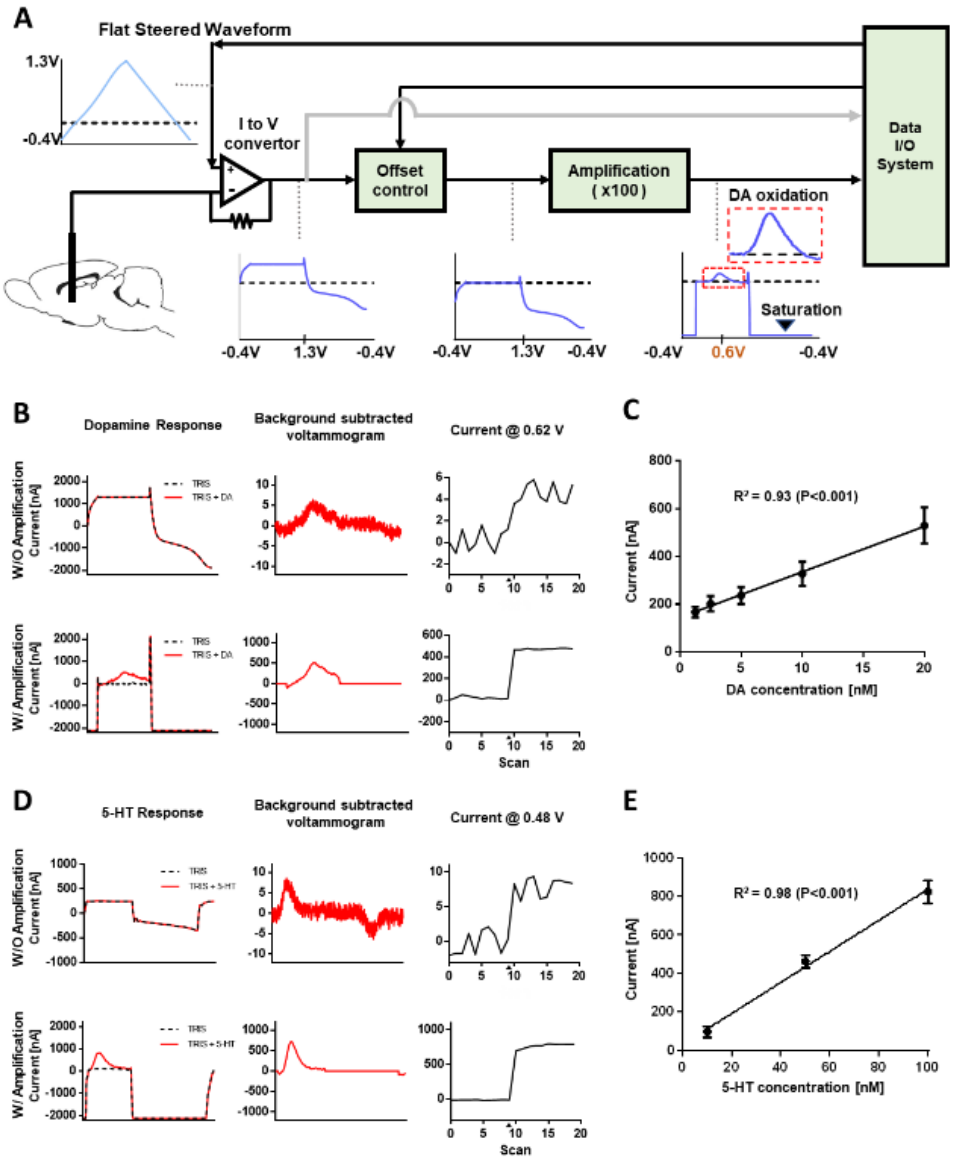


Figure 4 - Signal processing and dopamine response using the pre-amplifier. (A) Block diagram demonstrating the steps to alter the voltammogram. A flat voltammogram can be obtained by applying the steered waveform. The flat potential is adjusted to 0 V using an offset controller and amplified 100 times using an extra-amplifier. The dopamine oxidation peak is then measured from the flat part. (B) The upper row is the result of obtaining a flat dopamine voltammogram derived using a flat steered waveform and analyzing it using the background subtraction technique, and the lower row is the result of analyzing the Faradaic current after amplification. The left column shows the voltammogram, the black dotted line shows the non-Faradaic current, and the red solid line shows the Faradaic current at 20 nM of DA. The middle column shows the Faradaic current obtained from background subtraction. The right column shows the change in Faradaic current at 0.62 V over time. (C) Current resulting from 1.25 nM, 2.5 nM, 5 nM, 10 nM, and 20 nM dopamine after amplification. (D) The upper row is the result of obtaining a flat 5-HT voltammogram derived using a flat steered waveform and analyzing it using the background subtraction technique, and the lower row is the result of analyzing the Faradaic current after amplification. The left column shows the voltammogram and waveform, the black solid line shows the Faradaic current at 100nM of 5-HT, and the gray solid line shows the N-shape waveform. The right column shows the change in Faradaic current at 0.48 V over time. (E) Current resulting from 10 nM, 50 nM, and 100 nM 5-HT after amplification.

In order to derive the desired voltammogram using the waveform steering technique, a waveform with a variable scan rate was used, as opposed to the constant scan rate used in conventional FSCV. Figure 3A shows the output voltammograms of the conventional triangular waveform (increasing from -0.4 V to 1.3 V at a rate of 400 V/sec and returning to -0.4 V at a rate of 400 V/sec; black line) and the steered waveform to obtain a flat voltammogram (red dotted line). The potential where the peak faradaic current occurs and the magnitude of the peak faradaic current were only slightly changed between the two waveforms (Figure 3B-C). The average difference this peak potential between the two waveforms was about 3 mV and not significantly different (Fig. 3B, unpaired t-test, $n = 3$, $p = 0.89$). Dopamine sensitivity to these waveforms was not also significantly different (Fig. 3C, unpaired t-test, $n = 3$, $p = 0.062$). The change in the peak potential position depends on the shape of the waveform used to create the steered voltammogram, specifically relating to the rate of change of the waveform scan rate in the vicinity of the oxidation peak of DA. A high rate of change of the scan rate enables the steered waveform to more quickly reach the peak potential, so that the oxidation peak will occur at a lower absolute potential, and vice versa; however, the differences are nonsignificant, indicating that this technique can be safely used to measure DA concentrations.

Offset control and amplification of Steered Fast-Scan Cyclic Voltammetry

In order to amplify only the Faradaic current generated from the oxidation of dopamine, a special type of pre-amplifier is required; its composition and function are shown in Figure 4A. The pre-amplifier consists of a current to voltage converter (IVC), an offset controller, and an extra-amplifier. All analog devices are manufactured using a low noise operational amplifier (OPA2604, Texas Instruments). The IVC applies the steered voltammogram output from the data I/O system to the carbon fiber microelectrode and converts the resulting nano-current back to voltage. When amplifying in this state, the potential should be lowered to 0 V because there is a high possibility that a flat part with a positive potential would exceed the measurement range of the Data I/O system. The offset controller handles this problem. Adjusting the potential of the flat part of the steered voltammogram to 0 V has the same effect as removing the background current of the flat steered voltammogram using an analog circuit. The extra-amplifier then amplifies the adjusted flat part of the voltammogram. Because the location of Faradaic current generation due to the oxidation of dopamine was adjusted to 0 V through the offset controller, 0 V can be maintained despite passing through the extra-amplifier. If dopamine is present, the Faradaic current generated by the oxidation of dopamine appears as a hump above the flat baseline (red box, Figure 4A). The amplification of the extra-amplifier can be changed depending on the concentration of dopamine to be measured or the measurement range of the ADC of the Data I/O system. In this study, a 100-fold amplification was used.

Figure 4B shows the steered FSCV response to 20 nM of DA before and after amplification. The upper row shows the dopamine response before amplification, and the lower row shows the dopamine response after passing through the offset controller and extra-amplifier. The left column shows the total voltammogram generated when a steered waveform is applied. The black dotted line is the current response in the absence of dopamine, and the red solid line is the current response in the presence of dopamine. The middle column shows only the Faradaic current generated by dopamine redox using background subtraction. The right column displays the dopamine response at 0.62 V. The triangle mark below the X-axis indicates the injection time of dopamine into the flow-cell. In conventional FSCV, the limit of detection (LoD) is calculated as the ratio of 3*std of the temporal change of non-Faradaic current to the magnitude of the dopamine response. Therefore, if the change in the non-Faradaic current is small, the LoD will be lowered. In buffer, the magnitude of the change in the non-Faradaic current generated in conventional FSCV is 0.04 ± 0.95 nM (Mean ± std.); using steered-FSCV it is 4.38 ± 3.99 nM. Using Steered FSCV, the pre-amplifier was used to amplify the voltammogram by 100x, but the standard deviation only increased about 4.2x, mainly stemming from the amplified background noise. Therefore, LoD can be decreased by 32-fold compared to conventional FSCV (5.48 nM down to 0.17 nM). Figure 4C shows the dopamine current response vs. concentration in the flow-cell. DA concentrations were 1.25 nM, 2.5 nM, 5 nM, 10 nM, and 20 nM, with $n = 3$ per concentration. The calibration curve showed a linear pattern ($R2 = 0.93$, $p < 0.001$).

Figure 4D shows the steered FSCV response to 100 nM of 5-HT before and after amplification. The upper row shows the 5-HT response before amplification,

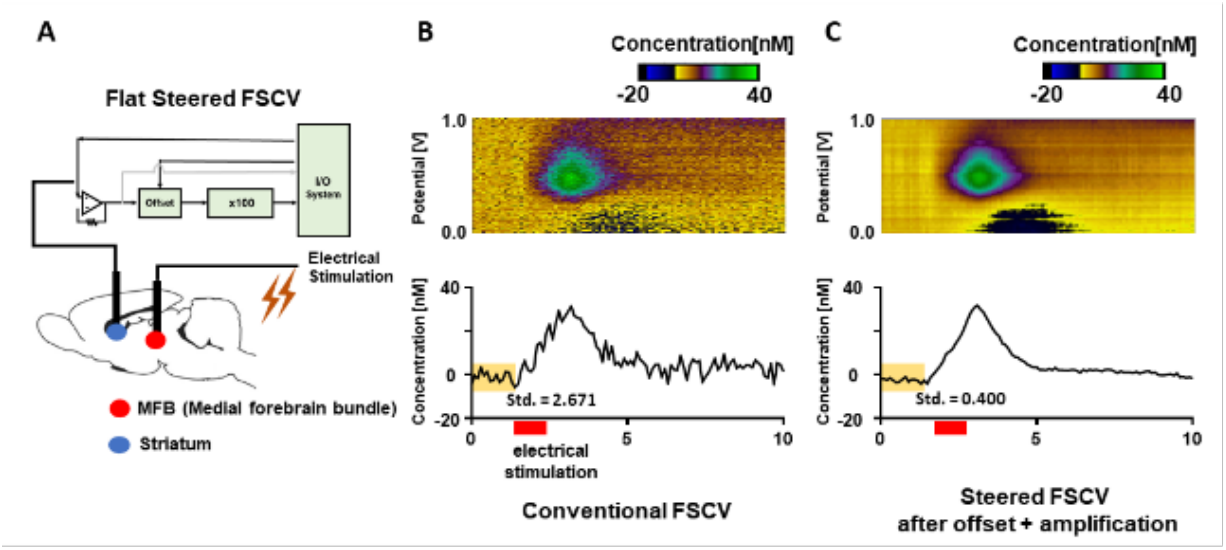


Figure 5 – In-vivo experiment results using Steered-FSCV. (A) A carbon-fiber microelectrode is located in the dorsal striatum, and electrical stimulation is applied to the medial forebrain bundle (MFB). (B) DA response measured using conventional FSCV and Steered-FSCV with amplification(C). A total of 10 seconds before and after stimulation was measured, with the position of the stimulation indicated by a red bar.

and the lower row shows the 5-HT response after passing through the offset controller and extra-amplifier. The left column shows only the Faradaic current generated by 5-HT redox using background subtraction. The right column displays the 5-HT response at 0.48 V. The triangle mark below the X-axis indicates the injection time of 5-HT into the flow-cell. LoD can be decreased by 39-fold compared to conventional FSCV (57.3 nM down to 1.46 nM) These results imply that Steered FSCV can improve the detection sensitivity for many neurotransmitters by modifying various waveforms. Figure 4E shows the 5-HT current response vs. concentration in the flow-cell. 5-HT concentrations were 10 nM, 50 nM, and 100 nM, with n=3 per concentration. The calibration curve showed a linear pattern ($R2 = 0.98$, $p < 0.001$).

As the DA concentration decreases, the magnitude of the Faradaic current decreases. In general, if the magnitude of the temporal noise (fluctuations in successive DA current measurements) is larger than the change caused by the Faradaic current, dopamine cannot be detected. In this study, when a signal is amplified using a flat voltammogram, a low concentration of dopamine can be detected because the amount of amplification of the magnitude of the Faradaic current surpasses the temporal noise.

In vivo application of Steered FSCV

This technique was then verified in vivo (Figure 5A). To verify the effectiveness of detection of dopamine induced by electrical stimulation, the stimulation parameters were set to 2 ms pulse width, 60 Hz, 100 uA, and stimulation was delivered for 1 second. In Figures 5B and C, the upper row shows a color plot of dopamine response pre- and post-stimulation, and the lower row shows the temporal change in dopamine oxidation current at 0.6 V. The dopamine response to MFB stimulation was about 32 nM as shown in Figure 5B. Using standard FSCV, the value of the current cannot be precisely determined due to the surrounding noise. In vivo especially, it is difficult to measure very low dopamine concentrations due to the large influence of noise. However, the Steered-FSCV technique is able to mitigate the influence of noise by amplifying only the Faradaic current, making the dopamine current response much easier to analyze. Both signals (Fig. 5B-C) have the same concentration because they were measured simultaneously at the same spot, but with different standard deviations of the temporal change: Conventional FSCV Std 2.67 nM and Steered FSCV Std 0.40 nM. This makes it possible to estimate small dopamine concentrations a 6.7-fold more accurately in vivo.

Conclusion

In this study, we have developed a technology that can induce various types of voltammograms by adjusting the input waveform using the waveform steering technique. By generating an output voltammogram with a flat response in the dopamine oxidation region, and by constructing a pre-amplifier that was able to amplify the current only from this voltage range, we were able to lower the limit of detection of dopamine, both in vitro down to 0.17 nM, a 32-fold reduction and in vivo down to 1.2 nM, a 6.7-fold reduction compared to conventional FSCV. The waveform steering technique can be applied to any waveform, such as the N-shape waveform for detecting 5-HT. It lower the limit of detection of 5-HT in vitro down to 1.46 nM, a 39-fold compare to conventional N-shape FSCV.

Acknowledgements

This research was supported by the NIH (R01NS112176), Minnesota Partnership for Biotechnology and Medical Genomics (MNP #19.13) and the National Research Foundation of Korea (2017R1A2B2006896).
This content was submitted to ACS Omega.

References

1. Arbuthnott, G.W. and J. Wickens, *Space, time and dopamine.* Trends Neurosci, 2007. **30**(2): p. 62-9.
2. Ungerstedt U, P.C., *Functional correlates of dopamine neurotransmission.* Bull Schweiz Akad Med Wiss, 1974. **30**: p. 44–55.
3. Lena F. Burbulla, et al., *Dopamine oxidation mediates mitochondrial and lysosomal dysfunction in Parkinson's disease.* Burbulla et al., Science, 2017. **357**: p. 1255–1261.
4. Rusheen, A.E., et al., *Evaluation of electrochemical methods for tonic dopamine detection in vivo.* Trends Analyt Chem, 2020. **132**.
5. Benveniste, H., *Brain Microdialysis.* Journal of Neurochemistry, 1989. **52**.
6. Darren Michael, E.R.T., R. Mark Wightman, *Peer Reviewed_Color Images for FSCV Measurements in Biological Systems.* Analytical Chemistry News & Features, 1998.
7. Gu, H., et al., *In Vivo Monitoring of Dopamine by Microdialysis with 1 min Temporal Resolution Using Online Capillary Liquid Chromatography with Electrochemical Detection.* Anal Chem, 2015. **87**(12): p. 6088-94.
8. BLAHA, C.D., A. COURY, and A.G. PHILLIPS, *Does Monoamine oxidase inhibitaion by pargyline increase extracellular dopamine in the striatum?* Neuroscience Letters, 1996. **75**: p. 543–550.
9. Puthongkham, P. and B.J. Venton, *Recent advances in fast-scan cyclic voltammetry.* Analyst, 2020. **145**(4): p. 1087-1102.
10. Venton, B.J. and Q. Cao, *Fundamentals of fast-scan cyclic voltammetry for dopamine detection.* The Analyst, 2020.
11. Peters, J.L., et al., *Ultrastructure at carbon fiber microelectrode implantation sites after acute voltammetric measurements in the striatum of anesthetized rats.* J Neurosci Methods, 2004. **137**(1): p. 9-23.
12. DeWaele, M., et al., *A baseline drift detrending technique for fast scan cyclic voltammetry.* Analyst, 2017. **142**(22): p. 4317-4321.
13. Puthongkham, P., C. Yang, and B.J. Venton, *Carbon Nanohorn-Modified Carbon Fiber Microelectrodes for Dopamine Detection.* Electroanalysis, 2018. **30**(6): p. 1073-1081.
14. Kavalali, E.T., *The mechanisms and functions of spontaneous neurotransmitter release.* Nat Rev Neurosci, 2015. **16**(1): p. 5-16.
15. Bouron, A., *Modulation of spontaneous quantal release of neurotransmitters in the hippocampus.* Progress in Neurobiology, 2001. **63**: p. 613–635.
16. Kaeser, P.S. and W.G. Regehr, *Molecular mechanisms for synchronous, asynchronous, and spontaneous neurotransmitter release.* Annu Rev Physiol, 2014. **76**: p. 333-63.

17. Keithley, R.B., et al., *Higher sensitivity dopamine measurements with faster-scan cyclic voltammetry.* Anal Chem, 2011. **83**(9): p. 3563-71.
18. Park, C., et al., *Fast Cyclic Square-Wave Voltammetry To Enhance Neurotransmitter Selectivity and Sensitivity.* Analytical Chemistry, 2018. **90**(22): p. 13348-13355.
19. Oh, Y., et al., *Tracking tonic dopamine levels in vivo using multiple cyclic square wave voltammetry.* Biosens Bioelectron, 2018. **121**: p. 174-182.
20. Yoo, J.S. and S.M. Park, *Programmed Potential Sweep Voltammetry for Lower Detection Limits.* Anal. Chem., 2005. **77**: p. 3694-3699.

P-065

Application of Fourier transform electrochemical impedance spectroscopy in fast cyclic square wave voltammetry for the detection of biofouling of electrodes

S.M. Hwang[1], C.H. Park[1], Y.M. Kang[1], H.U. Cho[1], D.P. Jang[1*]

Department of Biomedical Engineering, Hanyang University, Korea

dongpjang@gmail.com

Abstract

In our previous study, New voltammetry waveform, fast cyclic square wave voltammetry (FCSWV), that improves selectivity and sensitivity in detecting neurotransmitters *in-vivo* was suggested. Fourier transform electrochemical impedance spectroscopy (FTEIS) is an electrochemical analysis method that finds the impedance at all frequencies of an electrochemical cell in a short time. Through this method, the circuit characteristics of the cell, solution resistance, R_s, oxidation resistance, R_{ct}, and double layer capacitance, C_{dl}, can be known. In this study, we combine FCSWV and FTEIS to provide a new type of electrochemical spectroscopic information regarding the ability to estimate the degree of sensitivity loss due to biofouling of the electrode surface during in vivo measurements.

Background

Electrochemical measurement is the most widely used method to measure neurotransmitters *in vivo*. In particular, Fast Scan Cyclic Voltammetry (FSCV) with the high temporal and spatial resolution is suitable to measure dopamine that is phasic release and reuptake from synapses. Carbon fiber microelectrodes are inserted into the brain to measure the Faradic current that oxidizes and reduces neurotransmitters.

In a previous study, we reported a Fast Cyclic Square Wave Voltammetry (FCSWV) with enhanced selectivity and sensitivity of high-speed cyclic voltammetry. This method is a form of adding a square wave pulse of large amplitude to the staircase step. It can obtain a two-dimensional Faradic signal by continuously oxidizing and reducing neurotransmitters at high speed.[1]

Electrochemical impedance spectroscopy is a method for quantitatively viewing electrochemical signals. EIS is a method of inferring the values of R_s, R_{ct}, C_{dl} between the electrode and the electrolyte by analyzing the impedance value, which is the frequency information of the electrochemical cell. Fourier transform EIS (FTEIS), the latest technology among EIS, can obtain impedances of all frequencies in a step waveform within a short time through Fourier transform [2]. For this reason, it is suitable for application to the situation of measuring neurotransmitters whose concentration changes dynamically in a short time in vivo.

In this study, dopamine concentrations were measured in Flow Injection Analysis (FIA) and in vivo using the FCSWV method. By combining FTEIS, the C_{dl} value, which can confirm the characteristics of the electrode surface, was used as an indicator of electrode fouling. Through this, it was confirmed that the electrode was fouled, and the sensitivity of dopamine was reduced.

Methods

Data acquisition. An NI board (NI USB-6356, 16-bit, National Instruments) operated by LABVIEW was used as a device for applying a voltage to the electrochemical cell and measuring voltage and current. After voltage was applied to the electrochemical cell from the analog output channel of one channel, the current obtained through the analog input channel of the second channel and the voltage applied to the cell were also digitized to obtain data. Impedance is obtained through differentiation and Fourier transform in MATLAB. Through the function of fitting the impedance to the circuit, the values of the resistor and capacitor of the equivalent circuit were obtained (Figure 1A).

Electrode. The electrode used as the working electrode was made by insulating all of the fine carbon fibers except for the measurement part and was used. The reference electrode was used to make Ag/AgCl

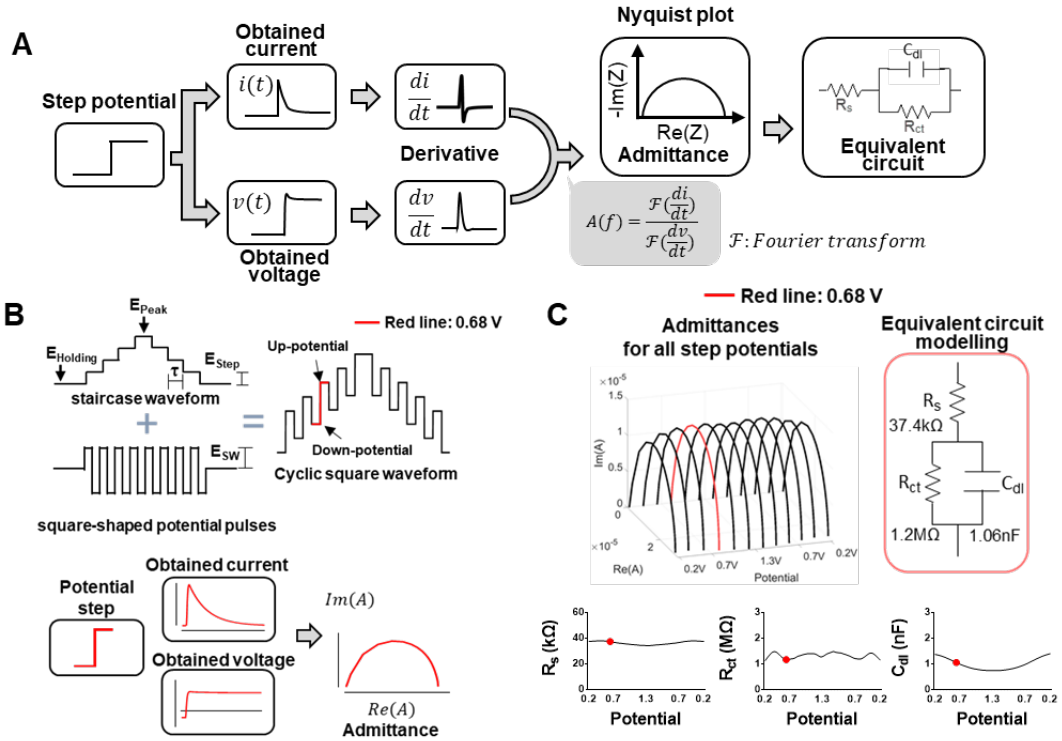


Figure 1. Scheme for FTEIS and FTEIS-FCSWV. (A) The basic concept of FTEIS (B) The application of FTEIS into FCSWV. (C) The estimation of the element value of the equivalent circuit from the admittance data and the reconstruction of three new types of components voltammograms: R_{ct}, R_s, C_{dl} voltammogram.

reference electrode by sufficiently oxidizing the Ag wire.

Chemicals. The solution used as the electrolyte is a tris buffer solution (15 mM tris (hydroxymethyl) aminomethane, 3.25 mM KCl, 140 mM NaCl, 1.2 mM CaCl2, 1.25 mM NaH2PO4, 1.2 mM MgCl2, and 2.0 mM Na2SO4, pH 7.4), which has a composition similar to that of artificial cerebrospinal fluid was used.

Waveform. The FCSWV data was acquired with the waveform depicted in Figure 1B. The staircase potential ramp starts with a holding potential ($E_{Holding}$), increases with each stair-step (E_{Step}) up to a peak potential (E_{Peak}), and then decreases back to $E_{Holding}$ (Figure 1B). The waveform parameters used in this study were $E_{Holding}$: -0.2V, E_{Peak}: 0.6V, E_{Step}: 0.0224V, the duration of a single stair step τ: 1 ms, and the magnitude of the upward and downward potentials E_{sw}: 0.4 V. The cyclic square waveform length is 200 ms with 200 stair steps Therefore, impedance analysis is performed at each of the 200stair steps (Figure 1C).

In-vivo. Adult male Sprague–Dawley rats (8-9 weeks old, weighing 250-300 g, Koatech, South Korea) were used for this study (n = 3). The rats were housed in 12 h light/dark cycles and were given food and water ad libitum. US National Institutes of Health (NIH) guidelines were followed for animal care, and the Hanyang University Institutional Animal Care and Use Committee approved the experimental procedures. Rats were anesthetized by intraperitoneal injection (anesthetic urethane, 1.5 g/kg, i.p.). Surgeries were performed using a stereotaxic frame (Model 900, David Kopf Instruments, Tujunga, CA). To evoke DA release, the medial forebrain bundle (from bregma, AP: -4.6 mm, ML: 1.4 mm, from dura, DV: -8.0 to -9.0 mm) was electrically stimulated, and a CFM was inserted into the striatum (AP: 1.2 mm, ML: 2.0 mm, DV: -4.5).

Results and Discussion

Estimation of the degree of biofouling using C_{dl} voltammograms. Biofouling, adsorption of biomolecules, and redox reaction by-products, result in a decrease in electrode sensitivity due to changes in the electrode surface. Flow injection analysis was performed. DA sensitivity decreases due to a decrease in dopamine by-products due to oxidation. 1 μM of dopamine was injected over a total of 30 cycles every minute for 10 seconds (Figure 2A).

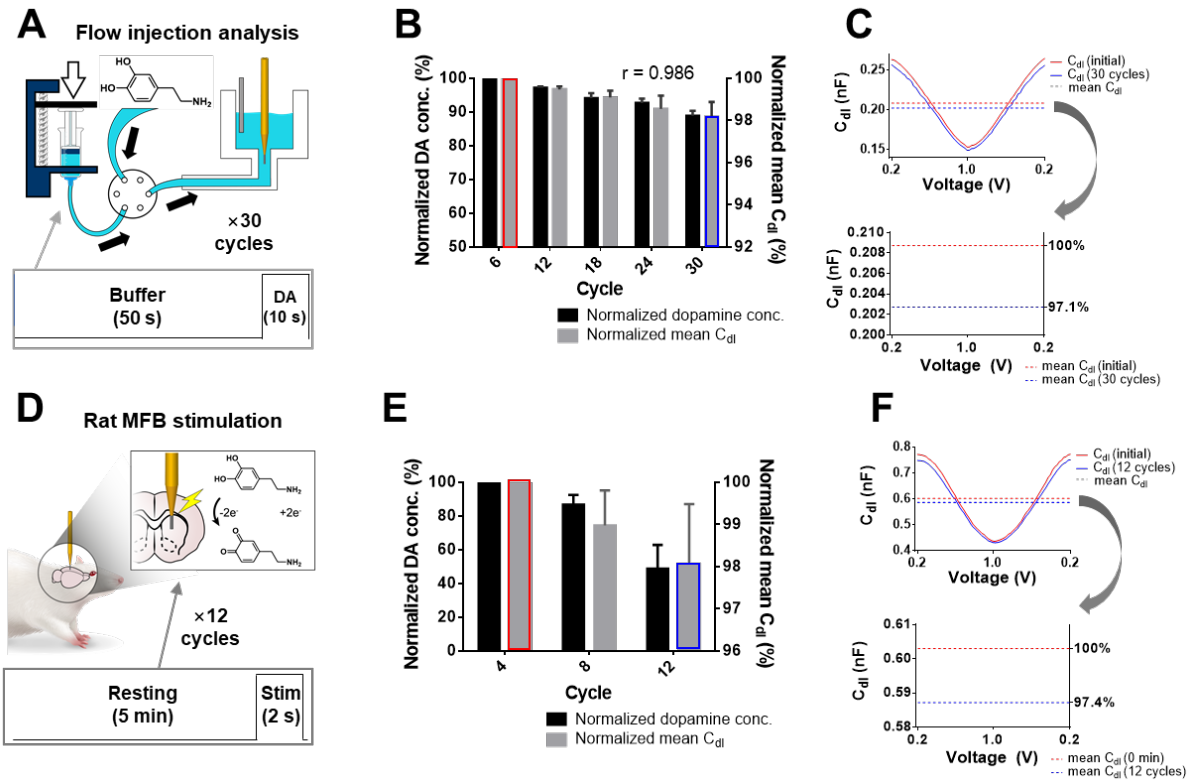


Figure 2. Concept of the experiments and the change of C_{dl} and DA response. (A, D) Experimental concept of flow injection analysis and *in-vivo* experiment. (B, E) Normalized C_{dl} change and normalized dopamine response change from DA flow injection and *in-vivo* stimulation. (C, F) Change of C_{dl} voltammogram during the experiment.

Dopamine injection lowered the sensitivity to dopamine by an average of 14.9% and C_{dl} by an average of 2.5%. The Pearson correlation coefficient between sensitivity and $C_{dl\%}$ was 0.993 (Figure 2B, C). These results suggest that the rate of change in C_{dl} can be used as an indicator of bio-contamination of electrodes during electrochemical measurements. Field impedance estimation using FTEIS-FCSWV can simultaneously observe the concentration of neurotransmitters and the degree of bio-falling. In vivo experiments were also conducted to observe changes in C_{dl} and decreased DA sensitivity (Figure 2D). Due to the dynamic environment of organisms, dopamine release was not correlated with C_{dl} change, but both DA sensitivity and C_{dl} tended to decrease (Figure 2E, F).

It is essential to check the condition of the electrode if the experiment lasts for a long time, such as a chronic experiment. In this study, FTEIS-FCSWV provides the impedance information which can be used to evaluate the sensitivity loss caused by biofilm formation on the electrode surface.

Acknowledgements

This research was supported by the National Research Foundation of Korea (NRF) grant funded by the Korea government (MSIT). (No. 2021R1A2B5B02002437).

References

1. Park, Cheonho, et al. "Fast cyclic square-wave voltammetry to enhance neurotransmitter selectivity and sensitivity." Analytical chemistry 90.22 (2018): 13348-13355
2. Park, Su-Moon, and Jung-Suk Yoo. "Peer reviewed: electrochemical impedance spectroscopy for better electrochemical measurements." (2003): 455-A.

A web-based multimodal platform for the evaluation and training of cognitive control in children

Jiseon Baik*[1,6], Sole Yoo*[1,3,5] and Hae-Jeong Park[1,2,3,4,5]

[1]Laboratory of Molecular Neuroimaging Technology, Department of Nuclear Medicine, Radiology, Yonsei University College of Medicine, Seoul, Korea
[2] Department of Cognitive Science , Yonsei University, Seoul, Korea
[3]Center for Systems and Translational Brain Sciences, Institute of Human Complexity and Systems Science , Yonsei University, Seoul, Korea
[4]Graduate School of Medical Science, Brain Korea 21 Project, Yonsei University College of Medicine, Seoul, Korea
[5]Department of Nuclear Medicine, Yonsei University College of Medicine, Seoul, Korea
[6]Department of English Language and Literature, Kyung Hee University, Seoul, Korea

Abstract — Cognitive control is essential for children to manage a healthy childhood by controlling appropriate attention. Despite its importance, not many online evaluation methods for cognitive control are available at home. We presented a multimodal web/app-based platform of cognitive control evaluation, based on which participants could train themselves at home. This platform includes a cognitive task presentation and response system called Cogmap, a training system called MindSome, and an interoception system called Mind-your-beat, independently or combined with eye-tracking and electroencephalogram (EEG). The Cogmap is composed of diverse scales of cognitive controls, including n-back task, stop-signal task, Stroop task, Wisconsin card sorting tasks, and self-report of GREET. MindSome is composed of 14 days' working memory and attention-related tasks. Mind-your-beat is a system for counting one's cardiac beats, which induces interoception performances. All tasks are constructed with children-friendly graphical images with a scenario of exploring one's cognitive map. The participants' responses are obtained from a touchpad in the tablet to magnify the gamification, with sound feedback and reward scores. The events and responses are recorded in the online database for detailed analysis, and the final reports are presented to the participant with the normalized scales corresponding to the age group of participants. Eye-tracking helps to test the level of attention in the presence of distractors and to evaluate emotional perceptions. During the cognitive performance and eye-tracking measurement, EEG is recorded, and events for cognitive tasks are marked on the EEG system via Bluetooth for the analysis at each brain state. The Cogmap, as a web-based platform, is advantageous in its accessibility without constraints on the acquisition locations and devices. Parents can access the evaluation system online without a site visit for evaluation. We expect the multimodal platform could be of great use in evaluating and enhancing the children's cognitive control capacity.

Acknowledgement:
This research was supported by Brain Research Program through the National Research Foundation of Korea(NRF) funded by the Ministry of Science and ICT(NRF-2017M3C7A1030750)

P-067

Decoding the performance of a memory task using single-trial intracranial EEG

H.-T. Lee[1,2], S. Jun[3], J. S. Kim[4], C. K. Chung[3] and H.-J. Hwang[1,2*]

[1]Department of Electronics and Information Engineering, Korea University, Sejong, Republic of Korea

[2]Interdisciplinary Graduate Program for Artificial Intelligence Smart Convergence Technology, Korea University, Sejong, Korea

[3]Department of Neurosurgery, Seoul National University Hospital, Seoul, Republic of Korea

[4]Research Institute of Basic Sciences, Seoul National University, Seoul, Republic of Korea

[*]hwanghj@korea.ac.kr

Abstract

The aim of this study is to decode the results of a memory task using intracranial EEG (iEEG) measured before (pre-task) and during (task) an encoding session in advance of a retrieval session. iEEG data were measured from two epilepsy patients during a memory task, and the power spectral density of the iEEG data was extracted as decoding features. Event-related spectral perturbation (ERSP) in beta band showed the significant difference between correctly and incorrectly memorized items in common along with the unique patterns of each patient. The highest decoding accuracy was 74.8% and 78.8% for pre-task and task periods, respectively, demonstrating the possibility of decoding the results of a memory task before and during an encoding session.

Background

Distinct brain activity patterns are shown when successfully remembering and forgetting a specific item in a memory task, respectively [1]. The memory task is divided into an encoding session to memorize presented items and a retrieval session to retrieve memorized items. Previous studies showed the possibility of decoding the performance of the memory task using brain activity; how many items are remembered or forgotten [2-3]. Most of previous studies attempted to decode the performance of the memory task using brain activity measured in the retrieval session, but which cannot predict whether the memory task will succeed or fail in advance. Decoding the performance of the memory task before or during the encoding session can not only predict whether the memory task will succeed or fail in advance, but also help to reveal neural mechanisms of encoding the memory task. In this study, we investigated the possibility of decoding the performance of the memory task using intracranial electroencephalography (iEEG) data measured around the hippocampus, known to be associated with memory task during and before encoding session.

Methods

Two epilepsy patients participated in this study. iEEG data were collected from the two patients using macro electrodes (Neuralynx, USA) implanted in the right or left hippocampus, respectively, at Seoul National University Hospital during the memory task. The numbers of electrodes were twenty for both patients.

Figure 1 shows the schema of the experimental paradigm used in this study, which consisted of encoding, distractor, and retrieval session. In the encoding session, each of 120-words items was presented to the patients and they were asked to memorize them as many as possible. In the distractor session, the patients took a break for 10 min during which they were asked to solve a simple math task for at least 5 min. In the retrieval session, the patients were asked to retrieve the 120 words, where new 60 words were also presented along with the 120 words; the patients were asked to press the three buttons depending on their memory whether the words had been presented before (“old”; button 1), not presented before (“new”; button 2), or not sure presented before (“no idea”; button 3).

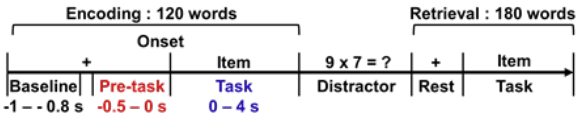


Figure 1. Schema of the experimental paradigm

The iEEG data measured during the encoding session were band-reject filtered between 59.5 to 60.5Hz and band-pass filtered between 0.5 to 50.5 Hz. The filtered iEEG data were segmented -1 to 4 s based on onset time of presenting each word. To decode correctly and incorrectly encoded items during a pre-task (-0.5 – 0 s) and task period (0 – 4 s) in the encoding session, respectively, we took advantage of the task results of the retrieval session as class labels. We assigned the correctly remembered trials as "correct", while others (forgotten and no idea) were assigned as "incorrect". We extracted power spectral densities (PSDs) using continuous wavelet transform (CWT) from five frequency bands: delta (δ: 1 – 4 Hz), theta (θ: 4 – 8 Hz), alpha (α: 8 – 13 Hz), beta (β: 13 – 30 Hz), and gamma (γ: 30 – 50 Hz). The PSDs were normalized using the Z-score of the baseline power (-1 – -0.8 s) and used as decoding features. The decoding accuracy was evaluated using a naïve Bayes classifier based on 10x5-fold cross-validation, where Fisher score was used to select the best subset of features to avoid an overfitting problem.

Results and Discussion

Figure 2 shows the event-related spectral perturbation (ERSP) maps of the two patients during the encoding session, which were obtained by averaging all channels and trials for correctly and incorrectly encoded items, respectively. The two conditions showed different ERSP patterns; correct items showed stronger ERS around beta band in common for the two patients (magenta rectangle in the third column) along with their unique patterns.

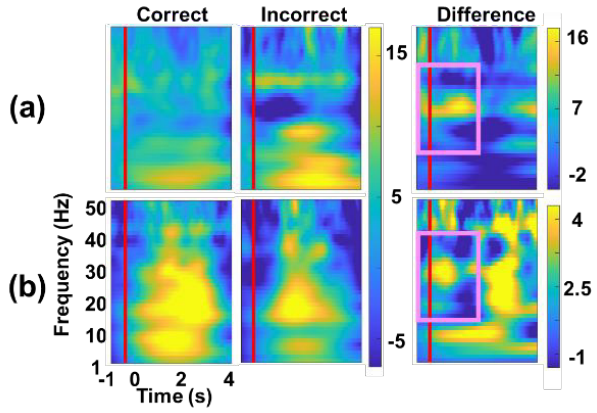


Figure.2 Event-related spectral perturbation (ERSP) maps of (a) Patients 1 and (b) Patients 2 during the encoding session. The red line indicates when the item was presented (onset time).

Figure 3 shows the decoding accuracy for each patient. The highest decoding accuracies of the pre-task and task periods were obtained when using delta spectral powers for both patients (Patient 1: 67.5 % and Patient 2: 78.8% for the task period; Patient 1: 74.8 % and Patient 2: 73.2% for the pre-task period). This result demonstrated that the results of the memory task can be successfully decoded before and during the encoding session using brain activity.

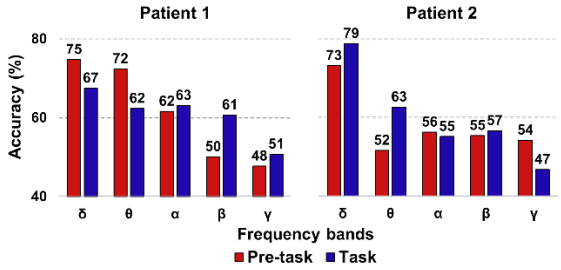


Figure.3 Decoding accuracy for each patient.

In our future studies, we plan to improve the decoding performance by introducing more advanced classification algorithms based on deep learning architectures [4].

Acknowledgements

This research was supported by the Bio & Medical Technology Development Program of the National Research Foundation (NRF) funded by the Ministry of Science & ICT (NRF-2021M3E5D2A01019547).

References

1. Burke, J. F., Zaghloul, K. A., Jacobs, J., Williams, R. B., Sperling, M. R., Sharan, A. D., and Kahana, M. J., "Synchronous and asynchronous theta and gamma activity during episodic memory formation." Journal of Neuroscience 33.1 (2013).
2. Noh, E., Liao, K., Mollison, M. V., Curran, T., and Sa, V. R. D., "Single-trial EEG analysis predicts memory retrieval and reveals source-dependent differences." Frontiers in human neuroscience 12 (2018).
3. Kerrén, C., Linde-Domingo, J., Hanslmayr, S., and Wimber, M., "An optimal oscillatory phase for pattern reactivation during memory retrieval." Current Biology 28.21 (2018): 3383-3392.
4. Schirrmeister, R. T., Springenberg, J. T., Fiederer, L. D. J., Glasstetter, M., Eggensperger, K., Tangermann, M., and Ball, T., "Deep learning with convolutional neural networks for EEG decoding and visualization." Human brain mapping 38.11 (2017).

P-068

A computational scheme for optimal control of brain with consideration of activity-dependent and homeostatic plasticity

Jiyoung Kang[1,2], Jinseok Eo[3,4], and Hae-Jeong Park[3,4,5]*

[1]Department of Scientific Computing, Department of Physics, Pukyong National University, 48513, Busan, Republic of Korea

[2]College of Liberal Arts, Pukyong National University, 48513, Busan, Republic of Korea

[3]Brain Korea 21 Project, Graduate School of Medical Science, Yonsei University College of Medicine, 03722, Seoul, Republic of Korea

[4]Department of Nuclear Medicine, Department of Psychiatry, Yonsei University College of Medicine, 03722, Seoul, Republic of Korea

[5]Center for Systems and Translational Brain Science, Institute of Human Complexity and Systems Science, Yonsei University, 03722, Seoul, Republic of Korea

[8]Department of Cognitive Science, Yonsei University, 03722, Seoul, Republic of Korea

parkhj@yonsei.ac.kr

Abstract

The brain is a nonlinear dynamic system with self-repairing processes. It protects itself from damage, but sometimes moves against the recovery from brain disease. Therefore, a framework that can induce the desired brain state by considering the self-recovery process of the brain is important. However, these properties have often been neglected in control studies for brain recovery. This study presents an optimal brain control framework for inducing normal brain function considering characteristic nonlinear brain dynamics and the self-restoration process of the brain.

Background

The goal of treatment for brain disease is to modify the brain circuit to obtain proper brain function. Although various clinical methods have been developed for treatment of brain disease, the optimal control of the brain still has many practical challenges due to the complexity of the brain and ethical issue. Computational approaches are advantageous in developing treatments for human brain diseases, which are difficult to test by experiments due to the ethical issue. Recently, several computational methods have been developed to overcome difficulties in optimal brain treatment problems. However, in most these computational models, the brain system's self-adjusting nature after treatments has not been fully considered, and the brain system was only regarded as a passive responding system. Thus, in the present study, we propose a computational framework for optimal control of the self-adjustment brain system [1].

Methods

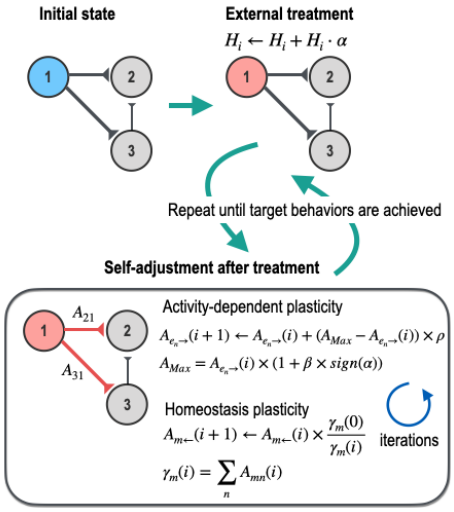
We considered two types of self-adjusting natures of the brain; activity-dependent plasticity and homeostatic plasticity (Figure 1). The active-dependent plasticity describes that the activity of presynaptic neurons increases synaptic strengths between connected neurons. The other plasticity, homeostatic plasticity mimics that numbers of receptors in the post-synaptic neurons are not rapidly changed by external stimulations, and the entire strength of incoming synaptic strengths are consistent. Then, we coupled brain dynamics model and self-adjustment brain models to describe brain network changes related with brain activity. To describe brain dynamics, we used the dynamic causal model (DCM), which consists of two models; neural state model and observation model.

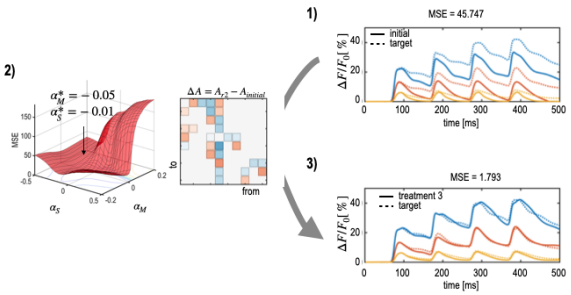
Constructing biological circuits based on our previous study [2], we tested the presented computational scheme. The hippocampus systems of mutant and wild-type mice were assigned as the initial and target systems estimated using the DCM method with the voltage-sensitive dye imaging (VSDI) data.

Results and Discussion

Starting with abnormal initial brain systems, which show different brain activities from the normal brain, we searched how we can recover the normal brain's brain activity patterns (Figure 2). The present scheme consists of three parts; 1) system evaluation (diagnosis) to understand the current state, 2) treatment based on the search for treatment parameters in a practically possible range, 3) system based on the system status evaluation result after treatment. This evaluation includes estimating plasticity and homeostasis parameters.

By adopting the treatment and self-adjustment rules, our scheme found optimal solutions that generated signals of the target brain system in various restrictions of clinical treatments such as one or two treatable nodes that mimic transcranial magnetic stimulation (TMS), global treatment that mimics medications, and mixed treatments (simultaneous treatments of TMS and drugs).





Simulation results showed that optimal control of the abnormal mutant system successfully approached the typical wild type signals under restrictions that mimic various clinical treatments. These results suggest that consideration of the brain system's self-adjustment properties is critical to find appropriate brain treatments, and the proposed computational framework can be a useful tool for searching for optimal controls of the dynamic brain after treatment. Our results also suggested that these recoveries could not be achieved without considerations of the brain system's self-adjustment properties.

Acknowledgements

This research was supported by Brain Research Program and Basic Science Research Program through the National Research Foundation of Korea (NRF) funded by the Ministry of Science and ICT, and the Ministry of Education (NRF- 2017M3C7A1049051).

References

1. Kang, J., Jung, K., Eo, J., Son, J., Park, H.J., 2020. *Neuroimage* **213**, 116755.
2. Kang, J., Eo, J., Lee, D.M., Park, H.-J., 2021. *Neuroimage* **230**, 117805.

P-069

Development of an Online Endogenous Brain-Computer Interface Based on Ear-EEG

S.-I. Choi[1] and H.-J. Hwang[2,3]

[1]Department of Medical IT Convergence Engineering, Kumoh National Institute of Technology, Gumi, Korea

[2]Department of Electronics and Information Engineering, Korea University, Sejong, Korea

[3]Interdisciplinary Graduate Program for Artificial Intelligence Smart Convergence Technology, Korea University, Sejong, Korea

hwanghj@korea.ac.kr

Abstract

In this study, we investigated whether an endogenous ear-electroencephalography (ear-EEG)-based brain-computer interface (BCI) with reasonable performance can be implemented in online environments. We measured ear-EEG while fourteen subjects performed three BCI experiments on three different days. An offline experiment was first conducted to determine the best pair of mental tasks for each subject, and online experiments were then conducted on two different days using individually selected best pairs. The mean online classification accuracy was almost 70% for most cases, which is equivalent to a marginal accuracy for a practical two-class BCI (70%), and the performance could be further improved by introducing deep learning algorithms, demonstrating the feasibility of implementing an online endogenous ear-EEG-based BCIs.

Background

Previous studies have demonstrated the feasibility of using ear-electroencephalography (ear-EEG) for the development of brain-computer interfaces (BCIs), but most of them have used exogenous paradigms in offline environments [1]. To verify the reliable feasibility of constructing ear-EEG-based BCIs, the feasibility of using ear-EEG should be further demonstrated using another BCI paradigm, namely the endogenous paradigm, in real-time environments. In this study, we investigated whether an endogenous ear-EEG-based BCI can be developed with reasonable performance in online environments that mimic real-world scenarios. Additionally, the deep learning algorithms were conducted to confirm the feasibility of implementing an endogenous ear-EEG-based BCI system with high reliability.

Methods

Ear-EEG data were acquired using eight electrodes mounted behind the ears while fourteen healthy subjects performed three BCI experiments on three different days. On the first experimental day (day 1), offline experiments were performed for three mental tasks (mental arithmetic: MA; mental singing: MS; word association: WA). The three mental tasks were randomly performed, with each task being performed 10 times, in a single session. Each subject completed five sessions, performing 50 trials for each of the three mental tasks. On the basis of the classification accuracies of all combinations of the three mental tasks performed in the offline experiment (i.e., MA vs. MS, MA vs. WA, and MS vs. WA), we selected the best pair of tasks for each subject and used them for the following online experiments performed on two online experimental days. The online experiment comprised three training and two test sessions, where we collected training data (30 trials for each task) to construct an online classifier and we tested the classifier for new inputs (test data: 20 trials for each task) in real-time, respectively. In the test session of the online experiment, real-time feedback based on classification results was provided right after the subject performs a mental task. In the first online experimental day (day 2), subjects performed three training and two test sessions. In the second online experimental day (day 3), subjects performed three training sessions, followed by two test sessions

repeated thrice independently using three different online classifiers. The three classifiers were constructed using different training data sets (the data set obtained on day 2, 3, and the combination of these two data sets) to check the test-retest reliability of the ear-EEG-based BCI.

Ear-EEG data were first band-pass filtered from 1 to 50 Hz using a zero-phase third-order Butterworth filter, and then down-sampled to 200 Hz to reduce the computation time. After that, we used multi-band common spatial pattern (CSP) and shrinkage linear discriminant analysis (LDA) for feature extraction and classification, respectively. Offline classification accuracies obtained using 10-fold cross-validation results were used to select the best pair of mental tasks for each subject on day 1, whereas real-time outputs obtained immediately after performing a single trial in the test sessions were used to estimate online classification accuracies on days 2 and 3.

To investigate the possibility of improving the classification performance of ear-EEG-based BCIs using deep learning algorithms, we calculated classification accuracy using the four different convolutional neural network (CNN)-based deep learning algorithms: ShallowNet, EEGNet, HybridNet, and DeepNet [2]. This was tested using only the offline datasets as a preliminary study.

Results and Discussion

Figure 1 shows the mean classification accuracies for the offline and online experiments using individual best pairs of mental tasks. The mean classification accuracy for days 1 was 77.7 ± 10.9%. The mean online classification accuracy for day 2 was 69.1 ± 14.5%, which was not statistically different from the offline classification accuracy, despite the reduced performances. The mean online classification accuracies for day 3 were 61.9 ± 13.2%, 65.7 ± 12.7%, and 69.5 ± 14.7%, which were obtained using training data measured on day 2, 3 and combination of day 2 and 3, respectively. Despite the lower classification performance in online experiments compared with that in offline experiments, the mean online classification accuracy was almost 70%, which was significantly higher than the theoretical 95% confidence limit of a chance accuracy for a two-class BCI (59.61%) and equivalent to a marginal accuracy for a practical two-class BCI (70%), demonstrating the feasibility of using ear-EEG for the development of endogenous BCIs.

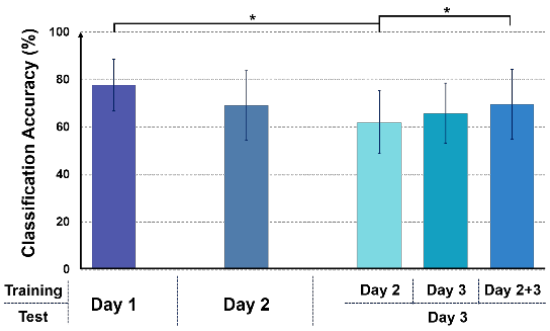


Figure 1. Mean classification accuracies of the offline and online experiments.

Figure 2 shows the comparison of the mean classification accuracies obtained using the four CNN-based deep learning methods and that obtained using the LDA-based machine learning method. The classification accuracies of ShallowNet outperformed those of the others for most cases, and they were significantly higher than those of the LDA method (paired t-test: $p < 0.05$). This result indicates that the deep learning algorithms can improve the classification performance for endogenous ear-EEG-based BCI.

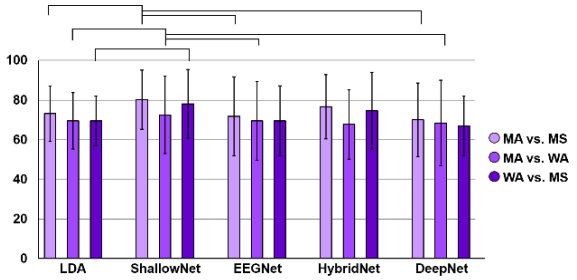


Figure 2. Mean classification accuracies for five different algorithms.

Acknowledgements

This work was supported by the National Research Foundation of Korea (NRF) grant funded by the Korea government (MSIP; Ministry of Science, ICT & Future Planning) (No. 2017R1C1B5017909)

References

1. R. Kaveh, J. Doong, A. Zhou, C. Schwendeman, K. Gopalan, F. L. Burghardt, et al., "Wireless user-generic ear EEG," IEEE Trans. Biomed. Circuits Syst. 14(4), 727–737 (2020).
2. K.-W. Ha. and J.-W. Jeong., "Motor imagery EEG classification using capsule networks," Sensors 19(13),2854 (2019).

Optogenetic stimulation on rat hippocampus for neuromodulation

Youjin Lee[1,2], Yena Lee[2], Seoyoung Hwang[2], Hyang Woon Lee[3,4], Sang Beom Jun[1,2,5*]

[1]Graduate Program in Smart Factory, Ewha Womans University, Korea

[2]Department of Electronic and Electrical Engineering, Ewha Womans University, Korea

[3]Department of Neurology, Ewha Medical Research Institute, Korea

[4]Department of Medical Science, Ewha Womans University School of Medicine, Korea

[5]Department of Brain and Cognitive Sciences, Ewha Womans University, Korea

***juns@ewha.ac.kr**

Abstract

It is well known that sleep plays an important role in cognitive functions as well as in physical recovery. However, the sleep mechanisms in the neural circuit are not fully identified yet. Since optogenetic technology enables the selective modulation of targeted neuronal cells in the brain, we are attempting to optogenetically control the signaling in sleep-related neural circuits. In this study, excitatory neurons in rat hippocampus are selected for the optical stimulation. As a preliminary study, the pyramidal neurons in hippocampal regions are genetically modified to express channelrhodopsin-2 (ChR2). The neurons are optically stimulated and the evoked neural activity is simultaneously recorded. The frequency of neural activity immediately increased during light stimulation. This result is expected to be useful for targeting sleep related brain region and finding an effective neuromodulation approach for sleep therapy.

Background

Sleep is essential not only for physical and mental recovery, but also for maintaining health by strengthening long-term memory by controlling physical function such as growth and preservation of energy metabolism or strengthening immune function, especially cognitive and emotional function. Sleep deprivation can increase the risk of metabolic, cardiovascular and Alzheimer's diseases [1]. Therefore, various studies have been conducted to improve the sleep quality through brain stimulation to modulate sleep related brain circuits. As the brain areas related to sleep, prefrontal cortex (PFC), thalamus reticular nucleus (TRN), and hippocampus are mainly studied, but exact neuronal mechanisms for sleep and wake regulation have not been clearly revealed yet [2]. Especially, it is known that hippocampus is crucial for memory consolidation, specifically related with hippocampus-dependent memory [3]. In addition, insufficient sleep affects the molecular signaling which is important for synaptic plasticity of the hippocampus.

Optogenetics, a technology that can selectively stimulate or inhibit cells by expressing opsin proteins that can respond to specific light on a specific type of neuronal cells. Therefore, optogenetics has been actively used to investigate neural signaling with selective neural modulation. Channelrhodopsin-2 (ChR2) is well known as a protein that induces cell activation by responding to light stimulation at 473 nm wavelength.

In this study, hippocampus, one of the key brain areas related to sleep, was targeted. We optogenetically excited hippocampal signal pathway using ChR2 virus. ChR2 was expressed in hippocampal pyramidal cells and light stimulation was applied. Simultaneously, electrophysiological recording was performed to verify the neural responses induced by light stimulation.

Methods

Figure.1 shows a conceptual diagram of optical stimulation setup. Light pulses from laser source are irradiated into the hippocampal region through the

implanted optical fiber and the neural signal is recorded using intan RHD interface board simultaneously. Adult SD male rat received 2 μl AAV-CaMKⅡα-hChR2(H134R)-EYFP in each hippocampus. The virus was delivered slowly over 20 min using 10 μl Hamilton syringe and left in place for an additional 5 min. after then withdrawn slowly. Five weeks after the AAV vector delivery, the neurons in the virus-injected brain region successfully expressed ChR2. The animal care and surgical procedures were approved by the Institutional Animal Care and Use Committee (IACUC) at the Ewha Medical Research Institute (approval No. 069-1**).**

Rat was anesthetized with a ketamine cocktail and optrode which is manufactured with 2x2 tungsten electrodes included an optical fiber which has 200 μm diameter was inserted into hippocampus (AP: 2.8 to 3.8 mm, ML: 2–3 mm, DV: −2.7 mm). Optical stimulation was performed with a 473 nm laser source.

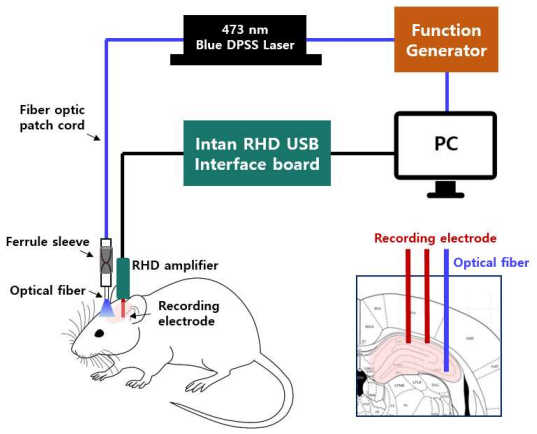


Figure 1. Conceptual diagram of optical stimulation and electrophysiological recording.

The light intensity was checked by power meter. 3 mW/mm^2 was measured at the end of the optical fiber tip. Stimulation parameters were set to 50 % duty cycle, and 10 Hz frequency by controlling function generator. Total light application time was twenty seconds. Electrophysiological recording was performed for twenty seconds each before, during, and after light stimulation. In order to identify changes of neural activities, the recorded data was analyzed by Matlab.

.

Results and Discussion

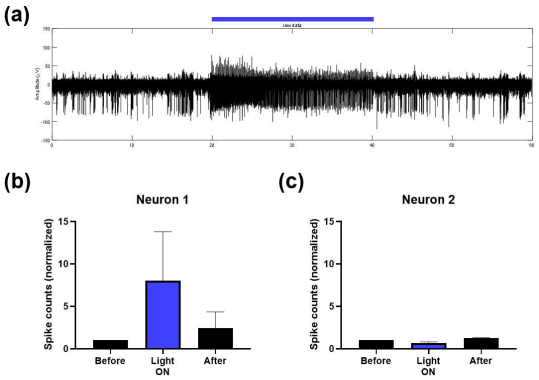


Figure 2. Neural recording with optogenetic stimulation (a) Raw waveform of recorded neural signal from hippocampus (blue light was ON for 20 sec). Sorted spike count during before, blue light ON and after from (b) neuron 1 and (c) from neuron 2

Figure. 2(a) shows the raw data of simultaneous neural recording and stimulation. Neural signals were activated during light stimulation. Spike sorting was conducted using Matlab, and two different neurons were detected based on spike waveforms. Normalized spike counts were calculated for each neuron. As a result, neuron 1 showed a rapid increase in firing rate. The result can be explained that neruon1 was an excitatory neuron and well expressed ChR2, so that it showed immediate activation under light stimulation. On the other hand, there was no significant change in the firing rate of neuron 2. Therefore, neuron 2 may not an excitatory neuron or ChR2 was not expressed. Distribution of CaMKIIα expression in the hippocampus is known to be about 70% [4].

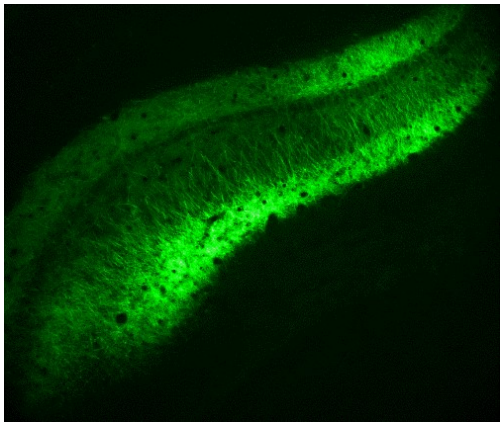


Figure 3. Expressed CaMKⅡα-ChR2- EYFP in hippocampal neurons.

In order to prove the validity of the results, the final step in optogenetics experiment is to test whether virus is expressed or not. Since ChR2 opsin itself is not fluorescent, virus containing EYFP, which is fluorescence reporter protein, was used in this study. As shown in Figure. 3, fluorescence was well expressed in the hippocampus. Therefore, it can be concluded that the results of an increase in the number of spikes during light stimulation was optogenetically induced.

Acknowledgements

This research was supported by Convergent Technology R&D Program for Human Augmentation through the National Research Foundation of Korea (NRF) funded by the Ministry of Science and ICT (NRF-2019M3C1B8090805), and was supported by a National Research Foundation of Korea (NRF) grant funded by the Korea government (MSIT) (no. 2019R1A2C1088909).

References

1. Lisa Marshall, Nathan Cross, Sonja Binder and Thien Thanh Dang-Vu," Brain Rhythms During Sleep and Memory Consolidation: Neurobiological Insights", PHYSIOLOGY, Vol. 35, Issue 1, 2020.
2. Antoine R. Adamantidis, Carolina Gutierrez Herrera and Thomas C. Gent, "Oscillating circuitries in the sleeping brain," Nature reviews neuroscience, Vol.20, 2019.
3. Nicolas Maingret, Gabrielle Girardeau, Ralitsa Todorova, Marie Goutierre & Michaël Zugaro, "Hippocampo-cortical coupling mediates memory consolidation during sleep", Nature neuroscience, Vol. 19, 2016
4. Xinjun Wang , Chunzhao Zhang, Ga´ bor Sza´ bo, Qian-Quan Sun, "Distribution of CaMKIIα expression in the brain in vivo, studied by CaMKIIα-GFP mice", Brain Res., 1518:9-25, 2013

P-071

Coincidence level estimation of bursting spike trains using jittering timestamp

Hyungsub. Lee[1] and Yoonkey. Nam[1]

[1]Department of Bio and Brain Engineering, Korea Advanced Institute of Science and Technology, Daejeon, Korea

mrmirocu@kaist.ac.kr, ynam@kaist.ac.kr

Abstract

For connectivity inference, significant correlation values need to be selected among coincidently generated correlation values. Jittering timestamp of spike trains can be one of the ways to generate surrogate spike trains for comparison of correlation peak and coincidence level. In this study, simple spike trains were simulated and the performance of jittering CL estimation method was investigated. The jittering CL estimation performed better for bursting spike trains.

Background

Understand of functional structure of neuronal circuit is one of the most interesting challenge in the neuroscience field. Many researchers have inferred connectivity from parallel spike trains measured from different neurons in order to reconstruct connection map and to figure out network characteristics. Correlation values between spike trains are calculated by many different ways like cross-correlation, transfer entropy, etc. After then, significant correlation peak is selected and inferred as connectivity. Coincidence level (CL) of correlation values should be estimated first in order to decide the correlation peak is significant or not. Correlation histogram bulges according to their temporal relationship when network activity like bursts, neuronal avalanches occurred, so it becomes hard to find significant peaks from CL.

Researchers have developed several methods picking out sharp peak from the CL estimation. Jittering spike time is a method for finding CL by generating surrogate spike trains and cross-correlation histogram (CCH) and comparing to original CCH. One previous research claimed that confidence interval of correlation values and z-score can be calculated by jittering method, and jittering method can be effective to different state of spike trains. However, less investigation has done for realistic bursting spike trains.

In this study, we generated bursting spike trains with different states, and the performance of jittering methods for CL estimation was investigated. According to the bursting characteristics of simulated spike trains, the jittering CL estimation was better than other methods.

Methods

Two methods for CL estimation were implemented. They resulted confidence intervals, represented by μ and σ. MFR CL estimation assumed two spike trains were randomly distributed with MFR of r_1 and r_2 where T was timespan and time bin for CCH was τ. Mean and s.t.d of MFR CL were represented:

$$\mu_{MFR} = r_1 r_2 \tau T, \sigma_{MFR} = \sqrt{\mu_{MFR}}$$

For jittering CL estimation, surrogate spike trains were generated by adding normal distributed random variables with mean of 0 and s.t.d of λ, jittering parameter to the spike timing of spike train 1, and 100 surrogate CCHs were calculated and averaged.

$$x_1(t) = \sum_{i=1}^{n_1} \delta(t - t_i), where\ n_1\ is\ the\ number\ spike$$

$$x_1'(t) = \sum_{i=1}^{n_1} \delta(t - t_i'), t_i' \sim t_i + N(0, \lambda)$$

, where λ is jittering parameter

$$\mu_{jittering}(\tau) = mean[CCH(x_{1,k}', x_2, \tau)]$$

$$\sigma_{jittering}(\tau) = std[CCH(x_{1,k}', x_2, \tau)]$$

Simple spike train simulation was performed in order to evaluate MFR and jittering CL estimation methods according to the conditions of spike trains condition. The condition of spike trains was targeting tonic or bursting states, and the cases with connection and without connection was assumed. The correlation between two spike trains without connection was assumed that it was occurred by pure coincidence, so CCH between spike trains without connection was used to be right CL and was compared to the estimated CL for calculating error.

Spike trains were simulated based on the Poisson process. Tonic spike trains were simply generated by repeating the Poisson process using mean firing rate (MFR). Bursting spike trains were designed to share burst timing, so the burst regime was defined first by the Poisson process using mean burst rate (MBR) and burst duration. After then, intra- and inter-burst spike rate were calculated, and spikes were filled according to them

Results and Discussion

Figure 1. (a, d) are representing the raster plot of examples of generated tonic and bursting spike trains. The bursting spike trains were sharing the burst regime which was marked by red lines above the raster plot. In order to investigate the characteristic of simulated spike trains, the ISI histograms of them were represented in Figure 1. (b, e). The ISI of tonic spike trains was following uni-modal distribution, and the peak of the distribution was close to 0.6 sec, which corresponded with the MFR of 1.5 Hz (Figure 1. (b)) On the other hand, the ISI of bursting spike trains was following bi-modal distribution. The larger peak was close to 0.025 sec, which was similar with intra-burst spike rate (36 Hz), and the smallar peak was representing inter-burst spike rate. (Figure 1. (e)) Cross-correlation histogram (CCH) between tonic spike trains was flat, and the sharp peak was occurred on the histogram when the connection was added. (Figure 1. (c)) CCH between bursting spike trains bulged close to zero, and the peak appeared on the histogram by connection. (Figure 1. (f)) In the both tonic and bursting cases, the connection between spike trains did not affected to the coincidence level (CL) of the CCH, and the sharp peak added on the CL.

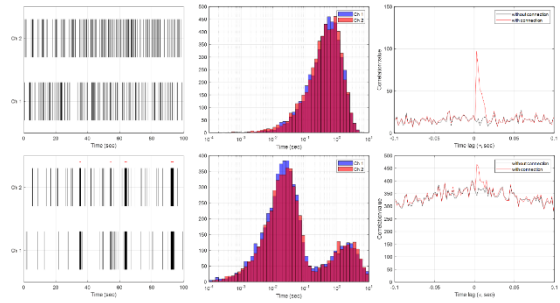


Figure.1 Spike train simulation and characterization.

The CL estimation of CCH of tonic spike trains without connection was successful for both methods. The correlation values in the range of interest were included in 99.9 % confidence interval by MFR and jittering CL estimation. (Figure 2. (a)) MFR CL estimation method was still successfully even though the sharp peak was added on the flat correlation histogram. (Figure 2. (b, red)) On the other hand, jittering CL estimation with small jittering parameter (20 msec) was affected by the peak by connection and big error was occurred near it. (Figure 2. (b, blue)) The sharp peak was indicating statistically larger correlation than coincidence level that could be inferred as connection based on both CL estimation. The error of jittering became similar level to the error of MFR when the jittering parameter was 200 msec. For the connectivity inference of tonic spike trains, both CL estimation methods worked, but MFR CL estimation showed better performance.

MFR CL estimation showed large difference for bursting spike trains. (Figure 2. (e, red)) The MFR of spike trains did not changed, but bursting activity raised spike train within the burst regime. The jittering CL estimation was well following the bulged CCH without (Figure 2. (e, blue)) and with (Figure 2. (f, blue)) connection. As the jittering parameter became larger, the estimation became flatter than real CL. (Figure 2. (g)) When the jittering parameter was between 20 and 50 msec, the error between CL estimation and real CL minimized. (Figure 2. (h)) For the connectivity inference of bursting spike trains, the jittering CL estimation showed good performance.

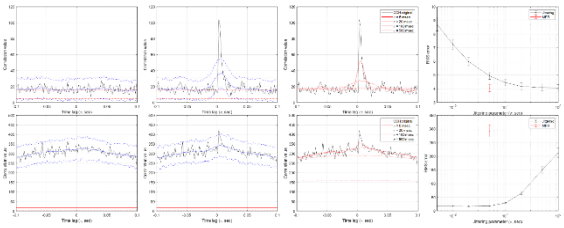


Figure.2 CL estimation of tonic and bursting spike trains.

In this research, jittering and MFR CL estimation was implemented and compared using simple spike train simulation with different states. Jittering CL estimation showed better performance for bursting spike trains than MFR CL estimation.

Acknowledgements

This work was supported by the National Research Foundation of Korea grant funded by the Korean government (MSIP) (NRF-2021R1A2B5B03001764).

P-072

Changes in activated astrocytes by the electrical stimulation

Uk Jegal[1], Sangyoon Oh[1], Eunmin Ko[1], Eunyoung Park[1] and Jennifer H. Shin[1]

[1] Dept. of Mechanical Engineering, KAIST, Republic of Korea

j_shin@kaist.ac.kr

Abstract

Astrocytes become activated after brain injury, exhibiting changes in function and gene expression. In the previous in vivo research, electrical stimulation(ES) of injury sites in a rodent model facilitates the acquisition of stemness in cortical astrocytes, suggesting therapeutic effects of ES. In this research, changes in activated astrocytes by ES were investigated in an in vitro model to perform a more detailed analysis. Upon ES, the expression levels of key biomarkers for stemness and neuroprotective function in astrocytes increased, suggesting possible therapeutic effects of ES on brain injury.

Background

Astrocytes, the most abundant type of glial cells, become activated after brain injury, then exhibit changes in gene expression and function, known as astrogliosis. During the astrogliosis, activated astrocytes show increased GFAP and S100B expressions, marked characteristics of activated astrocytes. Recently, two distinct states of activated astrocytes have been proposed, known as A1 and A2 astrocytes. A1 astrocytes cause neuronal deaths by secreting neurotoxins whereas A2 astrocytes have neuroprotective and tissue repair functions. In particular, S100A10 identified as a specific marker for A2 astrocytes is essential for membrane repair and inhibition of apoptosis [1].

Previous *in vivo* experiment from our laboratory demonstrated the acquisition of stemness in cortical astrocytes by ES on injury site in a rodent model, suggesting therapeutic effects of ES [3]. Since subpopulation of activated astrocytes has been shown to express several stem cell-associated proteins such as SOX2 after brain injury [2], it would be of great interest to investigate the mechanism of the ES-induced elevation of stemness in cortical astrocytes. In this study, we established an *in vitro* platform that allowed a more detailed mechanism study as well as a confirmation of the ES-induced changes in activated astrocytes.

Methods

Primary cortical tissue was separated from 1-3 days old SD rats, then cut into small fragments by mixing the tissue with papain solution. Then, the cells were cultured in Poly-D-lysine (PDL) coated flask. DMEM-based media supplemented with 10% FBS and 1% penicillin-streptomycin was used. After 10 days of culture, when astrocytes formed monolayer and microglia were exposed on the monolayer, the flask was shaken at 250 rpm for 18 hours to remove other cells except for astrocytes. The isolated astrocytes were then plated on the PDL-coated slide glass to generate the activated state of astrocytes mimicking the cellular state after the occurrence of brain injury. After 3 days of culturing the isolated astrocytes, cells were transferred to the ES chamber. Figure 1 shows a schematic representation of the ES device, consisting of a DC power supply, cell culture chamber, agar bridge, and Steinberg's solution chamber. The voltage level was set at 2.0 V/cm. After applying the ES to the astrocytes, the gene expression levels (GFAP, S100B: the marker for astrocyte activation and SOX2: the marker for stemness, S100A10: the marker for A2 astrocytes) were confirmed by qRT-PCR.

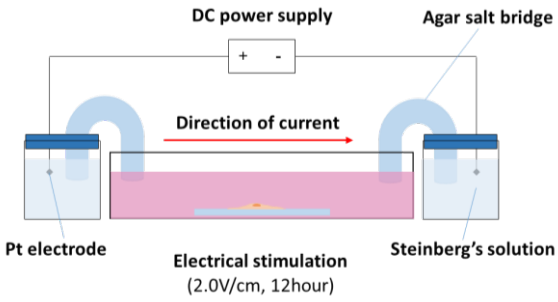


Figure 1. DC Electrical stimulation device.

Results and Discussion

The results indicated that the mRNA expression for GFAP and S100B as the marker for astrocyte activation decreased after ES (Figure 2). Since high extracellular concentration of S100B is known to induce mitochondrial dysfunction and apoptosis of neurons, the ES-induced decrease in S100B may be considered positive.

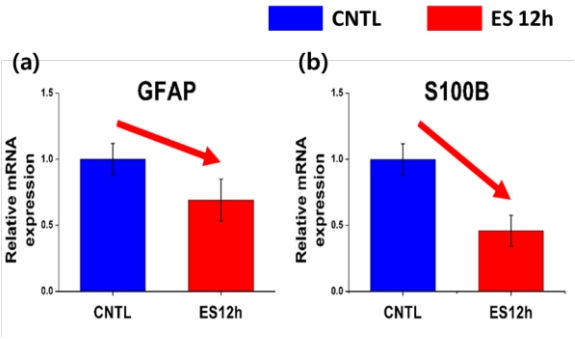


Figure 2. Relative mRNA expression changes in (a) GFAP and (b) S100B after electrical stimulation.

As shown in Figure 3(a), the mRNA expression for SOX2, considered as the marker for stemness in activated astrocytes, increased after ES, suggesting an encouraging effect of ES to the astrocyte function.

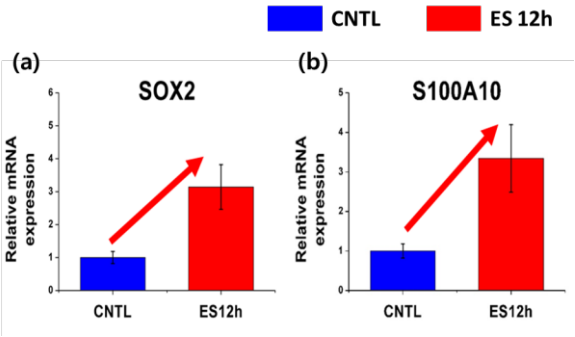


Figure 3. Relative mRNA expression changes in (a) SOX2 and (b) S100A10 after electrical stimulation.

The ES-induced increase in S100A10 shown in Figure 3(b) was also consider positive as S100A10 is the specific marker for the neuroprotective astrocytes promoting survival of neurons and synapse repair.

In summary, our results consistently demonstrated positive effects of12 hour stimulation of ES at 2.0 V/cm, suggesting its potential usage as a promising therapeutic strategy following the brain injury.

Acknowledgments

This research was supported by the Global Singularity Research Program funded by KAIST.

References

1. Li, T., et al. (2019). "An update on reactive astrocytes in chronic pain." J Neuroinflammation 16(1): 140.
2. Shimada, I. S., et al. (2012). "Self-renewal and differentiation of reactive astrocyte-derived neural stem/progenitor cells isolated from the cortical peri-infarct area after stroke." J Neurosci 32(23): 7926-7940.
3. Park, E., et al. (2021). "Enriching neural stem cell and anti-inflammatory glial phenotypes with electrical stimulation after traumatic brain injury in male rats." J Neurosci Res 99(7): 1864-1884.

Classifying the distracted state during exercise using Steady State Visual Evoked Potential (SSVEP) and EEGNet

H.M. Lim[1] and J.H. Ku[1]

[1]Department of Biomedical Engineering, Keimyung University, Daegu, Korea

kujh@kmu.ac.kr

Abstract

Concentration while rehabilitation training is critical for positive outcome. Therefore, concentration measurement and its feedback during exercise rehabilitation could help to maximize the effect of exercise rehabilitation. In this study, we investigated whether the concentration level could be detected by using the modulation effect of SSVEP amplitude by the external focus on exercise and be superiorly classified the concentration level. For this, we used dual-task paradigm that made users distracted in focusing on performing an exercise task. The experiment was conducted on 10 healthy adults. As results, it was shown that the distract modulated SSVEP amplitude, which means it could be influenced by the user's concentration on body movements. Also, the accuracy was superior when using SSVEP feature. Therefore, this SSVEP paradigm could provide an effective rehabilitation method of providing feedback and it could induce continuous focus on motor rehabilitation.

Background

It is important to focus on task during motor learning [1], but the patients usually have difficulty concentration on rehabilitation. It could be helpful to give quantitatively measures of concentration, subsequently it could lead to strong the effectiveness improvement of rehabilitation. Recently, one of the BCI techniques, steady state visual evoked potential (SSVEP) has been introduced to measure the user's concentration on stimulation [2]. Therefore, in this study, we propose the superiority of using the SSVEP technique in classifying concentration levels during exercise

Methods

1. Motor Task

The motor task was designed to move the mouse cursor and match to the moving target on the screen using dominant hand [figure 1].

2. SSVEP stimulation

For the features on the difference in concentration, the target was blinked at 15 Hz and the cursor at 12 Hz.

3. Distractions

- Visual distraction: A visual disturbance is provided to confuse the focus on the target's movement. Twenty circles similar in shape and color to the target were placed in the background. Each circle moves randomly as the target moves. The color of the circle is gray, which is the middle value of the target's blinking colors (black and white).

- Cognitive distraction (multi-task): Subjects were asked to do mental arithmetic tasks while performing motor tasks. A simple mental arithmetic task was presented once every 3 seconds. The mental arithmetic task was two digits minus one digit with regrouping. Participants gave their answers while performing the motor task.

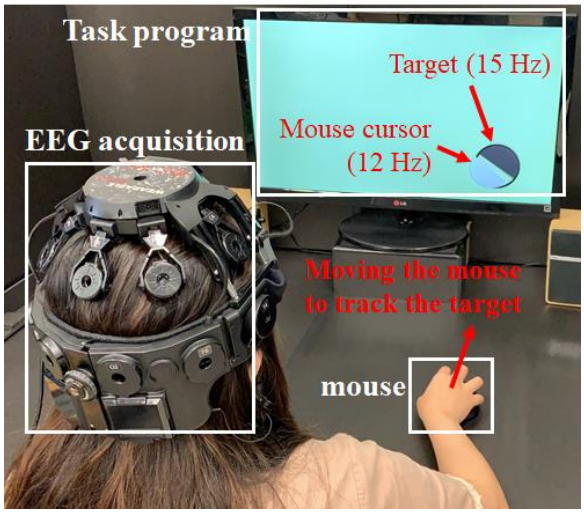


Figure 1. Experiment configuration

4. Conditions

There were four conditions [Table 1].

condition	distraction	flickering
1	O	O
2	X	O
3	O	X
4	X	X

Table. 1. Experiment conditions

(1) Motor training with distractions + flickering; There were visual distraction and cognitive distraction. The cursor and moving target on the screen were flickered.

(2) Motor training without distractions + flickering; There was only motor task. The cursor and target were flickered.

(3) Motor training with distractions + nonflickering;

(4) Motor training without distractions + nonflickering;

The cursor and moving target on the screen were not flickered in condition (3) and (4).

Each condition was performed for two minutes.

5. Subjects

Ten healthy adults were recruited in this study. All participants were right-handed.

6. EEG data acquisition

EEG was collected from 19 electrodes at 300 Hz sampling rate, using a DSI-24 (wearable sensing, San Diego, USA).

7. Classification methods

EEGNet model [3] was used to classify the distraction condition and non-distraction condition. We fit the model using the Adam optimizer, minimizing the categorical cross-entropy loss function. We run 100 training iterations (epochs).

8. Classifier validation

A 10-fold cross validation was performed to evaluate the performance of the classifier.

Results and Discussion

The classification performance of distraction level during motor task was superior in flickering condition. The classifier's average accuracy was 54.5% in the non-flickering condition [Table 2], while average 72% of accuracy was shown in the flickering condition [Table 3].

nonFlickering condition		
	nonDistraction	Distraction
nonDistraction	0.72	0.28
Distraction	0.63	0.37

Table. 2. Confusion matrix in non-flickering condition

Flickering condition		
	nonDistraction	Distraction
nonDistraction	0.75	0.25
Distraction	0.31	0.69

Table. 3. Confusion matrix in flickering condition

In this study, we investigated the effect of SSVEP paradigm on concentration classification. The results showed that SSVEP enhanced the improvement of the concentration classification performance during motor task. Therefore, we could conclude that the SSVEP paradigm could be an effective method in a neurofeedback system in rehabilitation that requires concentration such as motor, cognitive, and dual task rehabilitation.

Acknowledgements

This work was supported by the National Research Foundation of Korea (NRF) grant funded by the Korea government(MSIP) (No. NRF-2017R1A2B4011920).

References

1. Wulf G. Attention and Motor Skill Learning. Champaign, IL: Human Kinetics 2007
2. Tononi GSrinivasan RRussell DPEdelman GM (1998) Investigating neural correlates of conscious perception by frequency-tagged neuromagnetic responses PNAS 95:3198-3203.
3. Vernon J Lawhern et al, EEGNet: a compact convolutional neural network for EEG-based brain-computer interfaces. 2018, Journal of Neural Engineering, 15

Effect of auditory Vagus Nerve Stimulation on Pupillometry

Ji Yeon Lee[1,2], Hee Soo Jeong[1,2], Jee Eun Sung[3], and Sang Beom Jun[1,2,4*]

[1] Department of Electronic and Electrical Engineering, Ewha Womans University, Korea

[2] Graduate Program in Smart Factory, Ewha Womans University, Korea

[3] Department of Communication Disorders, Ewha Womans University, Korea

[4] Department of Brain and Cognitive Sciences, Ewha Womans University, Korea

***juns@ewha.ac.kr**

Abstract

Vagus nerve stimulation (VNS) bears therapeutic potential for medical conditions such as the treatment of drug-resistant epilepsy or depression. However, the invasive VNS method has limitations to be a first-line treatment due to surgical risks involved with device implantation. Noninvasive transcutaneous auditory VNS (aVNS) uses electrical stimulation that targets the branch of the vagus nerve of the ear. Due to its noninvasiveness, aVNS is developed to replace invasive VNS methods. However, it is questionable whether aVNS does mimic VNS. Thus, we studied the acute effects of aVNS on the pupillometry which is a typical measurement of VNS effects during visual fixation at rest. Short aVNS trials are performed while monitoring the pupil size of the subject. Pupil dilation in aVNS (peaking 7–8 sec after trial onset) was significantly higher than sham stimulus. This result shows that aVNS clearly leads to arousal state beyond the simple effects of somatosensory stimulation, thus supporting the hypothesis that aVNS stimulates autonomic nerve system and mimics conventional invasive VNS.

Background

Vagus Nerve Stimulation (VNS) modulates vagal afferent inputs to the brainstem nucleus of the solitary tract and activates locus coeruleus–norepinephrine (LC-NE) system [1]. VNS is applied to treat neurological diseases such as pharmaco-resistant depression and epilepsy [2]. However, since general VNS is an invasive method, it is inconvenient to apply a large population of people. Implantation is accompanied by surgical method, which is inherently risky, so non-invasive methods should be needed. Accordingly, a technology called transcutaneous auricular vagus nerve stimulation (aVNS or tVNS) that stimulates the auricular branch part of the vagus nerve at the cymba conchae of the ear has been proposed. Despite several studies of aVNS, it remains unclear if aVNS effectively mimics VNS. Thus, we need a reliable predictive biomarker for the simulation to verify this. Since pupil dilation is closely related with LC-NE activity, the pupil size and event-related pupil response can be considered as candidate biomarkers.

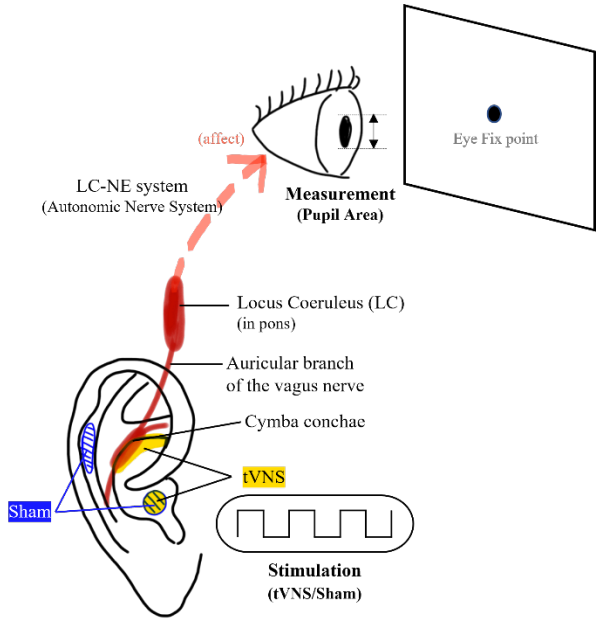
In this study, in order to investigate the effectiveness of aVNS, we performed the pupillometry while short (5 sec) trials of aVNS stimulation is delivered at the earlobe to activate the peripheral nerves.

Methods

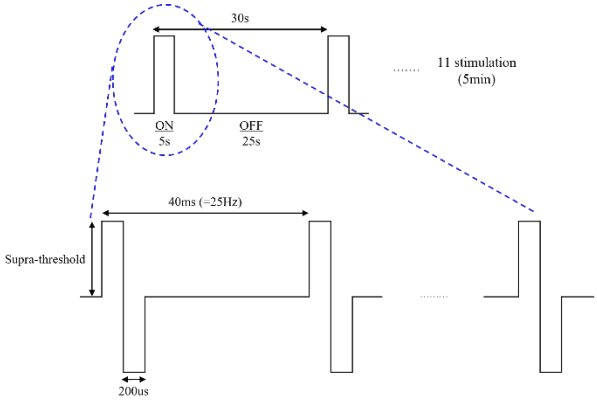
Figure.1 shows an overall experimental system. Simply, the experiment is designed to find out if auditory VNS induces any change of pupil size. The aVNS system is developed by TODOC Co. (Seoul, Korea). aVNS stimulates auricular branch part of the vagus nerve at the cymba conchae of the ear. As a control experiment, sham stimulation is applied to earlobe far from the vagus nerve branch. Auditory branch of the vagus nerve passes through Locus Coeruleus (LC) and controls autonomic nerve system which affects pupil size by LC-NE system. Since the pupil size is also sensitive to light, other emotional and physical stimuli, distance for pupillometry device, the subject constantly gazed at a black dot in white screen (not monitor) during stimulation for visual fixation.

Sequences of each stimulus in stimulation are shown in Figure 1(b). The same parameters for the electrical stimulation were used for both aVNS and sham stimuli shapes except the stimulation sites.

Before aVNS stimulation and pupil measurement, an appropriate stimulus parameters were determined just below the threshold of pain sensation. Each stimulation sequence lasts 5 minutes and includes 11 trials of 5 seconds stimulation epochs, which called 'ON' time, separated by interstimulus intervals of 25 seconds, which called 'OFF' time. 'ON' time consists of tonic stimuli of 25 Hz (40 ms last for each cycle), and 200 μs pulse width.



(a) Schematic illustration of the experimental system



(b) Stimulation design

Figure 1. Experimental Design

Pupil size is measured by pupillometry equipment (Eyelink Portable Duo, SR Research), and pupil size data are sampled at 1000 Hz. The data recorded by '.edf' type, should be converting data into '.m' file (MATLAB file, MATLAB). The pupil size varies greatly depending on the subjects, environments, and the conditions of the subject. Therefore, pupil dilation must be analyzed with variation ratio (%).

Results and Discussion

Figure. 2(a) shows pupil dilation data plot by aVNS and sham stimulation. Both stimuli enlarge the pupil, but aVNS (blue trace) leads to greater dilation than sham stimulus (red trace). The stimulations are applied during gray transparent area. Although, pupil area size is not fixed variable because of incomplete external stimuli control like sound or human blink, so baseline fluctuation is about $\pm 3\%$. After aVNS, pupil dilates about 14%, and shrinks into baseline after 7 seconds later. However, after sham stimulation, pupil dilates about 8%, and same event occurs as aVNS after 7 seconds later.

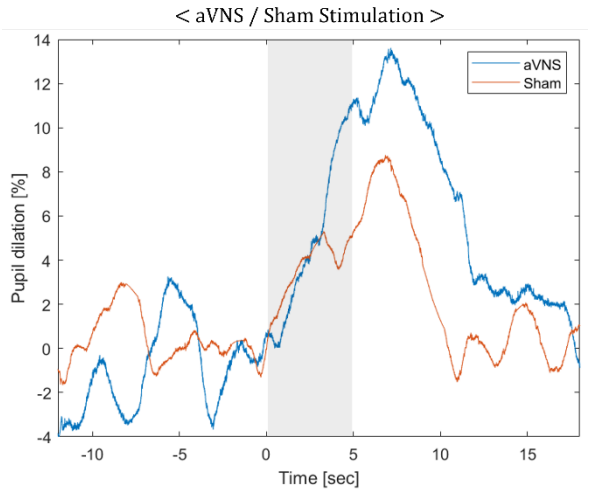


Figure 2. Pupil dilation (Area) by stimulation; aVNS (blue) vs. Sham (red)

Pupil dilation in aVNS (peaking 7–8 seconds after trial onset) was significantly higher than following sham stimulus. This shows that aVNS clearly leads to pupillary of arousal beyond the effects of somato-sensory stimulation, thus supporting the hypothesis that aVNS mimics invasive VNS.

Acknowledgements

This work was supported by the Graduate School of Ewha Womans University, the Korea Medical Device Development Fund grant funded by the Korea government (the Ministry of Science and ICT, the Ministry of Trade, Industry and Energy, the Ministry of Health & Welfare, the Ministry of Food and Drug Safety) (1711139110, KMDF_PR_20210527_0006), and the National Research Foundation of Korea (NRF) grant funded by the Korea government (MSIT) (NRF-

2019R1A2C1088909). The authors thank TODOC Co., Ltd. for providing auditory vagus nerve stimulation (aVNS) equipment and excellent technical assistance.

References

1. Omer Sharon, Firas Fahoum, Yuval Nir (2021). Transcutaneous Vagus Nerve Stimulation in Humans Induces Pupil Dilation and Attenuates Alpha Oscillations, The Journal of Neuroscience
2. Thompson SL, O'Leary GH, Austelle CW, Gruber E, Kahn AT, Manett AJ, Short B and Badran BW (2021). A Review of Parameter Settings for Invasive and Non-invasive Vagus Nerve Stimulation (VNS) Applied in Neurological and Psychiatric Disorders. Front. Neurosci.

Development of real time untact healthcare system for an infectious disease patient

S. J. Hong[1], J. H. JUNG, J.B. Park[1] and S.R. Lee[1*]

Osong Medical Innovation Foundation, Medical Device Development Center[1]

Sungjun86@kbiohealth.kr

Abstract

The Spread of new infection virus(COVID-19) around the world, the World Health Organization(WHO) declared a pandemic against COVID-19 on March 11, 2020. Against this background, the demand for a Telehealth and management system between infectious disease patients and doctors to prevent the spread of infectious diseases is increasing. In order to overcome these problems, we developed the real time Telehealth system and platform using wearable devices and cloud server.

Background

Due to the outbreak of novel coronavirus infection(COVID019) around the world, the World Health Organization(WHO) declared COVID-19 a pandemic on March 11, 2020. For this reason, there is an increasing demand for a untact remote treatment and management system between an infectious disease patient and a doctor to prevent the spread of an infectious disease. In COVID-19 situation, interest in remote patient management defense systems and screening treatment systems for national disasters and infectious diseases is increasing. In order to overcome these problems, it is necessary to establish a real-time untact remote treatment system and platform using wearable devices as a major means of protecting medical staff and patients and preventing the spread of infectious diseases[1].

Methods

In this study, we aim to develop a wearable device that can measure and analyze a patient's various biosignals and to build an administrator web server that can provide patient health and location information to on-site medical staff in real time.

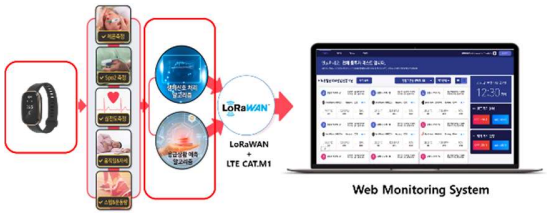


Figure 1. Untact Healthcare system using Wearable Device

1. Band Type wearable device

Health status can be checked based on biosignal data (Motion, Photoplethysmography (pulse, oxygen saturation), Location information (indoor/outdoor), Body temperature) and developed a wearable type system that can generate a notification in case of an emergency.

2. Biosignal acquisition RF Gateway system

As a gateway for RF communication with wearable devices, it is based on Lorawan communication that enables long-distance communication.

Security of personal biometric information is strengthened by applying “AES128” security protocol with wearable devices.

In addition, the patient's location information is collected indoors using the Gateway installed at each branch and the RSSI (RF signal strength) of the wearable device, and the Gateway transmits the collected biometric information to the cloud server.

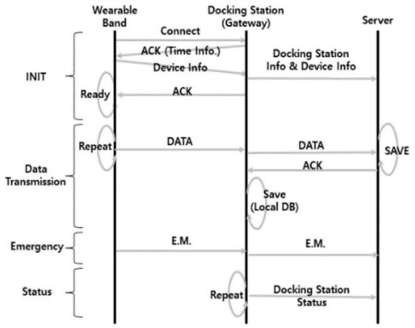


Figure 2. RF RX/TX Protocol

3. Real time health information monitoring

Development of a web-based monitoring program that can record bio-signal information of wearable devices and monitor them in real time.

It is possible to observe the bio-signals of multiple patients in real time, and when abnormal signs are found or deviated from a specific location, a notification is generated to help the field medical staff efficiently.

Results and Discussion

The wearable device worn by the patient transmits the collected biometric data to the gateway once every 2 min.

Also, in case of an emergency, the transmission frequency is reduced to 3sec and the communication speed is adjusted so that the patient's information can be delivered to the medical staff quickly.

Gateway is transmitted to the Cloud Server using the HL7 protocol for compatibility with the medical data platform, and the data transmitted to the server is outputted in real time through the web viewer program.

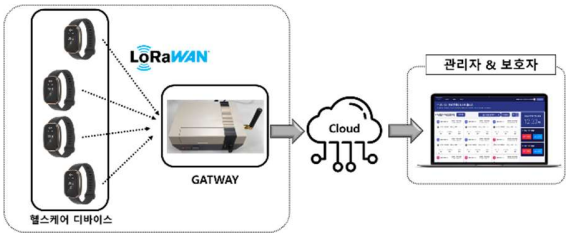


Figure 3. Untact Healthcare system

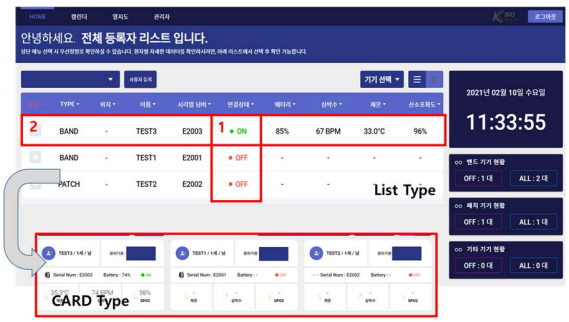


Figure 4. Web Monitoring System (Main Page)



Figure 5. Web Monitoring System (Detail Page)

There are lots of wearable devices that measure health information use a method of uploading personal health information to the cloud or a related server using a smartphone and Bluetooth communication. This method has limitations in that individual health cannot be continuously measured and transmitted to a server without a smartphone, and a large number of patient data cannot be continuously monitored.

In order to overcome these shortcomings, in this study, health information can be uploaded using its own wireless communication private network, and security for personal information is solved at the same time, and medical data standardization work is carried out using the HL7 protocol.

This enabled heterogeneous compatibility with medical record charts or platforms used in existing medical institutions, and the platform developed in this study is expected to provide efficient medical services to medical staff who need to manage a large number of patients.

Reference

[1] Channa, A., Popescu, N., Skibinska, J., & Burget, R. (2021). The rise of wearable devices during the COVID-19 pandemic: A systematic review. Sensors, 21(17), 5787.

Complete circumferential renal sympathetic denervation using a laparoscopic ablation system to treat hypertension

J. Baik[1] and S.M. Park[1*]

[1]Department of Convergence IT Engineering, Pohang University of Science and Technology, Pohang, Korea

jinhwan52@postech.ac.kr, *sungminpark@postech.ac.kr

Abstract

In clinical trials, the catheter-based renal denervation (RDN) have significantly lowered BP, but also resulted in many non-responders due to incomplete ablation of renal nerves. Here, we present a new laparoscopic ablation system (LAS) to conduct complete RDN regardless of anatomic variations on nerves and arteries. The ablation electrode of LAS wraps a target artery and generates heat by transmitting radiofrequency (RF) energy. Computational simulation and 28-day survival animal study using pigs demonstrated the feasibility of RDN using LAS. The ablation patterns of LAS were created circumferentially around the tunica externa and could be predicted during RDN. In the animal study, the systolic BP and diastolic BP decreased up to 22.8 mmHg and 14.4 mmHg ($P<0.001$) after RDN treatment, respectively. The intensity of immunostain targeting tyrosine hydroxylase (TH) was 108.2 ± 7.5 at control group and 63.4 ± 8.7 at treatment group ($P<0.001$). The reduction on the staining intensity, which means the degree of interruption of sympathetic nerve signals to kidneys, was associated with the reduction on BP after RDN. Thus, the proposed laparoscopic system could achieve circumferential RDN and improve the effectiveness of RDN treatment. It will be new therapeutic approach on uncontrolled hypertension.

Background

The elevated sympathetic nerve contributes to the pathogenesis of hypertension, chronic kidney disease, and heart failure. In the previous experience in surgical sympathectomy, which completely divide the thoracic and lumber sympathetic ganglia, we found that modulating sympathetic nerve activity could induce the reductions in BP. However, these methods were abandoned from clinical trials due to significant complications and perioperative morbidity. As an improved strategy, catheter-based RDN has been introduced, which reduces invasiveness and the duration of postoperative recovery. The catheter-based RDN demonstrated short-term safety and their feasibility but with non-uniform success in BP reduction [1]. While the negative results remain unexplained, the randomized and sham-controlled SYMPLICITY HTN-3 trial failed to demonstrate significant difference in BP reduction when compared to sham control at 6 months after RDN. Although the results evoked some suggestions about the efficacy of RDN on hypertension, the catheter-based procedure also generated some questions about complete interruption of the sympathetic nerve activity on renal arteries. Indeed, *post hoc* analyses of the catheter-based RDN clinical trial disclosed incomplete neural ablation [2]. The catheter procedure performed RDN only in arteries 3 mm or larger in diameter that did not include accessary arteries and early branched main arteries. The catheter tip was empirically rotated and pulled to ablate several endoluminal sites despite the renal nerve distributions were asymmetric. Further, partial damaged nerves presented due to the limited lesion depth of intravascular RDN. It is difficult to be solved by increasing ablation energy that may predispose the irreversible intima injury such as atherosclerosis, thrombosis, or stenosis. These retrospective analyses evoked the needs for further optimized RDN system.

In this study, to overcome the limitations of catheter-based modality, we introduce a novel laparoscopic RDN system for fully circumferential ablation in various size arteries without thermal damage to the tunica intima. We characterized the ablation patterns achieved by laparoscopic RDN through the use of computational models and swine model.

Methods

The laparoscopic RDN directly approaches renal artery through the posterior retroperitoneal approach and performs treatment outside the artery. Thus, we aimed to develop a new laparoscopic ablation system (LAS) to completely cover a target artery and ablate the entire renal sympathetic nerves without thermal damage to the tunica intima (Fig. 1). The ablation

electrode of LAS had a Nitinol substrate and a parallel bipolar electrode that were fabricated on a flexible printed circuit board with two thermocouples.

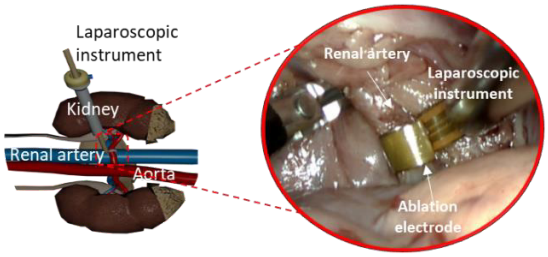


Figure 1. Laparoscopic renal denervation with LAS.

The computational modeling of LAS at a renal artery was conducted with the ANSYS Fluent by solving the Bio-heat equation that combines electric and thermal problems. We performed 28-day survival animal study using six pigs that were randomly allocated to two groups (4 for experiment and 2 for sham control).

Results and Discussion

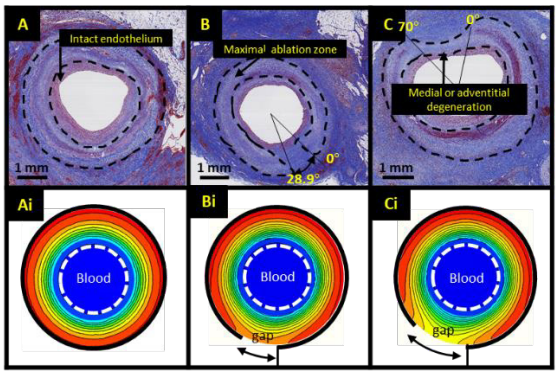


Figure 2. Ablation patterns of LAS on animal study (A, B, C) and simulation study (Ai, Bi, Ci).

Figure. 2 shows ablation patterns at the treatment sites by activating the parallel bipolar electrode. Maximal ablation patterns were classified as a ring-like pattern (Fig. 2A), a horseshoe-like pattern (Fig. 2B), and a crushed ring-like pattern (Fig. 2C). There was a gap between two tips of the horseshoe-like and the crushed ring-like patterns, which were variable as 27.39° - 83.36° (Fig. 2B, C). The RF stimulus damaged the outer layers of an artery, e.g., tunica adventitia and outer media, but this effect did not extend to the inner media and the endothelial layer. Quantitative morphometry conducted on the thermal damage zones showed that 36.41 ± 7.17% of the medial area were affected. Thus, the parallel bipolar electrode focused heat outside of an artery and efficiently protected the tunica intima from thermal damage. In simulation study, we could find that the ablation patterns were different due to the gap where the parallel bipolar electrodes did not cover the renal artery.

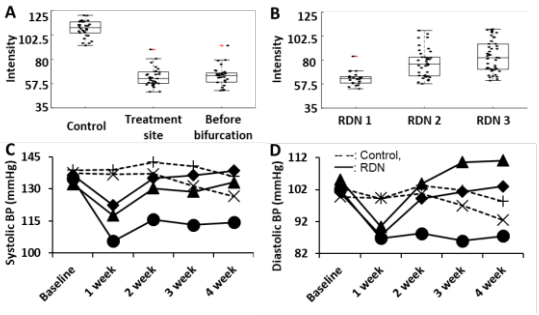


Figure 3. TH intensity and BP change at 4 weeks.

Figure. 3 shows BP changes after RDN using LAS. As comparing the baseline BP, laparoscopic RDN reduced SBP and DBP in all RDN group animals at 7 days after treatment; SBP and DBP was reduced by 29.2 mmHg (P<0.001) and by 15.2 mmHg (P<0.001) respectively. RDN on a main renal artery bilaterally showed significant BP reduction compared to the control group until 7 days after treatment. However, the degree of change in BP at 28 days after treatment differed between pigs. The reduction in BP maintained by 28 days in RDN 1 (at SBP & DBP P<0.001), but recovered in RDN 2 (at SBP P=0.245, at DBP P=0.235) and RDN 3 (at SBP P=0.539, at DBP P<0.001). These trends were similar to the increased TH staining intensity at the distal portion compared to the proximal portion. Thus, the result implied that the maintenance of the BP reduction after RDN may relates with the degree of TH synthesis at the distal portion of a renal artery, not at the proximal portion.

Acknowledgements

This research was supported by the National Research Foundation of Korea (NRF) grant funded by the Korea government (MSIT) (No. 2017R1A5A1015596) and funded by the Ministry of Education (No. 2020R1A6A3A13066375).

References

1. H. Krum et al., “Catheter-based renal sympathetic denervation for resistant hypertension: a multicentre safety and proof-of-principle cohort study”, Lancet, 373, 1275-1281 (2009).
2. D. E. Kandzari et al., “Predictors of blood pressure response in the SYMPLICITY HTN-3 trial”, Eur Heart J, 36, 219-227 (2015)

The effectiveness of noise cancelling function in different types of earphones

SeoHu Kim[1,2], Soojin Kang[4], Hye Yoon Seol[2,3], and Il Joon Moon[2,5]

[1]Department of Medical Device Management and Research, SAIHST, Sungkyunkwan University, Korea
[2]Hearing Research Laboratory, Samsung Medical Center, Seoul, Korea
[3]Medical Research Institute, Sungkyunkwan University School of Medicine, Suwon, Korea
[4]School of Humanities and Social Sciences, Korea Advanced Institute of Science and Technology, Daejeon, Korea
[5]Department of Otorhinolaryngology-Head and Neck Surgery, Samsung Medical Center, Seoul, Korea
moon.iljoon@gmail.com

Abstract

Noise-induced hearing loss is one of the most common form of sensorineural hearing loss. Although noise-induced hearing loss is preventable, the wide use of personal listening devices (i.e., earphones) has increased the prevalence of noised-induced hearing loss. In this study, we used noise cancelling earphones to acoustically confirm the effectiveness of the noise cancelling function. In addition, preferred listening levels for each individual was examined based on the type of the earphone. Ultimately, the noise cancelling function could contribute to hearing protection for people who use earphones frequently.

Background

Hearing loss means losing the ability to hear. There are various types of hearing loss. Among these types, noise-induced hearing loss is one of the most common form of sensorineural hearing loss, and the prevalence has recently increased due to earphone overuse. Noise-induced hearing loss is preventable. Earphones nowadays are equipped with noise canceling (NC) technology which reduces unwanted background noise by using a noise canceling system. This function allows users to enjoy music even in noise. Previous studies which examined the effected of the NC function in earphones and individuals' preferred listening levels (PLLs) reported that noise was attenuated up to 5.1 dB, and the PLLs for listeners was decreased by up to 3.0 dB [1]. Other studies reported that the degree of noise reduction varied depending on the earphone design, but the noise canceling function worked effectively for low frequencies [2]. The purpose of this study is to acoustically investigate the effect of the NC function of wired and wireless earphones that are currently available in the market and to investigate PLLs based on the earphone type.

Methods

The experiment was carried out with a total of 30 people (15 people with normal hearing (NH) and 15 people with hearing loss (HL)). Three types of NC earphones (A. canal-type wireless earphones, B. canal-type wired earphones, C. Open-type) were used. Two types of environmental noises, cafe and bus, were presented at around 80 dBA through louder speakers that were located at 90, 135, 225, and 315 degrees in a semi-anechoic chamber. The experiment was conducted in two conditions: NC ON and NC OFF.

KEMAR and real-ear measurement (REM) were utilized to examine the effect of the NC function of an earphone in terms of acoustics. The REM measured the sound pressure level (SPL) delivered to the eardrum by inserting a probe microphone into the ear canal. Through KEMAR, we analyzed frequency characteristics of the NC function. BTS's Dynamite, which has relatively little rhythm and frequency change acoustically, was presented in noise to examine the difference in PLLs. The PLL was defined as the most comfortable volume level that did not require a volume change.

Results and Discussion

The difference between NC OFF and ON conditions for the whole frequencies (250, 500, 750, 1000, 1500, 2000, 3000, 4000, and 6000Hz) were analyzed. The NH group showed the difference of 5.4 dB SPL, 3.9 dB SPL, and 2.3 dB SPL for earphone A, B, and C, respectively, when the bus noise was presented. The HL group showed the difference of 4.8 dB SPL, 1.1 dB SPL and 2.7 dB SPL for earphone A, B, and C, respectively. The NH group showed the difference of 5.1 dB SPL, 3.9 dB SPL, and 2.6 dB SPL for earphone A, B, and C, respectively, when the cafe noise was presented. The HL group showed the difference of 4.3 dB SPL, 3.5 dB SPL and 3 dB SPL for earphone A, B,

and C, respectively. For the NH group, for all earphones, the Wilcoxon's signed-rank test showed statistical difference ($p<0.001$) between the NC ON and OFF conditions for the cafe and bus noises. Statistical significance ($p<0.01$) was also observed for the HL group for the two environmental noises except earphone C which did not show any statistically significance for the bus noise.

For the low frequencies (250 and 500Hz), the NH group showed the difference of 12.1 dB SPL, 12.6 dB SPL, and 4.3 dB SPL for earphone A, B, and C, respectively, when the bus noise was presented. The HL group showed the difference of 10.9 dB SPL, 8 dB SPL and 6 dB SPL for earphone A, B, and C, respectively. The NH group showed the difference of 14.2 dB SPL, 11.8 dB SPL, and 4.4 dB SPL for earphone A, B, and C, respectively, when the cafe noise was presented. The HL group showed the difference of 12.1 dB SPL, 9.6 dB SPL and 6 dB SPL for earphone A, B, and C, respectively. For the NH group, the Wilcoxon signed-rank test showed statistical difference between the NC ON and OFF conditions for the cafe and bus noises for all earphones ($p<0.001$). Statistical significance was also observed for all earphones for the HL group ($p<0.01$).

For KEMAR, the difference in SPL was compared between the NC ON and OFF conditions for the whole and low frequencies. For the whole frequency, in the NC ON condition, the difference was 8dB SPL, 10 dB SPL for earphone A and B, respectively. In case of low frequency, the differences were 17 dB SPL and 15 dB SPL for earphone A and B, respectively. Earphone C did not show any difference for the whole frequency. For the low frequency, earphone C showed an increase of 1.5 dB SPL.

Table 1 shows the difference in PLLs between the NC ON and OFF conditions for the NH group. In the NH group, when the bus noise was presented, the PLL was decreased by 7 levels for earphone A. When the cafe noise was presented, the PLL was decreased by 6 levels. For earphone B, the PLL was decreased by 9 and 11 levels for the bus and cafe noises, respectively. For earphone C, with the bus noise, the PLL was decreased by 5 levels. The PLL was decreased by 3 levels with the cafe noise. Table 2 shows the difference in PLLs between the NC ON and OFF conditions for the HL. In the NC on condition, when the bus noise was presented, the PLL was decreased by 5 levels for earphone A. When the cafe noise was presented, the PLL was decreased by 3 levels. For earphone B, the PLL was decreased 11 and 10 levels for the bus and cafe noises, respectively. For earphone C, with the bus noise, the PLL was decreased by 4 levels. The PLL decreased by 1 level with the cafe noise.

(Level)

NC \ Earphone	A	B	C
Bus NC OFF-ON	7	9	5
Cafe NC OFF-ON	6	11	3

Table 1. Difference in PLLs in the NH group

(Level)

NC \ Earphone	A	B	C
Bus NC OFF-ON	5	11	4
Cafe NC OFF-ON	3	10	1

Table 2. Difference in PLLs in the HL group

Comparing the PLLs according to the earphone type, for the NH group, statistical significance was observed between earphone A and B for the cafe and bus noises when the NC function was activated ($p<0.01$). On the other hand, in the HL group, only earphone B showed significant reduction in PLLs when bus noise was presented ($p<0.05$).

The three types of NC earphones used in this study have different noise reduction effects depending on the type of earphone, but all of them statistically and significantly reduced sound pressure at low frequencies. This is consistent with the results of previous studies that NC earphones are effective at low frequencies. In the case of the PLLs, two of the three NC earphones statistically significantly decreased the PLLs. Therefore, it can be inferred that using canal-type earphones with a NC function could be used to protect hearing in a noisy environment.

References

1. W. S. Na, K. W. Kim, S. D. Jung, J. W. Lee, J. Y. Jung, and M. W. Suh, "Effect of active noise cancelling earphones on preferred listening level when listening to portable music players in noisy environments," Korean J Otorhinolaryngol-Head Neck Surg. 55(7), 415-421 (2012).
2. M. Liang, F. Zhao, D. French, and Y. Zheng, "Characteristics of noise-canceling headphones to reduce the hearing hazard for MP3 users", The Journal of the Acoustical Society of America, 131(6), 4526-4534 (2012)

P-078

Determination of the Counter-pulsation of the pneumatic Dual-parallel pulsatile extracorporeal membrane oxygenator

C.Y.Yoo[1], S.M.Kang[1] , S.W. Choi[1]

[1]School of Mechanical and Biomedical Engineering, Kangwon National University, Chun-cheon, Korea

swchoe@kangwon.ac.kr

Abstract

Existing commercialized Extracorporeal Membrane Oxygenator(ECMO) have problems with thrombosis and hemolysis due to their complex structure, which requires a pulsatile pump with a new structure. The ECMO with a new structure developed in this study is linked with a ventricular assist device(VAD) to construct a system and detects the contraction point of the VAD to perform a Counter-pulsation algorithm. This study aims to confirm the success rate of co-pulsation and counter-pulsation, which are conditions that operate regardless of cardiac load, by measuring blood pressure and blood flow while performing the counter-pulsation algorithm.

Background

ECMO is a device used to assist oxygen supply and blood circulation in patients with cardiopulmonary disease, and the number of applications due to the recent increase in patients with cardiopulmonary diseases such as COVID-19 is increasing every year. Existing ECMOs used centrifugal pumps and roller pumps to supply continuous blood flow, but due to the complex internal structure of the blood pump and the structure that applies direct force to the blood, the problem of thrombosis in the impeller and blood inlet and outlet and shear stress applied to the blood The development of a new structure of ECMO has been required due to problems such as hemolysis caused by stress and intracardiac load caused by continuous blood supply. Among ECMO products using centrifugal pumps, products have been developed that greatly vary the speed of the impeller to reduce the load in the heart by creating pulsatile blood flow.However, as the impeller speed changes, a direct force is applied to the blood, causing hemolysis, which makes it difficult to apply clinically. The patient's heart rate is linked to the pulsatile ECMO to automatically control the pulsatile ECMO, detect the time when the heart ejection blood, and set it as a variable called Delay from that point to confirm the pulsatile ECMO. This study propose a method to evaluate whether ECMO has become Counter-pulsation or Co-pulsation using BP (Blood Pressure).

Methods

As shown in Figure. 1, The manufactured system algorithm simulated the role of a heart using a single VAD developed by Libraheart, and the pulsatile ECMO manufactured for this research was linked. It consists of a power source for operating ECMO and an oxygen tank, control unit, membrane oxygenator, cannula, etc. Oxygenator used Maquet's product, a 24fr cannula of edwards was used in the inlet part, a blood circuit was formed using the 22fr cannula of the same company in the outlet part, and a mock system and other components were self-manufactured to conduct an experiment. The measured data were recorded on a computer by converting the measured value of analog voltage data into mmHg using

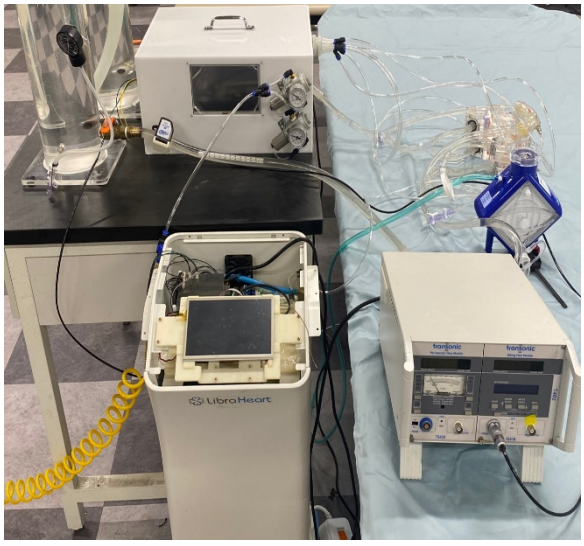


Figure 1. Mock circulation system structure used in ECMO and VAD field in-vitro experiments

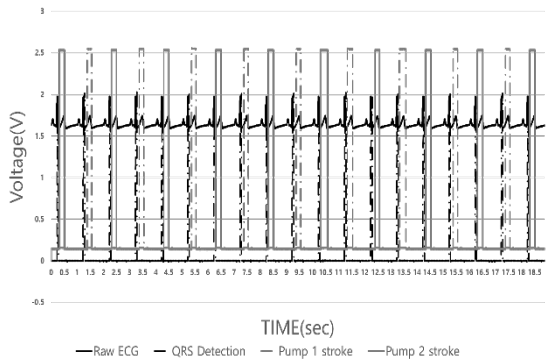


Figure.2 Counter-pulsation performance algorithm through detection of QRS waveform of ECG

Labview and DAQ (USB-6001, National Instrument, USA) devices from self-made pressure sensors (33A-003G-2210, SHIBA KOREA, KOREA) through sensor calculation. The operation method of the VAD is configured such that the internal blood of the VAD flows in one direction by supplying pneumatic pressure while the pneumatic cylinder moves up and down, and the internal stroke volume is fixed at 22cc and operates at 40BPM. In the system, the system was configured to enable control by interlocking a signal that drives the piston in the vertical direction with ECMO.

Results and Discussion

As shown in Figure. 2, that by connecting an ecg simulator in a mock system device, qrs was detected and a delay of 50 ms was given from that point in time, and pump 1 main blood sac and pump 2 main blood sac were cross-extruded. Connecting VAD and ECMO in a simulated circulation device, the discharge amount of pump according to BPM and the discharge amount according to Co-pulsion and counter-pulsion and BP change were measured. The BPM of ecmo was measured in conjunction with the BPM of vad, the preload was maintained at 30~40mmHg with the change of 40,45,50,55,60 bpm, and the afterload was measured to be maintained between 80-120mmHg. VAD operates as an actuator, and is connected to recognize the actuator's operation signal in conjunction with ECMO. A pump with a dual-parallel structure intersects according to the signal to supply blood to the heart. as shown in Figure 3 is the result of measuring the pressure of each node of the blood circuit by conducting a simulation using a VAD and pulsatile ECMO in the experiment. In this experiment, since the simulation was conducted using an artificial ventricular aid rather than an actual heart, it is not

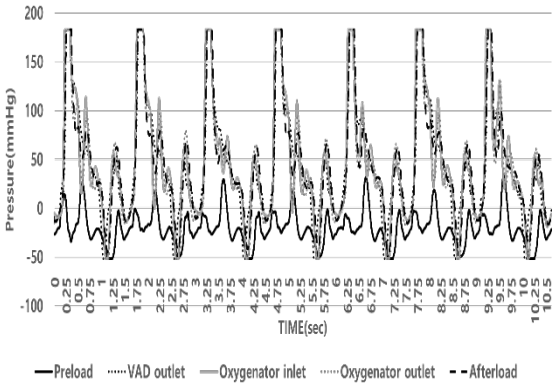


Figure.3 Pressure in the blood circuit when controlling the Counter-pulsation of the ECMO due to heart contraction.

possible to identify the areas where problems such as arrhythmia and ventricular tachycardia that occur during actual clinical trials. Since existing pulsatile pumps operate regardless of the heart's load because they cannot control the counter-pulsation, it is expected to reduce the heart's load when applied to clinical trials, and to improve practicality by using DNN to check the success rate of counter-pulsion and separate the actual heart and ECMO.

Acknowledgements

This research was supported by the Basic Science Research Program through the National Research Foundation of Korea (NRF) funded by the Ministry of Education (2020R1A4A1019475).

This work was supported by the Korea Medical Device Development Fund grant funded by the Korea government (Project Number: KMDF_PR_20200901_0159-2021-02)

References

1. Choi, S. W., Nam, K. W., Chung, J., Lee, J. C., Hwang, C. M., Won, Y. S., ... &Min, B. G. (2006). Development of a new pulsatile extracor-poreal life support device incorporating a dual pulsatile blood pump. The International journal of artificial organs, 29(6), 583-590
2. Kang, Seong Min, Keun Her, and Seong Wook Choi. "Outflow monitoring of a pneumatic ventricular as-sist device using external pressure sen-sors." Biomedical Engineering Online 15.1 (2016): 1-12.

Development of sleep classification algorithm considering medical significance using EEG and EOG

J.Y. Kim[1], B.R. Nam[2], M.S. Kim[1], J.K Choi[2], K.M Choi[1], S.J Choi[2], and I.Y. Kim[1,2]

[1]Department of Biomedical Engineering, Hanyang University, Seoul, Korea

[2]Department of Electronic Engineering, Hanyang University, Seoul, Korea

jykim1026@hanyang.ac.kr

Abstract

Sleep related diagnosis requires analysis of multiple biological signals for about 8 hours, which causes time and cost problems. To solve these problems, there are definitions and classification standards according to the characteristics of multiple biological signals during sleep, but the reliability of the automation algorithm is insufficient because the definition and the quantitative standard is ambiguous. Therefore, in this study, we propose a method to learn deep learning algorithms individually using electroencephalogram (EEG) and Electrooculogram (EOG) during sleep, and to improve performance by correcting the results based on medical definitions. When EEG and EOG were used, the F1-scores of the five stages of sleep classification were 0.6793 and 0.6678, respectively, and when the proposed algorithm was applied, the F1-score improved to 0.7252.

Background

Sleep analysis is performed based on the polysomnography (PSG) results. Sleep-related diseases are defined based on the ICSD-2 and include insomnia, sleep related breathing disorders, hypersomnias of central origin, circadian rhythm sleep disorders, parasomnias, sleep related movement disorders and other sleep disorders.

Polysomnography measures various vital signals such as electroencephalogram (EEG), electrooculogram (EOG), electromyogram (EMG), electrocardiogram (ECG), respiration, chest and abdomen movement, blood oxygen saturation, snoring, leg movement, etc. All these signals are analyzed to define events during sleep, classify sleep stages, and make a diagnosis accordingly. Carefully diagnosing 8 hours of sleep every 1 epoch (30 s) based on multiple biosignals during sleep causes excessive cost and diagnosis time. To solve this problem, various automated sleep stage classification technologies are being developed and can be divided into the following two categories.[1] 1. Step-by-step feature detection and classification based on signal processing 2. End-to-end automatic classification algorithm using deep learning algorithm

A limitation of research based on signal processing is that the definition and the quantitative standard of sleep stage is ambiguous.[2] On the other hand, in studies based on deep learning, the problem of reliability of training data and result evidence is pointed out.[3] In this study, to improve these shortcomings, we propose a deep learning method that supplements the classification results with a rule-based method based on medical definitions.

Methods

In this study, a public database Sleep Heart Health Study Database (SHHS DB) was used to develop a sleep stage classification algorithm. This database is a polysomnography database consisting of a total of 5,804 people aged 40 to 90 years. In this database, EEG (C3-A2, C4-A1), EOG (L, R), ECG, SpO2, Heart Rate, EMG, Respiration (signals such as Thorax, Abdomen, Airflow) are provided. This study was developed using 5,793 sleep polysomnography records collected in SHHS-1, 125Hz 1ch EEG (C4-A1) and 50Hz 1ch EOG (Right) were used.

Before the development and learning of the algorithm, about 10% of the 5,793 PSG records were separated into the test set. In the learning process, 5,211 PSG records were used as the train set, and 582 PSG records were used as the test set. Although there are 5,793 PSG records used in the study, each record is measured in units of one epoch based on 30 seconds and recorded

for about 8 hours. Therefore, the total epoch is as shown in the Table. 1.

Table.1 Number of epochs for each stage composing SHHS-1 and SHHS-2 database

Stage	SHHS-1	SHHS-2
Wake	1,691,108	1,208,326
Stage 1	217,576	111,456
Stage 2	2,396,989	1,147,780
Stage 3	739,306	313,790
REM	817,376	411,155
Total	5,862,355	3,192,507

Due to this imbalance problem, a problem occurred in which learning was not possible. Therefore, learning was made by applying a weighted loss to each sleep stage. The structures of the EEG classification network and the EOG classification network are identical except for the final fully connected size. In this study, a network consisting of a 5-layer 1D CNN and a 1 fully connected layer was developed in the Tensorflow environment.

PSG record was sequentially input to each network in epoch units, and post-processing was performed based on the results. Post-processing was carried out for each epoch, and conditional ensemble and filtering of two networks based on rules were performed. When the classification results of EEG and EOG are the same, the existing prediction results are used, and when EEG is predicted to be one of the two stages, stage 1 and REM stages, which are difficult to predict by EEG, are followed by the prediction of EOG. Also, in the case of stages 2 and 3, since there is no special EOG characteristic, the predicted value of EEG was used. And according to the definition, the first sleep transition time was replaced with stage 1, and smoothing was performed within 5 epochs to ignore short transitions.

Results and Discussion

As a result of the algorithm test, the micro F1-scores of the EEG network and the EOG network were 0.6793 and 0.6678, respectively. At this time, the classification result for stage 1 showed more than 60% recall performance in both algorithms. However, the precision for stage 1 was 15%. When the proposed algorithm was applied, the accuracy of the F1-score was improved to 0.7252, and the precision was improved to the 20% while maintaining the recall of the stage 1 classification performance at 60%. Also, in the case of REM, both recall and precision showed significant improvement. In order to apply this algorithm to the actual medical field, it is necessary to use a method such as visualization of a deep learning algorithm to check the algorithm predicted the sleep stage based on which part of data.

	Recall (%)		
	EEG only	**EOG only**	**Proposed**
Wake	86.36	81.50	87.15
Stage 1	64.94	63.66	60.43
Stage 2	66.28	65.86	72.13
Stage 3	90.81	84.51	90.57
REM	62.67	68.60	80.24
	Precision (%)		
	EEG only	**EOG only**	**Proposed**
Wake	90.69	90.79	91.25
Stage 1	15.62	15.84	22.82
Stage 2	91.68	87.04	90.52
Stage 3	76.19	67.01	70.38
REM	70.18	77.85	81.84

Table.2 Recall and precision of sleep stage classification algorithm

	EEG only	EOG only	Proposed
Accuracy	74.81	73.17	79.63
F1-Score	0.6793	0.6678	0.7252

Table.3 Accuracy and F1-Score of the proposed algorithm

Acknowledgements

This research was supported by the Brain Convergence Research Program of the National Research Foundation (NRF) funded by the Korean government (MSIT) (No. NRF-2021M3E5D2A01022397).

References

1. Malhotra, A., Younes, M., Kuna, S. T., Benca, R., Kushida, C. A., Walsh, J., ... & Pien, G. W. (2013). Performance of an automated polysomnography scoring system versus computer-assisted manual scoring. *Sleep*, *36*(4), 573-582.
2. Bankman, I. N., Sigillito, V. G., Wise, R. A., & Smith, P. L. (1992). Feature-based detection of the K-complex wave in the human electroencephalogram using neural networks. *IEEE transactions on biomedical engineering*, *39*(12), 1305-1310.
3. Lacourse, Karine, et al. "Massive online data annotation, crowdsourcing to generate high quality sleep spindle annotations from EEG data." *Scientific data* 7.1 (2020): 1-14.

Interim Results of 2021 Horizon Scanning Service for Emerging Health Technologies in NECA H-SIGHT – Digital Therapeutics -

Ah-Ram Sul[1,2*] and Kyun-Ik Park[2]

[1]Office of Project Management, Division of Research & Development, National Evidence-based Healthcare Collaborating Agency (NECA), Republic of Korea

[2]Big Data Cooperation, Division of Research & Development, NECA, Republic of Korea

ahramsul@neca.re.kr, ahram.sul@gmail.com

Abstract

Healthcare horizon scanning (HS) explores new and emerging health technologies which will be introduced to the market in few years. It is to provide timely information to various customers (i.e., healthcare industries, medical service providers, policy decision makers, and patients) by monitoring and assessment of the technologies. Utilizing the toolkit, we identified, filtered, and then prioritized the innovative technologies - digital therapeutics (DTx). Considering predefined criteria, DTx for insomnia, dementia and diabetes were selected for assessment. The potential impacts of selected technologies will be evaluated.

Background

Health technology assessment (HTA) is defined as "a multidisciplinary process that uses explicit methods to determine the value of a health technology at different points in its life-cycle (that is, pre-market, during market approval, post-market, through to the investment)." The health technology can be a test, device or procedure [1].

In the healthcare sector, HS focuses on early awareness and alert (EAA) of new and emerging health technologies (i.e., in translational research or pre-market stage). It is a tool intended to manage risks and uncertainties, enable preparation for appropriate introduction of those innovative technologies. By providing advance warning and information of the risks and benefits of the technologies, it can facilitate effective planning and investment in healthcare industries [3].

The purpose of HS is to comprehensively evaluate the aspects of technical properties, safety, efficacy and effectiveness, cost and other economic attributes, and other impacts (i.e., social/cultural, legal, ethical, organizational or political impacts) of early-stage health technologies. Numerous global agencies have conducted this activity for almost 20 years [5]. National Evidence-based Healthcare Collaborating Agency (NECA), which is the representative HTA agency in Republic of Korea, developed HS service for Innovative Global Health Technology (H-SIGHT) toolkit and has been performing HS of health technologies since 2014. A scan is to provide potential impacts and social effects of health technologies supposed to be adopted in the Korean medical market within 1 to 5 years [4].

The rapid growth in market of DTx over the past years has resulted a software-based medical device development. Since DTx is expected to transform healthcare service, it was selected for research topic [2].

Methods

This study was carried out under the expert consultation based on collected data (literature evidences) and did not use personal information of the participants (experts), thus it was exempt from IRB review (NECAIRB21-019).

Figure.1 shows flow chart of HS activities. They generally involve in the following process: identification of new health technologies and their filtration, priority setting of technologies to assess, assessment of potential role and value of those technologies, dissemination of unbiased findings to the customers, and monitoring the provided information [5].

In identification step, we searched for DTx technologies based on 13 electronic databases (6

domestic, 7 foreign). After that, in filtration step, relevant experts excluded inappropriate technologies. The predefined criteria were relevance, innovativeness, and potential to introduce to the Korean market. Then, in prioritization step, more than four experts independently determined the priority of the technologies. We took into account the social needs, quantity of evidence, and potential to adopt to the domestic market. By expert consultation, the selected technologies will be evaluated for their potential positive or negative impacts (i.e., dealing with unmet medical needs, effects on patient health condition, healthcare equity, acceptability of patient/ doctor, change of healthcare cost, and social/ ethical/ legal/ political/ cultural aspects). Then, assessment report will be uploaded in the NECA website (https://www.neca.re.kr/).

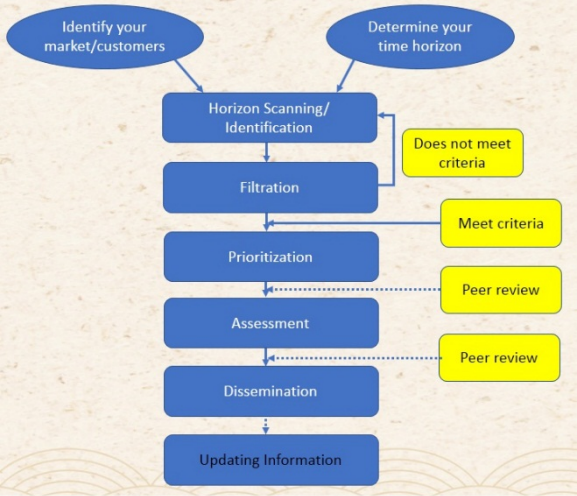


Figure. 1 Flow chart of HS activities

Results and Discussion

A total of 124 DTx technologies were identified. After classification and filtration, 8 technology groups were selected for candidates of prioritization (Table 1). Finally, technologies which obtained three highest score in prioritization were chosen for further review. The potential impacts will be assessed for DTx groups utilized in insomnia, dementia and diabetes. By supporting reliable information on emerging health technologies, HS will promote safe and rapid introduction of them in the market.

This study is expected to be utilized as basis of data for the development of the DTx industry.

Table. 1 Candidates for prioritization

No.	Intended Use of DTx
1*	Insomnia
2*	Dementia
3*	Diabetes
4	Anxiety disorder (Generalized Anxiety Disorder (GAD), Post-Traumatic Stress Disorder (PTSD), panic disorder or Obsessive Compulsive Disorder (OCD))
5	Attention-Deficit/Hyperactivity Disorder (ADHD)
6	Respiratory disease (Asthma or Chronic Obstructive Pulmonary Disease (COPD)) medication
7	Alcohol Use Disorder (AUD)
8	Neuro-rehabilitation

The technologies denoted by an asterisk (*) were chosen for further assessment.

Acknowledgements

This research was supported by National Evidence-based Healthcare Collaborating Agency (NECAIRB21-019) funded by the Ministry of Health and Welfare, Republic of Korea.

References

1. B. O'Rourke, et al., "The new definition of health technology assessment: A milestone in international collaboration", Int. J. Technol. Assess. Health Care. 36(3), 187-190 (2020).
2. G. Recchia, et al., "Digital Therapeutics - What they are, what they will be", Acta Scientific Med. Sciences, 4(3), 01-09 (2020).
3. L. Mundy, et al., "Sustainability of healthcare systems in Asia: exploring the roles of horizon scanning and reassessment in the health technology assessment landscape", Int. J. Technol. Assess. Health Care. 36(3), 262-268 (2020).
4. S-K. Lee, et al., "Study of Horizon Scanning and Potential Health Impact Assessment of Emerging Health Technology and Development of Operation System of H-SIGHT", NECA Research Report (2014).
5. W. Oortwijn, et al., "How can health systems prepare for new and emerging health technologies? The role of horizon scanning revisited", Int. J. Technol. Assess. Health Care. 34(3), 254-249 (2018).

P-081

Salivary gland stimulation system to promote radioiodine excretion

Sung Gyun Kim[1], Joo Hyun Hong[1], Myoung Nam Kim[2], Jeong Hyun Lee[2*]

1Department of Applied Technology, Daegu-Gyeongbuk Medical Innovation Foundation, Daegu, Korea

2Department of Biomedical Engineering, School of Medicine, Kyungpook National University, Daegu, Korea

pung@knu.ac.kr

Abstract

Radioiodine therapy is a treatment to prevent recurrence after thyroid cancer surgery. However, the therapy causes some inconvenience to the patients, such as damaging the salivary gland tissue and causing sialadenitis. So far, salivary gland massage, which stimulates the salivary glands, is recommended to treat sialadenitis. However, since this massage method is performed by inexperienced patients, there are uncertainties in terms of treatment effectiveness. To solve this problem, we propose a system that can automatically stimulate the salivary glands and verify the effect of radioiodine excretion through a preclinical trial.

Background

According to the cancer statistics in Korea in 2018, thyroid cancer is the second most common cancer, accounting for 11.8% of all cancers. In the case of thyroid cancer, surgery is performed when the cell findings are malignant [2]. In addition, if there is a possibility of recurrence of the cancer after surgery, radioiodine treatment is used in parallel [3].

Radioiodine therapy is known as a reasonable and safe method [4]. However, there are several side effects depending on the cumulative radiation dose, and the side effects experienced by most patients are related to the salivary glands. The reason is that about 2% of the injected amount is ingested into the salivary gland during radioiodine treatment. Penetrated radioiodine releases β-rays, damaging the salivary gland tissue and causing sialadenitis.

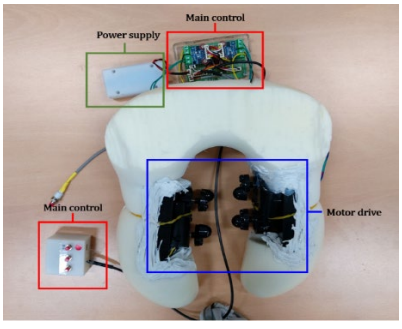
Destruction of these salivary glands is irreversible and therefore fundamental treatment is difficult. Therefore, clinicians focus on improving the symptoms of sialadenitis. It is recommended that if the salivary glands are constantly swollen, a squeezing massage is recommended [6]. However, there is a problem that the therapeutic effect is uncertain due to the lack of experience. In this study, we propose an automatic salivary gland massage system for the treatment of sialadenitis, which is a side effect of radioiodine treatment in thyroid cancer. Furthermore, a preclinical trial was conducted to verify the performance of the proposed system.

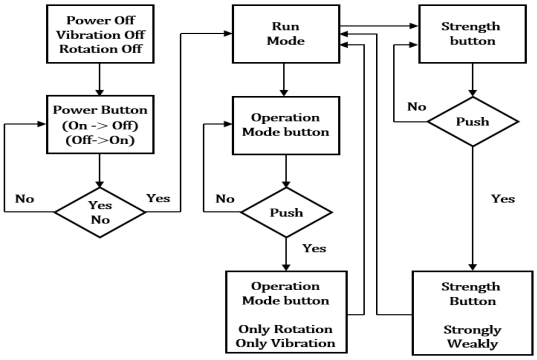
Methods

Proposed system design

The proposed system consists of three parts — main control that drives the device, power supply to charge the battery and drive the device, and motor drive that stimulates salivary glands. It is designed in the form of a neck pillow to continuously stimulate the patient's salivary glands. The main control unit consists of a microcontroller (ATmega328) and three switches (ON/OFF, motor driving mode, and speed control). The power supply operates the system and is designed to use a 3.7V 3000mAh battery. The motor drive unit consists of two vibration motors and two DC motors.

The system is programmed to power on by pressing the power button for more than 1 second and allow the user to select a mode. The system is also programmed to select the appropriate intensity for the user by pressing an intensity button. Figure 1 and Figure 2 show the flow chart and implementation result of the proposed system, respectively.

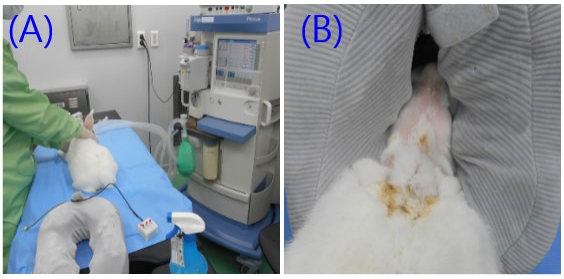




Preclinical trial

To confirm the radioiodine excretion performance of the developed automatic massage system for salivary glands, a rabbit preclinical experiment was conducted. The protocol of this study was approved by the Medikinetics Institutional Animal Care and Use Committee (DGMIF-21071202-00). Eight rabbits (about 2-2.5kg, male, 5-month-old, Newsealand White Rabbit) divided into two groups (experimental and control group) were used in the experiment.

All rabbits underwent total thyroidectomy 4 weeks before the test day, and 1 g/ml of potassium iodide was dissolved in water and drank daily from 5 days before the test day. After completion of anesthesia, salivary gland massage was performed for 30 minutes through the automatic salivary gland massage system. After the experiment, rabbits were sacrificed under deep anesthesia. We extracted and detected the left/right salivary glands of sacrificed rabbits. One of the salivary glands was checked for tissue morphology and pathology, and the other was stored frozen. Finally, the frozen salivary glands of the two groups were used to compare and analyze the amount of iodine remaining in the salivary glands.



Results and Discussion

In this paper, an automatic salivary gland massage system was proposed to promote the release of radioiodine from the salivary glands, and its performance was verified through the preclinical experiments. According to the results of the experiment, we confirmed the difference in the amount of iodine remaining in the salivary glands of the two groups. In the further study, it is considered that the proposed system may be applied in clinical practice if the stimulation factors are optimal.

Acknowledgement

This research was supported by High-tech medical complex One-stop support project for the future medical industry, funded by the Ministry of Health & Welfare, Republic of Korea (grant number: HI19C0760)

References

1. National Cancer Registration Project Annual Report, 2018). http://www.cancer.go.kr, [accessed:01-10-2021].
2. K. H. Lee, “2016 Revised Korean Thyroid Association Management Guidelines for Patients with Thyroid Nodules and Thyroid Cancer,” International Journal of Thyroidology, Vol. 9, No. 2, pp. 59-126, 2016.
3. J. H. Shin, Illness Experience of Thyroid Cancer Patients, Doctoral Dissertation of Chosun University of Nursing, 2018.
4. W. B. Kim, “Korean Thyroid Association Guidelines for Patients Undergoing Radioiodine Therapy for Differentiated Thyroid Cancers (First Edition, 2012),” International Journal Thyroidology , Vol. 6, No. 1, pp. 12-25, 2012.
5. K. S. Won, “Low Dose versus High Dose Radioiodine Therapy,” International Journal of Thyroidology, Vol. 8, No. 1, pp. 14-18, 2015.
6. I. C. Nam, “Radioactive Iodine-Induced Sialadenitis,” Journal of Korean Society of Otorhinolaryngology-Head and Neck Surgery, Vol. 58, No. 8, pp. 534-539, 2015.

P-082

Total sleep time estimation using an tri-axial accelerometer in daytime

S.J Choi[1], J.K Choi[1], J.Y Kim[2], B.R Nam[1], M.S. Kim[2], K.M Choi[2] and I.Y. Kim[1,2]

[1]Department of Electronic Engineering, Hanyang University, Seoul, Korea

[2]Department of Biomedical Engineering, Hanyang University, Seoul, Korea

csj1996@hanyang.ac.kr

Abstract

Getting adequate sleep is very important for mental and physical health. In the field of sleep medicine, Polysomnography has been used as a standard measurement, The actigraphy method, which can continuously measure for days or weeks by attaching an accelerometer to the wrist or waist, is also used to analyze sleep when PSG can be used only during sleep time. It is known as frequent physical exercise affects sleep. Therefore it was necessary to measure the total sleep time of the day by the amount of activity up to just before sleep. In this study, a method developed to estimate the sleep time of the day using the 3-axis acceleration data in daytime.

Background

It is very important to get adequate sleep because a lack of sleep has adverse effects on mental memory loss, anxiety symptoms, the immune system and the cardiovascular health[1,2]. The quality of sleep is mainly measured through polysomnography. Polysomnography is a standard measurement method in sleep medicine, but it has the disadvantage that several sensors must be attached, it can be measured only during sleep, and an expert who can interpret the results is required. On the other hand, the actigraphy method attaches an accelerometer to the wrist or waist so that it can be measured continuously for days or weeks, and sleep time can be measured without an expert[3]. Since it can be implemented in the form of a built-in smart band, it has the advantage of being able to measure the amount of activity without purchasing a separate device. However, it has been reported from wearable device users that excessive obsessive thoughts about getting a good night's sleep interfere with sleep and physical discomfort can lead to obsessive-compulsive thoughts, which can lead to insomnia[4,5]. It is known as frequent physical exercise affects various aspects of sleep[6]. Therefore, instead of measuring the sleep time during sleep, it is necessary to measure the total sleep time of the day by the amount of activity just before sleep. Based on the study of classifying sleep quality using weekly actigraphy and deep learning, a study was planned to estimate total sleep time using 3-axis acceleration.

Methods

Data were collected by wearing Actigraph wGT3X-BT set at a sampling rate of 100 Hz on a non-dominant left wrist of a 77-year-old female subject for 4 days. The collected raw data was processed as data of 30 second epochs X, Y, and Z-axis using the program (ActiLife version 6.13.4; available from ActiGraph, LLC), before using Vector Magnitude(VM) of each 3-axis data through Matlab R2021a.

$$VM = \sqrt{X^2 + Y^2 + Z^2}$$

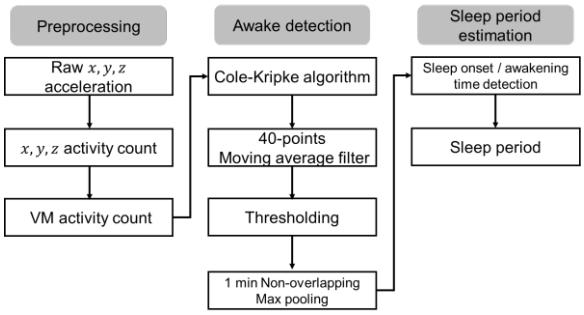


Figure 1. Process of estimating sleep period from Raw tri-axial acceleration data

After the preprocessing, sleep scoring was performed for 30-second epoch actigraphy using the Cole-Kripke algorithm used for subjects over 35 years of age. When the sleep scoring result is classified as 20 minutes of

continuous sleep, The first minute of consecutive 20 minutes is sleep onset time[7].

By 40-points moving average filter, thresholding the section that is determined sleep as 1 and 0 for the section that is not sleep. In order to shorten the data processing time, 1 minute non-overlapping max pooling was used to extract the maximum value out of 2 samples of 30 second epoch data, and the data was reduced in half (Figure 1).

In sleep period estimation, the 1 min epoch data that obtained in the awake detection process was divided into 1440 samples (24H). After 1440 samples were made, a matrix of (4, 2880) was created by 720 zero padding on both sides. Then, using the average value of the index determined as Awake in each row vector, a 1440-sized window 24H was set based on the average position. A total of three estimated sleep periods were obtained by setting the smallest index as the sleep awakening time and the largest index as the sleep onset time among the vectors determined to be awake within the window set in each row vector. Activity and sleep period based on sleep awakening / onset time are displayed below (Figure 2)

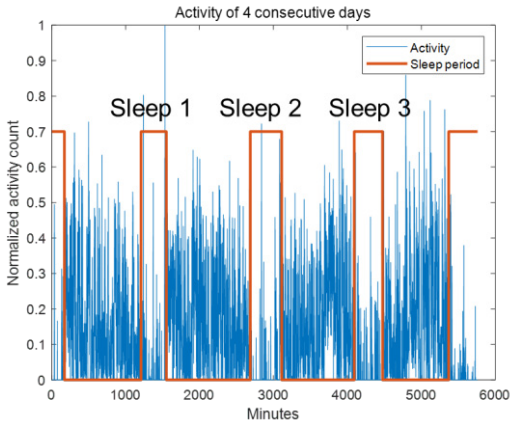


Figure 2. Activity measured for 4 consecutive days and estimated sleep period

	Estimation	Actilife6	Sleep diary
Sleep 1	5.72	5.40	5
Sleep 2	7.11	6.30	6
Sleep 3	6.42	5.97	6

Unit : Hour

Table 1. Sleep period results of estimation, Actilife6 and sleep diary along 3 different sleep

Results and Discussion

It was possible to estimate 3 sleep times from the raw 3-axis acceleration data (Table 1). Actilife6 and estimated sleep time in Table 1 show a difference even though the same sleep scoring algorithm is used due to the different data processing. Based on this result, it was possible to separate the accelerometer data measured for several consecutive days, and lay the foundation for applying the method for estimating sleep parameters with 3-axis accelerometer data for one day.

Acknowledgements

This research was supported by the Brain Convergence Research Program of the National Research Foundation (NRF) funded by the Korean government (MSIT) (No. NRF-2021M3E5D2A01022397).

References

1. Tempesta, Daniela, et al. "Emotional memory processing is influenced by sleep quality." *Sleep medicine* 16.7 (2015): 862-870.
2. Strine, Tara W., and Daniel P. Chapman. "Associations of frequent sleep insufficiency with health-related quality of life and health behaviors." *Sleep medicine* 6.1 (2005): 23-27
3. Walia, Harneet K., and Reena Mehra. "Practical aspects of actigraphy and approaches in clinical and research domains." *Handbook of clinical neurology* 160 (2019): 371-379.
4. Baron, Kelly Glazer, et al. "Orthosomnia: are some patients taking the quantified self too far?." *Journal of Clinical Sleep Medicine* 13.2 (2017): 351-354.
5. Patil, Sunil R. "An Overview of Insomnia." *Journal of Medical and Pharmaceutical Innovation* 6.33 (2019).
6. Vanderlinden, J., F. Boen, and J. G. Z. Van Uffelen. "Effects of physical activity programs on sleep outcomes in older adults: a systematic review." *International Journal of Behavioral Nutrition and Physical Activity* 17.1 (2020): 1-15.
7. Cole, Roger J., et al. "Automatic sleep/wake identification from wrist activity." *Sleep* 15.5 (1992): 461-469.

P-083

Duty cycle dependence of tumor-treating fields on glioblastoma spheroid cells

Eunbi Ye[1], Jung Eun Lee[2], Young-Soo Lim[1], Seung Ho Yang[2] and Sung-Min Park[1]

[1]Department of Convergence IT Engineering, Pohang University of Science and Technology, Pohang, Korea

[2]Department of Neurosurgery, St. Vincent's Hospital, College of Medicine, The Catholic University of Korea, Suwon, Korea

sungminpark@postech.ac.kr

Abstract

Tumor-treating fields (TTFields) are emerging cancer management therapies that use alternating low intensity electric fields that interfere with dividing cells and induce cancer cell apoptosis. However, little is known about the effects of changing duty cycles on outcomes. In this study, we aimed to evaluate the effect of TTFields with different duty cycles on glioma spheroid cells and the influence of TTFields. A customized TTFields system was developed to perform in vitro experiments with varying duty cycles. Three duty cycles (100%, 75%, and 50%) were applied to three types of glioma spheroid cells (U87 and U373). Our results confirmed that TTFields showed a significant anti-cancer effect even when duty cycle was lowered to 75%. These findings suggest that further in-depth studies are needed to optimize the duty cycle to enhance the safety of this emerging therapeutic modality.

Background

Tumor-treating fields (TTFields) is an emerging cancer treatment modality that uses alternating, low intensity (1–3 V/cm) electric fields at intermediate frequencies (100–300 kHz) to disrupt cancer cell proliferation [1]. The anticancer efficacy of TTFields was further demonstrated by clinical studies, and the TTFields system quickly received FDA approval for newly diagnosed and recurrent glioblastoma (GB) [2]. However, mechanistic investigations are needed to optimize the use of TTFields and elucidate the mechanism of TTFields. Although monolayer cell cultures are frequently used in mechanism studies for TTFields, two-dimensional cell cultures are oversimplified versions of tumors and do not recapitulate in vivo cellular organization and interactions. One way to reduce the gap between in vitro and live tissue is to use well-suited three-dimensional (3D) cultured cells. Here, we applied TTFields to 3D glioma spheroids for the first time.

In general, patients are advised to wear the device for impractical duration, 23 h/d, without any parametric evidence. As the TTFields device requires a high compliance rate, it is designed to be wearable and portable, with minimal impact on daily activities. Thus, a further improvement in the usability of the system, such as device miniaturization and operation time extension, is imperative to benefit more patients. In this study, we noted that energy efficiency can be further improved through duty cycle regulation. Reducing the duty cycle has advantages such as increasing energy efficiency, thereby reducing the size and weight of the battery, and these advantages increase the possibility of transforming the device type to an insertion type or one with wireless recharging.

In this study, we evaluated the duty cycle dependent effects of TTFields by using tumor spheroid cells. For the in vitro experiment, we designed a system that generates an electric field suitable for TTFields in a cell culture environment based on numerical electromagnetic simulations and fabricated a simple TTFields system that can modulate the duty cycle freely. In this study, details of TTF-induced cell damage to tumor spheroid cells were analyzed and compared according to the duty cycle.

Methods

We have developed an in-house TTFields system that allows for accurate adjustment of the duty cycle while maintaining a constant voltage of 2.5 Vpp between electrode plates (Fig. 1). The entire system was built using off-the-shelf components with easy-to-

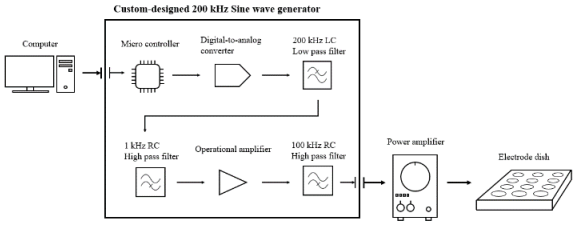


Figure 1. A schematic diagram of our experimental setup.

fabricate electrodes. For system verification, we performed computational simulations, which confirmed that the experimental setup generated a uniform electric field distribution between the electrodes. Calibration testing confirmed that our system did not induce significant heating when the worst case 100% duty cycle was applied; the temperature increase in the cell culture medium was <0.5 °C and maintained at <41 °C, which is below the temperature for thermal injury [3].

Results and Discussion

Our results confirmed that high duty cycles of TTFields effectively induced apoptosis in cancer cells. The evaluation of bioluminescence intensity revealed that TTFields application at 75% duty inhibited cell proliferation (average 85% decrease compared to control), which was very similar to that achieved using 100% stimulation (average 78.5% decrease compared to control), but slightly better (Fig. 2). By contrast, when applying 50% TTFields, the average reduction rate was only 43% compared to the control. The difference in the treatment effect depending on the duty cycle was more pronounced in the evaluation of the cell cycle. When comparing the apoptosis phase of the TTFields group and the control group, we found that apoptosis conspicuously increased in the 75% and 100% groups, but no significant change was seen in the 50% group. There was also a difference depending on the type of glioma spheroids, which we speculate is because of the gradients of proliferation, oxygen, nutrients, and pH observed from the external layer to the inner part of the spheroid [4].

. We believe that this is an important finding for advancement of TTFields therapy. TTFields devices have limitations in that they cause inconvenience to patients because of the size and weight of the battery and the presence of exposed cables outside the clothes. One approach to solving this problem is to evolve the device into an implantable form using wireless recharging technology. However, to implement this, energy saving, which can be achieved through duty cycle reduction, is a key requirement for device miniaturization and operation time extension. Finally, we believe that our study paves the way for enhancing the usability and safety of TTFields therapy through parametric optimization.

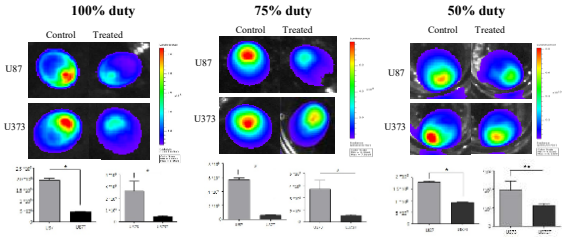


Figure 2. Bioluminescence imaging of U87 and U373 cells after applying tumor-treating fields (TTFields) for 72 h. Data are given as average ± SD (n = 5). *p-value < 0.001, **p-value < 0.05

Acknowledgements

This research was supported by Basic Science Research Program through the National Research Foundation of Korea (NRF) funded by the Ministry of Education (2020R1A6A1A03047902).

References

1. Kirson ED, Gurvich Z, Schneiderman R, Dekel E, Itzhaki A, Wasserman Y, Schatzberger R and Palti Y. Disruption of cancer cell replication by alternating electric fields. *Cancer Res* **64**, 3288-3295 (2004)
2. Stupp R, Wong ET, Kanner AA, Steinberg D, Engelhard H, Heidecke V, Kirson ED, Taillibert S, Liebermann F, Dbalý V, et al. NovoTTF-100A versus physician's choice chemotherapy in recurrent glioblastoma: A randomised phase III trial of a novel treatment modality. *Eur J Cancer* **48**, 2192-2202 (2012)
3. Toms SA, Kim CY, Nicholas G and Ram Z. "Increased compliance with tumor treating fields therapy is prognostic for improved survival in the treatment of glioblastoma: a subgroup analysis of the EF-14 phase III trial." *J Neurooncol* **141**, 467-473 (2019)
4. Carlsson J and Acker H. "Relations between pH, oxygen partial pressure and growth in cultured cell spheroids." *Int J Cancer* **42**, 715-720 (1988)

P-084

Development of radio-frequency generator for Radio-Frequency Ablation application

Jinsu An[1], Jin-Kyung Park [1], Jeong-Han Yi[1], Hyung-Sik Kim[1*]

Department of Biomedical Engineering, BK21+ Research Institute of Biomedical Engineering, School of ICT Convergence Engineering[1], College of Science & Technology, Konkuk University, Chungju, South Korea
*hskim98@kku.ac.kr

Abstract

In this study, Radio-frequency generator for Radio-Frequency Ablation (RAF) application is developed. The Radio-frequency generator is composed of a power supply unit, a control unit, and an output unit. The power supply unit rectifies the 220V AC power and uses it as an input. It is designed to be adjustable in the range of ±60V ~ ±100V using the flyback converter structure. The control unit was implemented to generate a radio frequency of 1 kHz to 500 kHz using a microcontroller and a waveform generator. The form of radio frequency that can be generated is a sine wave, a triangular wave, and a square wave. It consists of a voltage control system that adjusts the size of the output voltage, and a current monitoring system that feeds back the output current to the microcontroller so that the set output is maintained constant. It is possible to measure the impedance of the load. The output unit amplifies a transmitted signal from the control unit using a power operational amplifier to output a maximum voltage of 180Vpp (Peak-to-Peak) and current of 1A. To check the operation, wire-wounded resistor of 66Ω, 100Ω, and 200Ω were used. As a result of the experiment, it was possible to generate various radio-frequency waveforms from 1 kHz to 500 kHz.

Introduction

The radio-frequency electrosurgical device uses radio-frequency current to minimize the impact on living tissue and enables ablation, hemostasis, and coagulation.

For the above effect, thermal energy from the output of the radio-frequency surgical device is required. Thermal energy raises the temperature between cells by friction as the negative ions in the cells move from the negative electrode to the positive electrode by the electric current passed through the body. [1,2] As the tissue changes due to heat, the tissue impedance also changes, so a generator capable of generating a desired output for the changed tissue impedance is a very important element in the electrosurgical device.[1]

In general, radio-frequency electrosurgical devices used for treatment use alternating current with a frequency of 300kHz to 3MHz and a potential of 1V to 10kV.[2]

Radio-frequency heat treatment using alternating current of 460kHz to 500kHz generates heat by applying an electric current around the electrodes inserted into the tumor. The frictional heat generated in this way induces tumor necrosis.[3] Radio-frequency heat treatment is a non-surgical treatment for patients who cannot be treated with surgery. It is characterized by a short recovery period and excellent therapeutic effect even in metastatic cancer, which has low therapeutic effect due to vascular depression and abundant fibrous tissue.[4] However, due to the standardized size of the electrode and the attachment of the electrode to a thin needle or catheter, the range of ablation has a limited range in the form of a line, so sufficient ablation of the lesion is not performed. Specifically, 1) Insufficient ablation range in round-shaped lesions, 2) In the curved lesion area, only the area in contact with the electrode is cauterized, 3) The length and range of cauterized lesions are standardized with limited electrodes attached. In order to reduce these shortcomings to a minimum, research on the core technology of various local thermal treatments is being conducted.

In this study, we intend to develop a radio-frequency generator for RFA application. It is designed to use different frequencies (1kHz~500kHz) and waveforms of different shapes (sine wave, triangle wave, square wave) according to the characteristics of the target organ. It was confirmed that an output of up to 55 Watt is possible, and it was confirmed that the impedance of target tissue that changes due to heat can also be measured.

Methods

As shown in the block diagram proposed in Figure 1, a radio-frequency generator for radio-frequency ablation application is composed of a power supply unit, a control unit, and an output unit.

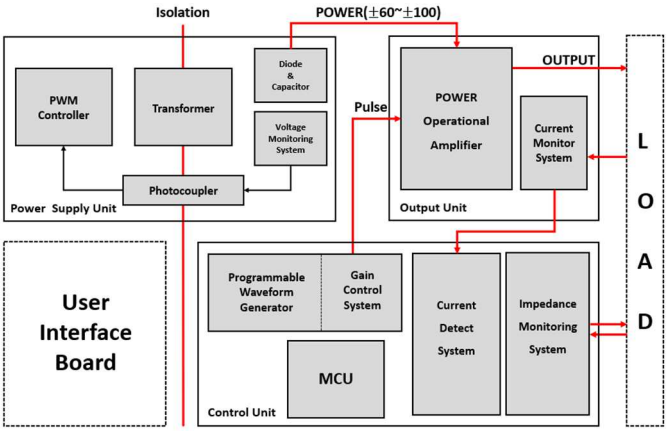


Fig 1. Diagram of radio-frequency generator.

The power supply rectifies the 220V AC power and uses it as the input power. By configuring a flyback converter using a voltage monitoring system and a photocoupler, it is possible to realize isolated powers with an output of up to 200Watt adjustable from ±60V to ±100V.

The control unit is controlled through an external user interface based on a microcontroller. Radio-frequency of 1kHz to 500kHz can be generated using programmable waveform generator, and it is possible to implement sine wave, square wave, and triangular wave. The pulse generated by the Waveform Generator controls the voltage applied to the load through the Gain Control System. Current detect system measures the current value flowing from the load so that the set output power is kept constant. If an amount of current greater than the set maximum current flows to the load, the output is cut off. Impedance Monitoring System measures the change in impedance of
the load due to heat.

The output unit amplifies the pulse generated by the control unit to a maximum of 180Vpp (Peak-to-Peak) using the Power Operational Amplifier and can output a maximum current of 1A. The current monitoring system feeds back the output current and converts it to a DC voltage with an RMS value. Based on this value, the control unit regulates so that the set output is maintained.

Results

3.1 Power supply operation according to load

The power supply consists of a flyback converter that uses an AC power of 220V as an input power, so that it can be adjusted in the range of ±60V ~ ±100V. The operation was confirmed by connecting a wire-wounded resistance of 100Ω to 1kΩ at both ends of the output. The output power at each load is shown in Figure 2, and it was confirmed that the output power of 200Watt was maintained.

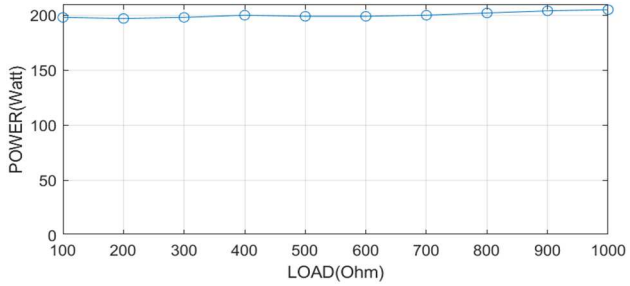


Fig 2. Power supply operation according to load

3.2 Various radio-frequency signal generation

It generates various radio-frequency signals using the microcontroller of the control unit and the Programmable Waveform Generator. It can be adjusted from 1kHz to 500kHz, and as shown in Figure 3 below, sine wave, square wave, and triangle wave can be implemented.

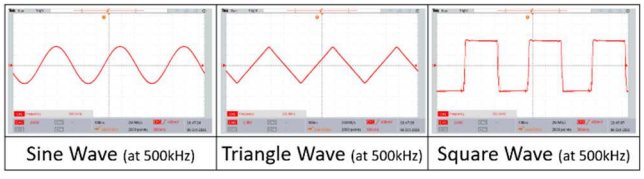


Fig 3. Various radio-frequency signals at 500 kHz

3.3 Output operation according to frequency change

The output operation of the radio-frequency generator was confirmed using wire-wounded resistor of 66Ω, 100Ω, and 200Ω. The output power at each load was checked by changing the frequency. The operation result is shown in Figure 4.

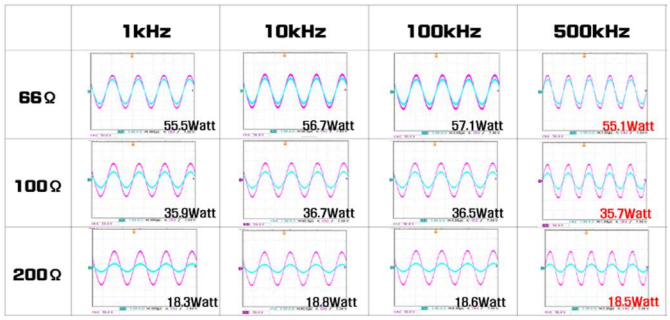


Fig 4. Output of a radio-frequency generator

3.4 Operation result of current monitoring system

The current monitoring system measures the feedback current flowing through the load. Figure 5 below shows the measurement of various radio-frequency signals of 500kHz, 1A (Peak-to-Peak). The measured value of CH1 (Red) is the actual RMS value of the current converted in the form of voltage, and the measured value of CH2 (Blue) is the output value of the current monitoring system. By measuring the value of the current flowing through the load, it was confirmed that it is possible to measure the DC voltage of the RMS value.

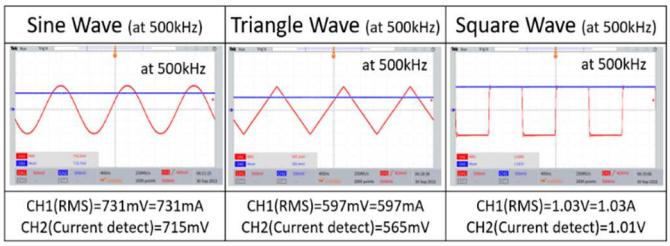


Fig 5. Current monitor system operation

Acknowledgements

This study was funded by the Korea Medical Device Development Fund (KMDF_PR_20200901_0079).

References

[1] Lee, Seok Min. (2021). A Study on Electrical Compensation for Deformation of Living Organisms in the Operation of High Frequency Electrosurgical Devices Using Power Amplifiers. (Doctoral dissertation). Hanyang University, Korea.

[2] Dosun Song, Hyen-Ho Choi, Dong-gyu Jeoug. (2005). Development of High Frequency Electro-surgical Instrument. Proceedings of KIIT Conference, 135-140.

[3] Jung Wook Seo. (2015). Current status and future of radiofrequency ablation for hepatocellular carcinoma. Journal of the Korean Medical Association, 58(6), 542-547.

[4] Young-sun Kim, et al. (2003). Transluminal Radio-Frequency Thermal Ablation Using a Stent-Type Electrode: an Experimental Study. Journal of Korean Radial Society, 48, 447-458.

P-085

A study on the identification of foreign substances in the intubation tube using respiration signals

Jin-Kyung Park [1], Jinsu An[1], Jeong-Han Yi[1], Hyung-Sik Kim [1,*]
[1]Department of Biomedical Engineering, BK21+ Research Institute of Biomedical Engineering, School of ICT Convergence Engineering, College of Science & Technology, Konkuk University, Chungju, South Korea
*hskim98@kku.ac.kr

Abstract

After intubation into the trachea, foreign substances in the tube interfere with the patient's smooth breathing. For this reason, the medical staff should periodically check the respiratory status of the airway intubation patient. This process increases the workload of medical staff. The present study was conducted to detect the degree of obstruction. Caused by foreign substances in the tube by obtaining respiratory signals from tubes for airway intubation and analyzing audio characteristics. To this end, a ventilator, an intubation tube containing artificial foreign substances, and a lung phantom were used, and a breathing signal was obtained by connecting a microphone to the intubation tube. When there is no foreign matter in the tube (0%) and when there is foreign matter (20%, 50%, 80%) four stages of artificial foreign matter were produced and controlled. MATLAB software was used to analyze the audio characteristics of the respiration signal. After convolution in the time-frequency spectrum Short-Time Fourier Transform (STFT), the generated feature points were quantified. As a result of the analysis, the number of feature points decreased as the number of foreign substances increased. This study will show the degree of clogging of foreign substances.

Background

Tracheal intubation is a medical technology that secures airway by inserting a tube into the patient's airway when artificial breathing is required due to poor spontaneous breathing due to respiratory failure or when airway maintenance is required during surgery. Since intratracheal intubation is mainly used in severe patients, if smooth breathing is not provided due to bending in the intubation tube or clogging by foreign substances, it can lead to very fatal consequences. Therefore, continuous management is very important for medical staff.

Airway obstruction by foreign substances means a state in which the airways are blocked by foreign substances generated outside and inside. Clogging by external foreign substances is mostly caused by food and clogging by internal foreign substances includes oral and nasal secretions, such as sputum, bleeding, and clogging by vomit. Symptoms of airway obstruction include shortness of breath, cyanosis (a phenomenon in which the skin or mucous membrane turns blue due to insufficient blood oxygen), and loss of consciousness, and if the oxygen supply is stopped for more than 7 minutes due to blockage, it can lead to death. Clogging due to such foreign substances may also occur in intubation tubes during intubation. In the event of such a blockage, the notification function of the respirator should be used to enable medical staff to respond quickly.

The alarm function of the ventilator contributes significantly to delivering the patient's condition. However, there is a phenomenon in which some alarm functions malfunction or the alert sensitivity of the medical staff decreases due to meaningless alarms[1]. An institution in Europe investigated the problem of alarm malfunction of a ventilator. Of the 17 randomly selected hospitals, only two alarms correctly identify the risk as a result of disconnecting the test connection between the ventilator catheter and the intubation tube[2]. As such, damage caused by malfunction of the ventilator alarm is frequently occurring[3,4]. Malfunctioning alarms are much more dangerous than alarms that do not work at all. Therefore, the sensitivity and accuracy of alarm functions are very important to patients. To prevent this situation, this study subdivides the function of the alarm of the ventilator to detect the presence of foreign substances in tubes for airway intubation and proposes a classification algorithm according to the degree of obstruction. When there is no foreign substance (0%) is a control group, and when there is a foreign substance (20%, 50%, 80%), respiratory signals according to the degree of obstruction were recorded and analyzed.

Methods

In order to classify respiratory signals according to the degree of obstruction caused by the accumulated foreign substances in the intratracheal insertion tube, an intubation tube containing artificial foreign substances was manufactured using Solidworks and 3D printers (Single Plus, CUBICON. Depending on the degree of clogging of foreign substances in the tube, it was produced in four stages: 0%, 20%, 50%, and 80%. After connecting the lung phantom to a ventilator actually used in clinical practice, a microphone was connected to the insertion tube to obtain a breathing sound. Recording was performed five times, 20 seconds per degree of obstruction. The breathing cycle provided by the ventilator is about one cycle per 4 seconds, and four cycles appear when recording for 20 seconds.

Figure 1 shows a series of preprocessing process using MATLAB. The respiratory sound data was divided into cycles based on a specific amplitude value generated every 4 seconds by the exhalation sound of the ventilation equipment. After obtaining the average with the divided data, one average waveform was extracted and noise removed. Short-Time Fourier Transform (STFT) was applied to the extracted average breathing signal and converted into time-frequency data. The basic concept of STFT is to introduce a window window that

moves according to a signal to calculate a time spectrum in addition to Fourier transform that divides waveforms such as voice into basic frequency and regular multiple frequency. In this study, the Blackman-Harris window was used, and the window and movement sizes were set to 512 and 256, respectively. STFT was applied to implement a spectrogram that shows the difference in amplitude as a color change according to the change in the time axis and frequency axis.

A power spectrum provides information on energy per unit time of a signal belonging to a given frequency band. Previous studies have shown that if clogging by foreign substances is present in the airways, the increased high frequency energy content appears in the audio signal, which corresponds to a distinct vertical texture in the power spectrum image of the sound signal[5].

In order to analyze the texture pattern, the time-frequency distribution of the audio signal determined in the spectrogram was stored as an image. In order to make the RGB image stored in color into a 2D image, a gray filter was applied and converted into a gray image. Convolution was applied to extract a distinct vertical texture. Mathematically, convolution means multiplying one function and another function by a convolution and then integrating it over the interval. Therefore, convolution in image processing is determined by the convolution mask while scanning the input image. There are smoothing methods that blur the image according to the arrangement of masks, and sharpening methods that make the image clear. In this study, in order to clarify the texture pattern, a sharpening method used to make the image clear or to detect edges was applied. The sharpening mask is a Laplacian mask and is set such that the sum of the mask arrangements is zero[6]. When applied to an image, the pixel value becomes 0 in an area where the pixel value remains unchanged, and the value is large in an edge area where the pixel value changes significantly. As a result of convolving the convolutional mask and the power spectrum image, it was confirmed that the vertical line became clearly clear in the audio signal.

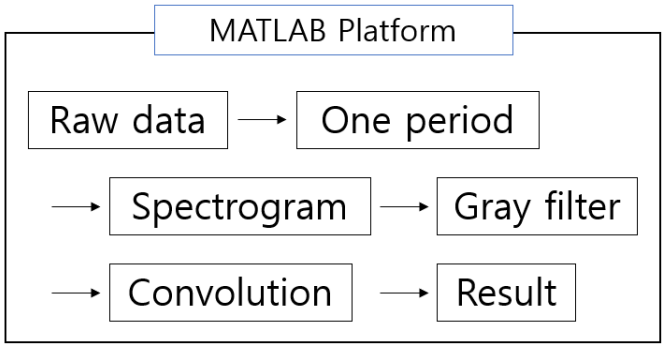


Figure 1. The preprocessing process.

Results and Discussion

Figure 2 shows the results of each convolution according to the degree of airway obstruction caused by foreign substances. In the result graph, the numbers of the X-axis and Y-axis mean the number of data. In Figure 2, the number of white vertical lines between the X-axis 500 and 1000 and the Y-axis 1 and 100 was quantified. As a result, as shown in Table 1, fewer feature lines were extracted because the control passed without clogging. And the feature line tended to decrease as it went to 20% 50%, and 80%.

In conclusion, there is no foreign substance in the intubation tube after airway intubation, so if normal breathing is performed without obstruction, the vertical line hardly appears. On the other hand, if there are foreign substances, it can be seen that a lot of vertical lines appear. In addition, when foreign substances are present, the degree of obstruction tends to gradually decrease when compared to each other, indicating that it is possible to compare according to the degree of obstruction.

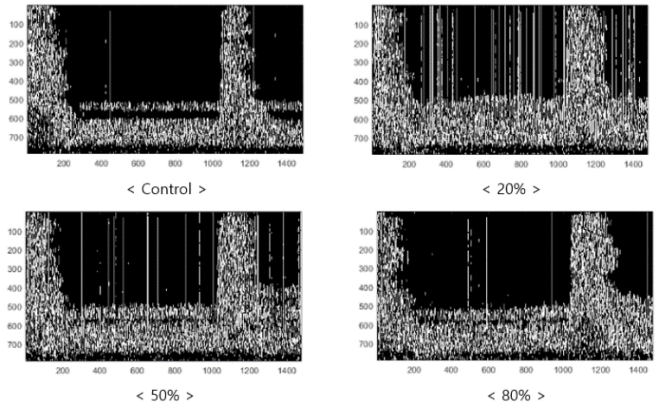


Figure 2. Convolution result graph

Control	20%	50%	80%
418	4662	1765	630

Table 1. Number of vertical lines

Acknowledgements

This study was funded by the Korea Medical Device Development Fund (KMDF_PR_20200901_0079).

References

[1] Lin, Z., Zheng, K., Shen, Y., Zheng, C., Cheng, X. (2017). Survey and Discussion on Ventilator Alarm Status in ICU. Chinese journal of medical instrumentation, 41(6), 460-463.

[2] Kang, Yoo-Jin, Jung-eun Cha, and Young Kyoo Choi. (2016). Effects of Fresh Gas Flow, Respiratory Rate, and Mode of Ventilation on Recovery of Tidal Volume after Circuit Disconnection. Kyung Hee University Medical Journal, 31(1), 15-21.

[3] Chatwin, M., et al. (2010). Analysis of home support and ventilator malfunction in 1,211 ventilator-dependent patients. European Respiratory Journal, 35(2), 310-316.

[4] Cvach, Maria M., et al. (2020). Ventilator alarms in intensive care units: frequency, duration, priority, and relationship to ventilator parameters. Anesthesia & Analgesia, 130(1), 9-13.

[5] Niu, Jinglong, et al. (2019). A Novel Method for Automatic Identification of Breathing State. Scientific reports, 9(1), 1-13.

[6] Ansari, Mohd Aquib, Diksha Kurchaniya, Manish Dixit. (2017). A comprehensive analysis of image edge detection techniques. International Journal of Multimedia and Ubiquitous Engineering, 12(11), 1-12.

A Multi – Channel Neural Stimulator with Passive Component Based on An Inductive Power Transfer

Kyungmo Sung[1] and Kyungsik Eom[1]

[1]Department of Electronic Engineering, Pusan National University, Busan, Korea

gkswnsgh6278@pusan.ac.kr

Abstract

A Wireless Power Transfer (WPT), such as Inductive Power Transfer (IPT), and Ultrasonic Power Transfer (UPT) has been used to design a neural stimulator. In particular, one of the best WPTs is an IPT because it has a Power Transfer Efficiency (PTE) higher than others. In this paper, we designed a multi-channel neural stimulator based on inductive power transfer, a device of an implantable power receiver by using only passive components (e.g. spiral coil, capacitor, diode, and resistor). we study based ORCAD simulation, and we get results both channel selectivity by resonant frequency and waveform of load voltage.

Background

An IPT has been widely used for neural stimulator devices because it reads to a high PTE in a narrow distance a primary coil (transmitter) to a secondary coil (receiver) and a high-frequency selectivity determined by an LC tank resonant frequency with a tuning capacitor(1). However, as a constraint, since one coil can match one capacitor, it can provide one LC tank, using only the secondary coil and tuning capacitor as power transfer. In addition, by using an integrated circuit designed with active components generally, channel selectivity is controlled. Unfortunately, this system with these components can cause generate its thermal generation which may result in damage to the tissue around an implanted device.

In this respect, we suggest a power receiver for implantable multi-channel neural stimulator with passive components and diodes(2N4148) to make up for disadvantages. An overall system consists of the power transmitter and the power receiver. The circuit of a neural stimulator in the power receiver contains one coil, but it is implemented with two LC tanks. So, this neural stimulator is composed of two channels. Each channel is only operated when an input signal frequency is matched to an intrinsic resonant frequency. In addition, we designed the power transmitter system with a power BJT (2SB649A, 2SD669A), coil, and capacitor. Here, because amplitude modulation(AM) can contain two data both a message signal and carrier signal, the amplitude modulation signal is used for an input signal of the system. It means that carrier frequency is controlled by the operation of each channel, and message frequency is fixed by the stimulation signal frequency at the Load.

Based on this principle, particular frequencies are theoretically calculated, which are the channel resonant frequency (i.e. $f1$ = 10 MHz and $f2$ = 1 MHz) and stimulation signal frequency (i.e. $fsti$ = 1 kHz). To verify a proper operation of this stimulator at these calculated frequencies, we perform the simulation, using ORCAD™. As a result, we observe the output signal applied to load (i.e. 1 kΩ) in both the time domain and frequency domain when an input AM signal is used. It is also found that this system can stimulate neurons more efficiently compared to the existing stimulation system.

Methods

An Inductance and a capacitance value of our system are summarized in Table .1. Fig .1 shows an overall system which is contained both the power transmitter and power receiver. A power transmitter is described in Section .A, with a power amplifier and a LC series resonant circuit(2). An AM signal is selected by the input signal of power amplifier because the AM signal has two frequency data both the message signal and carrier signal. At the carrier signal match with the resonant frequency of each LC tank in the power receiver, each channel is operating. A power receiver in Section. B by Fig .1 is realized with the secondary coil, capacitor, resistor, and diode only. The Selectivity of the power receiver is explained by an

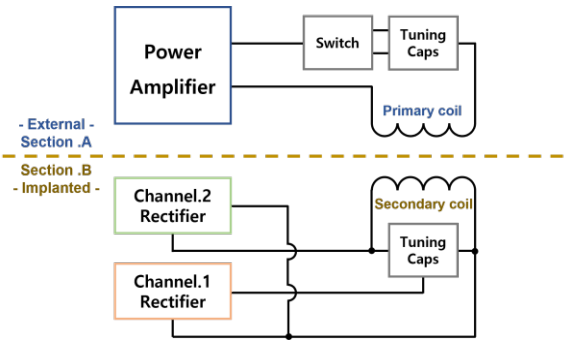


Figure .1 Overall system with power transmitter and power receiver (neural stimulator).

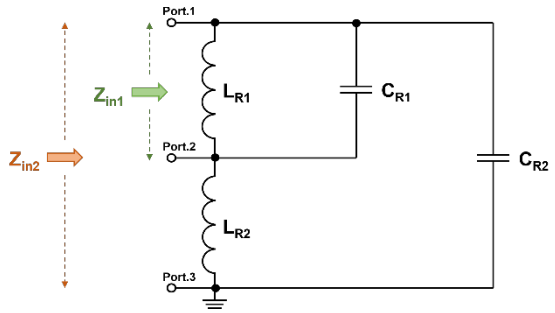


Figure .2 LC Tank Circuit about Power Receiver.

input impedance (e.g. *Zin1*, *Zin2*), as seen in Fig.2, It shows a Receiver LC circuit. Zin1 and Zin2 about a LC1 and LC2 were shown the equation (1), (2). Z_{in1} and Z_{in2} are calculated as follows :

$$Z_{in1} = (j\omega L_{R2} + 1/j\omega C_{R2}) \,||\, (1/j\omega C_{R1}) \,||\, (j\omega L_{R1}) \quad (1)$$

$$Z_{in2} = \{(j\omega L_{R1} \,||\, 1/j\omega C_{R1}) + (j\omega L_{R2}) \,||\, (1/j\omega C_{R2}) \quad (2)$$

If the $L_{R2}C_{R2} >> L_{R1}C_{R1}$,

$$Z_{in1} = j\omega L_{R1} \,||\, (1/j\omega C_{R1}) \quad (3)$$

$$Z_{in2} = j\omega L_{R2} \,||\, (1/j\omega C_{R2}) \quad (4)$$

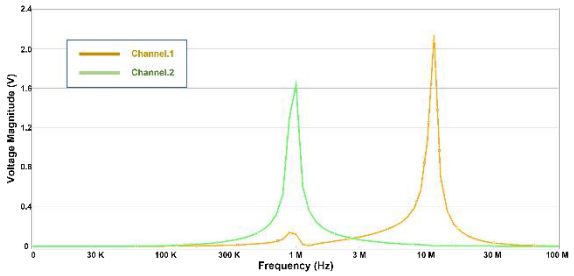
Based on our measurement, each resonant frequency is only affected by one pair of an inductance-capacitance.

Results and Discussion

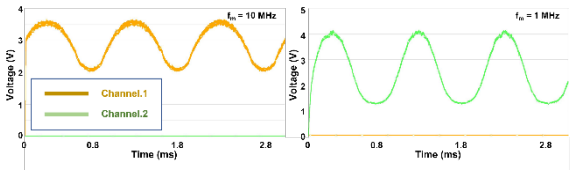
The simulation is performed with ORCAD™ CAPTURE™. Fig .3 (a) shows LC tank output voltage magnitude by analyzed of frequency domain. Each channel is operating when the transmitted signal carrier frequency is equal to a channel resonant frequency. Figs .3 (b) and (c) show the load output voltage in time domain. the carrier frequency of the input signal is optimized each channel's resonant frequency. At Fig .(b), Channel.1 peak-to-peat voltage(*Vpp*) is shown that :

	Inductance				Capacitance			
	L_T	L_{R1}	L_{R2}		C_{R1}	C_{R2}	C_{T1}	C_{T2}
μH	1	1	10	nF	0.25	25	0.25	2.5

Table .1 Component's value (L_T : transmitter coil , L_{R1} , L_{R2} : receiver coil 1 and 2 , C_{T1} , C_{T2} : transmitter tuning caps , C_{R1} , C_{R2} : receiver tuning caps.)



(a)



(b) (c)

Figure .3 (a) LC tank voltage (frequency domain) (b) load output voltage after rectified (message frequency(f_m) : 10 MHz) and (c) (f_m : 1 MHz)

$$V_{pp_ch.1} = 1.42\text{V} \text{ , } V_{pp_ch.2} = 2.79\text{V}$$

it means that the stimulation current is more than 1.42mA. the neural stimulator designed by this study is providing sufficient stimulation current. As a result, our study shows that this system can neural stimulation effectively, so we prepare the next study to implement about implantable and biodegradable neural stimulator based on this study.

Acknowledgements

This work was supported by National Research Foundation of Korea (NRF) grant funded by the Korea government (MSIT) (2020R1C1C1010505) and by BK21PLUS, Creative Human Resource Education and Research Programs for ICT Convergence in the 4th Industrial Revolution.

References

1. Young-Sik S, Minh Quoc N, Hughes Z, Rao S, Chiao JC. Wireless power transfer by inductive coupling for implantable batteryless stimulators: IEEE
2. Ali H, Ahmad TJ, Khan SA. Inductive link design for medical implants: IEEE

P-087

Evaluation of the role of perfusion of the pulsatile pump contributes to pressure fluctuations in the tube

K.H. Kim[1] and S.W. Choi[1]

[1]Department of Mechanical & Biomedical Engineering, Kangwon National University, Chun-cheon, Korea

swchoe@kangwon.ac.kr

Abstract

percutaneous transluminal coronary angioplasty(PTCA) is A method of releving the stenosis by expanding the ballon inserted the stenosis area and generating shear stress in the blood vessels. If it turns out that pulastile flow in blood vessel, it was possible to apply shear stress to blood vessels without using the instrment, it can prove that advantage of maintaing similar conditions as in the body is to specifically prevent blood vessel stenosis and thrombosis

Background

The extracorporeal membrane oxygenator (ECMO) is device that maintain blood gas concentration and blood circulation in patients with severe cardiopulmonary disease. Due to the recent rise expectancy and viruses such as COVID-19, The application cases of ECMO are steadily increasing. At this time, using a pulsatile pump can be Set similar condition , rather than using a non- pulsatile pump to flow through the heart, can be maintained the organ function longer. To assume that the coronary artery is subjected to the same shear stress and pressure as the actual cardiac ejection. We have developed a technique for ejecting pulsatile blood flow that is more similar to the pressure graph of the coronary artery. the extruded pulsatile blood flow was compared with the form of blood flow using roller pump and continous pump, and quantitatively evaluated for same preload as the same diameter.

Methods

Figure.1 shows the setting for circulation of the pulsatile pump. A blood circulation section composed of a compliance chamber and a reservoir system for preload and afterload setting, it is separated into sections for operating and has an inner diameter of 3mm and an outer diameter of 4mm. It passes through and circulates. The shear stress inside the tube is then measured through a pressure sensor at the end of the circulating tube. and air pressure using an actuator are compressed into sections for operating. The pulsatile flow is created by generating pressure from the blood sac inside the acrylic with an actuator, and the bpm is adjusted to at least 60bpm to 120bpm, and One way valve is mounted at the beginning and end part to prevent backflow in the process of generating pulsatile blood flow

We used the logic table of the NAND gate to obtain desire bpm, In this experiment, the motor driver used to control the BLDC motor inside the actuator. The signal of the FET was modulated to control the speed of the BLDC motor to pwm by connecting the logic circuit TC4469 to three bottom FETs. Due to the characteristic of NAND gate, a signal of pwm inversely proportional to the speed of the BLDC motor is displayed. All control signals generated by MCU are Arduino IDE(Using Arduino Mega 2560 REV3), the speed of the BLDC motor and the volume of air per time wer controlled.

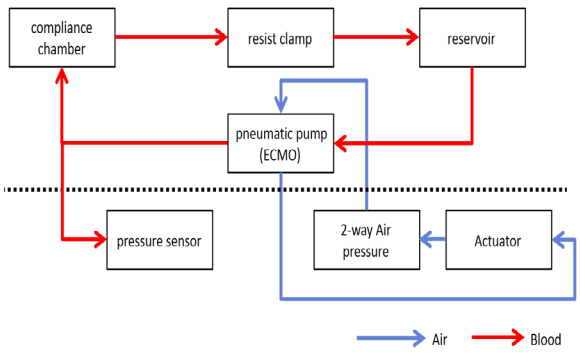


Figure 1. The mechanism of pulsating pump, block diagram.

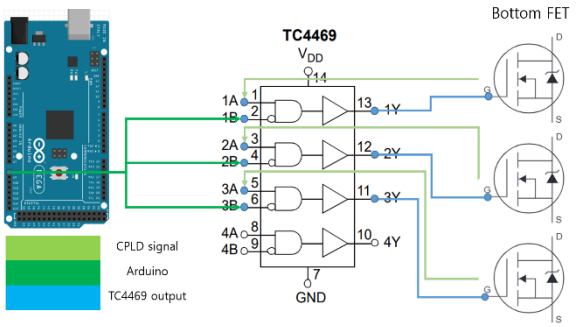


Figure.2 Three bottom MOSFET signals connected to TC4469 controlled to a NAND gate

To verify the fluctuation of pressure, It was graphitized using a temperature compensation type pressure sensor. preload, afterload, and resist clamp are all the same state to check difference in pressure form between the pulsatile pump and another pump. it was set and pump was replaced. the performance of the pumps at this time was all the same at 0.2 L/min. This verification was through an ultrasonic flowmeter(DEXCOM Transonic T4O3, Flowprobes) The output of the roller pump and the continuous pump

Results and Discussion

Fig. 3(a) shows that the stroke of actuator can be controlled separately from the bpm in accordance with the control of Arduino Mega, the MCU. This also affects the flow rate, but the shear stress of the target blood vessel. It is possible to create a pulsatile blood flow controlled by form. In the case of coronary arteries, the experiment was conducted in 64% area for polyethylene tube with an average inner diameter of a 4.7mm in the left main coronary artery (LMCA). The

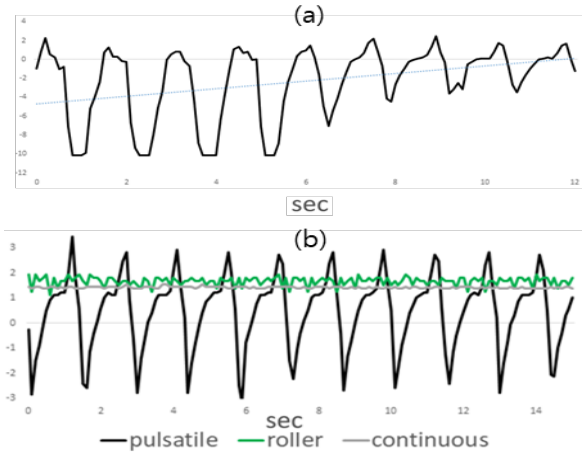


Figure.3 (a) controlled actuator air pressure graph (b) pump pressure shape form

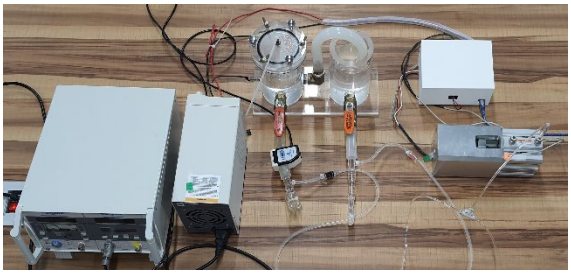


Figure.4 Blood flow reservoir to form the same experimental conditions

unit of pressure at this time was mmHg, it was measured in the section after the pulsatile blood flow passed one way valve. Figure 3(b) shows the pressure form of individual pump. The pressure of pulsatile pump be seen largest fluctuation, followed by the roller pump and the continuous pump. Under the same reservoir pressure conditions,Assuming that the blood pressure waveform is 120mmHg to 80mmHg, the most similar pressure waveform to the coronary artery was pulsatile pump, and the roller pump has relatively similar pattern to the continuous pump due to its low pressure fluctuation.

Acknowledgements

This work was supported by the Korea Medical Device Development Fund grant funded by the Korea government (Project Number: KMDF_PR_20200901_0159-2021-02)

References

1. SCHOEBEL, F. C., et al. Relevance of hemostasis on restenosis in clinically stable patients undergoing elective PTCA. Thrombosis research, 2008, 122.2: 229-236.

2. BELL, Robert M.; MOCANU, Mihaela M.; YELLON, Derek M. Retrograde heart perfusion: the Langendorff technique of isolated heart perfusion. Journal of molecular and cellular cardiology, 2011, 50.6: 940-950.

Machine learning-based cardiac output estimation using non-invasive photoplethysmogram in off-pump coronary artery bypass surgery

C. A. Callejas Pastor[1], C. Oh[2], B. Hong[2,*] and Y. Ku[1,*]

[1] Department of Biomedical Engineering, Chungnam National University College of Medicine, Daejeon, Korea
[2] Department of Anesthesiology and Pain Medicine, Chungnam National University College of Medicine, Daejeon, Korea
*koho0127@gmail.com, yunseo.ku@cnu.ac.kr

Abstract

Cardiac output (CO) monitoring is important for hemodynamic management in patients undergoing surgery. However, currently available methods for CO monitoring such as pulmonary artery catheter using thermodilution technique has limited clinical applicability due to its invasiveness. This pilot study with 19 patients aimed to investigate the feasibility of machine learning-based CO estimation using non-invasive finger photoplethysmogram (PPG) signals. When applying an exponential Gaussian process regression model with the selected features of the representative PPG signals, the correlation and root-mean-square error compared to the reference values were 0.93 and 0.75 (L/min), respectively.

Introduction

Hemodynamic monitoring plays an important role in the management of critical and major surgical patients. (1). With the development of technology, non-invasive monitoring devices have been introduced, expanding the scope of application of hemodynamic monitoring, and increasing clinical utilization. (2) photoplethysmogram (PPG) signals are widely used for non-invasive applications. (3) Although many previous studies on blood pressure estimation using PPG have already been performed, there are still few studies on cardiac output (CO) estimation. In particular, clinical studies on surgical human patients are very scant. The study aimed to develop and evaluate machine learning-based CO estimation models using PPG signals obtained from patients undergoing cardiac surgery.

Materials and Methods

This retrospective study was approved by the Institutional Review Board of the Chungnam National University Hospital (IRB No. 2019-08-039) and written informed consent form patients was waived. Nineteen subjects undergoing off-pump coronary artery bypass surgery (OPCAB) from February 2021 to September 2021 were included. The demographic information of subjects is listed in Table 1. Reference CO values by continuous thermodilution technique with a 7.5 F Swan-Ganz continuous cardiac output thermodilution catheter (HemoSphere advanced monitoring platform, Edwards Lifescience, Irvine, CA) and non-invasive finger PPG signals with a patient monitor (Intellivue MX800, Philips, Boeblingen, Germany) were obtained simultaneously. Data were integrated by a computerized data acquisition software called Vital Recorder. (4)

Demographic information

Age	62.42 ± 11.75 years
Gender	15 (male), 4 (female)
Height	158.67 ± 9.67 cm
Weight	66.15 ± 10.56 kg

Table 1 Demographic information

The overall development process including data pre-processing, feature extraction, machine learning model development, and performance evaluation was performed using MATLAB 2021a (Mathworks, Natick, MA). On the pre-processing stage, 125 Hz sampled PPG data was divided into windows of one minute (total 4877 windows) and each window contained a representative CO reference value obtained by the gold standard catheter method. Following this process, a bandpass filter (0.4 – 8 Hz), an averaging filter, and detrending process (DC offset removal) was applied to the signal. For each window, a representative PPG wave was extracted by first finding all peaks of the PPG signal and then obtaining a mean PPG signal. Noisy or missing data was discarded from the analysis. After this, a feature selection process was performed by neighborhood component analysis using the original, first, and second differentiate PPG signals. A total of 26 features such as kurtosis, skewness, and mean values were extracted. For the machine learning model development, the data was divided into a training and

validation set with 16 subjects (3956 windows, 81.11%) and a testing set with 3 subjects (921 windows, 18.89%). A 5-fold cross validation method was applied for the validation process. The exponential Gaussian process regression is a non-parametric Bayesian algorithm that predicts variance under Gaussian assumptions, which is that data points with similar input values will tend to be close in the output space (5). The signal standard deviation (σ_f) and the characteristic length scale (σ_l) of the exponential kernel were tuned during training session. For two different predictor values x_i and x_j ($i \neq j$, $i = 1, 2, ..., n$), the basic exponential kernel with parametrization vector θ is defined as follows:

$$k(x_i, x_j|\theta) = \sigma_f^2 \exp\left(-\frac{r}{\sigma_l}\right) \quad (1)$$

where r represents the Euclidean distance between x_i and x_j.

Results

Figure 1 shows an example of the representative PPG wave extracted on a one-minute length window.

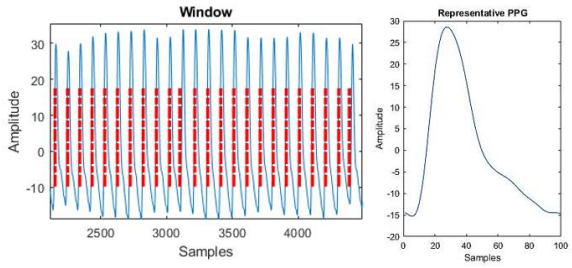


Figure 1 One-minute window PPG (left) with detection of PPG waves (red lines), and a representative PPG (right).

The trained Gaussian process regression model had a signal standard deviation of 4.32 and a customized length scale for each predictor. The results of the CO estimation of both training and test sessions are shown in Figure 2.

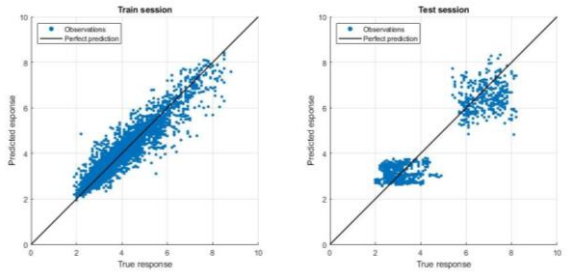


Figure 2 CO reference vs. model estimation result in training (left) and test (right) sessions (unit: L/min).

Table 2 shows the evaluation results of various metrics. In the test session, correlation and percentage error of prediction were 0.93 and 0.021, respectively. R2 and RMSE values were 0.86 and 0.75, respectively.

Metrics	*Training session*	*Test session*
Correlation	0.931	0.930
PE	0.00074	0.021
R-squared	0.87	0.86
RMSE	0.44	0.75

Table 2 Estimation performances

Discussion

In the present study, we proposed a machine learning-based CO estimation method using non-invasive PPG wave analysis. The results using 19 OPCAB patients demonstrate a strong relationship between reference and estimated CO values. The OPCAB is characterized to have a large dynamic variation of CO, which was advantageous to develop the estimation model. With this novel approach, our results showed that non-invasive CO monitoring using finger PPG is feasible. A deep learning approach can be applied with more data collection for future work. In addition, different types of surgical data can further broaden the scope of the proposed approach.

Acknowledgements

This work was supported by the Korea Medical Device Development Fund grant funded by the Korea government (the Ministry of Science and ICT, the Ministry of Trade, Industry and Energy, the Ministry of Health & Welfare, Republic of Korea, the Ministry of Food and Drug Safety) (Project Number: KMDF_PR_20200901_0144, 9991006817).

References

1. Shoemaker WC, Thangathurai D, Wo CCJ, et al. Intraoperative evaluation of tissue perfusion in high-risk patients by invasive and noninvasive hemodynamic monitoring. *Critical Care Medicine*. 1999;27(10):2147-2152.
2. Ameloot K, Palmers PJ, Malbrain ML. The accuracy of noninvasive cardiac output and pressure measurements with finger cuff: a concise review. *Curr Opin Crit Care*. Jun 2015;21(3):232-9. doi:10.1097/mcc.0000000000000198
3. Wang C, Huang C, Ye S. Noninvasive cardiac output monitoring system based on photoplethysmography. 2014:669-673.
4. Lee HC, Jung CW. Vital Recorder-a free research tool for automatic recording of high-resolution time-synchronised physiological data from multiple anaesthesia devices. Sci Rep. 2018 Jan 24;8(1):1527. doi: 10.1038/s41598-018-20062-4
5. Caywood MS, Roberts DM, Colombe JB, Greenwald HS, Weiland MZ. Gaussian Process Regression for Predictive But Interpretable Machine Learning Models: An Example of Predicting Mental Workload across Tasks. Front Hum Neurosci. 2016;10:647.

P-089

User needs analysis for multi-purpose smart neonatal incubator

H.K. Choi[1], S.E. Park[1] and W.S. Jang[1*]

[1]Department of Medical Device Engineering & Management, Yonsei University, Seoul, Korea

[*]W.S.JANG@yuhs.ac

Abstract

The neonatal incubator is an important medical device of life support, as the survival rate of low birthweight and preterm infants. In this study, we combine multiple functions such as warmer, patient monitoring with ECG, NIBP, SpO2, RESP, TEMP, phototherapy to neonatal incubator. We expect that this newly designed incubator, multi-purpose smart incubator, can improve workflows in NICU. In order to reduce risk and improve patient safety, it is important to incorporate user human factors into the medical device design process. In the human factors engineering process, it is recommended to make user population participate in user interface design and evaluate the device. To define industrial design needs, participatory design was applied gathering user preferences on design elements of neonatal incubators. Our research identified user needs and preferences for multi-purpose neonatal incubator. Human factors engineers translated those into functional and design needs as design inputs for the design process.

Background

Preterm infants are defined as babies born alive before 37 weeks of pregnancy are completed. An estimated 15 million infants were born preterm worldwide and this number is rising [1]. The neonatal incubator system that is central to the care of ill and/or pre-term infants in NICU such as physiological monitors, mechanical ventilators, and medication pumps [2]. It is an important medical device as the survival rate of low birth weight and preterm infants. After the first usage for maintaining thermal stability in preterm infants, little has changed in fundamental design [3]. Recently the way and environment of neonatal intensive care have been transformed into patient and family oriented and developmental oriented. Various functions such as warming using a radiant warmer, SpO2 monitoring have been added to traditional incubator. Additional functions, patient monitoring with ECG, NIBP and phototherapy, can be combined with existing incubators. Also, artificial intelligence can be adopted to help infant's developmental care and analyzing vital signs.

Methods

In order to reduce risk and improve patient safety, it is important to incorporate human factors into design process. According to IEC 62366-1, Figure 1 shows Human Factors Engineering (HFE) Process and User-Centered Design (UCD) cycle [4], [5]. In the HFE process, it is recommended to make user population participate in user interface design and evaluate the device. Especially, early consultation with user population is essential to assess needs and developing needs. Thus, HFE approaches are applied to identify user needs in accordance with HFE process and UCD cycle.

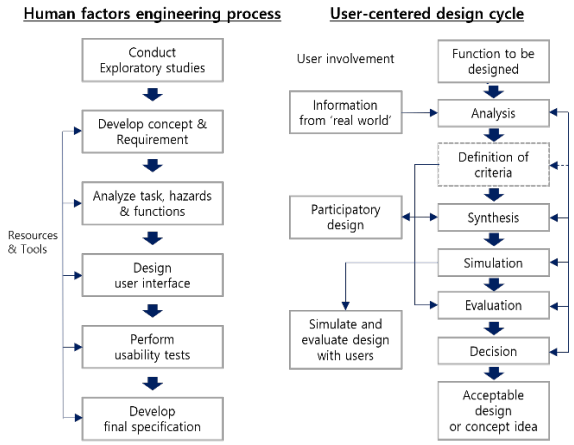


Figure 1. HFE process – UCD cycle

Brainstorming sessions and an online survey were conducted as methods to assess user needs for designing multi-purpose neonatal incubator. 37 medical staffs of NICU at Severance hospital participated. Human factor engineers analyzed user needs derived from the brainstorming session and translated into functional needs. The online survey aimed to assess importance and frequency of functions derived from user needs.

Results and Discussion

Applying IEC 62366-1 and UCD cycle, we used usability method such as expert reviews, function analysis, participatory design, literature. Participation of individuals from the user population is integral to HFE process [4]. The human factors integration in the design process of medical devices is crucial to reduce and provide the patient safety.

Table 1 shows user needs of smart neonatal incubator which are obtained by brainstorming sessions. One of the common needs related to weight measurement.

Table 1. User needs of neonatal incubator

Category	User Needs
Device	Bed tilting
	Location & shapes of hand port
	Storage space for X-ray plate
Humidity	Type of water tank of humidifier – bag type (like IV fluid bags) vs. bottle type
Monitor	Displaying vital signs on the incubator monitor as well as basic information for incubator operations
	Location of alarm indicator (LED) on the monitor
Weight	Weighing without lifting infants up from the mattress

Table 2 shows the results of the survey about incubator design preference. The survey used to apply the participation method. The survey was conducted to assess importance and frequency of functions derived from user needs. The survey consisted of 10 physicians and 25 nurses. Their career period ranges from 1 year to more than 10 years. Their average career period is 6.3 years. The important thing in incubator design is in order of function, usability, space efficiency and aesthetics. The importance of function and usability is almost the same.

Table 2. Survey result of neonatal incubator design

Category	User Preferences
Alarm indicator (Location)	Top of the monitor (82.4%)
	Better visuality
Canopy (Shape)	Flat top, wide bottom (80.7%),
	Easy to observe
Bed tilting (Controls)	Button (85.7%)
	Less chances to press wrong buttons than with touchscreen
Drawer (Shape)	2-tier drawer (54.5%)
	Different height between two tiers
Water bottle (Location)	Front middle (60.6%)
	Easy to check the residue

Bed tilting was one of the user needs founded in brainstorming sessions. Regarding controls, it was founded that users prefer hard keys (physical buttons) rather than soft keys (graphical buttons on touch screens). They pointed out that there are chances to press incorrect buttons on the screen without recognition.

To design better medical devices, it is important to understand specific user needs and preference of the device. In this study, user needs are analyzed and identified as design inputs for the multi-purpose smart neonatal incubator which combines several devices including a warmer, a patient monitoring system, a phototherapy. Designing new incubator is in progress reflecting the user needs in accordance with human factors principles.

Acknowledgements

This work was supported by the Korea Medical Device Development Fund grant funded by the Korea government (the Ministry of Science and ICT, the Ministry of Trade, Industry and Energy, the Ministry of Health & Welfare, the Ministry of Food and Drug Safety) (Project Number: KMDF_PR_20200901_0057-2021-03)

References

1. WHO, Preterm birth, https://www.who.int/news-room/fact-sheets/detail/preterm-birth (accessed on Oct 13, 2021)
2. Thomas Ferris and Mardelle Shepley, “A Multidisciplinary Human-centered Approach to the Design of Incubation System”, AR Andre (Chair), Symposium on Human Factors and Ergonomics in Health Care, 187-192, 2012
3. Ferris, T. K., and M. M. Shepley. "The design of neonatal incubators: a systems-oriented, human-centered approach." Journal of Perinatology 33.1 (2013): S24-S31.
4. IEC 62366-1 Medical device- Part1 Application of usability engineering to medical devices,2015
5. Van der Peijl, Jorien, et al. "Design for risk control: the role of usability engineering in the management of use-related risks." Journal of biomedical informatics 45.4 (2012): 795-812

Applying Human Factor Engineering Methods for Risk Analysis of the Breast Imaging Diagnostic System

J.Y. Jeong[1], S.E. Park[1,] W.S. Jang*

[1]Department of Medical Device Engineering & Management, Yonsei University College of Medicine, Seoul, Korea

***W.S.JANG@yuhs.ac**

Abstract

Mammography is the main pillar of breast cancer screening programs. Additionally, women with density breast tissue should be performed with a supplemental breast ultrasound. In this study, the purpose of this study is to make a safe medical device by exploring the use errors of this device and identifying and evaluating the risk factors through the usability problem. Usability issues of ABUS (automated breast ultrasound) were gathered from FDA's MAUDE (manufacturer and user facility device experience) and Recall database. As a risk factor for ABUS, there was no limit to the intensity of the compression paddle, and as a risk factor for DBT (digital breast tomosynthesis), it was a result of not considering the suitability of foot switch or C-arm. To solve the issues found in MAUDE, it is necessary to evaluate and plan in the development stage and establish an appropriate plan to make a safe fusion device.

Background

Mammography is a fundamental technique for breast cancer screening. However, sonography is recommended for a patient with dense breast tissue. There are limitations of traditional hand-held ultrasound such as examiner-dependency, long time for examination and interpretation. To overcome these problems, ABUS was developed. Because ABUS is indicated to use as an adjunct to mammography for breast cancer screening, there have been attempts to combine these two devices in a single device. During the examination the patient´s position is not changed between mammography and ABUS, so these are performed in the same projection as standing position [1].

This device to be developed is combined with ABUS & DBT, which has similar appearance and scanning procedures with mammography system. To improve patient safety and usability of the combination device, risk analysis related to usability errors was conducted in the early phase of the design process [2]. Main users, frequent tasks and major usability problems are also identified in this study prior to conduct risk analysis. Prioritizing human factors is imperative to decrease the occurrence of design flaws, eliminate or reduce use-related hazards. This ultimately ensures safe outcomes for end users of medical devices.

Methods

PMS data are needed to identify and analyze known problems and to identify known or foreseeable hazards and hazardous situations based on Annex B: External resources to identify known problems of IEC TR 62366.-2:2016. The PMS databases seek to guide manufacturers on using the FDA's MAUDE and Recall databases to gain knowledge about usability issues and develop safer devices. The MAUDE database contains adverse event reports that involve end user interactions with medical devices known as medical device reports. These adverse events describe suspected device-associated deaths, serious injuries, and malfunctions, with a wide range of causes such as usability issues. The FDA Recall database provides information about medical devices that are defective or otherwise pose a health risk and describes how manufacturers are responding to these issues [3].

Post-market surveillance data provide informative resources for usability-related improvements. In this study, usability issues of ABUS were gathered from FDA's database using product code for 'PAA(ABUS)' and 'OTE (DBT)'. Usability issues are categorized and analyzed according to risk management approach.

Results and Discussion

Considering the results of this study can contribute to improve usability and make a safer device that may reduce medical errors. Table 1 shows some examples of ABUS from MAUDE database are that patient rib injuries or breast silicone fluid leaks due to compression settings and scanning techniques during breast scans [4].

Looking at the following results, it is related to the intensity of breast compression, and there is no limit to the pressure during breast compression. To remove

such risk factors, it is necessary to set a limit value by placing a limit on the intensity of the compression, so that the pressure should be applied only up to that intensity.

Table 1. Summary of ABUS use-related issues found in the FDA's MAUDE database

The 1st main issue			
Date	2015.03.25	Type	Injury
Device Problem	Fluid leak		
Patient Problems	No information		
Brand Name (Manufacturer)	INVENIA SCAN STATION ABUS (GE)		
The 2nd main issue			
Date	2018.09.08	Type	Injury
Device Problem	Adverse event without identified device or use problem		
Patient Problems	Bone fracture(s)		
Brand Name (Manufacturer)	USYSTEMS INVENIA GEN2 (U-SYSTEMS, INC.)		

Table 2 also shows the summary of use-related risk analysis in DBT. Total 492 device problems related usability were searched [5]. Among the events resulting from human-device interaction, events leading to harm are summarized. By referring to the data obtained through these events, it can be used to reduce the risk related to usability by reflecting and evaluating the design.

Table 2. Summary of DBT use-related issues found in the FDA's MAUDE database

Harm	**Event**
Pain	The techs was injured by a loose foot switch pedal sliding out from under their foot
	Sore shoulder: the c-arm continued to rotate
Bruise/contusion	The patient was pinched between the c-arm and the chair
	Soft muscle tissue bruising (C-arm lowers after the foot pedal was released)
Burning sensation	The patient was unable to find any discoloration on the array or the array cover if the array had gotten that hot
Bone fractures	Fall: the patient had difficulty holding on to 'grooves' on dimensions system, lost balance, fell and broke a hip during acquisition of DBT.

As a result of searching ABUS & DBT in the recall database, there were no recalls related to usability, but recalls related to device defects.

Considering the results of this study can contribute to improve usability and make a safer device that may reduce medical errors. Further studies will also be performed through cognitive walkthrough, PCA analysis, and task analysis to analyze potential use errors for breast imaging diagnostic system.

Acknowledgements

This work was supported by the Korea Medical Device Development Fund grant funded by the Korea government (the Ministry of Science and ICT, the Ministry of Trade, Industry and Energy, the Ministry of Health & Welfare, the Ministry of Food and Drug Safety) (Project Number: KMDF_PR_20200901_0001-2021-04)

References

1. Benedikt Schaefgen, Joerg Heil, et al. "Initial results of the FUSION-US prototype combining 3D automated breast ultrasound and digital breast tomosynthesis", European Radiology (2018) 28:2499–2506
2. Jiajie Zhang, Todd R. Johnson, et al. "Using usability heuristics to evaluate patient safety of medical devices," Journal of Biomedical Informatics 36 (2003) 23-30.
3. Teresita C. Liebel, Tara Daugherty, et al. "Using the FDA MAUDE and Medical Device Recall Database to Design Better Design", Biomed Instrum Technol (2020) 54 (3): 178–188.
4. Food and Drug Administration. TPLC - Total Product Life Cycle: PAA https://www.accessdata.fda.gov/scripts/cdrh/cfdocs/cfTPLC/tplc.cfm?id=5641&min_report_year=2006 (accessed at 10/1/2021)
5. Food and Drug Administration. TPLC - Total Product Life Cycle: OTE https://www.accessdata.fda.gov/scripts/cdrh/cfdocs/cfTPLC/tplc.cfm?id=5640&min_report_year=2006 (accessed at 10/1/2021)

P-091

Design of Expandable High-Power Ultrasound Transducer Driving System Control Unit

J. H. Park[1] , S. Y. Lee[2] and J. Seo[1]

[1]Department of Biomedical Engineering, Yonsei University, Wonju, Korea

[2]Healcerion, Seoul, Korea

wn9609@yonsei.ac.kr

abstract

In this study, we aim to design an expandable High-Power Ultrasound Transducer Driving System Control Unit that can adjust the output amplitude for each channel based on PWM using low-cost FPGA. The system is composed of one Master Board and several Slave Boards, and each board was subdivided into modules by function. The subdivided modules implemented their functions with Verilog HDL and were evaluated through simulation. As a result of the simulation, it was confirmed that the pulse was output according to the input data such as Delay time, P-on time, P-off time, N-on time, and N-off time. 64-channel was implemented per one Slave Board, and it is expected that at least 1536-channel of the driving system can be realized when connecting additional Slave Boards.

Background

Ultrasound is used in various medical fields such as imaging diagnosis, surgery, rehabilitation, and drug delivery. High-intensity focused ultrasound(HIFU) is a treatment using heat generated by ultrasound energy and is used as a treatment that can recover quickly after treatment and minimizes side effects [1]. HIFU is a method of inducing tissue necrosis by concentrating ultrasound energy on tissues and raising the temperature of the area to 60°C or higher in a short period of time [2]. In the past, transducers with only one channel were widely used, but this requires adjustment using a mechanical method to change the location of the focal points during treatment, and it is difficult to treat large lesions due to the small size of the focal points. Therefore, most of them currently use multi-channel transducers. Accordingly, the driving system for these various multi-channel transducers needs to be designed to have a high degree of freedom in the number of channels and frequency control.

This study designed an expendable high-power transducer driving system control unit using Field Programmable Gate Array(FPGA) to drive multi-channel transducer more effectively in HIFU treatment. This system was designed to receive data from PC and give time delay to each channel so that the number and size of focal points could be controlled electronically and to adjust the amplitude of the energy output for each channel by adding PWM. The FPGA used in this study is XC7A35T-1FGG484C (Xilinx, US) allowed 64-1536 channels to be selected.

Methods

This system consists of a single Master Board and 64-channel unit Slave Boards, each modularized according to its function. Each module was implemented as Verilog HDL that could perform its function using Xilinx's Vivado program. The maximum operating frequency of the FPGA used is 484MHz, which requires at least 32 times the clock to give an appropriate delay, allowing it to be operated even with a transducer with a frequency of up to 15MHz [3]. However, since the frequency generally used in HIFU is less than 5MHz, we applied a system frequency of 200MHz.

Master Board exchanges data with PCs using FT245RQ(Future Technology Devices, International Limited, UK), which provides USB to parallel FIFO interface. Data entered through USB is processed by Master Control, as shown in Figure 1. and moved to the Sub Interface and Register File(Regfile). Meanwhile, data from the Regfile is also transferred back to the PC through Master Control so that data can be evaluated externally. Sub Interface selects which Slave Board to operate through the input data and exchanges data to and from the selected Slave Board.

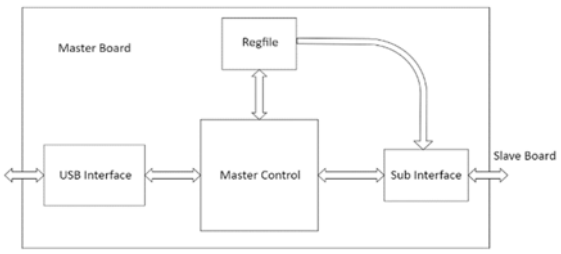


Figure 1. Master Board block diagram

Each Slave Board has 64 channels, and it is designed to allow additional expansion of channels by increasing the number of Slave Boards. In the Slave Interface of the selected Slave Board, data is exchanged with the Master Board, as shown in Figure 2. Data is later transferred to the Slave Regfile and the Pattern Memory(PM). The Slave Regfile stores the received data as 16 pattern tables, and each table contains four pattern information, so a total of 64 patterns can be stored. The patterns contain data on PRF, Duty, PWM and Delay time output through PM. This information is transmitted to Pattern Control and automatically determines whether to proceed to the next pattern. In addition, Slave Regfile selects and transmits the pulse type data(positive pulse first, negative pulse first, or single pulse only) at the final pulse output terminal to the Pulse Channel. This design enables selection among the type of analog amplifiers and driving methods to be added in the future. The Pattern Control sends the pattern to be executed through the pattern address received by the Regfile to the Pattern Memory Control (PM Ctrl), and when the transmission is over, the trigger signal is sent to Pulse Channel to operate it. Meanwhile, the PM processes the input data into information on the output pulse of each channel, such as PWM, Duty, and Delay time, and transmits the information to the PM Ctrl. The PM Ctrl transmits the received pulse information to the Pulse Channel, and when the Pulse channel receives a trigger, it finally outputs the pulse according to the pulse type received from Slave Regfile.

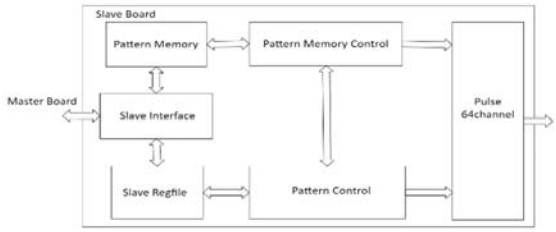


Figure 2. Slave Board block diagram

Result and Discussion

We simulated the written code and checked whether each board was operating normally. First, we proceeded with the simulation one by one and confirmed that each module was operating normally, and then the simulation was conducted by grouping two to three modules connected in the intermediate stage. As the final functional evaluation, we conducted the simulation in units of Master Board and Slave Board.

The simulation result for the Master Board is shown in Figure 3. First, when transmitting data from a PC, three data packets consisting of 16 bits are transmitted. The first 16 bits are Header information, 16'h ff5a, and then input the address and data in order. As a result of Figure 3, when the Header is input twice, 8 bits each, and becomes 16bits, rxf becomes low, and the Header is input. Then, incoming data 8'h 3f and 8'h e0 are input, and the top 2 bits are changed to 0, so 16'h 203f is input to sub1_addr_o. Finally, when the input data 8'h ff and 8'h 03 become sub1_we_o 1, it can be confirmed that 16'h 03ff data is input to sub1_data_io. Sub_sel_o is the value for selecting a Slave Board, and it can be seen that Slave04 is selected.

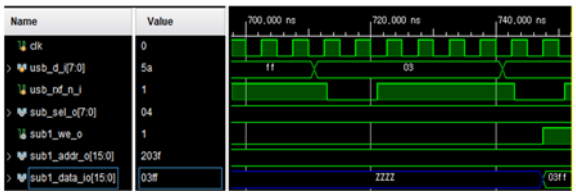


Figure 3. Master Board simulation result (As usb_rxf_n_i becomes low, sub1_we_o becomes 1, and data is entered.)

Slave Board selects which parameters to put data, such as Delay time, P-on time, P-off time, N-on time, and N-off time for each channel, through a 16-bit address, and the selected parameter has an input 16-bit data value. Figure 4 shows the results after entering an arbitrary value, and it can be seen from the input data that when the pulse type is positive pulse first, and when trigger(trig_prf) is in a high state, the positive pulse is 'ON' as much as P-on time and 'OFF' as much as P-off time, and then the negative pulse operates in the same way. After the trigger becomes high, the first pulse becomes 'ON' after 10ns than the input Delay time due to the delay occurring during the module operation.

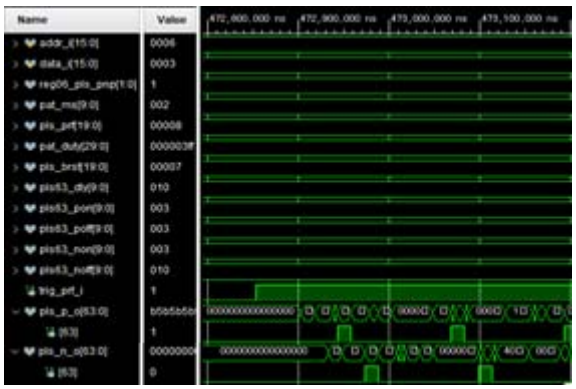


Figure 4. Slave Board simulation (Based on channel63, which is part of the entire channel, it can be confirmed that Delay time: 16*5ns (system clock), P-on time: 3*5ns, P-off time: 3*5ns, N-on

time: 3*5ns, N-off time: 16*5ns.)

As a result of the simulation of the Master Board and Slave Board, it was confirmed that when any address and data were entered, the results corresponding to the values were obtained, and the hardware functionality will be finally tested by implementing the driving system of the designed control unit in the future.

Acknowledgements

This work was supported by a National Research Foundation of Korea (NRF) grant funded by the Korean government. (MSIP) (2020R1A2C1008995)

Reference

1. Zhou YF. “High intensity focused ultrasound in clinical tumor ablation.” World J Clin Oncol, 2(1), 8-27, 2011.
2. Kennedy JE. “High-Intensity focused ultrasound in the treatment of solid tumours.” Nat Rev Cancer, 5(4), 321~327, 2005
3. Wang H, Ebbini E and Cain C A. “Effect of phase errors on field patterns generated by an ultrasound phased-array hyperthermia applicator.” IEEE Trans. Ultrason. Ferroelectr. Freq. Control. Vol. 38, No. 5, 1991

P-092

A study on the development of parallel robot for laparoscopic surgery

Y.J. Heo[1] and G.S. Jeon[1]

[1]Digital Health Care Research Center, Gumi Electronics & Information Technology Research Institute, Gumi, Korea

geumsang@geri.ac.kr

Abstract

The delta robot has the advantage that it can perform high-rigidity and high-precision work as a structure in which a plurality of legs support a mobile platform, and can have a high payload compared to a serial robot. Therefore, in this paper, we applied the delta robot to laparoscopic surgery to develop a delta robot with 7 degrees of freedom (translation, roll, pitch, yaw), and studied a laparoscopic collaboration robot that can replace simple repetition and continuous action.

Background

Serial robots used in most industrial sites have the advantage of being able to move flexibly with wrists and having a large work area, but they have a relatively heavy screwdriver attached to each joint, and the volume. There are drawbacks such as large size, limited high-speed movement, and low payload. On the other hand, the delta robot has the advantages of high payload, high rigidity, and high accuracy because the manipulator is supported by a large number of legs by the parallel robot [1]. In this paper, we designed a delta robot in a small size to minimize interference in laparoscopic surgery, and by operating the mechanism by one person, it is a simple operation that assists surgical instruments such as cameras. I would like to research a laparoscopic collaboration delta robot that can reduce the waste of human resources by replacing continuous actions repeatedly.

The kinematics of the delta robot

Fig.1 shows a kinematics diagram (diagram) showing the parameters of the delta robot for kinematics calculations. The following delta robot equation generates three vector loop closure equations in the kinematics diagram [2].

$$\{^{B}B_i\}+\{^{B}L_i\}+\{^{B}I_i\}=\{^{B}P_P\}+[^{B}_{P}R]\{^{P}P_i\}=\{^{B}P_P\}+\{^{P}P_i\} \quad i=1,2,3$$

$$[^{B}_{P}R]=[I_3]$$

I:

$$I_i=\|\{^{B}I_i\}\|=\|\{^{B}P_P\}+\{^{P}P_i\}-\{^{B}B_i\}-\{^{B}L_i\}\| \quad i=1,2,3$$

If you square both sides of the above constraint expression to avoid the square root in Euclidean norms:

$$I_i^2=\|\{^{B}I_i\}\|^2=i_{ix}^2+i_{iy}^2+i_{iz}^2 \quad i=1,2,3$$

Here, the kinematic equation of the delta robot is calculated using the following three constraint equations.

$$2L(y+a)\cos\theta_1+2zL\sin\theta_1+x^2+y^2+z^2+a^2+L^2+2ya-l^2=0$$

$$-L(\sqrt{3}(x+b)+y+c)\cos\theta_2+2zL\sin\theta_2+x^2+y^2+z^2$$

$$+b^2+c^2+L^2+2xb+2yc-l^2=0$$

$$L(\sqrt{3}(x-b)-y-c)\cos\theta_3+2zL\sin\theta_3+x^2+y^2+z^2$$

$$+b^2+c^2+L^2-2xb+2yc-l^2=0$$

Here, the kinematic equation of the delta robot is calculated using the following three constraint equations.

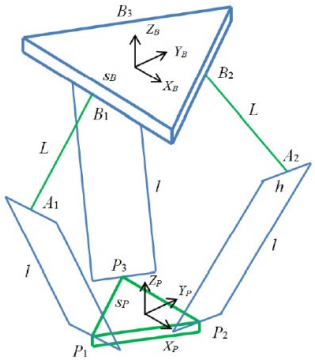


Figure.1 Delta robot kinematic diagram

Manipulator drive motor selection

The legs of the Delta Robot have x, y, and z translations by three motors connected to a fixed platform, and the specifications of the motors determine whether or not the Delta Robot is driven. It is possible to calculate the angular velocity and acceleration of the joint connected to the robot's foot operated by the output torque of the motor, and by utilizing the design of the Delta robot, including the weight of each part and the connected center of gravity. I calculated some variables. At this time, AL6061 is applied as the material of the parts that make up the robot, the weight of the robot is calculated, and the required torque that the motor can output is calculated in order to select the motor required for the operation of each leg that makes up the delta robot. Calculated.

Design of laparoscopic surgery robot

Figure.2 shows a laparoscopic surgery robot that applies the form of a delta robot for high rigidity and accuracy. The position between the platforms was changed to apply the shape of the existing Delta robot to laparoscopic surgery. The joint of each robot arm is designed to apply the existing rod end bearing in order to secure the rotation angle, and changed to the design to apply the knuckle joint to minimize the interference of the parts that make up the robot. Designed the shape of the robot's legs. Bearings were placed at each joint to minimize the load of motor torque due to rotational resistance and designed for miniaturization for laparoscopic surgery.

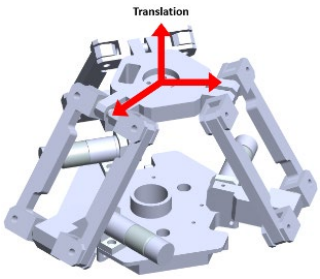


Figure.2 Design of delta robot for laparoscopic surgery

Results and Discussion

As shown in Fig.3, the maximum required torque for driving the Delta robot is calculated at 141 Nm, and the motor to output that torque was selected. In addition, the laparoscopic collaboration robot has x, y, and z translation 3 degrees of freedom, and the drive handle has roll, pitch, yaw, and grip 4 degrees of freedom, which is the movement of the wrist required for laparoscopic surgery.

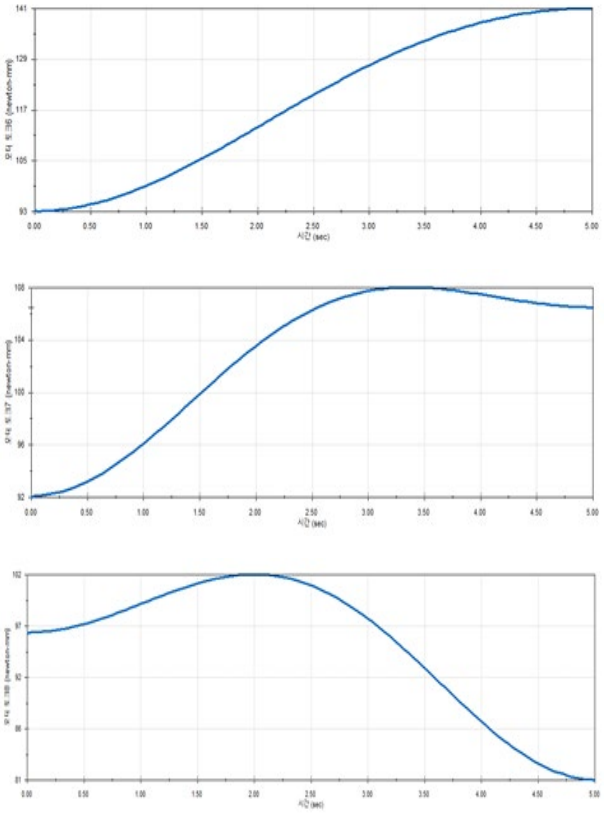


Figure.3 Calculate the required torque for the motor

Acknowledgements

This work was supported by Korea Evaluation Institute of Industrial Technology(KEIT) grant funded by the Korea Government(MOTIE) (20008821, Development of laparoscopic surgical collaborative assistive robot system comprising slave assistive robots for unconstrained placement of instrument and camera and a master assistive robot for the assistance of a surgeon.)

References

1. Tae-wook Kim, Han-sung Kim, “Development of a Delta-type Parallel Robot for High Speed Applications”, Institute of Control, Robotics and Systems, Vol. 2013, No. 5, 2013.
2. M. A. Laribi, L. Romdhane, and S. Zeghloul, “Analysis and dimensional synthesis of the DELTA robot for a prescribed workspace”, Mechanism and Machine Theory. 42, 859-870 (2007).

Design and Simulation of a Laparoscopic Surgical Robot by using the 3-DOF Parallel Robot

G.S. Jeon[1] and Y.J. Heo[1]

[1]Digital Health Care Research Center, Gumi Electronics & Information Technology Research Institute, Gumi, Korea

geumsang@geri.re.kr

Abstract

In this study, we developed a laparoscopic surgical robot by using the delta-type three-degree-of-freedom parallel robot. The parallel robot has higher rigidity and precision compared to the serial robot because several links are connected in a parallel structure and the load is shared on the links. Therefore, we designed delta-type parallel robot for laparoscopic surgery and performed simulations for verification the workspace of the robot.

Introduction

A surgical robot refers to a robot that automatically works on behalf of a doctor in part or the whole of the surgical process, works together with a doctor's control, or assists the doctor with haptic or image technology to increase the efficiency and effectiveness of surgery [1]. Surgical robots are largely divided into soft tissue surgical robots and hard tissue surgical robots. A soft tissue surgical robot is a laparoscopic surgical tool that performs operations such as incision and suturing of body tissues. The best-known system of a soft tissue surgical robot is Intuitive Surgical company's DaVinci. A hard tissue surgical robot is used to operate on bones in orthopedic or dental surgery and Stryker company's Mako is a representative of artificial joint surgery for knee and hip joints.

Machine tools used as manipulators in robots are mainly classified into series and parallel types [2]. The serial-type robot has a wide working area and good mobility, but it has many joints and links repeatedly connected, so its rigidity and load capacity are relatively low. The parallel-type robot which has a parallel structure with several links has higher rigidity and precision compared to the serial-type robot, but it has a limited working space due to its structure.

In this study, we designed a delta-type parallel robot for laparoscopic surgery and verified a workspace of the surgical robot by simulation.

Design and Verification

Figure. 1 shows a laparoscopic surgery robot that applies the form of a delta robot for high rigidity and accuracy. The joint of each robot arm uses a knuckle joint for the rotation angle and the shape of the robot arm is designed to minimize the interference of parts. Bearings were placed at each joint to minimize the load of motor torque due to rotational resistance and designed for miniaturization for laparoscopic surgery. The revolute joint point connected to the fixed base was designed to be constant at the base frame and the universal joint point connected to the moving platform was designed to be constant at the base frame.

In addition to avoiding excessively localized energy at proximal fiber, the convex lens was moved along the y- axis.

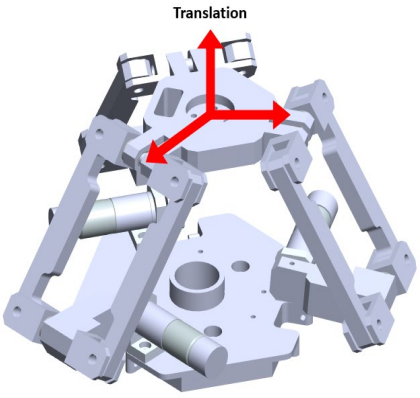


Table. 1 shows the main parameters of the robot designed by the kinematic analysis of the delta robot.

Table 1. Dimensions of the surgical robot.

name	meaning	value (mm)
s_B	base equilateral triangle side	162.97
s_P	platform equilateral triangle side	76.21
L	lower legs length	45
l	upper legs parallelogram length	90
h	upper legs parallelogram width	12
w_B	planar distance from {0} to a near base side	47
u_B	planar distance from {0} to a base vertex	94.1
w_P	planar distance from {P} to near platform side	22
u_P	planar distance from {P} to a platform vertex	44

Simulation was performed with Matlab to verify the robot's workspace using the parameters of the designed surgical robot. Figure. 2 shows the simulation results for the workspace.

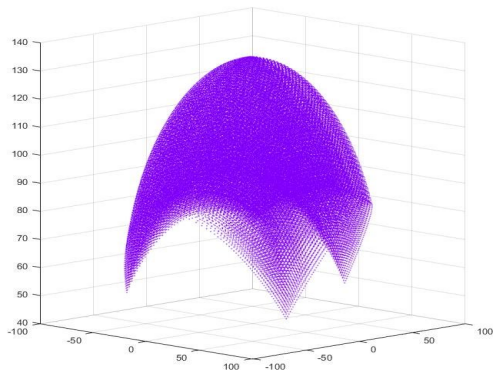


Figure 2. Simulation result of the workspace

Results and Discussion

In this study, we designed a delta-type parallel robot for laparoscopic surgery and simulated its working space. We demonstrated a limited workspace of a delta-type parallel robot due to its structural features. Based on our results, we indicated that the improvement of the workspace of a delta-type parallel robot is necessary for laparoscopic surgery..

Acknowledgements

This study was supported by Korea Evaluation Institute of Industrial Technology(KEIT) grant funded by the Korea Government(MOTIE) (20008821, Development of laparoscopic surgical collaborative assistive robot system comprising slave assistive robots for unconstrained placement of instrument and camera and a master assistive robot for the assistance of a surgeon).

References

1. W. J. Lee, “Current status and Competitiveness of Robot Surgery in Korea,” The Korean Hospital Association, 36(6), 64-74(2007).
2. Y. Y. Cha, “Parallel Robot with the developments,” Journal of Institute of Control, Robotics and Systems, 15(1), 22-28(2009).
3. X. J. Liu, J. S. Wang, K. K. Oh, J. G. Kim, “A New Approach to the Design of a DELTA Robot with a Desired Workspace,” Journal of Intelligent and Robotic Systems, 39, 209-225(2004).
4. L. Krystian, W. Piotr, K. Tomasz, G. Daniel, “Kinematic design of parallel delta system in Matlab,” Applied Mechanics and Materials, 844, 7-12(2016).
5. S. H. Jeong, G. S. Kim, G. M. Gwak, H. S. Kim, “Development of a Novel 3-DOF Hybrid Robot with Enlarged Workspace,” The Korean Society of Industry Convergence, 23(5), 875-880(2020).

Design of magnetic Traction clip for colonoscopic Perforation Suture.

S.E. Kim[1], C.H. Jung[1], Y.J. Kang[1], Y.H. Jung[2], Y.H. Jeon[1], M.G. Lee[1*]

[1]Department of Mechanical Engineering, Ajou University

[2]Instisute for Digestive Research, Soonchunhyang University College of Medicine

moonglee@ajou.ac.kr

Abstract

Perforation may occur when performing polypectomy and submucosal dissection using colonoscope and its tool. When the perforation occurs, suturing is performed using endoscopic clips. However, it is difficult to suture large perforations larger than a certain size due to the geometric limitations of the clip. In this research, we tried to propose a method for suturing large perforations by adding a permanent magnet to the existing endoscope clip to facilitate suturing through magnetic force. The size of magnet allows it to be inserted into an endoscopic working channel, and the magnitude of magnetic force is higher than 0.8N so that the magnet can tract circumferential tissue of a perforation with diameter larger than 15mm. To confine magnetic flux in the clip, yokes made of a material through which magnetic flux flows well was added to the upper and lower portions of the magnets. The magnetic punt of the device with magnets and yokes was analyzed and its force was predicted using a finite element analysis tool, Ansys maxwell. To confirm the applicability of the device, an experiment was conducted with endoscopists on swine colon. As a result of the experiment, it was verified that the proposed device reduced the width of large perforation by pulling two circumferential side of the perforation. After such traction, it was possible to proceed the suture with conventional clips. It is expected that the device can be widely applied to endoscopic suture for the large perforation.

Background

Endoscopic surgery is non-invasive, that the patients expect the quick recovery. The physicians also cannot on a better prognosis. Among them, colonoscopy is a useful tool for diagnosing and treating colon diseases. Sometimes, a perforation occurs during the diagnosis and treatment. This may lead to the patients suffering or medical disputes, requiring prompt treatment. If the perforation happens, serious complications such as peritonitis and sepsis may occur due to leakage of serous fluid and feces. [1] Small perforations less than 15 mm can be treated endoscopically, but large perforations lead to laparoscopic or open surgery. [2] The surgical operation takes longer time than endoscopic surgery as well as slows patient recovery. In our previous study, a traction clip that can pull and suture colon perforation tissue for non-invasive treatment was proposed. [3] By combining a magnet with a general endoscope clip, the diameter of the perforation can be partially reduced. If the diameter decreases after the primary traction, the secondary suture is performed using the general endoscope clips. In this study, the magnetic force for the traction was optimized so that the magnetic clips could maintain its state while the perforation is sutured.

Methods

In the previous study, a device capable of tracking a large perforation was designed by combining an existing endoscope clip with a rectangular magnet. However, the rectangular magnet cannot be applied to the conventional endoscope. Because it could not be inserted into endoscopic working channel. In this study, the shape of the magnet was modified to a circular shape and optimized through a finite element analysis. Yokes are added for magnetic flux confinement. In the previous study, a magnetic force of 0.8 N or more was specified to tract the two circumferential sides of large perforations with a diameter of 15 mm or more through an experiment. [3] Magnetostatic field analysis was performed using Ansys Maxwell to confirm the magnetic force. Fig. 1 is a model that combines magnets and yokes. The left assembly of a magnet and upper a lower yoke is for one clip. The right assembly is the case when it tracked. The magnetization directions of the two magnets are set opposite to each other. The total height (H) of the magnet and the yokes was fixed at 6 mm, and the distance (D) between the magnets was set at 0.1 mm considering a bonding agent to assemble the parts. For accurate analysis, the finite element was mashed in the size of 0.2 mm. The magnets are made of NdFe50, and their coercive force is 14 kOe. Yoke uses steel 1008.

As a result, the traction force of about 1.3N. During an actual fabrication, some errors are engaged due to the bonding agent and material properties of magnet and yoke. However, because the device made generates a sufficient magnetic force, it was determined that the traction of the organs could be achieved even though the large perforation occurred. The magnetic clip is harmless to human body because it is removed with a foreign body forceps after the traction and suture. Each part of the clip is assembled with ultra-violet cured adhesive which is harmless to human body. Figure 2 show two fabricated magnetic traction clips. They have tracked each other.

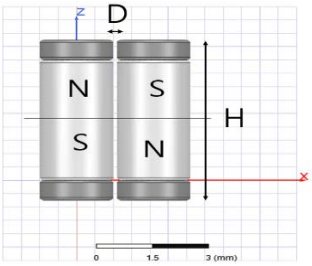


Figure 1. Finite element modeling



Figure 2. Fabricated traction devices

Results and Discussion

To confirm the applicability of the device, an experiment was conducted with gastroenterologists at Soonchunhyang University, Cheonan. The experiment was performed on swine colon. The simulated large perforation with a diameter of 20 mm was made randomly. The fabricated magnetic clips were fixed to both circumferential tissues of the perforation. The diameter of the perforation was partially reduced by the magnetic force of the device. Fig. 3-(a) shows the reduced diameter of the perforation after primary traction. Afterwards, secondary sutures were performed with a general endoscopic clip. Fig. 3-(b) shows the completely sutured perforation. Air was injected into the large intestine to confirm the closure. Fig.4-(a) and Fig.4-(b) show the air injected into the large intestine inflated without leakage. Through this, it can be confirmed that the suture of the perforation is well made. The size of large perforations is significantly reduced with only a pair of the proposed magnetic clip.



(a) (b)

Figure 3. (a) Primary traction
(b) Secondary suture



(a) (b)

Figure 4. (a) Colon before suturing with air leakage
(b) Colon after suturing without air leakage

By applying this study, it is possible to prevent the fatal complications such as peritonitis and sepsis by a large perforation. Because it does not lead to surgical operations such as laparoscopy, and open surgery it can be expected to have cosmetic advantages, shorten the recovery period, and reduce treatment costs. It is thought to be applicable not only to perforation of the colon, but also perforation of the stomach and duodenum during endoscopic procedures.

Acknowledgements

This work was supported by the Ajou University research fund.

References

1. Damore, L. J., Rantis, P. C., Vernava, A. M., & Longo, W. E. (1996). Colonoscopic perforations. Diseases of the colon & rectum, 39(11), 1308-1314.
2. Olympus EndoTherapy instructions. Tokyo: Olympus, 2004, p. 3.
3. C. H Jung, H. J. Choi, B. J Choi, B. H. Lee, S. H. Lee, M. S. Hong, Y.H. Jeon, M.G. Lee. (2019). Magnet design of endoscopic clip for large perforation suture.Proceedings of the Conference of KSMTE , 103 - 103.

P-095

Development of a system capable of diagnosing and treating Alzheimer's disease: a technique experiment using cadaver

E.B. Park[1,2] , J.C. Heo[1] , C.H. Kim[1] , S.M. Kwon[1] and J.H. Lee[1]

[1] School of Medicine, Keimyung University, Deagu, South Korea

[2]Inception LAB., Daegu, Korea

segeberg@kmu.ac.kr

Abstract

In this study, the following experiments were performed: improvement of memory and cognitive functions through hippocampus stimulation, investigation of treatment effects in Alzheimer's disease, development of a loop system-based electronic drug for simultaneous diagnosis and treatment of Alzheimer's disease using a closed-loop system based on pupil tracking. A new application method was proposed by confirming the clinical applicability of an implantable sensor in a cadaver experiment.

Background

Brain-derived neurotrophic factors (BDNF) affect specific neurons in the central and peripheral nervous systems, promoting the growth and differentiation of new neurons and synapses. BDNF is also involved in expression, learning, and memory functions in the hippocampus, cerebral cortex, and basal ganglia nucleus. In particular, BDNF is an important factor in long-term memory, and an increase in its expression helps stimulate and regulate neural development. An increase in BDNF also helps improve social and cognitive functions. To date, various studies have been conducted to increase the expression of BDNF using light.

Methods

A. Expression of BDNF by PBMT and confirmation of the related treatment mechanism in Alzheimer's disease

The expression and signaling pathway of BDNF, a memory-related factor, were identified in the hippocampus by PBMT (660 nm). The antioxidant activity of PBMT and related genes, glutathione peroxidase, superoxide dismutase 1, and glutathione reductase were also identified. Furthermore, PBMT was used to determine the optimal time and output conditions for BDNF expression in the hippocampus.

B. Non-invasive digital marker in computer diagnostic processing for Alzheimer's disease

Neurodegenerative diseases, including Alzheimer's disease, have pre-symptomatic stages that can develop several years before obvious clinical symptoms, which are related to eye movement and occur due to amyloid-β deposition (pigmentation) in the inner plexiform layer, RGC layer, nerve fiber layers, and outer nuclei according to studies on Alzheimer's disease transgenic models. The pupil response is associated with brain damage in Alzheimer's disease. A new neural decision tree was studied for tracking of microsaccades along with an algorithm for tracking of pupil expansion.

C. Application of techniques using PMBT sensors in patients

For the PBMT sensor to reach the hippocampus, an anatomical approach for the insertion of the sensor in the human body was developed through a cadaver experiment: a small incision was placed at the temporal lobe to remove the bones adjacent to the eye.

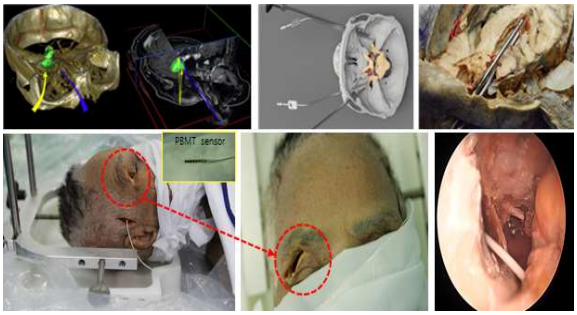


Figure 1. Surgical anatomical experiments for sensor application

Results and Discussion

In this study, treatment was performed by inserting a PBMT sensor directly into the human body and applying infrared or near-infrared rays (600-1,100 nm) and irradiating light energy into the hippocampus. In addition, a diagnostic method was suggested; this method uses a unique non-contact digital marker based on the analysis of microsaccades with a high-speed camera and computer vision algorithm. In particular, the multidimensional analysis data of the digital marker was transmitted to the PBMT sensor inserted into the human body and used as an optical parameter to obtain a closed-loop system that can produce an optimal treatment effect by stimulating the hippocampus directly. This paper suggests appropriate techniques related to the anatomical insertion of the PBMT sensor, its location, and sensor fixation for an optimal treatment effect while discussing its validity.

Acknowledgements

research was supported by Basic Science Research Program through the National Research Foundation of Korea(NRF) funded by the Ministry of Education (NRF-2017R1D1A1B04031182).

References

1. AlGhamdi, K. M., Kumar, A., & Moussa, N. A. “Low-level laser therapy: a useful technique for enhancing the proliferation of various cultured cells.” Lasers Med Sci, 27(1), 237-249. doi:10.1007/s10103-011-0885-2, (2012).
2. Kourtis, L. C., Regele, O. B., Wright, J. M., & Jones, G. B. Digital biomarkers for Alzheimer’s disease: the mobile/wearable devices opportunity. NPJ digital medicine, 2(1), 1-9, (2019).
3. Martinez-Conde, S., Otero-Millan, J., & Macknik, S. L. The impact of microsaccades on vision: towards a unified theory of saccadic function. Nature Reviews Neuroscience, 14(2), 83-96, (2013).
4. Crutcher, M. D., Calhoun-Haney, R., Manzanares, C. M., Lah, J. J., Levey, A. I., & Zola, S. M. Eye tracking during a visual paired comparison task as a predictor of early dementia. American Journal of Alzheimer's Disease & Other Dementias®, 24(3), 258-266, (2009).
5. Becker-Krail, D., Farrand, A. Q., Boger, H. A., & Lavin, A. Effects of fingolimod administration in a genetic model of cognitive deficits. Journal of neuroscience research, 95(5), 1174-1181, (2017)..

Performance evaluation of magnetic carrier controller for corneal endothelial cell transfer

B.G. Park[1], H. Lee[2], C.M. Hwang[3] and S.W. Choi[1]

[1]Department of Mechanical & Biomedical Engineering, Kangwon National University, Chuncheon, Korea

[2]Department of Ophthalmology, Asan Medical Center, University of Ulsan College of Medicine, Seoul, Korea

[3]Department of Convergence Medicine, University of Ulsan College of Medicine, Seoul, Korea

swchoe@kangwon.ac.kr

Abstract

Descemet Stripping Automated Endothelial Keratoplasty (DSAEK) is a surgical procedure in which a corneal endothelial tissue is inserted anterior chamber between the cornea and the iris, and then transferred to the correct position on the lower surface of the cornea. It is difficult to transport the fragile thin tissue to an appropriate location without damage. Instead of sharp conventional surgical tools that can damage tissues, a technology has been developed to transfer magnets attached to tissues using a magnetic field. It was confirmed whether the suggested new method could properly place the transplanted tissue into the rabbit's eye under anesthesia. In addition, it was also confirmed whether the transplanted tissue could be moved to an appropriate position after insertion in the eyes of a monkey's excised post-mortem.

Background

Descemet Stripping Automated Endothelial Keratoplasty (DSAEK) is one of the corneal endothelial transplantation procedure, in which a thin corneal endothelial tissue is inserted to anterior space between the cornea and the iris and adhered to the underside of the cornea where the pre-existing nonfunctional endothelial tissue was removed. Although the endothelial tissue is thin as 20~50 μm, wide as 10 ~ 12 mm diameter and difficult to move to the correct location without damage, it is frequently applied because of better prognosis compared to other procedures [1-3]. Due to the difficulty of the DSAEK operation, few doctors can perform the operation, and the operation takes 1 to 2 hours, longer time than other procedures. Recently, a technology for moving and transplanting a cell using magnets attached to the cell has been developed, so it is necessary to apply this technology to DSAEK. Techniques to transport magnets by controlling magnetic fields can replace the sharp forceps used in DSAEKs, despite the risk of damaging the tissue.

Methods

As shown in figure 1, four coils that generate a magnetic field were installed on the top, bottom, left and right sides, respectively, based on the center where the eye will locates during corneal endothelial cell transplantation. In order to form a high magnetic

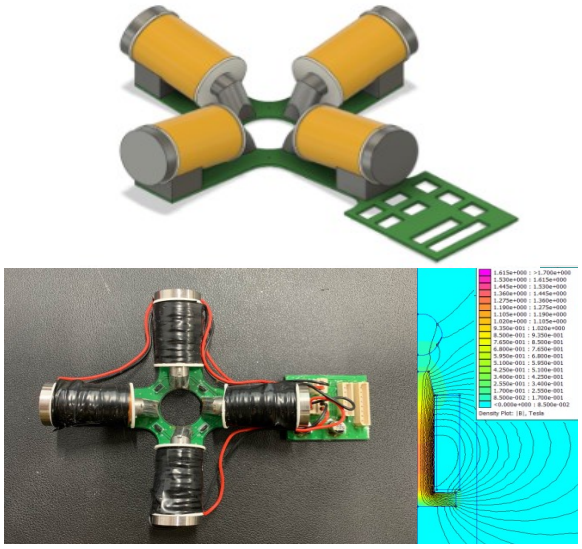


Fig. 1 Magnetic field generator with 4 coils

density, a core made of cobalt iron was installed in the coil. The operator checks the position of the magnet in anterior chamber and uses the joystick to determine the magnets' moving direction and force as shown in figure 2. The control unit selects one or two of the coils and supplies the appropriate amount of current to adjust the direction and strength of the magnetic field. The small magnets forced to move by the magnetic coils are in the form of thin wire made of stainless steel 316L and are attached to the sides of the corneal endothelial tissue to be transplanted, so that the shape

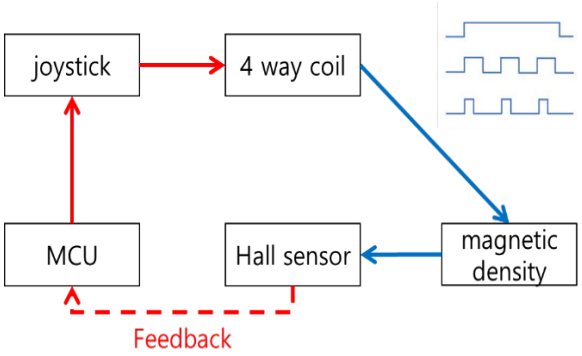


Fig. 2 Block diagram of a magnetic field controller

or size of the magnets is not disturbed when the tissue is inserted into the anterior chamber. When the magnet moves in a specific direction by the magnetic field generated by the coils, the corneal endothelial tissue to which the magnets are attached also moves. Animal experiments with New Zealand White rabbits were performed according to the protocol (2020-12-246) approved by the Animal Experiment Ethics Committee of Asan Hospital. After removing the existing corneal endothelial tissue under anesthesia with Zoletil 15 mg/kg, Rompun 5 mg/kg, a new corneal endothelial tissue was inserted into the anterior chamber. Most of the inserted endothelial tissue unfolded spontaneously in the anterior chamber and was transferred to an appropriate location using the magnetic field generator proposed in this study. After DSAEK, observation was carried out over 3 weeks to see whether endothelial cells were stably transplanted. In order to measure the transport speed of the corneal endothelial tissue by the magnetic field, a camera was installed on the microscope and recorded. The average transport speed and the maximum transport speed were measured using the interval times and the moving distance of the magnets in each consecutively taken photograph. A pulsed magnetic field was supplied to solve the problem of immobilization of endothelial tissue or magnets on the surface of the iris or cornea. An additional experiment was conducted in which corneal endothelial tissue was inserted into the eyes extracted from dead monkeys, and corneal endothelial cells were transplanted using a magnetic field in the same way.

Results and Discussion

The figure 3 shows the inserted endothelial tissue moving in the anterior chamber by magnetic force controlled by the operator. In animal experiments, the

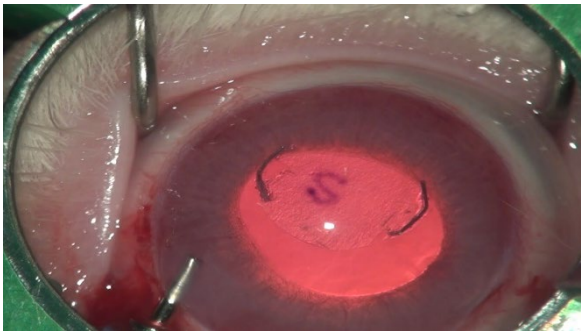


Fig. 3 Animal experiment of DSAEK in a rabbit

endothelial tissues were often immobile because those were attached to the inner surface of the cornea and iris. However, the pulsed magnetic force allowed the tissues to move more easily despite jamming of the surrounding tissue. When a pulsed magnetic field was applied, the endothelial tissue moved faster than when continuous magnetic field was applied. In addition, when the iris was removed from an eye taken from a monkey's cadaver, it became easier to control the movement of the endothelial tissue than before. This shows that the iris is the main cause of endothelial tissue immobilization.

Acknowledgements

This work was supported by the Korea Medical Device Development Fund grant funded by the Korea government (Project Number: KMDF_PR_20200901_0148-2021-02)

References

1. "Borroni, Davide, et al. "Tips, Tricks, and Guides in Descemet Membrane Endothelial Keratoplasty Learning Curve." Journal of Ophthalmology 2021 (2021).

2. "Soma, Takeshi, et al. "New graft insertion device for Descemet stripping automated endothelial keratoplasty." Cornea 36.11 (2017): 1432-1436."

2. "Bahar, Irit, et al. "Busin guide vs forceps for the insertion of the donor lenticule in Descemet stripping automated endothelial keratoplasty." American journal of ophthalmology 147.2 (2009): 220-226."

A development of an emergency automatic ventilator using AMBU Bag

Jong-Hyeok Lee[1], Beom-Seop Park[1], Hyun-Beom Kim[1], Jong-Hoon Lim[2], Yoonseok Yang[1]

[1]Division of Biomedical Engineering, Jeonbuk National University, Jeonju, Republic of Korea

[2]Department of Healthcare Engineering, Jeonbuk National University, Jeonju, Republic of Korea

babase98@jbnu.ac.kr, 201715451@jbnu.ac.kr, dlwhdgur317@jbnu.ac.kr, hun6949@gmail.com, ysyang@jbnu.ac.kr

Abstract

Since the massive spread of COVID-19 around the world, many people have died from this respiratory disease. In particular, due to the lack of ventilator, people with severe respiratory diseases often died because they could not breathe properly[1]. There is strong demand for the development of mass-produced ventilators since the world believes that these respiratory diseases could occur again. The AMBU bag is a simple, light, and low-cost ventilator. Therefore, the development of ventilator using AMBU bags is underway. Most ventilators using AMBU bags adopted robotic arms made of metal or plastic to compress AMBU bags. However, this not only can put a lot of load on the motor and gear, but it also has difficulty in portability. We adopted strings to manufacture ventilators using AMBU bags in our previous study, Now, we present a more advanced form of ventilator using AMBU bag by adopting a new frame that can hold the AMBU bag more stabling. We added a sensor to distinguish the patient's breathing period and encoder to the motor which enables of more reliable compression of the AMBU bag. The proposed ventilator could be a model which can be used to revive emergency patients in daily life as well as another respiratory disease pandemic that may appear in the future.

Background

Commonly used ventilators are less portable because they are large and heavy. In addition, because the ventilator is expensive and it's production period is long, it is not suitable for mass production and use. To overcome this, development of an automatic ventilator using the AMBU bag started, which is an inexpensive and portable manual ventilator.

Figure 1. shows our previous model[2], which mostly consists of a few off-the-shelf components such as an AMBU bag compressed by the winding of a string using a common wiper DC motor. In this study, we tried to prove the practicality of the model by integrating it with a flow sensor and a motor encoder for more accurate operation.

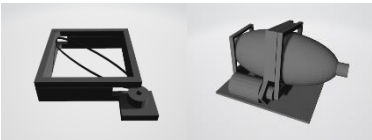


Figure 1. Previous model

Methods

Considering that the tidal volume should not exceed 500ml according to the regulations of the emergency ventilator in the Republic of Korea and that general human inhale volume is 200~300ml, the amount of the motor rotation was adjusted to supply about 250ml for each inspiration. Also, since general human breathing cycle is 4 seconds, the speed of the motor rotation was controlled so that the AMBU bag contracted for 2 seconds and relaxed for 2 seconds.

Figure 2 shows the respirator mask where a flow sensor is installed in the airway so that it can measure the patient's expiratory volume per second.

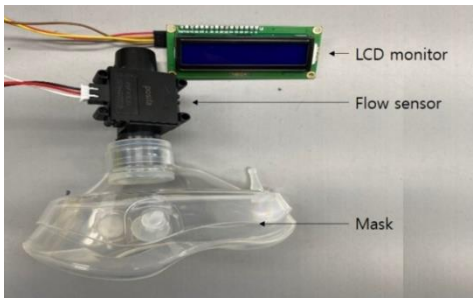
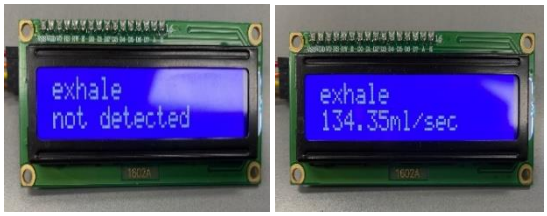


Figure 2. Mask with flow sensor and LCD monitor

The exhalation information and measurement (volume per second) is displayed on a small LCD along the patient's respiration cycle as shown in Figure 3.



(a) (b)

Figure 3. Exhale information on LCD (a) no exhalation detected, (b) exhalation speed

Figure 4 shows a typical graph of exhalation speed measured by the sensor.

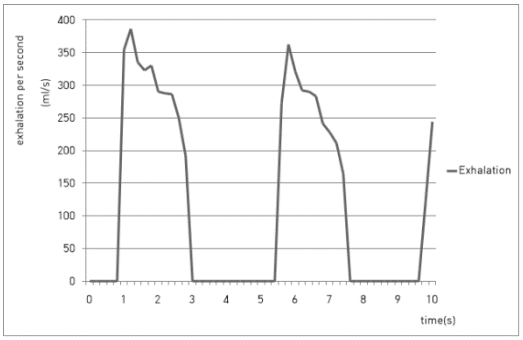


Figure 4. Measured exhalation

Figure 5 shows the 3D-printed frame for the compression of AMBU bag. Frame 1 supports all other devices and Frame 2 supports the AMBU bag. The rotational force of the motor rotates the bobbin to wind the strap. In this process, the rotational force is converted into tension, which compresses the AMBU bag.

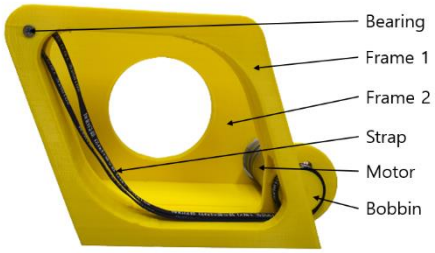


Figure 5. 3D-printed frame for AMBU Bag compression

As the motor rotates, the strap is wound around the bobbin, which causes the strap to contract and pressurize the AMBU bag to supply oxygen to the patient. Then, the motor rotates back to its original position, releasing the strap, and the AMBU bag inflates again, ready to supply oxygen.

Figure 6. shows the developed prototype of an emergency automatic ventilator using AMBU bag. The flow sensor enabled the monitoring of the emergency patient by observing the respiratory cycle and volume. In addition, the motor encoder controlled the tidal volume of the AMBU bag more accurately.

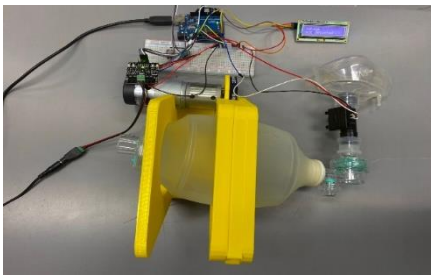


Figure 6. The developed ventilator prototype

Results and Discussion

The experimental results verified that the developed automatic ventilator using the AMBU bag integrated with a flow sensor and a motor encoder can be used in practice. It could supply as much oxygen to the patients as necessay with accurate sensing and precise control of respiratory cycle. Therefor, it is expected to provide customized medical care to patients in case of emergency.

Acknowledgements

This research was supported by Basic Science Research Program through the National Research Foundation of Korea (NRF), funded by the Ministry of Science and Technology Information and Communication. (NRF-2019R1F1A1061503).

References

1. Pia Daniel, Max Mecklenburg, Chanée Massiah, et al, “Non-invasive positive pressure ventilation versus endotracheal intubation in treatment of COVID-19 patients requiring ventilatory support”, The American Journal of Emergency Medicine, vol. 43, pp. 103 – 108, 2021
2. Kim H, Park B, Lee J, Lim J, Yang Y, “A novel design of emergency automatic ventilator using AMBU bag”, KIEE workshop, vol. 2021, No. 4, pp. 92 - 93, 2021

Development of mapping catheter for arrhythmia interventional procedure

H. Kang[2] and C. Hwang[1,2]

[1]Department of Convergence Medicine, Asan Medical Center, South Korea

[2]Department of Convergence Medicine, University of Ulsan College of Medicine, South Korea

hwang.changmo1@gmail.com

Abstract

A mapping catheter used for diagnosing an arrhythmic heart is a medical device that provides electro-anatomical information of the heart through tiny electrodes located at the tip of the catheter. A mapping catheter is a medical device used for electrode catheter ablation, a treatment for arrhythmias, and helps to understand the ECG information generated in the heart in real time. It is contributing greatly to the diagnosis and treatment of electrode catheter ablation by understanding the mechanism of arrhythmia along with the patient's disease information. The catheter inserted into the heart shortens the time it takes to diagnose according to the number of channels that can measure the electrocardiogram at the same time. This research team tried to secure a method for manufacturing a 64-channel mapping catheter with a basket deployment method for the development of an independent mapping catheter.

Background

Arrhythmia is a disease in which the heart beats abnormally or irregularly because the electrical impulses that cause contraction and expansion of the heart are not made well or the stimulation is not transmitted properly [1]. A general treatment is electrode catheter ablation, which uses a small action catheter to deliver high-frequency energy to the area where the arrhythmia has occurred to block the electrocardiogram nerve inside the heart tissue. Before and during electrode catheter ablation, a diagnostic catheter is used to obtain electrocardiographic information inside the heart and to determine the location of the arrhythmia [2]. The diagnostic catheter realizes the electro-anatomical information of the heart as a three-dimensional image structure in real time, and is used as an important tool for understanding and diagnosing the mechanism of arrhythmia, as well as for electrode catheter ablation treatment. Most of the diagnostic catheter electrodes are 4, 8, 12, and 20 channels, and the 64-channel diagnostic catheter developed by Boston Scientific is a product designed to enable three-dimensional diagnosis and mapping in a short time. It has the advantage of saving time. The goal of this study is to secure a manufacturing method for a 64-channel mapping catheter, a high-quality diagnostic catheter in Korea, and to secure the original technology by solving the shortcomings of the existing manufacturing method.

Methods

The difficulty in this study is that when manufacturing a 64-channel mapping catheter, as many wires as the number of electrodes are drawn in, it is difficult to assemble. Also, avoid affecting the wires adjacent to each other. To solve this problem, we applied a flexible PCB (FPCB) made of polyimide film and placed 64 electrodes and wires.

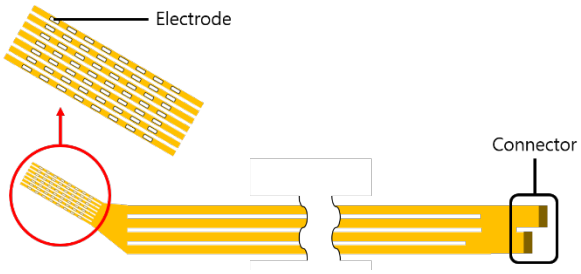


Figure. 1 Flexible PCB(FPCB)

At this time, a PCB board with a Hirose 35-pin connector (FH62-34S-0.25SHW) attached was manufactured so that the signal transmitted from the FPCB electrode could be received.

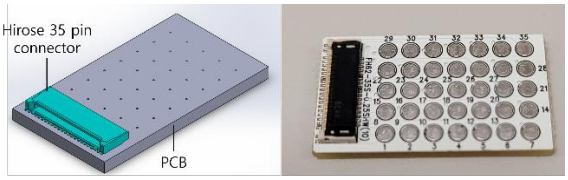


Figure. 2 PCB connector

The fabricated FPCB was wound around a metal tube using a heat gun and an electric drill, reduced to a size that can be put in a shaft tube with an inner diameter of 8.4Fr, and inserted into the shaft tube to confirm assembly feasibility.

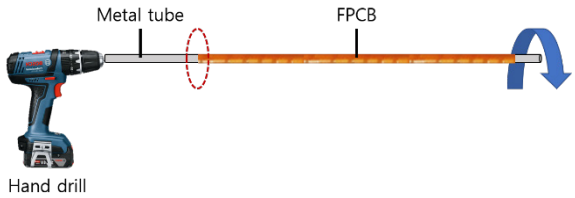


Figure. 3 Production process

In addition, in order to check whether each electrode is disconnected from the wire or some wires during the winding or insertion process, the PCB is connected to the FPCB and each connection number is checked.

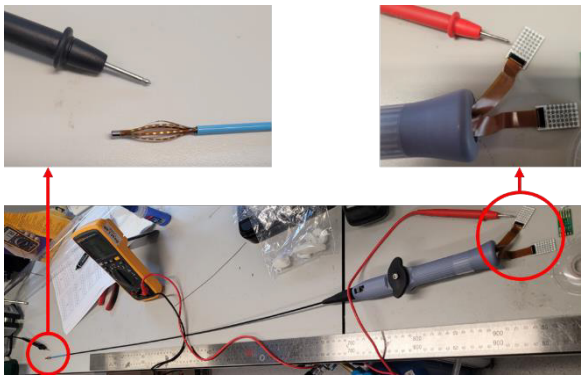


Figure. 4 Check electrode and PCB connection

Finally, by manipulating the deployment device of the handle, it was checked whether it was deployed in the form of a basket.

Results and Discussion

As a result of the manufacturing test, it was confirmed that the FPCB could be inserted into the shaft tube without any problem in the tube with an inner diameter of 8.4Fr. And as a result of checking the PCB number corresponding to each electrode using a multimeter, it was confirmed that there was no problem except for 14 electrodes. Since the absence of a signal from the 14 electrodes is a problem that occurred during the manufacturing process, it is judged that there is no problem if attention is paid. Finally, it was confirmed that there was no problem in electrode deployment by controlling the deployment device of the handle.



Figure. 5 Electrode deployment

Afterwards, we plan to conduct additional research and development to enable steering of the electrode part by adding a steering device.

Acknowledgements

This research was carried out with the support of the Ministry of Health and Welfare's Health and Medical Research and Development Project (HI14C0517).

References

1. "What Is Arrhythmia?". http://www.nhlbi.nih.gov. July 1, 2011. Retrieved 7 March 2015.
2. Y. Tanaka, M. Genet, L. C. Lee, A. J. Martin, R. Sievers, and E. P. Gerstenfeld. “Utility of high-resolution electroanatomic mapping of the left ventricle using a multispline basket catheter in a swine model of chronic myocardial infarction,” Heart Rhythm, 12(1), 144-154 (2015).

The noise removal by stationary wavelet transform filter in the phase contrast X-ray image using the instantaneous frequency

Jae-Suk Yang[1*] Myung-Joon Kwack[2], Sooyeul Lee[2], and Jang-Hwan Choi [1*]
[1] Division of Mechanical and Biomedical Engineering, Ewha Womans University, Seoul, Republic of Korea
[2] Medical Imaging Research Section, Electronics and Telecommunications Research Institute (ETRI), Daejeon, Republic of Korea
*corresponding author: mung07@empas.com
*corresponding author: choij@ewha.ac.kr

Abstract

We propose the extraction of the phase contrast X-ray image (PCXI) using the instantaneous frequency. The proposed method is that the row image is converted into the image with the instantaneous frequency values for the derivative of unwrapped phase of the 1D complex signal by Hilbert transform and the image multiplied by the conversion constant can be induced to the image with the phase derivative value. The merit of the proposed method can evade the loss of detailed information in an image by Fast Fourier transform (FFT) filtering and the error of the retrieved phase by 2D phase unwrapping. To remove the noise, we use the stationary wavelet transform filter (Matlab^{TM}). As a result, in comparison with the conventional x- ray images by FFT, we obtained the detailed and clear PCXI image by the instantaneous frequency.
Keyword: Phase contrast X-ray image, Instantaneous frequency, Fast Fourier transform, and Stationary wavelet transform filter

Background

Phase contrast X-ray imaging is a new biomedical and diagnostic method with a high resolution and real-time measurement. In general, compared to conventional X-ray absorption image, the phase contrast X-ray image by the imaging provide clear and detailed bio information. Thanks to this advantage, the phase contrast X-ray imaging is widely used in various fields such as medicine, substance analysis, and biological analysis **[1]**.

As a representative method, Wen et al. provided a way to simultaneously obtain three images: X-ray absorption, scattering (dark file image), and phase contrast X-ray images. Here, the X-ray absorption image provides information on a physical quantity of the product of the absorption and thickness of the object. The scattering image provides the detailed structure of the micro-unit in a sample. Meanwhile, the phase contrast X-ray image emphasizes the boundary of tissue by a difference of refractive index in a sample. Among the three images, the phase contrast X-ray image can show a detailed and clear internal structure of the sample without noise **[2]**.

However, in Figure 1(a) (top), the phase contrast X-ray image by Wen et al. can be obtained by Fourier transform and spatial frequency filtering. If the amplitude distribution of the sample on a spatial frequency is the superposition of the center peak (0st peak) and the first peak (1st peak), we cannot apply the filtering by Wen et al. in spatial frequency. In addition, to obtain a phase value, if wrapped phases by $\tan^{-1}$ are shown, we must use a 2D phase unwrapping algorithm. In general, a 2D phase unwrapping algorithm may cause many errors in reconstructed phases **[3-5]**.

In order to avoid a spatial frequency filtering and phase unwrapping algorithm mentioned above, we propose an acquirement of phase contrast X-ray image using instantaneous frequency. Figure 1(b) (bottom). To eliminate the noise of the phase contrast X-ray image by upper method, we introduce the stationary wavelet transform filter function in Matlab^{TM} and filtered phase contrast X-ray images by setting variables of the filter function are provided.

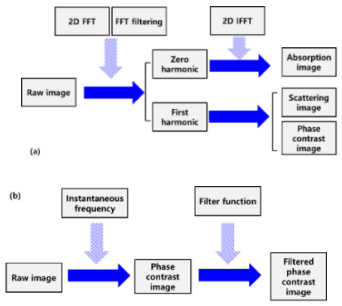


Figure 1. (a) FFT (top) and (b) proposed method (bottom) Flowchart.

Equipment setup and method

As shown in Figure 2, an equipment configuration is as follows. The X-ray source is driven under conditions of 22kVp, 630/exp., and 20mA. The local spot size of the source is 100 mm. The grid G0 has a grid pitch of 0.118 mm (215 dpi). The detector has a pixel size 7um and 3840 X 3072. The arrangements of the equipment components are SOD: 500 mm, SDD: 700 mm, and SGD: 1448 mm. The sample is an anchovy (Engraulis japonica).

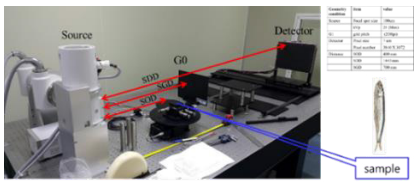


Figure 2. Equipment setup

Acquisition of the phase contrast X-ray image using instantaneous frequency is as follows. First, we transform the one-dimensional signal of the image into the Hilbert transform. Next, the one-dimensional signal and its Hilbert signal are combined to become complex signals and the phase of the complex signal is obtained by $\tan^{-1}$. We obtain a 1D unwrapped phase signal by the 1D phase unwrapping phase function. We can obtain the instantaneous frequency by multiplying a gradient of the unwrapped phase with a proportional constant [5]. The filtering process is as follows. We use the stationary wavelet transform filter function provided by Matlab^{TM}. The setting conditions of this study are wname = 'db3', lev = 3 **[6]**.

Result and discussion

As images to be compared with the proposed images in this study, Figure 3(a) X-ray absorption image, (b) scattering, and (c) FFT phase contrast X-ray images are presented in Figure 3. The X-ray absorption image Figure 3(a) well shows bone and internal tissue through the information of absorption and thickness. However, at an outer boundary between air and fin, the outer boundary of the scattering image Figure 3(b) and the FFT phase contrast X-ray images Figure 3(c) appears more unclear than that of the X-ray absorption image in Figure 3(a). In addition, the two images Figure 3(b) and (c) provide overlap of noise and internal structure.

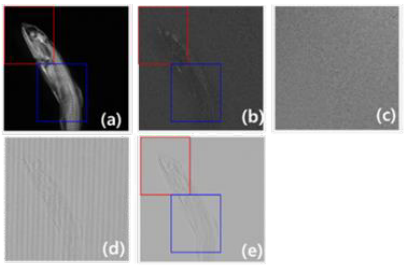
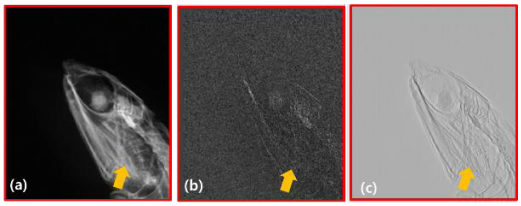


Figure 3. Images by FFT and instantaneous frequency methods. FFT method: (a) absorption, (b) scattering, (c) FFT phase contrast X-ray image, and Instantaneous frequency method: (d) original phase contrast X-ray image by instantaneous frequency and (e) filtered image of (d).

Meanwhile, compared with the original phase contrast X-ray image by instantaneous frequency Figure 3(d), the filtered phase contrast X-ray image by instantaneous frequency Figure 3(e) clearly shows the vertebrae of the anchovy and other internal structures.



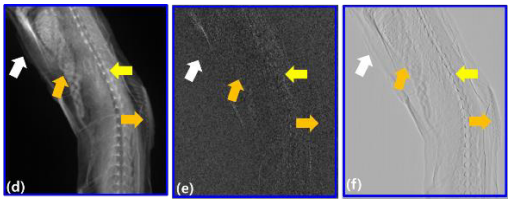


Figure 4. Six red box images: 4X enlarged images of Figure 3 (a), (b), and (e). Figure 4 (a) and (d) absorbed images, Figure 4(d) and (e) scattering images, Figure 4(c) and (f) filtered phase contrast X-ray images by instantaneous frequency.

We compare the six red box images in Figure 4 In the white arrow, compared to the absorption Figure 4(d) and scattering image Figure 4(e), the filtered phase contrast X-ray image by instantaneous frequency Figure 4(f) shows clearer outer boundaries (air and fin). In the yellow arrow, Thanks to noise, the scattering image Figure 4(e) dimly provides bone information. Meanwhile, compared to the absorbed image Figure 4(d), the filtered phase contrast X-ray images by instantaneous frequency Figure 4(f) clearly shows the internal information of the bone. In the orange arrow, compared to the absorbed images Figure 4(a) and (d), the filtered phase contrast X-ray images by instantaneous frequency Figure 4(c) and (f) provide the detailed structures of the gill, digestive organ, and dorsal fin.

We can confirm the effect of the stationary wavelet transform filter in Figure 3(d) and (e). Compared to the original phase contrast X-ray image by instantaneous frequency Figure 3(d), the filtered phase contrast X-ray image by instantaneous frequency Figure 3(e) clearly shows the removal of external noise. In particular, with a small loss of internal information of the sample, the noise inside the sample of the image Figure 3(e) was remarkably removed.

Acknowledgements

We thank the people who give to help for this study. This study is not related to the research assignment.

Reference

1. K. S. Morgan, and C. David, "A sensitive x-ray phase contrast technique for rapid imaging using a single phase grid analyzer." Opt. Lett., Vol. 38, No. 22, p. 4605- 4608, 2013.
2. H. W. Lim, and J. G. Kim. "Experimental setup and the system performance for single-grid-based phase-contrast x-ray imaging (PCXI) with a micro focus x-ray tube." Opt. Comm., Vol 348., p.85-89, 2015.
3. S. Li, and L. Xiang. "Eliminating the zero spectrum in Fourier transform profilometry using empirical mode decomposition." J. Opt. Soc. Am. A, Vol 26, No. 5, p 1195-1201, 2009.
4. E.M. Barj, and K. Nassim. "A digital spatial carrier for wavelet phase extraction." Optik, Vol 116, p507-510, 2005.
5. L. S. Jia., "Instantaneous frequency calculation with Hilbert Transform." instantaneous-frequency-calculation-with-hilbert-transform.
6. S. Bamerni," Image Denoising Based on Stationary WaveletTransform",https://www.mathworks.com/matlabcentral/fileexchange/55696-image-denoising-based-on-stationary-wavelet-transform

Low-dimensional representations of functional connectivity in migraine

Chae Hyeon Lee[1], Mi Ji Lee[2, 3], Chin-Sang Chung[2, 3], and Bo-yong Park[4, 5*]

[1]Department of Statistics, Inha University, Incheon, Republic of Korea

[2]Department of Neurology, Samsung Medical Center, Sungkyunkwan University School of Medicine, Seoul, Republic of Korea

[3]Department of Electrical and Computer Engineering, Sungkyunkwan University, Suwon, Republic of Korea

[4]Department of Data Science, Inha Unversity, Incheon, Republic of Korea

[5]Center for Neuroscience Imaging Research, Institute for Basic Science, Suwon, Republic of Korea

boyong.park@inha.ac.kr

Abstract

Migraine is a neurological condition characterized by episodic headaches. Recent case-control studies based on magnetic resonance imaging observed differences in functional connectivity in specific brain regions in migraine patients. However, how the whole brain functional network organization perturbs in migraine patients has not been fully explored. Here, we investigated functional connectivity alterations in migraine patients along the representative cortical axis running from sensory to transmodal regions using manifold learning techniques.

Background

The etiology of migraine is still on a debate due to complex interactions of molecular, neuronal, and network-level brain organization. Prior works in clinics based on magnetic resonance imaging (MRI) observed distinct patterns of functional brain networks in migraine patients [1]. These studies found atypical brain function in specific brain regions; however, how the whole brain-wide functional organization perturbs in migraine patients relative to healthy controls is largely unknown. Here, leveraging dimensionality reduction techniques, we characterized continuous axis along the cortex and compared between patient and control groups.

Methods

We recruited 50 migraine patients (mean ± SD; age = 33.5 ± 9.11 years; 70% female) and age- and sex-matched healthy controls (n = 50; age = 33.5 ± 9.11 years) from the Samsung Medical Center. Participants underwent T1-weighted and resting-state functional MRI (rs-fMRI). The rs-fMRI data were preprocessed using FuNP software [2], where the processing included slice timing and head motion correction, skull stripping, intensity normalization, registration to T1-weighted and subsequently to MNI standard space, nuisance variable removal, high-pass filtering with 0.01 Hz, and spatial smoothing with full width at half maximum of 5 mm. Processed volumetric data were mapped onto the cortical surface with a cortical ribbon-constrained volume-to-surface mapping algorithm. Based on the brain regions defined using Schaefer 200 atlas [3], we extracted time series and constructed connectivity matrix by calculating linear correlation of the time series between different nodes, and applied Fisher's z-transformation.

We then projected the functional connectivity matrix to the low-dimensional manifold space using diffusion map embedding algorithm [4], a robust and computationally efficient non-linear dimensionality reduction technique. Specifically, we first computed group averaged connectivity matrix and generated low-dimensional manifolds (henceforth gradients), and then aligned individual gradients to the template gradient using Procrustes alignment [5]. We selected a few gradients that explained enough information of the total data, and compared the gradient values between migraine patient and control groups via multivariate analysis with controlling for age and sex. We corrected multiple comparisons across the brain regions using false discovery rate (FDR) < 0.05. To assess which brain networks showed notable between-group differences, we stratified the effects according to the intrinsic functional communities [6].

Results and Discussion

Leveraging manifold learning techniques, we identified three gradients (61.36% information explained). The first gradient showed sensory-transmodal axis, second sensory-visual, and third multiple demand network-rest of the brain (Figure 1a). Multivariate analysis compared three gradients between migraine patients and healthy controls, and revealed significant (FDR < 0.05) between-group differences in early visual and somatomotor areas, as well as lateral temporal cortex and temporal pole (Figure 1b). Stratifying the effects according to seven functional communities, we could find the highest effect in dorsal attention network followed by visual and limbic networks (Table 1).

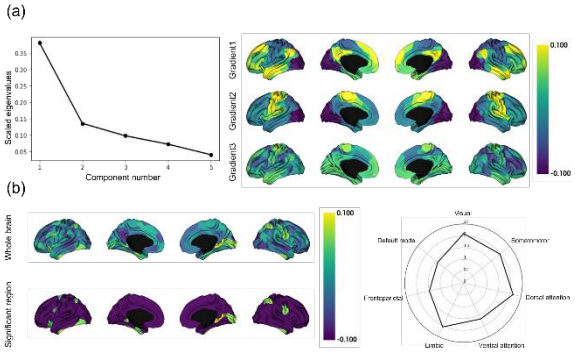


Figure 1. Functional connectivity differences between migraine patients and healthy controls. (a) Three gradients estimated using manifold learning techniques. The eigenvalues of each gradient are reported in the scree plot. (b) The t-statistics of between-group differences in the gradients are reported on the (top) whole brain, and (bottom) in the regions that passed for the significance level (false discovery rate < 0.05). The effects are summarized according to functional communities and reported in the spider plot.

Table 1. The t-statistics of between-group differences according to seven functional communities.

Visual	Somato motor	Dorsal attention	Ventral attention	Limbic	Frontop arietal	Default-mode
2.09	1.98	2.16	1.68	2.05	1.48	1.39

In this study, we investigated functional connectivity alterations in migraine patients using low-dimensional representations of cortex-wide connectivity. We found that low-level sensory as well as higher-order limbic cortices showed alterations in functional connectivity, indicating the migraine affects brain function along the cortical hierarchy. Our work may provide insights for understanding altered functional brain patterns at a whole cortex-level.

Acknowledgements

This research was supported by the National Research Foundation of Korea (NRF-2021R1F1A1052303, NRF-2020R1A2B5B01001826), Institute for Information and Communications Technology Planning and Evaluation (IITP) funded by the Korea Government (MSIT) (2020-0-01389, Artificial Intelligence Convergence Research Center, Inha University; 2021-0-02068, Artificial Intelligence Innovation Hub), and Institute for Basic Science (IBS-R015-D1).

References

[1] L. H. Schulte, A. Allers, and A. May, "Visual stimulation leads to activation of the nociceptive trigeminal nucleus in chronic migraine," *Neurology*, vol. 90, no. 22, p. e1973, May 2018, doi: 10.1212/WNL.0000000000005622.

[2] B. Y. Park, K. Byeon, and H. Park, "FuNP (fusion of neuroimaging preprocessing) pipelines: A fully automated preprocessing software for functional magnetic resonance imaging," *Frontiers in Neuroinformatics*, vol. 13, Feb. 2019, doi: 10.3389/fninf.2019.00005.

[3] A. Schaefer *et al.*, "Local-Global Parcellation of the Human Cerebral Cortex from Intrinsic Functional Connectivity MRI," *Cerebral Cortex*, vol. 28, no. 9, pp. 3095–3114, Sep. 2018, doi: 10.1093/cercor/bhx179.

[4] R. R. Coifman and S. Lafon, "Diffusion maps," *Applied and Computational Harmonic Analysis*, vol. 21, no. 1, pp. 5–30, Jul. 2006, doi: 10.1016/j.acha.2006.04.006.

[5] R. Vos de Wael *et al.*, "BrainSpace: a toolbox for the analysis of macroscale gradients in neuroimaging and connectomics datasets," *Communications Biology*, vol. 3, no. 1, Dec. 2020, doi: 10.1038/s42003-020-0794-7.

[6] B. T. Thomas Yeo *et al.*, "The organization of the human cerebral cortex estimated by intrinsic functional connectivity," *Journal of Neurophysiology*, vol. 106, no. 3, pp. 1125–1165, Sep. 2011, doi: 10.1152/jn.00338.2011.

Deep learning-based classification of autism individuals using functional connectivity

Yurim Jang[1], Kyoungseob Byeon[2, 3], Hyunjin Park[3, 4], and Bo-yong Park[3, 5*]

[1]Department of Electronic Engineering, Kyung Hee University, Yongin, Republic of Korea

[2]Department of Electrical and Computer Engineering, Sungkyunkwan University, Suwon, Republic of Korea

[3]Center for Neuroscience Imaging Research, Institute for Basic Science, Suwon, Republic of Korea

[4]School of Electronic and Electrical Engineering, Sungkyunkwan University, Suwon, Republic of Korea

[5]Department of Data Science, Inha University, Incheon, Republic of Korea

boyong.park@inha.ac.kr

Abstract

Autism spectrum disorder is one of the most common neurodevelopment conditions pervasive worldwide. Recent neuroimaging studies used image processing techniques to quantitatively assess autism brain and combined with machine learning algorithms to distinguish autism from normal controls. However, the classification performance was still relatively low. In this study, we proposed a deep learning-based classification model to distinguish between normal controls and autism individuals. The model was constructed based on multiple fully connected layers, and the performance was assessed using a leave-one-site-out approach. Our study demonstrated that neural network architecture shows better performance than conventional machine learning techniques, and provides new insights for understanding autism brain with an advanced computation model.

Background

Autism is a neurodevelopmental condition showing impairments in sensory and cognitive functions [1]. Prior studies using magnetic resonance imaging (MRI) observed perturbations in functional brain networks in individuals with autism. Combined machine learning and functional connectivity techniques were often used for assessing altered brain organizations in autism, but deep neural network-based stratification of functional networks is relatively scarce. In this study, we aimed to classify between autism individuals and normal controls using deep learning framework.

Methods

We obtained T1-weighted and resting-state functional MRI (rs-fMRI) of 107 individuals with autism (mean ± SD age = 20.85 ± 7.99 years) and 113 normal controls (age = 19.32 ± 7.28 years) from an openly accessible Autism Brain Imaging Data Exchange initiative (ABIDEI; http://fcon_1000.projects.nitrc.org/indi/abide) with three different sites (NYU Langone Medical Center (NYU): n = 35/51 autism/control; University of Utah, School of Medicine (USM): n = 20/22; University of Pittsburg, School of Medicine (PITT): n = 52/40). Only male participants were considered due to the low prevalence of females in the database.

The T1-weighted MRI was preprocessed using a conventional recon-all process in FreeSurfer, which includes bias field correction, registration to stereotaxic space, intensity normalization, skull stripping, tissue segmentation, surface generation, and spherical registration to fsaverage template surface [2]. The rs-fMRI data underwent slice timing and head motion correction, skull stripping, intensity normalization, nuisance variable removal, band-pass filtering with 0.01–0.1 Hz, and registration to T1-weighted and subsequently to MNI152 standard space. The volumetric data were projected onto the mid-thickness surface and resampled to Conte69 template. Surface-based smoothing with full width at half maximum of 5 mm was applied. We constructed functional connectivity matrix by calculating linear correlations of time series between different brain regions defined using Schaefer 200 atlas. The correlation coefficients were soft-thresholded [3] and Fisher's z-transformed.

The functional connectivity matrix was controlled for age and sex, and reordered according to seven intrinsic functional communities [4].We entered the matrix into the deep neural network architecture (Figure 1). The first layer flattened input functional connectivity matrix, and the second and third layers consisted of 128 units with 'relu' activation and 'he_normal' kernel initializer. The fourth layer used batch normalization, and the last output layer consisted of two units with 'softmax' classifier. We used 'adagrad' optimizer with learning rate of 0.0001. We opted for leave-one-site-out approach, where the data of two sites were used for model training and validation, and the left one site data were used as a test set. We repeated this procedure three times. Among 200 epochs, we applied the weights that showed minimum loss in training and validation dataset to the test dataset. The model performance was assessed using accuracy, sensitivity, and specificity.

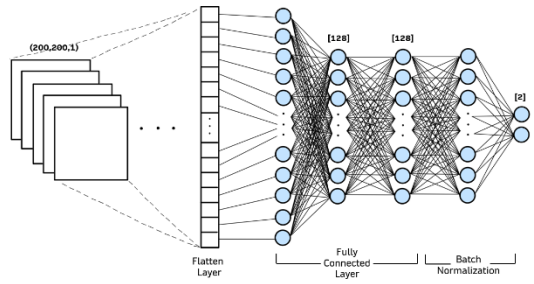
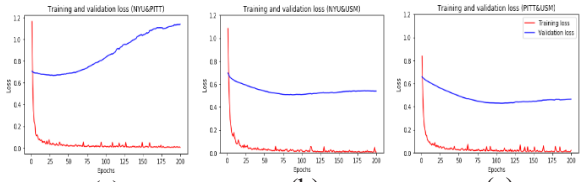


Figure 1. Proposed deep neural network architecture.

Results and Discussion

Figure 2 shows losses of training and validation dataset across the epochs with different subsets of data defined based on leave-one-site-out approach. We obtained high accuracy although one of the three datasets (i.e., USM) showed relatively low performance (Table 1). We confirmed better classification performance compared to previous studies based on random forest (accuracy of 0.59–0.67).



(a) (b) (c)

Figure 2. Loss function of training and validation dataset. (a) Loss curves calculated using NYU and PITT data; (b) NYU and USM; and (c) PITT and USM.

Table 1. Accuracy, sensitivity, and specificity of test datasets.

	USM	PITT	NYU
Accuracy	0.62	0.93	0.88
Sensitivity	0.60	0.95	0.80
Specificity	0.65	0.91	0.94

In this study, we demonstrated that the deep learning-based model outperformed conventional machine learning algorithms in distinguishing autism individuals from normal controls. In future works, we will consider interpretable models based on GradCAM and/or Integrated Gradients to assess which brain networks contributed most to classify the groups. Our work may provide insights on the application of deep learning framework to characterize autism brains.

Acknowledgements

This research was supported by the National Research Foundation of Korea (NRF-2021R1F1A1052303), Institute for Information and Communications Technology Planning and Evaluation (IITP) funded by the Korea Government (MSIT) (2020-0-01389, Artificial Intelligence Convergence Research Center, Inha University; 2021-0-02068, Artificial Intelligence Innovation Hub), and Institute for Basic Science (IBS-R015-D1).

References

[1] D. L. Christensen *et al.*, "Prevalence and Characteristics of Autism Spectrum Disorder Among Children Aged 8 Years — Autism and Developmental Disabilities Monitoring Network, 11 Sites, United States, 2012," *MMWR. Surveillance Summaries*, vol. 65, no. 3, Apr. 2016.

[2] S.-J. Hong *et al.*, "Atypical functional connectome hierarchy in autism," *Nature Communications*, vol. 10, no. 1, Dec. 2019.

[3] A. J. Schwarz and J. McGonigle, "Negative edges and soft thresholding in complex network analysis of resting state functional connectivity data," *NeuroImage*, vol. 55, no. 3, pp. 1132–1146, Apr. 2011.

[4] B. T. Thomas Yeo *et al.*, "The organization of the human cerebral cortex estimated by intrinsic functional connectivity," *Journal of Neurophysiology*, vol. 106, no. 3, pp. 1125–1165, Sep. 2011.

P-102

Cortical asymmetry of structural connectivity in autism spectrum disorder

Seulki Yoo[1,2] and Bo-yong Park[3,4*]

[1]Department of Biomedical Engineering, Sungkyunkwan University, Suwon, Republic of Korea

[2]Department of Intelligent Precision Healthcare Convergence, Sungkyunkwan University, Suwon, Republic of Korea

[3]Department of Data Science, Inha Unversity, Incheon, Republic of Korea

[4]Center for Neuroscience Imaging Research, Institute for Basic Science, Suwon, Republic of Korea

boyong.park@inha.ac.kr

Abstract

Autism spectrum disorder (ASD) is one of the most common neurodevelopmental disorder, and autism individuals show disrupted functional and structural connectivity of the brain. Our previous work observed perturbations in structural connectome based on manifold learning techniques, and here, we extended the prior findings by investigating cortical asymmetry in structural connectivity. We established that core regions in default-mode network as well as sensorimotor regions showed significant between-group differences in cortical asymmetry of structural connectivity. Our findings provide deeper insights for understanding structural connectome changes in autism.

Background

Autism is a pervasive neurodevelopmental disorder affecting an individual's behavior, social, and communication skills. Neuroimaging studies, magnetic resonance imaging (MRI) in particular, adopted advanced connectome modeling techniques to explore regional- and/or network-level alterations in the organization of autism brains. Our recent study investigated perturbations in structural connectivity based on diffusion MRI in individuals with autism and observed different susceptibility in structural reorganization in the cortex between hemispheres.[1] Here, we aimed to quantitatively investigate cortical asymmetry of structural connectivity in autism. We opted for manifold learning techniques to generate low dimensional representations of structural connectomes and calculated the asymmetry index (AI). We then compared the asymmetry patterns between individuals with autism and healthy controls.

Methods

We analyzed MR imaging data of 47 individuals with autism (mean ± SD age = 11.5 ± 5.7 years; 10.6 % female) and 37 healthy controls (mean ± SD age = 13 ± 4.6 years; 2.7 % female) obtained from the Autism Brain Imaging Data Exchange initiative (ABIDE-II; https://fcon_1000.projects.nitrc.org/indi/abide). All participants underwent MRI scans from two independent sites: (1) New York University Langone Medical Center (NYU) and (2) Trinity College Dublin (TCD). The multimodal imaging data including T1-weighted and diffusion MRI were acquired using 3T MRI. T1-weighted data were preprocessed using a standard pipeline of FreeSurfer[2], and the diffusion MRI data were preprocessed using MRtrix[3]. The structural connectomes were generated via anatomical constrained tractography. The multishell and multitissue response functions were estimated and constrained spherical deconvolution and intensity normalization were performed. The tractogram was generated based on a probabilistic approach, and spherical deconvolution informed fitering of tractograms (SIFT2) was applied to optimize a cross-section multiplier for each streamline. The structural connectome was built by mapping the reconstructed cross-section streamlines onto the Schaefer atlas with 200 parcels then log-transformed. We then generated cortex-wide structural manifolds (i.e., eigenvectors) using BrainSpace.[4] After constructing, a template manifolds using group representative structural connectivity matrix, and individual eigenvectors were aligned to the template via Procrustes alignment.

We performed multivariate analysis after controlling for age, sex, and site from the eigenvectors

and compared between individuals with autism and controls. We also calculated AI of the eigenvectors with the following formula: AI = (L-R)/|(L+R)/2|, where L and R indicate eigenvector scores of left and right hemisphere, respectively. After controlling for age, sex, and site, we compared asymmetry of the eigenvectors between the groups using multivariate analysis.

Results and Discussion

We generated three eigenvectors (E1, E2, E3) that explained approximately 50.6% of information (Figure 1), and calculated AI of the eigenvectors.

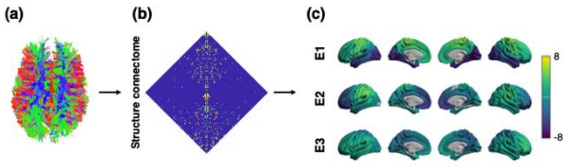


Figure 1. Structural connectome manifolds generation. (a) Fiber tracts generated from diffusion MRI, (b) structural connectivity matrix, and (c) the three eigenvectors estimated from the structural connectome.

The multivariate analysis identified significant between group difference in the AI in precuneus, dorsolateral prefrontal cortex, and lateral temporal cortex, which are the core regions of default mode network (false discovery rate (FDR) < 0.05, Figure 2a). Stratifying the effects according to the intrinsic functional communities, we found the highest effects in visual and default mode network followed by frontoparietal and ventral attention networks (Figure 2b).

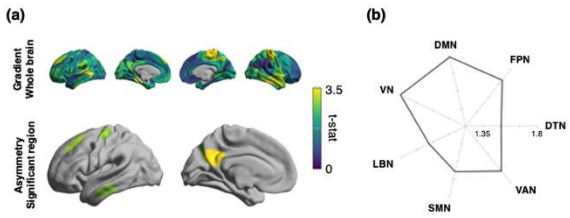


Figure 2. Between-group differences in structural connectome. (a) The t-statistics of between-group differences in three eigenvectors of the whole brain (top), and those in asymmetry index that showed significant between-group differences (bottom). (b) A spider plot summarized t-statistics of brain asymmetry according to functional communities. Abbreviations: VN, visual network; DMN, default-mode network; FPN, frontoparietal network; DAN, dorsal attention network; VAN, ventral attention network; SMN, sensorimotor network; LBN, limbic network.

In this study, we investigated cortical asymmetry in structural connectivity based on novel manifold learning techniques. We confirmed that the higher order areas showed significant cortical asymmetry in structural connectivity. In future works, we will explore the biological underpinnings of cortical asymmetry by associating with functional as well as microstructural profiles. Our work may provide insights for understanding underlying structural alterations in autism.

Acknowledgements

This research was supported by the National Research Foundation of Korea (NRF-2021R1F1A1052303), Institute for Information and Communications Technology Planning and Evaluation (IITP) funded by the Korea Government (MSIT) (2020-0-01389, Artificial Intelligence Convergence Research Center, Inha University; 2021-0-02068, Artificial Intelligence Innovation Hub), and Institute for Basic Science (IBS-R015-D1).

References

[1] B.-y. Park *et al.*, "Differences in subcortico-cortical interactions identified from connectome and microcircuit models in autism," *Nature communications,* vol. 12, no. 1, pp. 1-15, 2021.

[2] B. Fischl, "FreeSurfer," *Neuroimage,* vol. 62, no. 2, pp. 774-781, 2012.

[3] J.-D. Tournier *et al.*, "MRtrix3: A fast, flexible and open software framework for medical image processing and visualisation," *Neuroimage,* vol. 202, p. 116137, 2019.

[4] R. V. de Wael *et al.*, "BrainSpace: a toolbox for the analysis of macroscale gradients in neuroimaging and connectomics datasets," *Communications biology,* vol. 3, no. 1, pp. 1-10, 2020.

PointNet++ Based Method for Automated Prediction of Tooth Crown Center of Mass, Main Axis Angle and Mesiodistal Width

S.Y. Chun[1*], S. Yang[2], J.Y. Yoo[2], M.H. Choi[2], S.R. Kang[2], S.E. Choi[2], B.S. Jeoun[1], J. Kim[1], and W.J. Yi[3]

[1] Interdisciplinary Program in Bioengineering, Seoul National University College of Engineering, Seoul, Korea

[2] Department of Applied Bioengineering, Graduate School of Convergence Science and Technology, Seoul National University, Seoul, Korea

[3] Department of Oral and Maxillofacial Radiology, School of Dentistry and Dental Research Institute, Seoul National University

soyljh@snu.ac.kr*

Abstract

To design a patient-specific implant crown, it needs to consider the patient-specific tooth position, tooth angle, tooth size, and occlusion between maxilla and mandible, etc. In this study, we proposed a modified PointNet++ to automatically detect the position and size of the missing tooth. As the result, we expect that our method is applied to perform the automatic design of patient-specific implant crowns

Background

As dental CAD/CAM has been developed, it has become possible to produce sophisticated implant prostheses using computer-aided design software and a milling machine. Customized implants for patients are also possible with time-saving and cost. It needs to consider that tooth position, tooth angle, and occlusion between maxilla and mandible to design a patient-specific implant crown. However, this is a time-consuming and labor-consuming task both in the design and fabrication step due to it is often performed manually [1].

The process of designing an implant crown is a sequence of estimating and positioning the center of mass and angle of the crown to be manufactured in consideration of the center of mass and angle of each of the patient's remaining tooth crowns, then size adjustment and occlusion confirmation. In this study, we proposed a method for an automatic design of patient-specific implant crowns using deep learning, which detected the position, angle and mesiodistal width of the missing teeth from remain teeth of the patient.

Methods

We used maxillary clinical teeth scan dataset acquired from 30 adult males that visited Seoul national university dental hospital. We converted STL teeth scan data into point clouds with 1024 points and normalized it into [-1, 1] space for deep learning input shown in Figure1.

It has been known that deep learning is an algorithm applicable to various fields including the medical field[1]. The most common application is the classification or segmentation using 2D images, as the technology develops efforts are being applied to 3D data.

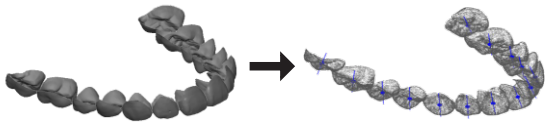


Figure 1. Data preprocessing: Converting patient's maxillary clinical tooth crown scan STL data to point clouds

There are several methods of handling 3D data, among which the representative methods are voxel and point clouds. Voxel and point clouds are the same in that containing 3D information, but voxel has a 3D data format, whereas point clouds have 1D. Therefore, there is a difference in the size of the data. Since deep learning itself requires computing power, it is more efficient to have a small data size. Therefore, we used point clouds to predict the center of mass and angle of the patient's clinical tooth crown.

We proposed a modified PointNet++ to directly detect the centers of mass, the main axis unit vectors and mesiodistal points of the missing tooth from the

dentition as shown in Figure2. The output layer of PointNet++ [2] was modified to detect the centers of mass, the main axis unit vector and mesiodistal point from input point clouds of dentition. The input point clouds are point set of the dentition with one missing tooth, and the outputs are coordinates of the main axis unit vectors, the centers of mass, and mesiodistal points from each tooth.

To evaluate the performance, the absolute error of the x, y, and z axes of the center of mass coordinates and the mesial points, the mean redial error (MRE) value for the center of mass coordinates and the mesiodistal points, and the scalar angle difference for the main axis unit vectors were calculated.

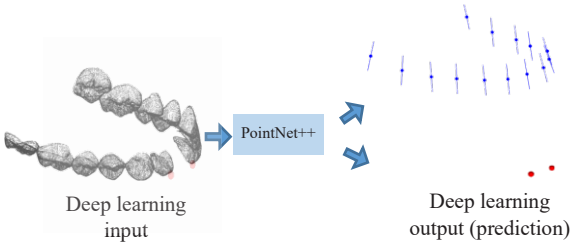


Figure 2. PointNet++ input and outputs (center of mass, main axis unit vector and mesiodistal point)

Table 1. Performance of center of mass and main axis prediction using PointNet++

# of Tooth	x(mm)	y(mm)	z(mm)	MRE (mm)	Angle(°)
11	0.95±0.83	0.33±0.23	0.37±0.23	1.18±0.75	2.75±4.05
12	0.74±0.51	0.50±0.28	0.50±0.47	1.18±0.48	1.15±1.34
13	0.64±0.26	0.73±0.45	0.74±0.44	1.32±0.45	2.74±2.41
14	0.49±0.37	0.68±0.53	0.39±0.28	1.03±0.54	1.44±1.27
15	0.74±0.67	0.53±0.53	0.36±0.23	1.15±0.64	0.49±0.64
16	0.92±0.78	0.36±0.27	0.25±0.26	1.16±0.66	0.28±0.38
17	1.43±1.51	0.75±0.67	0.55±0.47	1.92±1.48	0.85±0.78
21	1.05±0.91	0.17±0.13	0.42±0.27	1.25±0.81	2.58±3.92
22	0.83±0.61	0.39±0.35	0.39±0.33	1.17±0.47	2.22±2.42
23	0.89±0.56	0.62±0.38	0.62±0.29	1.36±0.51	4.23±2.18
24	0.53±0.34	0.60±0.43	0.35±0.28	0.97±0.45	2.08±1.48
25	0.51±0.31	0.46±0.33	0.30±0.31	0.88±0.30	0.34±0.34
26	0.52±0.34	0.44±0.32	0.32±0.21	0.87±0.28	0.19±0.22
27	0.81±0.48	0.49±0.30	0.77±0.42	1.34±0.42	0.87±0.84
mean	0.79±0.73	0.50±0.43	0.45±0.37	1.20±0.70	1.59±2.31

Table 2. Performance of mesiodistal point prediction using PointNet++

	x(mm)	y(mm)	z(mm)	MRE (mm)
Mesial point	4.05 ± 4.28	3.35 ± 2.78	0.43 ± 0.37	5.86 ± 4.44
Distal point	4.31 ± 4.53	2.8 ± 2.46	0.47 ± 0.32	5.64 ± 4.64
mean	4.18 ± 4.41	3.08 ± 2.64	0.45 ± 0.35	5.75 ± 4.54

Results and Discussion

Table 1, Table 2, Figure 3 and Figure 4 shows the performance of prediction using modified PointNet++.

In this paper, we proposed a modified PointNet++ that automatically predict the center of mass, main axis and mesiodistal width of each tooth in dentition with a missing tooth. We expect that our method would be applied to perform the automatic design of patient-specific implant crowns.

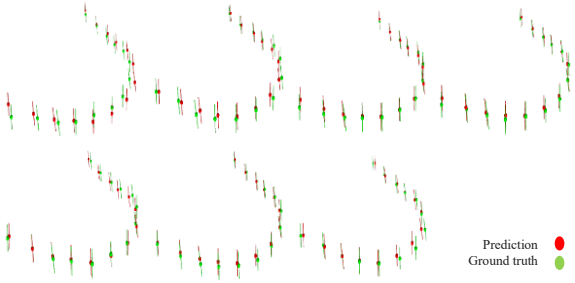


Figure.3 Ground truth and prediction : center of mass and main axis

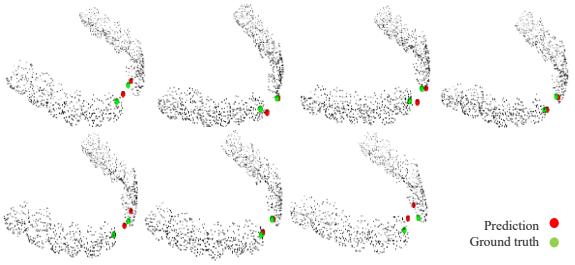


Figure.4 Ground truth and prediction : mesiodistal points

Acknowledgements

This work was supported by the Korea Medical Device Development Fund grant funded by the Korea government (the Ministry of Science and ICT, the Ministry of Trade, Industry and Energy, the Ministry of Health & Welfare, the Ministry of Food and Drug Safety) (1711137883, KMDF_PR_20200901_0011, 1711138289, KMDF_PR_20200901_0147).

References

1. Litjens, Geert, et al. "A survey on deep learning in medical image analysis." Medical image analysis 42, 60-88 (2017).
2. Qi, Charles R., et al. "Pointnet++: Deep hierarchical feature learning on point sets in a metric space." arXiv preprint arXiv:1706.02413 (2017).

Automatic segmentation of temporal bone structures in CT images using Deep Learning

Bo Soung Jeoun[1], Seryong Kang[2], Jiyong Yoo[2], MinHyuk Choi[2], Sieun Choi[2], Soyoung Chun[1], Su Yang[2], Jin Kim[1] and Wonjin Yi[3]

1. Interdisciplinary Program of Bioengineering, Seoul National University, Seoul, Korea

2. Department of Applied Bioengineering, Graduate School of Convergence Science and Technology, Seoul National University, Seoul, Korea

3. Department of Oral and Maxillofacial Radiology, School of Dentistry and Dental Research Institute, Seoul National University, Seoul, Korea

wjyi@snu.ac.kr

Abstract

Computed tomography (CT) is one of the most commonly used techniques for diagnosing various anatomical structures within the temporal bone and for treating ear diseases such as otitis media. Therefore, identification of anatomical structures near temporal bone such as facial nerve, inner ear bone, cochlea in temporal bone CT is very important. However, it is considered to be difficult task since they are highly complicated and small. In this study, we proposed automatic segmentation of temporal bone structures in CT using deep learning.

Background

Locating anatomical structures within the temporal bone using computed tomography (CT) is a basic task for clinical diagnosis of ear diseases. However, as the demand for both ear disease diagnosis and the number of CT images to be treated in clinical practice increases rapidly, the workload of doctors for temporal bone structures segmentation has increased at the same time. In addition, these temporal bone structures such as facial nerve, ossicle and the cochlea are very small in size and have a very sophisticated shape. Therefore, it is very difficult to distinguish in CT even for experts. In order to solve these difficulties, the demand for automatic segmentation for temporal bone structures has increased.

Recently, deep learning has been widely applied in the field of medical imaging. Various deep learning studies related to medical imaging such as object detection, classification, and image segmentation are being explored. Therefore, in this study, to overcome the aforementioned limitations, we proposed automatic segmentation of temporal bone structures using deep learning in CT.

Methods

The one of the typical deep learning networks used for medical image segmentation is U-Net [1]. U-Net is a U-shaped network with an encoder-decoder structure, that obtains information based on 2D images mage. It has a powerful performance in medical image segmentation so that many other deep learning networks combine or modify themselves using U-Net as a backbone. Thus, U-Net and two other modified versions were used for automatic segmentation of temporal bone structures such as Dense U-Net modified from DenseNet [2], and Efficinet U-Net modified from EffiecientNet [3].

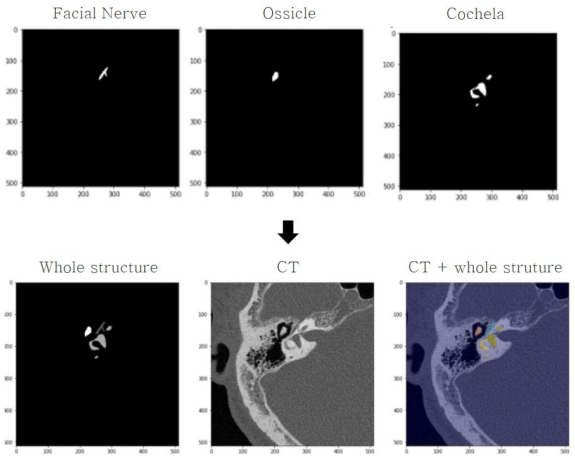


Figure.1 The temporal bone CT and labeled data of temporal bone structures.

The four experts manually labeled the 200 of CT data on both left and right temporal bone structures. Therefore, a total of 418 anatomical structure samples were acquired. The number of slices along the z-axis varies from 40 to 60 per patient in the size of 512 x 512. Figure. 1 shows the acquired labeled data and the original CT of temporal bone structures. Of the 418 structures data, we divided them into 331 for training and 87 for test at a ratio of 8 to 2. The data augmentation was performed through [-10,10] degree s rotation. Training was done based on Keras, Tensorflow using Nvidia GeForce GTX 1080 Ti GPU, set to 200 training epochs with Adam optimizer. Dice loss were used and Dice Similarity Coefficient Score (DSC) was calculated as an evaluation metric.

Results and Discussion

The quantitative evaluation results are shown in Table. 1 below. The DSC results for the facial nerves, the ossicle, and the cochlea, and the average DSC results for all three structures are shown. All used networks had similar results at 0.8 of DSC for the entire structure. Especially, Dense U-Net had the highest performance with 0.80 ± 0.18 among any others. The qualitative evaluation results are demonstrated in Figure. 3. The predicted results from each network are reconstructed in 3D shape. The Dense U-Net showed fewer false positives.

	Facial Nerve	Ossicle	Cochlea	whole
U-Net	0.72±0.23	0.84±0.15	0.82±0.21	0.79±0.20
Dense U-Net	0.74±0.21	0.85±0.14	0.83±0.19	0.80±0.18
Efficient U-Net	0.71±0.38	0.82±0.21	0.80±0.29	0.78±0.23

Table.1 The quantitative evaluation result of anatomical structures and each deep learning networks.

In this study, we proposed automatic segmentation of temporal bone structures in CT using deep learning for the diagnosis of ear disease. It showed a performance of about 0.8 of DSC, and it was possible to obtain a optimistic result that automatic segmentation of temporal bone structures using deep learning would be possible. However, since only 2D-based deep learning networks were used for this study, the 3D volumetric information of medical images was not sufficiently learned. In the future, we will try automatic segmentation of temporal bone structures based on the 3D networks.

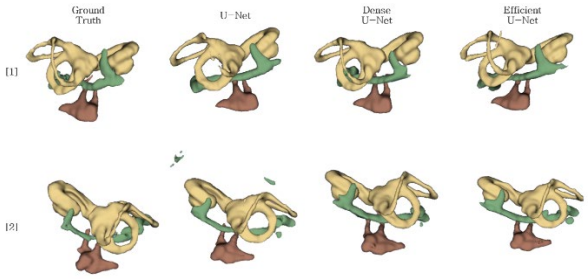


Figure.2 The qualitative evaluation result of anatomical structures and each deep learning networks.

Acknowledgements

This work was supported by the Korea Medical Device Development Fund grant funded by the Korea government (the Ministry of Science and ICT, the Ministry of Trade, Industry and Energy, the Ministry of Health & Welfare, the Ministry of Food and Drug Safety) (1711137883, KMDF_PR_20200901_0011, 1711138289, KMDF_PR_20200901_0147).

References

1. Ronneberger, O., Fischer, P., & Brox, T., "U-net: Convolutional networks for biomedical image segmentation. In International Conference on Medical image computing and computer-assisted intervention", Springer, Cham., pp. 234-24, 2015
2. Iandola, F., Moskewicz, M., Karayev, S., Girshick, R., Darrell, T., & Keutzer, K., "Densenet: Implementing efficient convnet descriptor pyramids", arXiv preprint arXiv:1404.1869, 2014
3. Tan, M., & Le, Q., "Efficientnet: Rethinking model scaling for convolutional neural networks. In International Conference on Machine Learning", PMLR., pp. 6105-6114, 2019
4. Çiçek, Ö., Abdulkadir, A., Lienkamp, S. S., Brox, T., & Ronneberger, O., "3D U-Net: learning dense volumetric segmentation from sparse annotation", In International conference on medical image computing and computer-assisted intervention, Springer, Cham., pp. 424-432, 2016

Deep learning based 3D Hand Segmentation for Computer Assisted Surgery

Sieun Choi[1], Seryong Kang[1], Jiyong Yoo[1], MinHyuk Choi[1], Bosoung Jeoun[2], Soyoung Chun[2], Su Yang[1], Jin Kim[2] and Wonjin Yi[3]

[1]Department of Applied Bioengineering, Graduate School of Convergence Science and Technology, Seoul National University, Seoul, Korea

[2]Interdisciplinary Program in Bioengineering, Seoul National University College of Engineering, Seoul, Korea

[3]Department of Oral and Maxillofacial Radiology, School of Dentistry and Dental Research Institute, Seoul National University

jjse1210@snu.ac.kr

Abstract

In computer assisted surgery, tracking the surgical tool and hand is an essential part to guide the surgeons. However, due to bleeding during surgery or complex background tissues, hand segmentation in surgical image is a difficult task. In this study, we used modified U-Net to improve the performance of hand segmentation in surgical image. Additionally, in order to track the hand in three dimension, we reconstructed the 2D segmentation results to 3D point clouds using RGB-D camera.

Background

In computer assisted surgery, surgical instrument pose estimation is an essential. Additionally, hand tracking is also essential because the surgical instruments are partially occluded by the hand during surgery [1]. However, due to bleeding during surgery or complex background tissues, hand segmentation in surgical image for tracking is a difficult task [2]. To solve this drawback, we used modified U-Net to segment the hand in the surgical image. Furthermore, in order to track the hand in three dimension, we reconstructed the 2D segmentation results to 3D point clouds using RGB-D camera.

Methods

Figure.1 shows the overview of our method. Our algorithm consists of two parts: segmentation in RGB image using deep learning and reconstruct the segmentation results to 3D point clouds using depth information.

First, we obtain RGB image and depth information using RGB-D camera. After that, using modified U-Net, we segment the hand in RGB image. Moreover, depth information which has 3D information corresponding to each pixel of RGB image is used to reconstruct the 2D segmentation results to 3D point clouds.

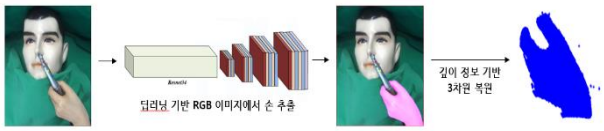


Figure 1. The overview of our method.

In order to improve the performance of U-Net in hand segmentation task, we modified the network architecture. Resnet34 which pre-trained by ImageNet was used as an encoder. In decoder part, expansive path of U-Net was used [3]. A skip connection is used for the encoder and decoder, and a residual block is added to the decoder part. Figure.2 shows the architecture of our deep learning network.

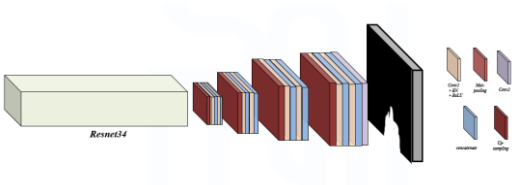


Figure 2. The architecture or our network

Two types of dataset were used for training: public dataset (HOF, EYTH) and surgical images. We augmented the public dataset and surgical images using horizontal flip, vertical flip, rotation and shift. A total of 4658 images were used to train the network. After that, 2448 surgical images acquired by augmentation were additionally used for training. The

image size was 256 x 256, and 80% of the entire dataset was used as train data and 20% as test data.

After hand segmentation using deep learning, depth information is used to reconstruct. We obtained 3D point clouds corresponding to each pixel from the depth information through the extracted 2D pixel information of the hand.

Results and Discussion

In order to evaluate the accuracy of our network, the ground truth and prediction were compared using dice similarity coefficients (DSC). The test was performed using surgical images. For the surgical image, an image obtained from an actual surgical video and an image made similar to the operating room using a phantom were used together. The mean DSCs was 0.94 ± 0.08. Figure.3 shows the result of hand segmentation.

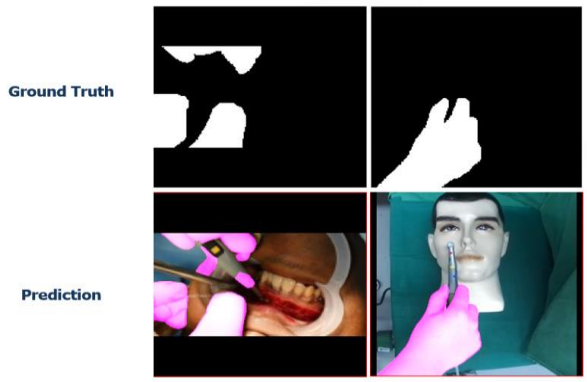


Figure 3. The result of hand segmentation.

The accuracy of the entire image was 0.94, however the image with a complex background showed slightly lower accuracy of 0.91. In future study, we will improve the accuracy of image with complex background, and hand tracking will be performed using the obtained 3D point clouds.

Acknowledgements

This work was supported by the Korea Medical Device Development Fund grant funded by the Korea government (the Ministry of Science and ICT, the Ministry of Trade, Industry and Energy, the Ministry of Health & Welfare, the Ministry of Food and Drug Safety) (Project Number: 1711138289, KMDF_PR_20200901_0147)

References

1. J. Hein, M. Seibold, F. Bogo, M. Farshad, M. Pollefeys, P. Furnstahl, N. Navab, “Towards markerless surgical tool and hand pose estimation” in *International Journal of Computer Assisted Radiology and Surgery 16, 799-808 (2021).*
2. A. A. Shvets, A. Rakhlin, A. A. Kalinin and V. I. Iglovikov, "Automatic Instrument Segmentation in Robot-Assisted Surgery using Deep Learning," *2018 17th IEEE International Conference on Machine Learning and Applications (ICMLA)*, 2018, pp. 624-628.
3. O. Ronneberger, p. Fischer, T. Brox, “U-Net: Convolutional Networks for Biomedical Image Segmentation”, MICCAI 2015, pp. 234-241, 2015

A Tooth Segmentation with Self-Attention U-Net

Jin Kim[1], Su Yang[2], MinHyuk Choi[2], Bosoung Jeoun[1], and Wonjin Yi[3]

[1]Interdisciplinary Program in Bioengineering, Seoul National University College of Engineering, Seoul, Korea.

[2]Department of Applied Bioengineering, Graduate School of Convergence Science and Technology, Seoul National University, Seoul, Korea

[3]Department of Oral and Maxillofacial Radiology, School of Dentistry and Dental Research Institute, Seoul National University

kimjin116@snu.ac.kr

Abstract

Segmentation of the tooth region is essential in the dental field to aid clinical diagnosis and make an appropriate surgical plan. However, this process is very tedious, challenging, and time-consuming. To address this problem, we propose a self-attention U-Net (SANet) for the fully automated tooth segmentation on panoramic dental X-ray images. Experimental results show that the SANet achieves higher performance than the baseline segmentation method.

Background

Accurate tooth segmentation is an important process in the dental field to aid clinical diagnosis and make an appropriate surgical plan. However, tooth segmentation mostly depends on manual or semi-automatic interactive segmentation by experts, which is very tedious, challenging and time-consuming, and it involves prior clinical knowledge.

In this study, we propose a self-attention U-Net (SANet) for the fully automated tooth segmentation on panoramic dental X-ray images.

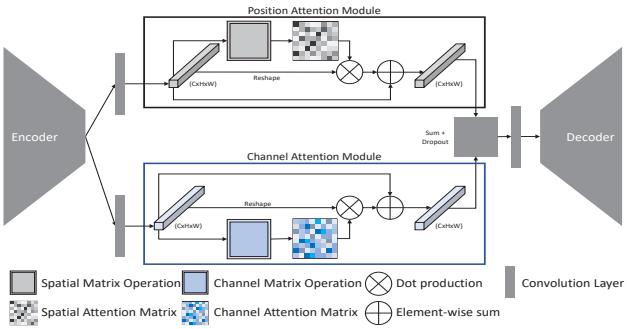


Figure 1) SANet deep network architecture

Methods

Network Architecture. The proposed network architecture, described in Fig. 1, was inspired by vanilla U-Net [1] and self-attention modules [2], which consisted of encoder, decoder parts, position and channel attention modules to predict the segmentation mask. We embedded the self-attention modules after the last encoder layer for adaptively integrating high-level local features with their global dependencies.

Training setup. The proposed network was trained for 300 epochs with a mini-batch size of 32. Data augmentation was performed with rotation(-30°- 30°), translation shift(0-10%), and zoom(0-10%). Soft dice loss was adopted for the multi-class segmentation. To train models, we employed Adam optimizer with learning rate of ⟦10⟧^(-4).

Experimental setup. In this study, we used a total of 499 panoramic X-ray images for network training and testing. The ground truths were annotated by an expert. The number of training, validation, and test sets was randomly split into 300, 100, and 99 images, respectively. We used precision (PR), recall (RC), and dice similarity coefficient (DSC) for evaluating performance.

TABLE I. COMPARISION OF SEGMENTATION PERFORMANCE

Models	DSC	PR	RC
Simple UNet	0.924±0.01	0.911±0.02	0.944±0.02
SANet	0.928±0.01	0.921±0.02	0.942±0.02

DSC, dice similarity coefficient; PR, precision; RC, recall.

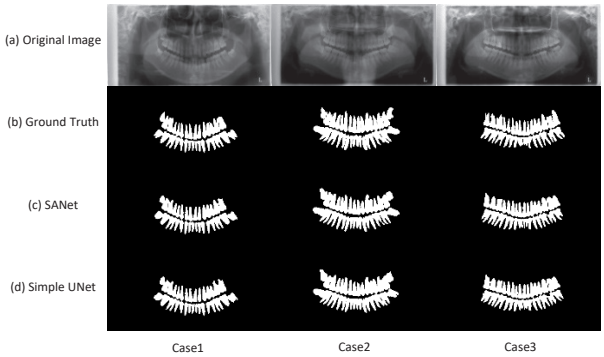


Figure 2) Examples of ground truth and segmentation

Results and Discussion

We compared the performance of SANet with simple U-Net. The experimental results show that SANet achieves higher performance than simple U-Net (Table 1). Fig. 2 shows the representative segmentation results of SANet and simple U-Net. Experimental results demonstrate that SANet can obtain superior performance for tooth segmentation on panoramic X-ray images.

Acknowledgements

This work was supported by the Korea Medical Device Development Fund grant funded by the Korea government (the Ministry of Science and ICT, the Ministry of Trade, Industry and Energy, the Ministry of Health & Welfare, the Ministry of Food and Drug Safety) (Project Number: 1711138289, KMDF_PR_20200901_0147)

This work was supported by the Korea Medical Device Development Fund grant funded by the Korea government (the Ministry of Science and ICT, the Ministry of Trade, Industry and Energy, the Ministry of Health & Welfare, the Ministry of Food and Drug Safety) (1711137883, KMDF_PR_20200901_0011-02)

References

1. Ronneberger, Olaf, Philipp Fischer, and Thomas Brox. "U-net: Convolutional networks for biomedical image segmentation." International Conference on Medical image computing and computer-assisted intervention. Springer, Cham, 2015.
2. Fu, Jun, et al. "Dual attention network for scene segmentation." Proceedings of the IEEE/CVF Conference on Computer Vision and Pattern Recognition. 2019

Automatic Leg Veins and Arteries Segmentation based on Deep Learning in CT images

Juhui Lee[1,2], Young Jae Kim[1,2] and Kwang Gi Kim[1,2,3]

[1]Department of Biomedical Engineering, College of Health Science, Gachon University, Incheon, Republic of Korea

[2]Medical Devices R&D Center, Gachon University Gil Hospital, Incheon, Republic of Korea

[3]Department of Health Sciences and Technology, Gachon Advanced Institute for Health & Sciences and Technology (GAIHST), Gachon University, Incheon, Republic of Korea

kimkg@gachon.ac.kr

Abstract

Deep vein thrombosis (DVT) is a disease in which stagnant blood clots and thrombosis occur due to venous blood flow disturbance in the deep veins. It can cause the risk of complications of pulmonary embolisms. Computed Tomography (CT) is a medical device to diagnose the condition of blood vessels and surrounding tissues, identify the cause of vein compression (May-Turner syndrome), and reflect on treatment. If the thrombus is excessive, the angiography is not good, so the vein has a color similar to the surrounding tissue. Also, if the artery and the vein are anatomically close, it is difficult to diagnose DVT. Therefore, this study aims to contribute to the diagnosis of DVT in clinical practice by automatically detecting the veins and arteries of the legs.

Background

Deep vein thrombosis (DVT) is a disease in which stagnant blood clots and thrombosis occur due to venous blood flow disturbance in the deep veins, and it occurs more frequently in the lower body than in the upper body [1]. At the onset, there is risk of complications of pulmonary embolisms, such as changes in skin color, swelling of the lower extremities, pain while walking, and ulceration if tissue is damaged or thrombus enters the pulmonary artery [2]. Computed Tomography (CT), which has a higher diagnosis rate than the Blood test and Doppler ultrasonography, diagnoses the condition of blood vessels and surrounding tissues, identifies the cause of vein compression (May-Turner syndrome), and reflects on treatment. After administering a contrast agent to the vein of the lower extremity, the CT scan performs. Depending on the amount of thrombus, the veins take color in black and white color with different brightness on the CT image. If the thrombus is excessive, the angiography is not good, so the vein has a color similar to the surrounding tissue, and even if the artery and the vein are anatomically close, it is difficult to diagnose DVT. Therefore, it is required to provide a DVT diagnosis range by automatically segmenting the vein region. This study aims to contribute to the diagnosis of DVT in clinical practice by automatically detecting the veins and arteries of the legs.

Methods

This study collected data from patients administered lower body angiography with approval from IRB at Gachon University Gil Hospital (Gachon University Gil Medical Center, GAIRB2021-225). Of the 192 lower body CT images and the region of interest (ROI) images used in the experiment, 116 were training data, 38 were validation data, and 38 were test data.

In order to clarify the boundary between tissues and blood vessels in the black and white image, the image's contrast was increased from 0 to 216 to 0 to 255.

We found a seed value using the OpenCV library and performed region-props to remove unnecessary search areas during the segmentation process and improve vascular segmentation performance. And as shown in Figure. 1, we crop and converted the image data into a square image of 64 x 64 size with a margin of all sides to preserve the ROI completely.

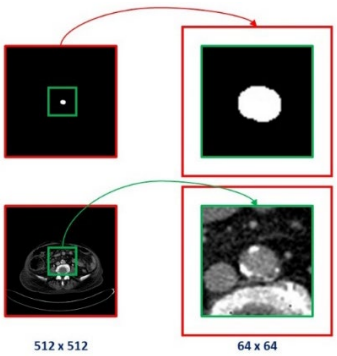
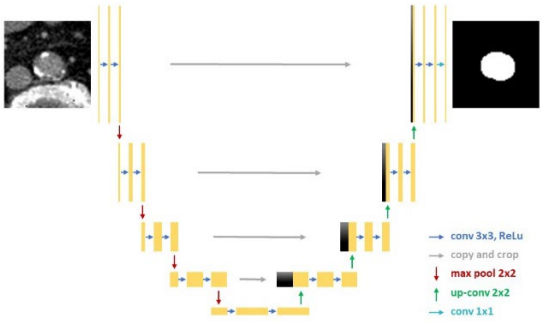


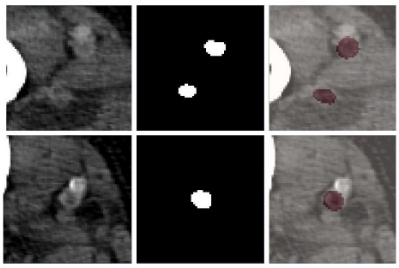
Figure. 2 shows the structure of U-net, a model used for learning. U-net is a modified model that allows more accurate detection with a small number of training images based on FCN. The network structure is U-shaped and consists of a contracting path and an expanding path. The contracting path is a general convolution network and uses ReLU without padding as 3x3 convolution. During downsampling, 2x2 max pooling is applied as stride 2, and the features are doubled in each downsampling step. The expanding path is upsampling to 2×2 convolution, and the channel is reduced in half. The feature map before max-pooling in the contracting path is cropped, repeated two 3x3 convolutions, and applied ReLU. In the last final layer, classification is performed into two classes using 1x1 convolution [3].

In this study, we set the image size to 64x64, the batch size to 5, and the epoch to 100, and learning was completed 52 times to prevent overfitting.



Results and Discussion

Figure. 3 shows the results of dividing the veins and arteries of both legs into the right leg veins. We evaluated the resulting images with the Dice Similarity Coefficient (DSC), respectively. DSC represents the similarity between the ROI image and the predict region as a value from 0 to 1. When DSC is 0, it means that there is no similarity, and when DSC is 1, it means that they are identical. Table. 1 shows the evaluation values for the learning model. The mean DSC of the veins and arteries for both legs is 84.479.



	Rt.vein	Rt.artery	Lt.vein	Lt.artery
Dice Similarity Coefficient	85.326	84.097	84.725	83.767

Table 1. U-net learning result: Dice Similarity Coefficient (DSC)

Acknowledgements

This work was supported by the Korea Medical Device Development Fund grant funded by the Korea government (the Ministry of Science and ICT, the Ministry of Trade, Industry and Energy, the Ministry of Health & Welfare, the Ministry of Food and Drug Safety) (Project Number: 202011B06-02), and by the MSIT(Ministry of Science and ICT), Korea, under the ITRC(Information Technology Research Center) support program(IITP-2021-2017-0-01630) supervised by the IITP(Institute for Information & communications Technology Promotion).

References

1. P.A. Kyrle and E. Sabine, "Deep vein thrombosis," The Lancet, Vol. 365, No. 9465, 1163-1174 (2005).
2. S. Z. Goldhaber and H. Bounameaux, "Pulmonary embolism and deep vein thrombosis," The Lancet, Vol. 379, No. 9828, 1835-1846 (2012).
3. O. Ronneberger, P. Fischer and T. Brox, "U-net: Convolutional networks for biomedical image segmentation," Proceeding of International Conference on Medical image computing and computer-assisted intervention, 234-241 (2015).

Ribs' Sequence Indexing using Deep learning-based method in the Chest CT images

Yu Jin Seol1,2, Young Jae Kim1,2,3, and Kwang Gi Kim1,2,3*

[1]Dept. of Biomedical Engineering, College of Health Science, Gachon University, Republic of Korea

[2]Medical Devices R&D Center, Gachon University Gil Hospital, Republic of Korea

[3]Dept. of Biomedical Engineering, College of Medicine, Gachon University, Republic of Korea

kimkg@gachon.ac.kr

Abstract

Manual indexing for 12 pairs of ribs is essential in the diagnosis field. However, this process is very tedious and time-consuming work. Also, the increasing demand of the chest computed tomography(CT)-based medical images reading makes burden for radiologists. To overcome this problem, we proposed the automatic system for indexing the ribs' serial sequence on chest CT images. Experimental results show that this system achieves high performance about labeling the whole ribs sequence in a short time.

Background

In most medical reading of upper body, the interested regions are usually referred to in terms of the sequence of ribs. Thus, the 12 pairs for ribs' sequence can be indicators of the nodule positions on chest CT images [1]. Accordingly, indexing the ribs in order is essential in the thoracic surgery to build a clinical diagnose with the ribs-based position of nodules that can be shared among radiologists. However, manually counting the order of the ribs is tedious, repetitive, and time-consuming work. Also, the increasing demand of chest CT imaging for thoracic surgical treatment makes radiologists feel burden about that works [2].

In this study, we proposed the automatic system for indexing the ribs' serial sequence on chest CT images, which is based deep learning-based method(U-net) and image processing algorithms.

Methods

We used a total of 50 chest CT datasets consisted of 5,250 sheets for network training and testing. Also, they are verified as subjects of the automatic ribs' sequence indexing system with cross-validation. The number of training, validation, and test sets was randomly split into 33,8, and 9 chest CT dataset, respectively. The ground truths were generated by image pre-processing including global fixed thresholding and morphological processing.

Also, template matching was used to remove vertebrae and sternum. These bones are connecting all of the ribs and make ribs' sequence labels be included in one, so that, pre-designated 20 templates with bones other than ribs were used to detect the most similar region based an equation (1) below on binary chest CT images. The equation means the sum of absolute differences (SAD), which is a technique for extracting regions with the minimal sum of absolute values of pixel-to-pixel errors for same coordinates (i.e. $[u, v]$) between consecutive pixels of the target input image($I1$) and predefined templates($I2$).

$$SAD = \sum_{(u,v)\in I} |I1[u,v] - I2[u,v]| \quad (1)$$

The proposed network architecture is simple U-Net to predict the segmentation mask of interested ribs region. The network(U-net) for segmented ribs to index the sequence was trained for 300 epochs and the batch size of 8 with early stopping to prevent overfitting to learn. The input images were consisted of a raw format of soft kernel with standard dose whose dimensions are 512x512. To implement generalized image processing to whole input datasets, the window widths and level setting of each images were unified to 400 and 40 emphasizing the bone on CT. Also, to verify the performance of ribs sequence indexing on CT images with same condition, the pixel spacing of the input images was unified to the mean value (0.798).

After the segmentation network, we indexed the 12 pairs of rib sequences based on the 3D(Three-Dimensional) region growing on the generated masks

from chest CT. It was implemented for the particularly relevant right-side ribs in images to annotate. 3D region growing method examines adjacent pixels from a seed pixel in the x, y, and z axes of the generated mask set as Figure. 1. In this study, if pixel value is 255 on binary masks and it is close to the seed pixel indicating the ribs, the pixel is included in the same index. And from the first CT slice corresponding to the upper part of the ribs, consecutive numbers are sequentially assigned to the index.

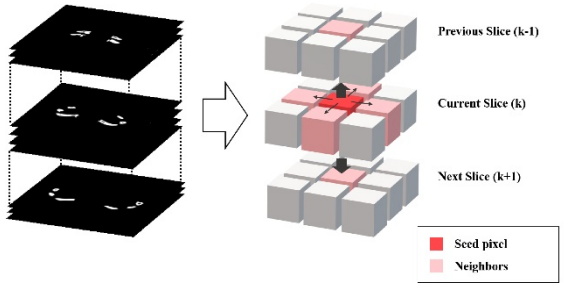


Figure.1 The architecture of 3D region growing.

Results and Discussion

We used dice similarity coefficient(DSC), precision, recall, specificity, and accuracy for verifying the segmentation performance to generate masks of interested ribs regions. And we evaluated the success rate meaning the rate of indexing appropriate ribs' sequences over whole pairs(1st-12th) for input 50 data sets and analyzed.

	U-net (CNN)				
	Sens (%)	Prec (%)	Spec (%)	Acc (%)	DSC
Average	81.93 (±2.74)	83.65 (±4.04)	99.85 (±0.05)	99.69 (±0.09)	0.83 (0.03)

Table. 1 The mean value of U-net performance to generate interested ribs' masks.

	The success rate	
	No. (Success cases No./ Total cases No.)	Successful sequence labeling rate about all ribs (%)
Indexing	48/50	96.0

Table. 2 The success rate of ribs' sequence indexing by the automatic process in this study.

The segmentation network we used achieved a DSC of 0.828, precision of 0.837, recall of 0.819, specificity of 0.999, and accuracy of 0.997 for each mean value of the 5-fold cross validation, as shown in Table. 1. Also, the success rate of the mask from the network achieved 96.0% for 50 data sets as shown Table. 2. Also, Figure. 2 shows the results included in the case of correctly indexing all 12 pairs of ribs.

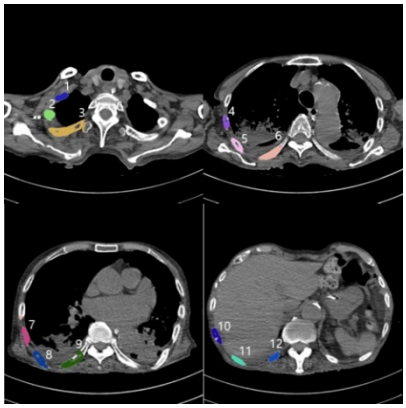


Figure.2 The results of ribs' sequence indexing over all 12 pairs of ribs

For the incorrect cases, we analyzed that the deep learning-based segmentation network responds ribs as outlier when the ribs appear dimly or morphologically similar with abdominal organs. In these case, the process annotated duplicated or omitted sequence index. Also, when a part of single rib is too adjacent or reaches another ribs' part, it leads to the ribs indexing as a single rib by 3D region growing.

We observed that the automatic system for indexing serial ribs' sequence perform accurate based on deep-learning and image processing. For future research, we aim to extend the data utilization and further increase the performance of the system. In addition, this we expect that this development improves the clinical environment of radiologists.

Acknowledgements

This work was supported by the National Research Foundation of Korea (NRF) grant funded by the Korea government (MSIT) (No. NRF-2019R1C1C1008381), and by the MSIT(Ministry of Science and ICT), Korea, under the ITRC(Information Technology Research Center) support program(IITP-2021-2017-0-01630) supervised by the IITP(Institute for Information & communications Technology Promotion).

References

1. Graeber GM, and Nazim M. "The anatomy of the ribs and the sternum and their relationship to chest wall structure and function.", Thorac Surg Clin. 17(4),473-89 (2007)
2. Pinto A and Brunese L. "Spectrum of diagnostic errors in radiology." World J Radiol. 2(10),377-83 (2010)

MSA-Net: Multimodal Spatial Attention Network for automatic head and neck tumor segmentation in FDG-PET and CT images

M.J. Cho[1], Y.J. Choi[2], D.H. Hwang[3,4], S.Y. Yie[3,5,6], H.V. Kim[7], and J.S. Lee[3,4,5,6]

[1]School of Electrical and Electronics Engineering, Chung-Ang University, Seoul, Korea
[2]Department of Biomedical Engineering, Kyung Hee University, Yongin, Korea
[3]Department of Nuclear Medicine, Seoul National University College of Medicine, Seoul, Korea
[4]Department of Biomedical Sciences, Seoul National University College of Medicine, Seoul, Korea
[5]Interdisciplinary Program in Bioengineering, Seoul National University Graduate School, Seoul, Korea
[6]Integrated Major in Innovative Medical Science, Seoul National University Graduate School, Seoul, Korea
[7]Department of Electrical Engineering, Ulsan National Institute of Science and Technology (UNIST), Ulsan, Korea
morra2014@gmail.com

Abstract

Quantitative positron emission tomography/computed tomography (PET/CT), owing to the functional metabolic information and anatomical information of the human body that it presents, is useful to achieve accurate tumor delineation. However, manual annotation of a volume of interest (VOI) is a labor-intensive and time-consuming task. In this study, we automatically segmented the head and neck (H&N) primary tumor in combined PET/CT images. Herein, we propose a convolutional neural network named multimodal spatial attention network (MSA-Net), supplemented with a modified multimodal spatial attention module. We evaluated this model on the MICCAI 2021 Head and Neck Tumor (HECKTOR) segmentation challenge dataset. Our method delivered a competitive cross-validation efficiency, with dice similarity coefficient (DSC) 0.757, precision 0.788, and recall 0.785. When we tested out the method on the test dataset, we achieved an average DSC and HD95 of 0.766 and 3.155 respectively, which is one of the best results according to HECKTOR 2021 leaderboard.

Background

PET/CT, an integrated imaging modality, can simultaneously acquire functional metabolic information and anatomical information of the human body. Accurate tumor delineation from PET and CT would allow for effective diagnosis, clinical decision-making, treatment planning, and personalized medicine. In this context, quantitative assessment of tumors provides valuable information and thus constitutes an important part of diagnostic procedures. Manual segmentation of VOIs in three dimensions is laborious, time-consuming, and error-prone, whereas automatic segmentation is desirable as it allows for a more fast, objective, and accurate process.

Herein, we propose an automated segmentation method for H&N tumors with PET/CT using a deep-learning approach. To achieve the goal of the MICCAI HECKTOR 2021 challenge [1, 2], we used a convolutional neural network named MSA-Net, supplemented with a modified MSAM [3].

Methods

The data used in this study were provided in the MICCAI HACKTOR 2021 challenge. The dataset consisted of information of 325 patients; 224 of them formed the training dataset, and the rest 101 formed the test dataset. As each patient image had a different voxel size, the origin 3D CT and PET images were resampled to 1 mm × 1mm × 1mm pixel spacing with trilinear interpolation. The primary gross tumor volume (GTVt) images were resampled to the same size spacing with nearest neighbor interpolation. Then, these images were cropped to a size of 144 mm × 144 mm × 144 mm using bounding box information. The intensities of CT images were clipped in the range of [-1024,1024] Hounsfield units. Then, these were mapped to the range of [-1,1]. PET intensities were normalized using Z-score normalization.

Our proposed MSA-Net consists of two main components: the modified spatial attention module (SAM) that consists of an image transformer network (ITN) [4], which is illustrated in Figure. 1, and encoder-decoder backbone CNN, which is UNet architecture with the SE norm layers. The SAM used the input PET image to create a spatial attention map that could be used to find the tumor location. The tumor was extracted from the PET/CT data using the backbone network. The spatial attention map of the PET was then multiplied by the PET/CT feature map generated at multiple stages of the encoder in the

segmented backbone. The feature map thus created was concatenated on the decoder. Therefore, the PET/CT feature map focused on the area where spatial interest of the PET was the strongest to produce the final segmentation. This model is illustrated in Figure. 2.

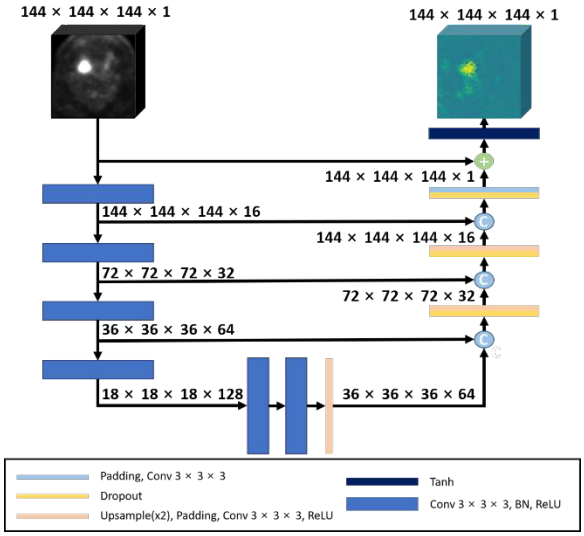


Figure 1. Architecture of modified multimodal spatial attention module.

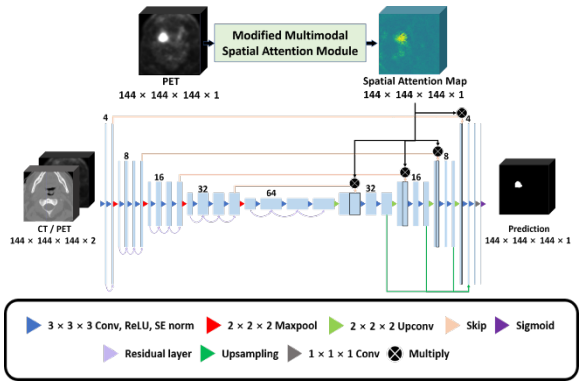


Figure 2. Architecture of proposed network.

Results and Discussion

We trained MSA-Net using the training dataset and evaluated its performance on the training set with 5-fold cross-validation. Table 1 presents the results for the five-fold cross-validation. To compare with the proposed MSA-Net model, we also performed training on the standard UNet. Table 2 presents the results of applying cross-validation in the same way. The DSC of our proposed model was 10.7% higher than that of the standard UNet.

	DSC	Precision	Recall
fold-1	0.769	0.796	0.797
fold-2	0.755	0.802	0.751
fold-3	0.793	0.815	0.828
fold-4	0.704	0.730	0.758
fold-5	0.764	0.797	0.793
Average	0.757	0.788	0.785

Table 1. Mean segmentation results of MSA-Net in the five-fold cross-validation splits.

	DSC	Precision	Recall
fold-1	0.704	0.704	0.719
fold-2	0.676	0.748	0.704
fold-3	0.760	0.770	0.779
fold-4	0.625	0.674	0.657
fold-5	0.654	0.724	0.675
Average	0.684	0.724	0.703

Table 2. Mean segmentation results of the standard UNet in the five-fold cross-validation splits.

Our results of the test set were obtained using ensembles of five trained models. The test set predictions were made by averaging the predictions of the different models and applying a threshold operation with a value of 0.4. For the test set, our proposed network achieved DSC and HD95 of 0.766 and 3.155, respectively.

References

1. Andrearczyk, V., Oreiller, V., Boughdad, S., Castelli, J., … & Depeursinge, A. (2021). Overview of the HECKTOR challenge at MICCAI 2021: Automatic Head and Neck Tumor Segmentation and Outcome Prediction in PET/CT images.
2. Andrearczyk, V., Oreiller, V., Vallières, M., Castelli, J., Elhalawani, H., Jreige, M., ... & Depeursinge, A. (2020, September). Automatic segmentation of head and neck tumors and nodal metastases in PET-CT scans. In Medical Imaging with Deep Learning (pp. 33-43). PMLR.
3. Fu, X., Bi, L., Kumar, A., Fulham, M., & Kim, J. (2021). Multimodal spatial attention module for targeting multimodal PET-CT lung tumor segmentation. IEEE Journal of Biomedical and Health Informatics.
4. Lee, M. C., Oktay, O., Schuh, A., Schaap, M., & Glocker, B. (2019, October). Image-and-spatial transformer networks for structure-guided image registration. In International Conference on Medical Image Computing and Computer-Assisted Intervention (pp. 337-345). Springer, Cham.

A study of lesion segmentation considering mechanism of ultrasound based on improved transfer learning

Y.H. Choi[1], H.L. Kang[1], D.Y. Kim[1], H.I. Koh[1], S.D. Na[2], and M.N. Kim[3]
[1]Department of Medical & Biological Engineering, Graduate School, Kyungpook National University
[2]Department of Biomedical Engineering, Kyungpook National University Hospital
[3]Department of Biomedical Engineering, School of Medicine, Kyungpook National University
kimmn@knu.ac.kr

Abstract

Recently, with the increase in the frequency and diversity of breast ultrasound images, the need for a computer-aided diagnosis system has emerged, and research on CNN-based medical artificial intelligence model is actively underway. The U-Net model is widely used for the segmentation of lesion regions in medical images. However, the existing U-Net model has limitations in feature extraction performance due to structural limitations. In addition, in the case of medical images, it is difficult to collect enough dataset to train a deep learning model. Recently, a transfer learning method that applies a pre-trained model from a large data set on solving a new problem is emerging as a new solution. Transfer learning method should effectively analyze the correlation between the data set of the pre-trained model and the data set of the problem to be solved. In this paper, to supplement the existing U-Net encoder structure, by using transfer learning method, U-Net encoder structure were replaced with the structure and weights of the pretrained VGG16 model. In addition, we proposed a transfer learning-based U-Net model to improve model accuracy by re-adjusting weights through additional breast ultrasound image learning.

Background

Recently, as the incidence of breast cancer continues to increase, ultrasonography, which is effective in detecting breast cancer lesion areas within dense breasts, is recommended. However, in ultrasound examination, the diagnosis and interpretation of the lesion area may vary depending on the examiner, causing variation in the diagnosis rates. Therefore, there are increasing cases that apply deep learning-based artificial intelligence technology to medical ultrasound images in order to supplement diagnosis that uses ultrasound images. In the study of medical image segmentation, CNN-based U-Net model is widely used. However, it is difficult to expect high accuracy in applying the conventional U-Net model to the ultrasound image due to speckle noise existing in the image and low contrast compared to general medical images. Also, there is a limitation in that the training data is insufficient to proceed with deep learning.

Transfer learning method has received great attention as an effective technology to solve these problems. Deepthy Mary Alex [1] and others built a transfer learning model with a fixed feature-extractor method using a pre-trained CNN model with ImageNet. However, since this study proceeds with training with fixed weights in the pre-trained model, accuracy is not guaranteed when training the unique features of ultrasound images.

In this paper, we proposed a transfer learning model that adopts the fine-tuning method that recalibrates the weights based on the extraction of additional features from the ultrasound image to improve the accuracy of the model.

Methods

In this paper, we selected the U-Net model as the backbone for segmentation of the lesion area in the breast ultrasound image, and the VGG16 model which is similar to the encoder structure of the U-Net model as the transfer learning model. The VGG16 model is

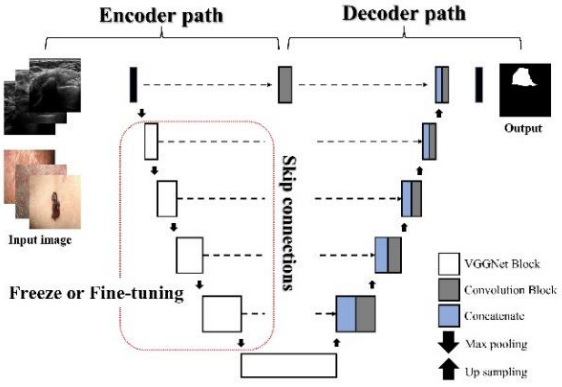


Figure .1 Proposed U-Net model

structurally similar to the encoder of the existing U-Net model, but because it has an additional convolutional layer, it is a model that can be expected to serve as a feature extractor with higher performance.

The data set used to train the model was constructed using 300 images provided by Kyungpook National University Hospital including breast ultrasound images, skin cancer images, and ground truth images. Figure. 1 shows the constructed U-Net model of the fine-tuning method and the U-Net model of the fixed feature-extractor. The Fine-tuning-based U-Net model was built to be trained by the given data set from all layers by importing the structure and weights of the pre-trained model by ImageNet. On the other hand, the fixed feature-extractor U-Net model was set to perform with pre-trained weights and structures as they are when training and extracting image features.

The overall implementation and training of the proposed model were conducted using the Pytorch framework. It was to compare the performance of the models between using and not using transfer learning and between transfer learning methods. For that purpose, a dice score of the prediction image was resulted by applying the train-completed model to the test image.

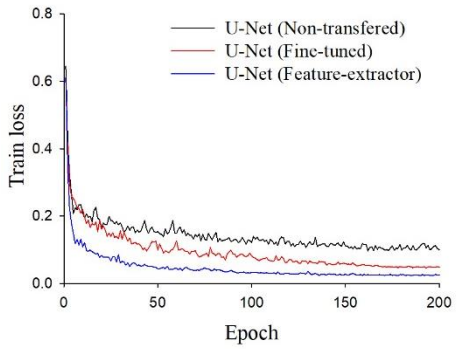
Results and Discussion

Figure. 2 shows the results of the loss function by the transfer learning method in skin cancer images and breast ultrasound images. (a) is a diagram that shows the loss function of the U-Net model by the transfer learning method in the skin cancer image. The result shows that the transfer learning method of the fixed feature-extractor is the most stable training pattern. (b) is a diagram that shows the loss function for each transfer learning method in the breast ultrasound image. The results shows that the fine-tuning transfer learning method is the most stable training pattern. Table. 1 shows the average dice scores calculated from the test images. In skin cancer images, the feature-extractor method recorded the highest score with 0.9287, and in breast cancer images, the fine-tuning method recorded the highest score with 0.7284 as the proposed method.

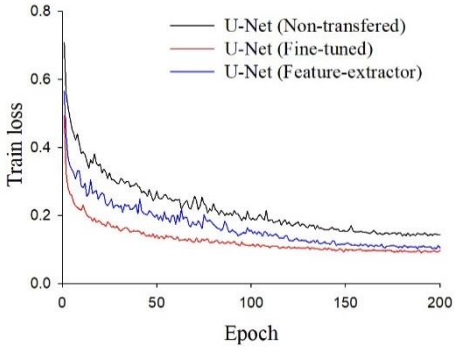
The results indicate that the fine-tuning-based transfer learning model can be an effective solution for improving the accuracy of breast ultrasound images.

Table. 1 The average dice scores

Models / Images	U-Net	Fine-tuning	Feature-extractor
Skin	0.8630	0.9116	0.9287
Ultrasound	0.6556	0.7284	0.6909



(a)



(b)

Figure. 2 (a) Training loss in skin cancer images, (b) Training loss in breast ultrasound image

In the ultrasound images, it is difficult to segment between the lesion region and the non-lesion region due to weak features such as speckle noise caused by scattered waves. These features are difficult to extract from natural images or other medical images. Therefore, a fine-tuning technique that readjusts the newly extracted features from the breast ultrasound image to the weight of the model is considered effective in analyzing the breast ultrasound. In the future, research on various deep learning techniques that consider the characteristics of ultrasounds will be continued.

Acknowledgements

This study was supported by the National Research Foundation of Korea (NRF) grant funded by the Korea government (MSIP) (No. 2017M3A9E2065284, 2019R1C1C1009013).

References

1. D. M. Alex and D. A. Chandy, “Investigations on performances of pretrained U-Net models for 2D ultrasound kidney image segmentation,” *in Proceeding of International Conference of Emerging Technologies in Computing*, pp. 185–195, 2020.

Complex chromosome dataset manufacturing and object detection for overlapped chromosome analysis

Seungyoung Kang[1], Junghun Han[1], Yerin Lee[1], Sena Lee[1], Inkyung Lee[2], Haemi Joo[2], Sejung Yang[1*]

[1] Department of Biomedical Engineering, Yonsei University, Korea

[2] Radiation Health Institute, Korea Hydro & Nuclear Power

tigerkang96@yonsei.ac.kr, *syang@yonsei.ac.kr

Abstract

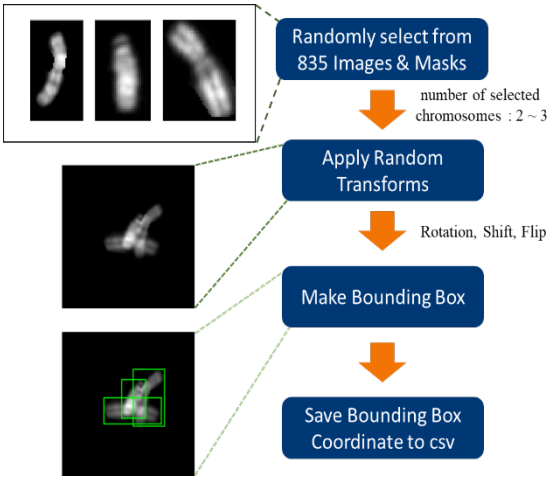
The number and shape of chromosomes are important characteristics that can determine whether a chromosome is abnormal. Thus, counting chromosomes through chromosome analysis is an important clinical procedure for diagnosing various genetic diseases. However, the complicated shape of overlapped chromosomes makes it difficult to analyze the chromosomes. So, we made various types of overlapped chromosome datasets and performed object detection on this data. Most overlapped chromosomes are separated by object detection deep learning model. This data may contribute to improving chromosome analysis in related research.

Background

Chromosomes are usually classified 22 pairs for autosomes and 1 pair for sex chromosomes. One chromosome consists of chromatid and centromere. Chromosome could mutate by radiation exposure, chemicals or genetic mutations. For example, if there is one more chromosome in the 21st, Down syndrome occurs. Counting chromosomes through chromosome analysis is an important clinical process for screening and diagnosing various genetic diseases [1]. Recently, there are attempts that have been made to segment or classify chromosomes. [2,3]. In actual chromosome data, many overlapped chromosomes are found, making it difficult to count the number of chromosomes. It consumes many costs when experts analyze chromosomes. For facilitating automatic counting chromosomes, separation of overlapped chromosomes is required. Thus, we manufactured the overlapped chromosome data and object detection was performed on the overlapped chromosomes to separate each other.

Methods

The data used in this study was manufactured based on the "chromosome Data set for Classification" provided by BioImLab [4]. This data consists of 5474 single chromosome images in which chromosomes are identified by number. All data were divided into train, validation, and test groups, and data production was carried out for each group. As shown in Figure 1, After randomly selecting 2 or 3 chromosomes, various



transform techniques were applied to make the chromosomes overlap, and bounding box information

Figure.1. Process of manufacturing datasets.

for object detection was also produced. In the same way as above, we augmented 3000 train data, 1500 validation, and 750 test data and employed it for deep learning.

We employed Faster R-CNN for object detection [5]. Faster R-CNN is an end-to-end object detection model that evolved from Fast R-CNN. The main idea is Region Proposal Network (RPN), which proceeds with region proposals with a neural network. A candidate bounding box is selected through RPN, and the bounding box and label are predicted through the same process as Fast R-CNN. In the extracting step, feature information was extracted by using MobilenetV3 that pre-trained with COCO train 2017

[6]. Figure 2 shows overall architecture of deep learning model that used in this study.

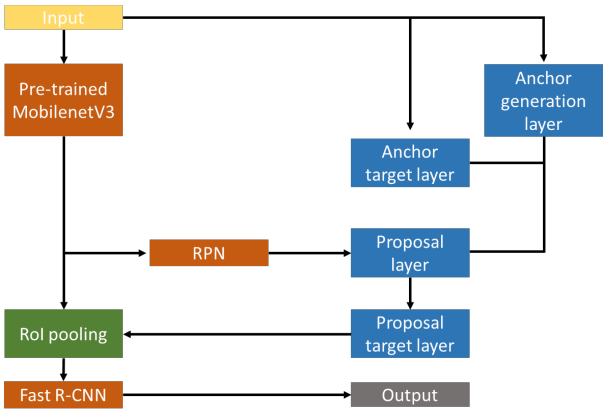


Figure.2. Architecture of object detection model.

Results and Discussion

Figure. 3 shows the ground truth and prediction results of object detection. As shown in Figure 3, Although there is a slight difference in the position and size of the box for the bounding box prediction, it was found that the bounding box prediction was performed accurately for two overlapped chromosomes and three overlapped chromosomes.

This study aimed to separate overlapped chromosomes to facilitate automatic chromosome counting. Since our data was made by stacking up single chromosome images, there might be differences from the actual overlapped chromosome data. However, this data could produce a large number of data and create various types of overlapped chromosomes. If the amount of actual chromosome data is small, transfer learning is performed using this data to learn the shape of the chromosome. Therefore, it is expected to contribute to improving learning outcomes in related studies.

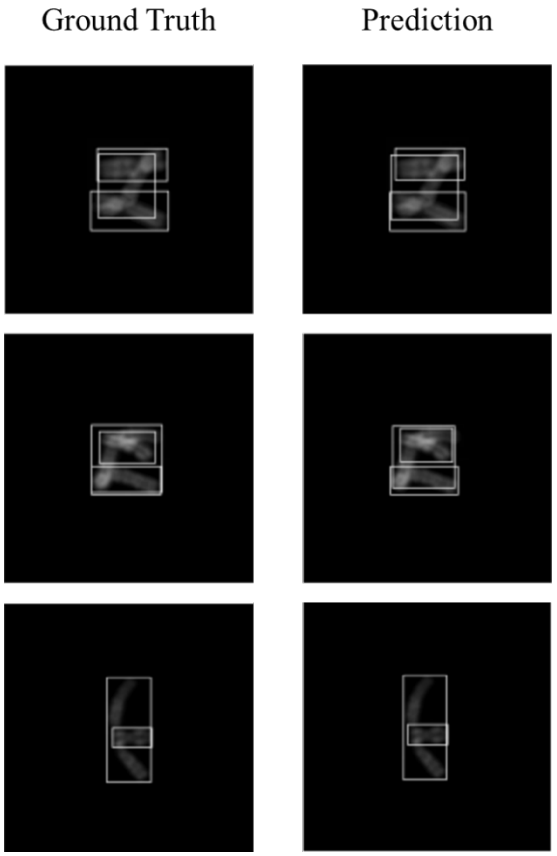


Figure.3 results of object detection in test data.

Acknowledgements

This work was supported by Korea Hydro & Nuclear Power Co., Ltd. (A21IF03)

References

1. S.L.Gersen, M.B.Keagle, “The principles of clinical cytogenetics,” Springer, 2013.
2. R.L.Hu, J. Karnowski, R. Fadely, J.P.Pommier, “Image Segmentation to Distinguish Between Overlapping Human Chromosomes,” arXiv preprint arXiv:1712.07639 (2017).
3. W. Zhang, S. Song, T. Bai, Y. Zhao, “Chromosome Classification with Convolution Neural Network Based Deep Learning,”
4. E. Poletti, E. Grisan, A. Ruggeri, “Automatic classification of chromosomes in Q-band images,” 30th Annual International Conference of the IEEE-EMBS, Vancouver, British Columbia, Canada, August 20-24, 2008.
5. S. Ren, K. He, R. Girshick, J.Sun, “Faster R-CNN: Towards Real-Time Object Detection with Region Proposal Networks,” Advances in neural information processing systems, 28, 91-99 (2015).
6. A.Howard, M.Sandler, G.Chu et al., “Searching for MobileNetV3”, arXiv:1905.02244v5 (2019).

P-112

Lung Cancer and Lymph Node Metastasis Segmentation on FDG PET/CT Images using Multiple Context Information

Si Eun Hwang[1,2], Donghwi Hwang[1,3], Seung Kwan Kang[1,4], Hongyoon Choi[1], Seunggyun Ha[1], Jae Seon Eo[5], and Jae Sung Lee[1,4]

[1]Department of Nuclear Medicine, Seoul National University, Seoul, Republic of Korea,
[2]Ewha Womans University, Division of Mechanical and Biomedical Engineering, Seoul, Republic of Korea,
[3]Seoul National University, Department of Biomedical Sciences, Seoul, Republic of Korea,
[4]Brightonix Imaging Inc., Seoul, Republic of Korea,
[5]Korea University Guro Hospital, Department of Nuclear Medicine, Seoul, Republic of Korea

Abstract

Accurate segmentation of primary tumors and lymph metastases plays an important role in staging lung cancer. Therefore, automatic segmentation using deep learning can help physicians to stage lung cancer by improving the accuracy and throughput. In this study, we applied three different methods to utilize context information to boost the segmentation performance. First, we used shared encoder blocks to co-learn the features between multi-modal PET/CT images. Cross-modality context information complements each other by characterizing tumors with spatial and visual consistency. Atrous spatial pyramid pooling block was adopted at the end of the encoder to obtain the multi-scale context information. In addition, 3D inter-slice context information was exploited for the accurate segmentation of volumetric medical images. The network has two decoders, which are segmentation decoder and context decoder. Two decoders interact with each other by attention mapping and context residual mapping, which transmit useful information for segmentation. We compared our network with baseline networks, and our proposed network showed better performance on FDG PET/CT clinical data.

Introduction

F-18-fluorodeoxyglucose (FDG) PET/CT scans play a vital role in the diagnosis of lung cancer. From FDG PET/CT scan data, location information, as well as quantitative indicators (glucose metabolism and tissue density) for tumors could be obtained for clinical use. In addition, accurate segmentation of primary tumors and lymph metastases is helpful for lung cancer staging, which is pivotal for determining possible treatments and predicting the prognosis of treatment.

We aim to capture multiple contextual information to further improve the segmentation performance of lung cancer and lymph node metastasis. PET/CT scans have complementary feature information which is very crucial in the segmentation task. Therefore, we used an encoder that can implement feature interaction by sharing the encoder block and help to capture the modality context information. In addition, we added atrous spatial pyramid pooling (ASPP) block at the end of the encoder. ASPP block can yield multi-scale context information by parallel atrous convolutions with different atrous rates. Also, we employed 3D inter-slice context information to boost the segmentation performance for 3D medical images. Voxel-wise differences between two adjacent slices were extracted which contain essential morphological information of tumors. Two decoders were each used to generate segmentation masks and inter-slice context masks.

Materials and Methods

A. Dataset

F-18 FDG PET/CT scan data of 930 lung cancer patients acquired from Seoul National University Hospital were used for the network training and evaluation (780 for training, 70 for validation, and 80 for test). Region of interests (ROIs) of the primary and lymph lesions were manually drawn by nuclear physicians, and used as two class labels for training and testing the network. The image size of CTs was 512 × 512 × ~490 (0.98 × 0.98 × 2 mm) and that of PET and ROI was and 200 × 200 × ~200 (2.43 × 2.43 × 4.95 mm). CT images were resampled to have the same voxel sizes as the other images.

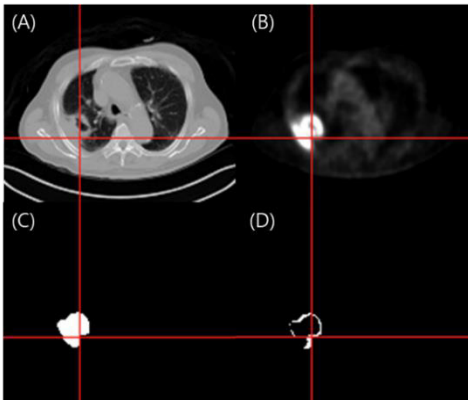


Figure 1. Exemplary case (A) CT, (B) PET, (C) ROI, (D) Inter-slice context

B. Network Architecture

In the analysis of multi-modal PET/CT images, PET images provide information about physiological metabolism and functional characteristics of organs, and CT images reflect anatomical localization information. However, PET and CT images also have spatial consistency as they are acquired from the same patient. Therefore, to extract complementary features from each modality, we employed a shared encoder block. In shared encoder blocks, we updated the weights twice for CT and PET each. The encoder blocks can learn from both

modalities and enable interaction between modalities while preserving spatial and structural consistencies.

At the last stage of the encoder, we added atrous spatial pyramid pooling (ASPP) block. It is composed of three parallel atrous convolutions with different atrous rates (6, 12, 18). The results of each convolution were concatenated and 1 × 1 convolution was applied to get the output. ASPP block helps the network to enlarge the field of view and prevent losing spatial information.

We used two decoders in the network; a segmentation decoder and a context decoder. In each stage of two decoders, they interact by residual mapping and attention mapping. The low-level features from the encoder were concatenated with the upsampled features in the segmentation decoder. Then, context residual features which reflect the discrepancy between the cross-sectional areas of the feature maps were extracted. The context residual features were transmitted to the context decoder and utilized to predict the residual mask. In addition, inter-slice context information generated in the context decoder is transmitted back to the segmentation decoder. It works as attention guidance by providing 3D context information for each slice.

C. Network Optimization

For the segmentation decoder, we combined dice loss and cross entropy loss. The context decoder used ground truth inter-slice context mask as target. Binary cross entropy loss was employed for the three predictions of the decoder. The influence of the loss of each prediction was controlled by parameter $\boldsymbol{\lambda}$, which was set to 0.5. All of the losses were combined and jointly optimized in an end-to-end manner.

Results and Discussion

Table 1. Comparison of results of the network

Metric	Mean Dice Score		F1 Score		95% Hausdorff Distance	
	Primary	Lymph	Primary	Lymph	Primary	Lymph
Residual U-Net	0.7218	**0.5224**	0.7766	0.4460	6.712	14.27
ConResNet[1]	0.8039	0.5099	0.7745	0.4398	7.780	10.80
Proposed	**0.8633**	0.4983	**0.8130**	**0.4574**	**2.919**	**10.19**

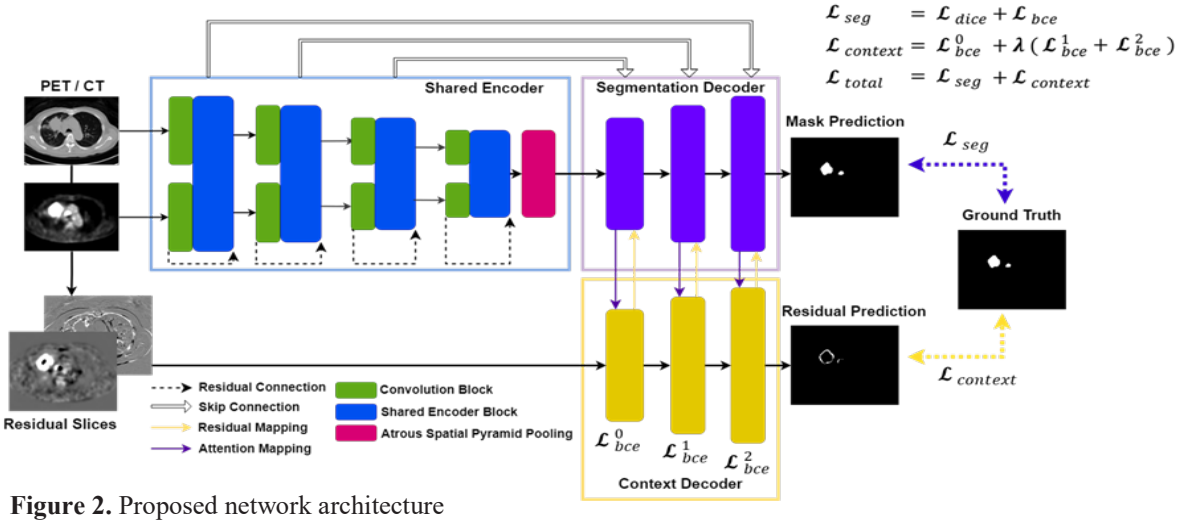


Figure 2. Proposed network architecture

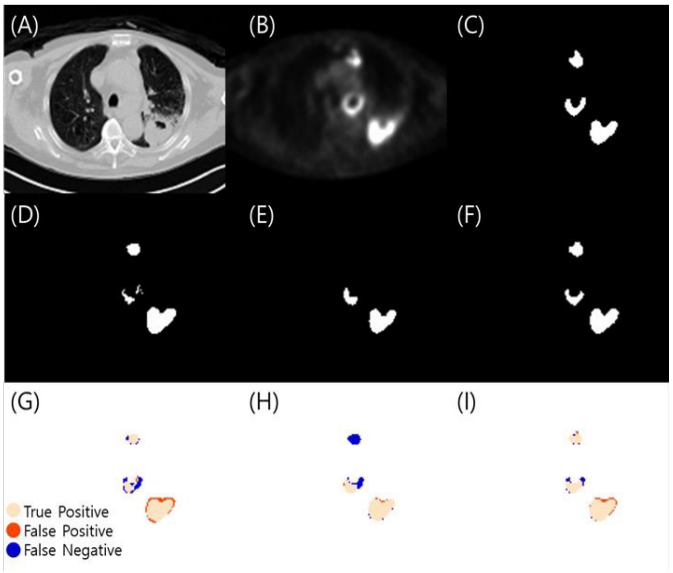


Figure 2. (A) CT, (B) PET, (C) Ground truth, Prediction Result ((D) ~ (F)), and Pixelwise Evaluation with True Positive, False Positive, and False Negative ((G) ~ (I)) of Residual U-Net, ConResNet, Proposed Network from Left to Right

Table 1 shows the comparison of our proposed network with Residual U-Net without any context learning and ConResNet [1] with inter-slice context learning only. The proposed network showed better results in most of the 3 metrics.

Figure 2 shows that after applying context learning, the network showed better performance in the segmentation of edge area. And proposed network segmented three tumor regions most accurately.

Our proposed network, which employed multiple context learning with three methods including co-learning between modalities, ASPP block, and 3D inter-slice context information showed improved segmentation performance.

References

1. J. Zhang *et al.*, "Inter-Slice Context Residual Learning for 3D Medical Image Segmentation," *IEEE Trans Med Imaging*, vol. 40, no. 2, pp. 661-672, Feb. 2021.
2. Z. Xue *et al.*, "Multi-Modal Co-Learning for Liver Lesion Segmentation on PET-CT Images," *IEEE Trans Med Imaging*, doi: 10.1109/TMI.2021.3089702.
3. Chen, Liang-Chieh, *et al.* "Rethinking atrous convolution for semantic image segmentation." *arXiv preprint arXiv*:1706.05587 (2017).

Segmentation knowledge distillation for Conjunctival microscopic image analysis

S.H. Jang[1] ,S.N. Lee[1], J.H. Han[1], Y.R. Lee[1], and S.J. Yang[1,*]

[1]Department of Biomedical Engineering, College of Software and Digital Healthcare Convergence, Yonsei university, Wonju, Korea

jangbi3486@yonsei.ac.kr, syang@yonsei.ac.kr

Abstract

To evaluate dry eye syndrome, microscopic images using moxifloxacin are analyzed with a deep learning algorithm. In this case, it is necessary to use a low-computational cost network for real-time processing. Therefore, we use Residual U-Net as the teacher network to distill knowledge into basic U-Net. We train the student network using pairwise loss and pixelwise loss. The results were evaluated by f1 score, recall, and precision, and the accuracy was increased by 4% compared to the basic unit based on the f1 score, and the parameters decreased by 15%.

Background

Due to the increased use of imaging equipment, more and more patients visit ophthalmology due to dry eye syndrome. According to a survey by the national health insurance, dry eye syndrome is a common disease among modern people, as it is reported that the number of patients visiting the hospital for dry eye syndrome increases by an average of 2.1% per year for the past 5 years (2015 ~ 2019). In order to accurately diagnose and treat dry eye syndrome, research on goblet cell non-invasive testing is underway.

Goblet cells present in the conjunctiva of the eye secrete mucin called mucin, and mucin plays an important role in maintaining the tear film. The conventional conjunctival goblet cell examination used the impression cytology method, which attaches a filter paper directly to the conjunctiva surface and stains the cells falling off the conjunctiva. Therefore, in this study, as a non-invasive test for conjunctival goblet cells, only conjunctival goblet cells were extracted from the image using moxifloxacin-based fluorescence microscopy (MBFM) and a deep learning algorithm [1]. MBFM had been developed for in-vivo CGC imaging by having a high image resolution (1.2μm), a high imaging field of view (FOV) (1.2mm x 1.2mm), a high imaging speed (30fps). We propose segmentation knowledge distillation to improve the inference speed of deep learning algorithms to match the high imaging speed of the MBFM. We set the network used for learning as the teacher network and learned the parameters using the basic U-Net as the student net [2]. The trained student network showed better performance than the result of basic U-Net.

Methods

Figure.1 shows the algorithm of segmentation knowledge distillation as a flow chart.

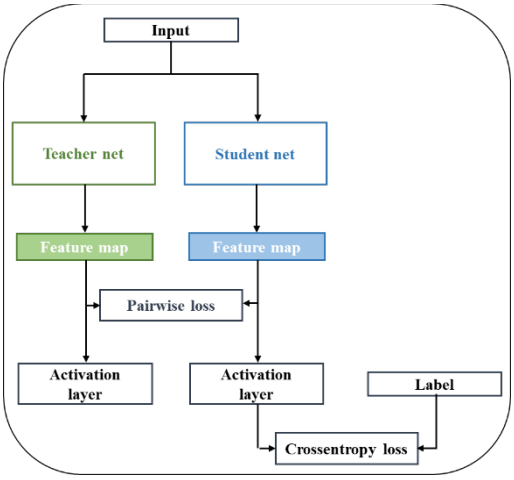


Figure 1. Segmentation knowledge distillation flow chart.

When meaning is grasped from data, it becomes information, and when context is grasped from information, it becomes knowledge. First, the concept of knowledge distillation is to distill the knowledge of the previously completed teacher network into a new, small student network. In the teacher network, parameters are transmitted using a complex model. In this study, the U-Net using the residual block used in the previous study was selected as the teacher network.

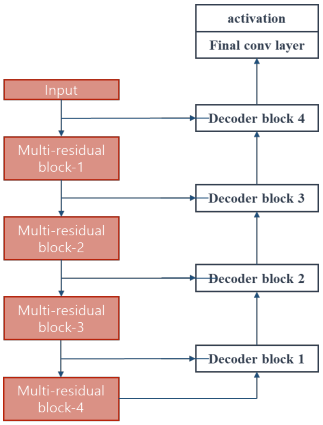


Figure 2. Residual U-Net flow chart.

The student network, which receives contextual information from the teacher network, adopts a basic U-Net structure that is small and relatively light. Two new loss functions were introduced for distillation, a pairwise loss that compares feature maps and a pixelwise loss that compares the outputs of hard labels and student nets. Pixelwise loss computes an error by comparing distributions between feature maps using KL divergence loss. The expression is as follows:

$$\ell_{pi} = \frac{1}{W' \times H'} \sum KL(q_s \parallel q_t) \qquad (1)$$

Pairwise loss analyzes the difference between the label and the output of the student network using binary cross entropy. The expression is as follows:

$$\ell_{pa} = \frac{1}{(W' \times H')^2} \sum (a_s - a_t)^2 \qquad (1)$$

For the experiment, we used a rabbit eye conjunctiva dataset taken with a fluorescence microscope using moxifloxacin. From the 10 rabbit images, 5000 cropped images were produced through data augmentation. The dataset was divided into 8:2 and verification was carried out. The algorithm applied to evaluate the performance of the classification algorithm is as follows:

$$F1\ score = 2 \cdot \frac{precision \cdot recall}{precision + recall} \qquad (1)$$

F1 score is an indicator that can evaluate model objectively without being unbalanced on a specific metric by using precision and recall at the same time.

Results and Discussion

The experiment compared the results of training with Basic U-Net and the results of training U-Net using knowledge distillation in the teacher network. As shown in Figure 3, the learning process was conducted for 20 epochs.

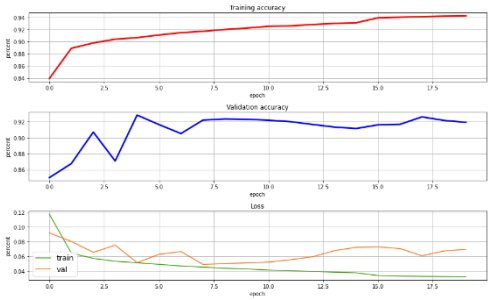


Figure 3. Model training results and losses

The results are shown in Table 1 below.

	Basic U-Net	U-Net with KD
F1 score	0.8749	0.9161
Execution time(sec)	2.29	8.81
Pass size (MB)	3074.00	9334.01
parameters	24,560,385	28,411,777

Table 1. Experimental results

From the training results, it was confirmed that the total number of parameters of the network was smaller than when only the existing model was trained, but the accuracy was higher. Therefore, inference through deep learning is possible even with a small computational cost, and high performance similar to a deep neural network was confirmed.

Acknowledgements

This research was supported by the 'BK21 FOUR (Fostering Outstanding Universities for Research)' in 2021 (II21SS7606007).

References

1. Lee, Jungbin, et al. "Moxifloxacin based axially swept wide-field fluorescence microscopy for high-speed imaging of conjunctival goblet cells." Biomedical optics express 11.9 (2020): 4890-4900.
2. Ronneberger, Olaf, Philipp Fischer, and Thomas Brox. "U-net: Convolutional networks for biomedical image segmentation." International Conference on Medical image computing and computer-assisted intervention. Springer, Cham, 2015.

Axial resolution enhancement of optical coherence tomography through STFT-based deep learning approach

W. Lee[1], H.S. Nam[1], S. Kim[2,3], and H. Yoo[1]

[1]Department of Mechanical Engineering, KAIST, Daejeon, Korea

[2]Department of Cardiology, Korea University Ansan Hospital, Gyeonggi-do, Republic of Korea

[3]Cardiovascular Center, Korea University Guro Hospital, Seoul, Republic of Korea

h.yoo@kaist.ac.kr

Abstract

We proposed a Short-time Fourier transform (STFT)-based deep learning model to enhance axial resolution of optical coherence tomography (OCT). The model was designed to directly process interference signal by applying STFT and fast Fourier transform (FFT). We demonstrated improvement on the data used for training, and further validated the performance on other sample data acquired in other systems. Through this, not only the performance but also the feasibility of independent application to a specific system or sample was verified. The current STFT-based deep learning approach will be highly helpful in overcoming existing limitations of OCT.

Background

Optical coherence tomography (OCT) is an optical medical imaging modality that provides non-invasive depth resolved imaging in vivo with high-sensitivity and high-speed [1]. Nevertheless, the systemic limitations of axial resolution inherent in the basic working principle of OCT using interferometric techniques limit its functionality as diagnostic tools for samples in the micron or sub-micron range. To overcome this, hardware or software-based research have been conducted, and one of them is a deep learning approach, a promising technology that has shown impressive advancements in various imaging fields [2, 3]. However, existing studies mainly utilized to 8-bit OCT images and did not fully utilize the raw data, which is the acquired interference signal. Furthermore, these studies had limited performance because they depended only on specific samples or systems. In this study, we propose a Short-time Fourier transform (STFT)-based deep learning to enhance axial resolution by directly accessing the interference signal. By overcoming aforementioned challenges of the previous deep learning OCT studies, we demonstrated the robust performance on the OCT images used for training, as well as additional data acquired from other OCT systems.

Methods

As shown in **Figure. 1**, the proposed STFT-based deep learning model for OCT signal processing was designed with a generative adversarial network (GAN)-based architecture. GAN is comprised of a generator and discriminator, where the generator is trained to infer a desired output and the discriminator is trained to distinguish which is real or generated data. The two of them compete with each other to train to the theoretical limit where the generated results are indistinguishable from the ground truth. The proposed model receives interference signals from two adjacent A-lines by applying fast Fourier transform (FFT) and STFT, and then enhances the axial resolution of A-lines. STFT generates a spectrogram and the FFT generates a typical OCT A-line. Accordingly, the depth-dependent frequency information contained in the spectrogram is provided in more detail to deep learning as two-dimensions (depth and frequency) by embedding local information as k changes. Finally, after completing the training, the generator in the trained model was used to process the OCT signal.

Training was conducted using swine and rabbit artery dataset acquired using previously reported swept-source OCT with an axial resolution of ~11 μm and a lateral resolution of ~ 21 μm in air [4]. All data were acquired in vivo from different regions of an artery by an imaging catheter. The total dataset consists of 35 helically scanned pullback sets, where each set comprised with approximately 400 frames. The ground truth was generated by conducting the dispersion compensation, k-linearization, and FFT,

which are the currently optimized processing for OCT, on the acquired interference signal. Then, bad dispersion compensation and bandwidth modification were processed on the same interference signal to degrade the axial resolution to generate the input. Note that, the axial resolution of OCT is inversely proportional to the bandwidth, and dispersion directly affects the axial resolution. Each process was randomly applied and can overlap.

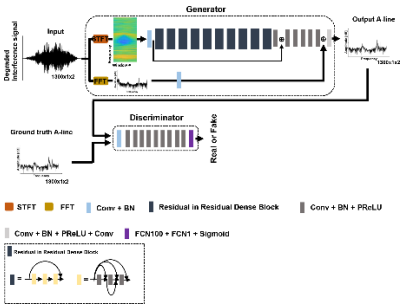


Figure 1. A schematic of the proposed STFT-deep learning-based OCT signal processing.

The training of model was started for 8,000 epochs, with no early stopping. The discriminator loss was defined as binary cross entropy, and the generator loss was defined as superposition using metrics that can evaluate the output of each model well. The model was sequentially optimized using the Adam optimizer with a learning rate of 0.01, and converged successfully in training without overfitting.

Results and Discussion

After training of the proposed models, the deep learning models was applied to the raw signals acquired from the OCT. Since the purpose here is to further enhance the optimal image obtained from the current OCT system, there is no ground truth or clear criterion for comparing the results. Therefore, the results were numerically evaluated using the conventional image quality evaluation metrics. The example results for data referenced during training are shown in **Figure. 2a**. It can be visually confirmed that the morphological features are more visible and even the speckle noise is suppressed. Furthermore, we additionally verified the resolution enhancement using the bead data acquired from the other bench top OCT system. The result can not only verify the resolution enhancement, but also prove the reliability of the proposed deep learning-based processing by applying it to other OCT systems. The example results for 1 μm TiO2 bead data are shown in **Figure. 2b**. It was confirmed that there was a clear enhancement in resolution visually, and the enhancement in axial resolution was particularly noticeable. For further investigation, numerical improvement of image quality metric and resolution results were demonstrated. On average, signal-to-noise ratio was improved by 7.6 dB, and contrast-to-noise ratio by 2.1 dB. In addition, the average axial resolution was improved by 2.2 times.

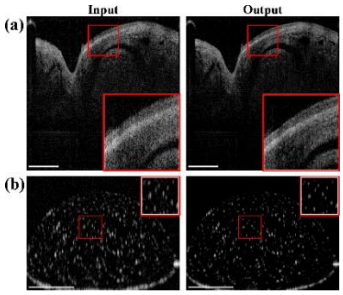


Figure.2 Example result with the proposed deep learning-based OCT signal processing applied. (a) are the results for the swine artery data used for training. (b) is the result for additionally acquired bead data not used for training. All scale bars are 1 mm.

This study demonstrated the robust performance of the newly developed deep learning-based OCT signal processing beyond the limitations of the existing OCT deep learning research. In the results for various samples, resolution enhancement was clearly demonstrated, and the reliable performance was also achieved independent of other systems or samples. This deep learning-based OCT signal processing will be a promising technology to improve OCT images by overcoming existing limitations of conventional OCT.

Acknowledgements

This research was supported in part by grants from the National Research Foundation of Korea (NRF) funded by the Ministry of Education, Science and Technology (2019M3A9E206688013).

References

1. Fujimoto, J.G., et al., *Optical coherence tomography: an emerging technology for biomedical imaging and optical biopsy.* Neoplasia, 2000. **2**(1-2): p. 9-25.
2. Liang, K., et al., *Resolution enhancement and realistic speckle recovery with generative adversarial modeling of micro-optical coherence tomography.* Biomedical Optics Express, 2020. **11**(12): p. 7236-7252.
3. Ma, Y., et al., *Speckle noise reduction in optical coherence tomography images based on edge-sensitive cGAN.* Biomedical optics express, 2018. **9**(11): p. 5129-5146.
4. Cho, H.S., et al., *High frame-rate intravascular optical frequency-domain imaging in vivo.* Biomedical optics express, 2014. **5**(1): p. 223-232.

P-115

Deep learning-based individual cell detection method to measure dielectrophoretic mobility

Sena Lee[1], Yerin Lee[1], Junghun Han[1] and Sejung Yang[1*]

[1] Department of Biomedical Engineering, College of Software and Digital Healthcare Convergence, Yonsei university, Wonju, Korea

bluesky9707@yonsei.ac.kr , syang@yonsei.ac.kr*

Abstract

Accurate cell tracking of dielectrophoretic (DEP) technology for non-contact manipulation of cells is critical for imaging-based characterization of cellular DEP mobility. Therefore, in order to accurately track each cell individually, it is necessary to accurately detect the cell in every frame. In this paper, we present a detection method using two deep learning-based models for the detection of Michigan Cancer Foundation-7 (MCF-7) cells. We use two models, Faster R-CNN and YOLOv5s, to obtain the coordinates of the bounding box representing the location of the cell in the image. To evaluate the performance of the proposed multi-cell detection algorithm, we evaluated the detection accuracy of MCF-7 (Michigan Cancer Foundation-7) cells by the DEP force oscillating between positive and negative numbers. The detection results of each cell were compared using the proposed deep learning-based detection model. Cell counting capacity was greater than 97% of the total cell count for both methods.

Background

Dielectrophoresis (DEP) technology is one of the cell manipulation systems for characterizing the dielectric properties of cells, and was defined by Pohl in the mid-20th century [1]. Dielectrophoresis is a technology that can control the movement of particles due to polarization by inducing charges on the surface of the particles according to the direction of the electric field when particles are placed in a non-uniform electric field. This DEP technique has been widely used in various fields such as cell detection and identification, cell manipulation, and cell characterization [2,3]. The reason that DEP technology has recently attracted attention is because it manipulates particles in a non-invasive and non-contact method, so it can preserve the electrical and genetic characteristics of cells compared to other particle movement control technologies, and can be manipulated with a simple design, and the detection time It has the advantage of being relatively short and inexpensive [4]. In previous studies, the limited field of view, the projected light pattern, and the non-uniform distribution of the light intensity from the microscope while the cells are moved by the DEP force act as a large noise effect is derived. Therefore, accurate detection should be the basis to accurately track hundreds of cells during long-term frame sequences.

Methods

In this study, we tried to develop a detection algorithm using a deep learning-based detection model for breast cancer cells on a given electrophoresis chip. The dataset used in this study is shown in table1.

Cell Num	Detection			
	Train & Validation		Test	
			Faster R-CNN	YOLOv5s
	Cell Type	Image	Image	
100~200	MCF-7	20	8	16
200~300		-	4	16
300~400		3	4	-
400~500		22	2	16
500~600		-	-	-
Total		45	18	48

The detector is the Faster R-CNN and YOLOv5s model was used for the deep learning model. The training set is augmented using geometric data augmentation techniques such as flipping left and right and symmetric origin. For the total training data, 180 images were used, and MCF-7 cell images were used. The original image size is 1024*1280 pixels, scaled to 1280*1280 pixels for training. The following figure 1

shows Detector pipeline. The deep learning model is trained as follows, and using the trained model, it receives images of continuous frames and acquires the coordinates of the bounding box, the result of which cells are detected.

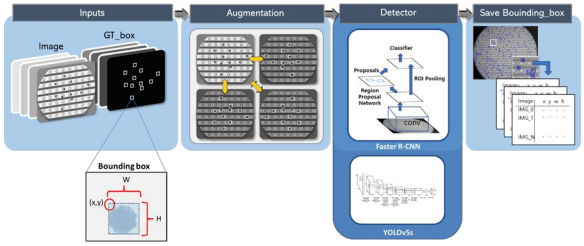


Figure 1. The entire pipeline for Detector

When training the deep learning model, the Faster R-CNN model used the SGD optimizer as the optimizer. The learning rate was set to 5e-3. In the YOLO model, we also used the SGD optimizer as the optimizer, and the learning rate was set to 1e-2. This training was conducted on a commercial central processing unit (Core i7-8700 3.20 GhZ, Intel Corp) and a graphics processing unit (GeForce RTX 2080 Ti, Nvidia Corp). The detection evaluation metrics used precision, recall, and f-meausre to evaluate the performance of the algorithm.

Results and Discussion

Figure 2 shows the quantitative results using Faster R-CNN and YOLOv5s models, respectively.

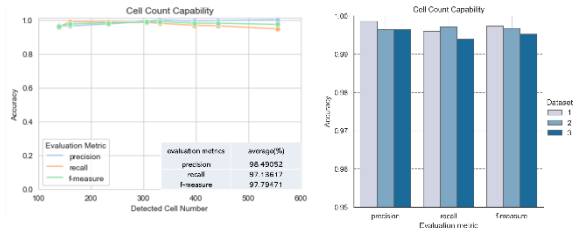


Figure 2. Faster R-CNN, YOLOv5s quantitative detection results on the test dataset.

The cell count capability of both models was over 97%. Figure 3 shows that cells were accurately detected in both nDEPtrap and pDEPtrap. In this study, we developed a deep learning-based detection algorithm for breast cancer cells on a given electrophoresis chip. Four significances can be stated in this study. The first can detect the first hundreds of cells for several individual cells. Because there are hundreds of cells in a DEP chip of limited size, when cells are moved by the DEP force, adjacent cells can be individually detected even if they are attached and detached.

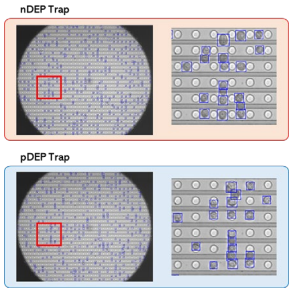


Figure 3. YOLOv5s qualitative detection results on the test dataset.

Second, cell detection was performed in the complex background of the DEP chip. Third, when cells are moved by the DEP force, the intensity of light emitted from the microscope is unevenly distributed, resulting in inaccurate detection results, but by learning about most images using various images for deep learning, hundreds of It can accurately detect canine cells. Finally, it was possible to image-based analysis of cells in their native state without staining. Therefore, the proposed cell detection algorithm is expected to be a more effective analysis for dielectrophoresis experiments in the future.

Acknowledgements

This research was supported by the 'BK21 FOUR (Fostering Outstanding Universities for Research)' in 2021 (II21SS7606007).

References

1. Pohl H, Pollock K, Crane J. Dielectrophoretic force: A comparison of theory and experiment. Journal of Biological Physics. 1978;6(3):133-60.
2. Pethig R. Dielectrophoresis: Status of the theory, technology, and applications. Biomicrofluidics. 2010;4(2):022811.
3. Su H-W, Prieto JL, Voldman J. Rapid dielectrophoretic characterization of single cells using the dielectrophoretic spring. Lab on a Chip. 2013;13(20):4109-17.
4. Munaz A, Shiddiky MJ, Nguyen N-T. Recent advances and current challenges in magnetophoresis based micro magnetofluidics. Biomicrofluidics. 2018;12(3):031501.

Prediction of bone mineral density in CT using deep learning

J.W. Kang[1] and M. Kim[2]

[1]Department of Information Convergence Engineering, Pusan National University, Yangsan, Korea

[2]School of Biomedical Convergence Engineering, Pusan National University, Yangsan, Korea

dnsdudwk1027@pusan.ac.kr

Abstract

Bone mineral density (BMD) is one of the key features to diagnose osteoporosis and build optimal operation plans. Although CT is the most common modality for imaging bone, most commercialized products, however, seldomly provide BMD information because they mainly focus on anatomical imaging. Thus, patients are additionally scanned by dual-energy X-ray absorptiometry (DXA) to measure BMD at the expense of additional radiation exposure and medical cost. In this study, we investigate BMD prediction methods based on deep learning using CT to improve patient convenience. As a result, the correlation coefficient between the BMD estimate and DXA BMD is more or less 0.89.

Background

Osteoporosis, which is characterized by reduced bone mineral density (BMD), is one of the main causes of fractures [1]. Physicians, thus, check BMD in addition to anatomical bone images to diagnose the disease or build surgery plan. Computational tomography (CT) is the main tool to study bone, but it is seldomly used for functional imaging or quantitative measuring. Therefore, a supplementary tool such as dual-energy X-ray absorptiometry (DXA) is used to obtain BMD information.

Many groups have studied methods to predict BMD using only a CT slice image to reduce additional cost [1]. Some reported that spatial attenuations represented by image pixels are enough even though it is from a single energy band, through experimental results that BMD estimates are close to DXA BMD values.

In this paper, we aim to develop novel methods based on deep learning to improve prediction performance and analyze the results.

Deep learning has widely been used in medical imaging fields such as classification and segmentation due to its strong generation power. Especially, convolutional neural network (CNN) showed high performance in visual tasks. We developed CNN models to estimate the BMD from a CT image and conducted supervised learning using DXA BMDs as labels. We cropped a section image to focus on the region of interest (L1 part) without any resizing and we performed training and testing using the CNN models. The performance was finally checked by Pearson's correlation between BMD estimate and DXA BMD.

Methods

In this study, we used 1 slice of axial CT image (L1 part) per one patient sample as input data and the BMD value (L1 part) measured by DXA as ground truth. The region of interest (L1 part) was extracted from DICOM format images through cropping processes (Fig. 1 (a) and (b)).



Figure 1. Images of U-net training (a)Original axial CT image. (512×512) (b) Cropped image for the input. (256×256) (c) binary label image. (256×256)

Next, we performed L1 segmentation using U-net [2] since the lumbar vertebra is known to have the most influence on the BMD value [1]. U-net was trained using 216 CT images and labeled L1 binary images. (Fig. 1 (b), (c)). Through the trained U-net, we could automatically segment the L1 vertebra from other CT images (Fig. 2). Fig. 2 (c) highlights the bone area through negative predictive area removal.

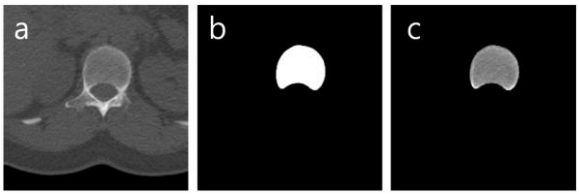


Figure 2. U-net segmentation test. (a) input image (256×256) (b) output binary image (256×256) (c) L1 segmented image (256×256)

To predict BMD value, we used CNN model. 627 CT images from 365 patients were used as train & validation, and 159 CT images from 93 patients were used as test set. The patient samples for train & validation were totally independent to those for the test.

Due to the lack of data samples, traditional image augmentation techniques such as image rotation, shift and flip were applied for robustness.

We constructed 2 structures as illustrated in Fig. 3. NET 1 consists of 5 convolutional layers and 2 fully connected layers. Each convolutional (filter size = 3×3) and fully connected layer were activated with a rectified linear unit (ReLU) function and the output layer of the model was activated with a linear function. Also, batch normalization was applied after each convolutional layer to stabilize learning. Hyperparameters for model training include loss function = mean square error, number of epochs = 150, batch size = 15, optimizer = Adam. NET 2 is the extended version of NET 1 for inputting 2 images.

We trained the models independently for 3 cases: 1) Case 1 used NET 1 inputting a cropped image, 2) Case 2 used NET 1 inputting a segmented L1 image, and 3) Case 3 used NET 2 inputting both cropped and segmented L1 images.

To evaluate the general performance, we used 20% of 627 images as the validation set and the rest as the train set. Also, we conducted cross-validations 10 times with different validation datasets for each case. Like ensemble techniques, 10 trained models independently predicted the BMD for the test set, and the average is set to the final BMD prediction.

All CT images and DXA BMD were obtained from Busan Medical Center orthopedic team. All imaging processes including deep learning were conducted using Python.

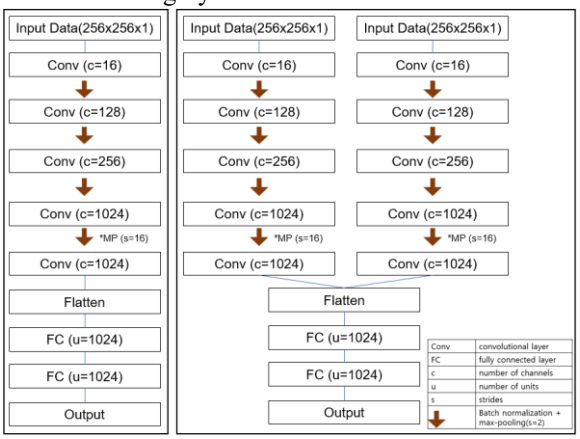


Figure 3. Schema of CNN structures. (Left: NET 1, Right: NET 2)

Results and Discussion

Table 1 and Fig. 4 show that Net 1 using only cropped images provided the highest correlation coefficient (r=0.8984, p<0.001). Net 2 using both cropped images and segmented L1 images provided a similar result (r=0.8880, p<0.001), but Net 1 using only segmented L1 resulted in the lowest value (r=0.8274, p<0.001). Our previous assumption was that the use of only L1 segment is enough for BMD prediction since the area is critical for BMD. On the contrary, the results showed that peripheral soft tissue areas contributed to the BMD estimation. Note that one limitation of this study is using not real BMD but DXA BMD as a ground truth. Since DXA transmits radiation (single view) to the human body and provides a projection image, DXA BMD is affected by not only bone but also surrounding soft tissue. Thus, the estimate of Case 1 and Case 3 using full area caused a higher correlation with DXA BMD than that of Case 2 using only the L1 part. Overall, the deep learning approach in common CT resulted in a high correlation with DXA, thus we concluded that they can be an alternative to DXA for accessing BMD, which medical professionals are accustomed to.

Table 1. Correlation coefficients (r) of three cases

	Case1	Case 2	Case 3
correlation coefficient	0.8984 (p<0.001)	0.8274 (p<0.001)	0.8880 (p<0.001)

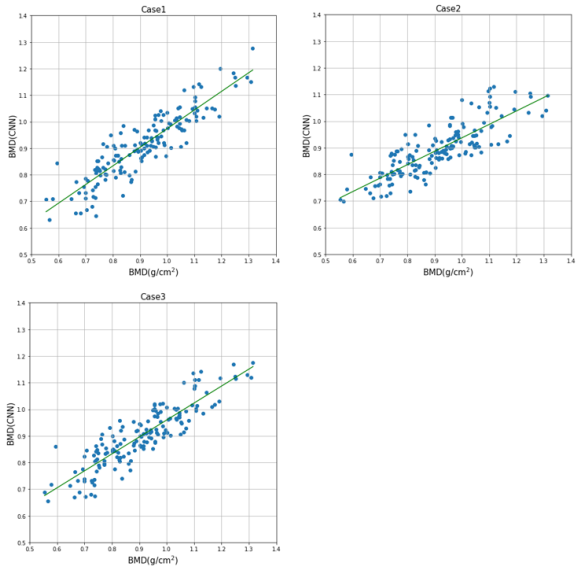


Figure 4. Scatter plots of the three cases. Every diagram shows the test results using the points on the horizontal axis (DXA BMD) and the vertical axis (BMD estimate).

Acknowledgements

This research was supported by Institute of Information & communications Technology Planning & Evaluation (IITP) grant funded by the Korea government (MSIT) (No. 2020-0-01450, Artificial Intelligence Convergence Research Center [Pusan National University])

References

1. Yasaka K, Akai H, Kunimatsu A, Kiryu S, Abe O Prediction of bone mineral density from computed tomography: application of deep learning with a convolutional neural network. Eur Radiol 30(6):3549–3557, 2020.
2. M. Drozdzal et al, The importance of skip connections in biomedical image segmentation, in Int. workshop Large-scale Annotation of Biomed. Data and Expert Label Synth., 2016

Computational modelling of neural interactions reflected in the calcium imaging signals using dynamic causal modelling

Jinseok Eo[1,2], Yoo Yong Lee[3,4], Jiyoung Kang[5,6] and Hae-Jeong Park[1,2,4,7*]

[1]Graduate School of Medical Science, Brain Korea 21 PLUS Project for Medical Science, Yonsei University, Seoul, Korea

[2]Center for Systems and Translational Brain Science, Institute of Human Complexity and System Science, Yonsei University, Seoul, Korea

[3]Department of Biomedical Engineering, Yonsei University, Wonju, Korea

[4]Department of Nuclear Medicine, Yonsei University College of Medicine, Seoul, Korea

[5]Department of Scientific Computing, Department of Physics, Pukyong National University, Busan, Korea

[6]College of Liberal Arts, Pukyong National University, Busan, Korea

[7]Department of Cognitive Science, Yonsei University, Seoul, Korea

parkhj@yuhs.ac

Abstract

Calcium imaging is widely used for research on neural plasticity and neural circuit. However, the analysis methods are not diverse. In this study, we extend a single neuron of calcium imaging generative model to multiple neurons. In addition, parameterizing the neuron type, can be obtained through the DCM framework which was based on the variational Bayes approach. The proposed model was validated by simulation and real data. The developed model can be utilized to find neuron types in bidirectional connectivity and calcium imaging.

Background

Calcium ions are being studied through multi-photon calcium imaging (CaI) as important ions for generating various intracellular signals [1]. Despite increasing interest in calcium imaging, most studies have focused on cell activities and correlative interactions, but less effort has been made to explore bidirectional causal interactions among neural cells. Exploring bidirectional interactions (called effective connectivity) among neuronal cells using CaI calls for computational modeling. In the current study, we introduce computational modeling to estimate effective connectivity from CaI of multiple neurons. The generative model was evaluated by simulations and rodent's barrel cortex experiment signal.

Methods

Figure 1. shows the developed model and DCM framework. The generative model has two parts, the neural state, and the observation model. As a neural state mode, we used a quadratic gaussian integrate-and-fire neural state model (QGIF), which generates spiking activities. In QGIF model membrane potential difference is calculated by sum of synaptic current, applied current, leaky current, spiking and repolarization voltage-current function. Calcium kinetics calculated based on membrane potential and Calcium ion base. The neural state model was combined with a calcium kinetic equation that led to CaI curves at each neuron. Calcium kinetic to fluorescence signal equation is modeled by a saturating Hill-type function. To obtain interactions of multiple neurons the proposed model extends Rhamati et al. [2] to model interactions of multiple nodes using a conductance-based approach. Bayesian model optimization was applied to find optimal model parameters (e.g., effective connectivity) using a variational expectation maximization scheme implemented in the dynamic causal modeling framework.

To validate the reliability of the proposed modeling and model inversion, simulation study was conducted. Most CaI data does not provide neuron type (excitatory or inhibitory) and determining origination of the CaI is one of the critical issues in the CaI data analysis. But biophysical parameters and effective connectivity could be obtained through the developed generative model in DCM framework. To confirm this, from various ground truth (GT) DCM models, we simulated fluorescence signals using 3 neurons. Then, inferred biophysical parameters and connectivity using DCM. For simplicity, we used 3 nodes which

can be an excitatory or inhibitory neuron, and in all simulations, the input went only to the first neuron. (The first neuron is fixed an excitatory neuron to perturb the system)

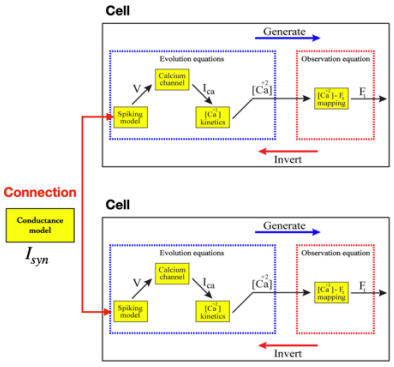


Figure 1. developed generative model and DCM(inversion) framework.

To apply the proposed method to real data, CaI of the rodent barrel cortex during successful and failed whisking signal was used [3]. Neuron types are manually classified based to empirical criteria [4]. Four neurons (excitatory 3, inhibitory 1) were selected to confirm model inversion according to the criteria of being in the same plane, having a correlation greater than 0.9 and a distance less than 100. All simulations and inversion was conducted based on DCM framework in SPM 12 (https://www.fil.ion.ucl.ac.uk/spm/software/spm12/).

Results and Discussion

Figure 2 shows the predefined parameter simulation result. (left) GT: Excitatory means a simulation in which all neurons are excitatory neurons. Ex bars (green) are the EV values when all neurons are excitatory inversion, and bars (red) are the results of inversion when one neuron is inhibitory. (right) GT : Inhibitory means a simulation one neuron is inhibitory neuron. In both cases, the inversion with the correct parameters had higher EV values.

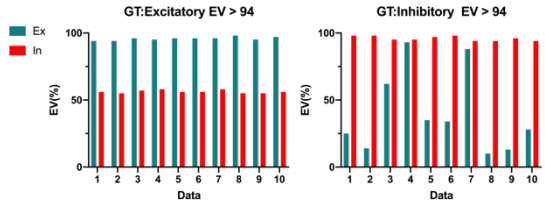
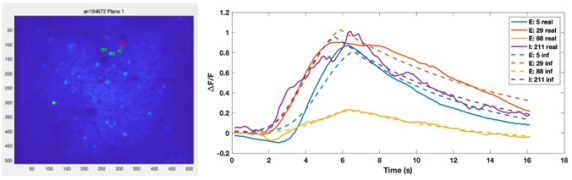


Figure 2. Simulation - Excitatory/Inhibitory classification result

Figure 3(a) shows the four neurons selected by criteria which are correlation under 0.9 and distance under 100. Figure 3(b) shows developed model could infer observed signals in the DCM framework. The solid line is the observed signal and the dashed line is the estimated signal.



(a) (b)

Figure.3 (a) selected 4 neuron by criteria (3E, 1I) (b) inferred observed signal by DCM

The results suggest the plausibility of the proposed method in the analysis of neural interactions observed in the CaI at the neuron level. Through this study, (1) we expanded the generative model considering the connection at the cell level and (2) using a developed model to classify neuron types that could not be provided by Cai data, and (3) can also estimate unknown connectivity.

Acknowledgements

This research was supported by Basic Science Research Program through the National Research Foundation of Korea (NRF) funded by the Ministry of Education, Science and Technology (NRF-2014R1A1A2060112) and a grant from Marine Biotechnology Program (20150220) funded by Ministry of Oceans and Fisheries, Korea

References

1. Grienberger, C. and Konnerth, A. Imaging Calcium in Neurons. Neuron 73, 862-885 (2012).
2. Rhamiti, V., Krimse, K., Marković, D., Holthoff, K. and Kiebel, S. J. “Inferring Neuronal Dynamic from Calcium Imaging Data Using Biophysical Models and Bayesian Inference”, Plos Comput Biol 12, e1004736 (2016).
3. Peron, S.P., Freeman J., Iyer, V., Guo, C. and Svoboda, K. “A cellular Resoultion Map of Barrel Cortex Activity during Tactile Behavior”, Neuron 86, 783-799 (2015).
4. Jung, K., Kang J., Chung, S. and Park, H.-J. “Dynamic causal modeling for calcium imaging: Exploration of differential effective connectivity for sensory processing in a barrel cortical column”, Neuroimage 201, 116008(2019).

P-118

Development of dental biomaterials consisting of various ratios of hydroxyapatite and tricalcium phosphate

Hyun-Soo Park[1], Ki-Joon Kang[1], Yu-Jin Kim[1], Yeun-Wook Kim[1], Hee-Joon Park[2], Ju-Wan Cha [3]

[1]Department of Advanced Materials Engineering, Keimyung University, Daegu, Korea

[2]Department of Biomedical Engineering, Keimyung University, Daegu, Korea

[3]Dentis Co., Ltd., Daegu, Korea

hjpark@kmu.ac.kr

Abstract

Synthetic bone graft materials are products made by synthesizing materials similar to those of the human body. Since human bones are mainly composed of hydroxyapatite, the initial synthetic bone graft materials consisted of hydroxyapatite alone or calcium phosphate products with a high hydroxyapatite ratio were commercially available. After that, products with a high ratio of tricalcium phosphate, which absorb faster than hydroxyapatite, were mainly products. The performance of synthetic bone graft materials is determined by several factors such as phase fraction, pore structure, pore size, porosity, and particle strength, but the degree of bone regeneration may vary depending on the condition of the patient undergoing the procedure. According to the investigation, the optimal phase fraction of the synthetic bone graft material suggested in each literature was different, and users often used their preferred product. For this reason, most of the manufacturers of synthetic bone graft materials are composing their lineup with products composed of various ratios of hydroxyapatite and calcium triphosphate.

Background

By mixing hydroxyapatite and beta-tricalcium phosphate in various ratios, data is obtained and synthetic bone graft material is manufactured at the desired ratio. The manufactured synthetic bone graft material is not simply used as a synthetic bone graft material, but it is possible to develop a derivative product that improves the ability to form new bone and the convenience of use by mixing it with a polymer material such as collagen [1, 2]. By controlling the ratio of hydroxyapatite and beta-tricalcium phosphate, the absorption capacity of the synthetic bone graft material is controlled and the new bone formation ability is improved to improve product performance competitiveness.

Methods

High-purity synthetic bone graft material is synthesized by mixing calcium carbonate and phosphoric acid. Calcium carbonate and phosphoric acid are mixed using ultrapure water so that they can be mixed evenly. Calcium carbonate is first added to ultrapure water and stirred for a certain period of time to dissolve the calcium carbonate. Phosphoric acid is slowly added dropwise to the dissolved calcium carbonate solution for reaction. The mixed calcium carbonate and phosphoric acid solution is stirred for at least 10 hours to ensure sufficient reaction. The mixed solution is completely dried in a dryer at 100°C and then heat treated at 1120°C or 1350°C to produce high-purity hydroxyapatite and beta-tricalcium phosphate. For the manufactured synthetic bone graft material, the phase fraction was confirmed using MP-XRD of the Korea Institute of Basic Science. As a result of confirming the phase fraction, it was confirmed that high purity hydroxyapatite and beta-triphosphate with a phase fraction of 100% were prepared.

Prepared by mixing high-purity hydroxyapatite prepared by mixing calcium carbonate and phosphoric acid and beta-tricalcium in various ratios so that the hydroxyapatite: beta-tricalcium ratio is 70:30, 60:40, 50:50. When hydroxyapatite and beta-tricalcium phosphate are mixed and heat-treated to produce calcium phase phosphate, the phase fraction does not come out the same as the ratio mixed before heat treatment. This is because beta-tricalcium phosphate is partially converted to hydroxyapatite during the heat treatment pro-

cess. According to the results of a number of experiments, hydroxyapatite: beta-tricalcium phosphate was prepared in 70:30, 60:40, 50:50 ratios. The phase fraction analysis method includes the intensity method and the Rietveld method. In this study, the phase fraction was confirmed by the Rietveld method, which is a more precise analysis. Phase fraction analysis confirmed the phase fraction using MP-XRD of Korea Basic Science Support Institute.

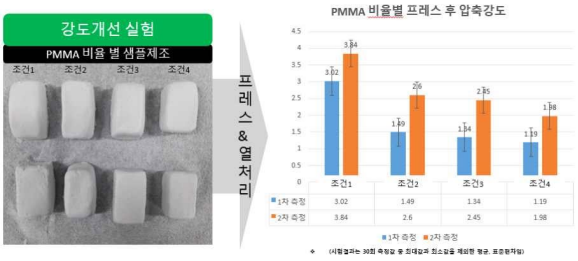
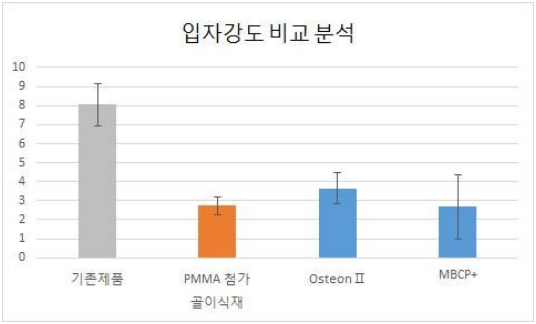


Figure 1. Example of decreasing in particle strength according to the amount of pore-forming agent added.

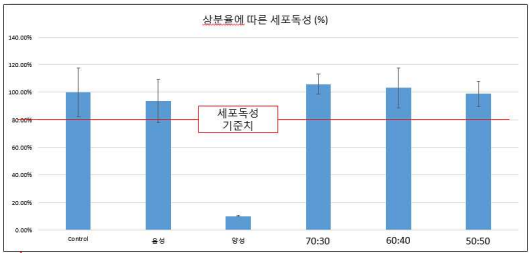
Results and Discussion

The manufactured synthetic bone graft material uses a push-pull gauge to check the particle strength of the bone graft material. The grain strength of the bone graft material should not be too strong or too weak, as it affects the formation of new heights depending on the degree of absorption and space retention according to the particle strength when implanted in the bone defect site. Comparison with the particle strength of competitive products with excellent performance to realize particle strength suitable for new bone formation. As a result of comparison, it was confirmed that the synthetic bone graft material manufactured using PMMA was about 3 MPa compared to the existing synthetic bone graft material manufactured using sugar, which is similar to that of the competitor's bone graft material.

Synthetic bone graft material composed of hydroxyapatite and beta-tricalcium phosphate can exhibit cytotoxicity due to hydroxyapatite, which has strong alkalinity. In order to confirm the biological safety of the manufactured synthetic bone graft material, the cytotoxicity according to the phase fraction of calcium phase phosphate was checked. Cytotoxicity was analyzed using the MTT method, and it was confirmed that there was no cytotoxicity when the cell viability was 70% or more compared to the control. Cytotoxicity analysis was analyzed using our laboratory and reagents, and as a result of the analysis, it was confirmed that there was no cytotoxicity in all phase fractions.



(a)



(b)

Figure.2 (a) Particle strength measurement result: about 3MPa and (b) Cytotoxicity according to phase fraction.

Acknowledgements

This research was supported by the Daekyung Innovative University Project (HuStar), promoted by Daegu City.

References

1. Mengjing Wang, Xiang Ge, Zhenduo Cui, Shuilin Wu, Shengli Zhu, Yanqin Liang, Zhaoyang Li, William Weijia Lu, Influences of strontium on the phase composition and lattice structure of biphasic calcium phosphate, Ceramics International, 10.1016/j.ceramint.2021.01.295, (2021).
2. Alexandra J. Barker, et al., Plant-derived soybean peroxidase stimulates osteoblast collagen biosynthesis, matrix mineralization, and accelerates bone regeneration in a sheep model, Bone Reports, 10.1016/j.bonr.2021.101096, 14, (101096), (2021).

Development of a IoT technology based personal digital pill box

Ho-Keun Hur[1], Kyung-Seop Kim[2], Hee-Ji Yu[2], Hee-Joon Park[2], Won-Seo Kim[3], Hyung-Ho Do[3]

[1]Department of Statistics, Keimyung University, Daegu, Korea

[2]Department of Biomedical Engineering, Keimyung University, Daegu, Korea

[3]HealthAll Co., Ltd., Daegu, Korea

kim.busung77@gmail.com

Abstract

The need for smart healthcare technology to increase medication adherence. The problem of patients taking wrong medications can cause great social costs and medical problems. Many patients take their medicines on time, and those who take health functional foods are burdened with taking their medicines or health functional foods consistently on time. Development of communication function for medication management and status provision. Development of firmware that enables medication management and status monitoring based on Bluetooth BLE communication using ESP32 module. Analysis and application of operating requirements after establishing an ESP-IDF development environment. ESP32-WROOM-32SE development board hardware analysis and ESP-IDF development environment setting are completed. Firmware development in accordance with the requirements for medication management and status information.

Background

It is expected to bring economic effects such as reduction of medical costs by reducing the direct or indirect costs of patients and high treatment effects according to the adherence to medication. Many patients take their medicines on time, and health functional food users (the general public) have a great burden of taking medicines or health functional foods on time. According to the announcement of the Korea Institute for Health and Social Affairs, the proportion of the elderly population in Korea is 14.3% as of 2013, and this number is expected to increase as life expectancy increases and have fewer children. A shocking forecast of 49.4% in 2060 is coming out, and it is expected that the increase in drug use by the elderly and chronically ill will steadily increase. One out of three (35.1%) patients with severe disease for which drug treatment was important took medication more than once arbitrarily. 1 in 4 patients (24.7%) said that they did not take the drug regularly at the set time. In various domestic and foreign surveys, the response rate that they have forgotten to take their medication exceeds 50%, and this phenomenon of 'non-compliance with medication' is known to be a long-standing concern in the medical community. As a result of these side effects, more than 35 tons of unused medicines are recalled annually in Korea. In the United States, it is investigated that patients do not take medicines, resulting in a cost loss of 300 billion dollars and 125,000 deaths every year. It is becoming a serious problem not only in terms of environmental pollution, but also in terms of environmental pollution. Informing the user of the time to take the medicine is one of the most simple but important factors in the medication guidance, to the extent that 44.4% of the reasons for not taking all of the prescribed medicines are "forgetting to take the medicine". As a way to solve this phenomenon, the global industry is turning its attention to smart healthcare technology early to solve the medication compliance problem, and as a result, various medication tracking systems such as smart medicine box and smart medicine box have been developed/released.

Methods

Simple and small smart medicine box product development. Methodology research and prototype development of the medication box that has a simple structure and does not impair the intrinsic function of medication detection and medication management. Simple design applied to external design and working mockup production. Communication function for medication management and status provision in conjunction with mobile-only apps. Researches IoT communication such as Bluetooth BLE, Lora, and NBIoT, and develops a prototype medicine box with a suitable communication method. Algorithm research and application plan development to improve medication compliance.

Algorithm research and prototype application to improve medication compliance by using medication status data collected from participating companies

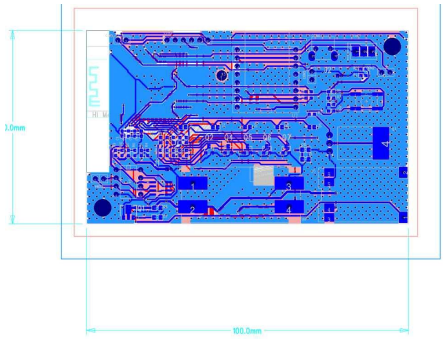
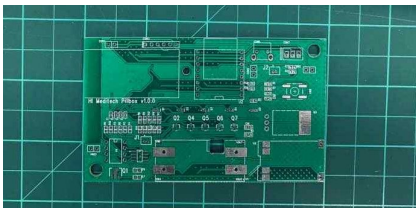


Figure 1. Artwork design of the proposed IoT technology based personal digital pill box.

Results and Discussion

The external design of the medicine box that can check the medication status in the form of a simple box (Lock & Lock, etc.) on the market. Process research that can check various medication states and reflect external design accordingly. It is necessary to perform external design considering the sensor part that can check the medication status. Development of firmware equipped with medication function using complex MCUs and modules such as ESP32. It is equipped with a medication detection module that reflects the research method that can detect medication. Medication circuit design according to the study of methods that can help in various medication situations. Development of Android-based medication detection service and mobile app prototype for guardians. It is equipped with a concept that allows you to easily check the medication status in the test kit box, and allows the guardian to manage the medication remotely by using the function. Development of mobile app function to set medication time, etc.

One circuit design including the function of medication management using medication detection and wireless communication. It consists of main MCU control unit, communication module unit, charging power unit, LED display unit, medication detection sensor unit, switch, and debugging pins. Printed circuit board design and anti-interference measures. Stable power supply and noise prevention by routing considering PCB layout. PCB Gerber extraction and manual shovel production. Design verification and rendering imaging. 2D drawing production Mockup for design working 3D output production, painting and post-processing.



(a)



(b)

Figure.2 (a) Manufactured PCB and (b) case of the proposed IoT technology based personal digital pill box.

Acknowledgements

This research was supported by the Daekyung Innovative University Project (HuStar), promoted by Daegu City.

References

1. Granger BB, Locke SC, Bowers M, Sawyer T, Shang H, Abernethy AP, Bloomfield RA Jr, Gilliss CL. The Digital Drag and Drop Pillbox: Design and Feasibility of a Skill-based Education Model to Improve Medication Management. J Cardiovasc Nurs. 2017 Sep/Oct;32(5):E14-E20. doi: 10.1097/JCN.0000000000000402. PMID: 28282304; PMCID: PMC5559183.
2. Subbaraman R, de Mondesert L, Musiimenta A, Pai M, Mayer KH, Thomas BE, Haberer J. Digital adherence technologies for the management of tuberculosis therapy: mapping the landscape and research priorities. BMJ Glob Health. 2018 Oct 11;3(5): e001018. doi: 10.1136/bmjgh-2018-001018. PMID: 30364330; PMCID: PMC6195152.

식품의약품안전처

혁신의료기기 지정제도

혁신의료기기란?

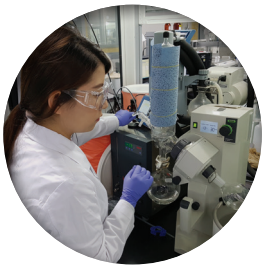
"혁신의료기기"란 「의료기기법」 제2조제1항에 따른 의료기기 중 정보통신기술, 생명공학기술, 로봇기술 등 기술집약도가 높고 혁신 속도가 빠른 분야의 첨단 기술의 적용이나 사용방법의 개선 등을 통하여 **기존의 의료기기나 치료법에 비하여 안전성·유효성을 현저히 개선하였거나 개선할 것으로 예상되는 의료기기로서 「의료기기 산업 육성 및 혁신의료기기 지원법」** 제21조에 따라 식품의약품안전처장으로부터 지정을 받은 의료기기를 말합니다.

www.dgmif.re.kr

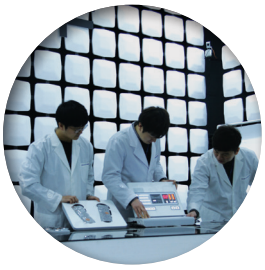
인재·장비·기술 집약 의료산업의 허브
메디밸리만의 최첨단 R&D지원시스템!

글로벌 경쟁을 위한 기업의 든든한 파트너가 되겠습니다.





신약개발지원센터
후보물질 개발 및
제약기업 기술이전



첨단의료기기개발지원센터
시제품제작부터
공인시험검사까지



실험동물센터
첨단 동물실험을 통한
신약 · 기기 안전성 평가



의약생산센터
공공기관 최초 GMP 획득
의약품 수탁 생산 및 공급

Medivalley
대구경북첨단의료복합단지

- 위　　치 대구시 동구 신서동 '대구혁신도시' 내
- 면　　적 1,054천㎡(혁신도시 4,216천㎡)
- 사업기간 2009~2038년(단지조성 : 2009~2013년)
- 총사업비 4.6조원(국비 1.1, 지방비 0.7, 민자 2.8)

KMEDIhub
대구경북첨단의료산업진흥재단

문의 053)790-5114

사용적합성이란?

의료기기가 의도한 특정 사용자가 실제와 유사한 환경에서 의료기기의 의도된사용 목적을 달성할 수 있는지를 평가하는 시험입니다.
의료기기와 사용자의 시각, 청각, 촉각, 기억, 해석, 행동을 조사하여 의료기기의 설계 유효성을 확인하고 안전성을 평가할 수 있습니다.

“ 이런분들께 사용적합성평가를 추천드립니다. ”

01	사용성이 증진된 프리미엄 의료기기를 제작하시는 경우
02	의료기기 제조 및 품질관리를 위해 사용적합성평가가 필요하신 경우
03	국내외 제품 인허가를 받으시는 경우
04	검증된 공인시험기관에서 제품을 개선하고자 하는 경우
05	연구과제의 성과를 성취하고자 하는 경우

서울대학교병원 사용적합성평가실은?

서울대학교병원 사용적합성평가실은 2015년 국내 최초로 구축된 사용적합성평가기관 및 국내 유일의 사용적합성평가 공인시험기관으로서 사용적합성 분야를 선도하고 있습니다.

서울대학교병원 사용적합성평가실은 최근 5년간 100건의 사용적합성평가 경험, 70건 이상의 의료기기 국내외 인증에 기여하는 등 의료기기 인허가의 큰 축을 담당하였습니다.

장점

- 국내 최고의 의료 인프라
- 연구자 우선 지원
- 최상의 시설
- 국제공인 시험성적서



장소

서울대학교병원 융합의학기술원 9층 사용적합성평가실



상세문의

전화 02) 2072-4400
홈페이지 utc.snuh.org

원주 의료기기 산업의 발상지!

(재)원주의료기기테크노밸리는 항상 여러분과 함께 하겠습니다

Mission	원주 의료기기 산업의 지속가능한 발전을 위한 산업생태계 활성화
Vision	" Global Connected-Health Leading Platform"
경영원칙	고객 중심 | 전문성 제고 | 사회적 책임



아이디어 컨설팅
- 의료기기 시장정보·규격 열람 지원
- 아이디어 컨설팅 및 제품화 연구
- 제품의 기술적 타당성 검토

마케팅·수출 지원
- 국내외 전시회 참가 지원
- 강원의료기기전시회 개최
- 광고·홍보물 제작 지원

디자인·설계 및 시제품 제작
- 제품 디자인 컨셉 설정
- 디자인 설계 및 모델링·렌더링
- 2D 도면화 & 3D 모델링
- 구동부 메커니즘 설계
- 부품 정밀 가공
- 3D 프린팅
- 후처리 가공 조립· 검토

인·허가 지원
- 국내외 인·허가 획득을 위한 컨설팅 지원
- 임상시험 및 사용적합성평가 연계 지원
- 규제과학(RA) 전문가 교육

시험검사
- 개발된 신제품의 신뢰성·내구성 검증
- 국내외 공통 시험 환경 제공
- 계측 장비 및 안전성 예비시험 지원
- EMC 시험 및 디버깅 전문기그룹 지원



느껴지는 차이

The Finest Experience







CE 1434

로리앙 홈페이지

(주)레오헬스케어

DATREND Systems Inc.



vPad-IV
Infusion Device



vPad-Rugged 2
Safety Analyzer



vPad-A1
Patient monitor



vPad-RF
Erectrosurgical



VenTest
Ventilator



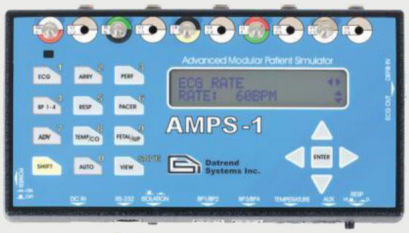
vPad-IN
Incubator



vPad-CO2



FMS-3
Fetal Simulator





㈜레오헬스케어
서울시 강남구 삼성로 624,502호
Tel : 02-3446-9618
Fax: 02-3446-9585

심정지 발생 위험 감시 AI 의료기기

VUNO Med®-DeepCARS™

ABOUT VUNO Med® DeepCARS™

뷰노메드 딥카스는 일반병동 입원 환자의 전자의무기록(EMR) 등에서 수집한 혈압(이완기, 수축기), 맥박, 호흡, 체온의 4가지 활력 징후(Vital Sign)를 기반으로 환자의 24시간 이내 심정지 발생 위험도를 0-100점의 점수로 제공하여 입원환자의 모니터링 및 사전 조치를 돕는 인공지능 의료기기입니다.

세계 응급의학과 최상위 학술지로 꼽히는 Resuscitation을 포함하여 미국심장협회지(JAHA), 세계중환자의학회지(CCM) 등 다수 학술지에서 우수한 심정지 예측 성능을 입증하였습니다.

- DeepCARS™ · 심정지 위험 실시간 감시
- · 사전적 예방조치
  · 효율적인 병동 운영
- · 사망률 감소
  · 삶의질 향상
- · 국민건강 증진
  · 사회적비용 절감

SIMPLE

4가지 활력 징후(Vital Sign)만을 이용해서 심정지 발생 위험도를 제공합니다.

OPTIMIZABLE

도입 병원이 보유한 과거 데이터를 이용해 **제품 성능 검증 및 병원 최적화**를 위한 추가 학습이 가능합니다.

SUPERIOR

다기관 후향 임상시험(173,368명) 결과를 통해 다양한 임상환경에서 **높은 정확도**를 입증하였습니다*

다기관 후향 임상시험에서 DeepCARS의 24시간 이내 심정지 예측 정확도(AUROC)는 내부코호트 0.860, 외부코호트 0.905로 높은 수준을 입증하였습니다*

DeepCARS™는 고도화된 AI기술을 기반으로 개발된
국내 최초의 심정지 발생 위험 감시 AI 의료기기로서
의료자원의 효율적인 운영과 **환자의 안전**에 기여할 수 있습니다.

* A multicentre validation study of the deep learning-based early warning score for predicting in-hospital cardiac arrest in patients admitted to general wards. Resuscitation. 2021 Apr 22;163:.78-85



SAFE LOCK REGULATOR

IV ADMINISTRATION INFUSION SET

안전성

- 잠금 시 최대 유량 이상 주입 방지
- 약물 과주입으로 인한 문제 발생 최소화
- 의료진 외 임의 조작 방지

사용성

- 손 쉬운 사용
- 원터치 잠금
- 잠금 해제 및 재 잠금 가능

호환성

- 다양한 부품 적용 가능
- 다양한 수액 세트 적용 가능
- 다양한 약물 적용 가능

(주)메디라인액티브코리아

본 사 | 경기도 안산시 단원구 원포공원 1로 70, 407, 408호 (초지동, 키즈타워 1)
TEL : 031 – 485 – 9402 | FAX : 031 – 485 – 9403

서울사무소 | 서울특별시 금천구 가산디지털 1로 219, 1401호(가산동, 벽산디지털밸리6차)
TEL : 02 – 2627 – 3530 | FAX : 02 – 2627 – 3534

Medi Line Active Korea

www.mek-ics.com

우리의 숨은 노력이 대한민국의 더 나은 숨이 되도록

우리는‘호흡’이라는 주제로 인류의 건강과 사회발전에 기여하고자 합니다.
멕아이씨에스는 지속성장의 기업문화로 열정적이고 창의적인 인재의 일터’가 될 것입니다.
사람을 존중하고 인재의 성장을 돕는 기업. 이것이 우리 인력관리 철학입니다.

호흡 치료 관련 모든 기술력을 겸비한, MEKICS



HFT700

기도삽관이 필요없는 중환자실 이전단계 적용장비



MTV1000

이동 중 중환자 용



MV2000

중환자실 입원단계 기도삽관이 필요한 환자용

Mild Condition — Critical Condition

인재채용 관련 안내

멕아이씨에스는 젊은 인재의 도전을 기다리고 있습니다. 자세한 내용은 QR코드를 확인 해주세요.

근무처 : 본사 – 경기도 파주시 상지석길 21 / 서울 사옥 – 서울특별시 마포구 성산동 133-7
지원 방법 : 이력서, 자기소개서 제출 (서류 평가 후 면접 진행) / E-mail : insa@mek-ics.com / Tel : 070-7119-2551

MEK 멕아이씨에스

오송첨단 의료복합단지

| 세계 최고 수준의 바이오클러스터 |

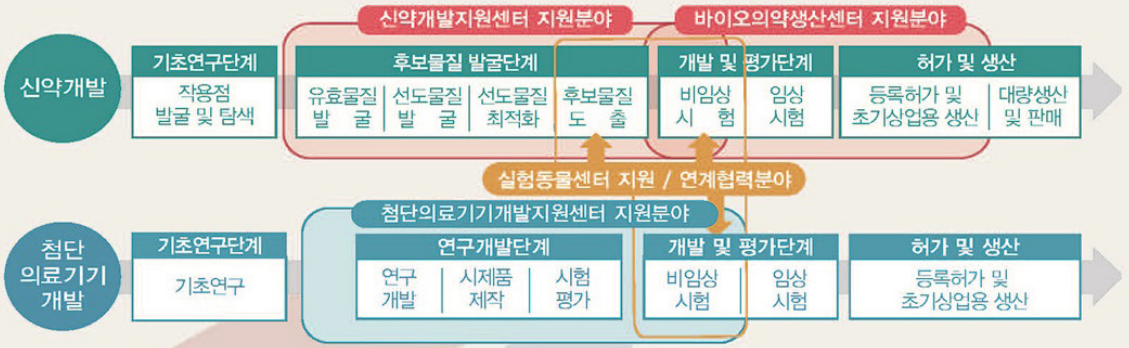
- 의료산업을 국가발전의 신성장동력으로 키워 나가기 위해 첨단의료로 특화된 연구개발단지
- 글로벌 신약과 첨단의료기기에 필요한 인적, 물적 인프라가 집적된 세계 최고수준의 의료연구개발 산업단지

편의시설 | 연구지원 CORE 인프라 | 바이오 메디컬시설 | 연구기관 | 보건의료 행정타운

오송첨단 의료산업 진흥재단

| 핵심 4개 센터 지원분야 |

- 바이오의약품 / 첨단의료기기의 연구 개발부터 인허가, 상용화까지 오송첨단의료산업진흥재단은 글로벌 수준의 우수 인력과 첨단 장비, 보건의료산업 사업화 지원 시스템을 통해 **'Death Valley' 를 극복하기 위한 지원 서비스를 제공합니다.**



첨단의료기기 개발지원센터

| 비전 | 첨단의료기기 개발을 위한 글로벌 수준의 One-stop 서비스 지원

대·내외 협력 네트워크 구축

- 국내외 의료기기 관련 기관과 협력 체계 구축
- 심포지엄 및 학회 개최
- 첨단의료기기 개발을 위한 전문 인력 양성

인프라를 활용한 제품화 기술 지원

- 제품화를 위한 시제품제작
- 장비 및 시설을 활용한 기술 지원
- 시제품의 안전성, 성능, 생체적합성, 전자파 시험검사

BT기반 의료기기 공동연구개발 지원

- 인체삽입형 3,4등급 의료기기 집중 지원
- 수요자 맞춤형 공동연구개발
- 기반기술구축 공동연구개발

산업체수요조사

- 의료기기 시장 및 기술 동향
- 의료기기 IP 현황
- 의료기기 클러스터 정책 동향

| 주요업무 |

기초연구	연구개발	시제품제작	시험평가	임상 및 상용화
산·학·연 기초연구	〈기술지원〉 미래선도형 핵심기술 수요자맞춤 공동기술	시설장비 활용 시제품 제작 지원 · 설계 해석 · 3D 조형제작 · 초정밀가공 및 측정 · 핵심부품 정밀가공	· 의료기기 인·허가 시험지원 · 의료기기 비임상시험 (GLP)지원 · 국제공인시험(KOLAS) 지원	임상시험 ∨ 품목허가 ∨ 생산판매
시장분석	인프라를 활용한 공동연구수행			

| 지원방향 및 역할 |

국내 의료기기 기업의 시장 진입을 위한 인프라 지원, 애로기술 해결, 성능/신뢰성 강화 등 제품화 중심의 One-stop Total Solution 지원

[공동연구개발] 기초 R&D 기술검증 및 제품화 애로기술 해결 지원

[설계·시제품 제작] 의료기기 설계 및 해석을 통한 시작품 및 시제품 제작, 초정밀 가공을 통한 광학계 제작 지원

[시험검사 및 평가] 품목허가를 위한 시험검사, 성능·신뢰성평가 및 전임상시험 지원

MEGA DERM

SILVER

We change life with creative biotechnology



MegaDerm® is derived from human skin which is processed using a Allo-Clean® technique. The Alloclean® process inactivates or removes cell debris, antigens and potential viruses while maintaining the structural integrity inherent in the pre-processed collagen.

www.lncbio.co.kr

Life and Creative L&C BIO

MxT Biotech
MICROFLUIDICS X THERAPY

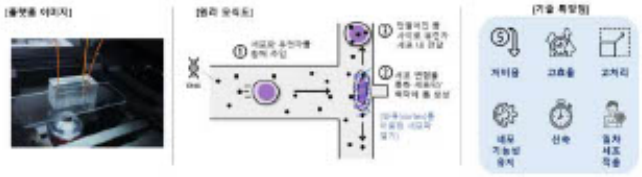
MxT Biotech | ㈜엠엑스티 바이오텍

MxT Biotech은 고려대학교 바이오의공학부 정아람 교수 연구실 창업 기업으로, 미세유체 기반 세포 내 물질 전달 원천기술인 "유체천공기"(Hydroporator™)를 이용하여 암 면역치료에 새로운 방향을 제시하고자 합니다.



Hydroporator™ (유체천공기)

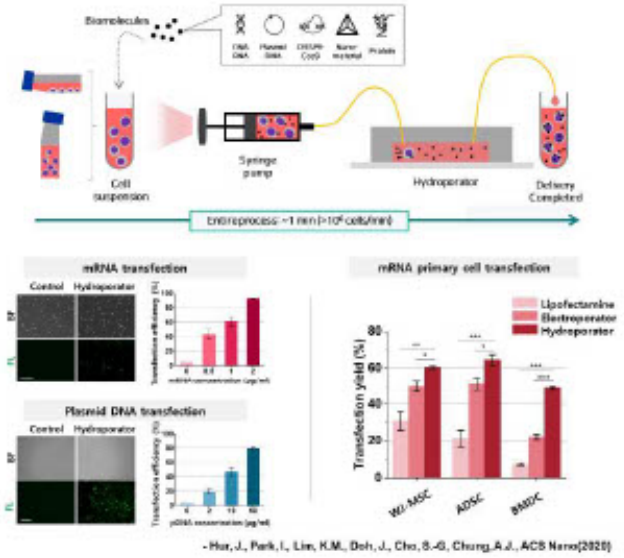
유체천공기는 미세유체관(microfluidic channel) 내에서 일어나는 특이적 유동을 이용하여 세포막과 핵막을 열어 그 속으로 외부 유전자를 전달하는 기기입니다. 본사는 유체천공기를 활용하여 유전자 편집을 통한 고효능 암 면역 세포 치료제 및 치료제 생산플랫폼을 개발하여 현재 바이러스 기반의 세포치료제 시장의 패러다임을 바꾸고자 합니다.



Simple, Rapid & High Performance

유체천공기는 사용자 위주의 간편한 시스템 구성 및 프로세스를 특징으로 일반인도 손쉽게 이용 가능합니다. 그리고, 분당 10^6-10^7개 이상의 세포를 연속적으로 신속하게 처리할 수 있는 고처리 플랫폼입니다.

최근 보고한 연구 논문(ACS Nano, 2020)에서는 유체천공기를 사용하여 mRNA와 plasmid DNA의 고효율 전달 및 형질변환(transfection)이 가능함을 입증하였으며, 경쟁 기술인 지질입자(Lipofection) 및 전기천공(Electroporation) 기법들과 비교함에 있어 전달/형질변환 효율의 비교우위를 확인하였습니다. 또한, 일차 줄기 및 면역세포(primary stem and immune cell)에도 적용 가능함을 확인하여 높은 활용성을 입증하였습니다.



- Hur, J., Park, I., Lim, K.M., Doh, J., Cho, S.-G., Chung, A.J., ACS Nano(2020)

Primary T cell transfection and biostability

인간의 혈액으로부터 채취한 T 세포를 이용하여 mRNA의 전달 및 형질변환에 대한 최적화 실험을 현재 진행중에 있으며, 다양한 유전체 분석을 통하여 프로세스의 안정성에 대하여 검증을 진행하여 세포 치료제 생산 플랫폼으로서의 가능성을 입증하고 있습니다.

Contact

본사는 유전자 전달 이외에 단백질, 나노입자, 유전자 가위 물질 등의 세포 내 물질 전달에 대한 우수한 연구결과를 확보하였으며, 이를 활용하는 다양한 공동연구와 함께 나아갈 파트너 또한 찾고 있습니다. 앞으로 많은 성원과 관심 부탁드립니다.



Tel: 02-2157-4808
E-mail: contact@mxtbiotech.com
Homepage: https://www.mxtbiotech.com

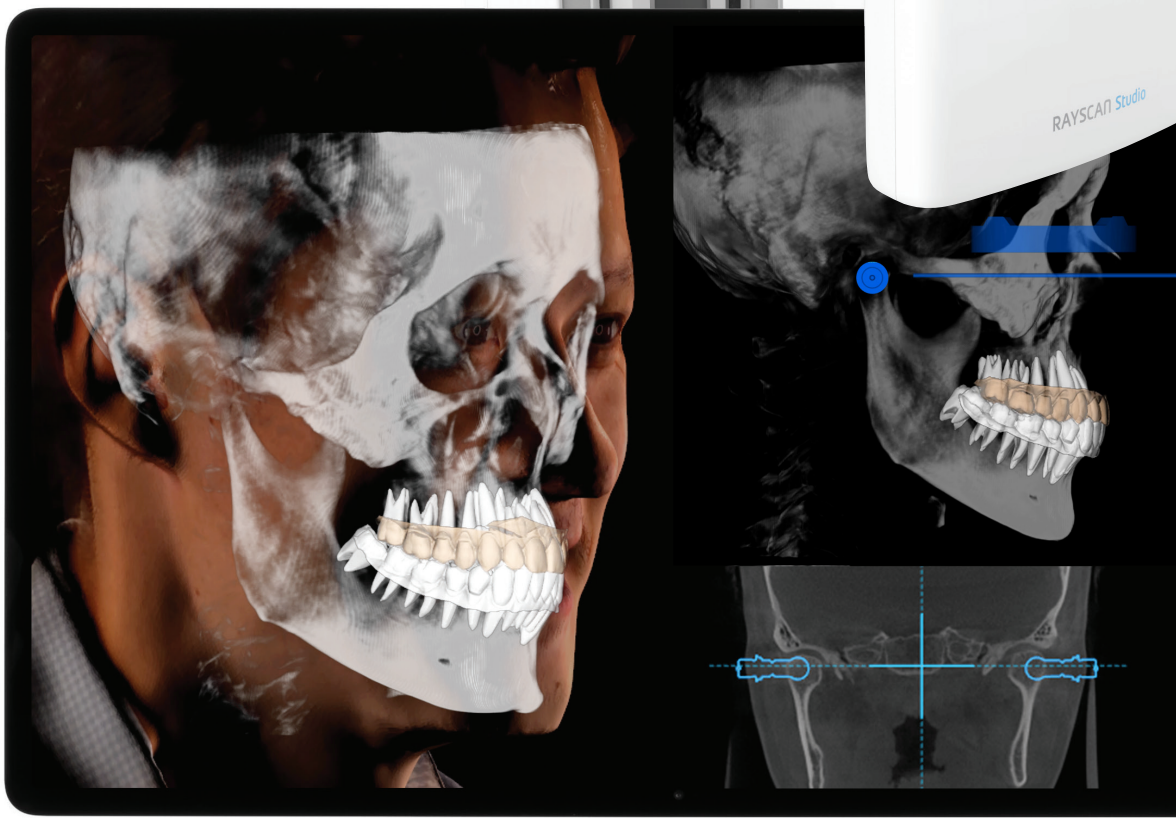
SILVER

THE TRUE DIGITAL

DENTAL AVATAR

5 in 1 CBCT

RAYSCAN Studio





RAYFace

One-shot 3D Face Scanner



RAYiOS

Intraoral Scanner

Ray

주식회사 레이

Tel. 031-605-1000 **Email.** ray_sales@raymedical.co.kr **Web.** www.raymedical.co.kr



대한민국을 넘어 더 큰 세상으로
메디아나의 끊임없는 도전은 계속 됩니다!

의료기기의 선진화를 추구해온 (주)메디아나는 기업활동의 이익을 사회에 환원하는데
솔선 수범하며, 열정과 도전이 가득한 글로벌 의료기기 회사로의 성장을 지향합니다.

MEDIANA

Healthcare Solutions You Can Trust

제품문의 : T.02)542-3375 / www.mediana.co.kr

(주)메디아나 본사:강원도 원주시 문막읍 동화리 1650-1 동화첨단의료기기 산업단지 (우)220-801
서울사무소:서울시 서초구 방배동 793-3 메디아나 빌딩 (우)137-830

OsteoSys

VET DXA
New Gold Standard

SILVER

iNSiGHT

DXA
Original
Technology

DR Image

FAST Scan
25sec.



<Parameter>
BMC
FAT
FAT Ratio
LEAN
Total Mass
BMD
Bone Area
Tissue Area

Hicardi®

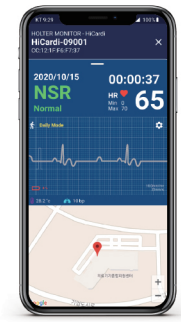
SILVER

MEZOO
MEDICAL EQUIPMENT ZOO

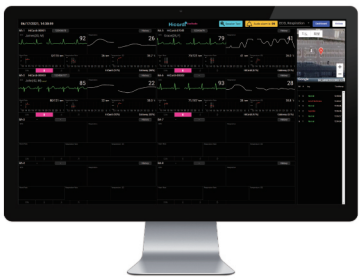
Wearable ECG & Arrhythmia diagnosis and monitor, HiCardi



HiCardi®



SmartView



LiveStudio

Hicardi LiveStudio

Remote Patient monitor
ECG diagnosis and Interpretation
Monitoring for COVID-19 Patients



BIO SIGNAL
TOTAL SOLUTION

bistos

SILVER

제조사 : ㈜비스토스
경기도 성남시 갈마치로 302
우림라이온스밸리 5차 7층

Tel : 031-750-0340
Fax : 031-750-0344
Website : www.bistos.co.kr
E-mail : domestic@bistos.co.kr

Fetal Monitor & Doppler



BT-350L



BT-380



BT-250



BT-200L



BT-220C



BT-200V(Vascular)

Patient Monitor



BT-710
(Puls Oximeter)



BT-720
(Vital Sign)



BT-740
(8.4")



BT-770
(12.1")



BT-780
(15.6" Patient Monitor)

Neonatal Care



BT400
(Photottherapy)



BT-500
(Infant Incubator)



BT-550
(Infant Warmer)



BT-450
(Biliblanket)

ETC





Medical Head Lamp





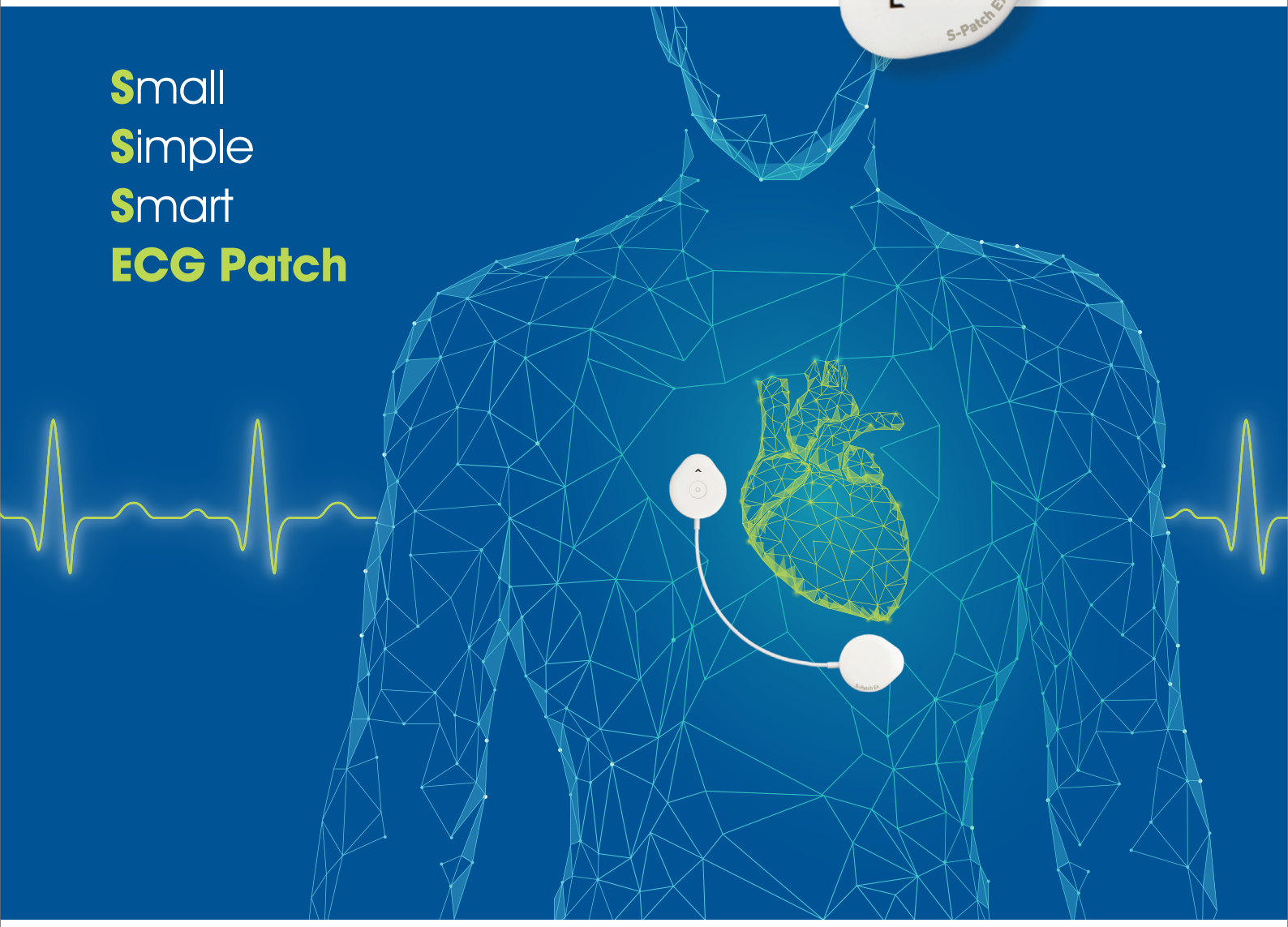
Breast Pump

SAMJIN 삼진제약

S-PATCH EX

패치형 연속측정
심전도 분석 솔루션

※ 실제 제품 크기



연속 심전도 모니터링
Continuous ECG Monitoring

다양한 검사기간 선택가능
Various Test Duration Options

환자 편의성 증대
Customer Convenience

운영 효율성 제고
Operational Efficiency

비용 합리화
Cost Saving

[품목명] 홀터 심전계 **[사용목적]** 심근이 활동할 때 발생하는 활동 전위가 신체의 표면에 전달되어 발생하는 전위차를 일정 부위에 전극을 부착시켜 신호를 감지하고, 이 심전도 데이터를 무선신호를 이용하여 표시해주는 기구 *주의 : 이 제품은 의료기기이며 '사용상의 주의사항'과 '사용방법'을 잘 읽고 사용하십시오. ※ 보다 상세한 내용은 사용자 설명서를 참조하시거나 삼진제약 (sjhealthcare@samjinpharm.co.kr, 02-3140-0773)으로 문의하십시오.

판매원 : 삼진제약(주) | 제조원 : 주식회사 웰리시스